VARIABILITY OF THE MANCOS SHALE: DEVELOPING PRELIMINARY DEPOSITIONAL AND SEQUENCE STRATIGRAPHIC MODELS OF A DEVELOPING SHALE GAS PLAY

by

Brendan Horton

A thesis submitted to the faculty of
The University of Utah
in partial fulfillment of the requirements for the degree of

Master of Science

in

Geology

Department of Geology and Geophysics

The University of Utah

August 2012

The University of Utah Graduate School

STATEMENT OF THESIS APPROVAL

The thesis of **Brendan Horton**

has been approved by the following supervisory committee members:

Lauren Birgenheier	, Chair	**6/12/2012** Date Approved
Cari Johnson	, Member	**6/12/2012** Date Approved
William Parry	, Member	Date Approved

and by **D. Kip Solomon** , Chair of

the Department of **Geology and Geophysics**

and by Charles A. Wight, Dean of The Graduate School.

ABSTRACT

With shale resources becoming increasingly more important in the global energy fuel mixture, a thorough understanding of heterogeneities present within individual units is crucial to an accurate assessment of resource potential. A wide variety of core data collected from the Lower Blue Gate Member, Mancos B, Juana Lopez Member, and Tununk Member of the Mancos Shale shed light on the scale and variety of heterogeneities present in this siliciclastically influenced mudstone/shale system. 11 lithofacies were identified over five cored intervals throughout the Uinta Basin, and a depositional model was thereby developed. Three environments of deposition are identified: the prodelta, the mudbelt, and the sediment starved shelf. Within this depositional model, subtle proximal to distal trends are interpreted. Mechanisms of transport and deposition of sediment are different within each of the three environments, with river influence dominant in the prodelta environment, combined flow as well as hyperpycnal flow dominating the mudbelt environment, and hypopycnal settling of sediment dominating in the sediment starved shelf. Individual parasequences are identified in each cored interval based on identification of flooding surfaces. Each parasequence (roughly 15 feet thick) records the local landward progression of depositional environments. Proximal to distal trends relating overlying and underlying parasequences is used to determine stacking patterns throughout each cored interval. Highstand systems tracts record aggradational stacking patterns. Transgressive systems tracts demonstrate a retrogradational stacking pattern. Lowstand systems tracts record a significant landward shift in facies at their base,

and are aggradational to progradational. Systems tracts are 20-50 foot-scale in thickness.

Two potential shale gas reservoir targets emerge from this study, and each target fits a very limited sequence stratigraphic interval. High gas storage potential along with a relative brittleness responsive to hydraulic fracturing is expected in the most landward lithofacies with the coarsest grained siltstone (lithofacies 9), deposited in the proximal mudbelt environment. In the sequence stratigraphic model presented herein, this lithofacies occupies the late, proximal highstand systems tract, or the lowstand systems tract. High organic carbon content, as well as high porosity values and increased calcite content (which may impart brittleness) are found in a separate lithofacies (lithofacies 8) that is deposited exclusively in the distal sediment starved shelf during the transgressive systems tracts. The systematic classification of environments of deposition allows refined interpretations of the sequence stratigraphic framework of the Mancos Shale without the necessity to correlate mudstones to updip, more proximal, shallow marine expressions of the depositional system.

TABLE OF CONTENTS

Appendices

LIST OF FIGURES

LIST OF TABLES

ACKNOWLEDGEMENTS

I hope I am not too vain to think that I am sole author of my victories. My time as a graduate student has been spent compiling this document in one way or another, but it was through the combined efforts of many colleagues that it has taken the shape that it currently holds. I am tremendously grateful to my thesis advisor, Dr. Lauren Birgenheier, for her guidance and friendship. She has truly shown me what it takes to mature as a scientist and as a person. Dr. Cari Johnson and Dr. William Parry have also been sources of inspiration as well as springs of knowledge throughout my graduate career. James Taylor has been a thoughtful and dedicated lab technician who has helped me prepare, measure, and sift through many hundreds of data points. Patrick Dooling, Luke Pettinga, Casey Kidney, and Andrew McCauley have provided irreplaceable assistance in my so-called "field area." The efforts of Nora Nieminski and William Gallin in this project must also be acknowledged. EGI has provided needed financial assistance, along with the RPSEA project for investigating the Mancos Shale. Thanks to Utah Core Research Center staff, including Tom Dempster, Brad Wolverton, and Mike Laine for their help with laying out the core and their sharp lithologic observations. Thanks to Tekla Harms for still serving as a motivator to do high quality research, Jack Cheney for instilling a geological work ethic, and my colleagues at Amherst College. I also acknowledge the assistance provided by the staff at the University of Utah, including, but not limited to, Dr. Dave Chapman, Dr. Tony Ekdale, Dr. Frank Brown, Dr. John Bartley, Dr. David Dinter, Judy Martinez, Thea Hatfield, Chris Carver, as well as

others. My time at the University of Utah has been tremendously rewarding in all aspects. To get me here, I would also like to thank Mark Norville and Dr. Lee Billingsley. John Green mentioned that "the truth resists simplicity" and his sentiments are especially applicable to shales and the energy industry. I would finally like to thank my wonderful wife, Tiffany, for her unwavering support, and insights that I would miss without her keen eye.

CHAPTER 1

FACIES VARIABILITY AND A DEPOSITIONAL MODEL OF A SILICICLASTICALLY INFLUENCED MUDSTONE SYSTEM: THE MANCOS SHALE, UINTA BASIN, UTAH

Abstract

As shale gas plays continue to expand in importance and productivity globally, a thorough sedimentological understanding of mud-dominated systems is increasingly important to maximize production and profitability. Heterogeneity in shales, particularly in thick, siliciclastically influenced mudstone systems such as the Mancos Shale, has not been well-characterized, and depositional facies models are still in their infancy. In this study, six cored intervals of the Mancos Shale from varying geographic regions of the Uinta Basin as well as varying levels of maturity were examined in order to evaluate facies heterogeneity. A centimeter-scale lithological description of each of the cored intervals of the Mancos Shale was performed, and thin section analysis was used to augment visual inspection. A wide array of geochemical tests was run to further describe the core intervals, including non-destructive X-ray fluorescence, oriented X-ray diffraction of clay separates, QEMSCAN, and TOC-RockEval pyrolysis.

Results demonstrate that the Lower Blue Gate, Juana Lopez, and Mancos B members of the Mancos Shale in the Uinta Basin of Utah exhibit substantial, multi-scale

facies variability that suggest equally variable environments of deposition. 11 distinct lithofacies are identified in the Questar and Pioneer cored intervals in this study, with an additional 12 lithofacies identified in the River Gas Unit #1 core by Kennedy (2011). Significant heterogeneities, including grain size, lamination style, sedimentary structures, bioturbation index, and mineralogy, are documented on multiple scales, both macro and micro-scale. Intrabasinal heterogeneities are also identified. Further chemofacies analysis defines meaningful trends in elemental and mineralogic composition between lithofacies. However, indiscriminate inference of geological characteristics based solely on elemental composition is found to be statistically unreliable.

A unified facies model scheme for offshore environments of deposition is proposed, in which the offshore realm is subdivided into three environments of deposition, including the prodelta, mudbelt, and sediment starved shelf. The defined 11 facies are interpreted in the context of these three environments of deposition, based mainly on primary structures, mineralogical composition, and bioturbation index. Further, within each environment of deposition, proximal to distal trends are categorized. Organic carbon values and porosity values increase in environments of deposition that are found to be more offshore.

Above all, these data suggest that the Mancos Shale's lithology is highly complex, shattering widespread beliefs that shales are by and large, homogenous. This work provides a framework for facies variability in siliciclastically influenced mudstone systems that can be used to identify ideal shale gas reservoir intervals. Furthermore, it presents a new facies model for offshore deposits that draws upon recent advances in mud sedimentology and can be applied in analogous siliclastically influenced mudstone systems.

Introduction

Between 2000 and 2006, shale gas production in the United States grew at an average annual rate of 17% (Energy Information Administration, 2011). In this period, the most successful shale play was the Barnett Shale in Texas. Refined completion practices in the Barnett Shale coupled with high natural gas prices drove exploration in other shale plays, and between 2006 and 2010, shale gas production had an annual growth rate of 48% (Energy Information Administration, 2011). Projections of shale gas production in the next 20 years are often plagued by uncertainty brought on by estimating vast resources over very large areas. Commonly, estimations made regarding recoverable gas from a formation include an average value for 1 well averaged over thousands of acres, however it has been demonstrated that production rates for wells drilled next to each other can have initial rates that differ by up to a factor of three (Energy Information Administration, 2011). This problem is compounded when comparing wells that are miles apart. In many cases, this variability may be a product of heterogeneity within the formation.

Vertical and lateral variability of sandstones and carbonates has been comprehensively studied. These vertical and lateral variations tend to exist on the macro to large scale in outcrop and (until recently) were the main type of reservoir rock in conventional oil and gas plays. In contrast, shales and their vertical and horizontal variability have received comparatively less attention. This is due in part to shale formations being very difficult to observe in outcrop (Sorby, 1908). Only very recently have comprehensive systems been emplaced to accurately describe the lithology of rocks whose grain size is mostly less than 63 micrometers (Macquaker et al., 2003; Schieber et al., 2010). Unsurprisingly, the majority of publicly available papers regarding the heterogeneity (or lack thereof) in shales and mudstones have focused on the most productive shale plays, but there

is still a lack of detailed publically available data on shales and mudstones that have yet to be explored for oil and gas production.

The Mancos Shale presents an excellent subject for a thorough analysis because of its very high ratio of detrital quartz relative to carbonate content. The Mancos Shale is the most carbonate-poor out of any large shale play in North America, and has a comparatively high ratio of detrital quartz (Figure 1). Productive shale plays to date tend to be either rich in clays (e.g. the Marcellus Shale (Boyce et al., 2009; Bruner et al., 2011)), rich in carbonate content (e.g. the Eagleford Shale (T. Anderson, 2012)), or rich in biogenic silica (e.g. Barnett Shale (Bruner et al., 2011; Loucks et al., 2007)) (Figure 1). Extensive siliciclastically influenced shales exist throughout North America and include formations in the Liard Basin in northern British Columbia through the Mancos Shale in southern Utah. These plays are very recently being explored as potential reservoirs. Imperial Oil has been exploring the Liard Basin within the last year, and XTO Energy drilled the first multistage horizontal well in the Uinta basin targeting the Mancos Shale in late 2010 – the first and only horizontal well in the Mancos in the Uinta Basin (Chidsey et al., 2011; Ressetar et al., 2012).

So-called "traditional" thought on the deposition of mudstones and siltstones in wave and storm dominated shallow marine environments, as well as deltaically influenced systems has long been under debate. It has recently been demonstrated that mud and silt can settle out of suspension far more quickly than previously identified, with mud aggregates settling out of suspension within 10 kilometers of river mouths due to clay flocculation in saline environments (Allison et al., 1998; Bhattacharya, 2010; Plint, 2010; Schieber, 1998). However, no comprehensive facies model has yet been refined with respect to shale and mudstone deposition.

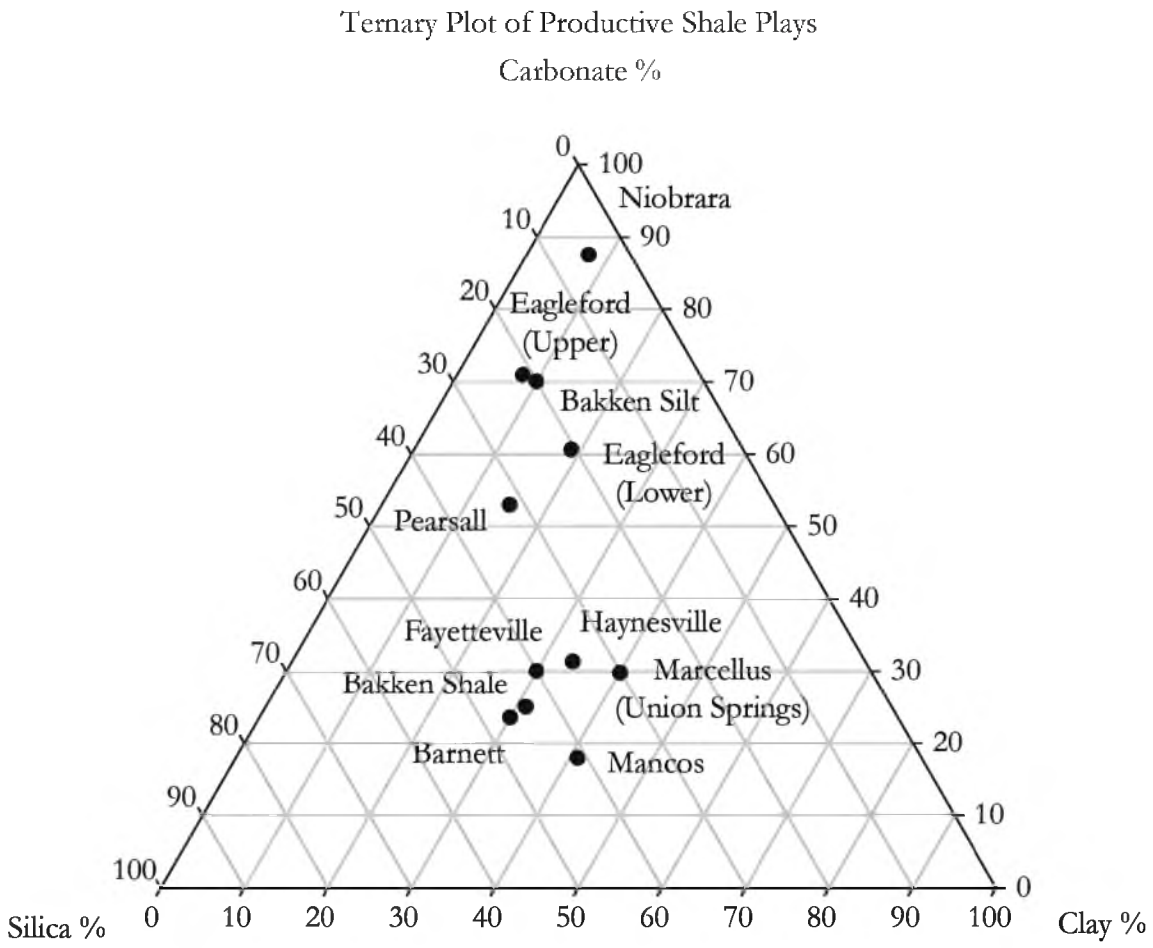

Figure 1: A ternary diagram plotting clay, carbonate, and silica content against each other for productive shale plays in North America. The Mancos shale is the most carbonate poor out of any of the producing shales, due in large part to the large detrital influx into the Uinta Basin in the Late Cretaceous.

Modified from Anderson (2012), Boyce & Carr (2009), and Bruner & Smosna (2011)

Previous work on the Mancos Shale includes research that focuses on sandstone-rich to heterolithic units such as the Prairie Canyon Member or the Mancos B member (D. S. Anderson et al., 2006; Cole, 1997; Hampson et al., 1999; Pattison, 2005), and studies that have identified the Mancos Shale as a potential source rock in the petroleum system (Kirschbaum, 2003). However, there is limited literature available that focuses on the sedimentology and geochemistry of the Mancos Shale as a whole. Previous work has focused on comparatively thin condensed intervals of the Mancos Shale (D. S. Anderson et al., 2006; Dumitrescu, 2002) . Previous examination of the clays present in the Mancos Shale are best summarized in Nadeau & Reynolds (1981) showing that clays collected throughout the southern Rocky Mountains and the Colorado Plateau contain interstratified illite smectite with increasing amounts of illite present according to burial depth and contact metamorphism. To that end, this study aims to look at large intervals of the Mancos Shale (intervals that are 120 feet or greater) in high resolution (centimeter scale) to characterize and quantify the vertical heterogeneity that exists in the Mancos Shale.

The goals of this study are two-fold. The first goal is to provide much needed detailed description of the siliciclastically influenced rocks of the Mancos Shale in the Uinta Basin, as a model for facies variability in silciclastically influenced shales as a whole. The second goal is to establish a facies model for variations in offshore depositional environments within siliciclastically influenced systems. Such basic framework is crucial to a thorough understanding of the Mancos Shale and other similar siliclastically influenced mudstones that are currently being explored for oil and gas production. Without such an understanding, vertical and horizontal variations within the formation itself can in no way be accurately quantified, and thus, reliable reservoir models cannot be constructed to estimate production. Hence, accurate estimations of recoverable resources are impossible to assess.

Geologic Setting

In the late Cretaceous, the geology of western North America was controlled on a large scale by the tectonic action of the Farallon plate subducting beneath the North American plate. This subduction – and the associated compressive forces – led to the thickening of the crust by a combination of thrusting and folding (Livaccari, 1991). These thrust fault systems tend to be low angle, with detachments generally above Precambrian basement rocks, especially in easternmost faulting (Dickinson et al., 1988; Johnson, 2003), with the oldest thrusts being most westward and structurally highest (DeCelles, 1994). Total shortening along the Sevier aged thrust faults in Utah was approximately 100 kilometers, with a structural relief of approximately 25 kilometers (DeCelles, 1994). Subsidence due to loading of the crust, created a foredeep basin east of the thrusting (Johnson, 2003), and in southern Utah, sediment began to fill the newly formed Rocky Mountain foreland basin east of the Sevier orogenic belt (DeCelles et al., 1996).

During the Cretaceous, the Western Interior Seaway covered large parts of the North American continent (Kauffman, 1977), and hundreds of meters of sediment accumulated in the basins that bordered the Western Interior Seaway (Kauffman, 1984) (Figure 2). The Mancos Shale was first described in the Mancos River Valley, in southwestern Colorado by Cross and Purington(1899). Subsequently, outcrops of the Mancos Shale can be found throughout much of southern and southeastern Utah (Leckie et al., 1997). The Mancos Shale was deposited as a largely marine shale from 95-75 million years ago and is on average, 4000 feet thick across the Uinta Basin (Council, 2009; Johnson, 2003).

The Mancos Shale, being deposited in the fordeep, is generally considered a distal expression of more proximal, synchronously deposited units, e.g., the Ferron and Emery

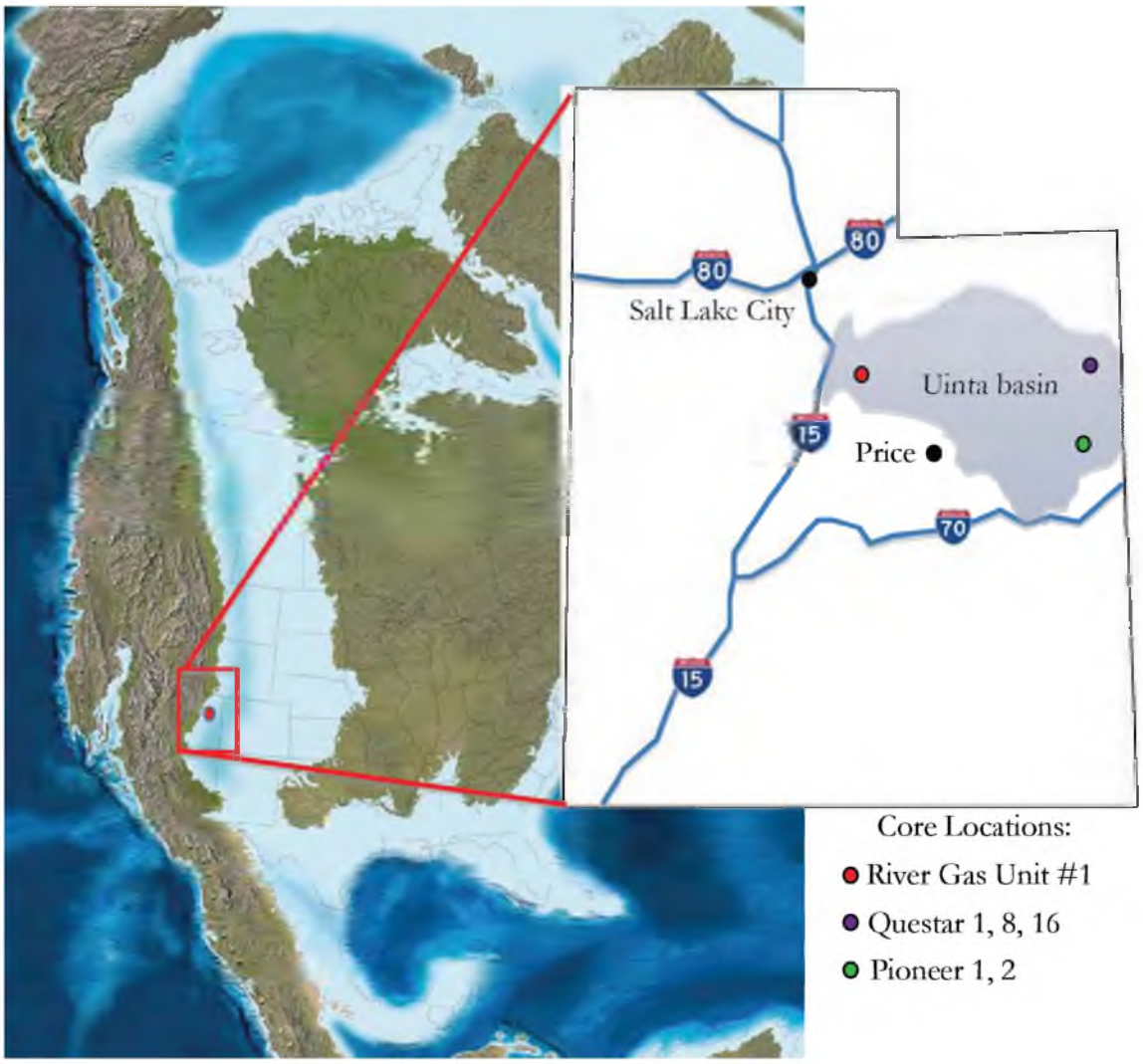

Figure 2: Paleogeographic map of the Western Interior Seaway during the Cretaceous (modified from Blakey, 2011), and location of the Uinta Basin.

Modified from Kennedy (2011).

Sandstones, Blackhawk Formation, and (in the Piceance Basin) the Lower Castlegate Sandstone. Throughout the late Cretaceous, these shoreline deposits of the Western Interior Seaway recorded multiple transgressive and regressive cycles on multiple time scales (Yoshida, 2000). In this study area, the Mancos is underlain by nonmarine Dakota Sandstone, and overlain by the Mesaverde Group (Molenaar et al., 1991)(Figure 3). To the west of the study area, the Mancos Shale interfingers with coarser-grained clastic sediments shed from the Sevier Orogenic belt, including the Ferron and Emery Sandstones and the Blackhawk Formation (Ressetar et al., 2011).

The Mancos Shale has several members that have been identified as potential shale-gas reservoirs: the Prairie Canyon (also referred to as the Mancos B), the Lower Blue Gate, The Juana Lopez, and the Tununk Shale (Schamel, 2006). All four of these intervals have been investigated in this study (Figure 3, modified from Birgenheier et al., 2011). While most of these intervals are laterally continuous, the Mancos B is an isolated heterolithic sandstone rich body that is bounded above, below, and laterally by the Blue Gate Member.

Following the Sevier orogeny and deposition of the Mancos Shale, the tectonic environment shifted to a different style of deformation. The Laramide orogeny was characterized by deeply rooted reverse faults extending into crystalline basement rocks (Johnson, 2003). While the stresses that caused the Laramide orogeny were similar to those that caused Sevier orogenic thrusting, the orientation of Laramide faults is widely variable – a stark contrast to the broadly north-south trending thrusts characteristic of the Sevier orogeny. Indeed, the Rocky Mountain foreland basin present at the end of the Sevier orogeny was then subdivided into multiple basins by Laramide aged structures. The boundaries of the Uinta basin are controlled, in large part, by these Laramide aged structures. To the north, The Uinta basin is bounded by the Uinta uplift. Bounding the south sits the

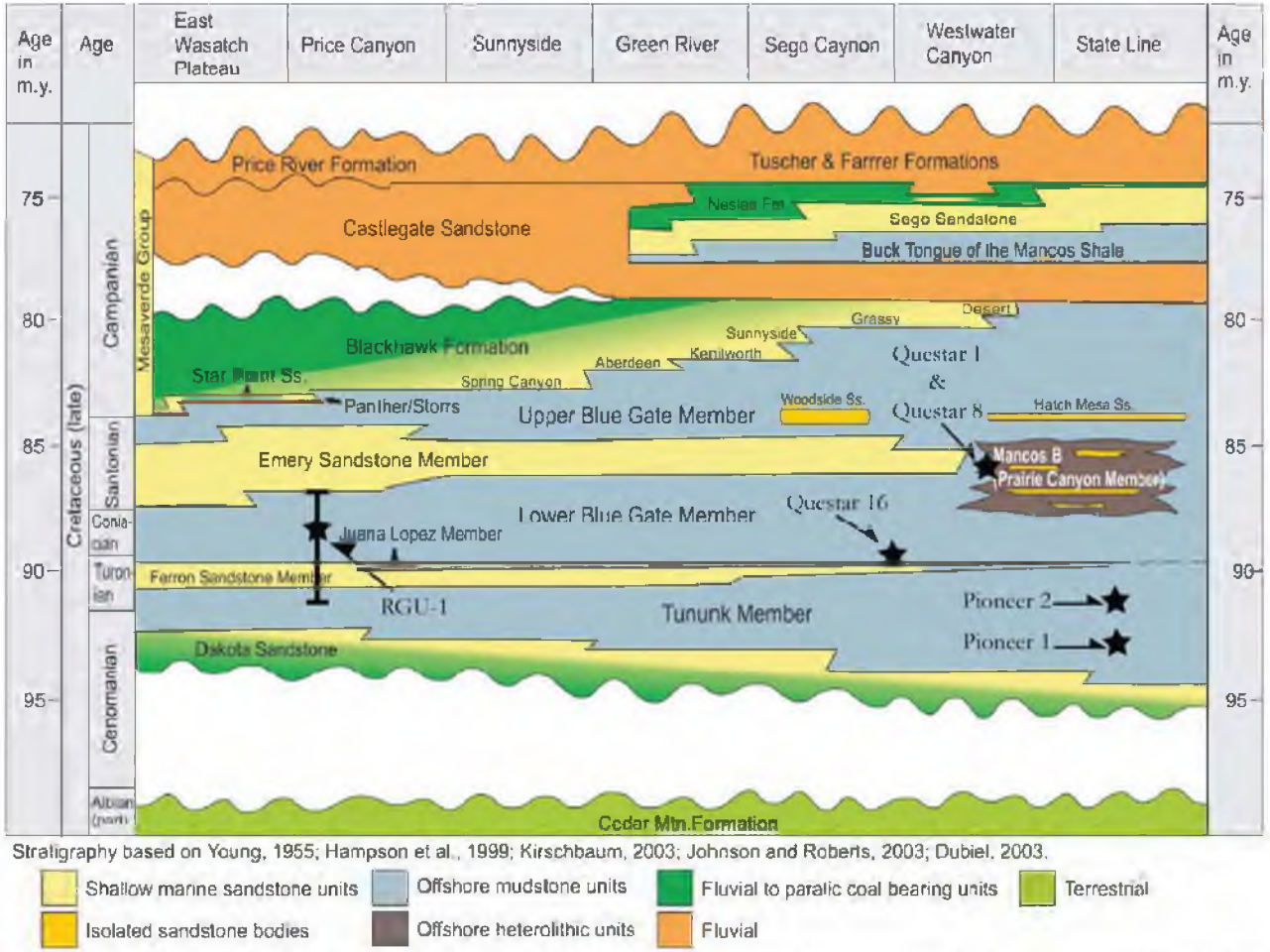

Figure 3: Stratigraphy of the Mancos Shale. Four stratigraphic intervals are potential targets as shale-gas reservoirs: the Prairie Canyon, the Lower Blue Gate, the Juana Lopez, and the Tununk. All four of these intervals are cored and examined in this study. Approximate well locations are represented by black stars.

Modified from Birgenheier et al. (2011)

San Rafael Swell. The Douglas Creek Arch forms the geologic boundary to the east separating the Piceance basin and the Uinta Basin (Figure 4).

Datasets

For this study, six cored intervals were studied. These cored intervals spanned a broad portion of the Uinta basin and represent different stratigraphic domains as well as different maturity levels (Birgenheier et al., 2011; Kirschbaum, 2003; Nuccio et al., 2003) (Figure 5).

River Gas Unit #1

The River Gas Corporation drilled the River Gas Unit #1 (hereby referred to as the RGU-1) well 3 miles southwest of Price, Utah (Figure 5). In 1991, 1712' of the well was cored, and the core has since been housed at the Utah Core Research Center at the Utah Department of Natural Resources. This is the thickest core that was studied for this project, and it has been the subject of previous work by Kennedy (2011). The core is nearly complete, with only 8% of the core missing (Kennedy, 2011). The core is divided into two sections – an upper half and a lower half – separated at 920'. The lower half of the core is unslabbed, with the upper half of the core slabbed at $1/3^{rd}$ and $2/3^{rd}$ increments. Donated datasets for this core include a gamma ray log collected during logging, along with a neutron density log and calculated sand percentages from the density log. Three units are present in the RGU-1 core: the 52' of the uppermost Tununk Shale member, which is overlain by the full thickness (237') of the Ferron Sandstone, and capped by 1423' of the Lower Blue Gate Member (Kennedy, 2011). Kennedy (2011) identified 12 lithofacies that are correlative to

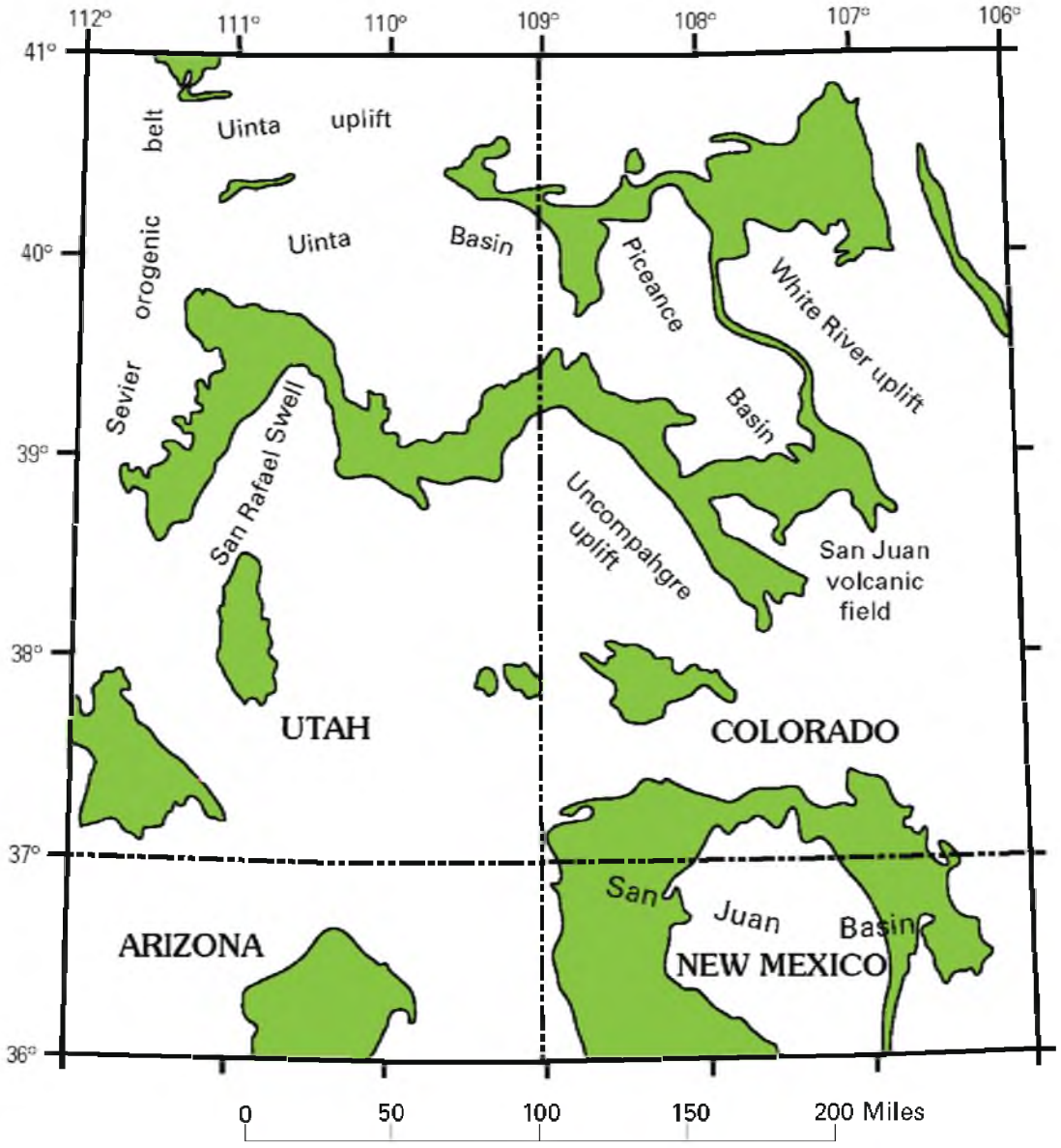

Figure 4: Map showing the regional context of the Uinta Basin, which is bounded by Laramide aged structures: the Uinta uplift to the north, the San Rafel Swell to the south, the Uncompahgre uplift to the Southeast. Outcrops of Cretaceous rocks in green.

Modified from Johnson (2003)

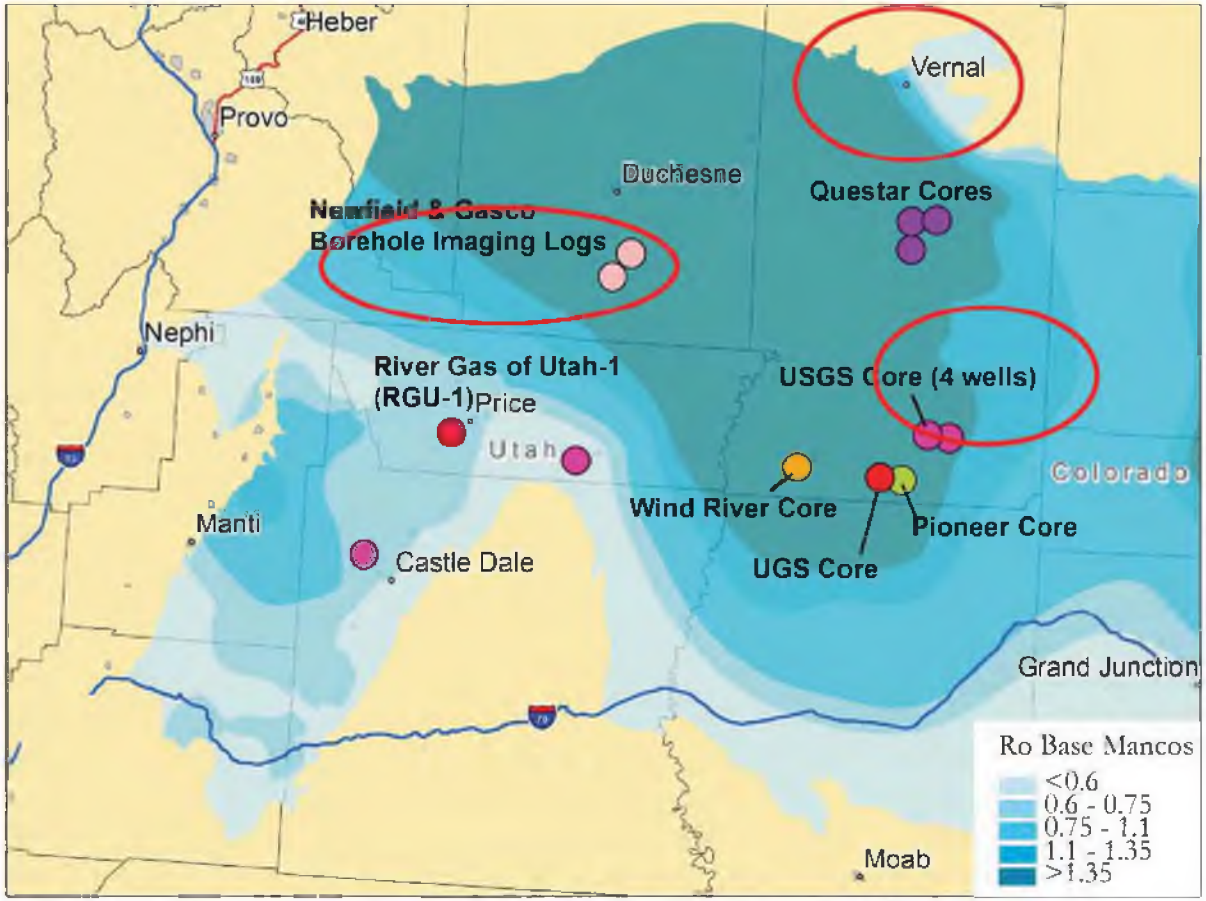

Figure 5: A map displaying the location of all cored intervals available for study in the Uinta Basin. Map represents approximate thermal maturity (from calculated vitrinite reflectance) by shading (based on Nuccio & Roberts (2002) and Kirschbaum (2002)). Cores circled are cores examined in this study.

Modified from Birgenheier et al. (2011)

some degree with the identified lithofacies in this study (Table 1). These RGU-1 lithofacies are discussed thoroughly in Kennedy (2011).

Questar Cores

Three cores from Questar were made available for study. These three wells are all located approximately 25 miles south of Vernal, Utah. The Questar Glenn Bench #1M-4-8-22R (hereafter referred to as Questar 1) was a gas well drilled in the White River field to a 17,114' depth. The cored interval is from 13,375' – 13,494', penetrating the Mancos B. Reports from the company suggest that the Mancos B formation begins at 13,125', and the Frontier (Ferron) Sandstone begins at 15,900'. The well was perforated at 45 intervals from 13,516' through 17,027', which suggests that the Mancos, Frontier, and Dakota sandstone were all targeted for production. Seven of these intervals were then hydraulically fractured from 13,383' – 17,027'. Initial production was 12 barrels of oil per day, 4,236 MCF of gas per day, and 1,514 barrels of water per day on a 16/64 choke (IHS, 2012b).

The Questar Red Wash #8ML-6-9-24 (hereafter referred to as Questar 8) was a gas well drilled in the Natural Buttes field and completed at a depth of 13,400'. The cored interval was from 9,631' – 9,746', penetrating the Mancos B. Questar marked the top of the Mancos B at 9,000', the top of the Frontier Sandstone at 11,700', and the top of the Dakota Sandstone at 12,600'. This well was perforated at 32 depths from 4,462' through 9,324' covering the Wasatch, Mesaverde, Sego, Castlegate, Blackhawk, Mancos and Mancos B formations. Of these 32 perforated intervals, 6 were hydraulically fractured from 4,462' – 9,324'. Initial production was 60 barrels of oil per day, 1,438 MCF of gas per day, and 1,330 barrels of water per day on a 26/64 choke (IHS, 2012d).

Table 1: Correlation between lithofacies identified in the RGU-1 core (Kennedy 2011) and those identified in the Questar and Pioneer cores in this study.

RGU-1	Description	Questar/Pioneer
F1	Massive to faitly laminated silty claystone	LF 4
F2	Low angle laminated calaystone to siltstone with intermittent shell	LF 2
F3	Bentonite	LF 10
F4	Non to minorly bioturbated heterolith; interlaminated claystone and siltstone with ripples and minor sandstone lamination	LF 1
F5	Moderately to heavily bioturbated heterolith; interlaminated claystone and siltstone with ripples and minor sandstone lamination	LF 1
F6	Massive bioturbated siltstone to claystone	LF 5
F7	Moderately to heavily bioturbated heterolith: interlaminated coarse siltstone and very fine sandstone	
F8	Admixed siltstone to sandstone; heavy bioturbation	LF 5
F9	Massive very coarse silt to very fine sandstone; heavy bioturbation	Not observed
F10	Fossiliferous shale	Not observed
F11	Hummocky, cross-bedded sandstone	Not observed
F12	Bioturbated sandstone	LF 9

The Questar Glenn Bench #16M-28-8-21 (hereafter referred to as Questar 16) was a gas well drilled in the Natural Buttes field and completed at a depth of 16,490'. The cored interval was from 15,145' – 15,263' penetrating a silt rich distal expression of the Frontier formation. In the northeastern part of the Uinta Basin, the Frontier is thought to be equivalent to the Ferron in the southern part of the basin. Thus, the Questar 16's siltstones are similar to Juana Lopez deposits in the southern Uinta Basin. Questar marked the top of the Mancos B at 12,480' and the top of the Dakota Sandstone at 16,040'. This well was perforated at 126 different depths from 10,454' – 16,412' perforating the Mesaverde, Castlegate, Blackhawk, Mancos, Mancos B and Dakota formations. Of these 126 perforated intervals, 15 were hydraulically fractured. Initial potential tests recorded 2,191 MCF of gas per day, with 974 barrels of water per day on a 18/64 choke (IHS, 2012c).

Pioneer Core

Pioneer Natural Resources donated two cored intervals of the same well located approximately 40 miles south of the Questar wells, and 25 miles west of the Utah/Colorado boarder. The Pioneer Natural Resources Main Canyon Federal #23-7-15S-23E is a gas well drilled in the Main Canyon field, and completed at a depth of 10,370'. The first cored interval was from 7,480' – 7,597' (hereafter referred to as Pioneer 1) and the second core interval was cored from 6,995' – 7,135' (hereafter referred to as Pioneer 2). According to documentation provided from the operator, the Mancos B interval began at 5,534' depth, and the Morrison formation began at 8,800'. This well was perforated at five intervals from 8,574' – 9,841', and was then stimulated by hydraulically fracturing four of these perforations. Initial potential tests recorded eight barrels of oil per day, 629 MCF of gas per day, and 73 barrels of water per day (IHS, 2012a).

Methods

Lithologic Description

The first analysis performed in this study was a detailed lithologic descriptions of the cores outlined above. Observations were made on a centimeter by centimeter scale. A log was generated for each of the six cored intervals with the following features noted: grain size, lamination style, lamination frequency, primary sedimentation structures, current indications, trace fossil abundance, trace fossil identification, degree of reactivity with acid, fossil presence, fossil identification, and any outstanding features (e.g., carbonaceous debris, dewatering structures, soft sediment deformation, etc.).

Grain size was determined by performing a grit test on the core every fifth of a foot. This grit test was then verified using a method described by Bohacs in 2011, whereby a scratch tool is used to determine the ratio of silt to mud in a sample (Bohacs, 2011). In the grit test, a large number of samples were first examined to calibrate any member of the research group. Once calibrations were made, any individual can estimate three orders of grain size in the silt domain – fine, medium, and coarse silt. These variations can also be tracked using the scratch test, as finer grained siltstones would have a higher percentage of particles that were clay-sized. These ultra-fine grains will "smear" on each other, rather than scratch, giving the surface a shiny or oily texture.

Acid reactivity was determined by comparing the reaction that occurred when a drop of hydrochloric acid was applied directly to a rinsed and dried portion of the core. These reactions were widely variable, with some portions of cored intervals reacting very vigorously, and other intervals being completely nonreactive. The degree of reaction was placed on a seven point scale with higher values assigned to more vigorous reactions.

Bioturbation indices were described on a scale of zero through six as outlined in depth by Bann et al. (2008) whereby a value of zero corresponded to an interval where bioturbation was absent, and a value of six corresponded to an interval that was completely bioturbated, and all sediment was biogenically homogenized (Bann et al., 2008). Bioturbation levels were generally averaged every third of a foot. If there were unique intervals where bioturbation was significantly different on a sub-one third foot scale, it was noted appropriately. Additionally, these bioturbation levels refer exclusively to macro-scale bioturbation. Any micro-scale bioturbation seen in thin section analysis is noted later in the study.

X-Ray Fluorescence

A total of 1,448 depths ere sampled for X-ray fluorescence (hereby referred to as XRF) data. Samples were taken from the Questar 1, Questar 8, Questar 16, and RGU-1 (1931.2' – 929.9') cores at one foot intervals. In the RGU-1 core from 929.9' – 220.3' samples were taken at three foot intervals. All sample results are expressed in weight percent, unless otherwise specified. Samples were taken directly from core, after the core had been lightly cleaned and dusted, for major and trace elemental composition using the Brüker AXS TRACER III-V energy dispersive handheld X-ray Fluorescence unit. Raw data was collected as a spectrogram, and to convert to weight percent, a matrix specific calibration was required (Rowe et al., 2012). To ensure accuracy, a standard pressed pellet was run periodically throughout testing.

X-Ray Diffraction

A total of 26 samples were prepared for X-ray diffraction (XRD) analysis for oriented XRD sample preparation. To prepare samples, intervals were first selected to examine all identified lithofacies from the initial lithologic interpretation. These intervals were selected as "type intervals" from the core, and were generally approximately one to two inches thick. From these type intervals, a number of samples would be prepared, so only a portion was used in XRD sample preparation. The initial disaggregation was performed by hand using a mortar and pestle. Care was taken to pulverize samples to an appropriate grain size such that nonclay minerals were not crushed to clay mineral size. The crushed sample was then peptized by adding approximately 10mL of a 5% solution of Calgon, which was then dispersed by a high shear stress blender. Particle size separation was then achieved through two centrifuge steps. First, the peptized suspension was centrifuged at 1000 rpm for five minutes to separate a two micrometer size fraction in suspension. The two micrometer size fraction was then centrifuged at 4000 rpm for 4 minutes, after which, the liquid was discarded, and the remaining slurry was smeared on a cleaned glass slide and air dried for at least 24 hours.

The oriented slides were analyzed using a Rigaku x-ray diffractometer. Analyses were conducted at 40kV and 30mA, from 2 to 30 degrees 2θ at a rate of two degrees per minute. Data were collected at every 0.02 degrees of rotation. These data were then summarized by the program Right Measurement and peaks were analyzed using the computer program Jade. Following initial analysis after being air dried, samples were then vapor glycolated at 60°C for 12 hours. Six samples were glycolated per batch, and each batch was immediately analyzed using the same settings after glycolation.

Mineral identification was contingent on the successful identification of multiple peaks at specific values of 2θ. Illite was present in all samples, producing a (001) peak at ~8.7° 2θ, a (002) peak at ~17.5° 2θ, and a (003) peak at ~26.5° 2θ. Chlorite was present in many samples producing a (001) peak at ~5.9° 2θ, a (002) peak at ~12.3 2θ, a (003) peak at ~18.6° 2θ, and a (004) peak at ~25.1° 2θ. Kaolinite produced a (001) peak similar to chlorite at 12.3° 2θ, but the (002) kaolinite peak was slightly lower than chlorite (004) at ~24.8° 2θ. Quartz produced a (100) peak at ~20.7° 2θ, and a (011) peak at 26.5° 2θ. Calcite, where present, produced a (104) peak at ~29.3° 2θ.

QEMSCAN Analysis

Type samples that were identified from the lithofacies were also prepared for quantitative evaluation of minerals by scanning electron microsopy (QEMSCAN) analysis. QEMSCAN samples were taken from identical laminations that were selected for XRD analysis. XRF data were taken from either side of the core, with one half designated for XRD and the other half designated for QEMSCAN.

After having XRF data collected from the designated sample area, the samples were cut to fit a one centimeter diameter epoxy mold. Stratigraphic direction was marked on the rear of the epoxy. The epoxy was mixed and allowed to impregnate the sample over 24 hours in a vacuum chamber. Following this, the epoxy pots were removed and the epoxy cylinders were polished using progressively finer meshes. To finish the preparation process, the cylinders were coated in carbon.

The samples were run on a model 4300 Zeiss Eco 50 SEM platform QEMSCAN, with a tungsten filament and four light element Brüker Xflash energy dispersive X-ray detectors, where the Spectral Analysis Engine automatically identifies elemental composition

at every predetermined spacing interval. Low resolution scans were performed with 10 micron spacing, and performed on all samples. High resolution scans were performed with two micron spacing. Once elemental composition is determined, the software determines concentrations of elements, and assigns each space on the grid to a predefined mineral. The S.M.A.R.T. method runs through several sets of mineral definitions and is outlined further in Haberlah et al. (2011) but at the completion of the QEMSCAN analysis, each step has been assigned to a mineral. This result can then be manipulated and examined in iDiscover (a program bundled with the QEMSCAN) wherein microfabrics can be analyzed, and area percentages of numerous minerals can be identified.

TOC-RockEval Pyrolysis

One hundred and twenty-eight samples from all six cored intervals were submitted to Weatherford Laboratories for RockEval Pyrolysis. Of these 128 samples, 20 of the darkest in color were selected to undergo additional total organic carbon (TOC) tests. These values were then compared to percent organic carbon values from elemental analysis of carbonate free samples for carbon isotope analysis. Samples sent for RockEval were both whole rock samples and powdered samples of the same depth.

Thin Section Analysis

A total of 64 intervals were selected for thin section analysis. These intervals were selected because of immediate proximity to XRD and QEMSCAN analysis, as well as proximity to other geochemical tests run on the core. Each slide was impregnated with red fluorescent epoxy to highlight porosity.

Lithofacies

Lithofacies 1 - Well Laminated Siltstone Dominated Sandstone Heterolith

Lithofacies 1 occurs in five of the six cored intervals (Table 2; Figure 6; Figure 7; Figure 8; Figure 9). It does not occur in the second cored interval of the Pioneer core (Figure 10). Lithofacies 1 is composed of fine to medium grained siltstone with very fine grained sandstone interlaminations (Table 2; Figure 11; Figure 12; Figure 13). Laminations are generally approximately one millimeter in thickness, and occur between millimeter and multiple-centimeter intervals. Sandstone laminations can contain a wide range of primary structures including ripples, low angle laminations, and planar laminations (Figure 11; Figure 13). Claystone interlaminations can also be present, although very few primary structures are visible in these claystone interlaminations. Bioturbation index (Bann et al., 2008) ranges between two and three with visible horizontal and vertical burrows (Figure 11; Figure 12). Burrows include *Skolithos*, *Planolites*, *Arenicolites,* (Figure 14) and others. The interlaminated siltstone is generally nonreactive with HCL, but minor reactions can occur, especially in sandstone rich intervals. Thin sections reveal that the more coarse grained laminations are quartz rich, and the muddy laminations have a higher clay content, and lower quartz content (Figure 11; Figure 12; Figure 13; Figure 15). Burrows are most dominant in quartz rich laminations (Figure 12).

X-ray diffraction data was collected from all occurrences of Lithofacies 1 throughout all 6 cored intervals for comparing clay mineralogical presence in lithologically similar intervals across multiple cores (Figure 16; Figure 17; Figure 18; Figure 19). A summary of all XRD data is listed in Table 3. Lithofacies 1 contains illite, chlorite, quartz, and calcite in all samples with one exception. In Questar 8, kaolinite is present in addition to the four other

Table 2: Summary of identified lithofacies across all cored intervals.

Lithofacies #	Brief Description:	Present in:	Key Mineralogical/ Geochemical Characteristics:	Environment of Deposition:
1	Well laminated, bioturbated siltstone dominated sandstone heterolith	Questar 1, 8, 16, Pioneer 1	Medium to high quartz content, ripple laminations	Intermediate mudbelt
2	Poorly laminated siltstone dominated sandstone heterolith	Questar 1, 8	Medium to low quartz content, ripple laminations	Distal mudbelt
3	Dewatered well laminated siltstone dominated sandstone heterolith	Questar 1	Dewatering destroys primary structures	Distal prodelta
4	Claystone rich poorly laminated siltstone	Questar 1, 8	High illite content	Very distal mudbelt
5	Admixed siltstone and sandstone	Questar 1, Pioneer 1	Very high quartz content, very high bioturbation	Very proximal mudbelt
6	Rhythmically bedded, discontinuously horizontally laminated siltstone	Questar 16, Pioneer 1, 2	High illite content, no ripple laminations	Proximal shelf
7	Extensively bioturbated siltstone	Questar 16	High quartz content, very high bioturbation	Intermediate mudbelt
8	Massive siltstone	Pioneer 2	Very high illite content, no quartz laminations	Distal shelf
9	Intensely laminated sandstone dominated siltstone heterolith	Pioneer 1	Very high quartz content, very high bioturbation	Very proximal mudbelt
10	Bentonite	Pioneer 1		
11	Claystone dominated siltstone heterolith	Pioneer 2	Very high illite content, very few quartz laminations	Intermediate shelf

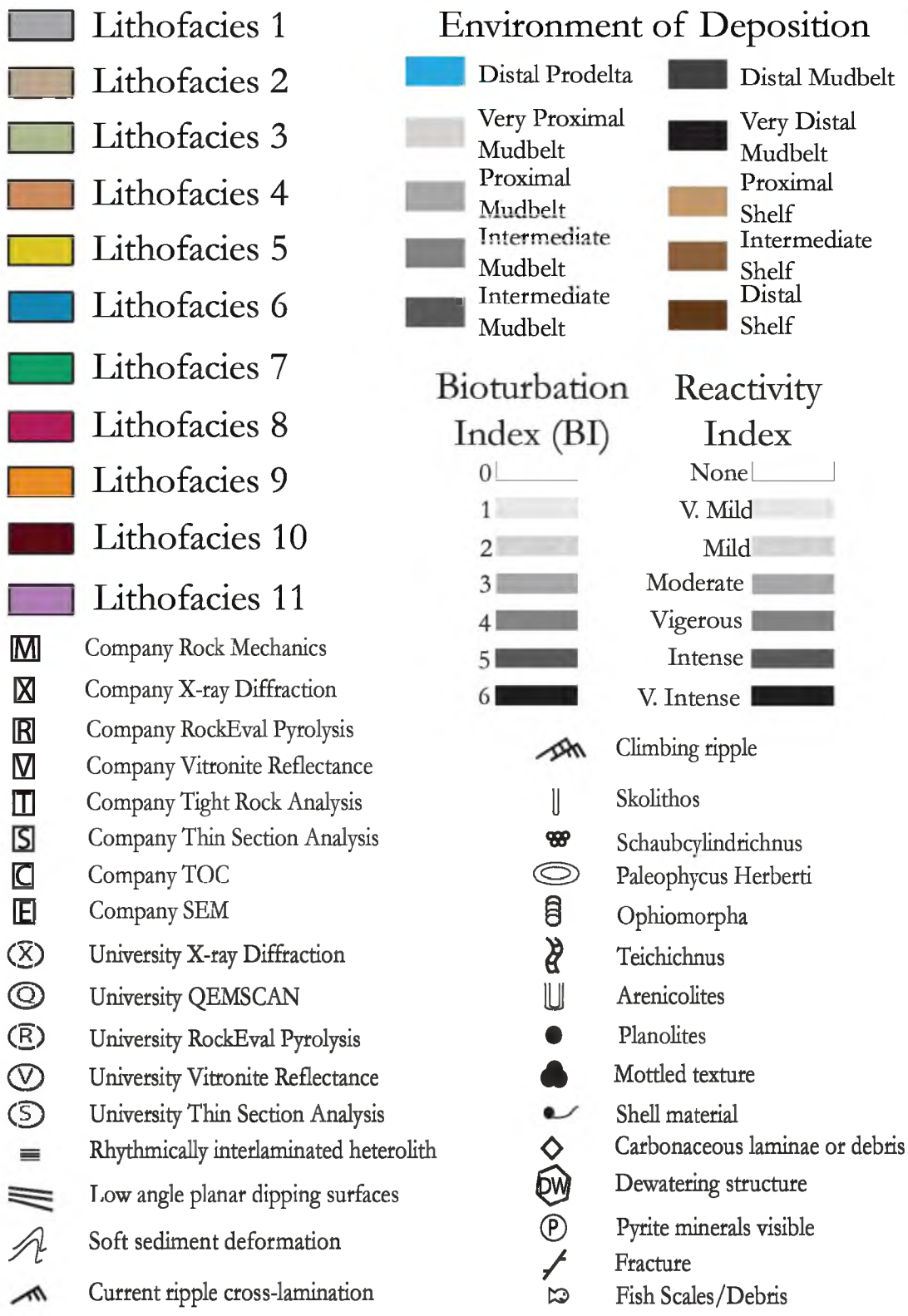

Key for Figures 6 – 10

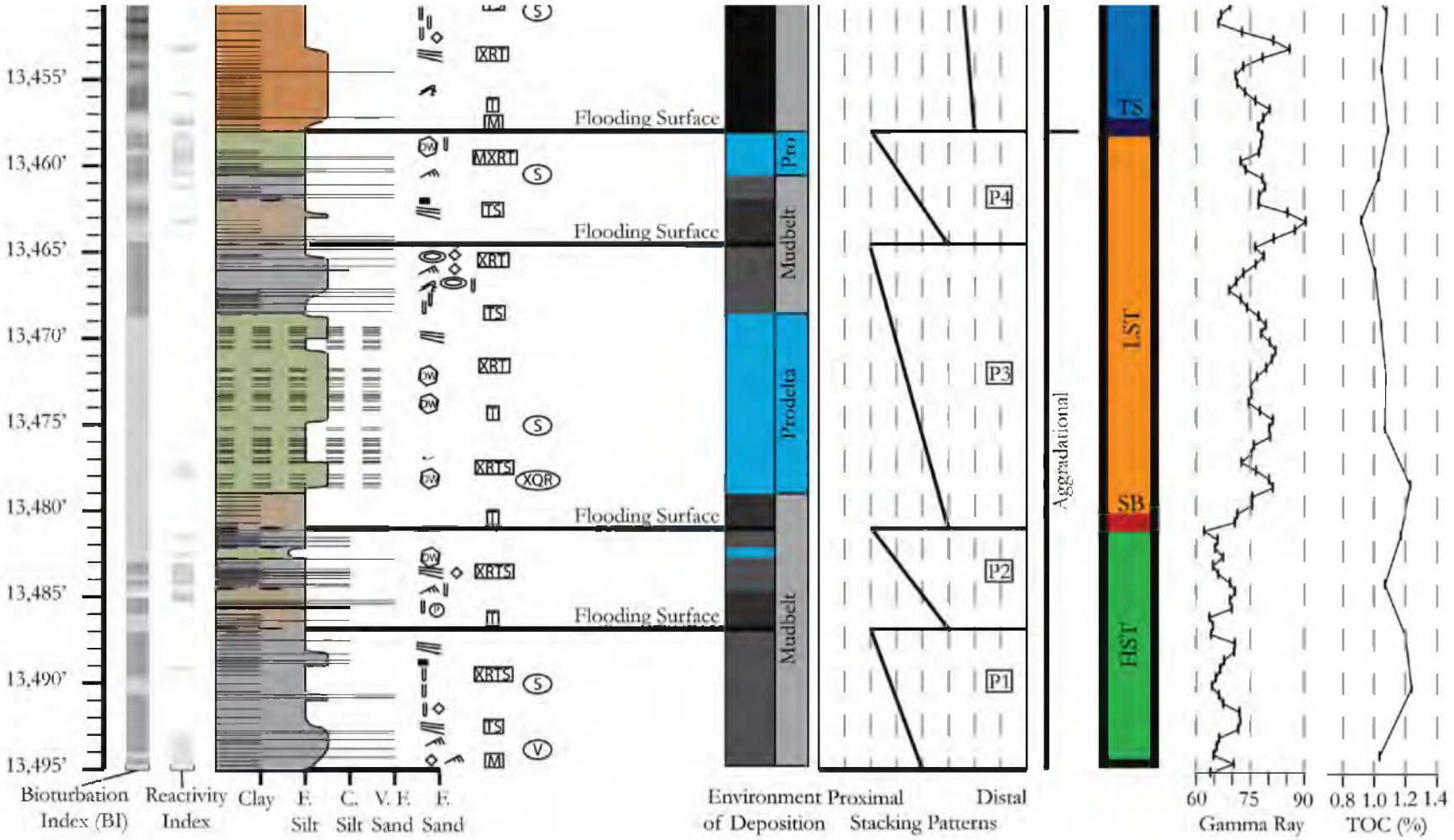

Figure 6: Core log of the Questar 1 Core

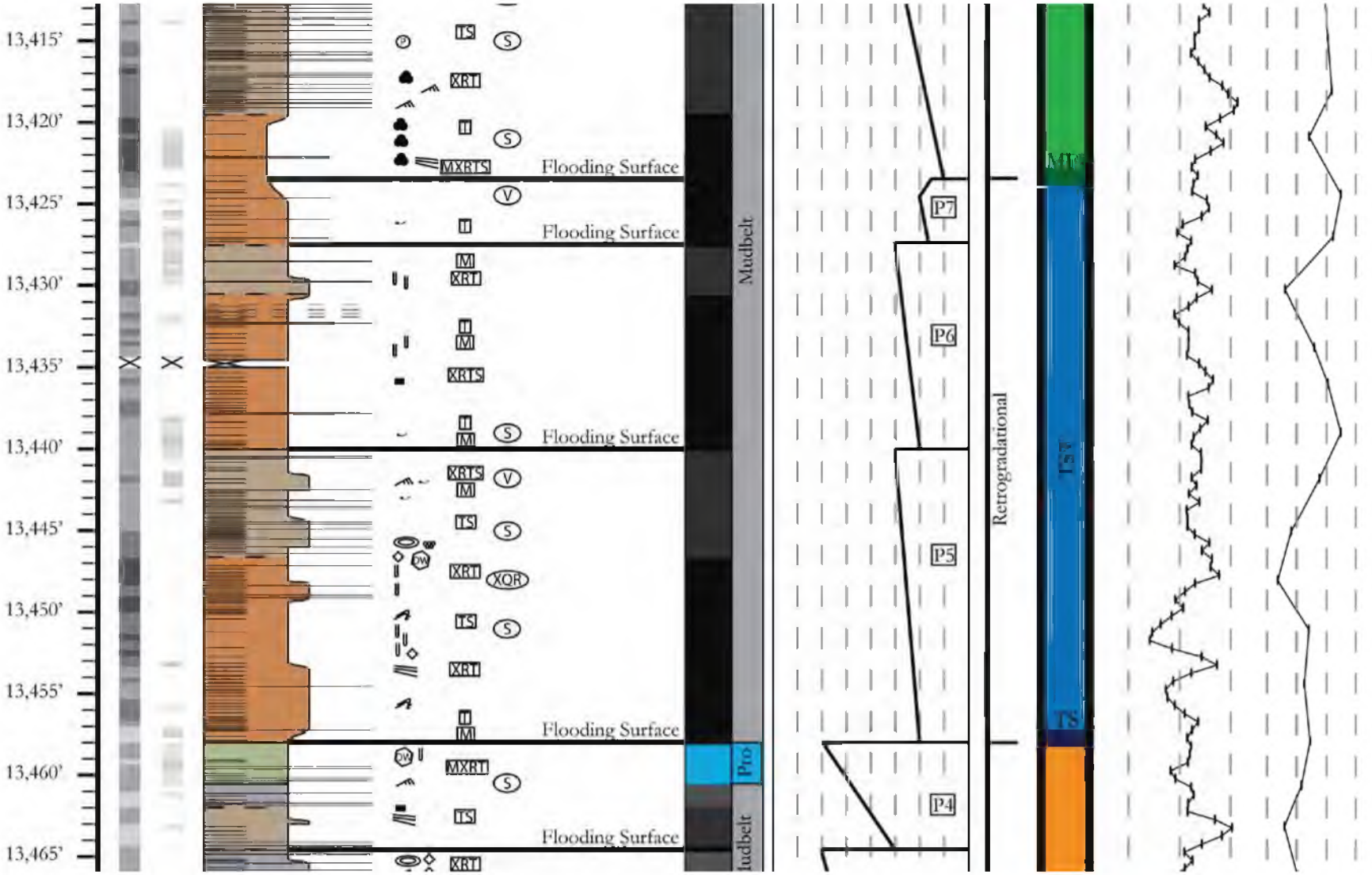

Figure 6: Continued

Figure 6: Continued

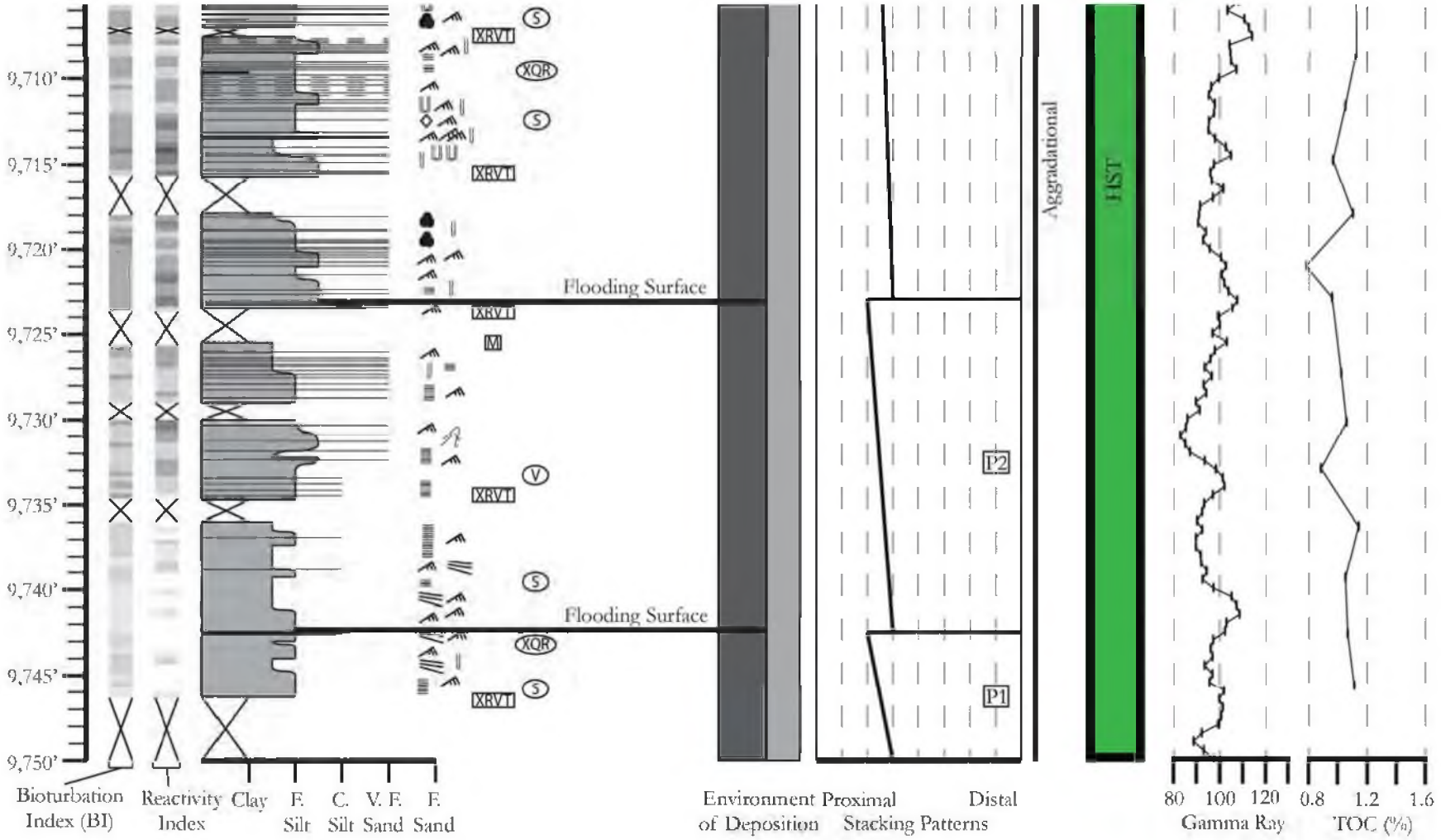

Figure 7: Core log of the Questar 8 Core

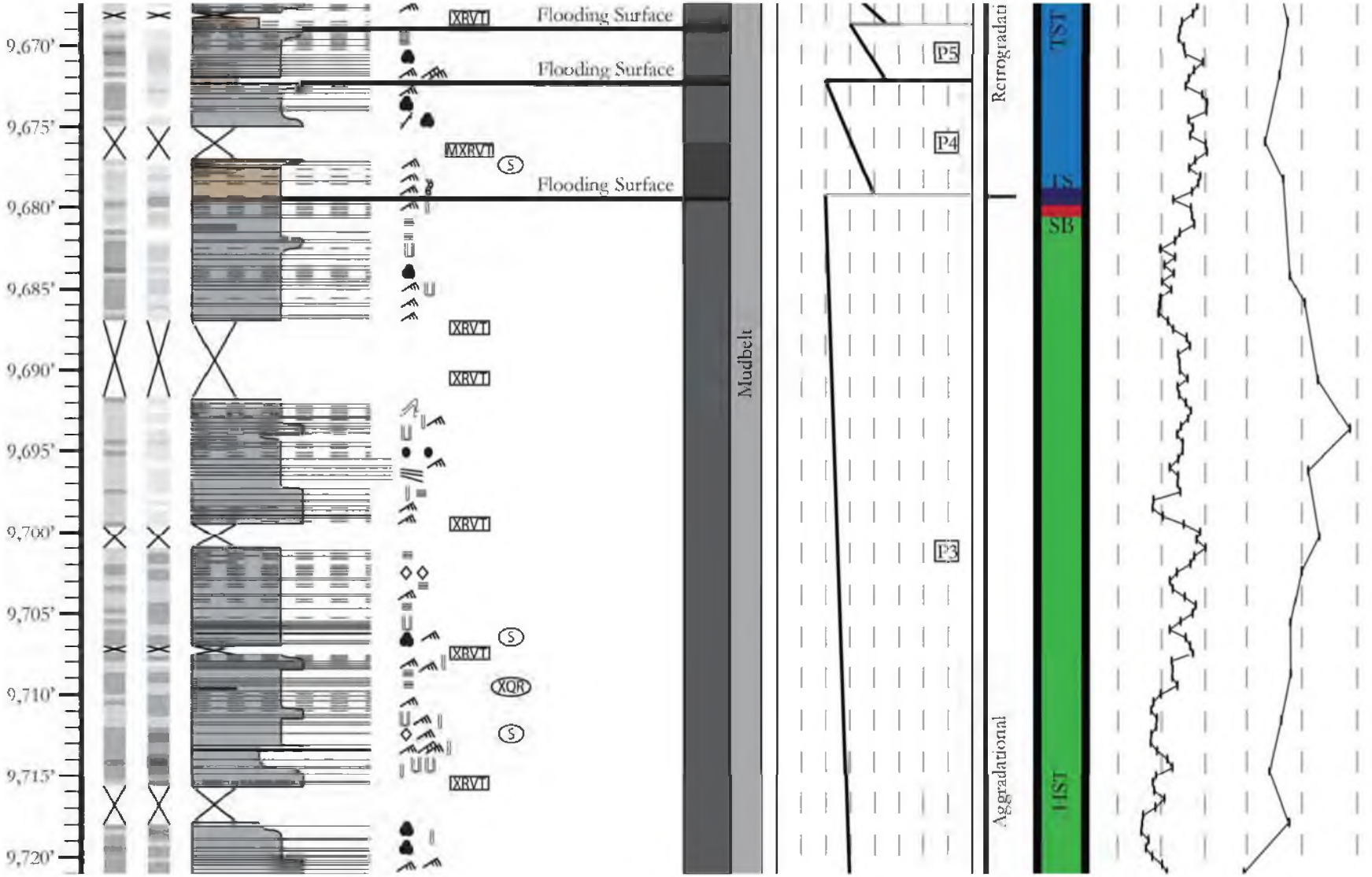

Figure 7: Continued

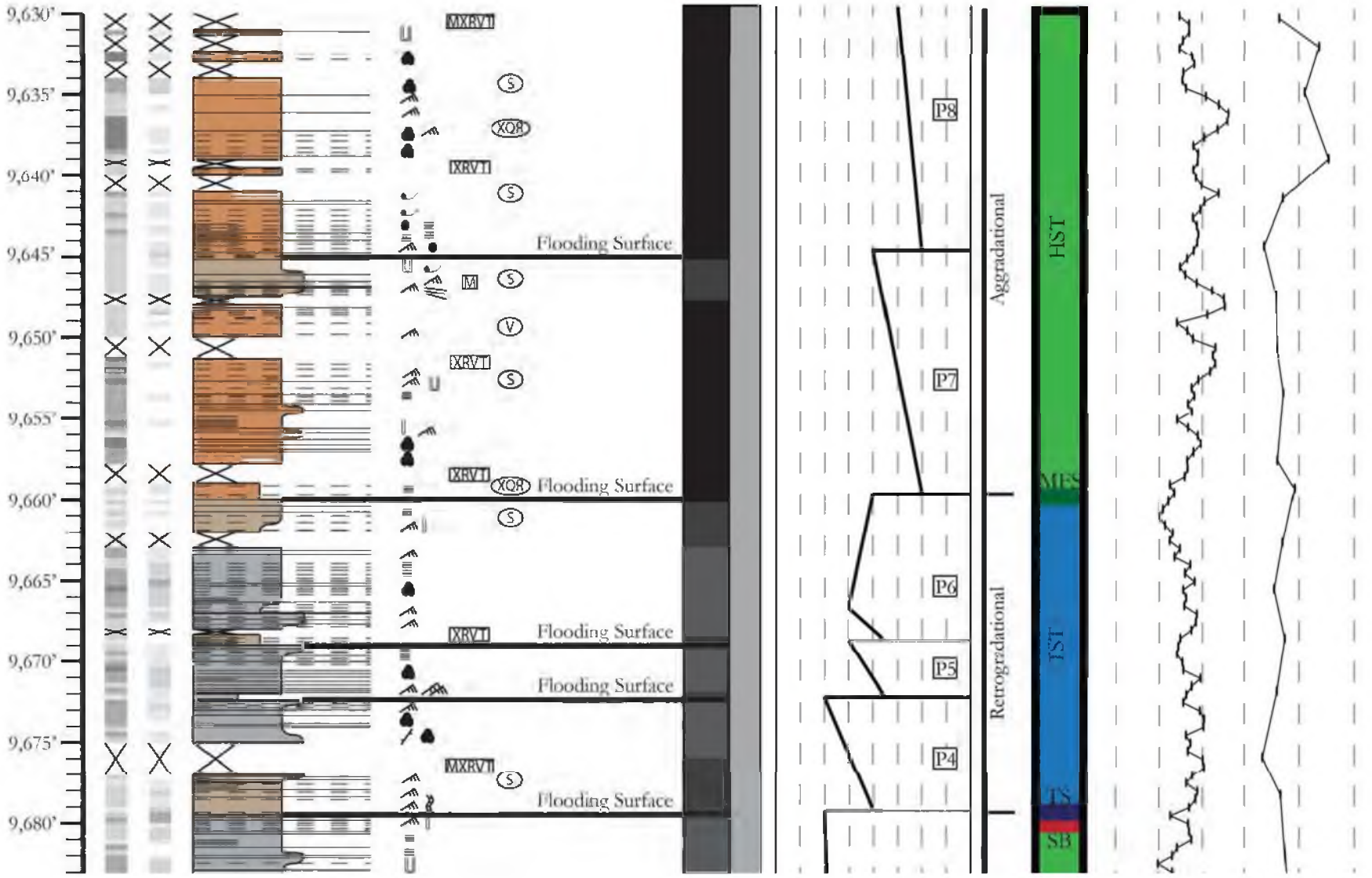

Figure 7: Continued

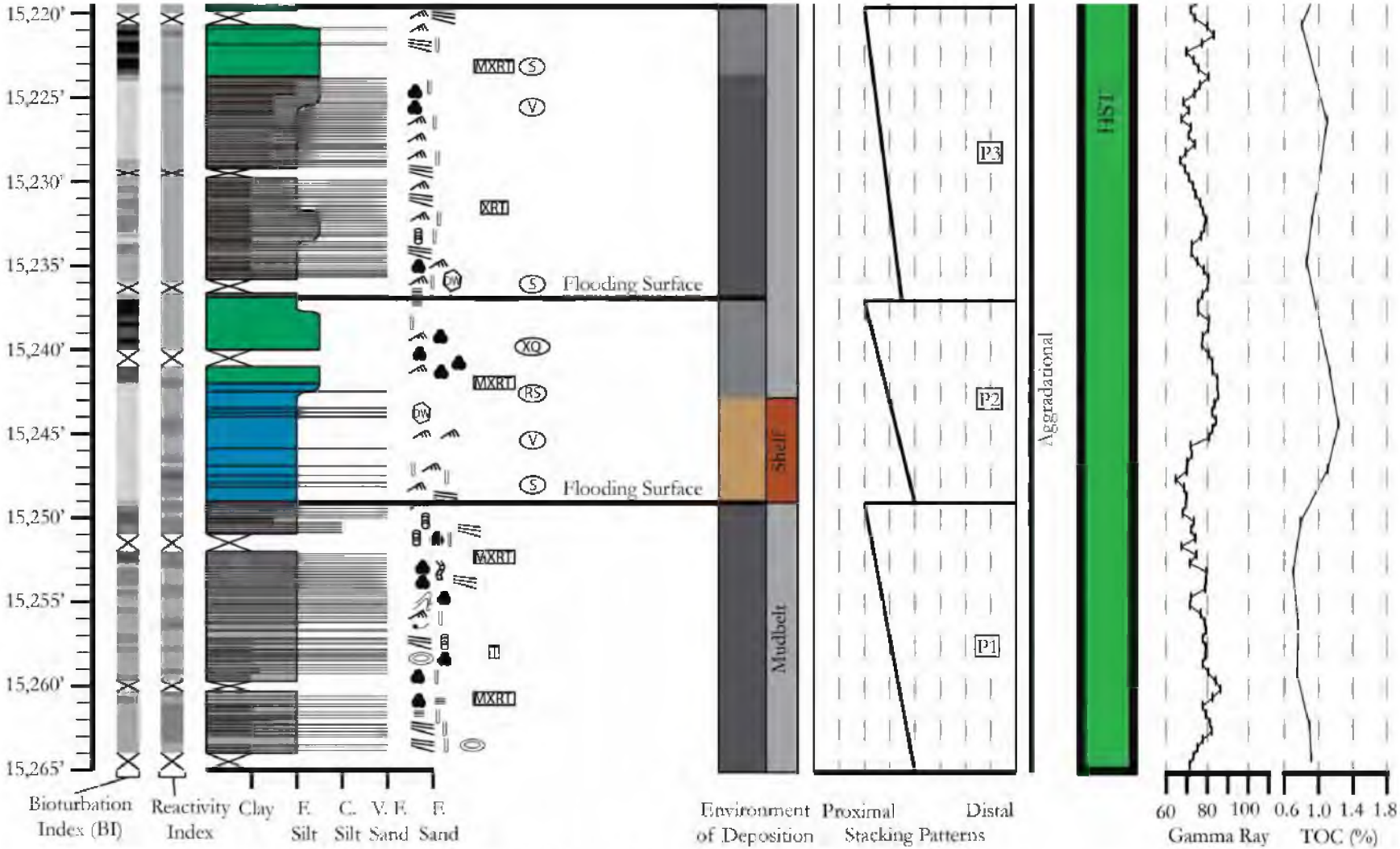

Figure 8: Core log of the Questar 16 Core

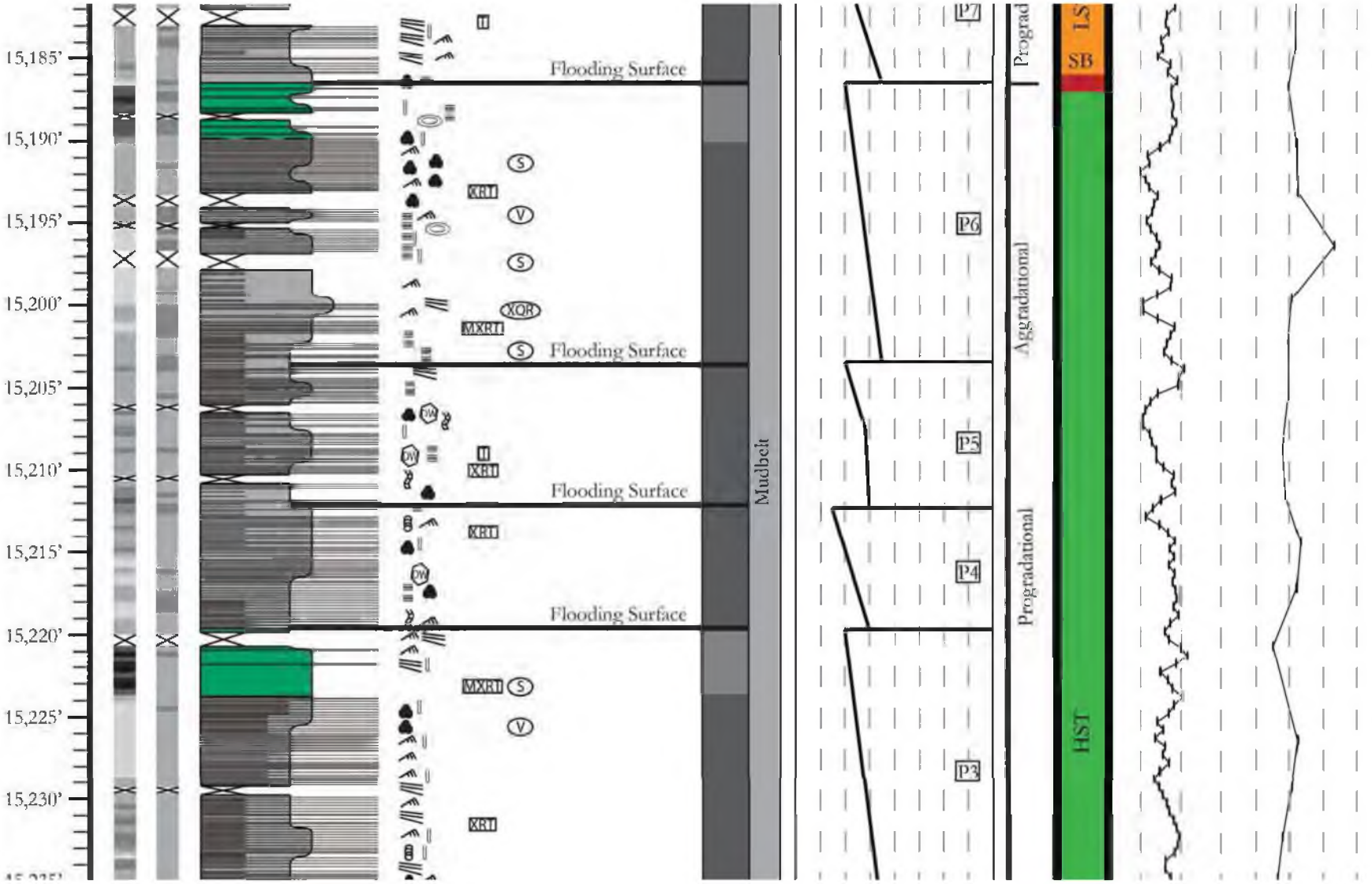

Figure 8: Continued

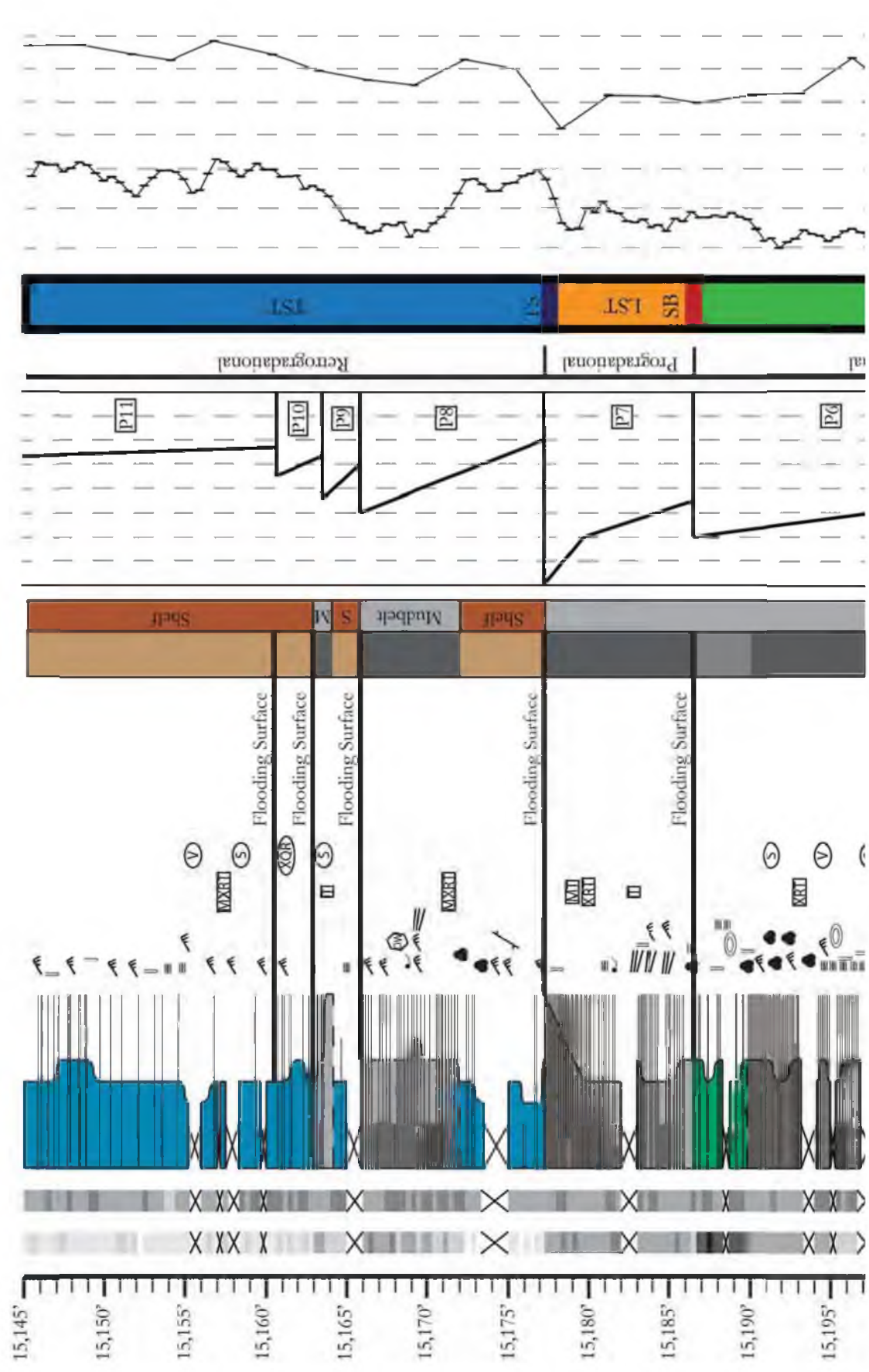

Figure 8: Continued

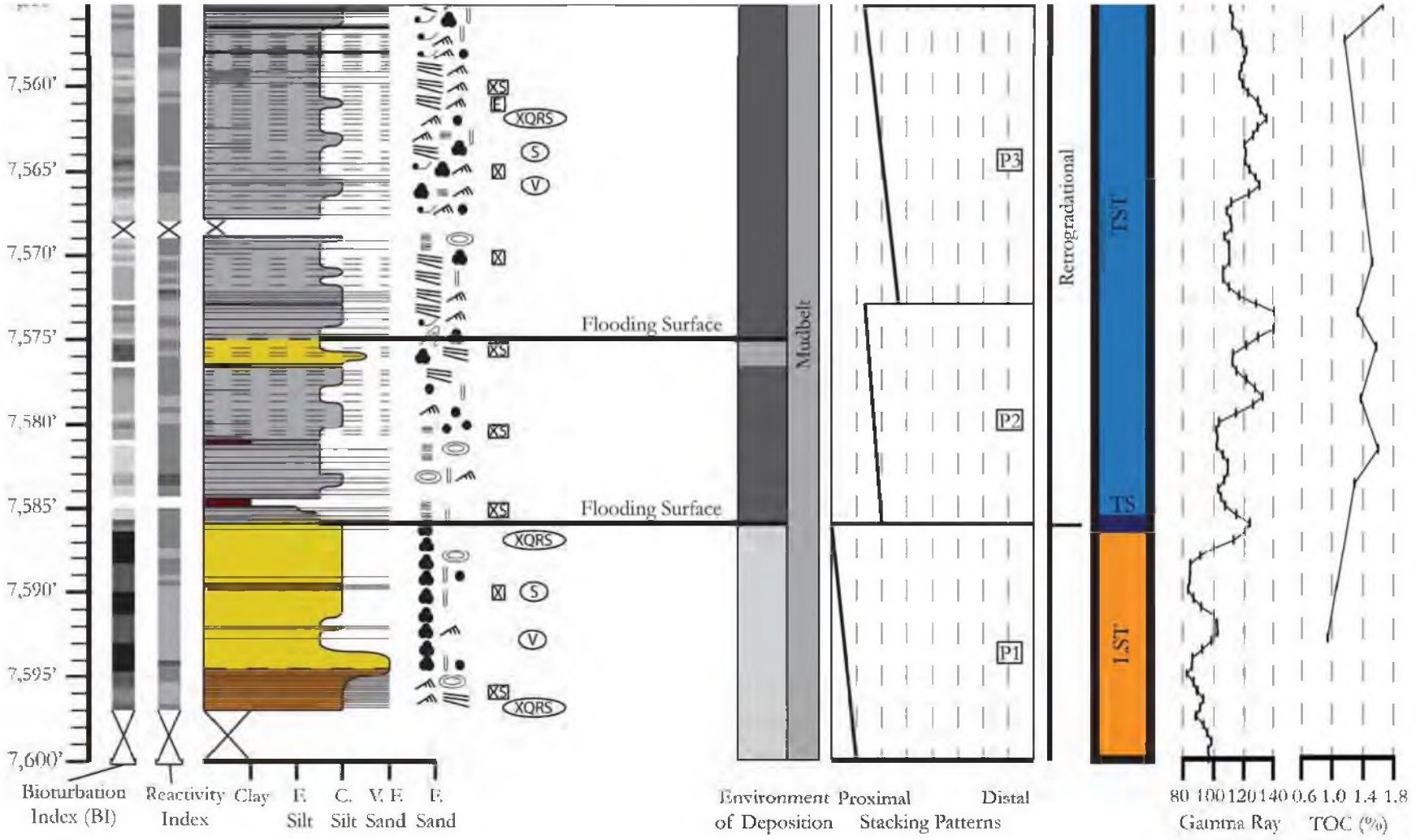

Figure 9: Core log of the Pioneer 1 Core

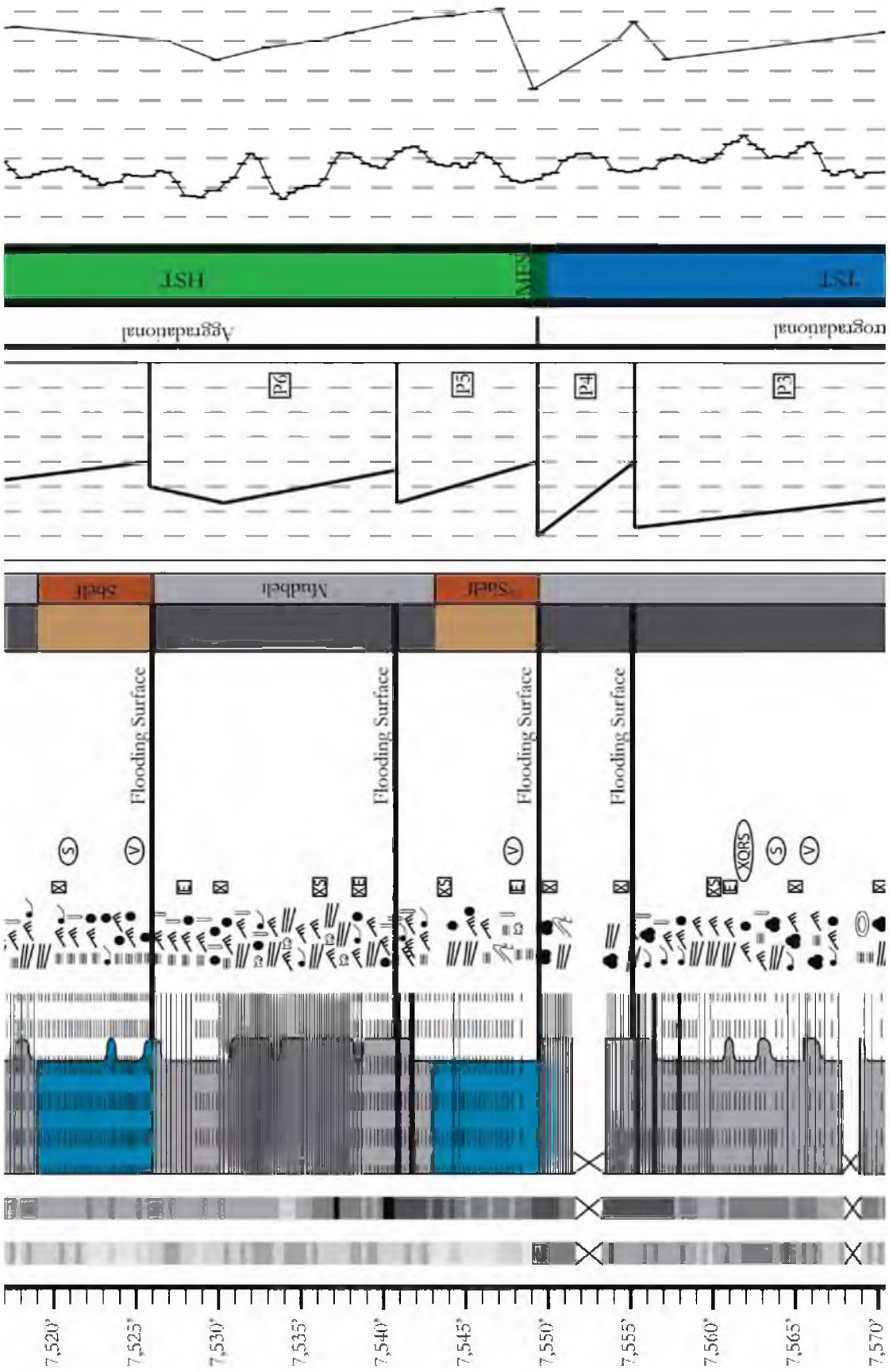

Figure 9: Continued

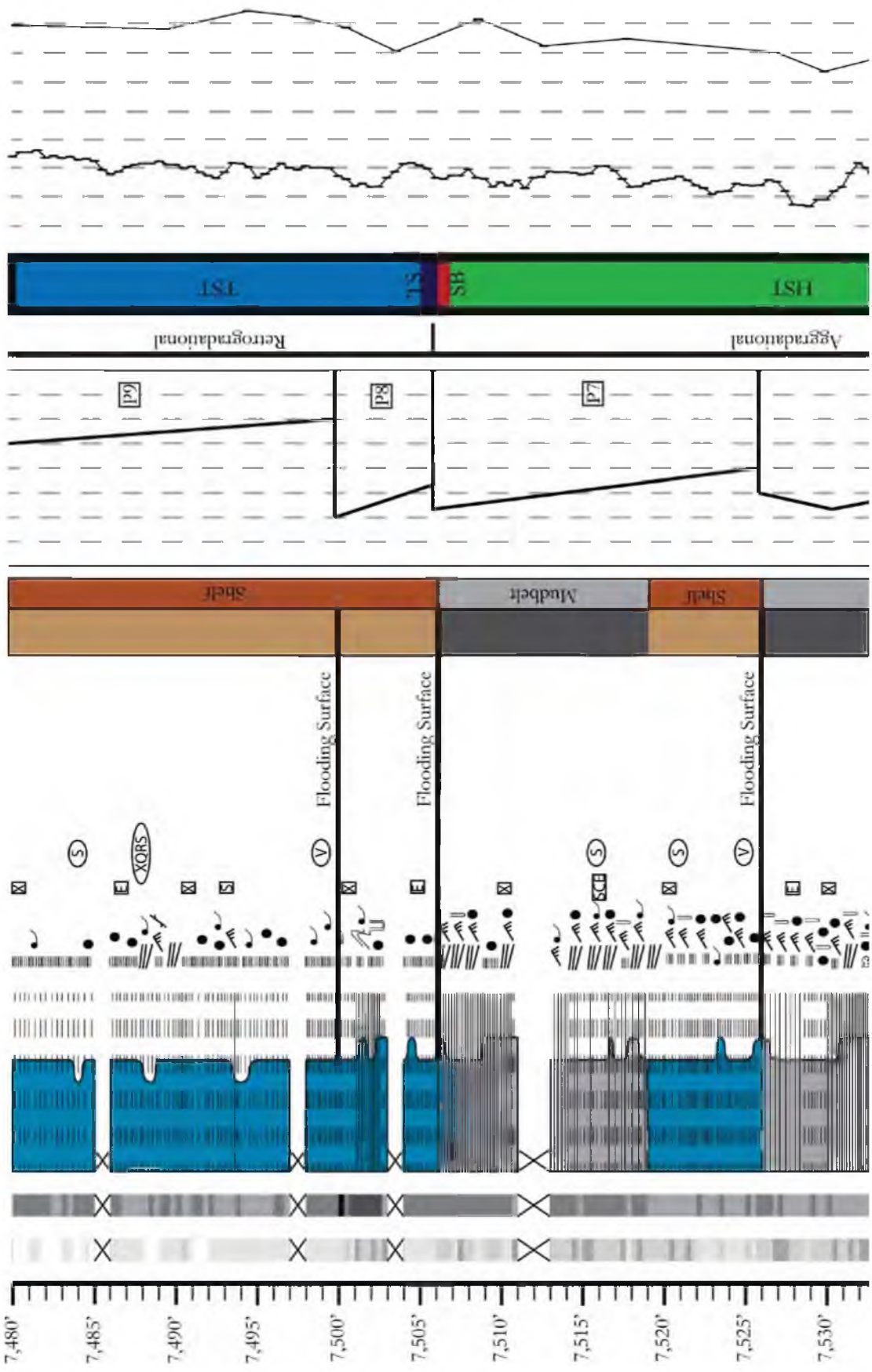

Figure 9: Continued

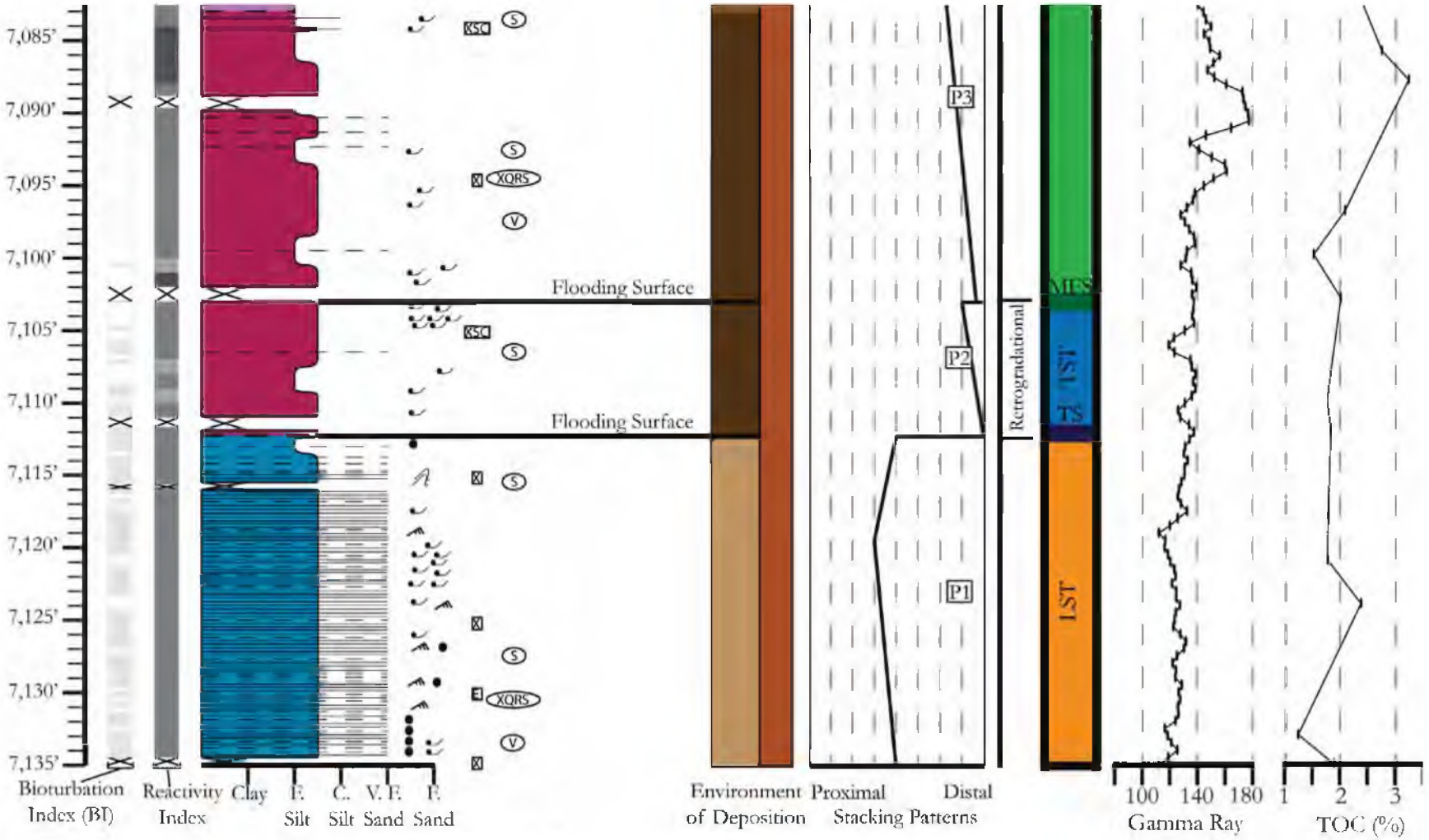

Figure 10: Core log of the Pioneer 2 Core

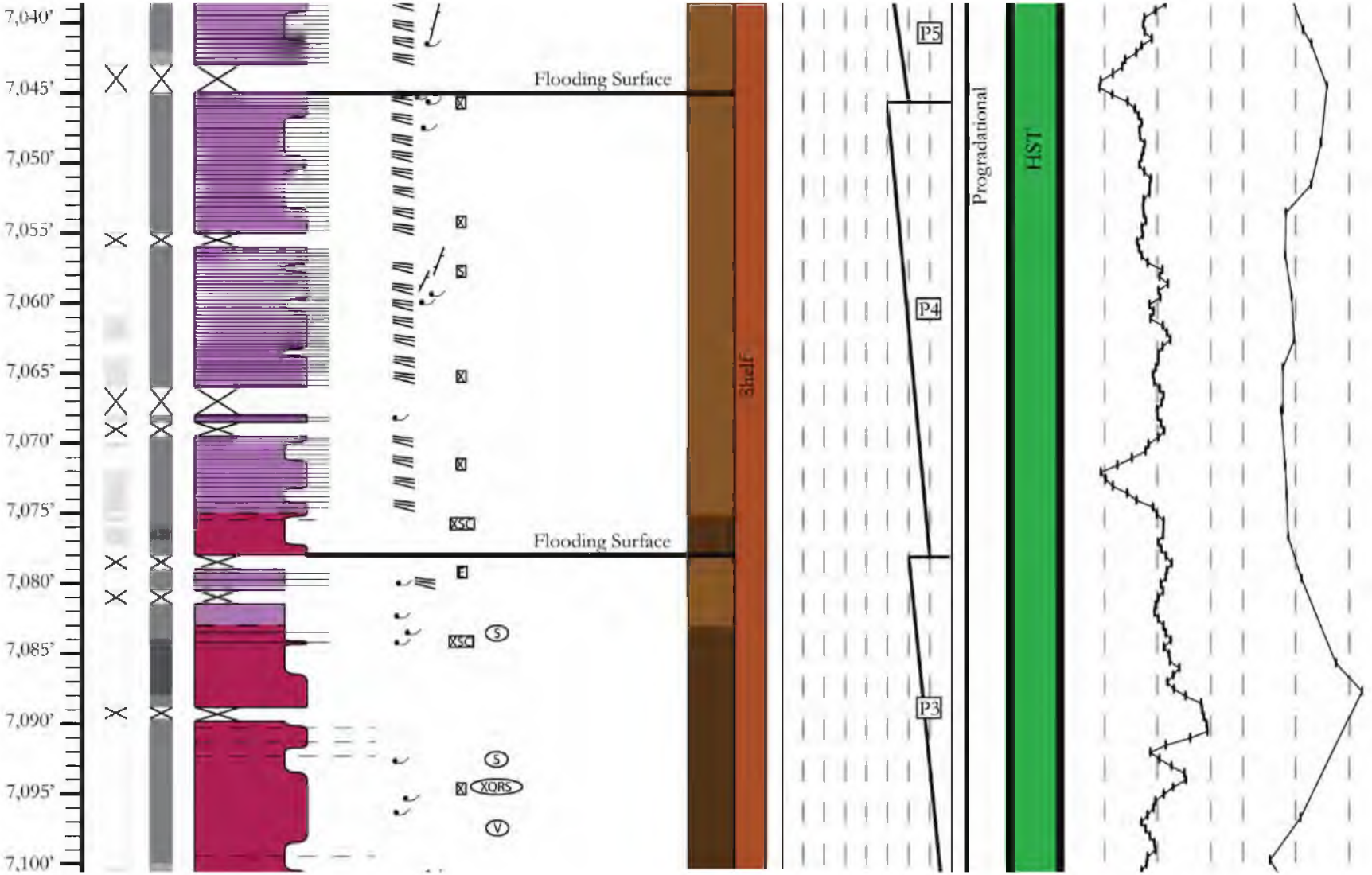

Figure 10: Continued

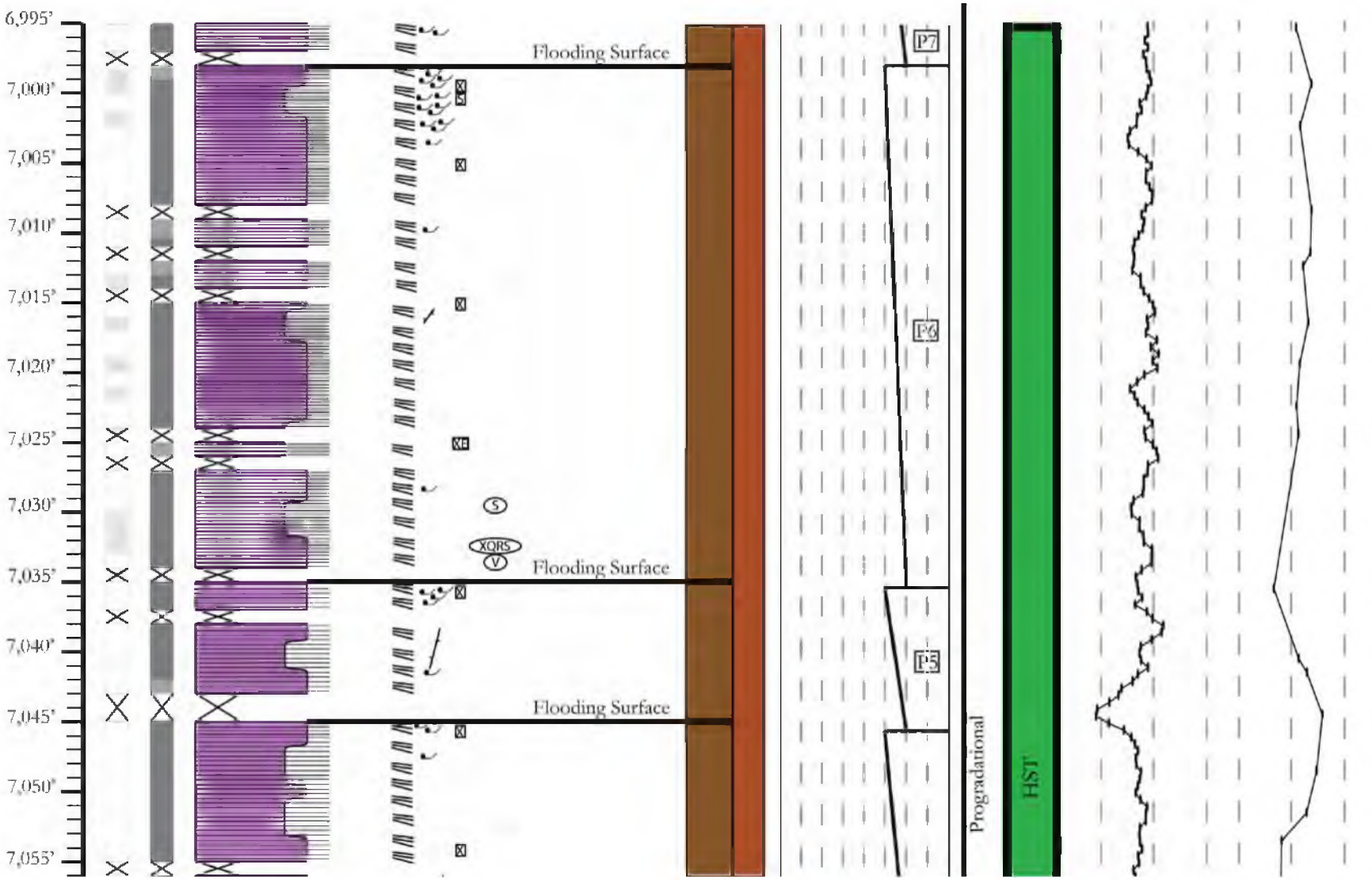

Figure 10: Continued

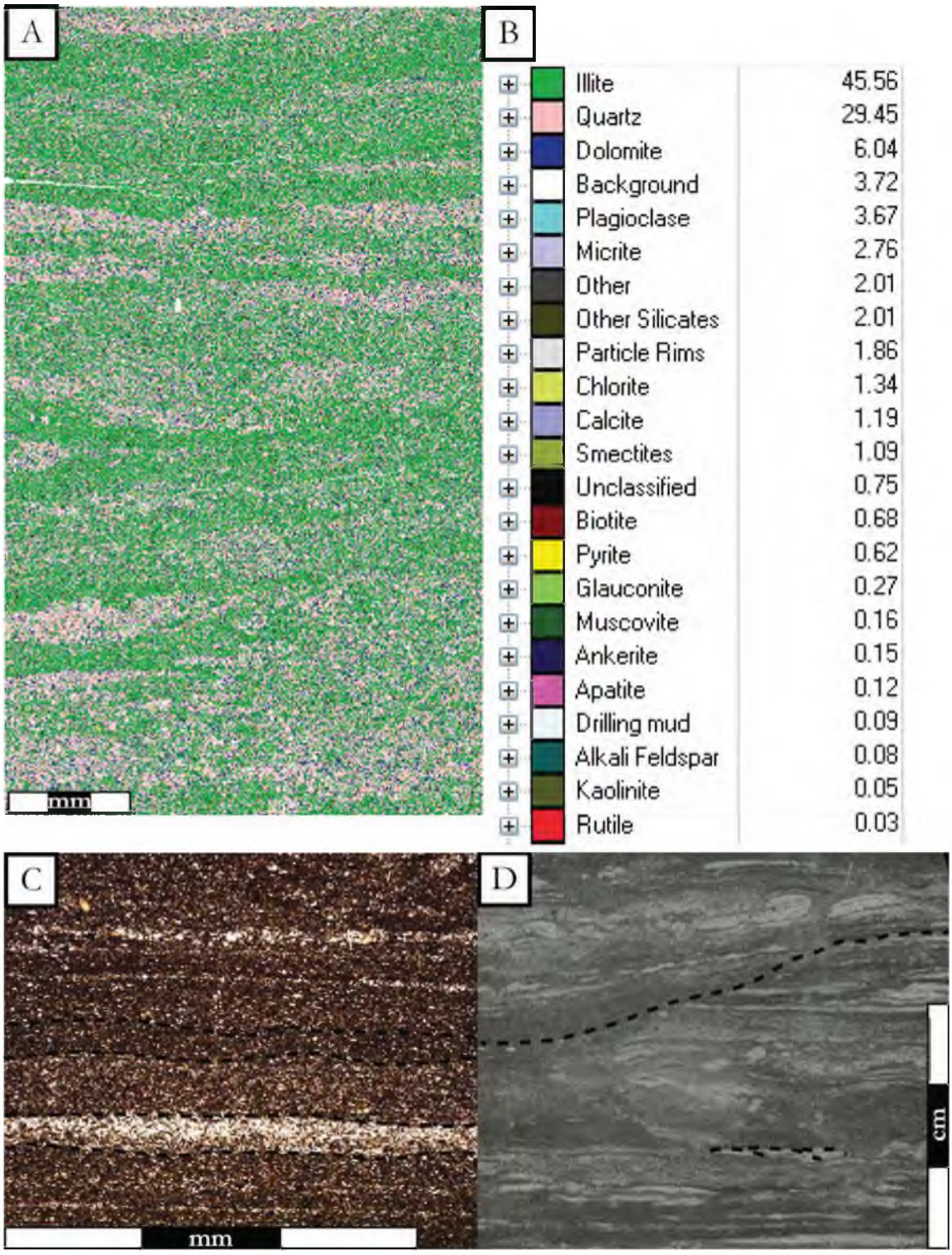

Figure 11: Lithofacies 1 in Questar 1. A) QEMSCAN slide with minerals color coded. B) Table expressing QEMSCAN minerals in area percent. C) Type thin section (13,490'). Note the well defined, quartz rich laminations alternating with darker, clay rich laminations. D) Type core sample (13,493'). Note abundant primary structures indicative of flow, including ripples and scour surfaces (dashed line). Abundant trace fossils are also pictured.

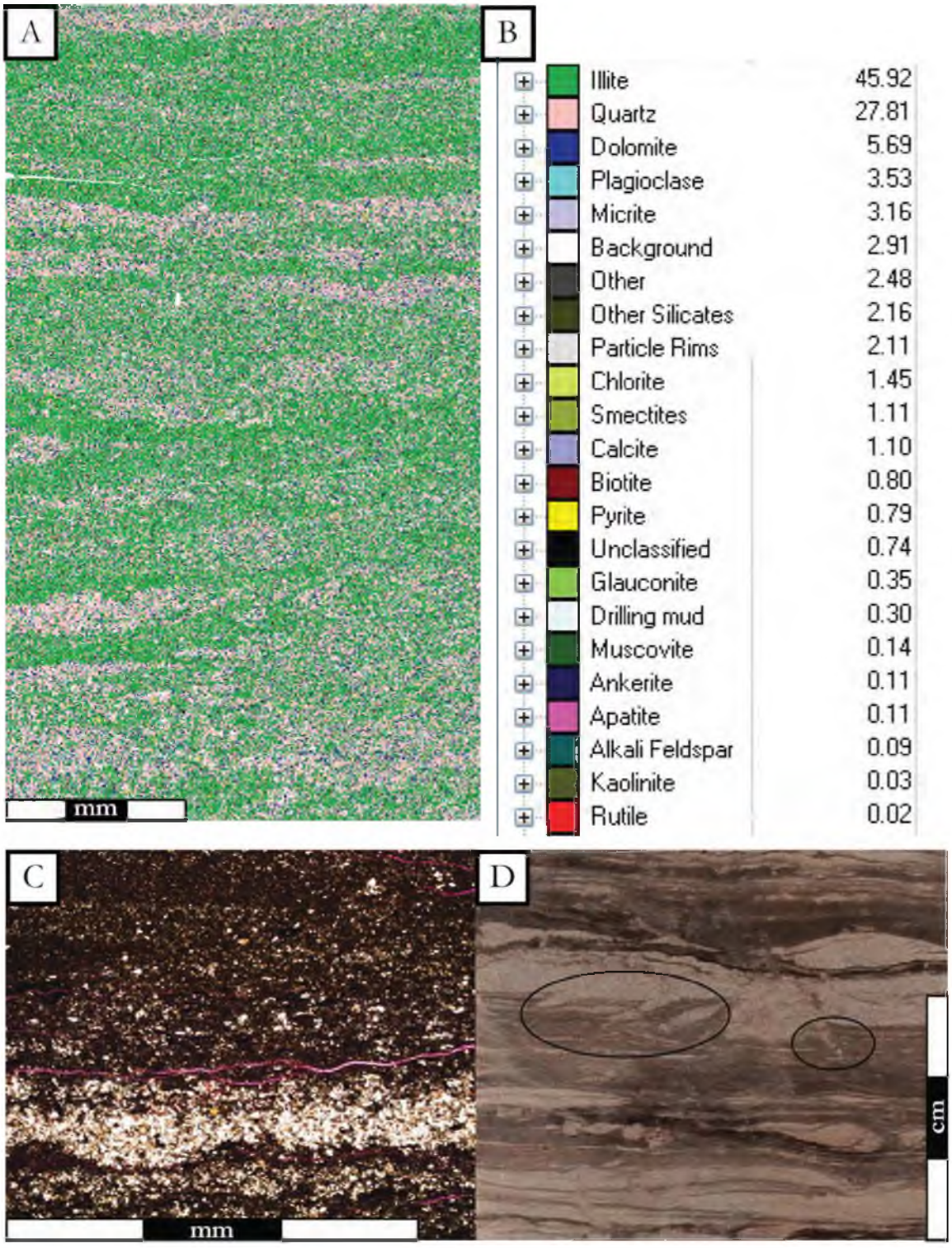

Figure 12: Lithofacies 1 in Questar 8. A) QEMSCAN slide with minerals color coded. B) Table expressing QEMSCAN minerals in area percent. C) Type thin section (9,646'). Scour surfaces are evident where the coarser quartz rich sediment scours the darker clay rich sediment. D) Type core sample (9,705'). Multiple sub-vertical burrows are circled in the center of the image.

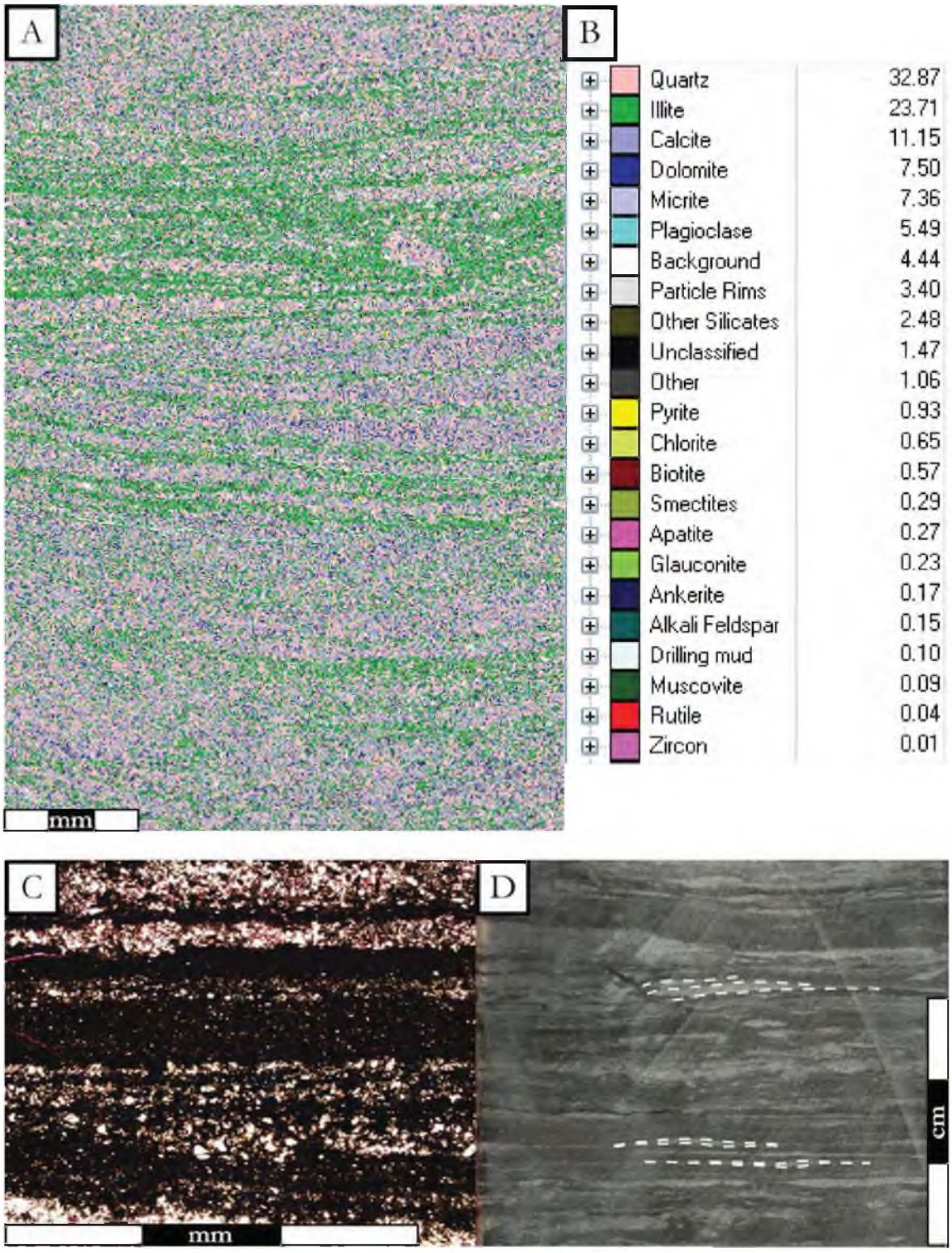

Figure 13: Lithofacies 1 in Questar 16. A) QEMSCAN slide with minerals color coded. B) Table expressing QEMSCAN minerals in area percent. C) Type thin section (15,199'). Well defined laminations exist in both darker clay rich intervals and lighter quartz rich intervals. D) Type core sample (15,261'). Ripples, discontinuous laminations and bioturbation are all evident in this image. Several examples are highlighted with white dashed lines.

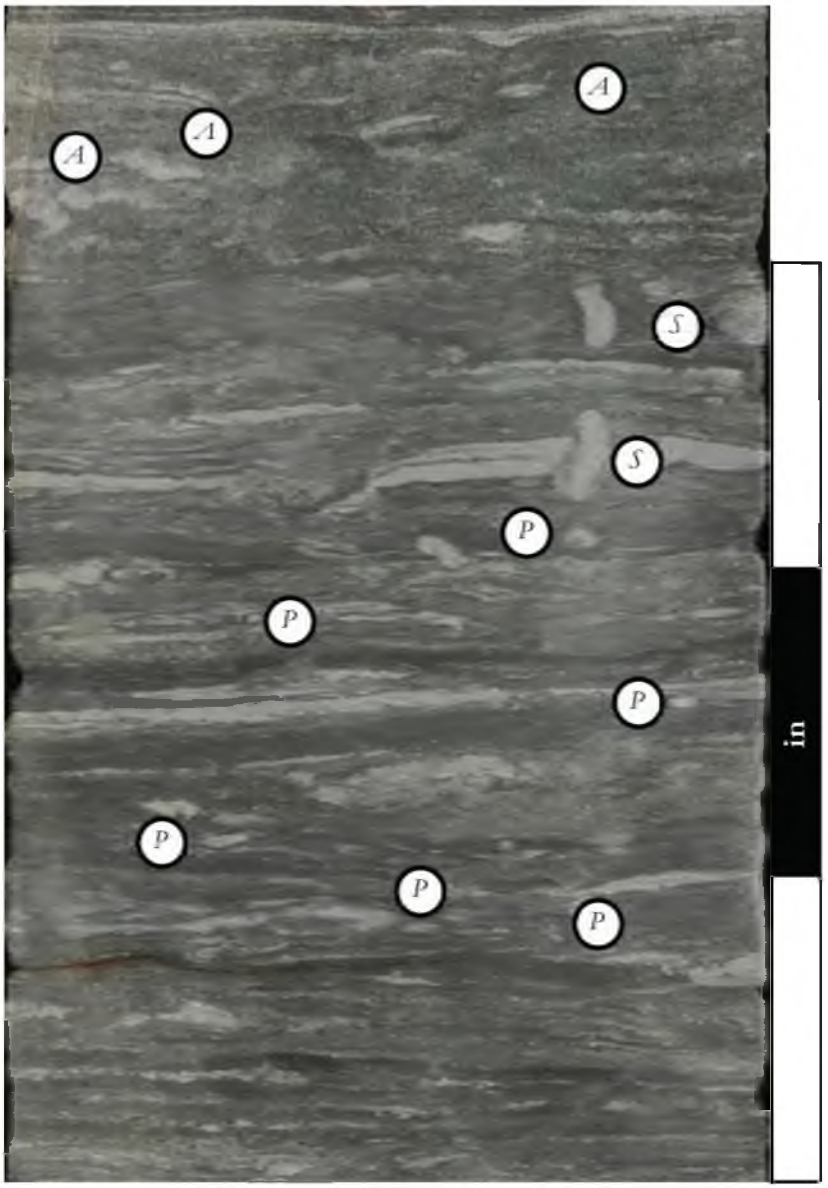

Figure 14: trace fossil assemblage found throughout lithofacies 1. A – Arenicolites, S – Skolithos, P – Planolites. In this image, most of the traces are filled with light colored quartz rich siltstone. Burrows are filled in with dark clay rich material in some other examples. Image from Questar 1, 13,492.7' to 13,493.0' depth.

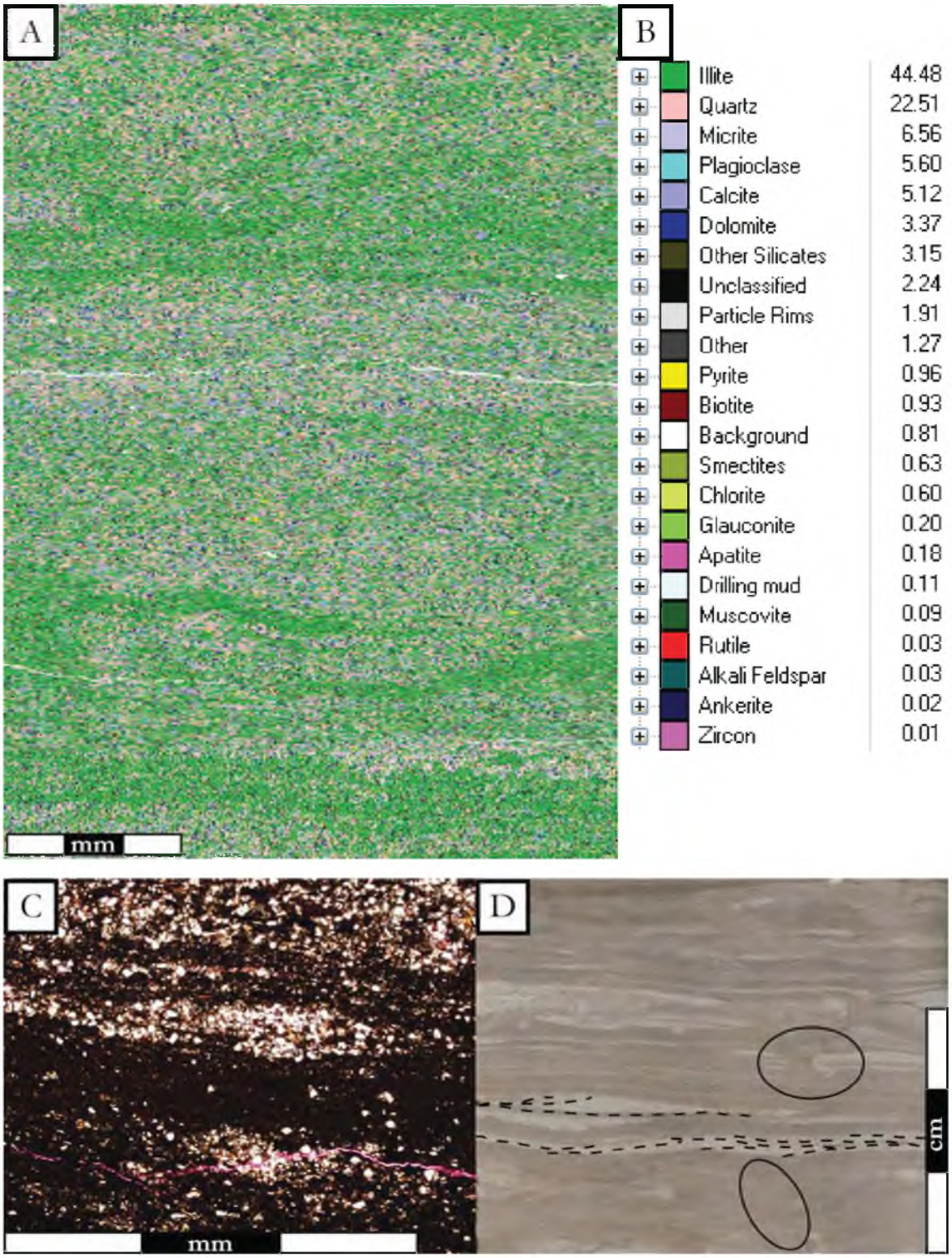

Plate 15: Lithofacies 1 in Pioneer 1. A) QEMSCAN slide with minerals color coded. B) Table expressing QEMSCAN minerals in area percent. C) Type thin section (7,562'). Non-parallel laminations are present, but still well defined between quartz rich and clay rich layers. D) Type core sample (7,560'). Very fine ripple laminations (dashed lines) as well as bioturbation (circled) are evident in this image.

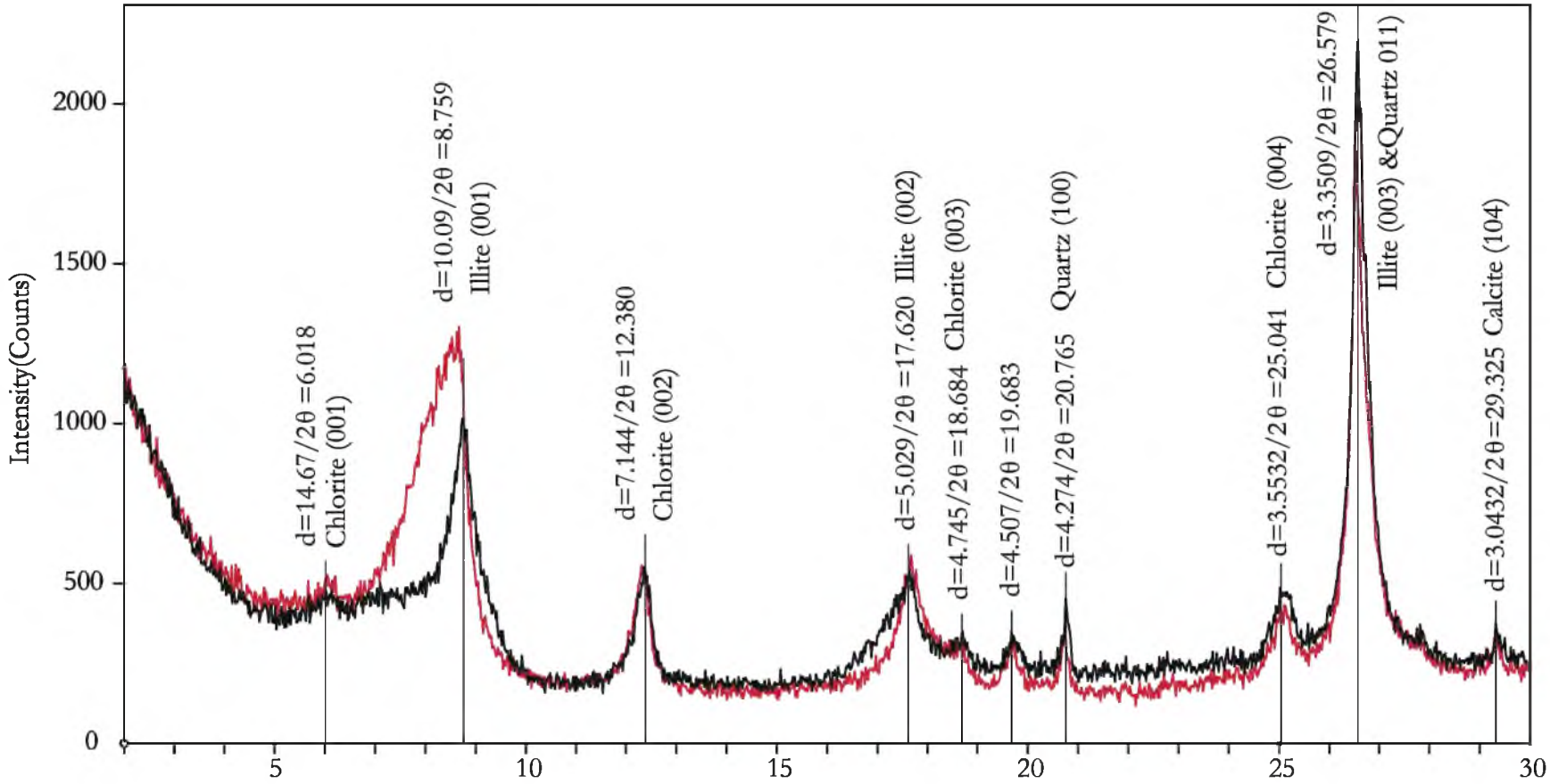

Figure 16: Lithofacies 1 in Questar 1 XRD peaks from oriented sample with minerals identified. Red pattern represents an air dried sample, black pattern represents a glycolated sample.

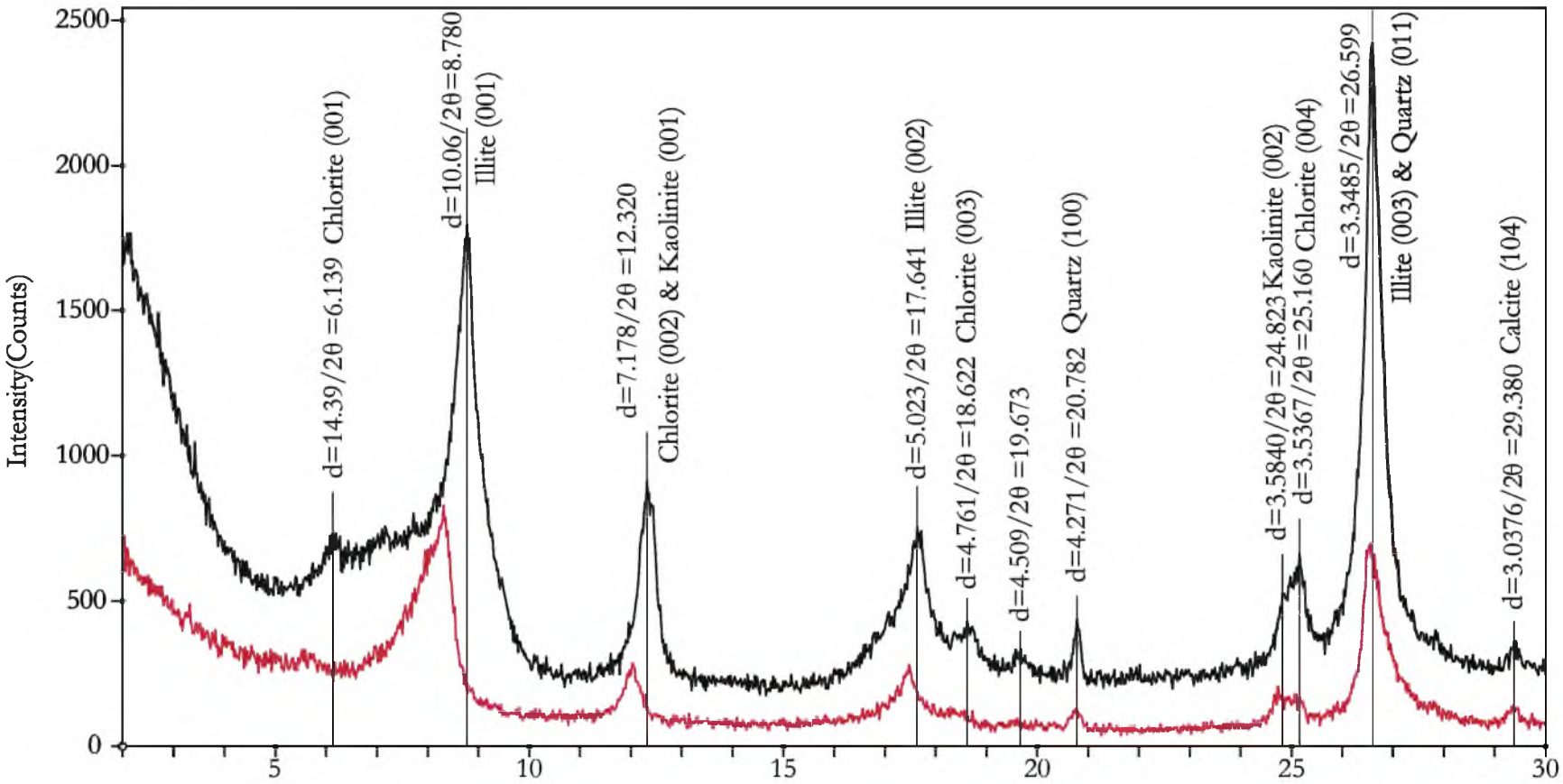

Figure 17: Lithofacies 1 in Questar 8 XRD peaks from oriented sample with minerals identified. Red pattern represents an air dried sample, black pattern represents a glycolated sample.

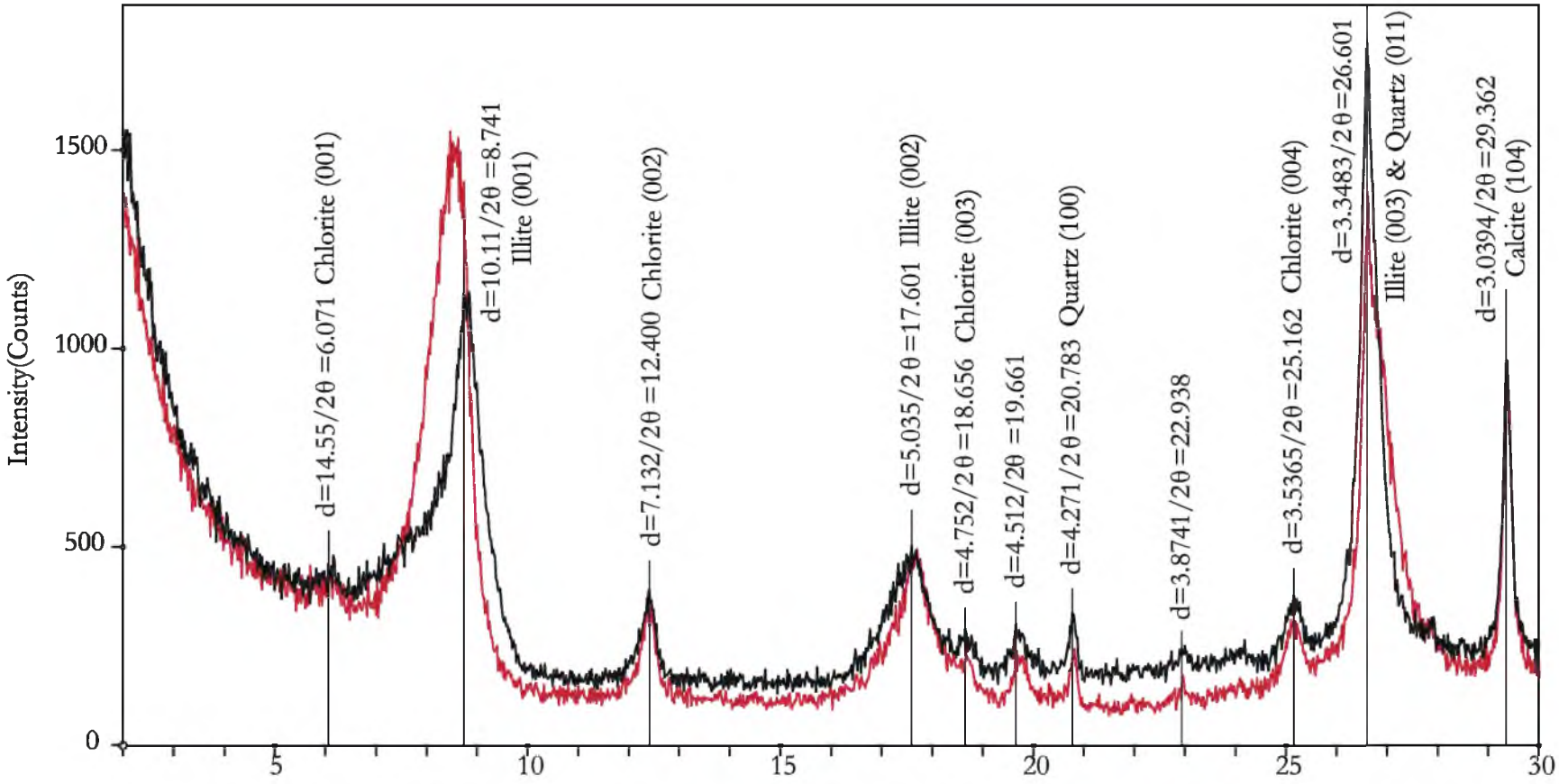

Figure 18: Lithofacies 1 in Questar 16 XRD peaks from oriented sample with minerals identified. Red pattern represents an air dried sample, black pattern represents a glycolated sample.

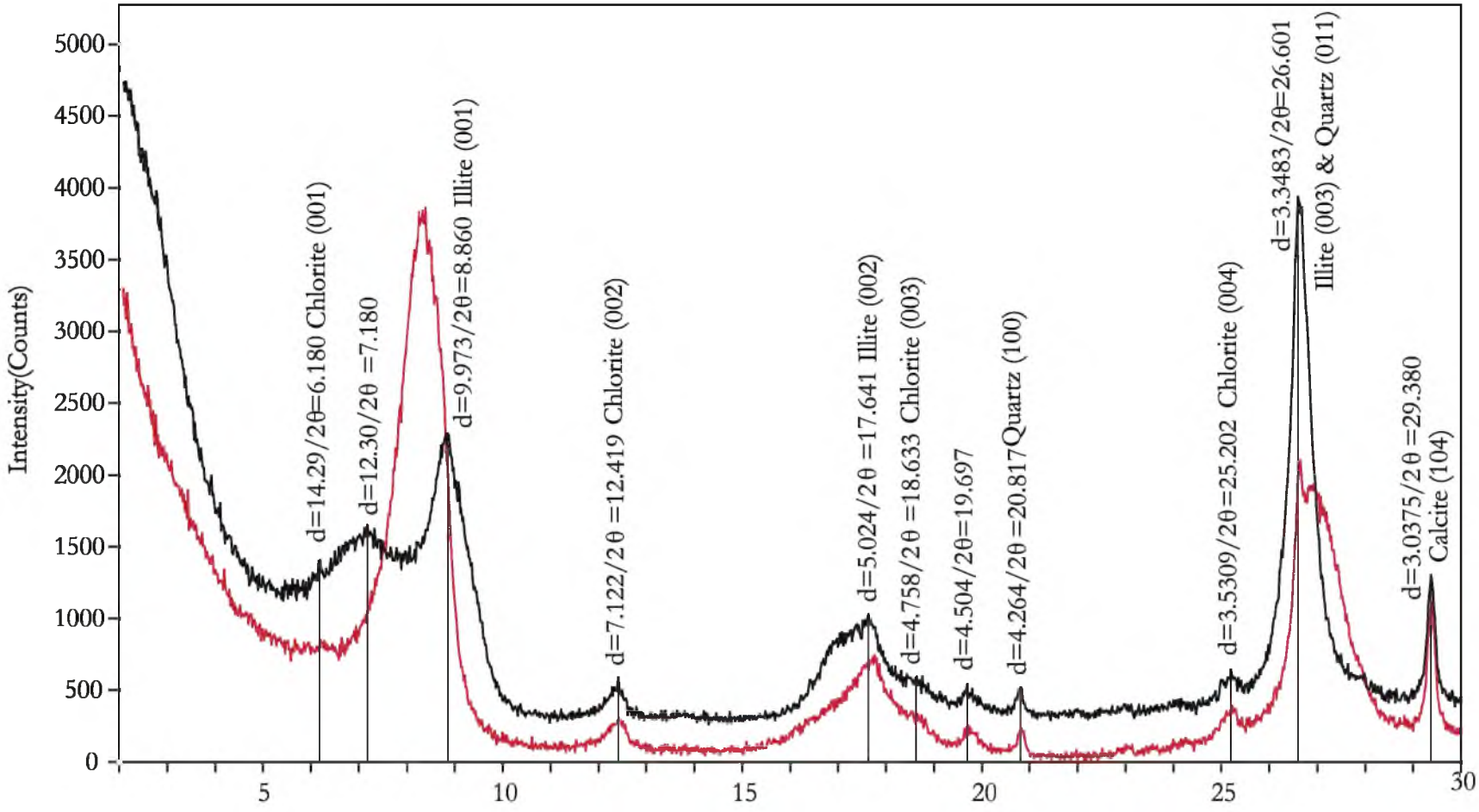

Figure 19: Lithofacies 1 in Pioneer 1 XRD peaks from oriented sample with minerals identified. Red pattern represents an air dried sample, black pattern represents a glycolated sample.

Table 3: Clays identified in glycolated XRD samples across all cored intervals sorted by lithofacies.

Sample	Lithofacies	Brief Description	Smectite	Illite	Kaolinite	Chlorite	Quartz	Calcite
Q1F1	1	Well lam. siltstone dom. sandstone heterolith		X		X	X	X
Q8F2	1	Well lam. siltstone dom. sandstone heterolith		X	X	X	X	X
Q16F1	1	Well lam. siltstone dom. sandstone heterolith		X		X	X	X
P1F3	1	Well lam. siltstone dom. sandstone heterolith		X		X	X	X
Q1F2	2	Poor lam. siltstone dom. sandstone heterolith		X		X	X	X
Q8F3	2	Poor lam. siltstone dom. sandstone heterolith		X	X	X	X	X
Q1F3	3	Dewatered siltstone dom. sandstone heterolith		X	X	X	X	X
Q1F4	4	Claystone rich poor lam. siltstone		X		X	X	
Q8F4	4	Claystone rich poor lam. siltstone		X	X	X	X	X
Q1F5	5	Admixed siltstone and sandstone		X	X	X	X	
P1F2	5	Admixed siltstone and sandstone		X		X	X	X
Q16F2	6	Rhythmically bedded horiz. laminated siltstone		X		X	X	X
P1F5	6	Rhythmically bedded horiz. laminated siltstone		X		X	X	X
P2F5	6	Rhythmically bedded horiz. laminated siltstone		X	X	X	X	X
Q16F3	7	Extensively bioturbated siltstone		X		X	X	
P2F6	8	Massive Siltstone		X	X	X	X	X
P1F1	9	Intensely laminated sandstone dom. siltstone heterolith		X		X	X	X
P2F7	11	Claystone dom. siltstone heterolith		X	X	X	X	X
RF1			X	X	X	X (no 001)	X	X
RF2			X	X	X	X	X	X
RF4			X	X	X	X	X	X
RF5			X	X	X	X	X	X
RF6				X	X		X	
RF9			X	X	X	X	X	X

Table 4: TOC values for each lithofacies along with sample size description (Figure 20).

Lithofacies	Max	Min	Mean	StDev	n
1	1.85	0.68	1.13	0.24	83
2	1.24	0.92	1.06	0.13	11
3	1.23	0.97	1.07	0.08	9
4	1.42	0.87	1.14	0.14	18
5	0.95	0.77	0.84	0.10	3
6	2.39	1.11	1.66	0.26	25
7	1.13	0.81	0.98	0.17	3
8	3.25	1.53	2.14	0.57	8
9	no data	no data	no data	no data	0
10	no data	no data	no data	no data	0
11	2.60	1.68	2.11	0.25	25

minerals (Figure 17). Organic carbon values average 1.13% with minimum values of 0.68%, and maximum values of 1.85% (Table 4; Figure 20).

QEMSCAN results largely agree with the XRD data. Calculated mineral percentages are widely variable, due to the variability associated with precise sample selection. Over a large interval (greater than one foot) the lithofacies are very similar. On a three centimeter slide, however, there can be considerable variability in the number and thickness of laminations. Questar 1 and Questar 8 slides show approximately 45 percent area of quartz and 27 to 29 area percent of illite (Figure 11; Figure 12). Conversely, Questar 16 and Pioneer 1 slides suggest 32 to 22 area percent coverage by quartz, and 17 to 44 area percent coverage by illite (Figure 13; Figure 15). While this variation is great, it is clear that this is caused by an increased number of sand laminations present in Questar 16 and Pioneer 1 relative to Questar 1 and Questar 8. Indeed, lamination thickness can vary dramatically even within a single 3 centimeter slide. In Questar 16, the thickest laminations are nearly two millimeters thick, and the thinnest quartz rich laminations are no greater than a half of a millimeter (Figure 13).

QEMSCAN data disagree slightly with XRD data from a mineralogical standpoint. QEMSCAN data identify kaolinite in Questar 1 (Table 5), where XRD showed no evidence for kaolinite (Table 3). Additionally, QEMSCAN data suggest the presence of slight amounts of smectite in all four instances of lithofacies 1, and indeed in all samples for all cored intervals (Table 5). It is likely that the smectite is present in the cores as interstratified illite/smectite. This interstratification occurs as a result of burial. When ratios of illite to smectite exceed 95% illite, the interstratified peak appears as a slightly broader peak of illite. Thus, the illite peak can represent interstratified illite smectite of sufficiently illite rich

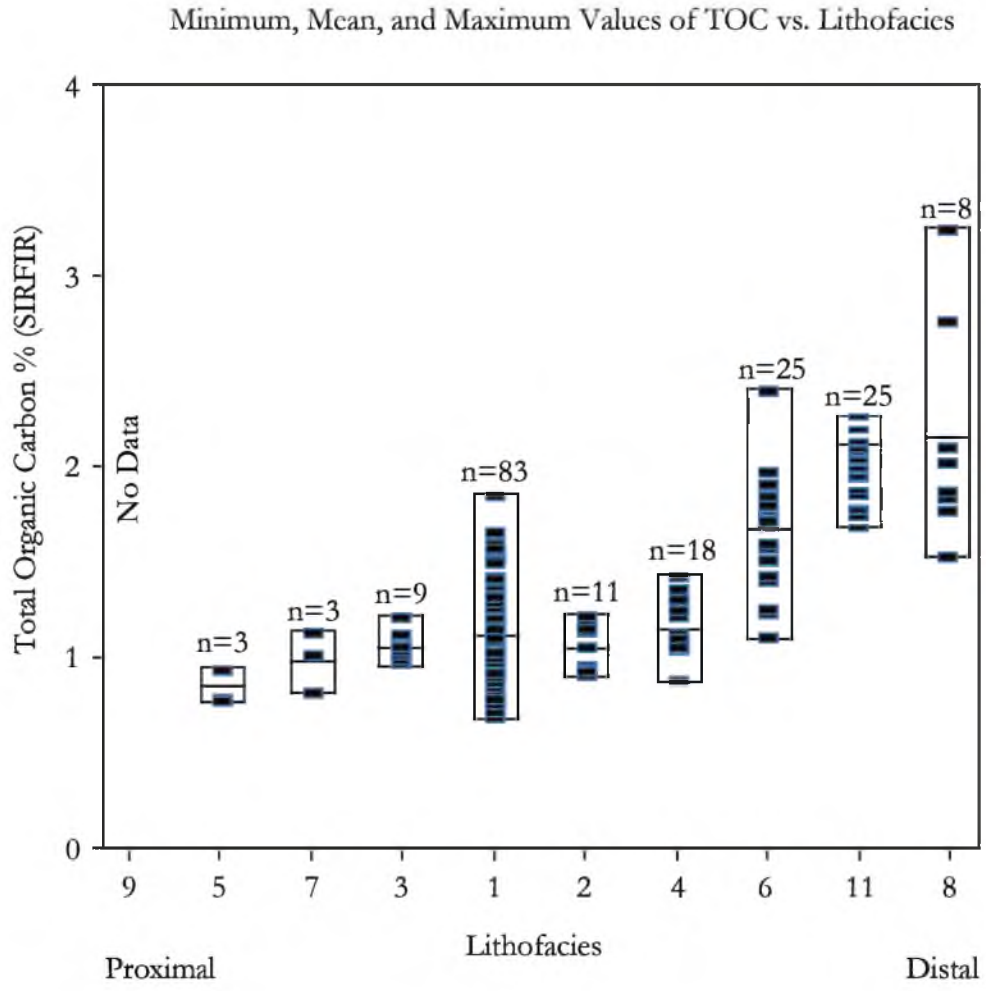

Figure 20: Total organic carbon percentages vs. lithofacies. Minimum, maximum and mean values are plotted vertically for each lithofaceis (sorted by proximity to shoreline), along with the number of datapoints that constitute each lithofacies. Most proximal lithofacies have mean values that are systematically lower than more distal lithofacies. The most distal lithofacies (6, 8, and 11 - found on the sediment starved shelf) have distinctly higher TOC values than mudbelt lithofacies.

Table 5: Clays identified by QEMSCAN analysis sorted by lithofacies.

Sample	Lithofacies	Brief Description	Smectite	Illite	Kaolinite	Chlorite	Quartz	Calcite
Q1F1	1	Well lam. siltstone dom. sandstone heterolith	1.09	45.56	0.05	1.34	29.45	3.95
Q8F2	1	Well lam. siltstone dom. sandstone heterolith	1.11	45.92	0.03	1.45	27.81	4.26
Q16F1	1	Well lam. siltstone dom. sandstone heterolith	0.29	23.71	0.00	0.65	32.87	18.51
P1F3	1	Well lam. siltstone dom. sandstone heterolith	0.63	44.48	0.00	0.60	22.51	11.68
Q1F2	2	Poor lam. siltstone dom. sandstone heterolith	1.62	46.76	0.33	1.23	26.54	3.89
Q8F3	2	Poor lam. siltstone dom. sandstone heterolith	1.09	50.92	0.08	1.17	23.92	4.98
Q1F3	3	Dewatered siltstone dom. sandstone heterolith	1.15	51.52	0.04	0.93	24.21	3.72
Q1F4	4	Claystone rich poor lam. siltstone	1.00	41.90	0.03	2.35	31.71	3.48
Q8F4	4	Claystone rich poor lam. siltstone	1.40	57.87	0.11	1.13	19.68	3.57
Q1F5	5	Admixed siltstone and sandstone	1.09	36.14	0.15	1.22	40.59	2.54
P1F2	5	Admixed siltstone and sandstone	0.59	28.09	0.01	0.84	39.86	9.17
Q16F2	6	Rhythmically bedded horiz. laminated siltstone	0.63	42.17	0.00	0.80	29.92	10.24
P1F5	6	Rhythmically bedded horiz. laminated siltstone	1.24	54.49	0.00	0.29	13.48	10.12
P2F5	6	Rhythmically bedded horiz. laminated siltstone	0.74	35.33	0.18	0.27	25.73	17.44
Q16F3	7	Extensively bioturbated siltstone	0.61	39.58	0.00	0.90	31.31	8.72
P2F6	8	Claystone dom. siltstone heterolith	1.04	48.16	0.04	0.16	18.61	13.13
P1F1	9	Intensely laminated sandstone dom. siltstone heterolith	0.19	17.20	0.00	0.23	39.72	26.31
P2F7	11	Massive siltstone	1.09	45.31	0.06	0.24	17.48	14.63

samples. In these samples, illite represents roughly 98% of the illite and smectite, and thus, it is unsurprising no separate interstratified peak can be identified.

Lithofacies 2 – Poorly Laminated Siltstone Dominated Sandstone Heterolith

Lithofacies 2 occurs in the Questar 1 and Questar 8 cored intervals (Table 2; Figure 6; Figure 7). Lithofacies 2 is a fine to medium grained siltstone with very few very fine sandstone interlaminations as well as medium to coarse siltstone interlaminations (Table 2; Figure 21; Figure 22). Claystone laminations are more prevalent in lithofacies 2 than lithofacies 1. Sandstone laminations are commonly discontinuous through the width of the core (Figure 21; Figure 22). Ripples and low angle laminations are uncommon, but can occur in siltstone and sandstone interlaminations (Figure 22). Bioturbation index generally ranges between 2 and 3, but higher bioturbation index values can exist locally up to a value of 5 (Figure 21; Figure 22). This lithofacies is generally non-reactive with hydrochloric acid, but very minor reactions were rarely observed (Figure 6; Figure 7). These minor reactions were more common in the Questar 1 core (Figure 6).

X-ray diffraction data was analyzed from both the Questar 1 and Questar 8 cores (Table 3; Figure 23; Figure 24). Similar to lithofacies 1, the Questar 1 core had illite, chlorite, quartz and calcite composing clay sized particles, and the Questar 8 included kaolinite in the mineralogical assemblage (Figure 23; Figure 24)). Organic carbon values average 1.06% with minimum values of 0.92%, and maximum values of 1.24% (Table 4; Figure 20).

QEMSCAN results largely agree with the XRD data. Structures and laminations bear a striking resemblance to those found in lithofacies 1, with distinct quartz bearing laminations set against illite rich laminations. Kaolinite was identified in both Questar 1 and Questar 8 in QEMSCAN data. Kaolinite is absent in the Questar 1 XRD data.

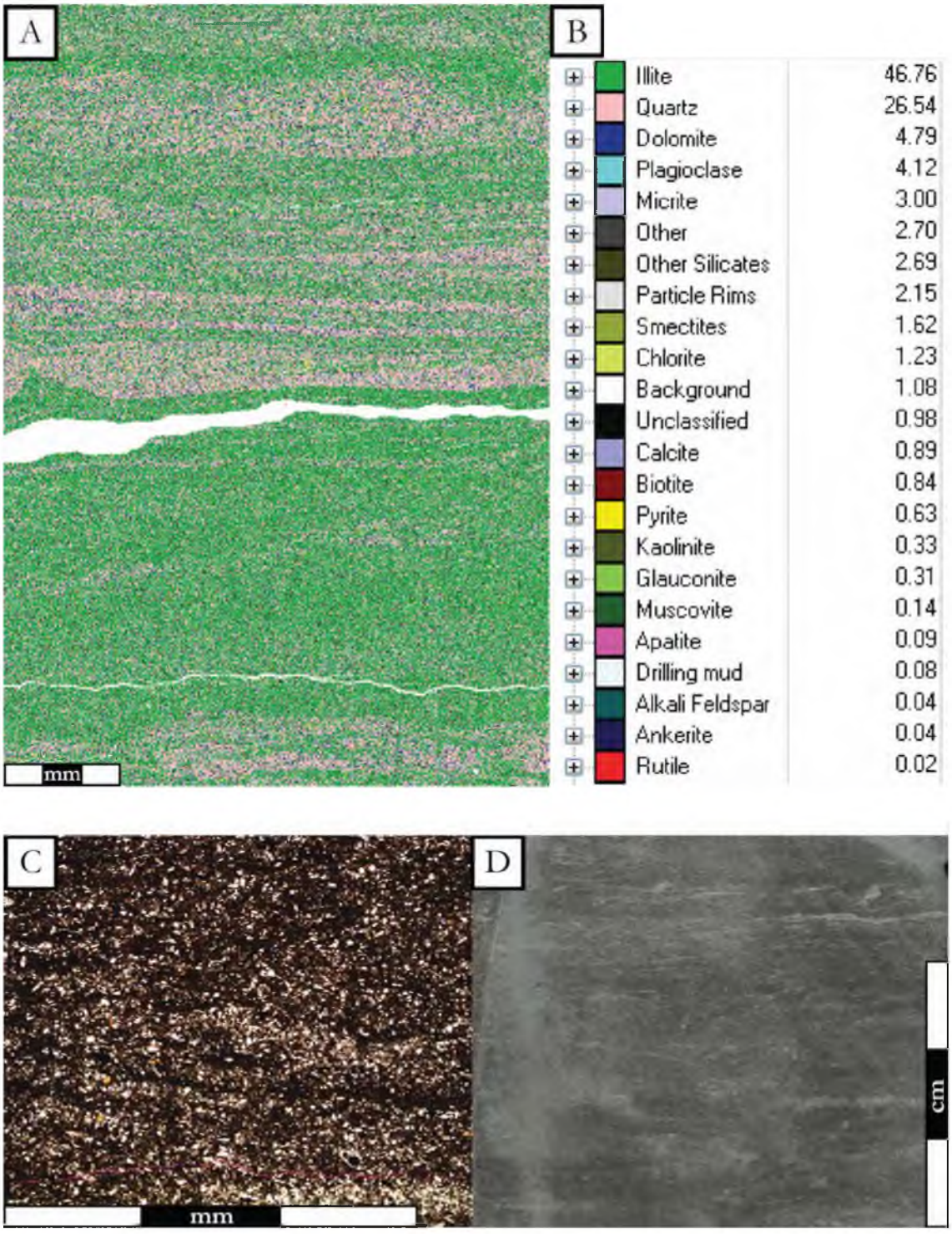

Figure 21: Lithofacies 2 in Questar 1. A) QEMSCAN slide with minerals color coded. B) Table expressing QEMSCAN minerals in area percent. C) Type thin section (13,445'). Laminations are poorly defined. Quartz grains are still present in the sample lending an average grain size that is unchanged from lithofacies 1. D) Type core sample (13,445'). Discontinuous and poorly defined laminations are evident as well as bioturbation.

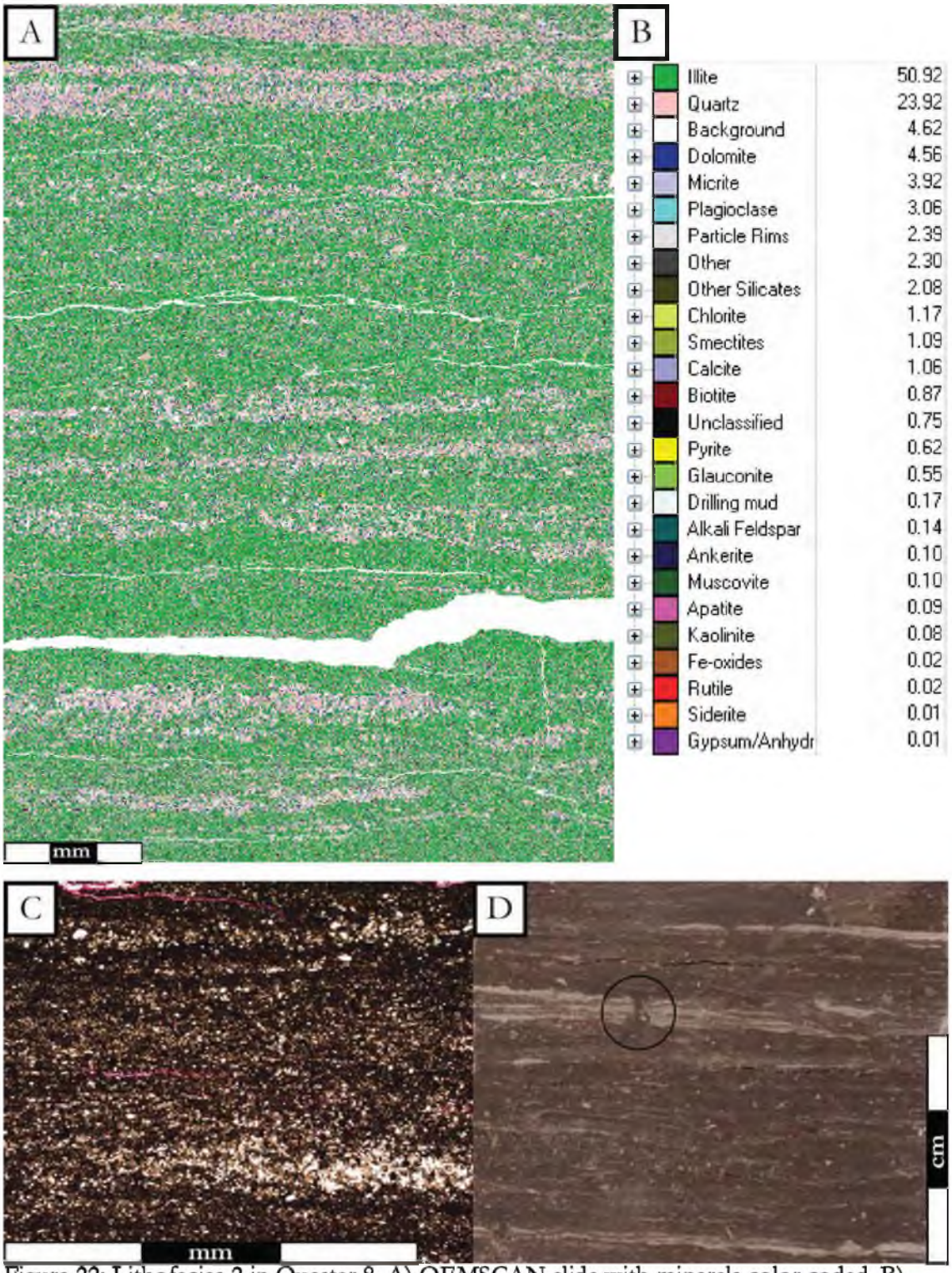

Figure 22: Lithofacies 2 in Questar 8. A) QEMSCAN slide with minerals color coded. B) Table expressing QEMSCAN minerals in area percent. C) Type thin section (9,677'). Some laminations are well defined, but by and large laminations are poorly defined. D) Type core sample (9,661'). Well defined laminations present in the center of the image (circled) are bioturbated. Most laminations are poorly defined or discontinuous.

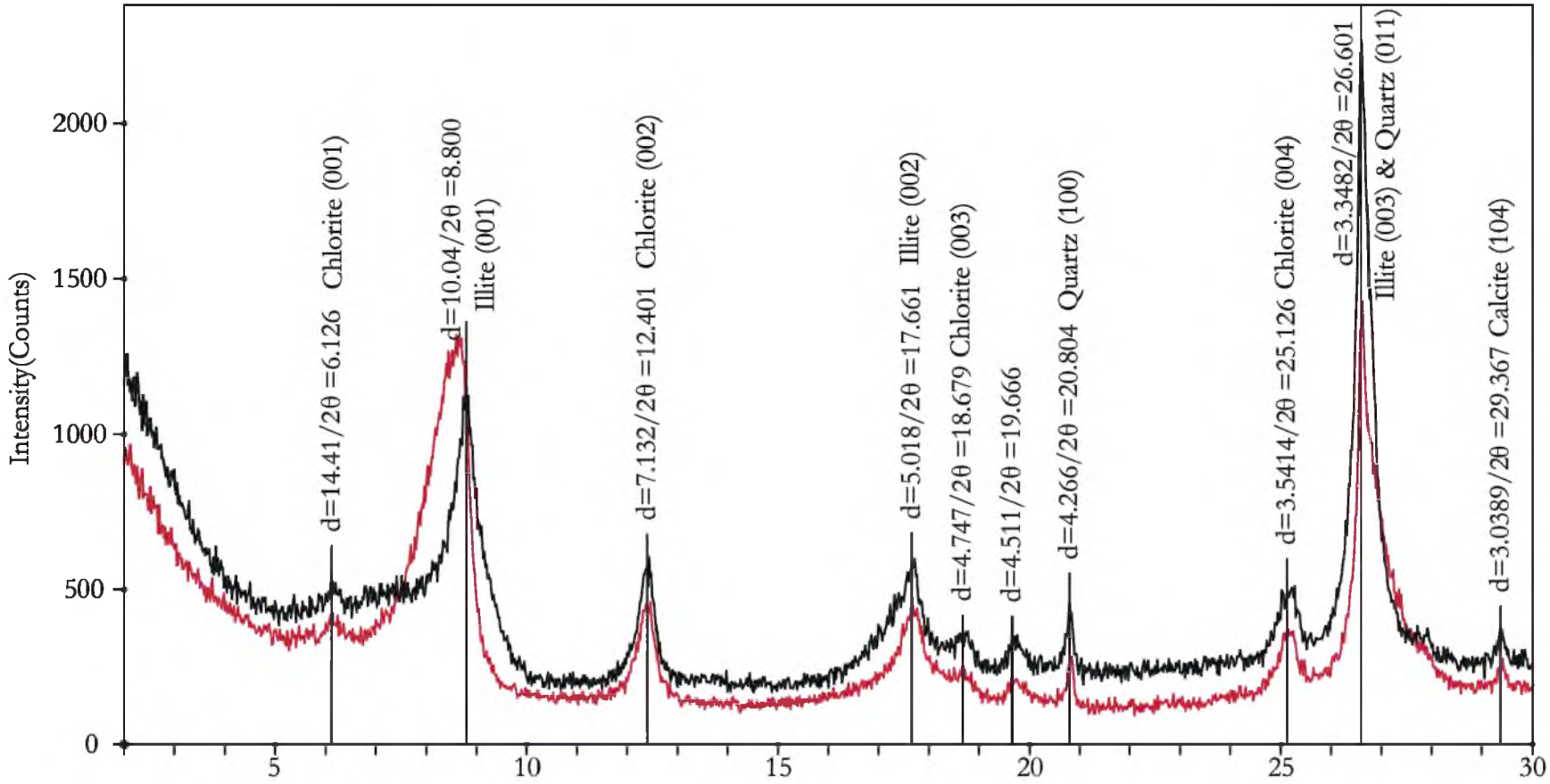

Figure 23: Lithofacies 2 in Questar 1 XRD peaks from oriented sample with minerals identified. Red pattern represents an air dried sample, black pattern represents a glycolated sample.

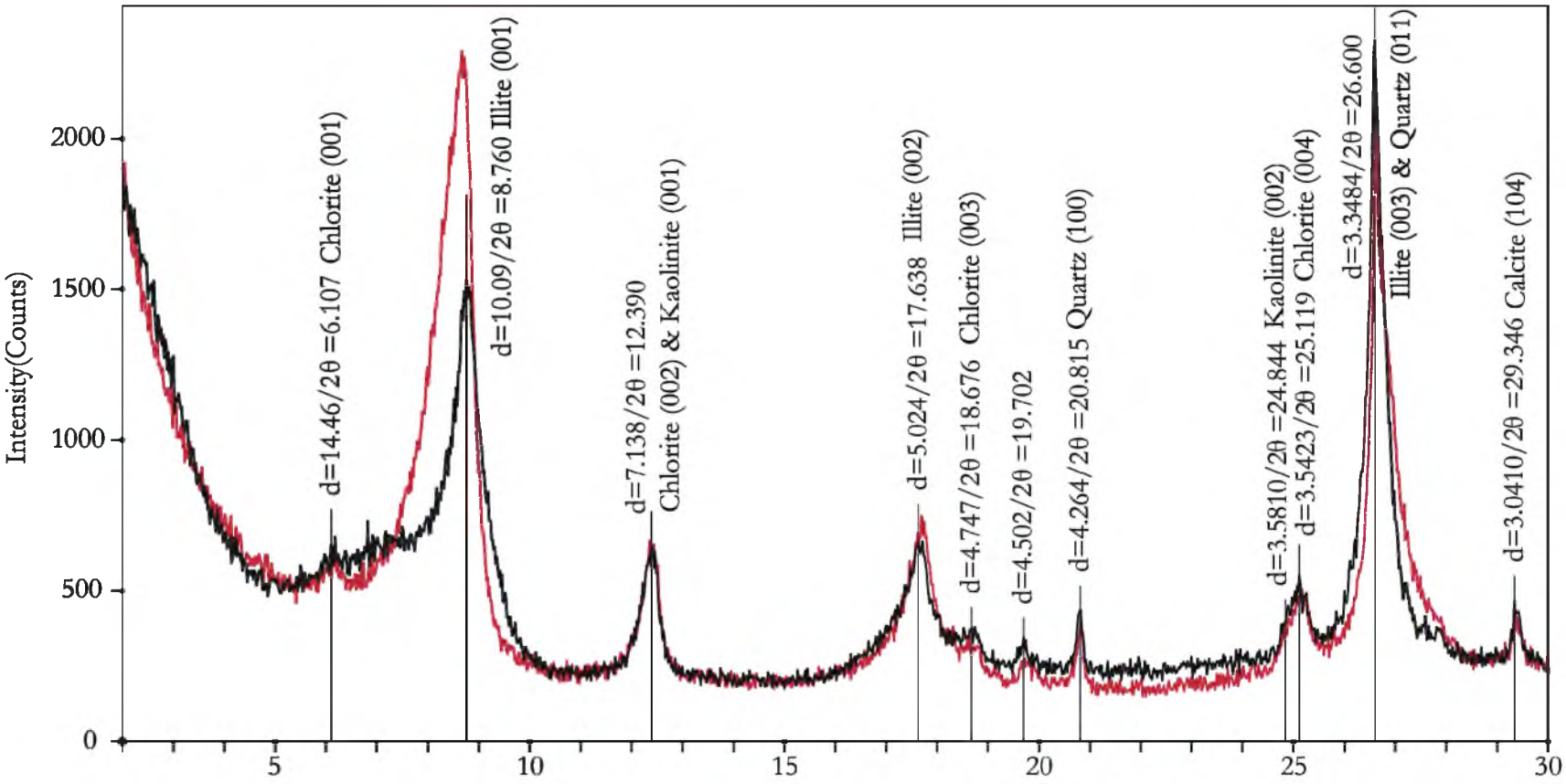

Figure 24: Lithofacies 2 in Questar 8 XRD peaks from oriented sample with minerals identified. Red pattern represents an air dried sample, black pattern represents a glycolated sample.

QEMSCAN data suggest the composition of lithofacies 2 doesn't change dramatically between Questar 1 and Questar 8. Illite accounts for 47% of the area of the slide in Questar 1, and 50% in Questar 8 (Figure 21; Figure 22). Similarly, quartz is the second most abundant mineral accounting for 27% of the area in Questar 1, and 24% in Questar 8 (Figure 21; Figure 22). Both of these datasets show that illite is a more dominant mineral in lithofacies 2 than in lithofacies 1, which agrees with direct observations.

Lithofacies 1 and 2 represent a proximal to distal shift in depositional style. Primary structures that include current ripples and high quartz content suggest that the deposition of lithofacies 1 is dominated by detrital transport from the shelf by undercurrent flows. Lithofacies 2, by contrast, has primary structures such as low angle, discontinuous laminations, and lower quartz content that suggests deposition is accomplished by sediment fallout and winnowing of depositional horizons. Similarly, lithofacies 1 exhibits slightly coarser detrital quartz grains than lithofacies 2. Commonly, however, lithofacies will exhibit features that do not fall exclusively in one category or the other. Lithofacies 1 and 2 are thereby end members on a spectrum of depositional styles (Figure 25).

Lithofacies 3 – De-watered, Siltstone Dominated Sandstone Heterolith

Lithofacies 3 is unique to the Questar 1 core. It is a fine to medium siltstone dominated heterolith consisting of massive siltstone units that vertically and laterally crosscut coarse siltstone to very fine sandstone laminated regions, so that the laminated intervals are discontinuous through the width of the core (Figure 26). In the laminated regions, low angle laminations are common and ripples are very rare (Figure 26). The massive siltstone bodies could be the result of fluid flow throughout the interval, and are interpreted to have formed through dewatering of the sediment. Bioturbation index can approach 3 in the siltstone and sandstone interlaminated regions, but is 0-1 in the massive siltstone layers (Figure 6). This

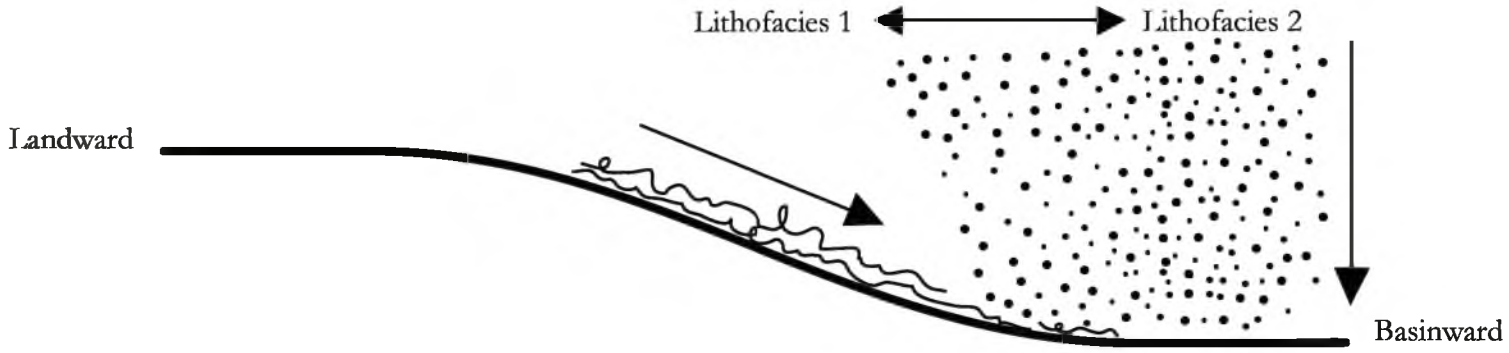

Lithofacies 1 = Traction flow
More proximal
Coarser Grained
Current induced sedimentary structures
Higher sedimentation rate

Lithofacies 2 = Sediment falls out of suspension and winnowing
More distal
Finer grained
Loading induced sedimentary structures (e.g. soft sediment deformation)
Lower sedimentation rate

Figure 25: Schematic illustration of the gradational nature of lithofacies 1 and lithofacies 2. Either lithofacies is an endmember in a spectrum of depositional environments.

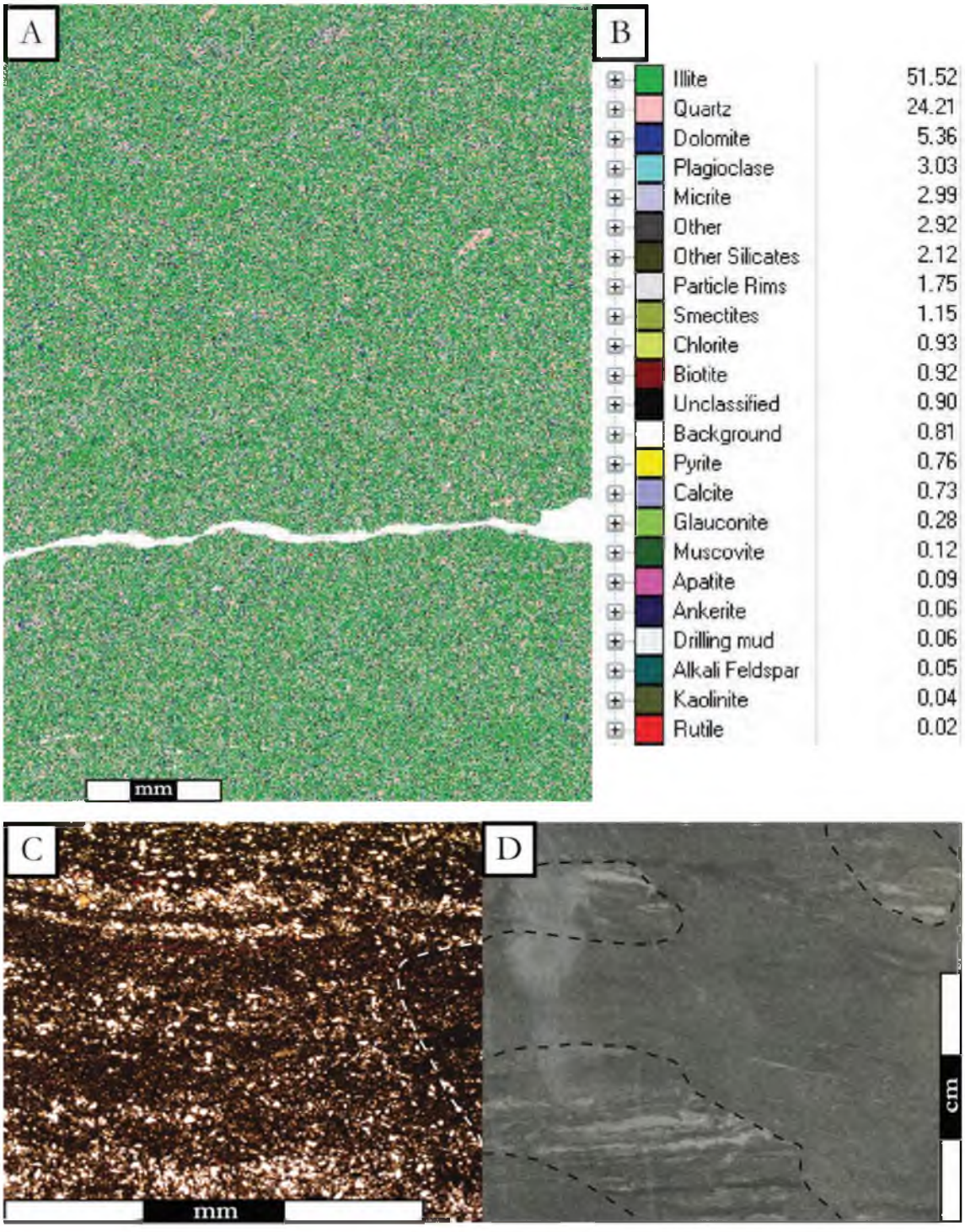

Figure 26: Lithofacies 3 in Questar 1. A) QEMSCAN slide with minerals color coded. B) Table expressing QEMSCAN minerals in area percent. C) Type thin section (13,391') with scale in millimeters. Dewatering structure is present on the far right side (outlined in white). Note that it cross cuts all laminations. D) Type core sample (13,475'). Note that a large dewatering structure cross cuts all laminations (outlined in black). The preserved initially deposited unit closely resembles lithofacies 1.

lithofacies is generally completely nonreactive with hydrochloric acid, but there are a few localized minor reactions, particularly in interlaminated regions. In intervals that are not dewatered, this reaction tends to increase in intensity to slight reactions, as seen in lithofacies 1 (Figure 6).

If the massive siltstone is the result of fluid flow, namely dewatering, originally deposited lithofacies can be identified. Given the frequency with which laminations occur, and given the amount of silt in the nonhomogenized sediment, it seems reasonable to postulate that lithofacies 1 was present prior to the dewatering effects. As previously established, lithofacies 1 represents an environment with a higher rate of sediment influx into the system based on the higher presence of coarser-grained, detrital quartz. If there was a sudden pulse of sediment into an otherwise stable system, the sediment load would increase substantially as well. This increased sediment load resulted in increased pore pressure on the underlying sediment, forcing water occupying pore spaces out of the unit.

We would expect, then, that the deposition of lithofacies 3 should be similar to lithofacies 1 in interpreted sedimentation processes, in that it was dominated by detrital sedimentation transport from the shelf in a higher sedimentation rate regime relative to lithofacies 2. In fact, in most stratigraphic occurrences in the core, lithofacies 3 occurs between lithofacies 2 and 1, suggesting that it represents a shift from lower to higher sedimentation rates that may have initiated dewatering.

X-ray diffraction data from lithofacies 3 indicate that there are small, but nonetheless significant, amounts of kaolinite present in lithofacies 3 (Figure 27), thus not matching either lithofacies 1 or 2 previously mentioned (Table 3). The unique presence of kaolinite could be explained by the chemical composition of dewatering fluid itself. If the fluid was rich in iron, silica, and aluminum, kaolinite could be generated (Rodriguez-Clemente et al., 1987). Such a

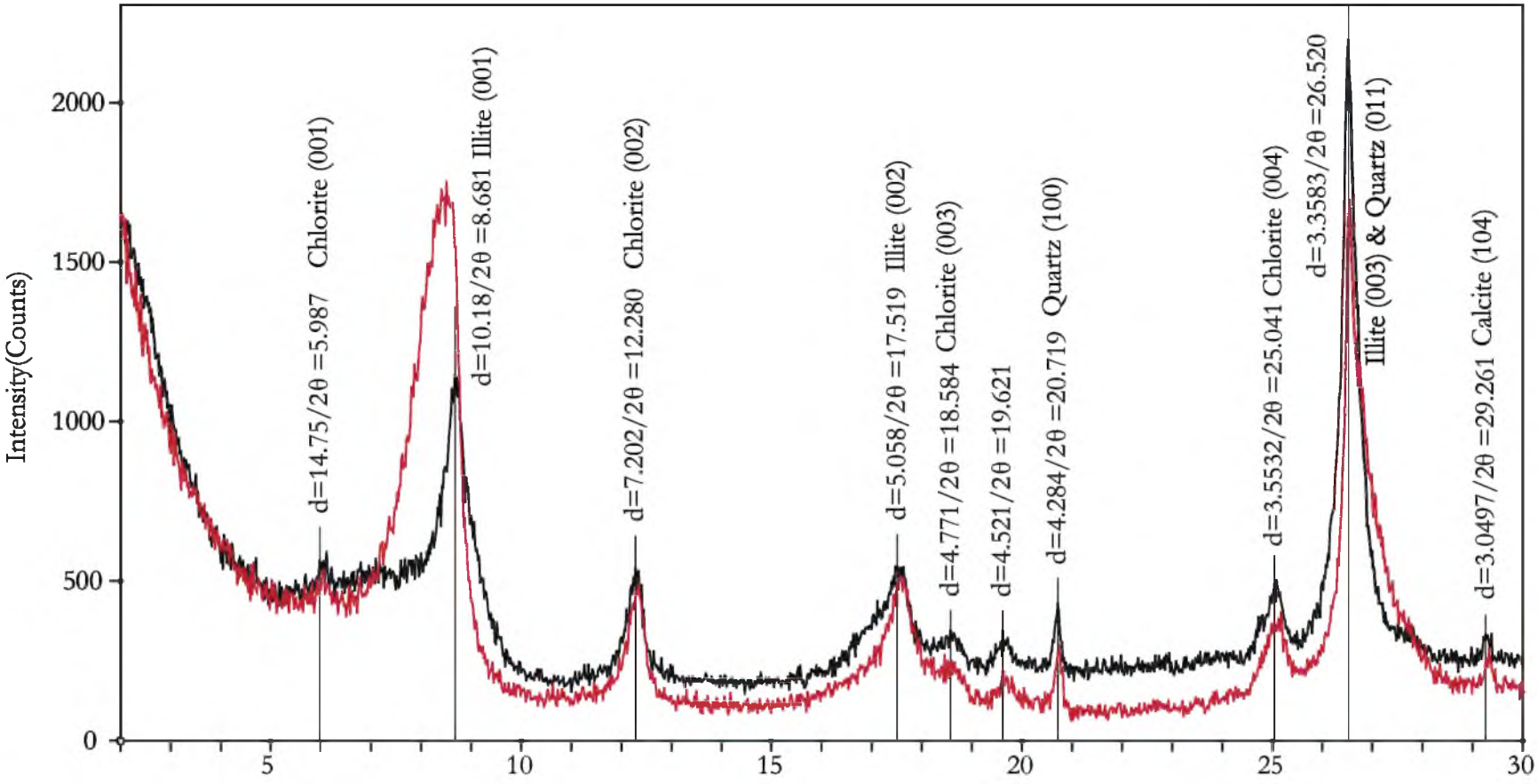

Figure 27: Lithofacies 3 in Questar 1 XRD peaks from oriented sample with minerals identified. Red pattern represents an air dried sample, black pattern represents a glycolated sample.

fluid composition is plausible given the elemental and mineralogical composition of lithofacies 1 and lithofacies 2. Organic carbon values average 1.07% with minimum values of 0.97%, and maximum values of 1.23% (Table 4; Figure 20).

QEMSCAN data further complicates the diagenetic history. As previously mentioned XRD was unable to distinguish kaolinite in Questar 1, but QEMSCAN did identify slight amounts of kaolinite. Thus, an alternate reason for the presence of kaolinite in lithofacies 3 is the presence of kaolinite in the lithofacies that were altered.

QEMSCAN analysis of the massive portions of lithofacies 3 reveal a massive texture at the micron scale as well. The mineralogical composition of lithofacies 3 is most similar to that of lithofacies 2 with 52% of the area composed of illite, and 24% covered by quartz (Figure 26).

Lithofacies 4 – Clay Rich Poorly Laminated Siltstone

Lithofacies 4 occurs in the Questar 1 and Questar 8 cores (Table 2; Figure 6; Figure 7). Lithofacies 4 is a fine to medium grained siltstone with dominantly claystone interlaminations and very few, poorly developed coarse siltstone to very fine sandstone interlaminations (Figure 28; Figure 29). Since there is a dramatically lower sand and silt content in this lithofacies, laminations are far less continuous and frequent. This lithofacies is clay rich, as evidenced by its behavior when sprayed with water. It becomes fragile, swells, and breaks apart. Bioturbation indices are medium to high, with values generally ranging between 3 and 5 (Figure 6; Figure 7). This lithofacies is unique in having a high degree of bioturbation (compared to previous lithofacies) despite low amounts of coarse quartz silt grains. However, the burrows that are evident in the core tend to be quite small, on the sub-millimeter scale (Figure 30). Rarely, small-scale, dewatering structures exist throughout

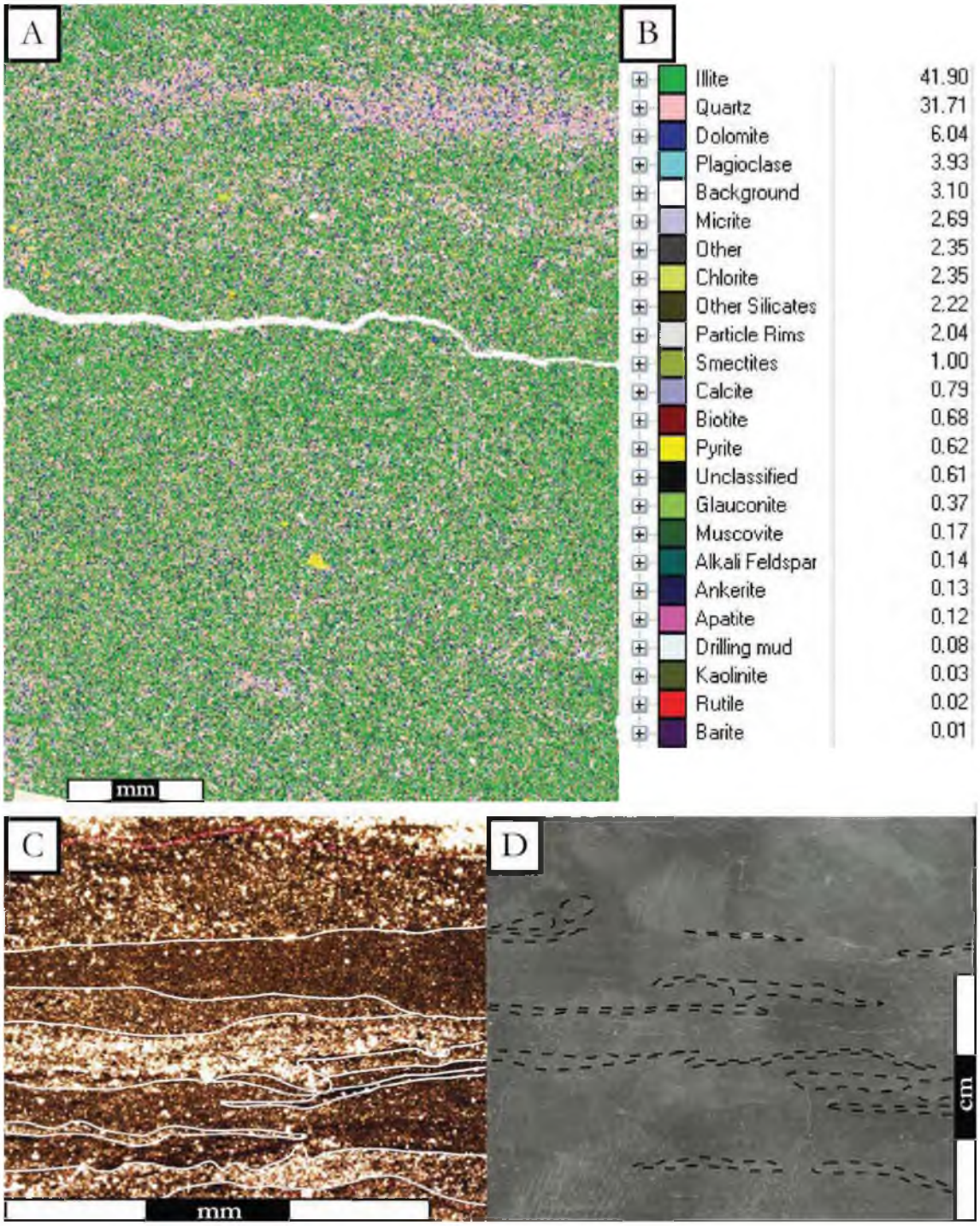

Figure 28: Lithofacies 4 in Questar 1. A) QEMSCAN slide with minerals color coded. B) Table expressing QEMSCAN minerals in area percent. C) Type thin section (13,421'). Quartz rich laminations are less common than in lithofacies 1 or 2 and laminations tend to be mixed rather than exclusively clay or quartz rich. Laminations (outlined in white) are quite distinct in thin section. D) Type core sample (13,436'). Laminations (outlined in black) are very subtle. Color differences between quartz rich and clay rich laminations are muted compared to lithofacies 1 or 2.

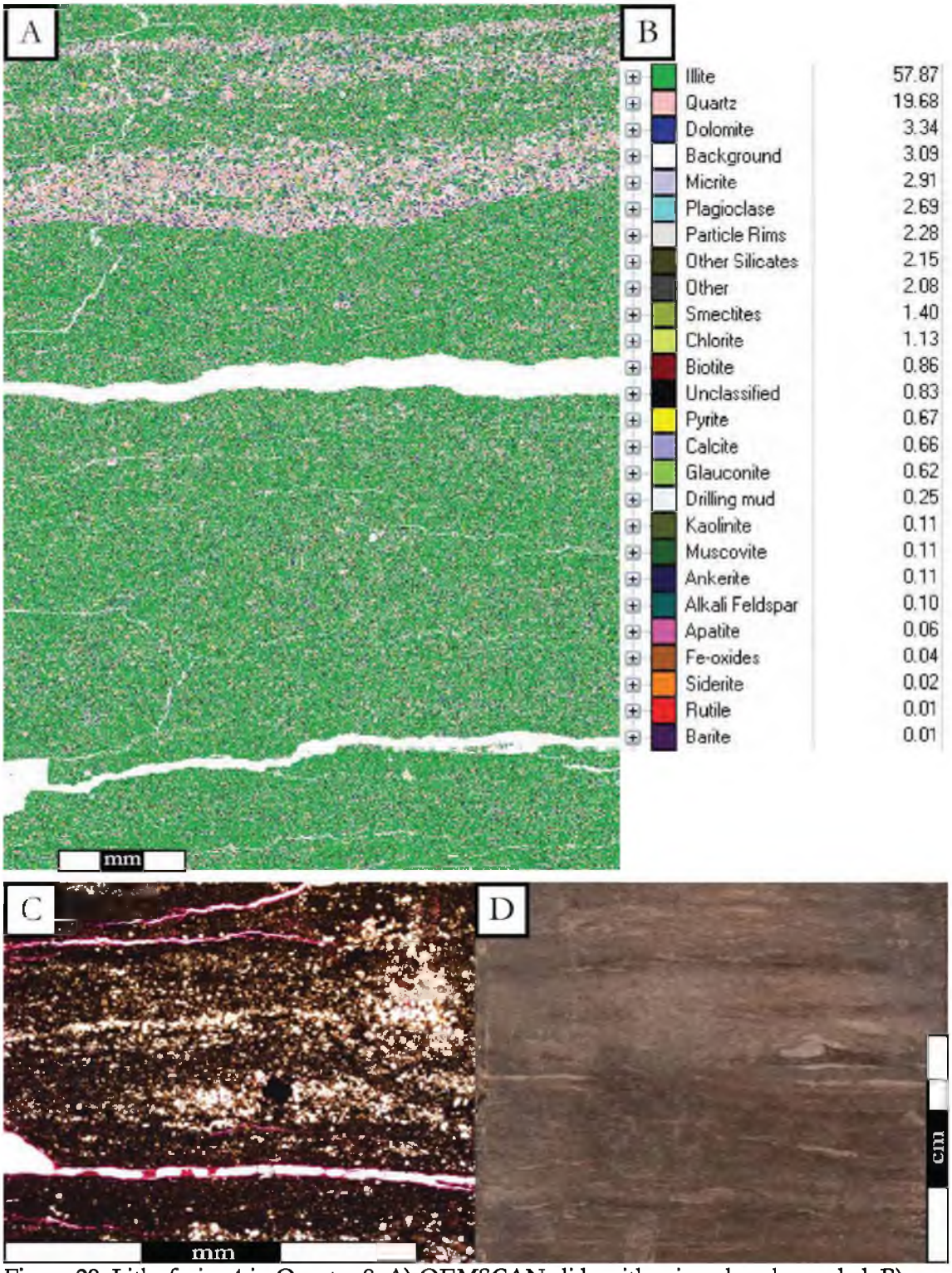

Figure 29: Lithofacies 4 in Questar 8. A) QEMSCAN slide with minerals color coded. B) Table expressing QEMSCAN minerals in area percent. C) Type thin section (9,652'). Clay laminations have gotten significantly thicker and more prevalent. D) Type core sample (9,656'). Rather than distinct heterolithic laminations, there are faint grey laminations agains darker grey laminations.

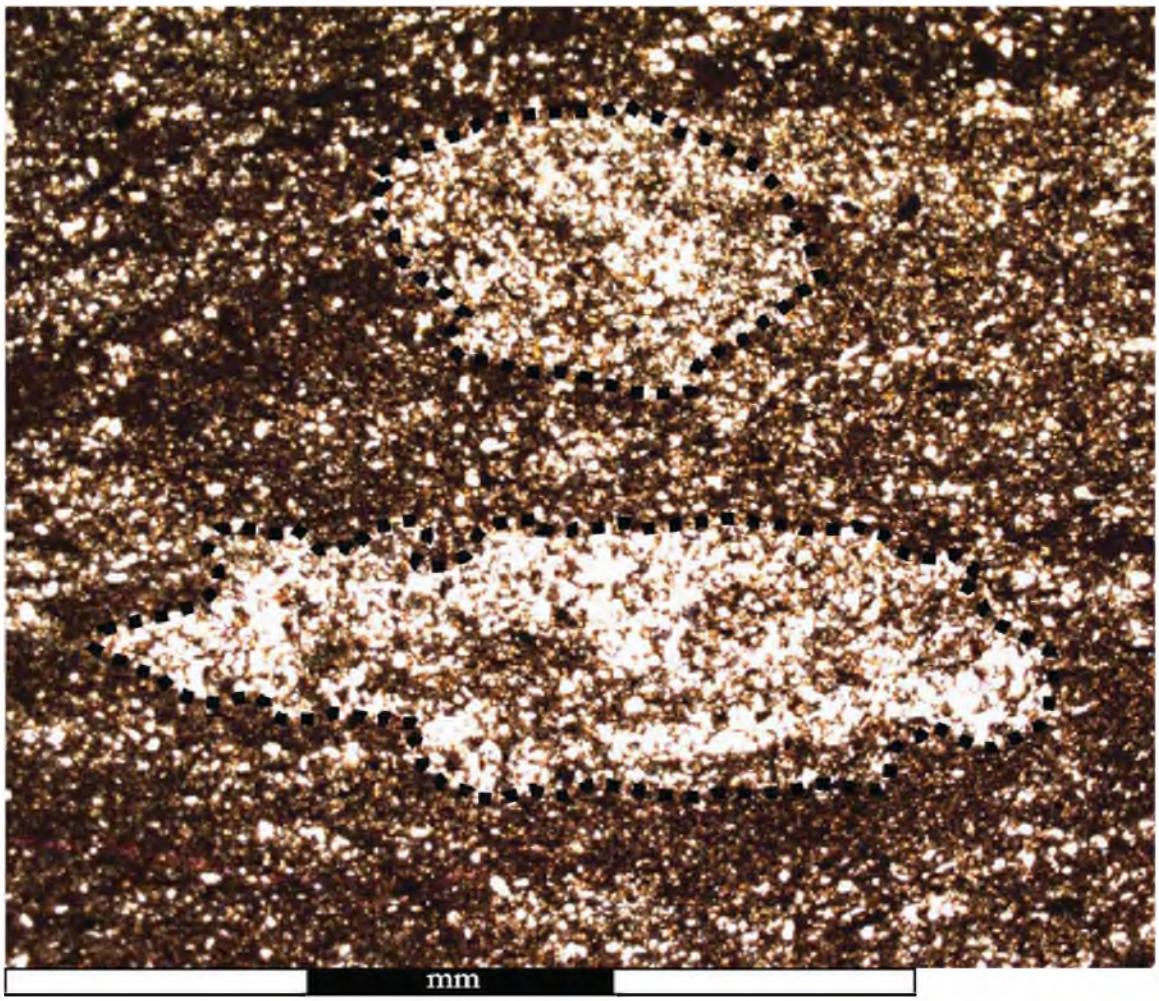

Figure 30: 'Two Planolites (outlined in black) present in the Questar 1 lithofacies 4 at 13,421'. The top Planolites in this image is 1.3 millimeters across, and 730 micrometers tall. The lower is 2.7 millimeters across, and 730 micrometers tall.

Questar 1, but they are far less common than in lithofacies 3. Reactivity with hydrochloric acid is moderate, especially when compared to lithofacies 1 or lithofacies 2, and locally, is strongly reactive (Figure 6; Figure 7).

X-ray diffraction data indicate that in the Questar 8 core, illite, kaolinite, chlorite, quartz, and calcite are all present (Figure 31). However, a sample from Questar 1 contains only illite, chlorite, and quartz (Figure 32; Table 3). In this instance, clay mineralogy is appreciably different between two cores. In the case of kaolinite, Questar 8 was likely in the depositional path of kaolinite whereas Questar 1 was not. Hydrochloric acid reaction tests in the two cores confirm the difference in calcite content (Figure 6; Figure 7). Questar 1 was non-reactive, confirming the lack of calcite. Questar 8 did react, albeit a very slight reaction, supporting the presence of calcite. Organic carbon values average 1.14% with minimum values of 0.87%, and maximum values of 1.42% (Table 4; Figure 20).

QEMSCAN results suggest that calcite is present in nearly identical quantities in both Questar 1 and Questar 8. Due to the limited amounts of calcite present in either core, appropriately oriented calcite grains were not present in the XRD pattern. Additionally, the composition of both samples is dominated by illite accounting for 42% of the area in Questar 1, and 58% of the area in Questar 8 (Figure 28; Figure 29). These values are quite different, considering how both samples contain similar structure – that is both samples have several sand laminations in them. This means that the illite rich laminations must have a different composition between the two cores. Indeed, in Questar 1, very fine quartz grains are present throughout the illite rich matrix (Figure 28), whereas the Questar 8 sample contains limited very fine quartz grains in the illite rich matrix. This suggests further heterogeneity exists within this lithofacies on the micron scale.

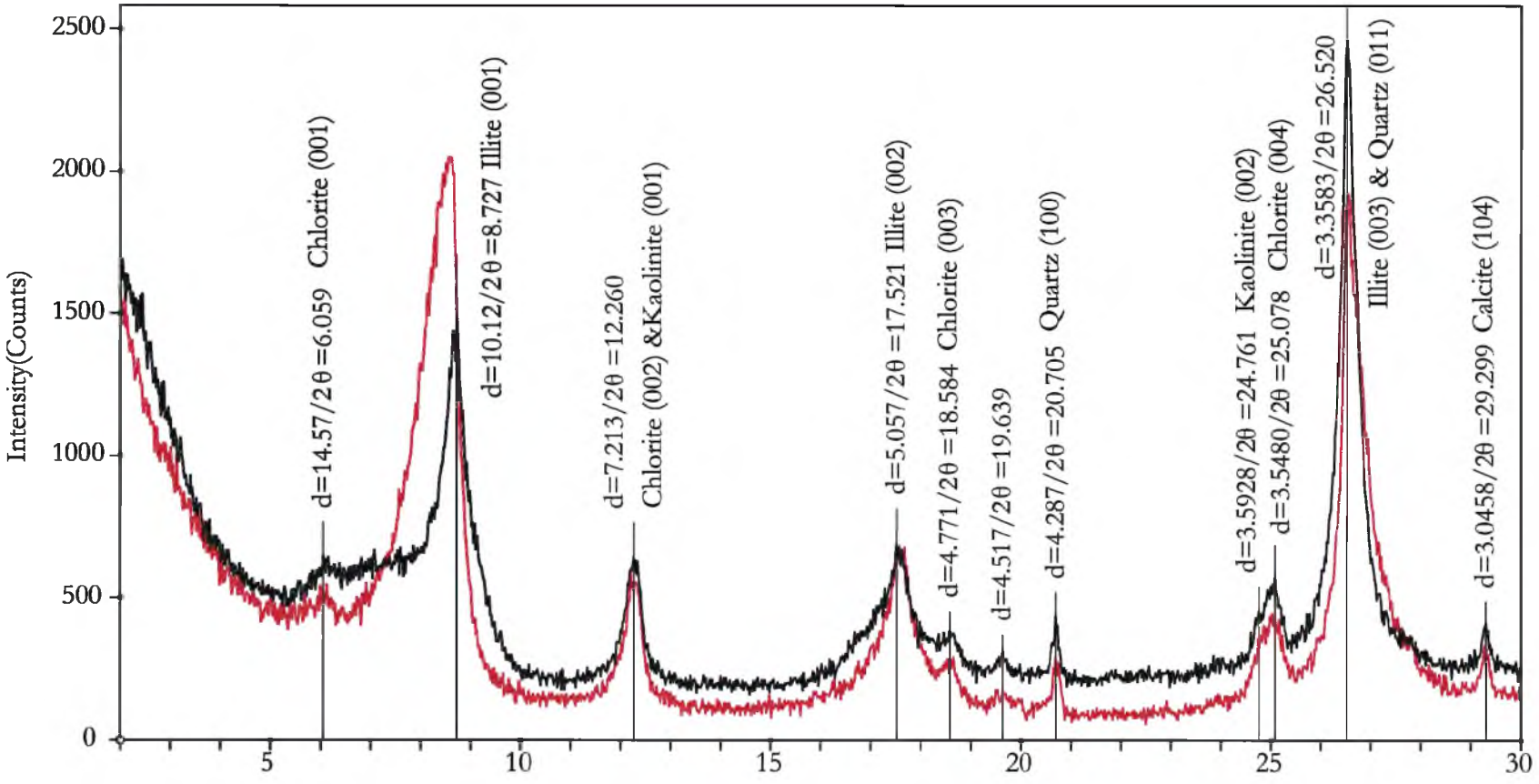

Figure 31: Lithofacies 4 in Questar 8 XRD peaks from oriented sample with minerals identified. Red pattern represents an air dried sample, black pattern represents a glycolated sample.

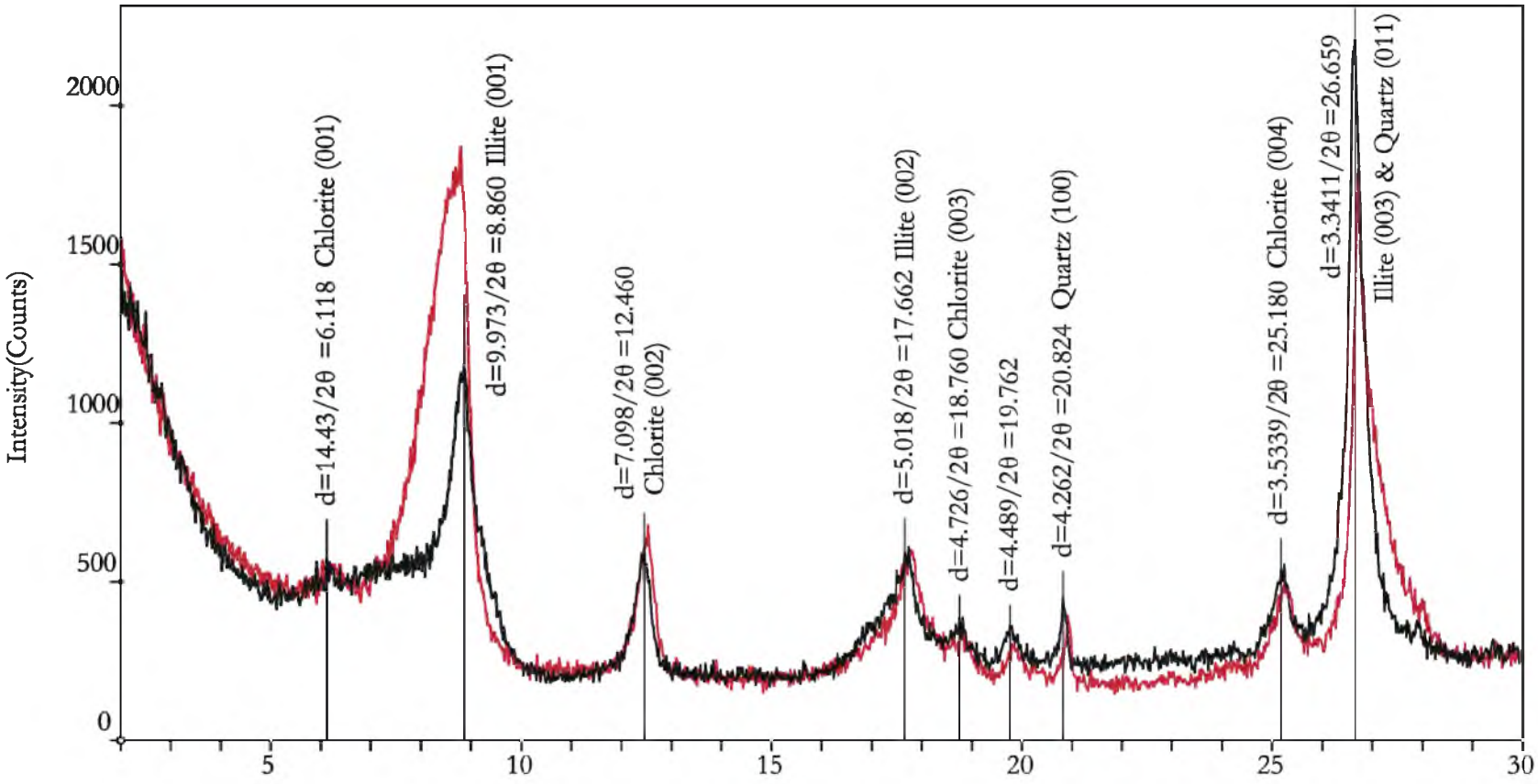

Figure 32: Lithofacies 4 in Questar 1 XRD peaks from oriented sample with minerals identified. Red pattern represents an air dried sample, black pattern represents a glycolated sample.

Lithofacies 5 – Admixed Siltstone and Sandstone

Lithofacies 5 can be found in the Questar 1 and Pioneer 1 cores (Table 2; Figure 6; Figure 9). Lithofacies 5 is a medium siltstone that is admixed with very fine sandstone. This lithofacies is consistently highly bioturbated, which causes the admixed grain sizes, and is distinctly coarser grained relative to other lithofacies (Figure 33; Figure 34). Bioturbation levels range between a 5 and 6 with values of 4 occurring very rarely (Figure 6; Figure 9). The texture is mottled or admixed, and is the result of total (or near total) obliteration of primary structures by bioturbation. Individual burrows are identifiable, and include *Diplocraterion*, *Palaeophycus Heberti, Skolithos, Planolites,* and *Schaubcylindrichnus* (Figure 35).

X-ray diffraction provides differentiation between the Questar 1 lithofacies 5 and the Pioneer 1 lithofacies 5. Both Questar 1 and Pioneer 1 contain illite, chlorite and quartz. However, Questar 1 contains kaolinite and Pioneer 1 contains calcite (Table 3; Figure 36; Figure 37). The disparate location of these cores could explain the difference in calcite and kaolinite content (Figure 5). Organic carbon values average 0.84% with minimum values of 0.77%, and maximum values of 0.95% making it the leanest lithofacies in the study (Table 4; Figure 20).

QEMSCAN analysis shows that Questar 1 is composed of large detrital quartz grains accounting for 41% of the area of the sample, and illite composing 36% of the area of the sample (Figure 33). Pioneer 1 has a very different mineralogical composition with illite being the most dominant mineral composing 44% of the area of the sample, and quartz accounting for only 23% of the sample (Figure 34). The difference in these two compositions is seen in the quartz rich laminations of the samples. In the Questar 1 core, the quartz rich laminations contain almost no illite. Conversely, in the Pioneer 1 core, the quartz rich laminations are in fact diluted by a comparatively large amount of illite. This difference suggests further

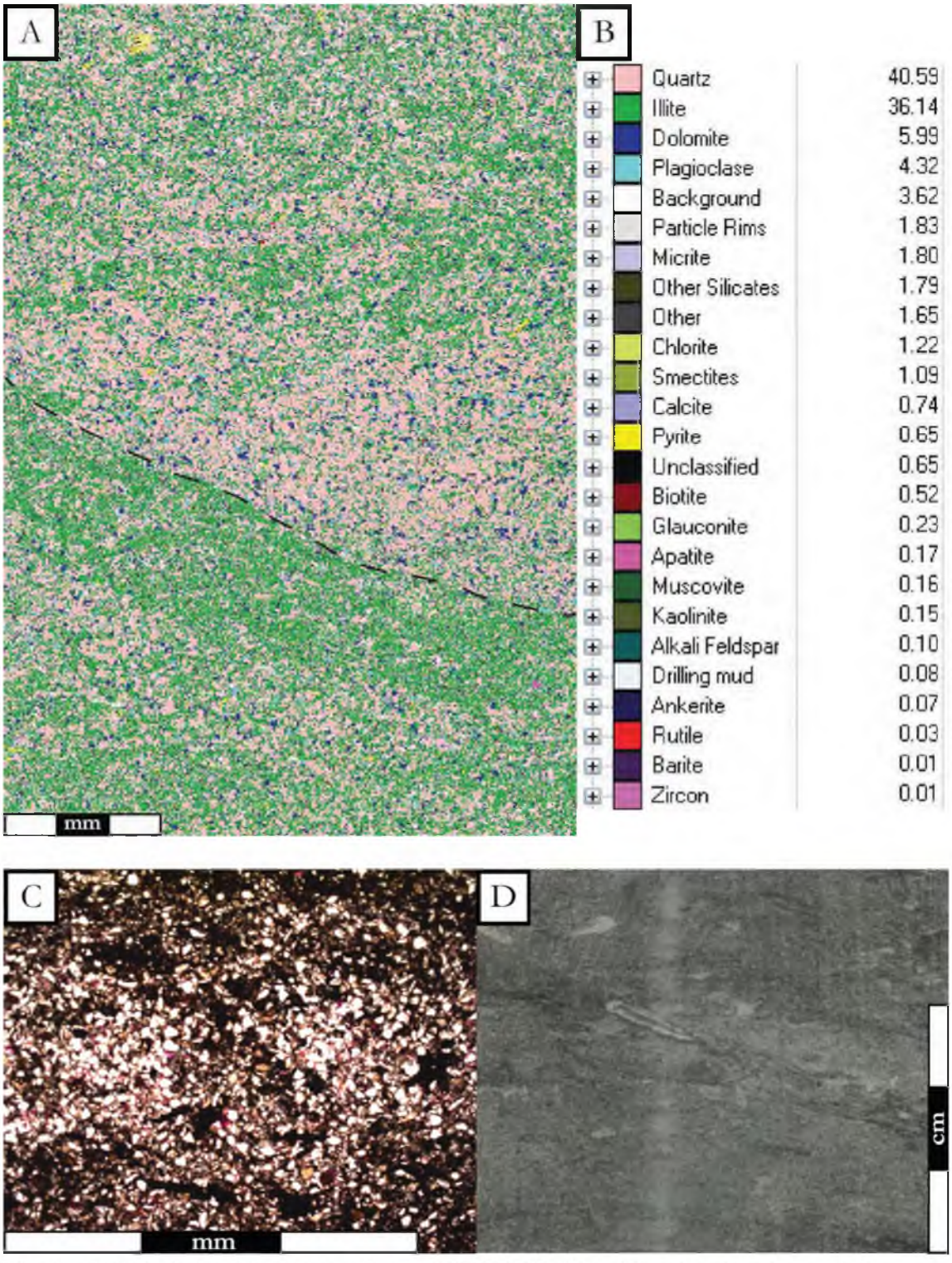

Figure 33: Lithofacies 5 in Questar 1. A) QEMSCAN slide with minerals color coded. Possible scour surface in black. B) Table expressing QEMSCAN minerals in area percent. C) Type thin section (13,376'). Laminations have been destroyed by bioturbation. D) Type core sample (13,379'). All laminations have been homogenized and primary structures have been destroyed by bioturbation.

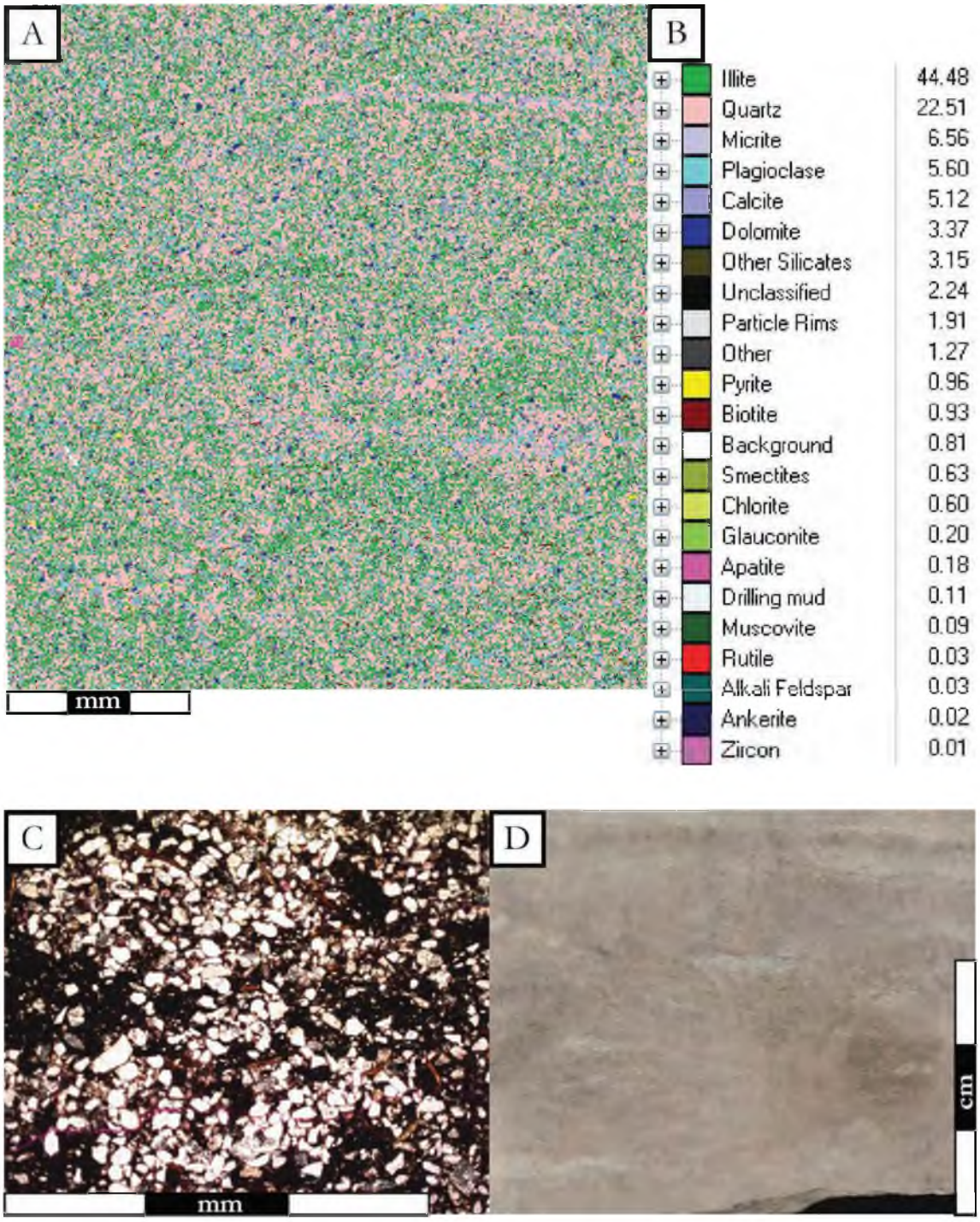

Figure 34: Lithofacies 5 in Pioneer 1. A) QEMSCAN slide with minerals color coded. B) Table expressing QEMSCAN minerals in area percent. C) Type thin section with scale in millimeters. Sediment has been largely homogenized. D) Type core sample. There is less contrast between quartz rich and clay rich layers than that in the Questar cores. Laminations and primary structures have been destroyed by bioturbation.

Figure 35: Trace fossil assemblage found in lithofacies 5 in the Questar 1 core from 13,376.0' to 13,376.6'.
D – Diplocraterion, PH – Palaeophycus Heberti, P – Planolites.
Schaubcylindrichnus and Skolithos are found in other intervals of lithofacies 5

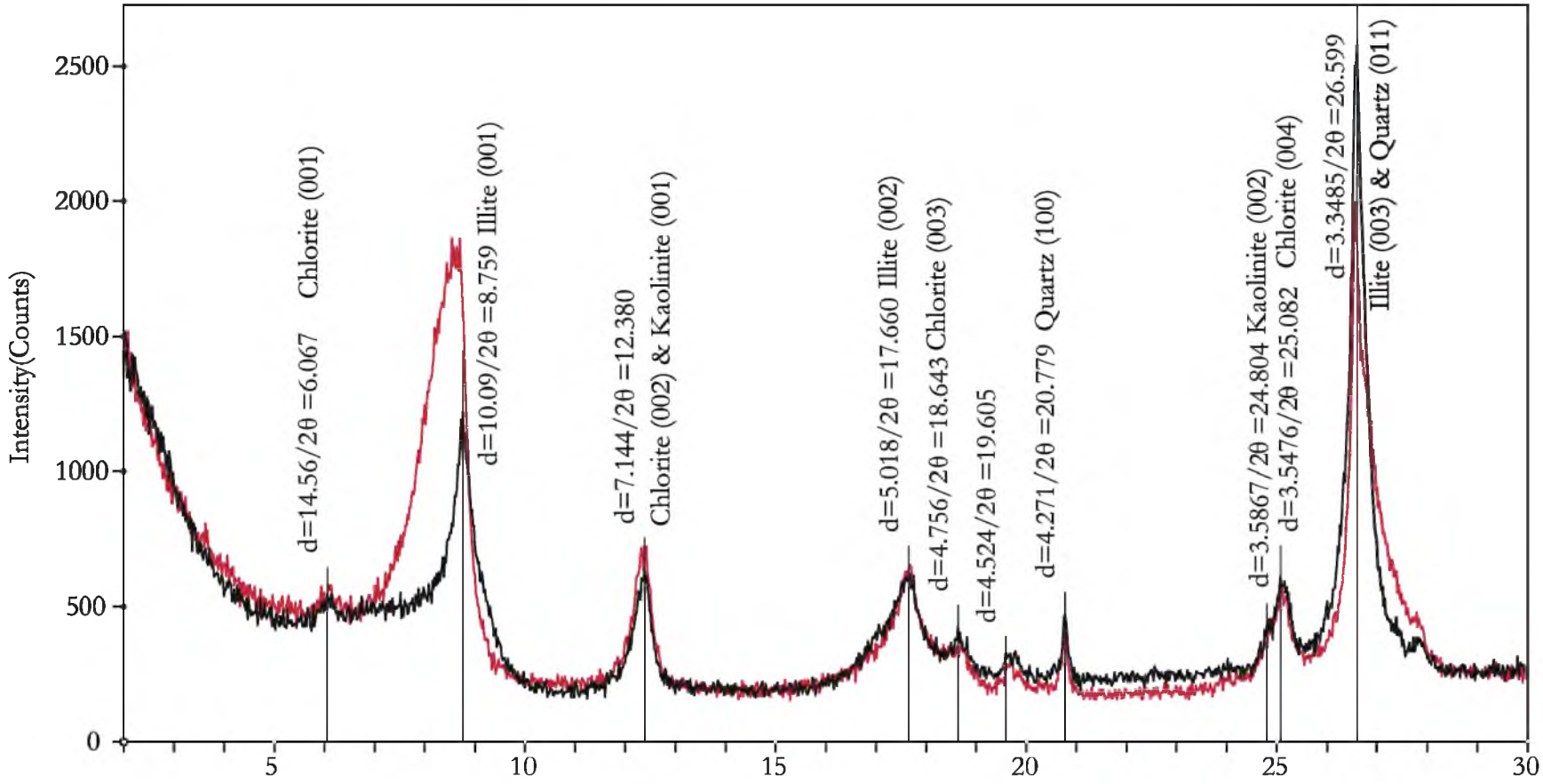

Figure 36: Lithofacies 5 in Questar 1 XRD peaks from oriented sample with minerals identified. Red pattern represents an air dried sample, black pattern represents a glycolated sample.

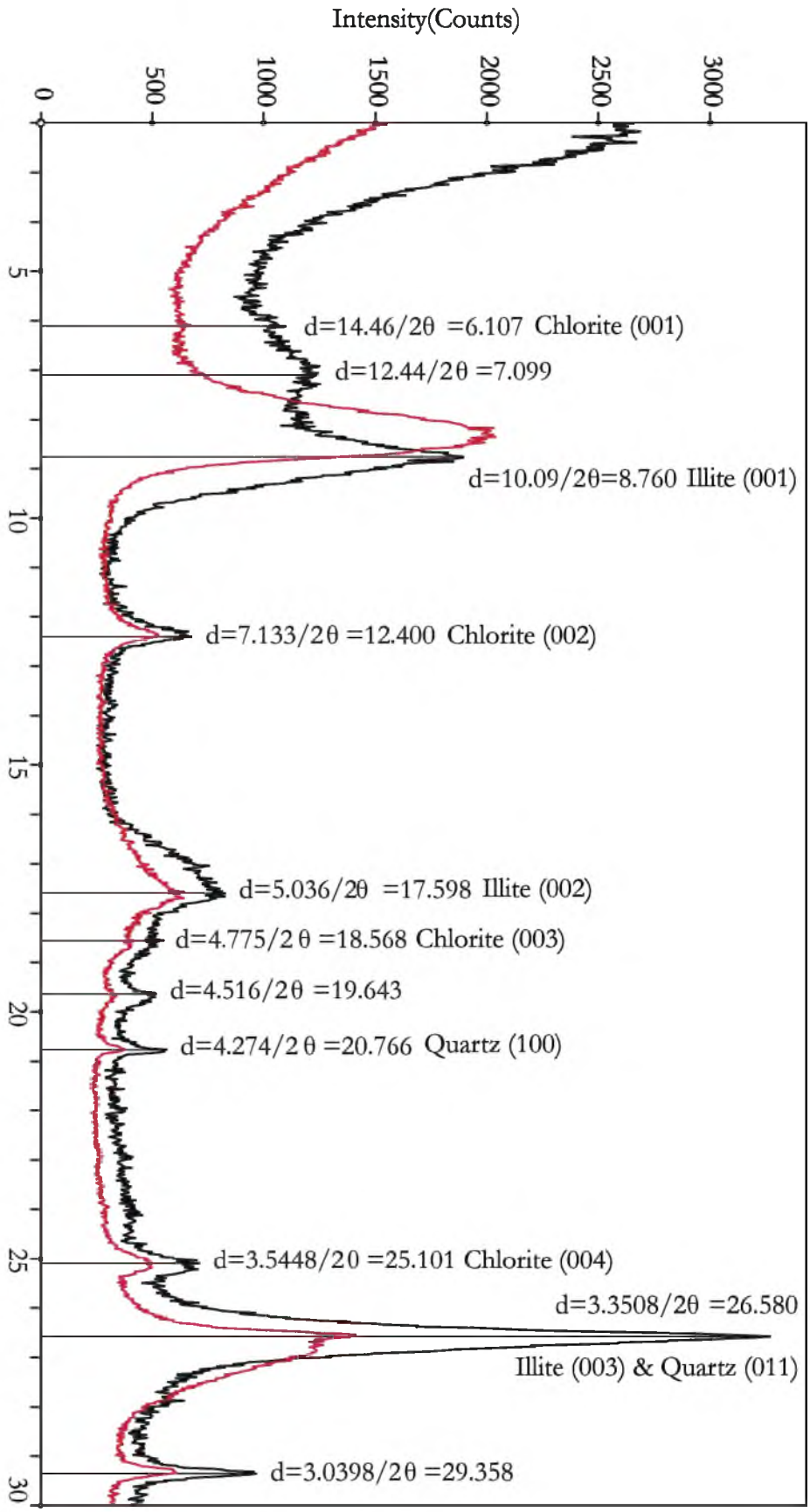

Figure 37: Lithofacies 5 in Pioneer 1 XRD peaks from oriented sample with minerals identified. Red pattern represents an air dried sample, black pattern represents a glycolated sample.

heterogeneity within the same lithofacies that is revealed only by a thorough micron scale analysis of samples.

Lithofacies 6 – Rhythmically, Discontinuously, Planar Laminated Siltstone

Lithofacies 6 occurs in the Questar 16, Pioneer 1, and Pioneer 2 cores (Table 2: Figure 8; Figure 9; Figure 10). This lithofacies consists of a fine to medium grained siltstone. It contains rhythmically interlaminated light grey coarse grained siltstone and dark grey to black fine to medium grained siltstone (Figure 38; Figure 39; Figure 40). In the lighter colored coarse siltstone laminations, primary structures are common and include ripple laminations and soft sediment deformation. These coarse siltstone laminations are, by and large, discontinuous across the length of the core (Figure 39; Figure 40). Bioturbation indices are generally low, with values of 1 or 2 on average. Locally values can be as low as 0 or as high as 3 (Figure 8; Figure 9; Figure 10). Reactivity with hydrochloric acid is common, with reactions tending to be moderate to vigorous. In more intensely laminated sections, however, more vigorous reactions were observed (Figure 8; Figure 9; Figure 10). This would suggest that the hydrochloric acid was most reactive with the lighter laminations.

X-ray diffraction data were consistent across the three cored intervals where lithofacies 7 co-occurred, with clay sized minerals including illite, quartz, chlorite, and calcite (Figure 41; Figure 42). In Pioneer 2, however, kaolinite is also included (Figure 43). The Pioneer 2 cored interval is unique in this aspect. Throughout the interval, kaolinite occurs in all lithofacies. Organic carbon values average 1.66% with minimum values of 1.11%, and maximum values of 2.39% (Table 4; Figure 20).

QEMSCAN data support the XRD data very well in this lithofacies, with no kaolinite identified in the Questar 16, and Pioneer 1 cores, and kaolinite identified in the

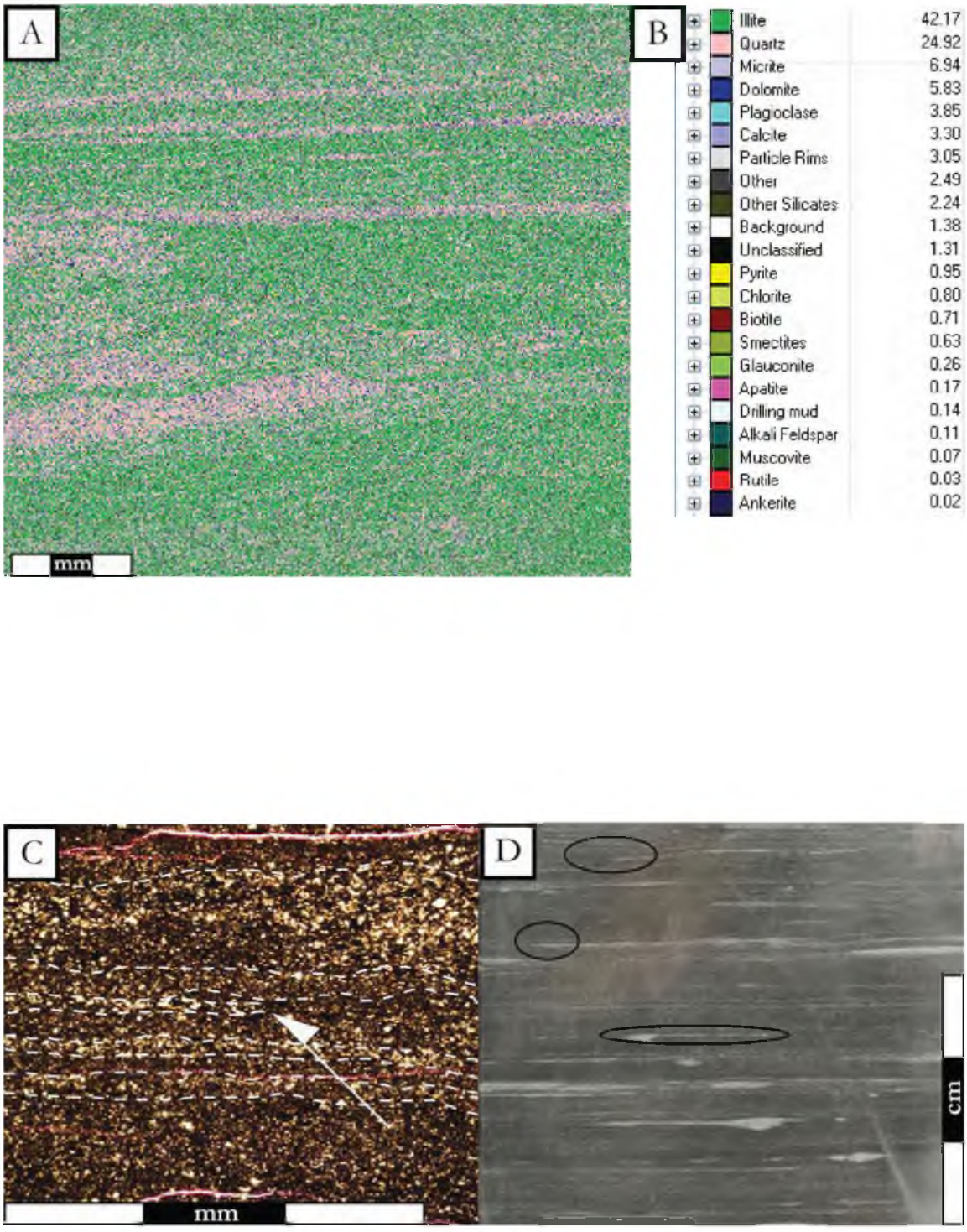

Figure 38: Lithofacies 6 in Questar 16. A) QEMSCAN slide with minerals color coded. B) Table expressing QEMSCAN minerals in area percent. C) Type thin section (15,151'). Laminations (white) are discontinuous in the center of the image (white arrow) D) Type core sample (15,160'). Note the discontinuous laminations that are characteristic of this lithofacies (circled in black).

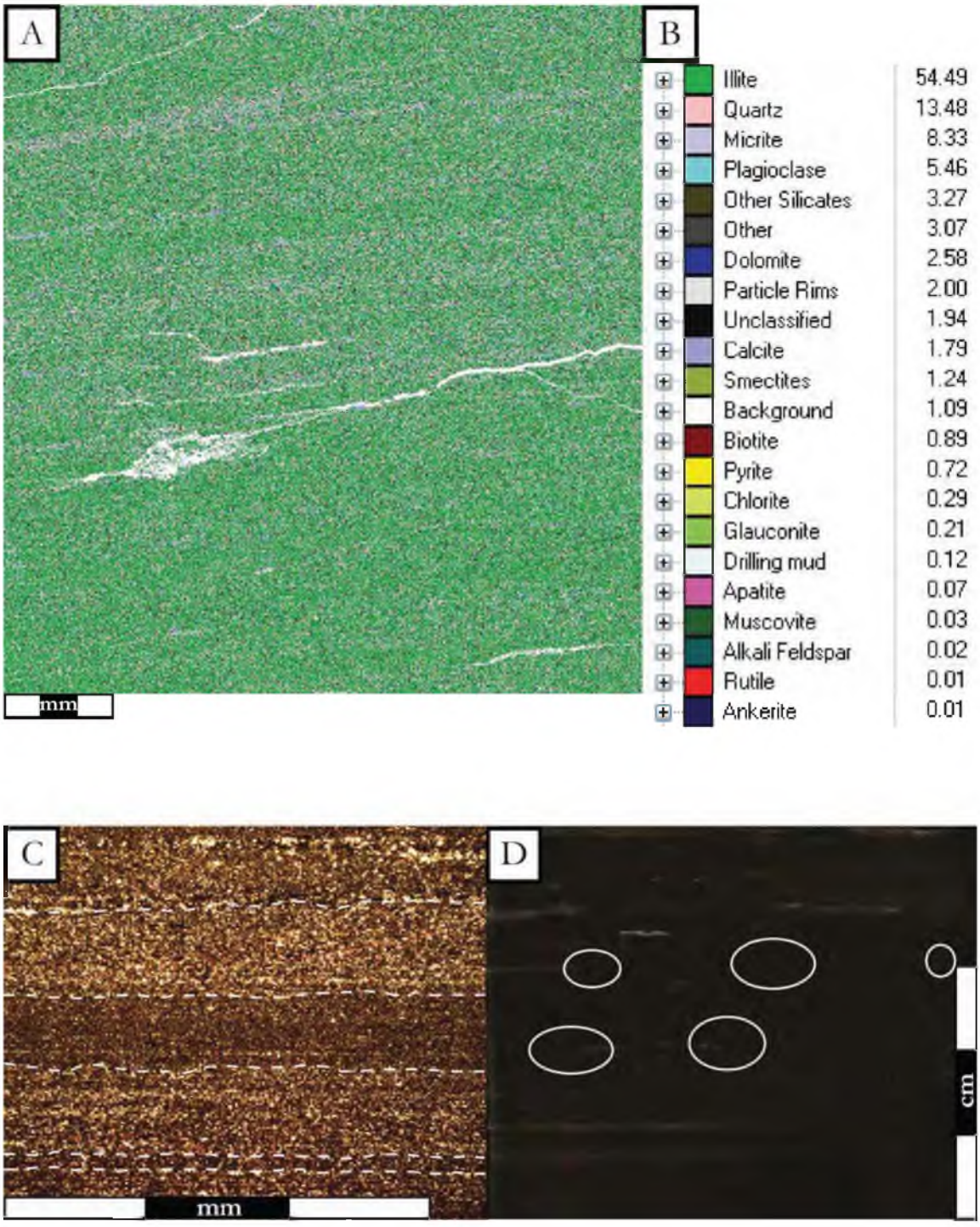

Figure 39: Lithofacies 6 in Pioneer 1. A) QEMSCAN slide with minerals color coded. B) Table expressing QEMSCAN minerals in area percent. C) Type thin section (7,484'). Laminations (white) are well defined and rhythmic. D) Type core sample (7,495'). Note terminations of the discontinuous laminations (circled in white).

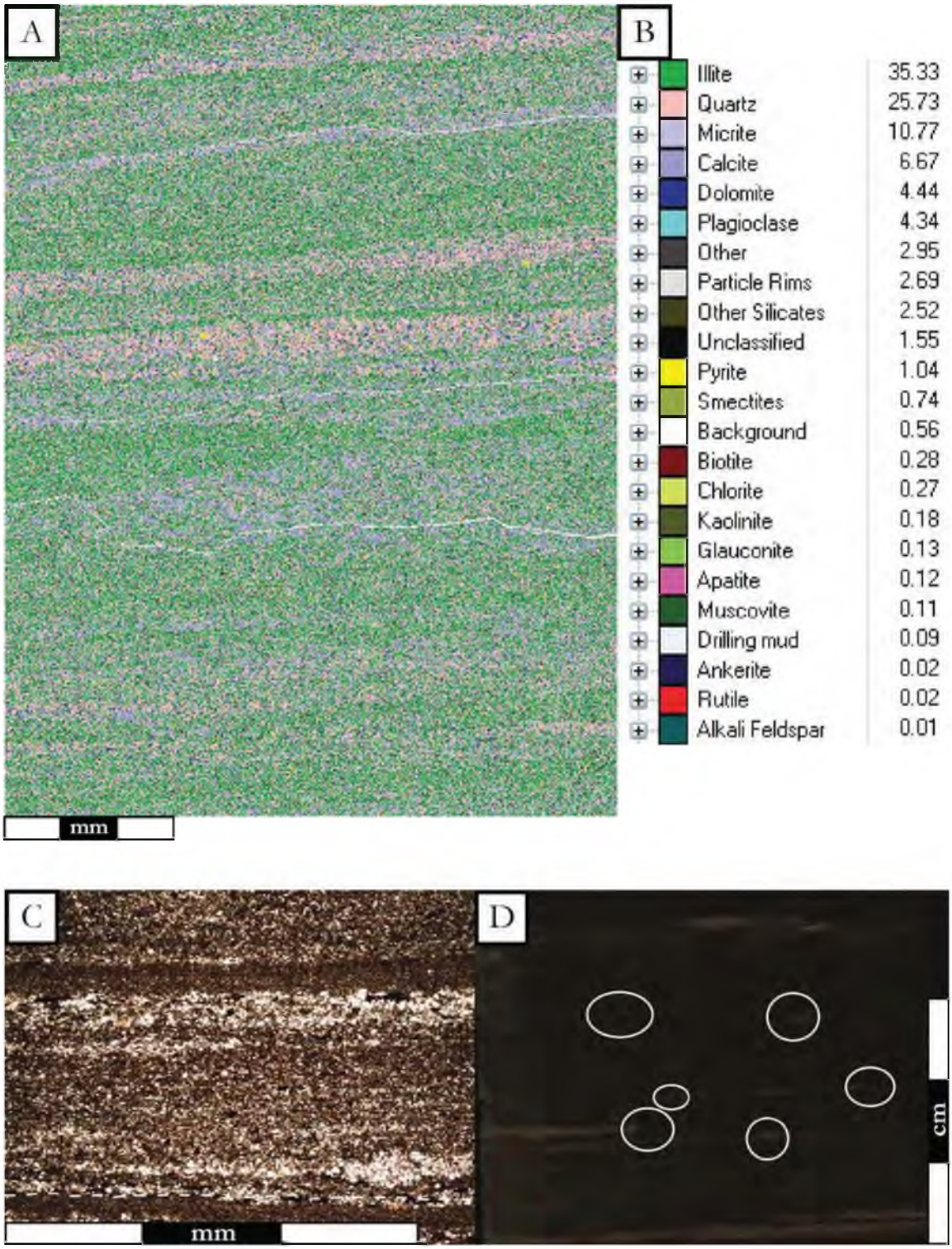

Figure 40: Lithofacies 6 in Pioneer 2. A) QEMSCAN slide with minerals color coded. B) Table expressing QEMSCAN minerals in area percent. C) Type thin section (7,130'). Note the variable grain size in the seperate laminations. D) Type core sample (7,133'). Note terminations of the discontinuous laminations (circled in white).

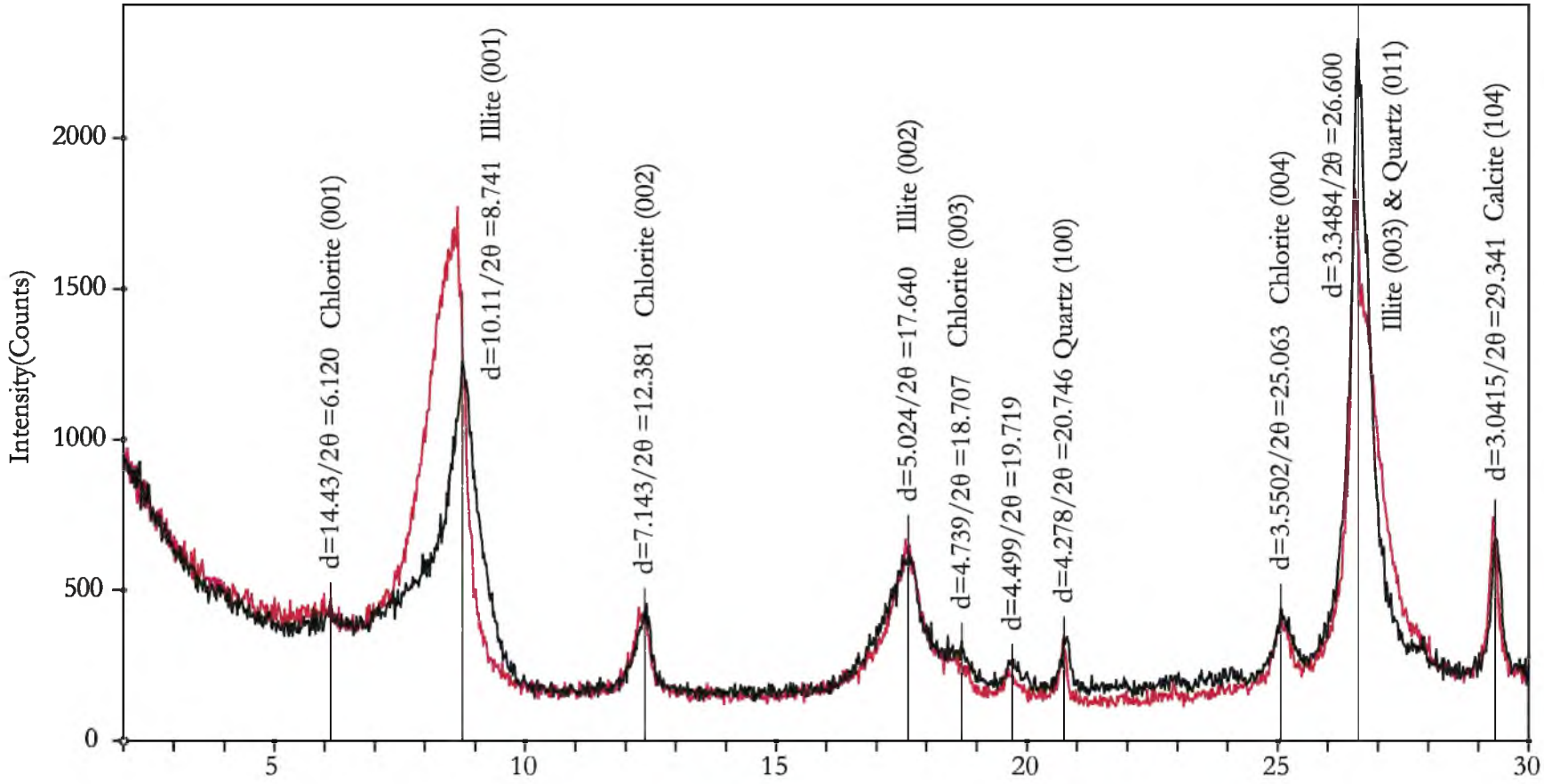

Figure 41: Lithofacies 6 in Questar 16 XRD peaks from oriented sample with minerals identified.
Red pattern represents an air dried sample, black pattern represents a glycolated sample.

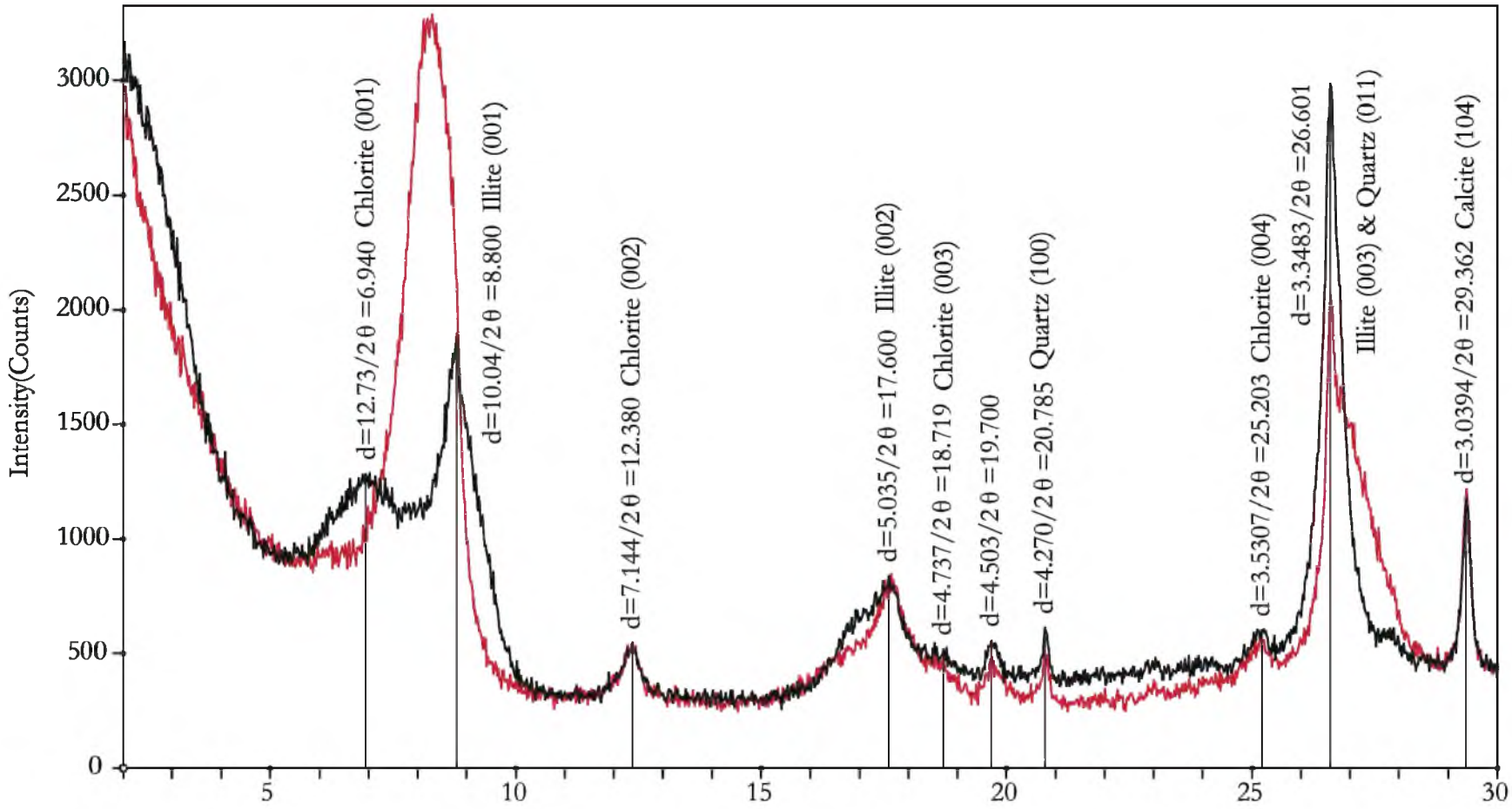

Figure 42: Lithofacies 6 in Pioneer 1 XRD peaks from oriented sample with minerals identified. Red pattern represents an air dried sample, black pattern represents a glycolated sample.

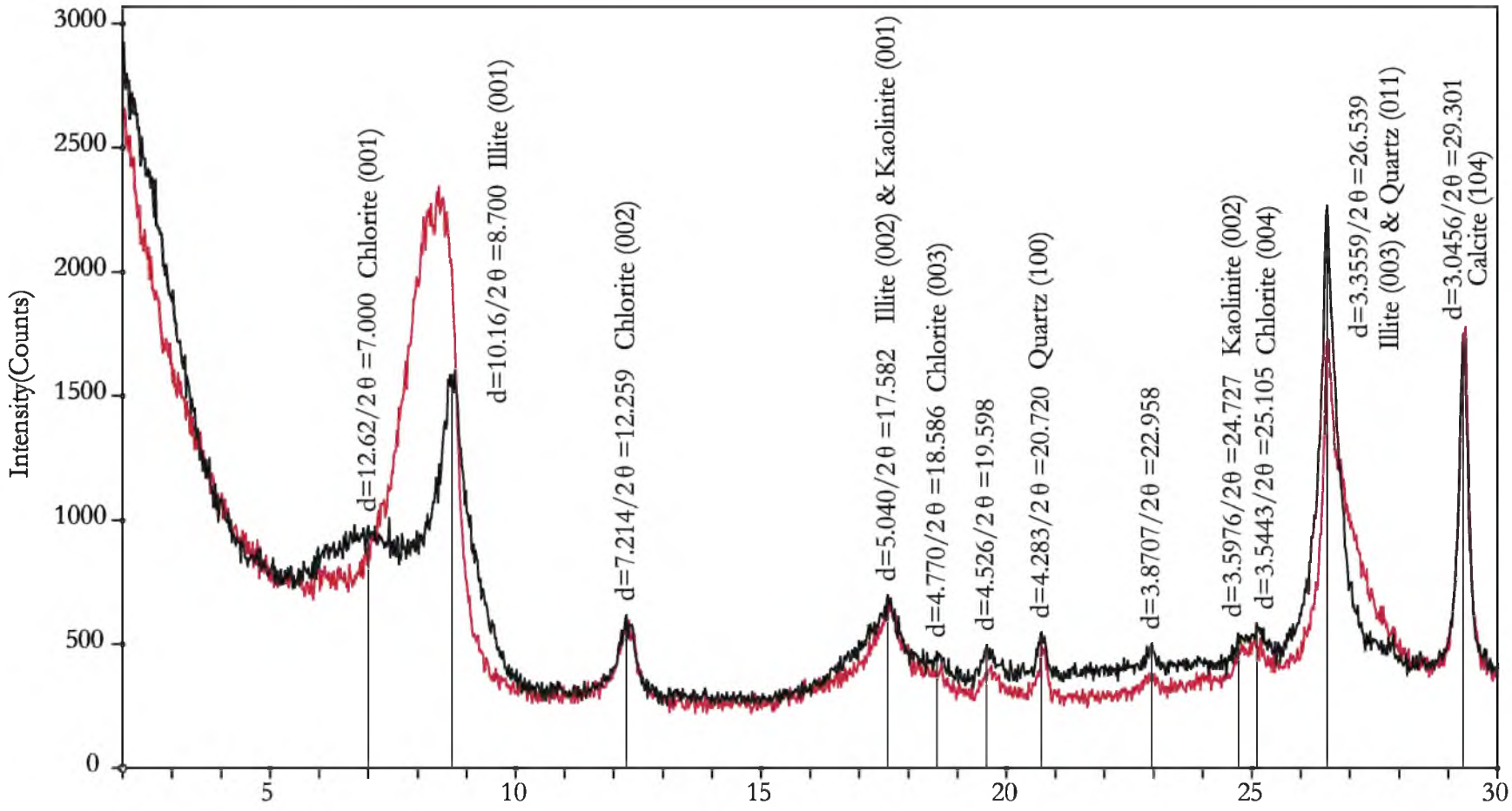

Figure 43: Lithofacies 6 in Pioneer 2 XRD peaks from oriented sample with minerals identified.
Red pattern represents an air dried sample, black pattern represents a glycolated sample.

Pioneer 2 core. Micrite/calcite growths grow around quartz rich laminations, with an exception in very coarse grained quartz laminations (Figure 44). Micrite/calcite does not appear to grow in illite rich laminations with the frequency that it does in quartz rich laminations.

Lithofacies 7 – Extensively Bioturbated Siltstone

Lithofacies 7 occurs exclusively in the Questar 16 core (Table 2; Figure 8). Lithofacies 7 is dominantly medium grained siltstone with local fine grained siltstone intervals (Figure 45). This lithofacies is marked by extensive bioturbation. Bioturbation indices range between 4 and 6 but are most commonly 5 (Figure 8). It varies from the similar lithofacies 5 in that it is considerably finer grained. This lithofacies can be slightly reactive to hydrochloric acid (Figure 8). Individual burrows are difficult classify, but primary structures have clearly been destroyed through burrowing. X-ray diffraction identified illite, quartz and chlorite in this lithofacies (Table 3; Figure 46). Organic carbon values average 0.98% with minimum values of 0.81%, and maximum values of 1.13% (Table 4; Figure 20).

QEMSCAN analysis generally agrees with XRD data. The QEMSCAN data also reveal pyritized burrows present in the core (Figure 45). These burrows were not seen in direct analysis of the core, but the size of the burrows that are pyritized (sub millimeter) would make direct observation difficult. The mottled texture that was observed in the core is supported in QEMSCAN samples – the quartz rich laminations are seen to be very discontinuous, with no primary structures preserved.

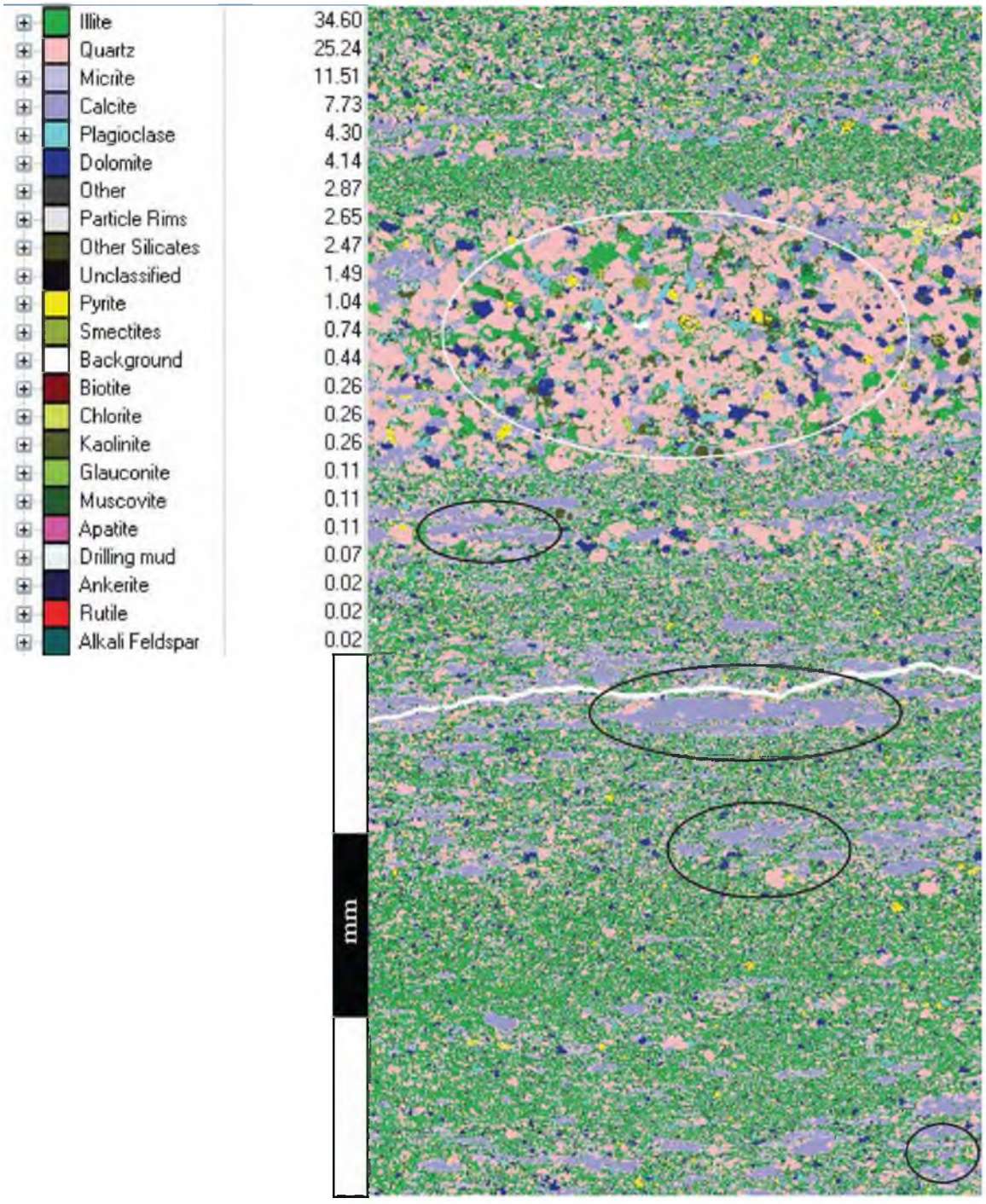

Figure 44: High resolution (2 micron spacing) QEMSCAN image of lithofacies 6 in Pioneer 2 (7,130'). Micrite/calcite preferentially grows in quartz rich laminations and around quartz grains (examples circled in black), but coarse quartz grains are not replaced (white).

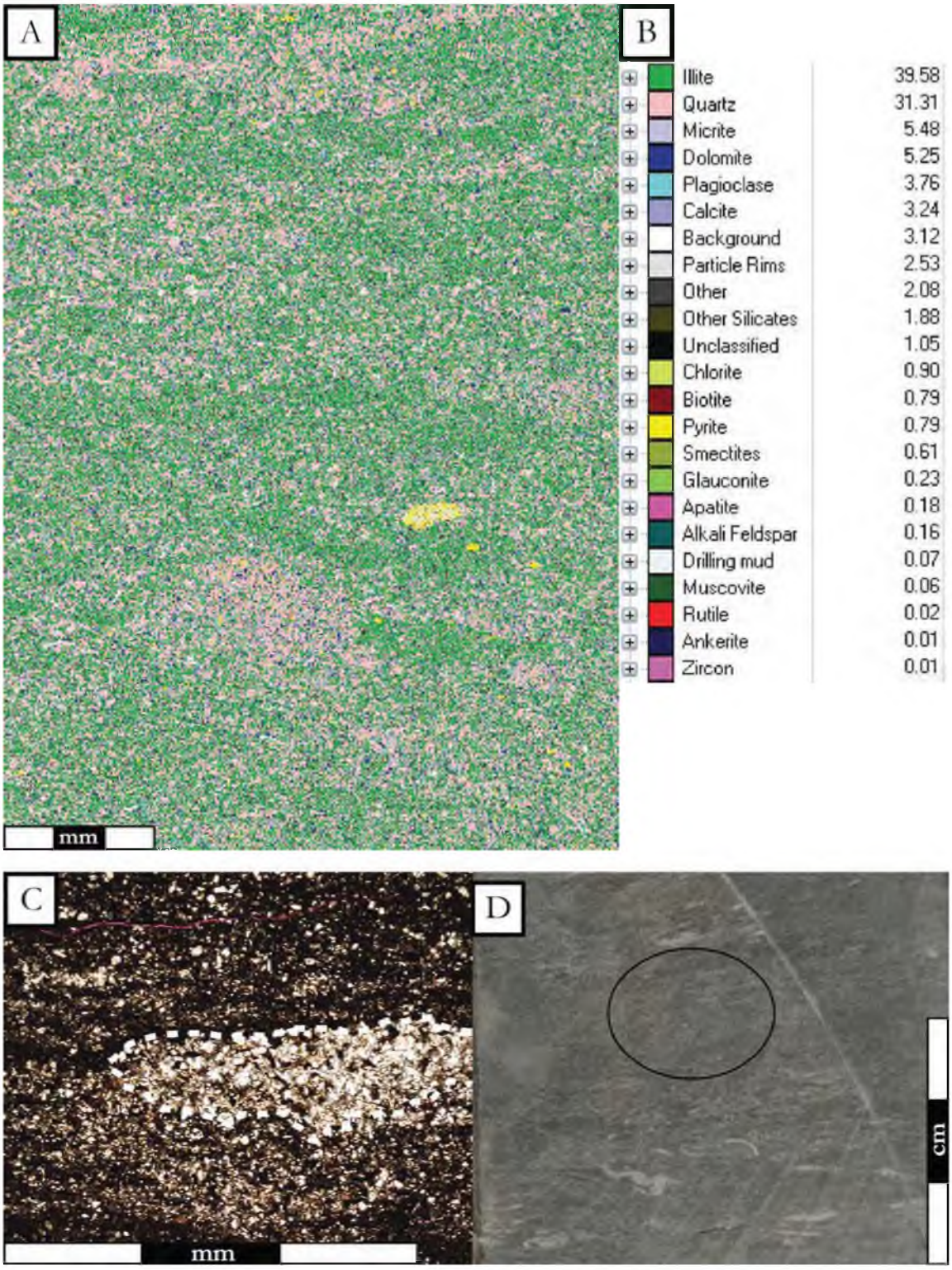

Figure 45: Lithofacies 7 in Questar 16. A) QEMSCAN slide with minerals color coded Note the pyrite (yellow) zone. Potentially a pyretized burrow. B) Table expressing QEMSCAN minerals in area percent. C) Type thin section (15,241'). Planolites burrow (white dashed line) is filled with coarser grained quartz grains than surrounding laminated quartz rich layers. D) Type core sample (15,238'). Mottled texture (circled in black).

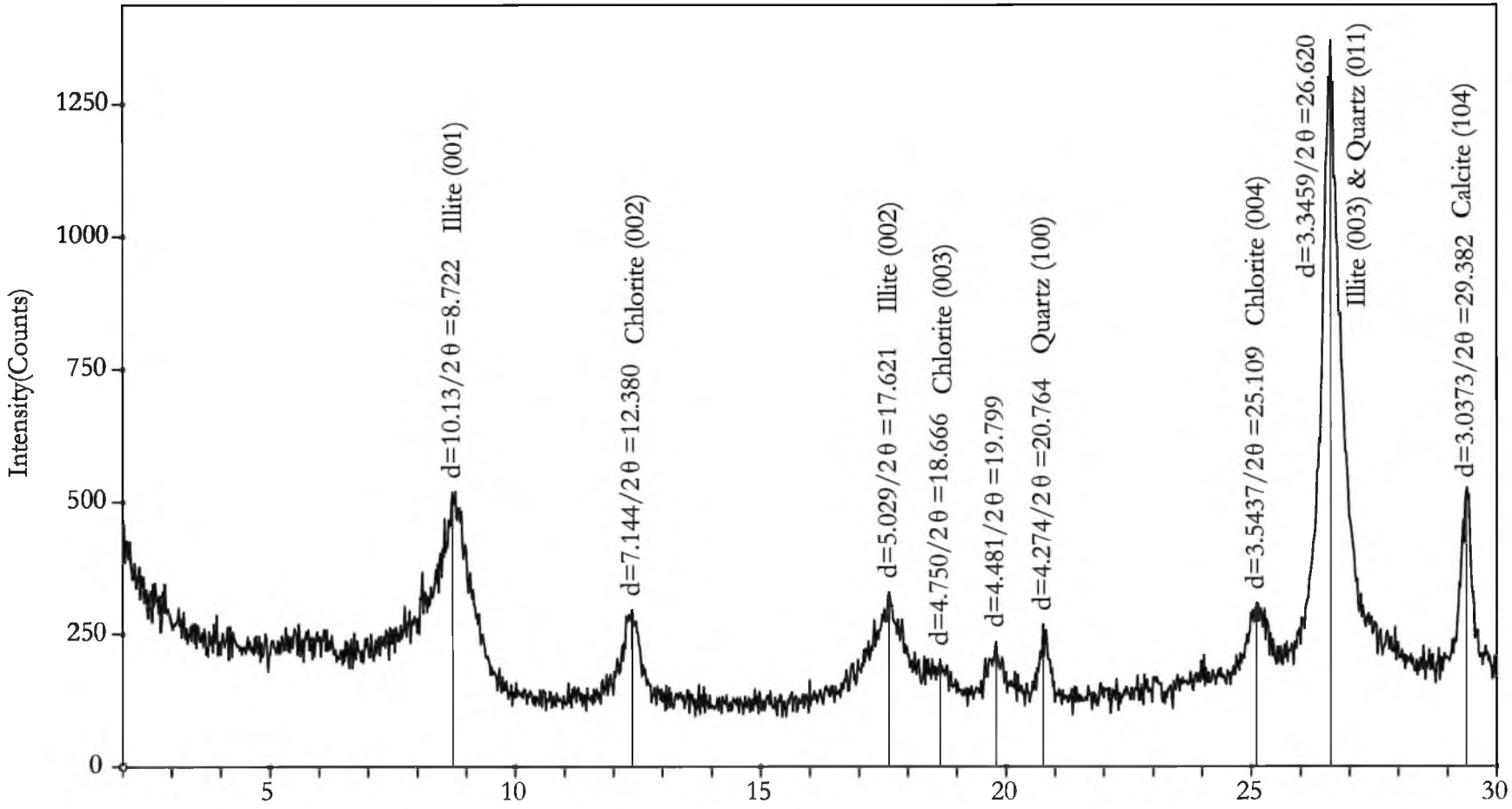

Figure 46: Lithofacies 7 in Questar 16 XRD peaks from oriented sample with minerals identified.

Lithofacies 8 – Nonlaminated Massive Siltstone

Lithofacies 8 occurs exclusively in the Pioneer 2 cored interval (Table 2; Figure 10). Lithofacies 8 is a fine to medium grained siltstone. This lithofacies is unique in that it best embodies the preconception that shales are thick homogenous intervals of dark grey to black fine grained rock. Indeed, the siltstone is massive, meaning laminations are mostly absent, with very few laminations present (Figure 47). This unit is marked by several shell beds featuring a hash of inoceramid shells (Figure 48). Other than the shell beds, there are no primary features that are preserved. Additionally, bioturbation is nearly non-existent (Figure 10). Where bioturbation is present locally, burrows are small and sporadically spaced with bioturbation indices of 0 to 1. This lithofacies is moderately reactive with hydrochloric acid (Figure 10).

X-ray diffraction data indicate lithofacies 8 contains illite, kaolinite, chlorite, quartz, and calcite in the clay size fraction (Figure 49). Interestingly, the mineralogical composition of this lithofacies is identical to lithofacies 6 in the Pioneer 2 core, despite the differences in lamination style, namely the complete lack of quartz rich laminations in lithofacies 8 as compared to lithofacies 6 (Figure 43). Organic carbon values average 2.14% with minimum values of 1.53%, and maximum values of 3.25% making it the richest lithofacies (Table 4; Figure 20).

QEMSCAN analysis indicates that this apparently homogenous lithofacies is, in fact, quite heterogeneous at the micro-scale. The dominant mineral is illite, composing 48% of the sample (Figure 47). However, there are heterogeneities that are clearly evident. Quartz grains comprise 18% of the area of this sample, and compose a very weakly laminated texture (Figure 50). Secondly, micrite and calcite account for a combined 15% of the area of the sample. Micrite tends to line the larger calcite grains, but several micrite rich zones exist

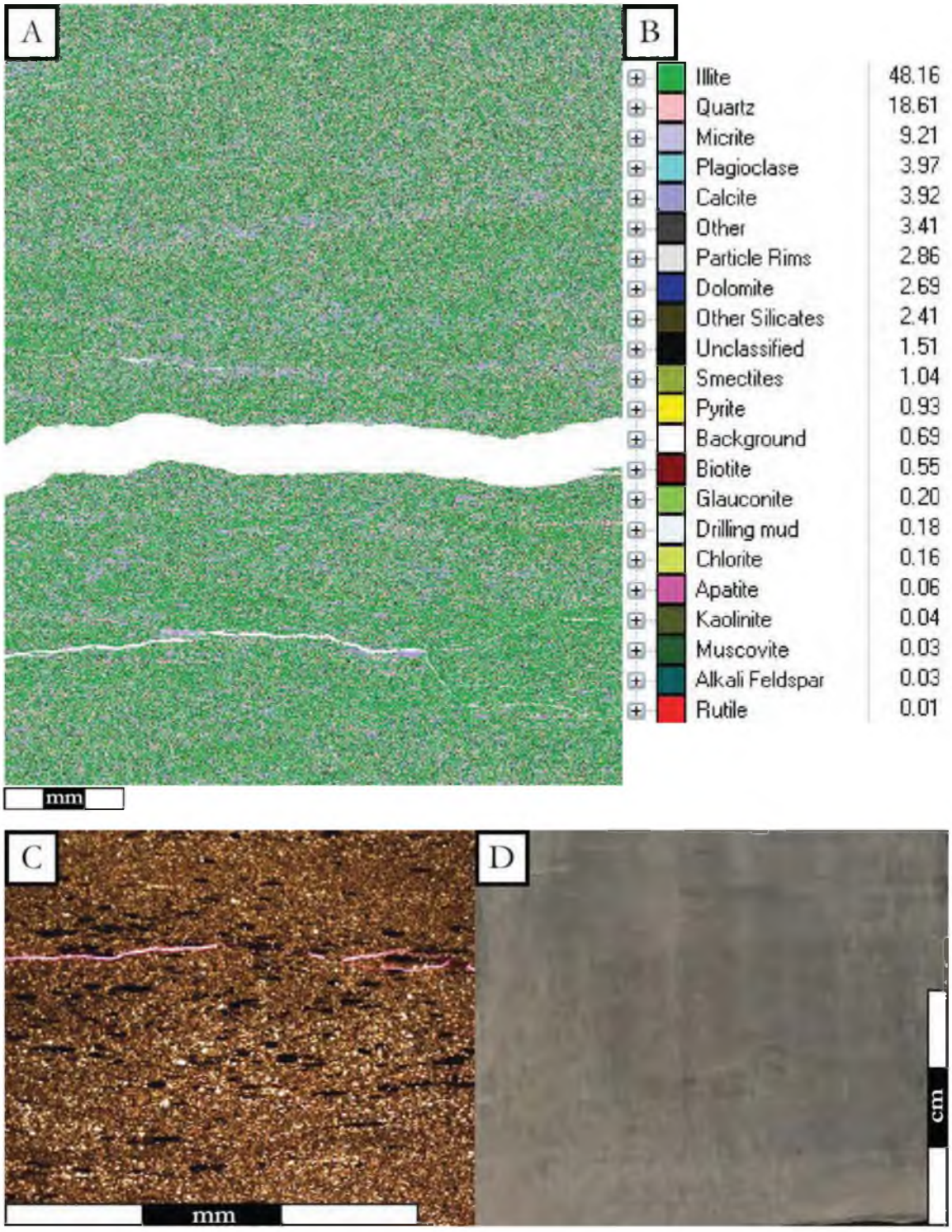

Figure 47: Lithofacies 8 in Pioneer 2. A) QEMSCAN slide with minerals color coded. B) Table expressing QEMSCAN minerals in area percent. C) Type thin section with (7092'). Faint laminations are visible in thin section that are otherwise invisible. D) Type core sample (7098'). This hand sample is quite homogenous with no laminations or primary structures visible without magnification.

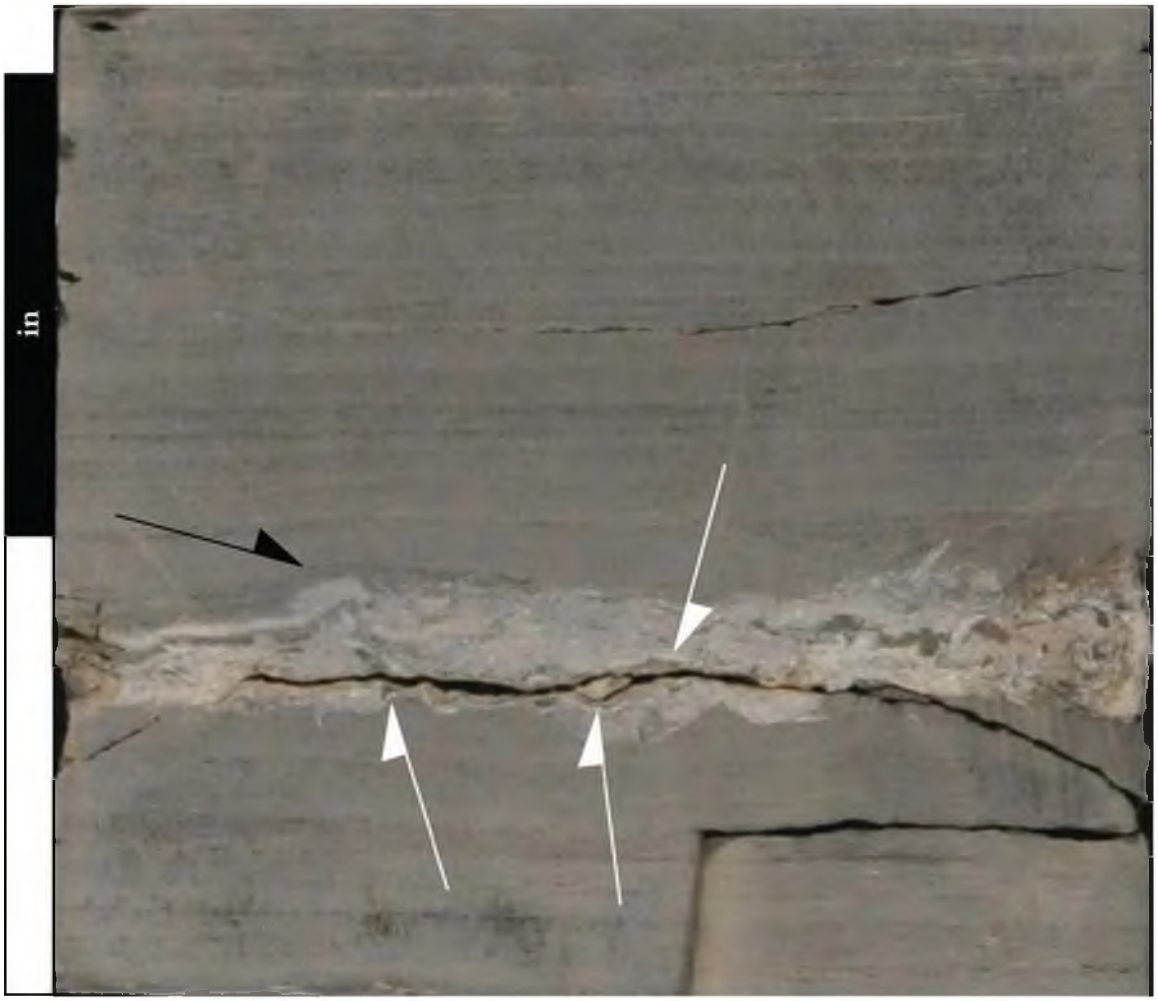

Figure 48: Shell bed in Lithofacies 11 in Pioneer 2 (7,045.3'). Similar shell beds occur throughout the Pioneer 2 core in lithofacies 8 and lithofacies 11. Shells are very thin and bold white (white arrow) against the surrounding dull grey silt. Also, note the mud drapes capping the shell bed (black arrow).

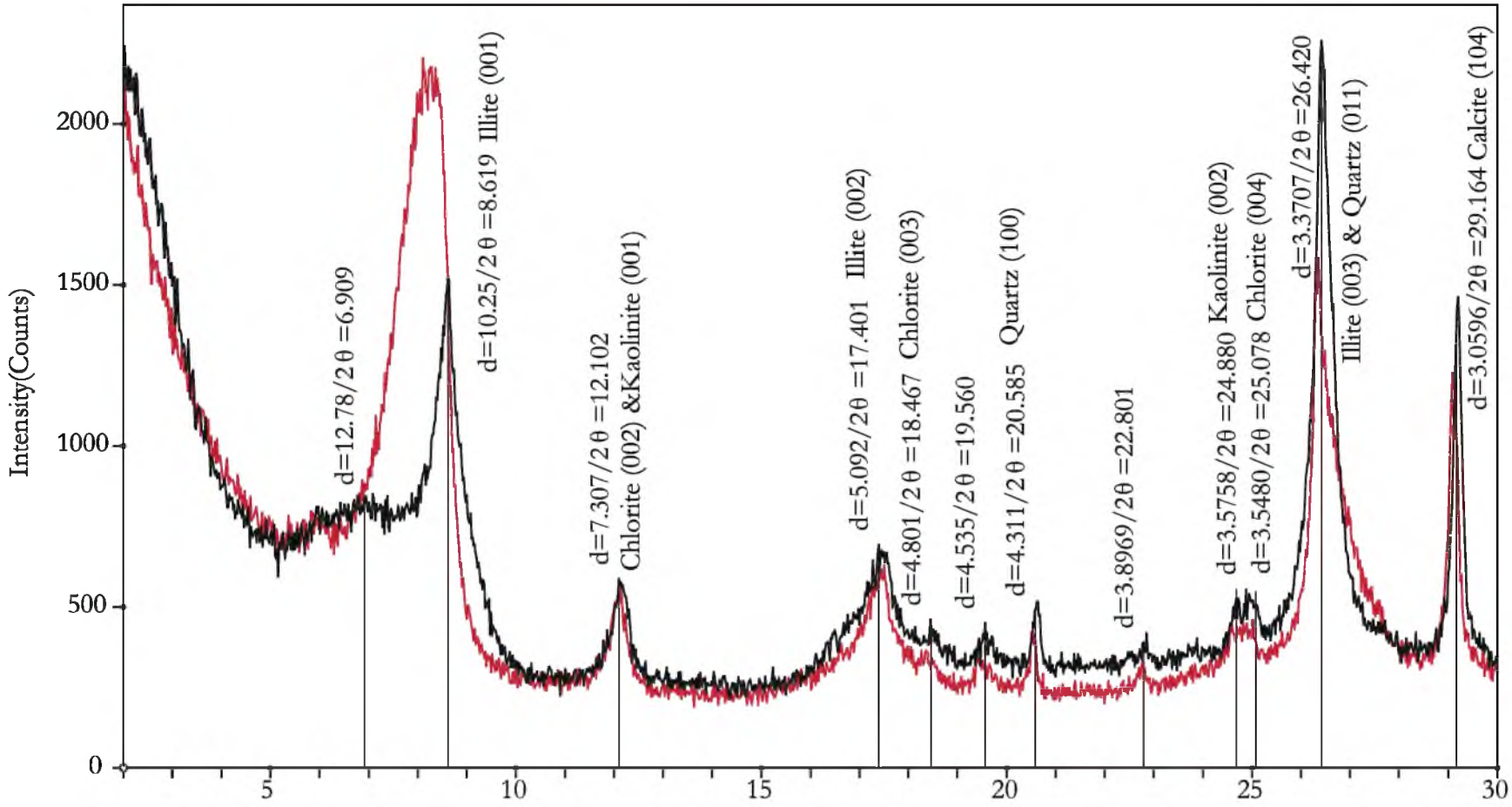

Figure 49: Lithofacies 8 in Pioneer 2 XRD peaks from oriented sample with minerals identified. Red pattern represents an air dried sample, black pattern represents a glycolated sample.

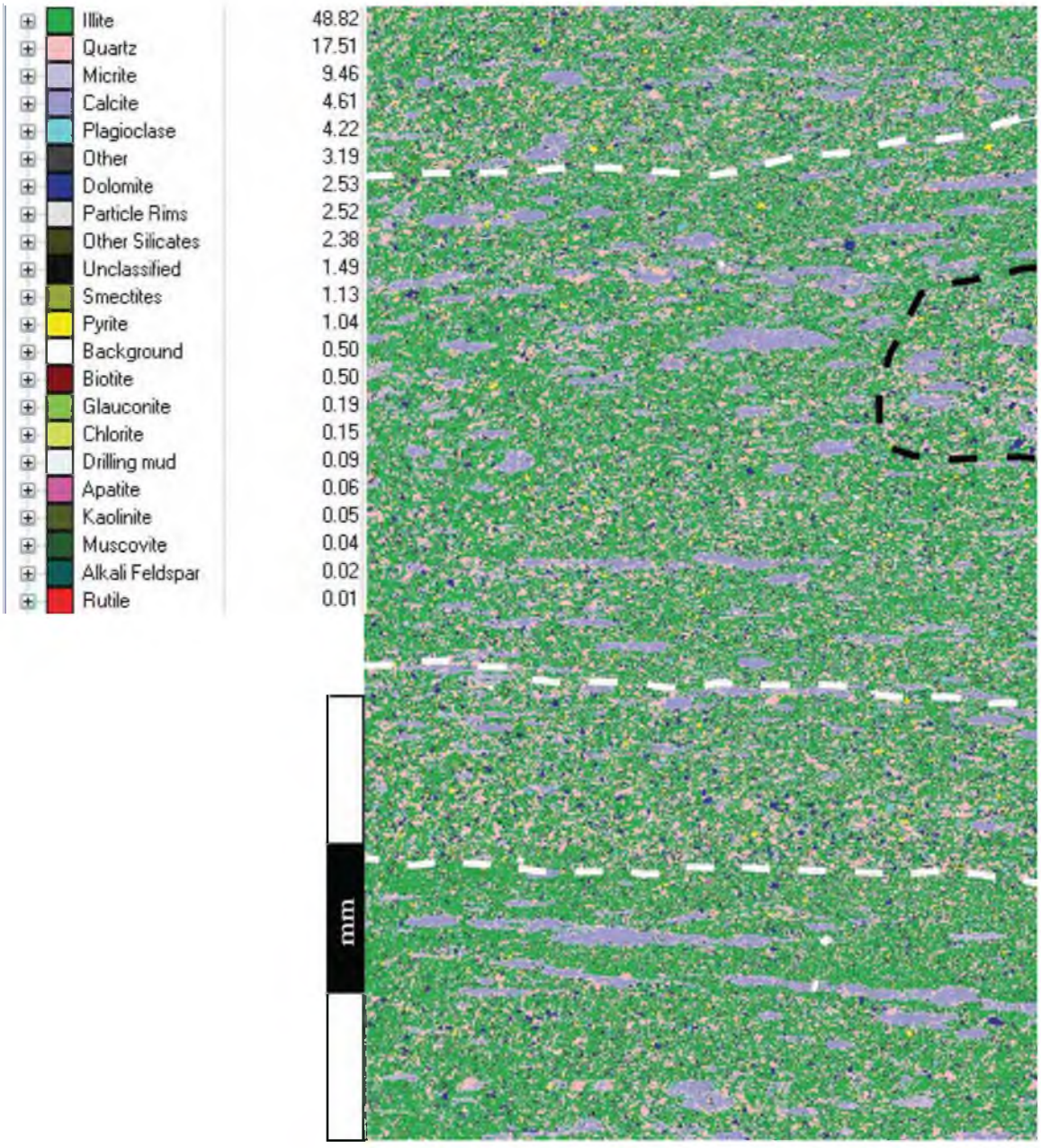

Figure 50: A high resolution (2 micron spacing) QEMSCAN image of lithofacies 8 (7,094'). Note horizontal linear pattern of quartz (peach) grain distribution that reveals a weakly laminated texture (outlined in white). Possible bioturbation also exists (outlined in black). Additionally, the micrite/calcite grains (purple) appear to cross cut depositional fabrics, with a preferential growth along lamination direction.

within the calcite grains. Because the minerals appear as oval shaped growths throughout the entire sample, we interpret them to have formed secondarily as diagenetic nodules or concretions that grew generally parallel to laminations (Figure 50).

Lithofacies 9 – Intensely Laminated Sandstone Heterolith

Lithofacies 9 is found only in the Pioneer 1 cored interval (Table 2; Figure 9). Lithofacies 9 is a heterolith consisting of dominantly coarse siltstone to very fine grained sandstone interlaminated with siltstone. Primary structures are visible and include ripples and low angle laminations (Figure 51). This lithofacies is associated with moderate levels of bioturbation, with values ranging from 3 to 5 (Figure 9). This lithofacies is similar to lithofacies 5, but is less bioturbated and can be a slightly coarser grained. Reactivity with hydrochloric acid is moderate to vigorous (Figure 9).

X-ray diffraction shows that the clay mineral assemblage contains illite, chlorite, quartz, and calcite (Figure 52). This is an identical assemblage to that of lithofacies 5 in the Pioneer 1 core (Table 3). Because lithofacies 5 and lithofacies 9 alternate stratigraphically in the base of Pioneer 1, this similarity suggests the provenance of the sediment is mineralogically unchanging. No Organic carbon data were collected from this lithofacies.

QEMSCAN data reveal mineral assemblages consistent with the XRD data (Figure 51). The QEMSCAN image additionally highlights disturbed laminations, bioturbation and scour surfaces characteristic of this lithofacies (Figure 53). Two interlaminated lithologies that compose this lithofacies are evident in the QEMSCAN image, and these include finer grained, darker in color, silt laminations that are rich in clays, and coarser grained, lighter in color, coarse silt to very fine sand laminations that are rich in quartz. QEMSCAN data

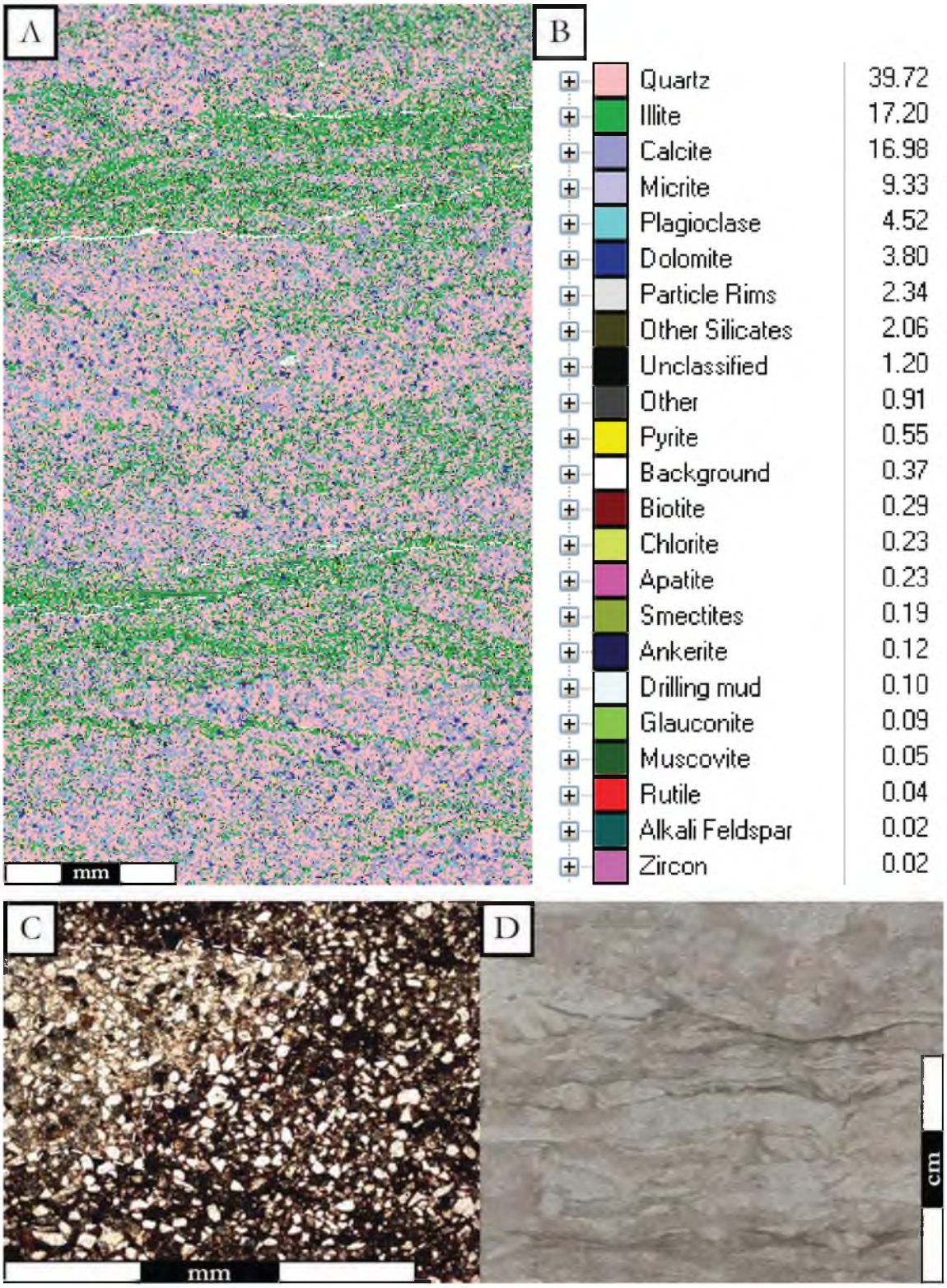

Figure 51: Lithofacies 9 in Pioneer 1. A) QEMSCAN slide with minerals color coded. B) Table expressing QEMSCAN minerals in area percent. C) Type thin section (7,597'). A clay rich lamination is cut by a quartz filled burrow. D) Type core sample (7,595'). Distinct Trace fossils are visible (outlined in white), as are relict laminations.

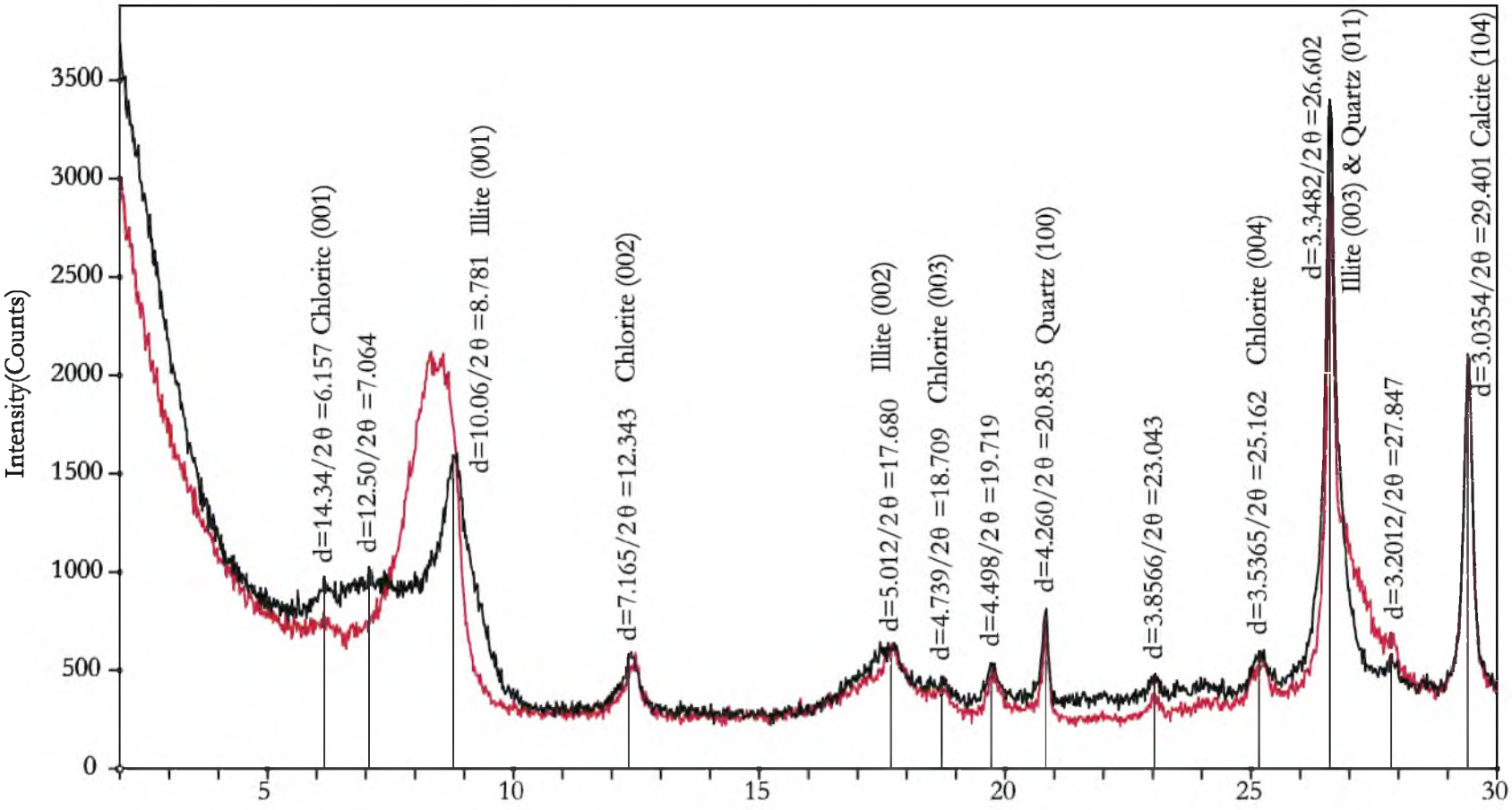

Figure 52: Lithofacies 9 in Pioneer 1 XRD peaks from oriented sample with minerals identified. Red pattern represents an air dried sample, black pattern represents a glycolated sample.

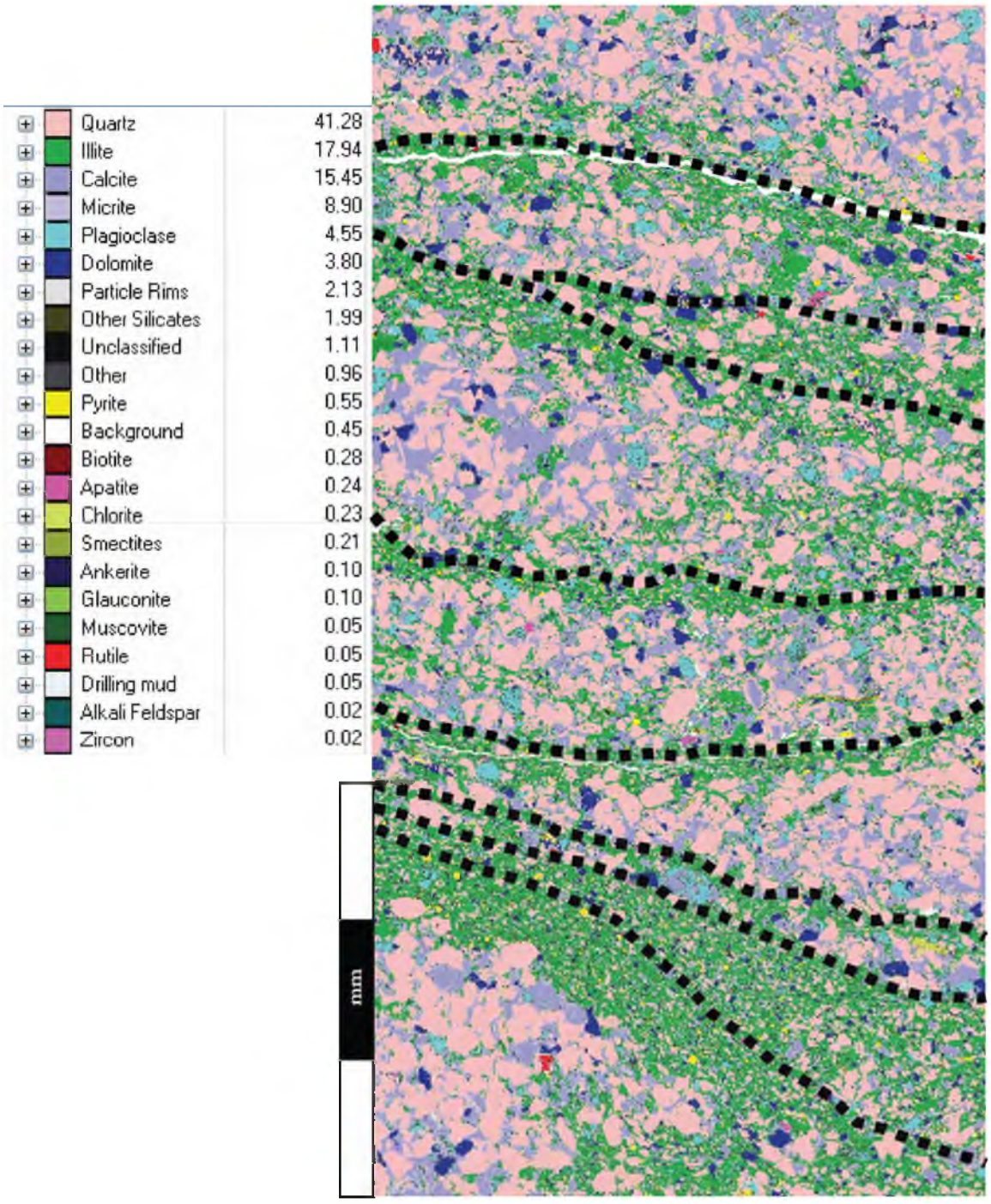

Figure 53: High resolution (2 micron spacing) QEMSCAN image of lithofacies 9 in Pioneer 1 (7,597'). Note distinct mineralogy following interlaminations. Detrital quartz (peach) dominated laminations scour (lined in black) clay laminations and consist of coarser grains.

suggest that the lighter laminations are composed almost exclusively lithics. The darker, clay rich laminations consist mostly of illite, with interspersed accessory minerals (Figure 53).

Lithofacies 10 – Bentonite

Lithofacies 10 is found exclusively in the Pioneer 1 cored interval (Table 2; Figure 9) (Table 2). Lithofacies 10 consists of light grey to white, massive, chalky claystone composed of bentonite. No primary structures are visible, but igneous minerals such as biotite are visible. This lithofacies is interpreted as ashfall deposits.

Lithofacies 11 – Claystone Dominated Siltstone Heterolith

Lithofacies 11 was found exclusively in the Pioneer 2 cored interval (Table 2; Figure 10). Lithofacies 11 is a fine to medium grained claystone dominated heterolith interlaminated with siltstone (Figure 54). Its most characteristic feature is the faint lamination style. Unlike previously described heteroliths, this lithofacies contains laminations that are nearly the same color. Upon initial inspection this lithofacies appears massive, but when wet, two colors, a light grey and a slightly darker grey, are visible. The thickness of these laminations ranges from sub-centimeter to multiple centimeters. Primary features are subtle, but low angle laminations dominate (Figure 54). There are several shell beds that contain a hash of inoceramids (Figure 10). Bioturbation is nearly non-existent in this core with values of 0 to 1 (Figure 10). Reactivity with hydrochloric acid is consistently moderate (Figure 10).

X-ray diffraction shows that the mineralogy of this lithofacies is identical to other lithofacies in the Pioneer 2 core (Figure 55; Figure 49; Figure 43). Clay sized minerals include illite, kaolinite, chlorite, quartz, and calcite (Table 3). Lithofacies 11 is most similar to lithofacies 8 in its lithologic characteristics, but is distinguished from lithofacies 8 by its

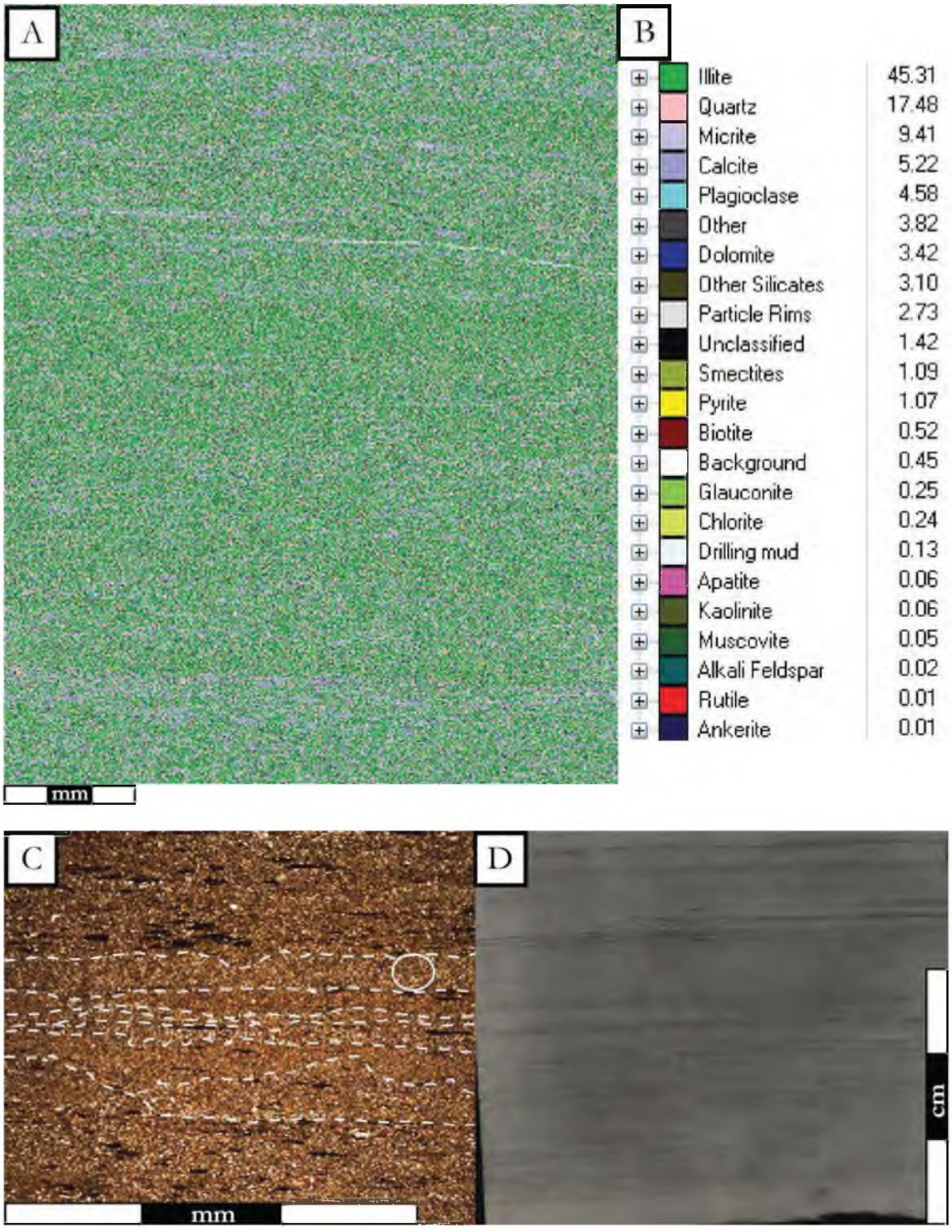

Figure 54: Lithofacies 11 in Pioneer 2. A) QEMSCAN slide with minerals color coded. B) Table expressing QEMSCAN minerals in area percent. C) Type thin section (7,032'). Laminations are very faint (several are outlined in white) and lithologically similar. Bioturbation is present (circled in white) but also faint. D) Type core sample (7,016'). Laminations are more clear in the core photo compared to the thin section. Laminations are very thin, can be discontinuous.

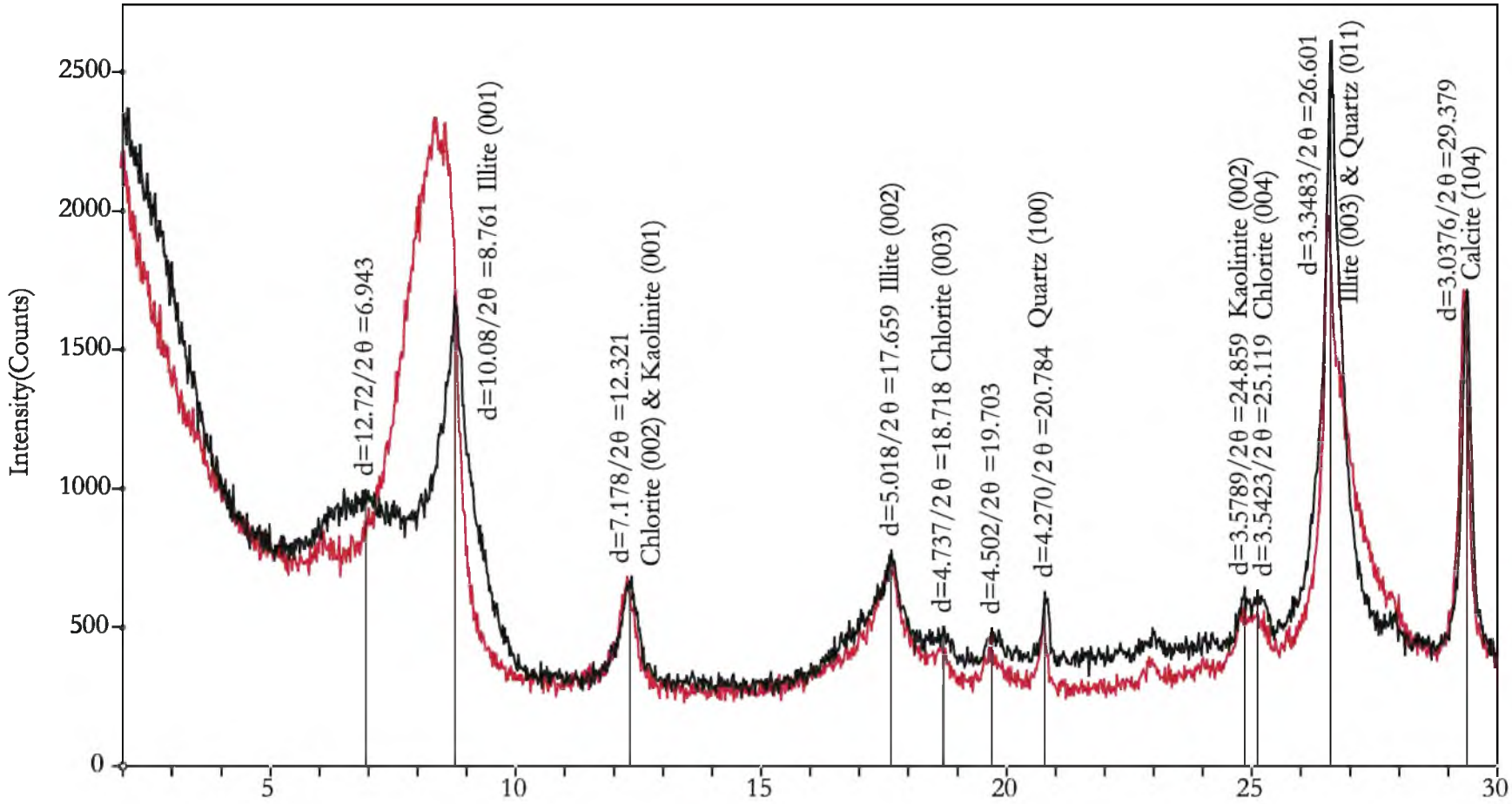

Figure 55: Lithofacies 11 in Pioneer 2 XRD peaks from oriented sample with minerals identified. Red pattern represents an air dried sample, black pattern represents a glycolated sample.

subtle laminations. Organic carbon values average 2.11% with minimum values of 1.68%, and maximum values of 2.60% making it nearly as rich as lithofacies 8 (Table 4; Figure 20).

QEMSCAN data suggest that the diagenetic growth of calcite nodules post-deposition contributes to the faint lamination style (Figure 56). The laminations are poorly defined by alternating layers of quartz rich and illite rich layers. However, micrite/calcite grains are an order of magnitude larger than mean grain size of quartz grains. Additionally, the micrite/calcite grains are nodular, and cross cut faint depositional fabrics. This suggests that the micrite/calcite is secondary. The micrite/calcite growths appear to grow preferentially around quartz rich laminations (Figure 57). Preferential horizontal growth, coupled with preferential growth around quartz grains suggest that the micrite/calcite growths contribute to the faint horizontally laminated fabric despite the fact that they are secondary.

Porosity and Permeability

Porosity and permeability (collected by both pulse decay and pressure decay methods) data were donated to the project by third parties. Selections for where tests were performed were therefore not based on the identified lithofacies. Additionally, data only exists for the Questar 1, 8, and 16 cores – not for the Pioneer 1 and 2 cores. Porosity and permeability data are summarized on Table 6.

Because of the sampling methods, only the Questar 1 core has substantial data. The correlations are thereby biased towards the five lithofacies that appear in that core. The statistical variance between lithofacies is quite broad (Table 6). Additionally, since some lithofacies occur considerably less frequently than others (e.g. lithofacies 7 and lithofacies 1), there are fewer data points for some lithofacies.

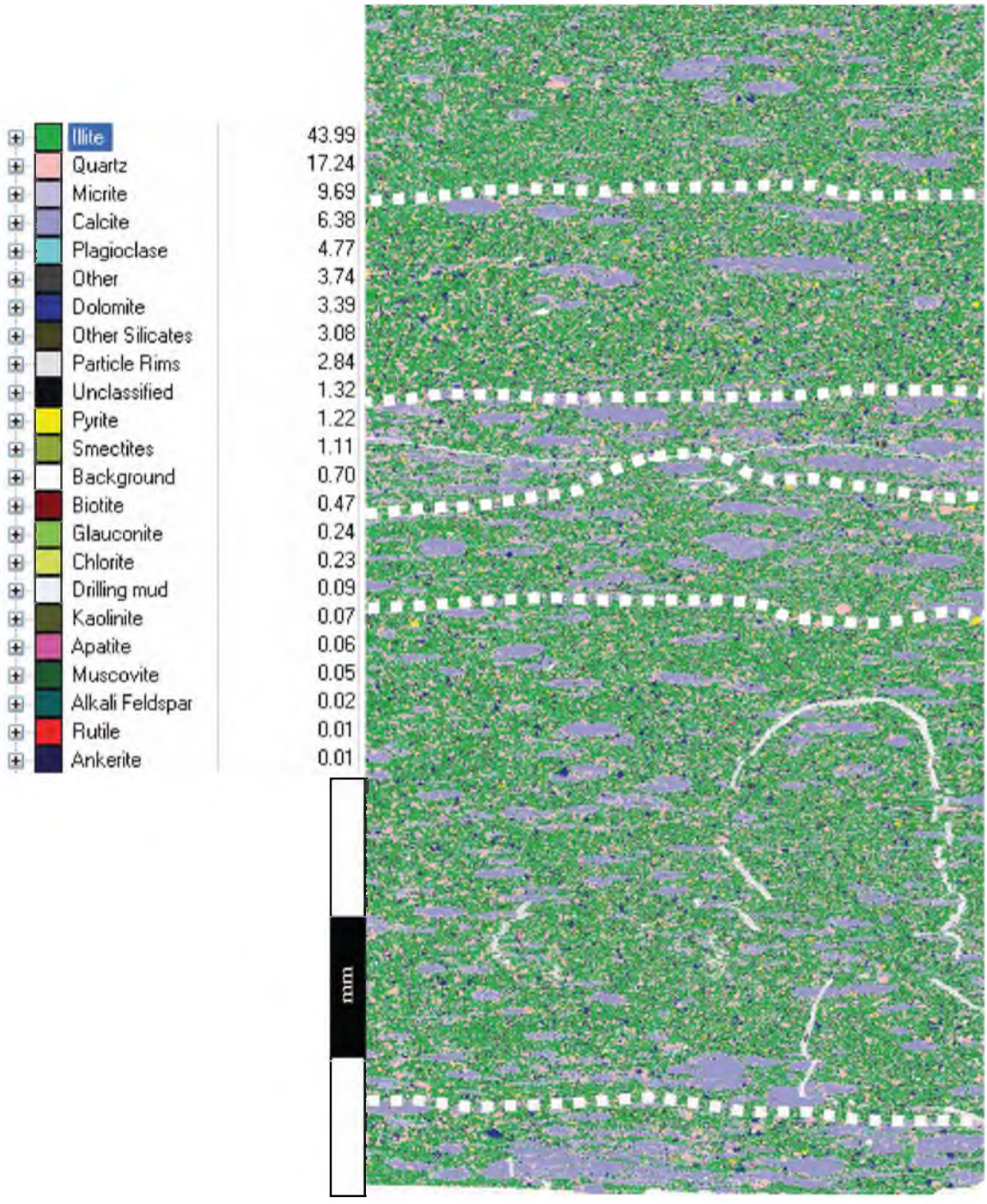

Figure 56: High resolution (2 micron spacing) QEMSCAN image of lithofacies 11 in Pioneer 2 (7,032'). Note the weakly defined lamination (outlined in white). Micrite/calcite grains (purple) appear to cross cut depositional fabrics, with preferential growth along lamination direction.

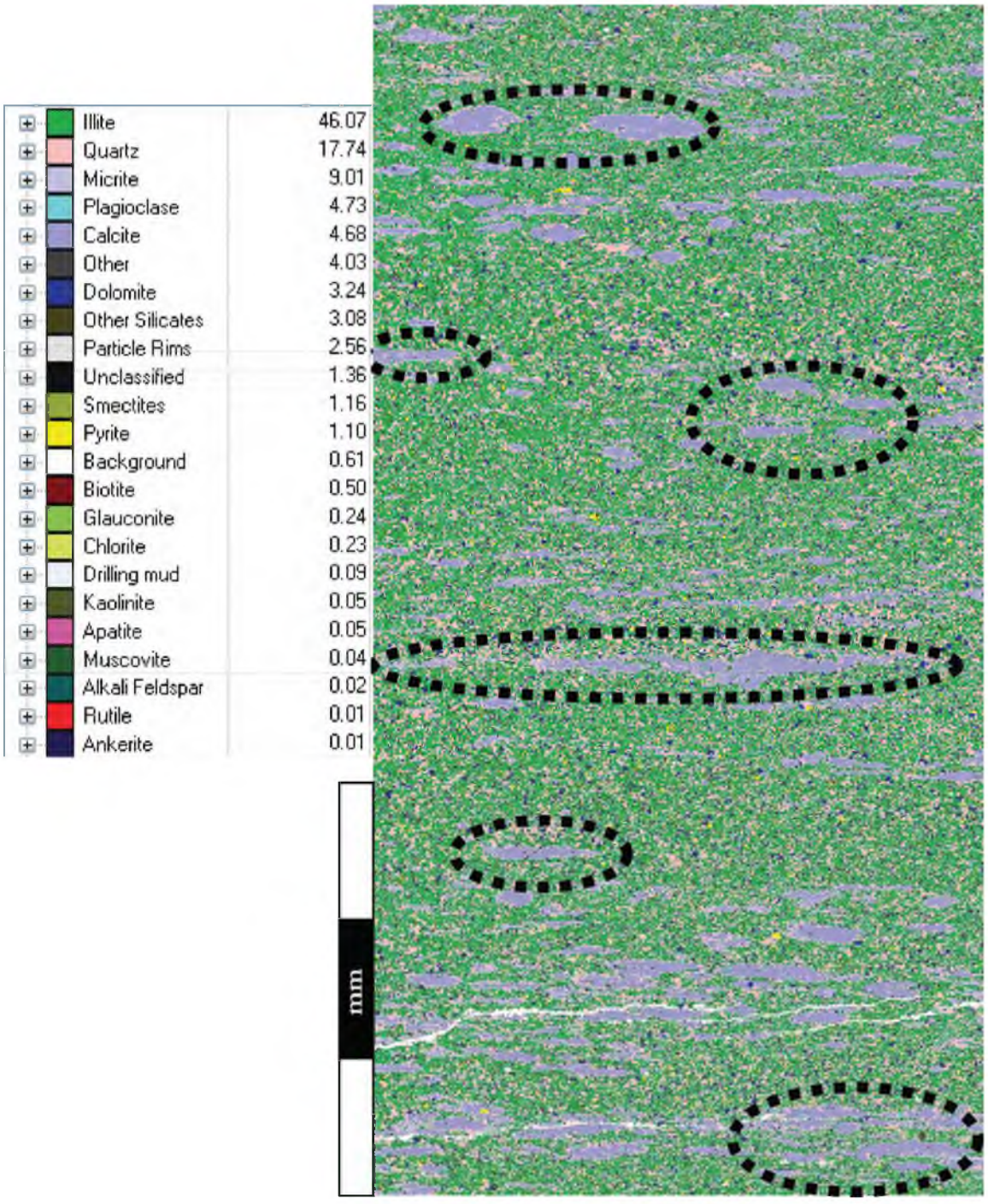

Figure 57: High resolution (2 micron spacing) QEMSCAN image of lithofacies 11 in Pioneer 2 (7,032'). Micrite/calcite preferentially grows in quartz rich laminations and around quartz grains (examples outlined in black).

Table 6: Porosity and Permeability statistical analysis.

Core Prefix	Max Poro (%)	Max Poro Lithofacies	Max Perm (nD)	Max Perm Lithofacies	Min Poro (%)	Min Poro Lithofacies	Min Perm (nD)	Min Perm Lithofacies
Q1	8.01	4	100	1	4.63	1	43	1
Q8	7.81	1	11.9	4	5.79	4	0.3	1
Q16	8.68	6	396	1	5.74	1	0.05	1

		Porosity (%)				Permeability (nD)			
Lithofacies	n	Max	Min	Mean	StDev	Max	Min	Mean	StDev
1	29	8.12	4.63	6.55	0.82	396.00	0.05	47.37	75.89
2	9	7.58	6.21	6.97	0.51	88.00	2.20	59.13	24.31
3	7	7.21	5.36	6.36	0.76	87.00	46.00	59.14	14.67
4	14	8.01	5.79	7.00	0.68	96.00	0.45	50.25	32.13
5	3	5.14	4.80	4.97	0.17	71.00	53.00	64.00	9.64
6	4	8.68	7.04	7.83	0.69	129.00	28.30	98.58	47.75
7	3	7.08	6.73	6.89	0.18	4.33	0.17	2.23	2.08

Lithofacies 6 displays the highest porosity of 7.83%, with lithofacies 5 displaying the lowest of 4.97% (Figure 58). This is counter-intuitive, since lithofacies 6 is clay rich, and lithofacies 5 is rich in quartz. Lithofacies 1 through lithofacies 4 all fall within the same statistical variation, however, the mean values systematically decrease with increased quartz content. Permeability within the cored intervals is low across all lithofacies, with a maximum value of 396 nanodarcies and a minimum of 0.05 nanodarcies. No clear pattern emerges with permeability data (Figure 58).

Chemofacies

Chemofacies analysis aims to construct narrow and consistent quantitative definitions of discrete rock units using elemental data. These chemofacies definitions should be consistent not only for a given core, but across any cored interval anywhere. In essence, a chemofacies is defined compositionally by certain percentages of a set of elements. A chemofacies defined as 50% silicon and 50% calcium will be the same regardless of its provenance or geographic location.

The previous section illustrates that there are considerable lithological variations in the Mancos Shale. In the QEMSCAN and XRD analysis the major minerals identified are quartz, illite, calcite/micrite, chlorite, and other silicate minerals. These major minerals vary in critical elements, and thus, we predict, should be traceable through XRF elemental data. Quartz (SiO_2,) is rich in silicon. Clays, mainly illite (highly variable chemical composition of $(K,H_3O)(Al,Mg,Fe)_2(Si,Al)_4O_{10}[(OH)_2,(H_2O)]$ which is often simplified to the muscovite composition of $KAl_2(Si3Al)O_{10}(OH,F)_2$), hold the majority of aluminum. Calcite and micrite are comparatively rich in calcium.

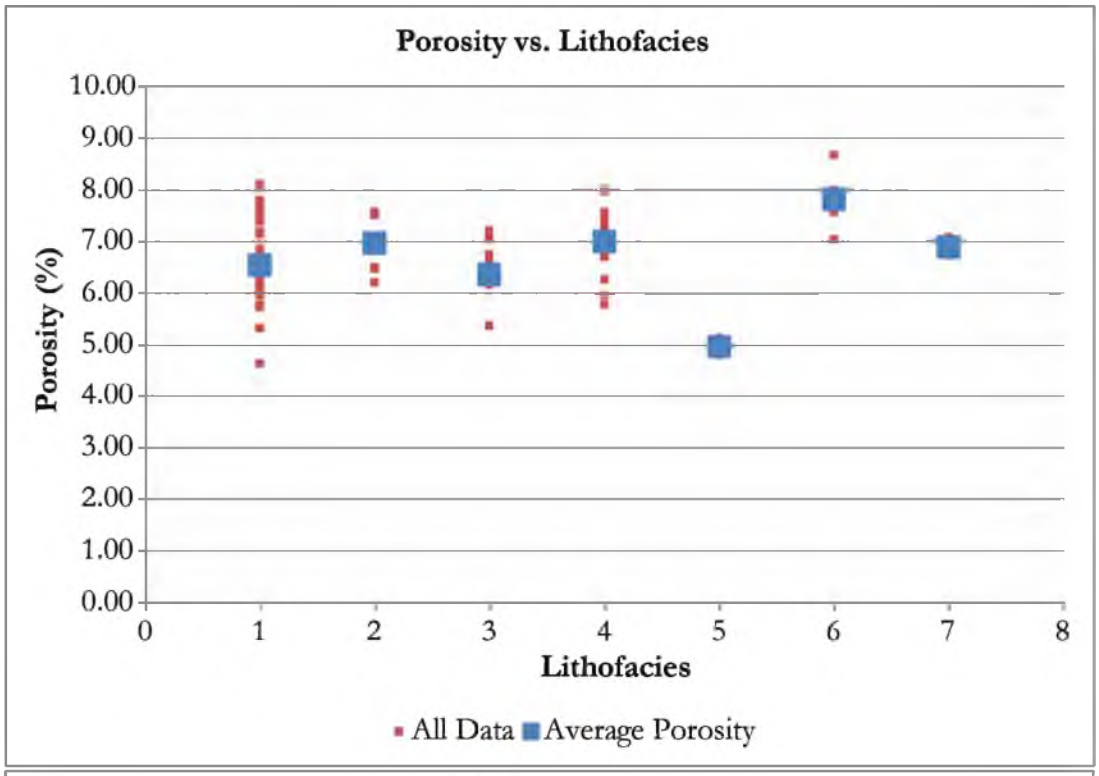

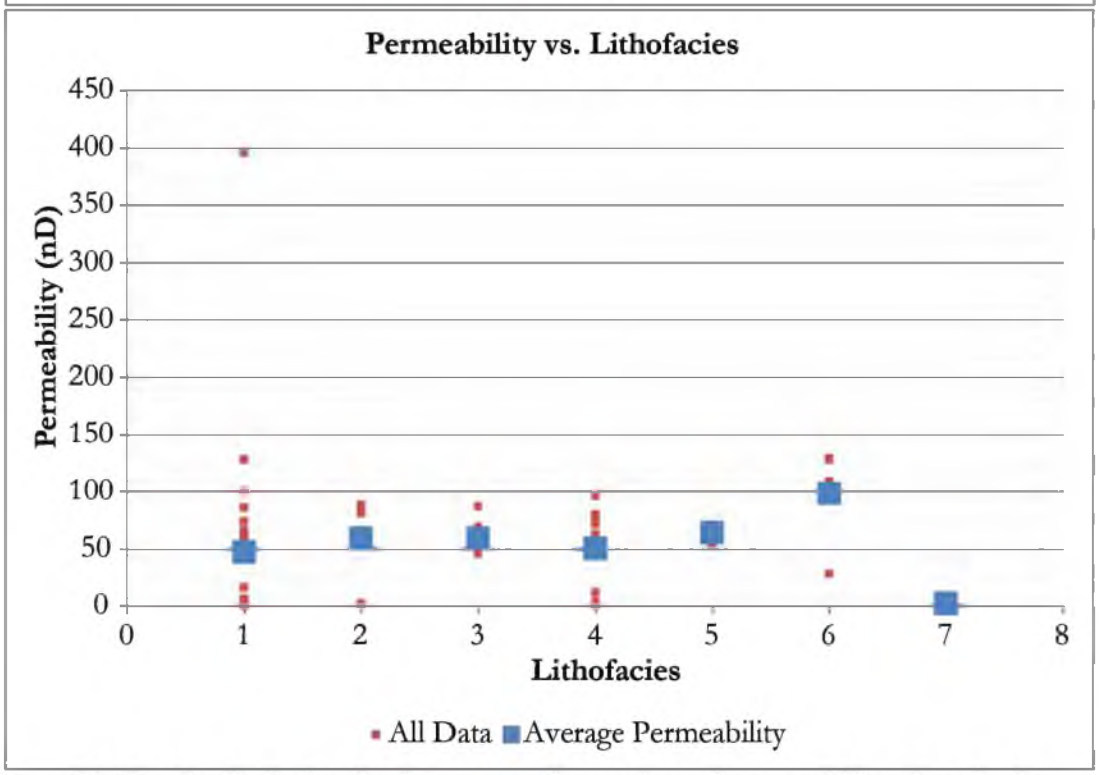

Figure 58: Graphs displaying the data range of porosity and permeability values in the Questar 1, 8, and 16 wells. Mean porosity values decrease with environments that range from distal to proximal. Lithofacies 6, being the most porous and the most distal environment, followed by 4, 2, 1, and 3. No simple trend is seen in the permeability data relating permeability to lithofacies.

For example, in a simplified system consisting of only quartz, the ratio of silicon to, aluminum should theoretically be infinite, or at least very high. Conversely, if there were only illite in this simple system, the ratio of silicon to aluminum should be 3/2 (assuming a simplified formula for illite). It would follow that if there were a mixture of quartz and illite, the silicon to aluminum ratio should be greater than 3/2 and less than infinity.

For the purposes of this study, we will be focusing on the following ratios. Calcium to aluminum ratios (Ca/Al) will be examined to trace the change of calcite and micrite relative to clays. Similarly, silicon to aluminum (Si/Al) ratios will be used to identify the change of quartz relative to clays. Since zirconium is found dominantly in zircon crystals, which are themselves the product of igneous processes, zirconium to aluminum ratios (Zr/Al) are used to indicate detrital input to the system. It follows then that a strong correlation between the Si/Al and Zr/Al ratios is highly indicative that the quartz is indeed detrital rather than biogenic. Titanium to aluminum (Ti/Al) ratios along with the niobium to aluminum (Nb/Al) ratios, indicate the amount of heavy mineral variability as both niobium and titanium are found in rutile, the most abundant heavy mineral throughout all cored intervals. Thorium to aluminum (Th/Al) and potassium to aluminum (K/Al) ratios show radioactive element variation throughout the cored interval.

R-squared values of .62, .56, and .68 for the Questar 1, Questar 8, and Questar 16 respectively imply 62%, 56%, and 68% of the variation in Zr/Al is related to the variation in Si/Al (Figure 59). This suggests that the majority of quartz in the cored intervals of study is detrital rather than biogenic or diagenetic. An inverse relationship between clay indicators (K/Al and Th/Al) is less well developed (Figure 60), but extends this finding suggesting that during comparatively quiescent periods of detrital input, there is an associated increase in clay content.

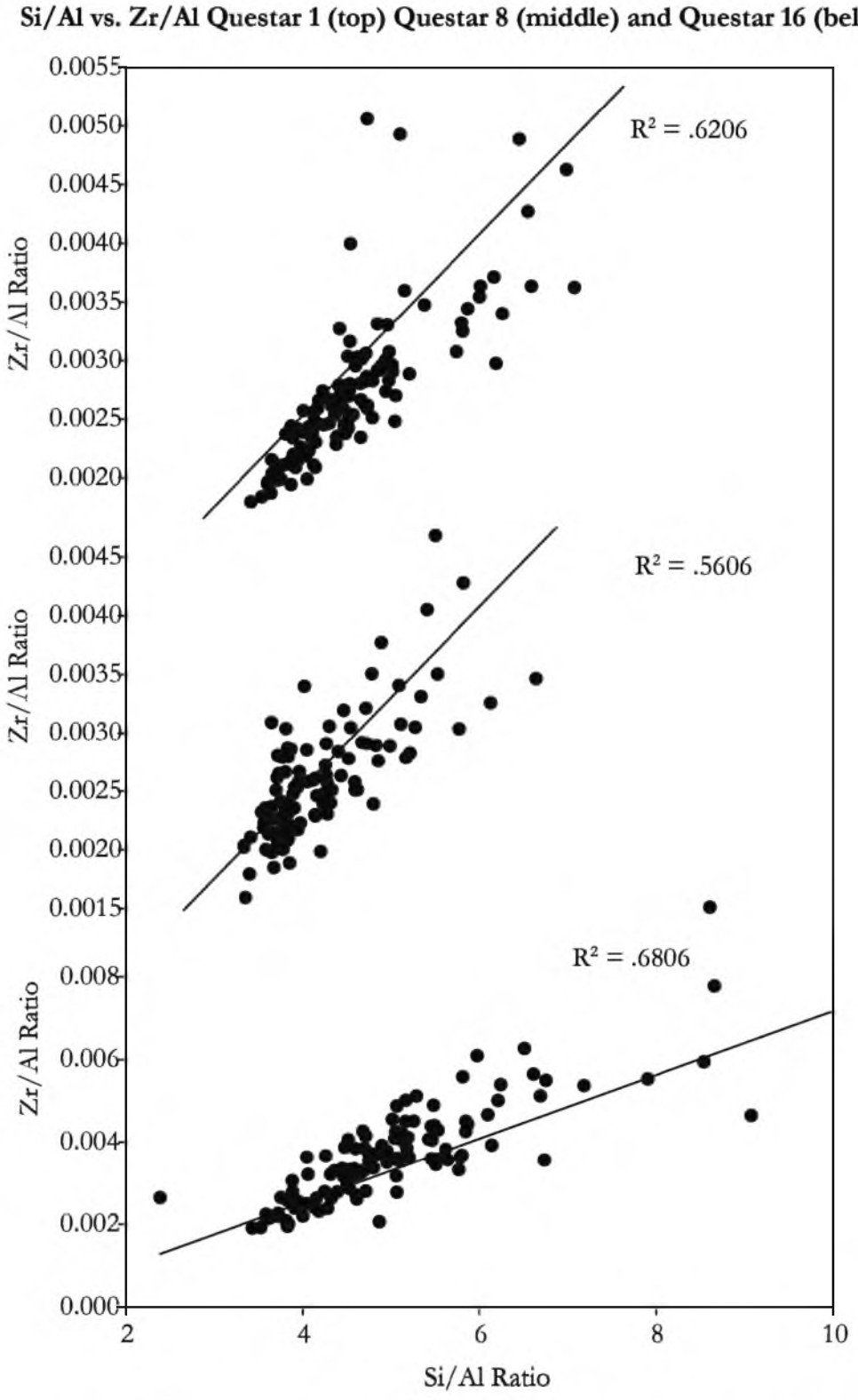

Figure 59: Cross-plot of Si/Al ratios and Zr/Al ratios in Questar 1, Questar 8, and Questar 16. The positive correlation shows that the detrital signal of Zr/Al is strongly related to the quartz signal of Si/Al. This suggests that the majority of quartz in these cores is detrital.

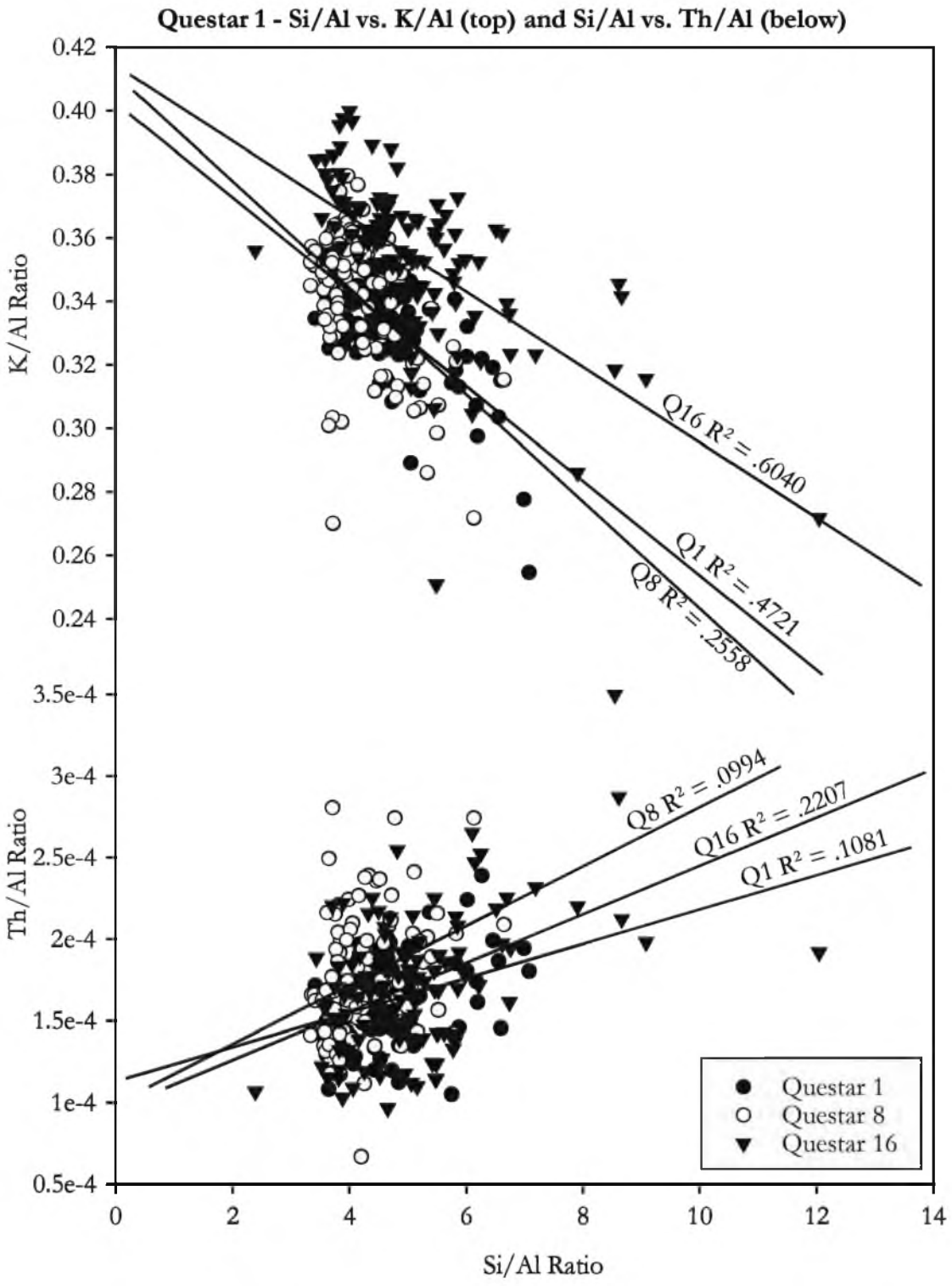

Figure 60: Cross-plot of Si/Al ratios against K/Al (top) and Th/Al (below) ratios in all Questar wells. Note the inverse relationship found in Si/Al vs. K/Al. This relationship suggests that it is possible to use gamma-ray logs to infer detrital quartz influence in the Mancos shale. This relationship does not extend to Si/Al vs. Th/Al.

The practical application of chemofacies analysis is that should identified chemofacies align with identified lithofacies, then one can reliably estimate lithological components (e.g. lamination style, bioturbation index, clay content – to as well as these parameters have been constrained through lithological analysis) given a specific chemical composition. A chemofacies that does not align well with identified lithofacies is less useful because no reliable connection can be made between chemical content to geologic parameters of interest. Because the usefulness of chemofacies is tied directly to the ability to differentiate between lithofacies, the established lithofacies are used to define our chemofacies. In other words, to use chemofacies analysis as a first order tool, a chemofacies is defined by the lithofacies present at the depth of XRF measurement.

Chemofacies 1 – Testing Cross-core Viability

In this study, there is an excellent opportunity to test the viability of chemofacies analysis across several cored intervals. Lithofacies 1, for instance, occurs in Questar 1, Questar 8, Questar 16, and Pioneer 1 cored intervals. Lithofacies 1, previously described in detail, is similar lithologically across all three cored intervals. It follows that chemical similarities should exist across all cored intervals (as well as within a single cored interval). Elements of particular interest include calcium, silicon, and aluminum. Calcium is used as a proxy for calcite and micrite, silicon as a proxy for quartz content, and aluminum as a proxy for clay content.

Normalized for the purposes of plotting all these data on a ternary plot, a clear pattern emerges across all three cored intervals (Figure 61). All three cored intervals have similar ranges of weight percent silicon and aluminum (ranging from 30 to 55 weight percent), but there is a wide variability in weight percent calcium (ranging from under 10 to

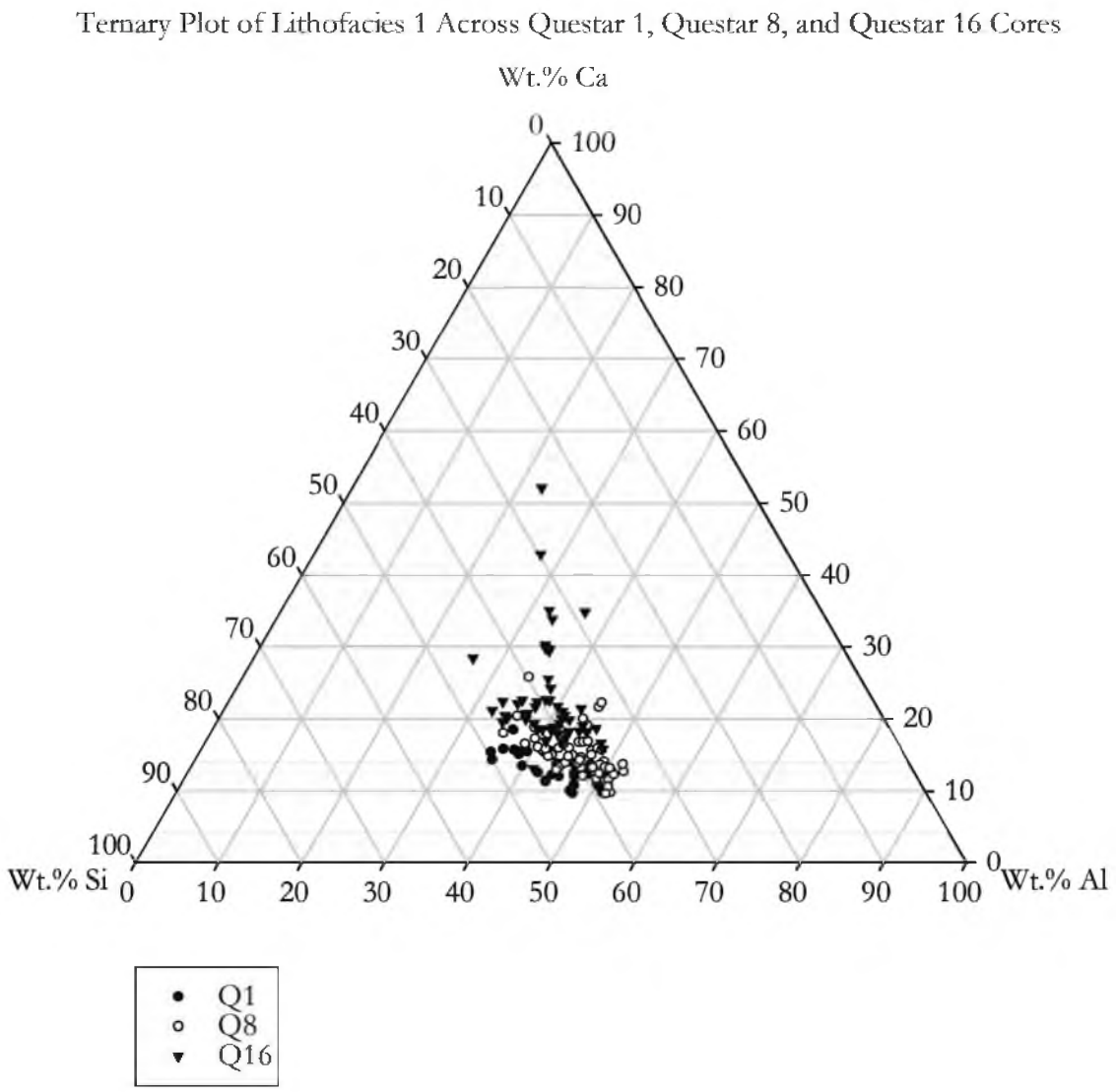

Figure 61: Ternary plot of normalized XRF data comparing weight percent of aluminum, calcium, and silicon in lithofacies 1. In all three cores, there are similar aluminum and silicon ratios, but there is highly variable calcium content. Questar 1 has the lowest calcium content, with Questar 8 containing intermediate calcium content, and Questar 16 with the highest calcium content.

55 weight percent). This variability shows a consistent pattern wherein Questar 1 is the least calcium rich cored interval, followed by Questar 8, with Questar 16 being the most calcite rich of the three. Eight data points from the Questar 16 cored interval fall well outside the range of other data. With the exception of these few anomalous data points, there appears to be some across core variability, particularly in regards to calcite content. These data are summarized on Table 7. Chemofacies 1, the chemically defined facies that corresponds to lithofacies 1, has a 95% certainty within the following ranges: aluminum weight percent ranges from 30% to 55%, calcium weight percent ranges from 5% to 30%, and silicon weight percent ranges from 32% to 48% (Figure 62).

While the chemofacies is well defined statistically, it is not chemically different enough from the remaining XRF data to be of applicable use (Figure 63). In essence, there is a problem with chemofacies 1 overlapping with large portions of the remaining data. While chemofacies 1 data are clustered well, the error associated with them is simply too large to differentiate them from other chemofacies.

Chemofacies 1 can also be effectively analyzed to address critical assumptions that have been made for chemostratigraphic and chemofacies analysis. In a simplified system consisting of only quartz (SiO_2), calcium carbonate ($CaCO_3$), and illite $KAl_2(Si3Al)O_{10}(OH,F)_2$), there should be trends relating silicon, calcium, and aluminum.

If the assumption holds that the rocks in the cored intervals are behaving similarly to those in the simplified model mentioned at the beginning of this section, then aluminum, which is being used as a proxy for clay content, and silicon, which is being used as a proxy for detrital quartz content, should demonstrate a clear inverse relationship. Figure 64 represents a collection of cross-plots of aluminum weight percent versus silicon weight percent separated by each core interval. In Figure 64a, most of the data points display an

Table 7: Statistical analysis of chemofacies 1.

Lithofacies 1:		Al wt% norm	Ca wt% norm	Si wt% norm
Q1	N=	37.00	37.00	37.00
	mean=	43.91	13.04	43.05
	std dev=	4.75	2.13	3.34
	std error=	10.82	16.30	7.77
	2 sigma=	9.50	4.25	6.69
	96% -	34.41	8.79	36.36
	96% +	53.41	17.30	49.73
Q8	N=	72.00	72.00	72.00
	mean=	46.13	14.86	39.01
	std dev=	4.40	3.16	2.70
	std error=	9.53	21.25	6.92
	2 sigma=	8.80	6.31	5.40
	96% -	37.34	8.54	33.61
	96% +	54.93	21.17	44.41
Q16	N=	74.00	74.00	74.00
	mean=	37.53	22.29	40.17
	std dev=	5.43	6.20	4.70
	std error=	14.46	27.81	11.71
	2 sigma=	10.85	12.40	9.41
	96% -	26.68	9.89	30.77
	96% +	48.39	34.69	49.58

		Al wt% norm	Ca wt% norm	Si wt% norm
All Cores	N=	183	183	183
	mean=	42.21	17.50	40.30
	std dev=	6.28	6.03	4.02
	std error =	14.87	34.45	9.97
	2 sigma=	12.55	12.06	8.03
	96% -	29.65	5.44	32.27
	96% +	54.76	29.55	48.33

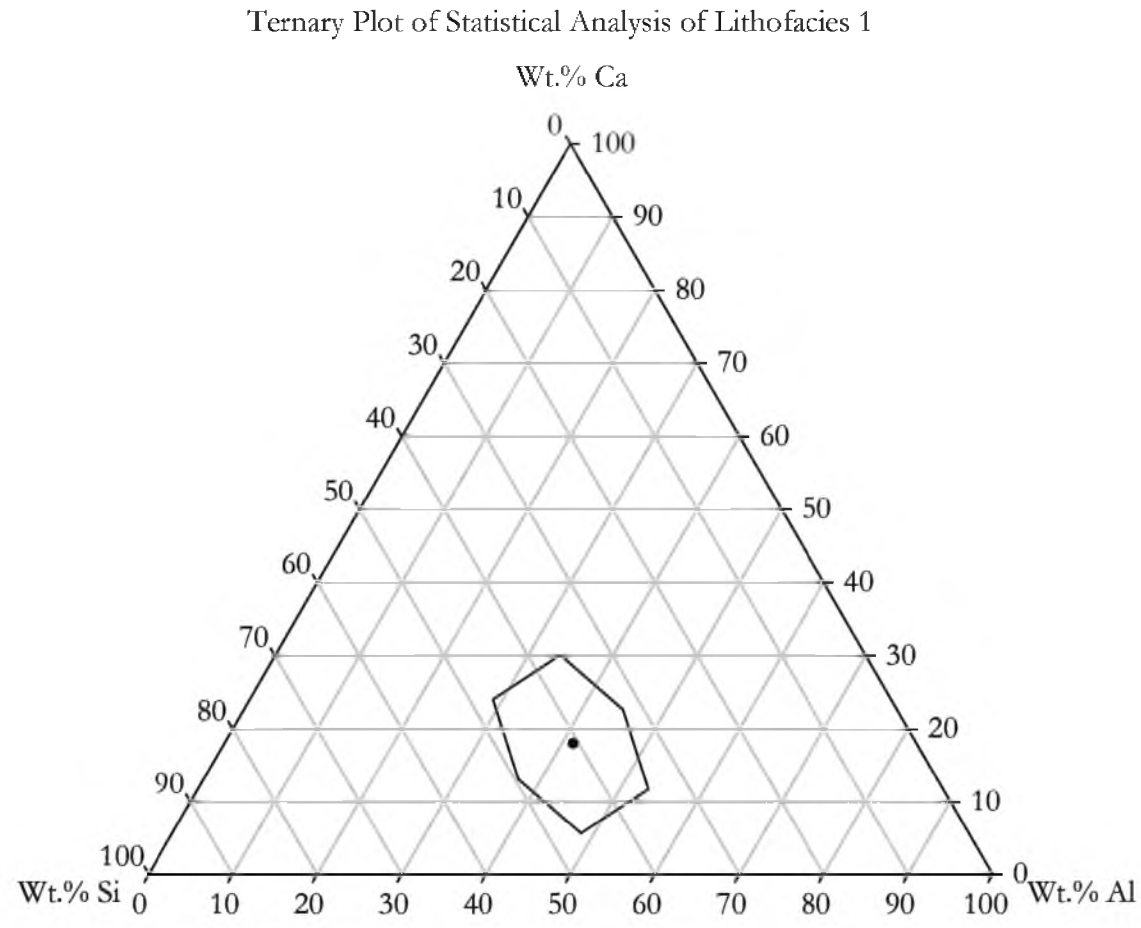

Figure 62: Ternary plot summarizing the statistical analysis of lithofacies 1. The point plotted represents the mean value of normalized data across all cores for lithofacies 1. Outline represents 95% statistical certainty that sample belongs to chemofacies 1. Data are summarized on Table 3.

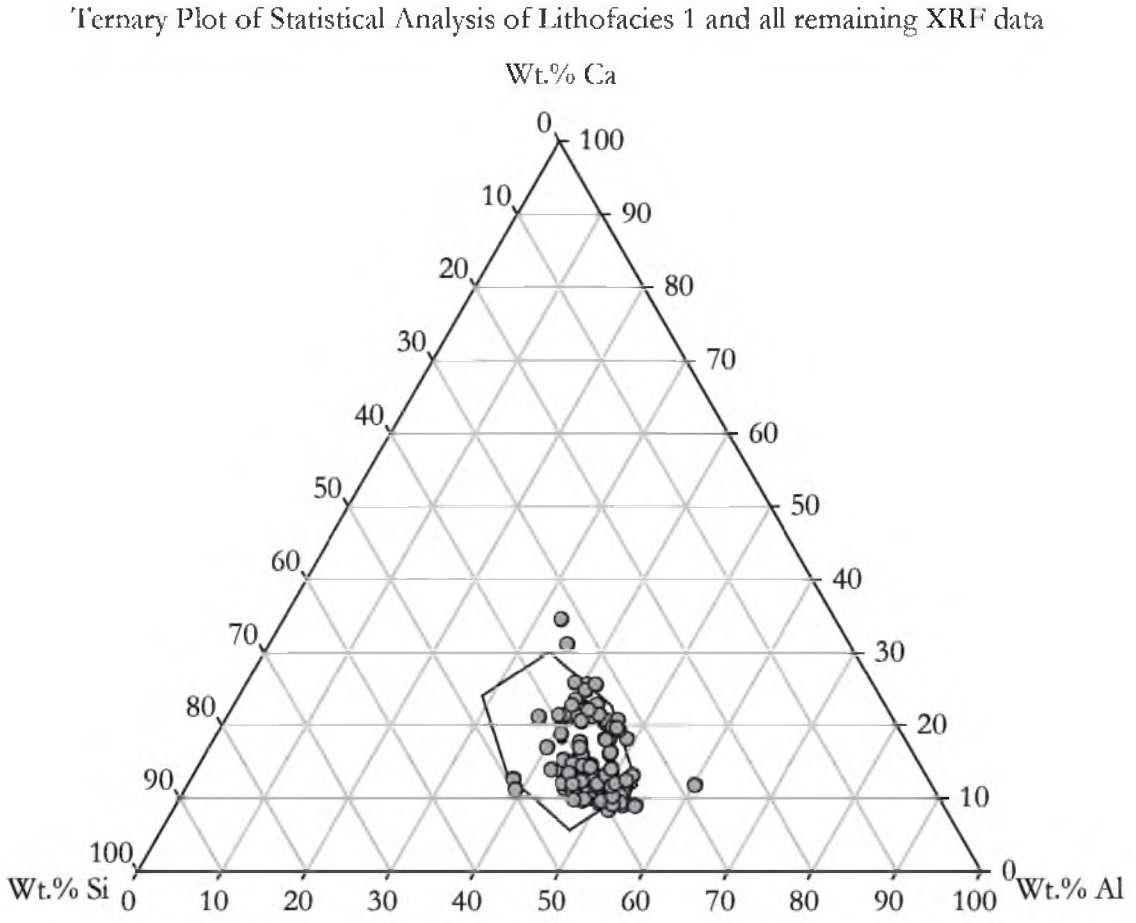

Figure 63: Ternary plot of lithofacies 1 with all other XRF data overlain. Lithofacies 1 is defined by the black outline. All other XRF data (lithofacies 2, 3, 4, 5, 6, and 7) are plotted in grey. These data suggest that lithofacies 1 is not narrowly enough defined to chemically differentiate between it and other data.

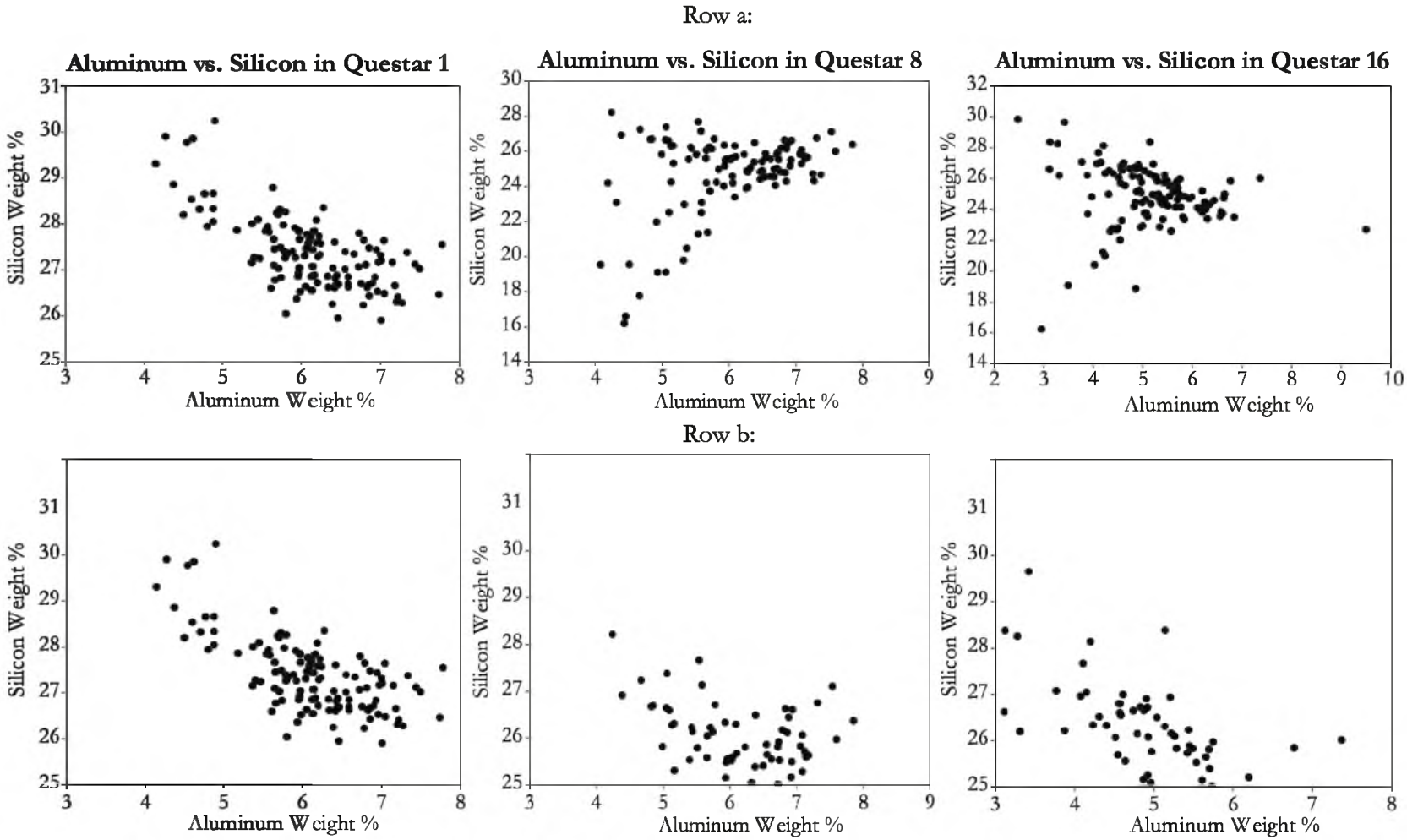

Figure 64: Cross-plots of Aluminum vs. Silicon in Questar cores. Row a (top) shows all data collected, and row b (below) shows data on the same scales. Row a shows that there are outliers in all datasets. Row b highlights that there are rough inverse correlations between aluminum and silicon. Also note that silicon values are generally higher in the Questar 8 well and highest in the Questar 1 well.

inverse relationship, but in Questar 8 and Questar 16, there are numerous data outliers illustrating a more far more complex relationship. If the values in Questar 1 are used as a model relationship, and the axes in Questar 8 and Questar are changed to match those in Questar 1, then a similar, inverse relationship emerges (Figure 64b).

However, there are several trends worth noting in this standardized view of silicon and aluminum. First, if these cores were behaving similar to the simple system, all three plots should plot on top of each other. This is not the case. Given these axes (Figure 64b), it becomes clear that the Questar 1 core is somewhat silicon enriched relative to aluminum (i.e. for a given aluminum weight percent, there is a higher corresponding silicon weight percent). Questar 16, similarly, is silicon poor relative to aluminum. Questar 8 has intermediate values compared the other two cored intervals.

A similar relationship emerges when examining the relationship between calcium, a proxy for carbonate content, and aluminum, a proxy for clay content (Figure 65). Figure 65a demonstrates that there are outliers from the simplified system in all three cores. In Figure 65b, in contrast to Figure 64b, we see that Questar 16 is the most enriched in calcium relative to aluminum (i.e. for a given weight percentage of aluminum, there is a higher weight percentage of calcium). Questar 1 is the more calcium poor relative to aluminum, with Questar 8 again displaying intermediate values compared to the two end members.

Figure 60 demonstrates an important finding. Correlation between K/Al and Si/Al is relatively good, with an R^2 value of .4721 in the Questar 1 core. While this is not the strongest correlation that is seen, it is a far better correlation than that which is seen between Th/Al and Si/Al (Figure 60) which has an R^2 value of .1081. Commonly, potassium and thorium are thought to reside in clays in shales (the operating principal behind use of the gamma ray tool as a grain size indicator) yet the poor correlation between thorium and silica

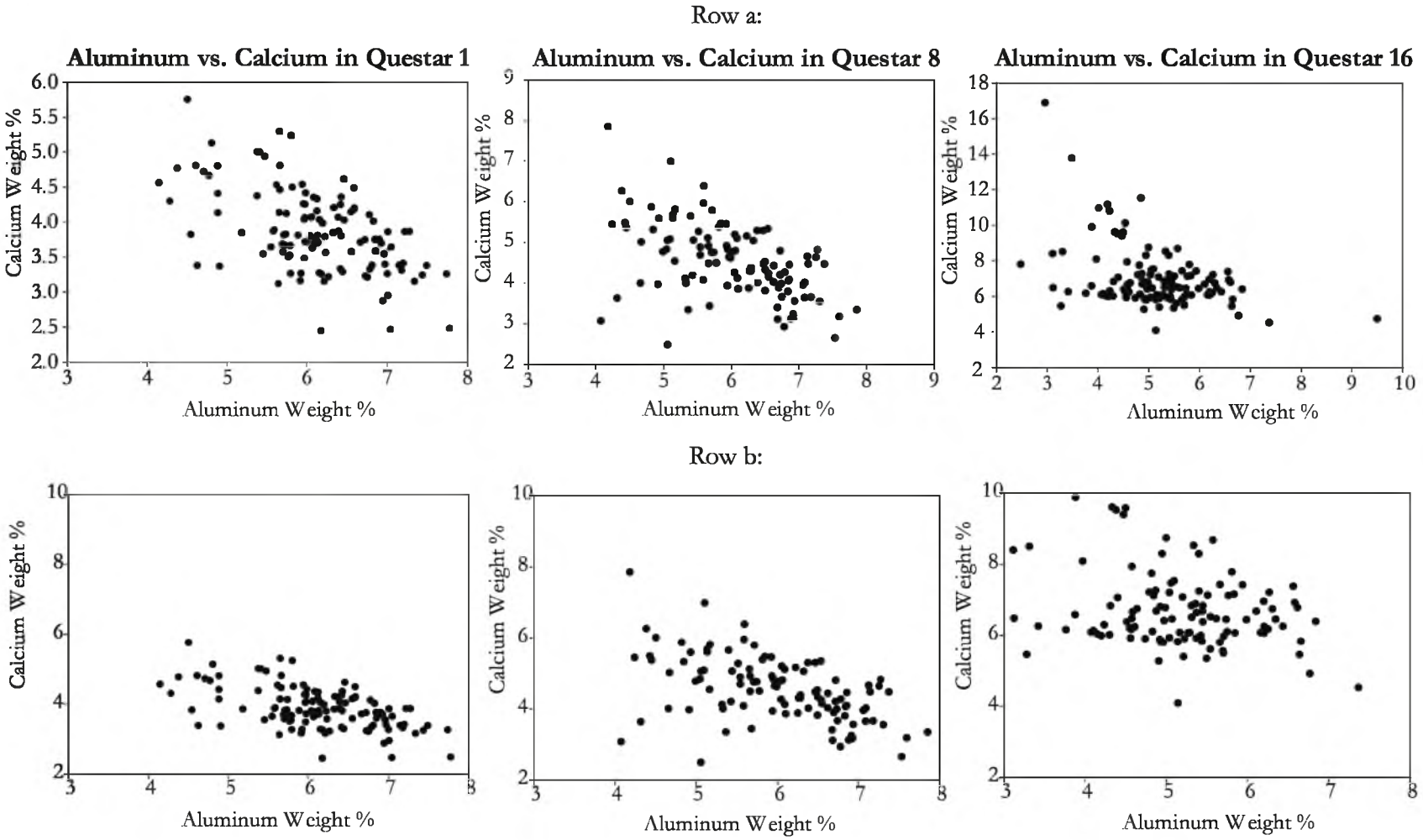

Figure 65: Cross-plots of Aluminum vs. Calcium in Questar cores. Row a (top) shows all data collected, and row b (below) shows data on the same scales. Row a shows that there are outliers in all datasets. Row b highlights that there are rough inverse correlations between aluminum and calcium. Also note that calcium values are generally higher in the Questar 8 well and highest in the Questar 16 well.

is worth noting. The inverse correlation between potassium and silica supports the notion that potassium is largely disseminated throughout clays (as Si/Al increases, K/Al decreases). Additionally, this correlation would imply that if the majority of radiation in these cores comes from potassium, then that radiation would be traced in the gamma ray curves – thus, the gamma ray tool could be used cautiously as an indicator of detrital clays. An increase in detrital clays would be accompanied by a corresponding decrease in the detrital quartz signal. This relationship suggests that it is possible to use gamma-ray logs to infer detrital quartz influence in the Mancos shale. If radiation were suspected to be coming from other radioactive elements, then a spectral gamma ray could achieve the same results.

Chemofacies 3-7 – Chemical Variability Between Different Lithofacies

Approaching the problem of differentiating specific chemofacies from each other is somewhat resolved in examining chemofacies 3 through chemofacies 7. Chemofacies 1 is the most commonly occurring chemofacies throughout the Questar cores accounting for 183 of the 345 measurements. Chemofacies 2 (present only in the Questar 1 and Questar 8 cores) was also a common chemofacies accounting for an additional 35 measurements. The remaining 127 XRF measurements in the Questar cores are spread between chemofacies 3 through chemofacies 7. These data present a picture very different from that of chemofacies 1 and chemofacies 2.

In Figure 66 chemofacies (as defined by lithofacies) are displayed on a truncated ternary diagram. All of these data plot within the 95% certainty area of chemofacies 1. In this figure, it becomes clear that although there are not wildly different elemental properties associated with any of the chemofacies, several distinctions can be made. First, chemofacies 3 through 5 are chemically distinct from chemofacies 6 and 7. Chemofacies 6 and

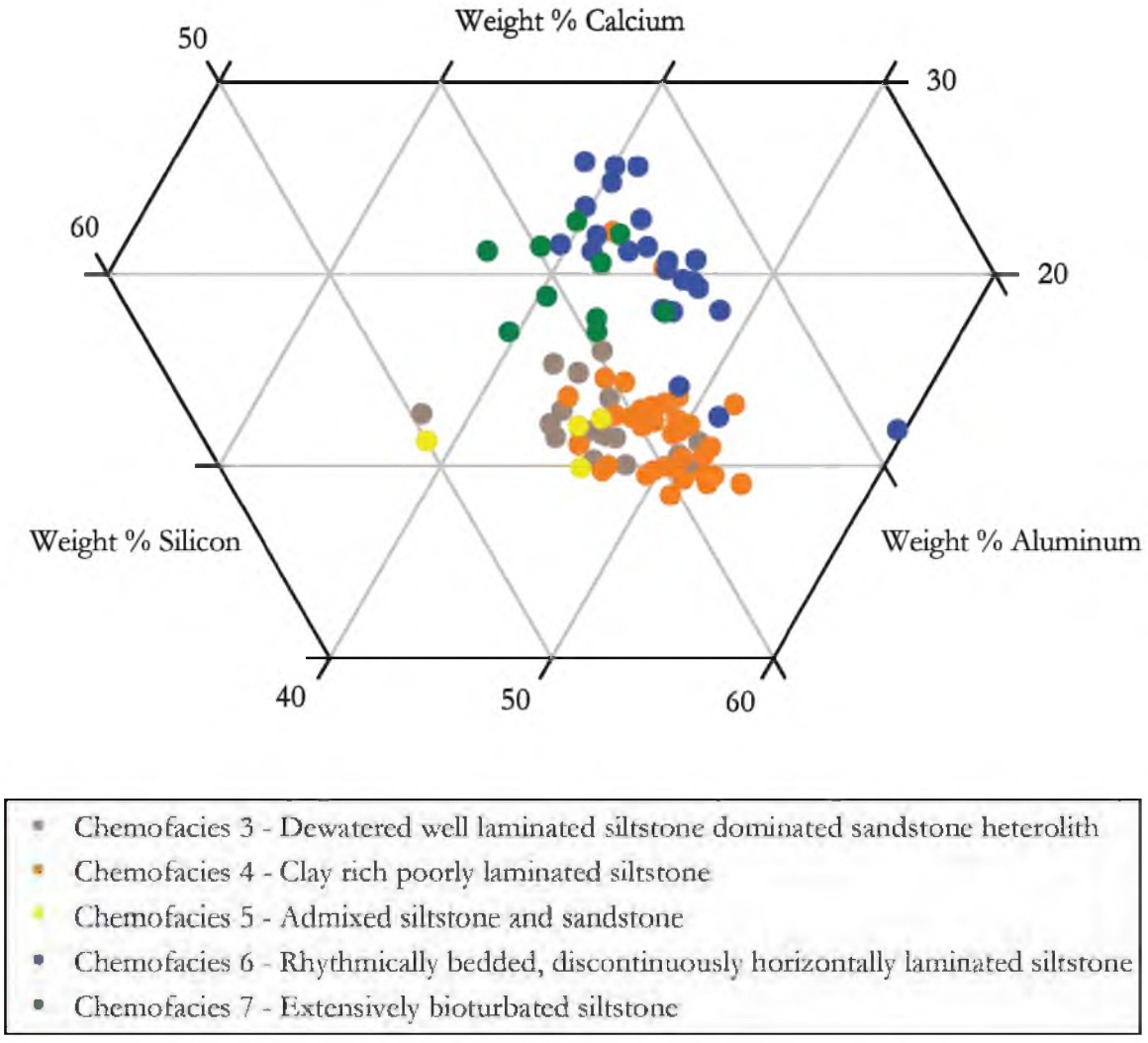

Figure 66: Cropped ternary plot of chemofacies 3 through chemofacies 7. Individual chemofacies begin to separate from each other. Variability between cores is also highlighted, as chemofacies 6 and chemofacies 7 only occur in Questar 16 which is notably enriched in calcium relative to aluminum compared to Questar 1 and Questar 8.

chemofacies 7 are found in Questar 16 but neither Questar 1 nor Questar 8. In chemofacies 1, it was demonstrated that throughout the Questar 16 cored interval there were higher weight percentages of calcium than in any of the other cores. This is further supported when examining chemofacies 3 through 7. Thus the difference in weight percentages of calcium between chemofacies 6 and chemofacies 7 with respect to chemofacies 3 through 7 is attributed to the consistent measurable difference in calcium content in the Questar 16 cored interval. Additionally, other than the difference in calcium, there is little difference in the silicon and aluminum weight percentages between chemofacies 6 and chemofacies 7 with respect to chemofacies 3 through 5.

With chemofacies 3 through chemofacies 7, a similar statistical analysis yields confidence values in an area surrounding the mean value of each chemofacies (Figure 67). This confidence interval helps determine statistical viability of inferring geologic parameters based on chemical data.

Figure 67 demonstrates several key concepts. First, that the statistical variation present suggests that it is difficult to infer specific geologic parameters based solely on elemental variation. For example, a sample that had 11 weight percent calcium, 47 weight percent aluminum, and 42 weight percent silicon would belong (with similar degrees of statistical confidence) to chemofacies 3, chemofacies 4, or chemofacies 5. Consider the lithofacies on which these chemofacies are tied: lithofacies 3 is a dewatered well laminated siltstone heterolith, lithofacies 4 is a clay rich, poorly laminated siltstone, and lithofacies 5 is an admixed siltstone and sandstone. This lithologic variability is far greater than the chemofacies analysis would suggest. Statistically, then, it seems as though chemofacies analysis has failed – while it is possible to construct narrow definitions of chemofacies with statistical reliability, these definitions overlap between various lithofacies making inference to

Ternary Plot of all Lithofacies across Questar 1, Questar 8, and Questar 16

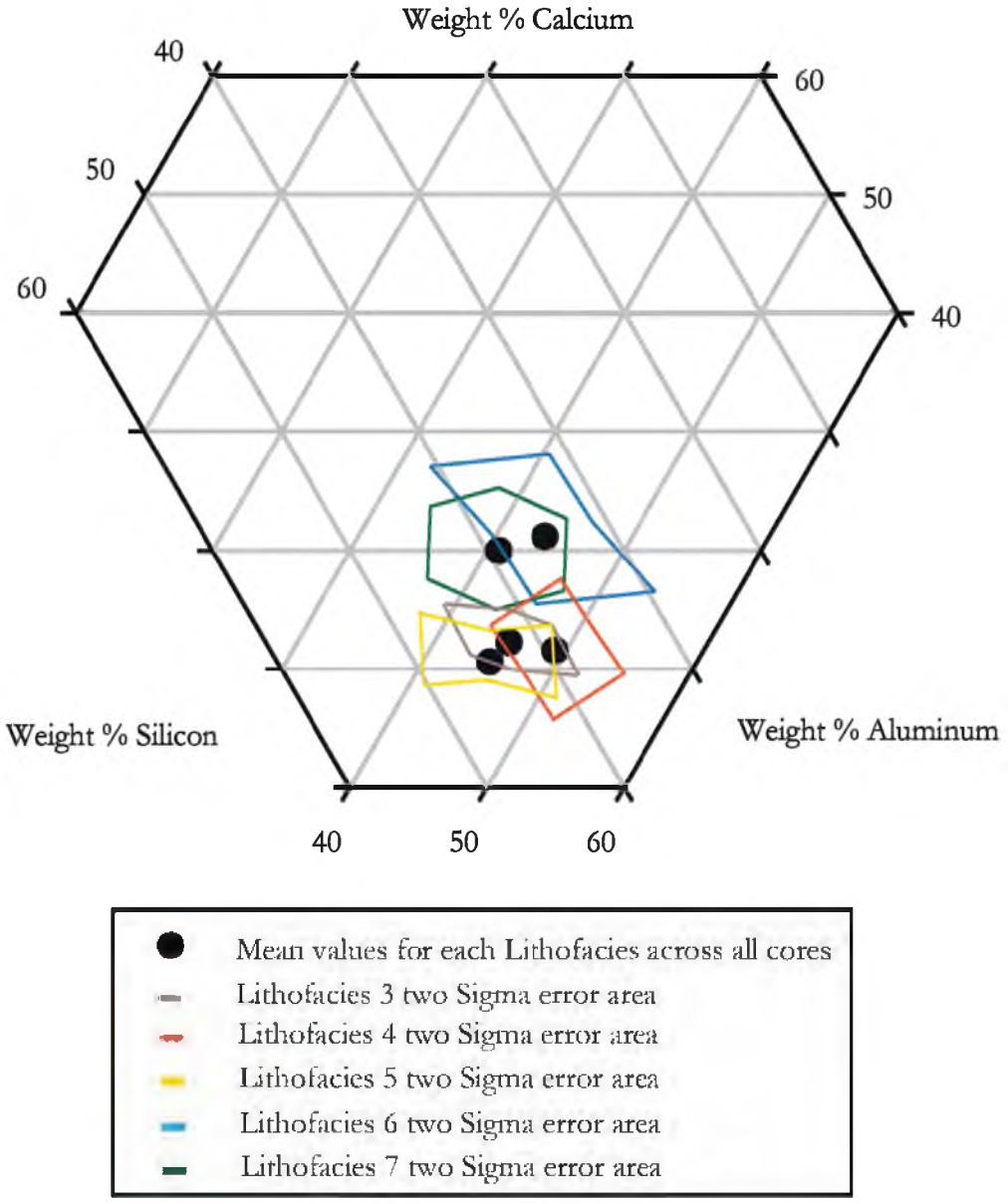

Figure 67: Ternary plot of mean normalized data comparing weight percent of aluminum, calcium, and silicon. Each point represents the mean of all normalized data for a single lithofacies across multiple cores. Surrounding each point is an error area including two sigma lengths in the direction of each axis. Each area then becomes a 95% confidence area for each individual lithofacies. Note that these areas overlap considerably between lithofacies. Also note that lithofacies 6 and lithofacies 7 occur only in the Questar 16 core. The Questar 16 has already been shown to have a high calcium content relative to the other cores.

geologic parameters with statistical reliability difficult. The complete data for Figure 67 is found in Table 8.

A second concept, however, is also well illustrated in Figure 67 – that although it is difficult to infer geologic properties from elemental composition, there are in fact clear patterns and trends that have emerged. Consider lithofacies 4 and lithofacies 5 – a very clay rich lithofacies and a very quartz rich lithofacies, respectively. In our simplified model, where rocks were composed entirely out of calcite, quartz, and illite, these two should plot in very different regions of the ternary plot. Lithofacies 4 should plot very close to the aluminum axis, and lithofacies 5 should plot close to the silicon axis. In practice, this system is far more complex, yet the predicted pattern emerges (Figure 67). The mean values across all Questar cored intervals plot lithofacies 5 approximately five weight percent silicon richer than lithofacies 4. Similarly, lithofacies 3 (a dewatered siltstone dominated sandstone heterolith) plots directly in the middle of lithofacies 4 and lithofacies 5. Additionally, in describing the Questar cores, the Questar 16 core had an average reactivity with acid that was considerably higher than the average reactions encountered in Questar 1 or Questar 8. Seeing all data from Questar 16 plot upwards of 10 weight percent calcium greater than values found in Questar 1 and Questar 8 confirms this observation. To this end, despite the inability to reliably infer statistically significant geologic parameters from given data, chemofacies analysis has confirmed direct observations, and trends have emerged that have been consistent across multiple cored intervals and multiple lithofacies, which has confirmed many assumptions and simplifications implicit to the chemical analysis process.

Table 8: Statistical analysis of chemofacies 3 through 7 over all Questar cores.

Lithofacies 3:	Al wt% norm	Ca wt% norm	Si wt% norm
N=	23	23	23
mean=	45.46	12.28	42.26
std dev=	3.16	1.85	2.50
std error=	6.94	15.06	5.92
2 sigma=	6.31	3.70	5.00
96% -	39.15	8.58	37.25
96% +	51.77	15.98	47.26

Lithofacies 6:	Al wt% norm	Ca wt% norm	Si wt% norm
n=	30	30	30
mean=	43.66	21.19	35.16
std dev=	5.07	4.65	2.01
std error=	11.61	21.96	5.73
2 sigma =	10.14	9.30	4.03
96% -	33.52	11.88	31.13
96% +	53.80	30.49	39.18

Lithofacies 4:	Al wt% norm	Ca wt% norm	Si wt% norm
n=	53	53	53
mean=	49.20	11.58	39.22
std dev=	2.97	2.71	1.93
std error=	6.04	23.43	4.92
2 sigma =	5.94	5.43	3.86
96% -	43.26	6.15	35.35
96% +	55.14	17.01	43.08

Lithofacies 7:	Al wt% norm	Ca wt% norm	Si wt% norm
n=	14	14	14
mean=	40.88	19.99	39.14
std dev=	3.07	2.78	2.73
std error=	7.52	13.90	6.98
2 sigma =	6.14	5.56	5.47
96% -	34.73	14.43	33.67
96% +	47.02	25.54	44.61

Lithofacies 5:	Al wt% norm	Ca wt% norm	Si wt% norm
n=	7	7	7
mean=	44.93	10.59	44.48
std dev=	3.00	1.63	2.72
std error=	6.68	15.38	6.11
2 sigma =	6.00	3.26	5.43
96% -	38.93	7.33	39.05
96% +	50.93	13.85	49.91

Environments of Deposition

Facies Model

Past work has shown conclusively that mud and silt rich fine grained sediments deposited more than 100 kilometers off shore can be correlated to more proximal near shore facies (Plint, 1988; Varban et al., 2005). However, to date, there is no single comprehensive facies scheme that ties together multiple identified mud-rich or silt-rich facies into associated offshore environments (Plint, 2010). In part, this is due to the difficulty of outcrop study of mudstones and siltstones, as they are typically poorly exposed. Additionally, it wasn't until recently that mudstones were cored for unconventional resource exploration. The emergence of new models of mud transport and deposition that focus on flocculation of clays, hyperpycnal flows and associated rapid sedimentation rates of fine-grained sediments have revolutionized previously held notions that most mud was deposited as a blanket of sediment that settled slowly out of suspension.

Flocculation of clays occurs at the interface between freshwater and saline water conditions (Parry, 2011). There are numerous modern and ancient examples of heightened clay density within 10 kilometers of river mouths (Hyne et al., 1979; Milligan et al., 2007). Flocculation is the result of electric double layer repulsion being surpassed by attractive Van der Waal's forces in saline environments (Van Olphen, 1965). Through flocculation, rivers drop vast amounts of muddy sediment rapidly in the transition from freshwater fluvial environments to saline marine environments.

Hyperpycnal flows are defined by Mulder et al. (2003) as negatively buoyant flows that flow along the basin floor due to density in excess of ambient density of the standing water-body. This density difference is driven by particle load suspended within the water

itself. These density flows can transport sediment tens or even hundreds of kilometers along a low grade into a basin.

The combination of flocculation and hyperpycnal flows result in a very different picture of mud deposition than previously envisioned – one where mud deposition is a very dynamic and in some cases, high energy, proximal process. Additionally, rates of mud deposition have been revised accordingly. Because of flocculation and hyperpycnal flows, sedimentation of muds can be on the order of 1-10 centimeters per year (Bhattacharya, 2010; Mulder et al., 2003).

Here, we draw upon current studies of mud transport and deposition from a variety of sources and present a new facies model for siliciclastically influenced offshore environments that include three main environments of deposition: the prodelta, the mudbelt, and the sediment starved shelf. Previously, these have been described (Bhattacharya, 2010; Schieber, 1998) as areas of possible mud deposition, yet limited description of primary structures, bioturbation levels, and lamination styles have accompanied these descriptions.

Prodelta Deposits

The first of these environments is shaped by deltaic influence exerted over sediments. Mud is transported into marine environments almost exclusively through rivers (Plint, 2010). By definition then, all marine mudstones are to some degree influenced by deltas. If mudstones are deposited immediately downstream of a river, it is included in the prodelta depositional environment (Figure 68). Transport from the river mouth to the prodelta is achieved mainly through hyperpycnal flows (Bhattacharya, 2010; Mulder et al., 1995; Vakarelov, 2006). Thus, grading (either normal or inverse) is a diagnostic feature of prodelta mudstones (Bhattacharya, 2010). Additionally, prodelta mudstones are marked by

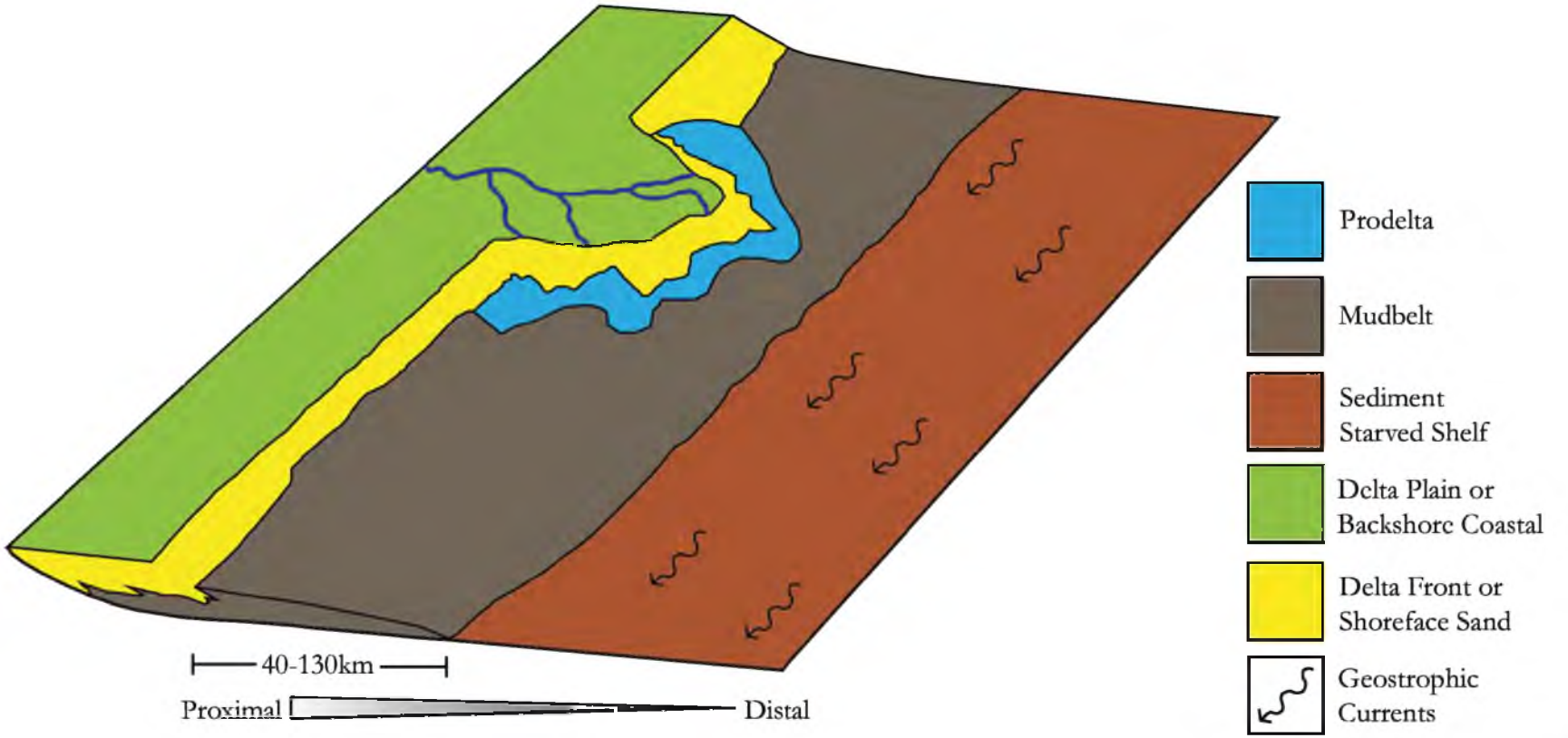

Figure 68: Schematic illustraion of three identified environments of deposition, with lithofacies location labelled, within the cored intervals of this study. Most proximal to a river is the prodelta (blue) containing lithofacies 3. Down flow from the prodelta are re-worked sediments that compose the mudbelt (grey) containing lithofacies 1, 2, 4, 5, 7, and 9. Sediment that is farthest away from a source comprises the sediment starved shelf floor deposits (brown) including lithofacies 6, 8, and 11.

Modified from Bhattacharya (2010) and Vakarelov (2006)

very high sedimentation rates. This can result in loading of structurally unsound fluid muds and water saturated silts and consequently, soft sediment deformation as well as dewatering structures. A separate effect of rapid sedimentation rate is a low diversity of trace fossils (also associated with brackish water conditions) and diminutive trace fossils where they do exist (MacEachern et al., 2010).

Mudbelt Deposits

While all mud is initially deposited in a delta dominated setting, muds and silts can be subsequently re-suspended by storms and wave action and advected alongshore by geostrophic currents as well as permanent along-shelf currents (Bhattacharya, 2010; Milligan et al., 2007; Plint, 2010). This results in a second environment of deposition – the mudbelt (Figure 68). Transportation of sediment is mostly achieved in this environment by currents, but can also include hyperpycnal flows. Storm and wave action can also create offshore directed hyperpycnal flows that transport coarser grained material (i.e. sand and silt) offshore. Thus, primary structures that include current indicators (e.g. ripples), as well as scour surfaces representing where mud and silt has been re-suspended by storms and wave action are particularly diagnostic of this environment of deposition. Because of lower sedimentation rates, and the comparatively lower influence of freshwater relative to the prodelta, a larger diversity of bioturbation can be seen. Since this environment is affected mostly by wave action, it is equivalent to the lower shoreface/offshore transition and offshore zone in conventional shallow marine siliciclastic facies schemes. It has been documented that this mudbelt can be quite large, extending 100's of kilometers alongshore as well as into the basin (Bhattacharya, 2010; Plint, 2010).

Following this model, proximal expressions of the mudbelt would be coarser grained (increased sand and silt content) than distal expressions. In sediment starved distal expressions, discontinuous sandstone and/or siltstone interlaminations would be evident. Correspondingly, organic carbon values should be lowest in the most proximal lithofacies due to extensive dilution effects. Systematic increases in organic carbon should be identified in more distal expressions of this environment.

Sediment Starved Shelf

Basinward of the influence of hyperpycnal flows, the third environment of deposition is a sediment starved shelf floor. Here, hypopycnal flow dominates the transport of sediment – with most sediment settling out of suspension. Winnowing of the sea floor creates scour surfaces that fill with silt and clay. Because of this low sedimentation rate, organic carbon values should be relatively higher than mudbelt environments as a result of low sediment dilution. Primary structures are limited due to sediment starvation as well as low energies. Lamination style is faint and discontinuous. If bioturbation is present, it would be expected to include *zoophycos* or *cruziana* ichnofacies. In all occurrences of this environment in this study, bioturbation levels are low, and where traces exist, they are diminutive.

The lack of trace fossils in the studied cores indicated either an environmental stress or a preservational bias that makes trace identification difficult. There is little evidence that the lithofacies present in the sediment starved shelf deposits are stressed from an environmental standpoint. There is evidence of ample nutrients (lithofacies 6, 8, and 11 have the highest amounts of organic carbon) and little evidence of anoxic conditions. Given that the fossils present in these environments are most likely horizontal, it is entirely possible that

through compaction and winnowing there is simply a low probability of preservation of biological activity.

Environmental Interpretations of Lithofacies

The mudbelt environment is best represented in this study. As described above, the mudbelt is characterized by abundant current indicators as well as moderate bioturbation levels. Lithofacies 1, 2, 4, 5, 7, and 9 are interpreted to be mudbelt deposits. More proximal mudbelt expressions are silt and sand rich, compared to the distal mudbelt expressions, which are clay dominated. Following this classification, lithofacies 9 is the most proximal mudbelt deposit with its very high sandstone and siltstone content. Lithofacies 5, being the second most detrital quartz rich lithofacies, is interpreted to be the second most proximal lithofacies. Lithofacies 7 is interpreted to be the third most proximal representation of the mudbelt attributed mostly to its high bioturbation level, yet finer average grain size than lithofacies 5. Lithofacies 1 is the third most distal expression of the mudbelt. Clay content is much higher in lithofacies 1 compared to lithofacies 5, 7, and 9, indicating a more distal environment. Ripples and current indicators are present in lithofacies 1, however, indicating mudbelt deposition. Lithofacies 2 is then the second most distal expression of the mudbelt with its lower silt content, yet abundant current indicators. The most distal expression of the mudbelt is lithofacies 4. In lithofacies 4, silt laminations are discontinuous, yet silt is still present along with current indicators (Figure 68; Table 9).

Table 9: Environments of Deposition and associated facies.

Environment of Deposition	**Lithofacies contained within (proximal to distal)**
Prodelta	3
Mudbelt	9, 5, 7, 1, 2, 4
Sediment starved shelf	6, 11, 8

Organic carbon values for the mudbelt are lowest in most proximal expressions, with mean values increasing systematically into more distal mudbelt expressions (Figure 20). Mean porosity values also decrease with distal to proximal shifts in environments of deposition (Table 6) with lithofacies 6 (most distal) having the highest porosity, followed by lithofacies 4, 2, 1, and 5 respectively. Lithofacies 7 appears to be an outlier, although to make any assertions, more data would be required.

In this study, the prodelta environment of deposition is underrepresented. Lithofacies 3 has diagnostic features that include dewatering structures. These structures indicate that the sedimentation rate has increased to such a degree that fluid-muds and water saturated silts expel water throughout the deposited sediment. This increase in sedimentation rate is interpreted to indicate an encroaching prodeltaic wedge. Lithofacies 3 is interpreted to represent a distal prodelta environment (Figure 68; Table 9).

Underrepresentation of the prodelta environment can attributed to several key factors. First, an ideal signature of a prodelta environment succession involves documenting a transition from a high sedimentation rate to vast amounts of mud deposited by flocculation. To document this, it is required that the cored interval cross directly through the delta. This is unlikely due to the far smaller area that prodelta deposits would cover in the Western Interior Seaway relative to the area of the mudbelt. Additionally, if small river systems fed the Uinta Basin at the time of Mancos deposition, the prodelta environment would be similarly small. The Ferron Sandstone is typically thought of as a relatively small delta system, as compared to most modern commonly cited examples of river-dominated deltas, like the Mississippi River. Increasingly wave dominated shorelines, like that interpreted for the updip partially equivalent Blackhawk Formation, would have a similar

effect on prodelta environments, as the delta would reach a shorter distance into the basin as compared to a river-dominated delta.

Finally, lithofacies 6, 8, and 11 are all interpreted to be expressions of the sediment starved shelf, where sediment transport is driven by hypopycnal fallout. Since coarser (silt) grains settle out of suspension before finer (mud) grains, the presence of silt indicates proximity to the shoreline. Thus, lithofacies 6 with its rhythmic interlamination style is interpreted to be the most proximal sediment starved shelf deposit. Similarly, Lithofacies 8 is interpreted to be the most distal sediment starved shelf deposit with no laminations. Lithofacies 11 is laminated, albeit very subtly. It follows, then, that lithofacies represents an intermediate environment between proximal and distal sediment starved shelf (Figure 68; Table 9). Also of note, the lithofacies present in the sediment starved shelf have demonstrably higher organic carbon values than mudbelt or prodelta deposits.

In Figure 69, the environments of deposition of all 5 cored intervals are compared to each other. It is demonstrated that the dominant environments of deposition have a clear pattern throughout geologic time. The Pioneer 1 and Pioneer 2 cores both show shifts from proximal environments to distal (the most distal studied). Stratigraphically, this shift corresponds to the transgression recorded by the Tununk member in the Late Cenomanian (Figure 69). Questar 16 shows intermediate mudbelt environments that don't shift to sediment starved shelf environments until a dramatic shift near the top of the core (Figure 69). This shift represents the top of the Juana Lopez siltstone, topped by the Lower Blue Gate member of the Mancos Shale. Questar 1 and Questar 8 both record comparatively proximal environments with respect to the other 3 cored intervals. The Mancos B represents a detached shoreline that records lowstands throughout the Santonian (Hampson et al.,

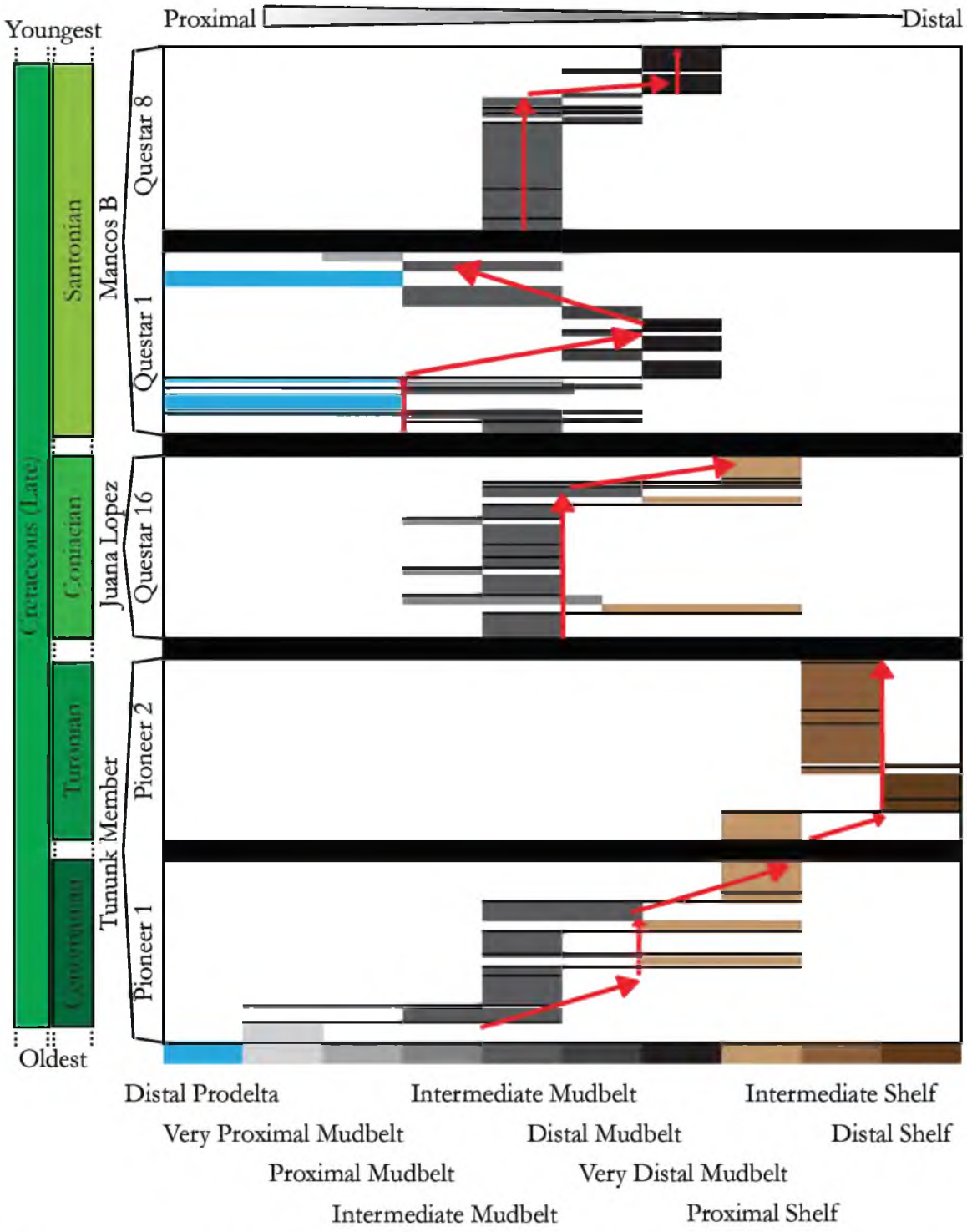

Figure 69: Cross-plot diagram of proximity of deposition and age of cores. Colors correspond to environment of deposition. Where intermediate environments are absent, adjacent envrionments have been expanded horizontally. Flooding surfaces are represented by black lines within each cored interval. Arrows represent overall patterns of deposition (e.g., shifting to more distal environments). Intervals not cored are thick black rectangles between cores (not to scale).

1999). Questar 1 and 8 are both consistent with this interpretation with overall more proximal environments than those represented in the three other studied cores (Figure 69).

Conclusions

With shale formations becoming an ever important resource in domestic natural gas and oil production, high resolution, detail oriented, geological studies of potential targets are essential to fully understand complex heterogeneities which exist on a multitude of scales. The Mancos Shale is no exception; in this study, heterogeneities were identified on micro, macro, and intrabasinal scales. Eleven distinct lithofacies have been identified within the Uinta basin, and within those lithofacies there is conclusive evidence that further heterogeneity exists on a micro scale. The degree of bioturbation, lamination intensity, and other primary depositional qualities vary within single lithofacies. On a chemical scale, the composition of a single lithofacies can span a wide range of chemical makeup.

In all XRD patterns, there is a trend for the illite peak to span a smaller range when glycolated. This suggests that there is some amount of expendable clays present in all samples. A peak at ~12.5Å in several samples also suggests some amount of interstratified clays, specifically the presence of R1 interstratified illite/smectite. While precise ratios of illite and smectite are not determined in this study, their presence is unsurprising given the findings of Nadeau et al. (1981). By and large, QEMSCAN data agreed with XRD observations, with slight changes in the presence of less common clay minerals such as kaolinite.

Mineralogically speaking, the majority of these samples are composed of widely varying percentages of quartz, illite, calcite, and other accessory clay minerals. XRF analysis demonstrated that a single chemical composition is not substantial evidence to generate a

lithological interpretation of a sample, although clear trends emerged when comparing multiple lithofacies to each other.

Additionally, this study classifies three major environments of deposition for this siliciclastically influenced mudstone system, including the prodelta, mudbelt, and sediment starved shelf environment. This new comprehensive facies model will aid in the interpretation of shales and mudstones and fills a significant knowledge gap in mudstone facies models. In the depositional model described above mud depositional forces, including hypopycnal flows, geostrophic currents, winnowing of the seafloor, and flocculation of muds merge to form a complex model for shale deposition. This model relies on bioturbation indices, primary structures (e.g., ripples, and graded laminations), indicators of rapid sedimentation (e.g., dewatering), and siltstone content to make accurate environmental interpretations. Within these environments, organic carbon values ranged from 0.68% – 3.25% and were found to increase as distance from the shoreline increased (i.e. environments of deposition that were more distal were seen to have higher organic carbon values). Porosity, ranging from 4.63% - 8.68%, was demonstrated to slightly increase in a similar fashion where more distal environments had higher porosities. Permeability ranged from .05nD – 396nD, but no significant trends were identified.

Thus, the heterogeneities that exist in the Mancos Shale exist on a variety of scales, and to significant degrees. Recognition of this heterogeneity can be used to guide the selection of ideal shale gas reservoir targets in this thick formation. Heterogeneity may also have significant impact on the design, execution, and effectiveness of stimulation methods of the Mancos Shale. Moreover, these heterogeneities are not unique to the Mancos Shale, and the facies variability documented and facies model presented here are applicable to other siliciclastically influenced shales.

CHAPTER 2

A PRELIMINARY SEQENCE STRATIGRAPHIC MODEL OF A SILICICLASTICALLY INFLUENCED MUDSTONE SYSTEM: THE MANCOS SHALE, UINTA BASIN, UTAH

Abstract

The establishment of sequence stratigraphy has been hailed as the third, and most recent revolution in geological thought. Sequence stratigraphic models were initially developed from sedimentary records of shallow marine environments, in part from world class Cretaceous outcrops in the Uinta Basin Book Cliffs succession. The downdip mudstone depositional system – the Mancos Shale – on the contrary, has yet to be thoroughly described from a sequence stratigraphic perspective. In this study, a preliminary sequence stratigraphic model of five cored intervals in the Mancos Shale in the Uinta Basin is presented. A highly detailed lithological description and associated depositional environment model (Figure 68) are reinterpreted with a focus on identifying parasequences and stacking patterns in core. Progradational, aggradational and retrogradational stacking patterns of parasequences are used to define highstand, lowstand, and transgressive systems tracts within the cored intervals, along with intervening sequence boundaries, maximum flooding surfaces, and transgressive surfaces. This description was complemented with the addition of stratigraphic x-ray fluorescence data. Results demonstrate that parasequences can

be routinely identified on the ~10 foot scale. In these data, retrogradational stacking patterns of parasequences, and hence transgressive systems tracts, are most easily identifiable. Chemostratigraphic data show that large scale trends (~20 -100 feet) agree with sequence stratigraphic interpretations, whereas smaller scale trends (e.g., individual parasequences) do not provide robust correlations. By thickness, the majority of the succession occupies highstand systems tracts, punctuated by intervals of transgression. Lowstand systems tracts, which are associated with sudden, distinct landward shifts in lithofacies, are thin and commonly omitted. Sequence stratigraphic analysis reveals an architectural motif dominated by progradation of the mudbelt system through time.

These systems tracts are found to be a higher order than those identified in the RGU-1 core (Kennedy, 2011), yet the style and architecture of these systems tracts is similar to those identified in the RGU-1 core. Future research should aim to test this preliminary sequence stratigraphic model regionally throughout the basin. Traditional sequence stratigraphic models are thereby demonstrated to fit siliciclastically dominated mudstone systems like the Mancos Shale with minimal alteration. Possible shale gas target intervals within the Mancos are found to occur in either transgressive systems tracts or early distal expressions of highstand systems tracts. Using sequence stratigraphic applications, sweet spots, ideal reservoirs, and other useful lithologic characteristics can be interpreted throughout the Uinta Basin.

Introduction

Sequence stratigraphic models provided a great revolution in geological study. Rather than rely on lithostratigraphic correlation between wells, sequence stratigraphy provided the ability to integrate chronostratigraphy (and biostratigraphy) to lithostratigraphy and

chemostratigraphy. This, in essence, ties together notions of relative and absolute timing with the deposition of various sediments. When it was first proposed, it provided a new, powerful predictive tool to describe and explain along-dip variations in rock units. Additionally, complexities within reservoirs became immediately apparent, and revolutionized modeling their capacities.

Sequence stratigraphy in some form or another can be traced back in its roots into the 19th century (Catuneanu, 2008). However, it was not until the revolutionary paper published in the 64th AAPG memoir by John Van Wagoner that sequences were explicitly named, and separated from global eustasy curves. This seminal work was based in part from outcrops of Cretaceous sandstones that outcropped in southern Utah (Van Wagoner, 1995). The Mancos Shale, in fact, represents the distal equivalent of the rocks upon which the book was literally written. Surprisingly, sequence stratigraphic models, which themselves have been written and re-written addressing shortcomings of this original text, have never been systematically applied to these distal equivalents.

Today, when developing conventional oil and gas plays a sequence stratigraphic interpretation of reservoirs provides an indispensable framework useful in calculating net pay, well costs, and other critical variables (Houseknecht et al., 2001). Sequence stratigraphic models of unconventional mudstone systems that exist in the public domain (e.g., Bohacs et al. (2008)) however, remain scarce. In part, this is due to the difficulty associated with studying mudstone systems (Sorby, 1908). Unlike their shallow marine counterparts that were used to develop sequence stratigraphy, mudstones rarely outcrop, making direct observation and analysis difficult, if not impossible. Furthermore, changes in mudstone systems may go unrecorded by visual hand-specimen inspection alone. As a result in mudstone systems, chemostratigraphic analysis is an important tool to resolve otherwise

invisible trends or corroborate subtle trends. Additionally, sequence stratigraphic analysis hinges on the ability to trace proximal to distal trends and patterns. With no unifying facies scheme that exists for mudstone offshore depositional systems, the ability to identify such trends was very difficult.

Recent studies on the sequence stratigraphy of distal equivalents of the book cliffs successions include work done by Hampson et al. (1999), and MacQuaker et al. (2007). Hampson et al. (1999) focused specifically on the Mancos B member, and identified incised valleys that were then filled with pulses of transgressively stacked sediment. MacQuaker et al. (2007), on the other hand, focused on lithofacies variability of the members of the Mancos Shale that correlate updip to the Blackhawk formation. Both of these studies, as well as others (e.g. Pattison (2005)) have been outcrop based in specific sandy or heterolithic bodies that exist within the marine shales. These studies are then limited by their exposure, and exist as islands of study, rather than part of a larger, basin-wide framework. By using cored intervals throughout the entire basin, exposure is laterally limited, but a larger framework is observed.

The goals of this study are twofold. The first goal is to apply established sequence stratigraphic models to the Mancos Shale, a siliciclastically influenced mudstone deposited in the offshore realm. The second goal is to use the resulting sequence stratigraphic model to predict ideal zones for horizontal completions. These intervals should be traceable throughout the entire Uinta Basin, making intelligent exploration decisions and reservoir estimations based on refined scientific findings.

Datasets

Datasets for this study include six cored intervals. The River Gas Unit #1 (hereby RGU-1) core is described in great detail in Kennedy (2011). It is the thickest core studied at 1712' thick, and penetrated the Tununk Shale, Ferron Sandstone, and the Lower Blue Gate Member of the Mancos Shale. Unless specifically mentioned, this core is not referred to in association with the remaining five cored intervals. The remaining five cored intervals form the bulk of the data for this study. The Questar Glenn Bench #1M-4-8-22R, Questar #8ML-6-9-24, and the Questar 16M-28-8-21 (hereafter Questar 1, Questar 8, and Questar 16) are each 120 feet thick. Questar 1 and Questar 8 cores each cored the Mancos B interval, with the Questar 16 coring a distal, siltstone rich expression of the Frontier formation. The Pioneer Main Canyon Federal #23-7-15S-23E was cored at two different depths; 7,480' – 7,597' (hereafter Pioneer 1) and 6,995' -7,135' (hereafter Pioneer 2). For a detailed discussion of each of these cored intervals, please refer to Chapter 1.

Methods

All five core intervals were initially described on centimeter scale. Initial descriptions of cored intervals focused on determining heterogeneity on multiple scales. See chapter 1 for a detailed description of core description methodology. Interpretations focusing on sequence stratigraphy expand on this initial core description with particular attention paid to the vertical changes in frequency and thickness of coarser-grained siltstone and even sandstone interlaminations. These interlaminations were utilized as a proxy for relative shoreline position. Vertical increases in frequency and thickness of coarse-grained interlaminations represent a progressively more proximal location to the shoreline. See Chapter 1 for an expanded explanation of this interpretation.

Proximity to relative paleo-shoreline is an integral variable to determine in sequence stratigraphic analysis. 11 distinct lithofacies have been identified in the five cored intervals (see Chapter 1 for detailed discussion on these lithofacies). These 11 lithofacies are placed in the context of a facies model to aid in determining relative proximity to shoreline (Figure 68). In this depositional model, three major environments are identified – the prodelta, the mudbelt, and the sediment starved shelf.

Features recording variable but overall high deposition rates and unidirectional flow are characteristic of the prodelta depositional environment. These features include relatively low bioturbation indices, diminutive trace fossils, and soft sediment deformation. Dewatering structures found in lithofacies 3 are also indicative of high deposition rates in the prodelta environment. Heterolithic strata that contain abundant current indicators, variable bioturbation levels and a generally continuous lamination style (lithofacies 1, 2, 4, 5, 7, and 9; Chapter 1) are placed in the mudbelt environment. Remaining lithofacies (lithofacies 6, 8, and 11; Chapter 1) are characterized by their discontinuous or absent siltstone interlaminations along with surfaces that had been winnowed away, a generally darker color, and a lack of bioturbation features. These lithofacies are interpreted to have been deposited in the sediment starved shelf environment. See Chapter 1 for an expanded discussion of key recognition criteria and sediment transport processes in these environments, along with the relationships between these three environments.

A total of 1,448 depths were sampled for X-ray fluorescence (hereby referred to as XRF) data. Samples were taken from the Questar 1, Questar 8, Questar 16, and RGU-1 (1931.2' – 929.9') cores at 1 foot intervals. In the RGU-1 core from 929.9' – 220.3' samples were taken at 3 foot intervals. Samples were taken directly from core, after the core had been lightly cleaned and dusted, for major and trace elemental composition using the Brüker AXS

TRACER III-V energy dispersive handheld X-ray Fluorescence unit. Following raw data collection, the results are interpreted using the calibrations outlined in Rowe et al. (2012). To ensure accuracy, a standard pressed pellet was run periodically throughout testing. All sample results are expressed in weight percent, unless otherwise specified.

Samples were collected from cores for percent organic carbon analysis. In the RGU-1 core, samples were collected at approximately ten foot intervals, totaling 164 samples. In Questar 1, Questar 8, and Questar 16, samples were collected at approximately three foot intervals, totaling 40 samples per core. Sixtyfive samples were analyzed from the Pioneer core at two to three foot spacing. In preparation for analysis of percent organic carbon samples were powdered using a shatterbox. Each sample was acidified to remove inorganic carbonate via hydrochloric slurry acidification. In this method, an aliquot of powdered sample was mixed in a beaker with approximately 30 mL of 1M hydrochloric acid and reacted for at least 24 hours or until pH stabilized at a value less than 2. If the pH was measured greater than two, additional 1M hydrochloric acid was added and allowed to react until the pH stabilized at a value less than two. The hydrochloric acid was then removed and separated from the immersed powdered sample via vacuum filtration. The samples were dried in an oven at 60° Celsius and removed from the filter paper. Approximately 20 milligrams (+/- two milligrams) of each carbonate free sample was weighed into a 5×9 milimeter^2 tin-foil cup. Samples were analysed using a Carla Erba 1108 elemental analyzer connected to a Thermo Finnigan Delta XL stable-isotope gas-ratio mass spectrometer at the University of Utah Stable Isotope Ratio Facility for Environmental Research (SIRFER) laboratory. Analytical precision (1σ) for determinations of C_{org} is .013 weight percent. In Chapter 1, organic richness was demonstrated to vary with proximity to shoreline, increasing

in more distal environments as a result of low clastic dilution and low biogenic destruction of organic matter.

In this study, the combination of all of these techniques is used in order to determine the proximity to paleo-shoreline – the most crucial variable in a sequence stratigraphic analysis of the cored intervals. This determination of proximity to paleo-shoreline exists on multiple scales: the parasequence scale, the systems tract scale, and the sequence scale.

Results

Parasequences

Parasequences are defined as "a relatively conformable succession of genetically related beds or bedsets bounded by flooding surfaces" (Van Wagoner, 1995). In classic sequence stratigraphic studies, parasequences are characterized by coarsening upwards trends (Catuneanu, 2008; Coe, 2003). These coarsening upwards trends represent proximal environments building over more distal environments. In a shallow, wave-dominated shoreline, this coarsening upward sequence could be typified: fine, hummocky cross stratified sediment packages of the lower shoreface are overlain by parallel laminated sands representing the middle shoreface, and into trough cross bedded, medium sandstones of the upper shoreface (Catuneanu, 2008; Coe, 2003). The key feature of these coarsening upward packages is not the change in grain size. Rather, it is the change in environment of deposition from a comparatively more distal environment to a comparatively more proximal environment (Figure 6; Figure 7; Figure 8; Figure 9; Figure 10). In this study, coarsening upwards trends are not reliably observed to define parasequences. The grain size in all cored intervals is variable, but this variation was not found to be a reliable indicator to dictate the presence of a parasequence. A more reliable indicator of parasequence boundaries was found

in examining the occurrence of the coarse fraction, or siltstone, interlaminations. Towards the top of a parasequence, siltstone and very fine sandstone interlaminations occur more frequently, and commonly, their individual thicknesses increase towards the top of a parasequence (Figure 6; Figure 7; Figure 8; Figure 9; Figure 10).

As demonstrated in Chapter 1, the siltstone interlaminations are composed almost entirely of detrital quartz. Grain sizes of these interlaminations are, in some instances, the same grain size as the clay particles that bound the interlaminations (i.e. detrital quartz had a range of grain sizes from under two microns through silt grain sizes). Thus, the average grain size does not necessarily increase, but the detrital quartz signal does become more abundant upwards within a parasequence.

Each parasequence is topped by a flooding surface. Flooding surfaces are defined as "a surface separating younger from older strata across which there is evidence of an abrupt increase in water depth. This deepening is commonly accompanied by minor submarine erosion or non-deposition" (Van Wagoner, 1995). This definition is very broad, as multiple processes can fit under this single characterization, including within trend facies contacts and localized flooding caused by delta lobe switching. In this study, flooding surfaces are found to distinctly separate individual parasequences (Figure 70; Figure 6; Figure 7; Figure 8; Figure 9; Figure 10). Directly overlying the flooding surface, by definition, is the most distal expression of the overlying parasequence. Flooding surfaces are easily identified when separating environments of significantly varying grain size. However, packages that contain relatively subtle changes in grain size or frequency and thickness of siltstone interlaminations produce subtle flooding surfaces. Flooding surfaces are more subtle still when siltstone laminations are rare or nonexistent. Interpretation of flooding surfaces in these instances relies heavily on defining a flooding surface as a surface which is accompanied by non-

Transgressive systems tract (discontinuously laminated, lithofacies 6)

Transgressive Surface (Flooding Surface)

Lowstand systems tract (very sandy, heavily bioturbated, lithofacies 1)

Figure 70: Core photo from Questar 16 at 15,177'. A very sandy and heavily bioturbated lithofacies 1 is sharply overlain by lithofacies 6. This represents a significant shift from a proximal mudbelt facies to a proximal sediment starved shelf environment. This flooding surface is interpreted to be a transgressive surface, with the lower lithofacies 1 representing a lowstand, and lithofacies 6 representing an early transgressive sustems tract.

deposition. During these hiatuses, there is an implied cessation of sedimentation, and this allows for two primary features to build up: bioturbation, and biogenic beds.

In the first case, organisms that exist in an environment at the time of the flooding surface will have an extended period of time to disturb the sediment below the flooding surface. At the end of the hiatus, sedimentation will begin again, and organisms will mill the newly deposited sediment. This results in increased amounts of bioturbation directly at and below flooding surfaces and a sharp decrease in bioturbation above the flooding surface.

In this study, biogenically produced material is limited to shells (see Chapter 1 – chemofacies analysis). These biogenically produced materials are produced regardless of the sedimentation rate in the water column and above the sediment water interface. During a hiatus in sedimentation, then, increased amount of biogenic (shell) debris accumulated at the flooding surface would be expected (Figure 48).

Both of these secondary methods of defining flooding surfaces are encountered throughout the cored intervals. Increased bioturbation at the flooding surface is best exemplified in Questar 16 at parasequences capped with lithofacies 7 (i.e., parasequences P2, P3, and P6 in Questar 16; Figure 8). Shell bed accumulation is exemplified in Pioneer 2, where shell beds are used to define parasequences with the total absence of laminations in lithofacies 8 (i.e. parasequences P2, P4, P5, and P6 in Pioneer 2; Figure 10).

Throughout all cored intervals, the one method that is most reliable to produce convincing parasequences is to use environmental interpretations to imply flooding surfaces. If a more distal environment (or a more distal expression of the same environment) overlies a more proximal environment, then a flooding surface must exist separating the two environments. Lamination frequency and thickness, bioturbation levels, and shell beds can

all aid in the identification of flooding surfaces, but the main feature of flooding surfaces is a sudden shift to a more distal environment.

Parasequences are documented in all five cored intervals (Figure 6; Figure 7; Figure 8; Figure 9; Figure 10). Each core has slightly different assemblages of parasequences, but each core has, on average, 9 parasequences that are on average 14 feet thick. In Questar 1, 8 parasequences are identified, ranging in thickness from 5 feet to 46 feet thick (Figure 6). In Questar 8, 8 parasequences are identified, ranging in thickness from 4 to 43 feet (Figure 7). Questar 16 has 11 parasequences identified, and these parasequences are between 3 and 17 feet (Figure 8; Table 10). Pioneer 1 contains 9 parasequences that range from 5 through 21 feet thick (Figure 9). In Pioneer 2, 7 parasequences are identified ranging in thickness from 3 to 40 feet (Figure 10; Table 11).

Stacking Patterns

Following the identification of parasequences within each cored interval, parasequences are then compared to each other for the purpose of identifying stacking patterns. A stacking pattern defines the relationship of a single parasequence to the parasequence below. There are three types of stacking patterns observed in this study: progradational, aggradational, and retrogradational. A progradational parasequence was defined as such if the base and top of the parasequence was more landward than the underlying parasequence. A parasequence was classified as aggradational if the base and top of the parasequence are equally proximal to the shoreline as the underlying parasequence. Retrogradational parasequences are more distal at their bases and tops relative to the underlying parasequences.

Table 10: Parasequence statistics for all Questar cores.

Core	Parasequence	Thickness (feet)	Stacking pattern	Systems Tract
Questar 1	1	8		HST
Questar 1	2	6	Agg	HST
Questar 1	3	17	Agg	LST
Questar 1	4	6	Agg	LST
Questar 1	5	18	Ret	TST
Questar 1	6	14	Ret	TST
Questar 1	7	5	Ret	TST
Questar 1	8	46	Agg	HST
Questar 8	1	4		HST
Questar 8	2	20	Agg	HST
Questar 8	3	43	Agg	HST
Questar 8	4	7	Ret	TST
Questar 8	5	4	Ret	TST
Questar 8	6	9	Ret	TST
Questar 8	7	15	Ret	HST
Questar 8	8	15	Agg	HST
Questar 16	1	15		HST
Questar 16	2	12	Agg	HST
Questar 16	3	17	Agg	HST
Questar 16	4	8	Pro	HST
Questar 16	5	8	Agg	HST
Questar 16	6	17	Agg	HST
Questar 16	7	10	Pro	LST
Questar 16	8	11	Ret	TST
Questar 16	9	3	Ret	TST
Questar 16	10	3	Ret	TST
Questar 16	11	15	Ret	TST

Table 11: Parasequence statistics for Pioneer cores.

Core	Parasequence	Thickness (feet)	Stacking pattern	Systems Tract
Pioneer 1	1	11		LST
Pioneer 1	2	11	Ret	TST
Pioneer 1	3	21	Ret	TST
Pioneer 1	4	5	Ret	TST
Pioneer 1	5	8	Agg	HST
Pioneer 1	6	15	Agg	HST
Pioneer 1	7	20	Agg	HST
Pioneer 1	8	5	Ret	HST
Pioneer 1	9	21	Ret	TST
Pioneer 2	1	23		LST
Pioneer 2	2	9	Ret	TST
Pioneer 2	3	25	Pro	HST
Pioneer 2	4	33	Pro	HST
Pioneer 2	5	10	Pro	HST
Pioneer 2	6	40	Pro	HST
Pioneer 2	7	3	Agg	HST

By the way that parasequences are compared, it is impossible to reliable characterize the most basal and uppermost parasequences. The most basal parasequences can't be compared to parasequences below. Similarly, complete analysis of uppermost parasequences is impossible, as the tops of the parasequences fall outside the cored interval.

There are nuances concerning stacking patterns that can help with interpretation that fall outside these strict definitions. It is not uncommon, for instance, for a parasequence to be aggradational at its base, and progradational at its top. In these cases, discretion has to be used, and the parasequences must be analyzed in context with the surrounding parasequences. As an example, in Questar 1 (Figure 6), the capping parasequence is slightly retrogradational at its base (13,421'), but its top is very proximal relative to the remainder of the core. In this case, this parasequence would be classified as progradational, despite the slightly retrogradational base.

Using the tops of parasequences as hard and fast indicators of proximity to paleo-shoreline is also potentially problematic. The tops of parasequences are at the mercy of processes that occur during the deposition of the flooding surface. If this interval of time includes a hiatus in which biological activity can burrow significantly through the sediment, then the interpreted environment may appear to be either more proximal or more distal than it was during deposition. Similarly, it is possible for flooding surfaces to erode away sediment (Catuneanu, 2008). If this were the case, then the top of the parasequence in question would appear more distal than it was during initial deposition.

In Questar 1 (Figure 6; Table 10), the first four parasequences are aggradational. However, in parasequence 3 and 4 there is a significant landward shift to prodelta environments. Parasequences 5 through 7 are all retrogradational. The final parasequence in

Questar 1 is strongly progradational, the top of which is the most proximal to shoreline seen throughout the entire core.

Questar 8 (Figure 7; Table 10) is characterized by its largely aggradational stacking patterns. The first three parasequences are all aggradational, and they account for over half of the core at 67'. The next four parasequences (4-7) are all retrogradational. The final parasequence is interpreted to be aggradational, although the top of the parasequence isn't exposed in the cored interval.

Questar 16 (Figure 8; Table 10) is based with a thick series of aggradational parasequences. Parasequences 1 through 3 are aggradational, with parasequences 4 and 5 being very weakly progradational. Parasequence 6 is aggradational. Parasequence 7 is strongly progradational, and shows a significant landward shift in depositional environment. Parasequences 8 through 11 are retrogradational on a broad scale. Parasequence 9, however, is progradational at its base, and retrogradational at its top. Retrogradational stacking patterns dominate the upper portion of this core, and parasequence 9 is therefore interpreted to be retrogradational as well.

The first parasequence in Pioneer 1 (Figure 9; Table 11) is significantly landward compared to all subsequent parasequences in the core. Parasequences 2 and 3 are retrogradational. Parasequence 4 has a base that is strongly retrogradational, and a top that is very weakly progradational. It is interpreted to be overall retrogradational. Parasequence 5 through 7 are aggradational. Parasequences 8 and 9 are both retrogradational.

In Pioneer 2 (Figure 10; Table 11), the lowest parasequence is significantly landward compared to all subsequent parasequences in the core. Parasequence 2 is very strongly retrogradational. Parasequences 3 through 6 are progradational, and parasequence 7 is aggradational. In this core, shell beds record flooding surfaces between parasequences.

Systems Tracts and Sequence Stratigraphic Surfaces

Following the classification of stacking patterns, sets of parasequences can be grouped into diagnostic systems tracts. Each individual systems tract places the units deposited at those times on specific places on a sea level curve. Three types of systems tracts have been identified in this study: the highstand systems tract, the lowstand systems tract, and the transgressive systems tract.

The highstand systems tract is traditionally defined as being dominated by a combination of aggradational to progradational stacking patterns (Catuneanu, 2008). In this study, progradation in a highstand systems tract was far less common than aggradation in a highstand systems tract. This is attributable to deposition occurring in a distal shallow marine environment that has virtually limitless accommodation space. Highstand systems tracts tend to become progradational as sediment supply outpaces accommodation space. In this distal environment, however, this progression from aggradation to progradation may not apply..

The lowstand systems tract is commonly associated with progradation and low rate aggradation (Catuneanu, 2008). In this study, lowstand systems tracts are associated with aggradational stacking patterns, but are distinguished from highstand systems tracts by a sudden and significant shift to more landward lithofacies at the base, marked by a sequence boundary. Additionally, the context of underlying and overlying systems tracts must be taken into account.

The transgressive systems tract is associated with retrogradational stacking patterns. These retrogradational stacking patterns are well evidenced in this study.

Questar 1 contains a highstand systems tract at its base (Figure 6; Figure 71; Figure 72). Parasequences 3 and 4 exhibit characteristics of being significantly landward of

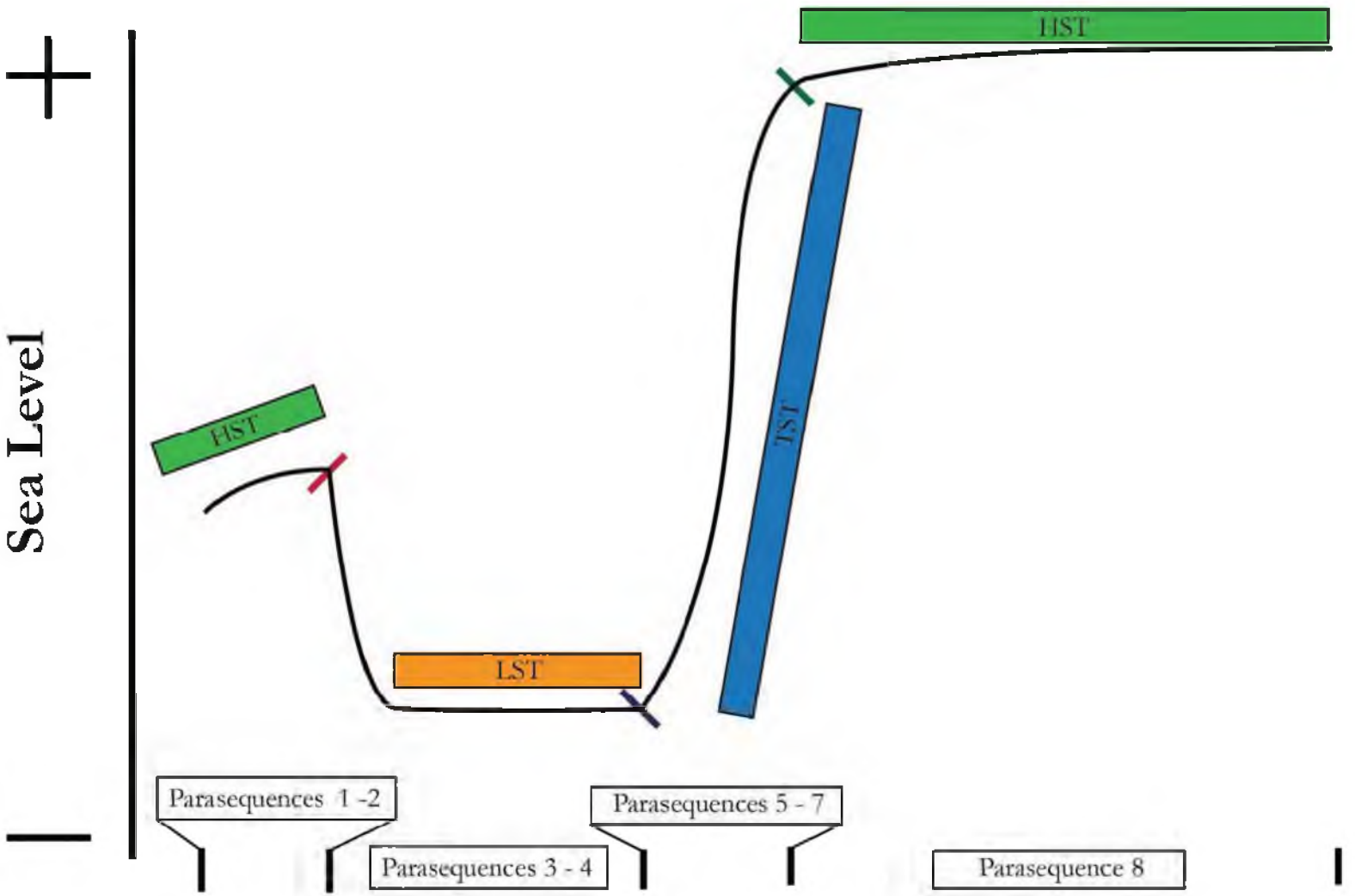

Figure 71: Relative sea level in Questar 1 through time.

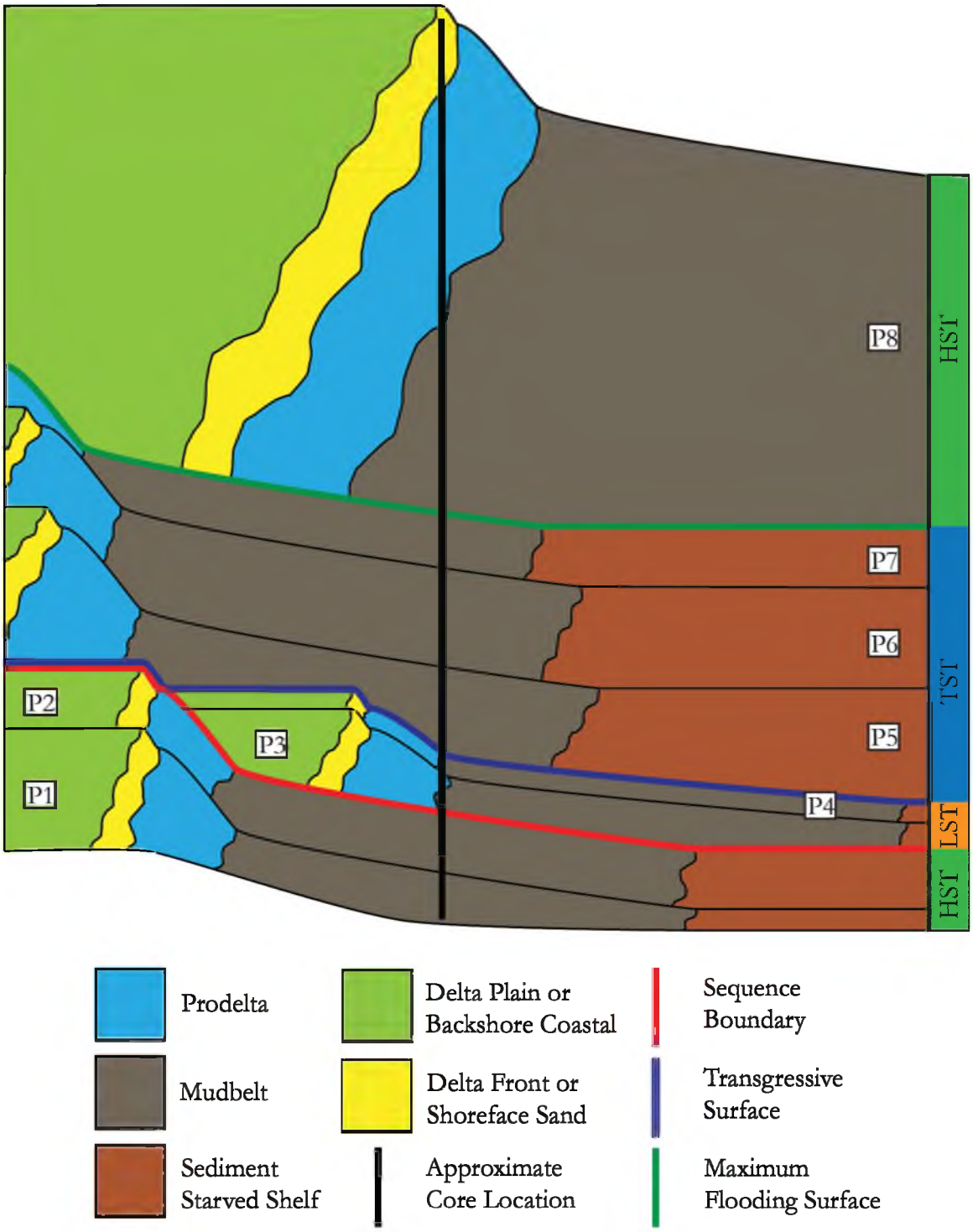

Figure 72: Schematic two dimensional cross section of the Questar 1 cored interval. Black line represents approximate location of the core.

parasequences 1 and 2, and therefore, they occupy the lowstand systems tract. By definition, a sequence boundary is interpreted at the flooding surface overlying parasequence 2. Parasequences 5 through 7 all comprise the transgressive systems tract, with a transgressive surface at the flooding surface that underlies parasequence 5. The uppermost parasequence (parasequence 8) represents the beginning of the overlying highstand systems tract. The maximum flooding surface is interpreted at the flooding surface underlying parasequence 8 between the transgressive systems tract, and the highstand systems tract.

Questar 8 is dominated by two thick highstand systems tracts characterized by aggradational sediment accumulation (Figure 7; Figure 73; Figure 74). Parasequences1 through 3 are all aggradational and belong to the lowermost highstand systems tract. Parasequences 4 through 6 are all retrogradational and are interpreted as a transgressive systems tract. Within the basal 6 parasequences, there is no evidence of a landward shift in deposition, and thus, there is no lowstand systems tract between the highstand systems tract and the transgressive systems tract (Figure 7). By definition, a transgressive surface underlies parasequence 4. There could also be a sequence boundary between the lower highstand systems tract and the overlying transgressive systems tract. Parasequences 7 and 8 are aggradational, and are interpreted to record the highstand systems tract, with an interpreted maximum flooding surface underlying the seventh parasequence.

Questar 16 also contains a prominent highstand systems tract (Figure 8; Figure 75; Figure 76). The basal 6 parasequences are aggradational and interpreted to record the highstand systems tract. Parasequence 7 marks a significant landward shift in facies, and is therefore classified as a lowstand systems tract with a sequence boundary at its base. The overlying uppermost four parasequences are all retrogradational, and are therefore assigned to the transgressive systems tract. A transgressive surface is interpreted at the base of the

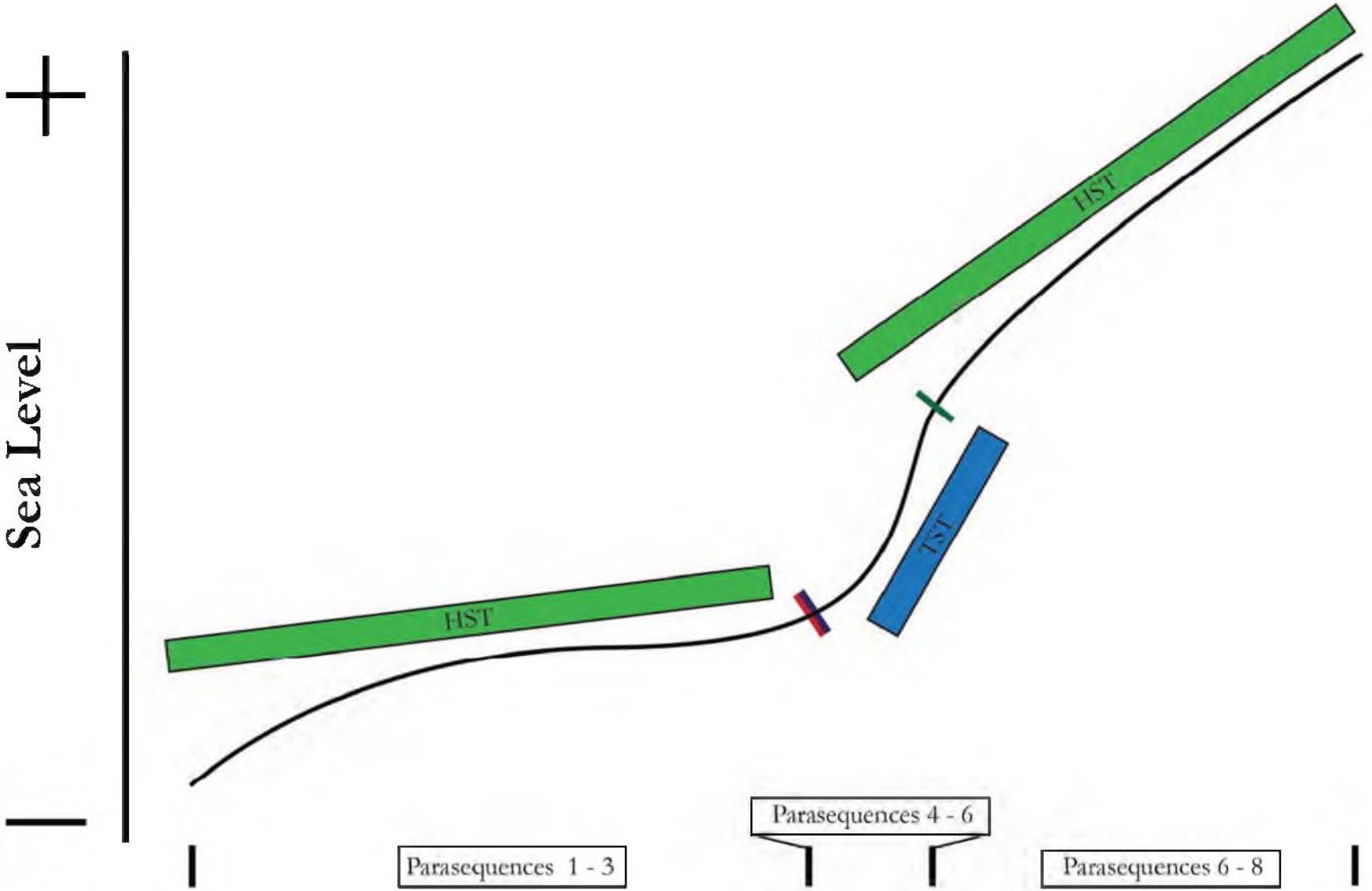

Figure 73: Relative sea level in Questar 8 through time.

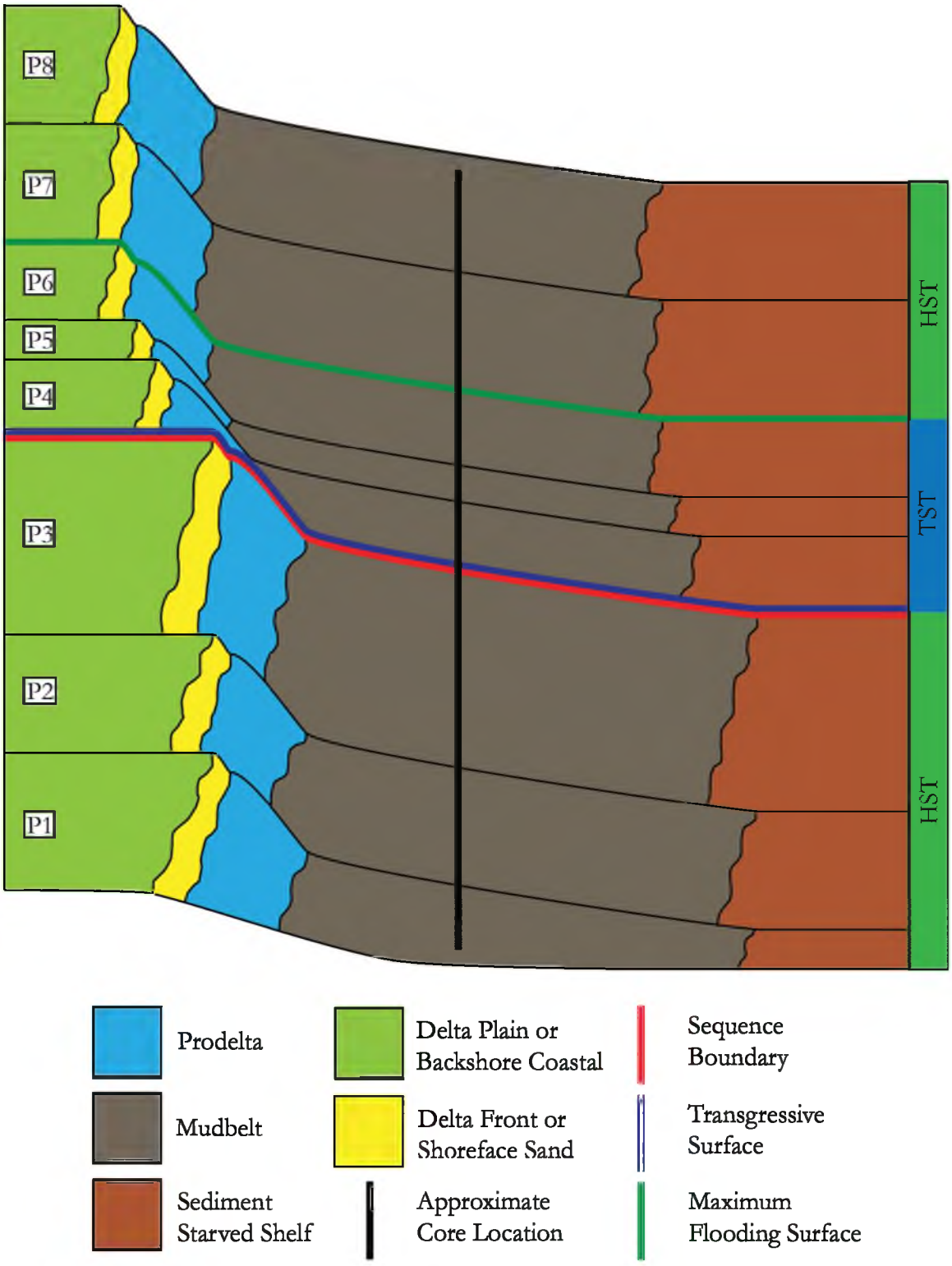

Figure 74: Schematic two dimensional cross section of the Questar 8 cored interval. Black line represents approximate location of the core.

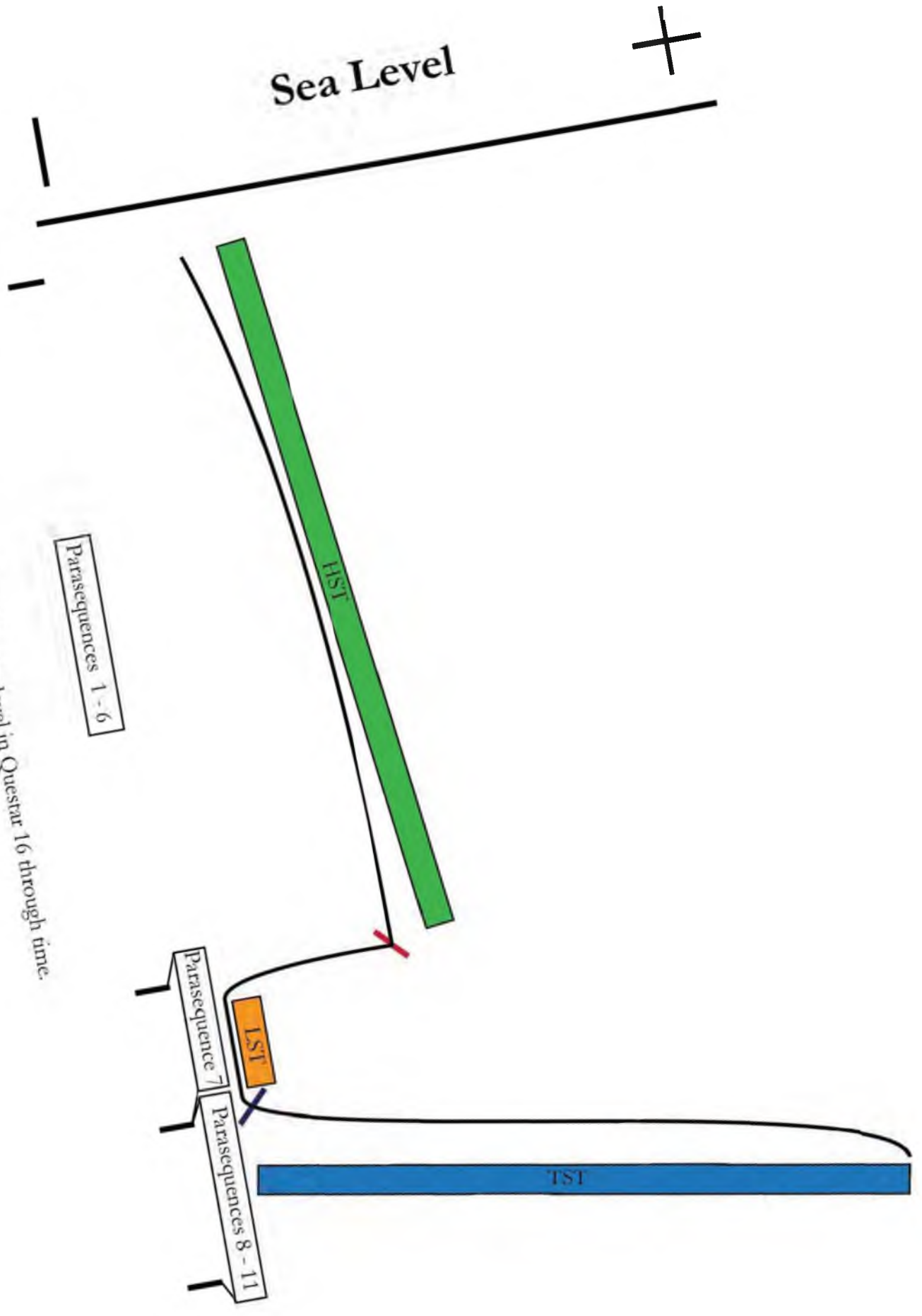

Figure 75: Relative sea level in Questar 16 through time.

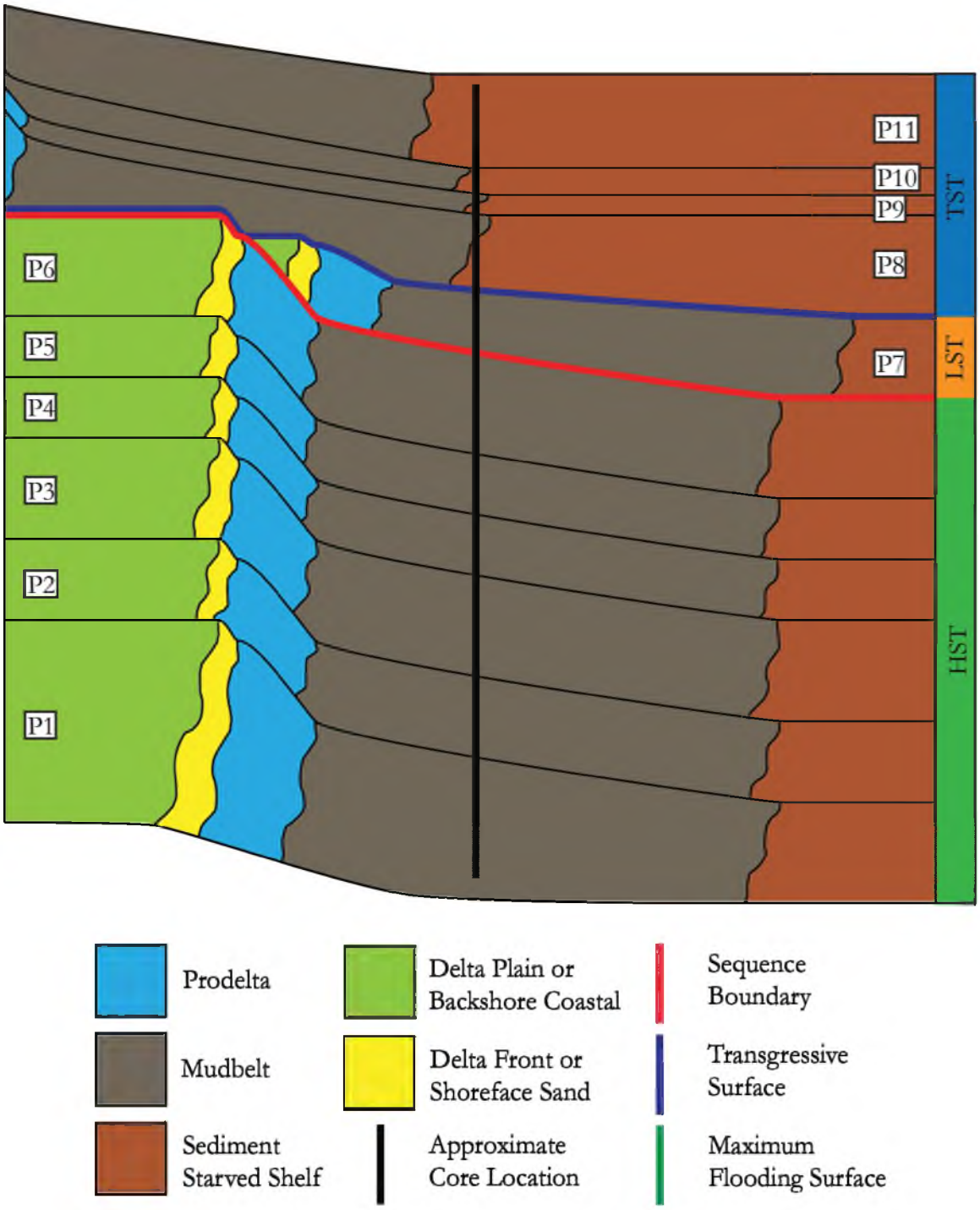

Figure 76: Schematic two dimensional cross section of the Questar 16 cored interval. Black line represents approximate location of the core.

eighth parasequence, between the underlying lowstand systems tract and the overlying transgressive systems tract.

The lowermost parasequence of the Pioneer 1 cored interval is interpreted to have been deposited very proximal to the shoreline, and is therefore interpreted to record part of the lowstand systems tract (Figure 9; Figure 77; Figure 78). Parasequences 2 through 4 all stack retrogradationally, and are therefore classified as the transgressive systems tract. A transgressive surface is interpreted at the base of the second parasequence, between the underlying lowstand systems tract, and the overlying transgressive systems tract. Parasequences 5 through 7 comprise a highstand systems tract, with a maximum flooding surface between the fourth and fifth parasequences. The upper two parasequences belong to a transgressive systems tract. There is no evidence of a landward shift in depositional environment in parasequences 5 through 7, and therefore there is no evidence of a lowstand systems tract recorded between the highstand systems tract and the transgressive systems tract at the top of this cored interval. Rather, a transgressive surface exists at the flooding surface at the base of the eighth parasequence. It is possible that a sequence boundary is also recorded at this flooding surface.

The first parasequence in the Pioneer 2 cored interval was deposited significantly landward as compared to the other environments present in the core (Figure 10; Figure 79; Figure 80). This suggests that the first parasequence records a lowstand systems tract. The second parasequence comprises the transgressive systems tract, with a transgressive surface at the base of the second parasequence. The third through the seventh parasequence are all interpreted to record the highstand systems tract. An associated maximum flooding surface is found at the base of the third parasequence.

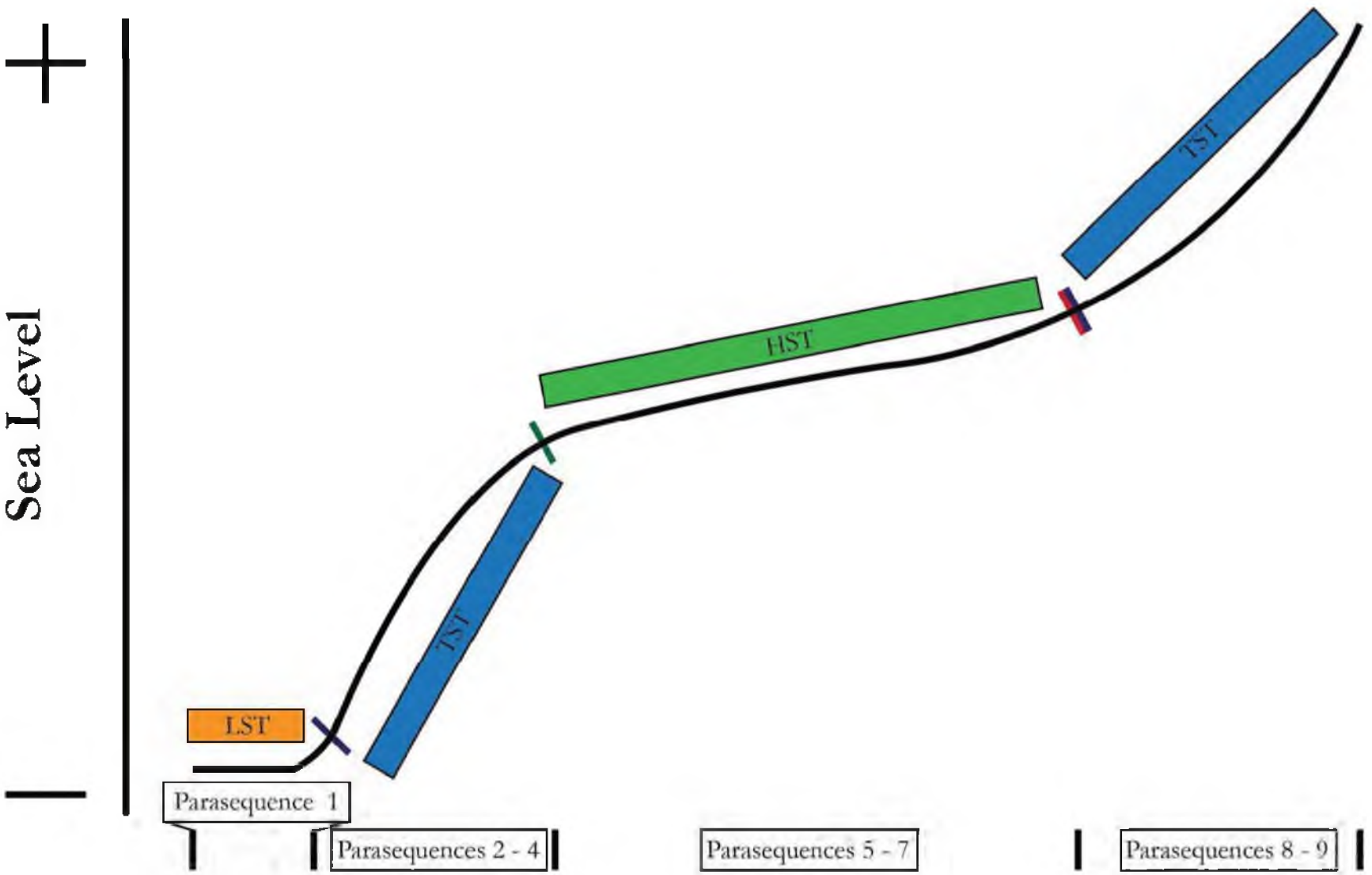

Figure 77: Relative sea level in Pioneer 1 through time.

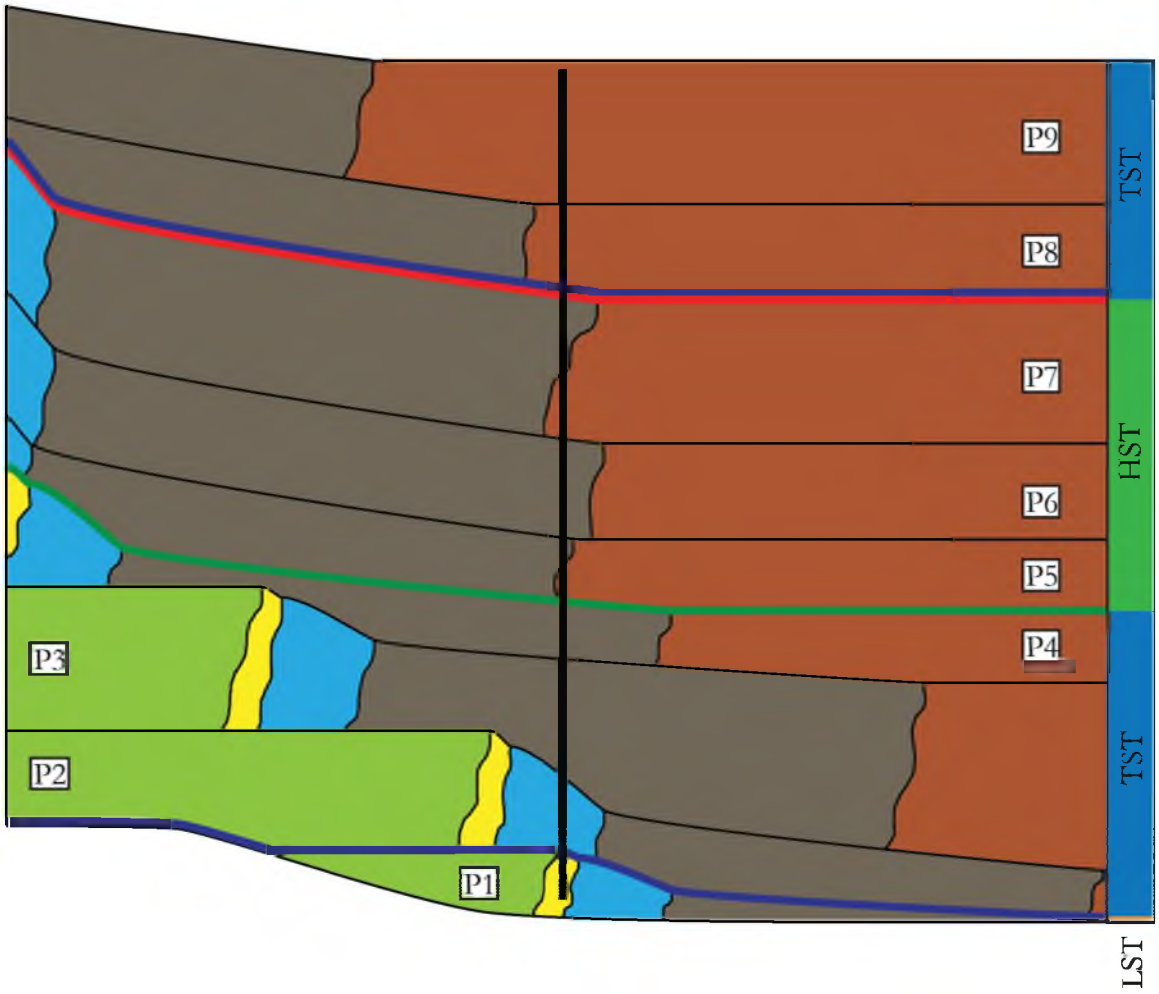

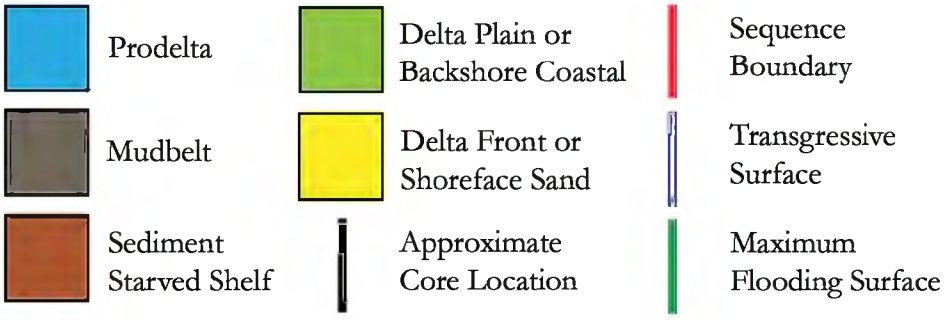

Figure 78: Schematic two dimensional cross section of the Pioneer 1 cored interval. Black line represents approximate location of the core.

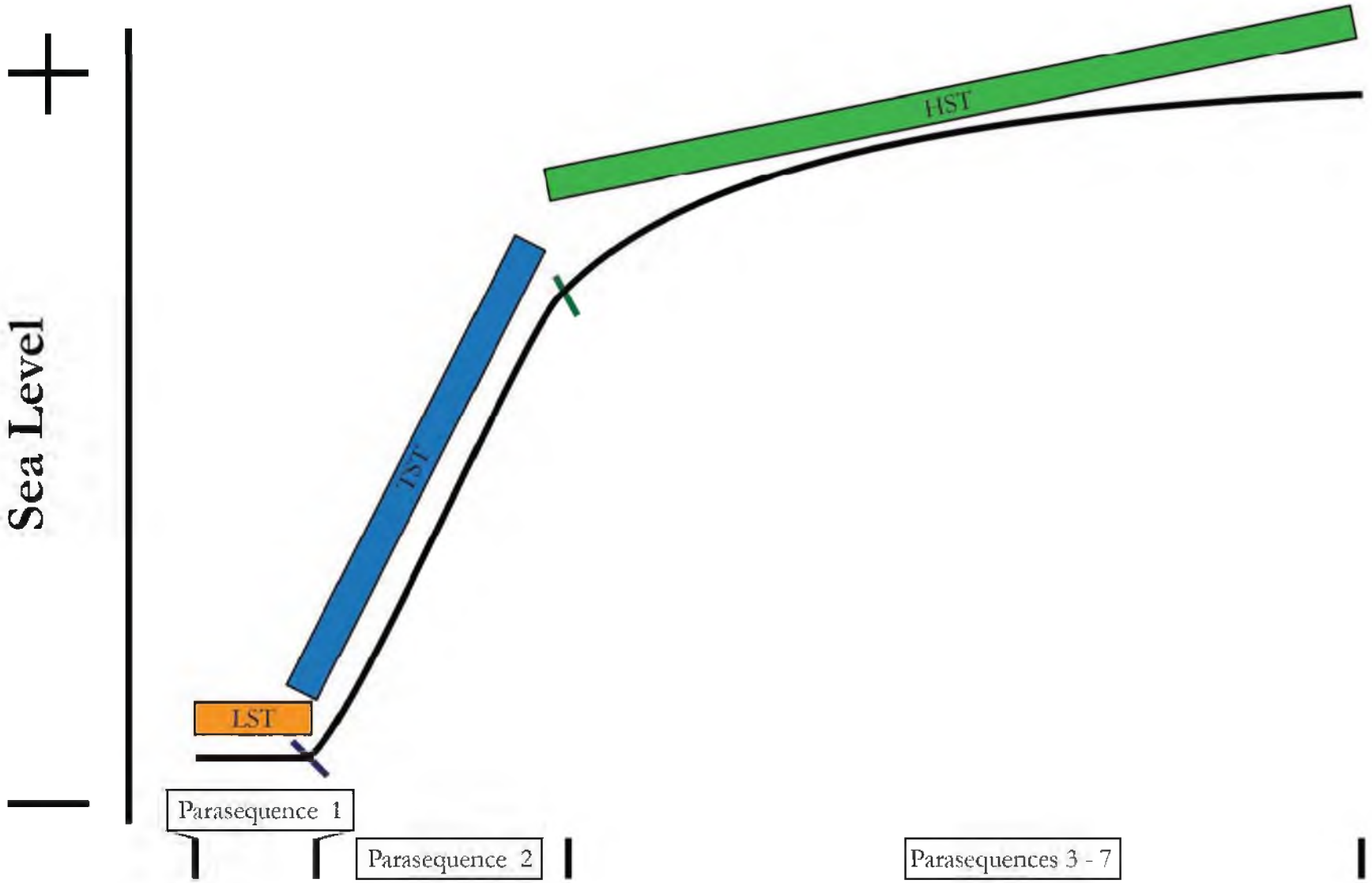

Figure 79: Relative sea level in Pioneer 2 through time.

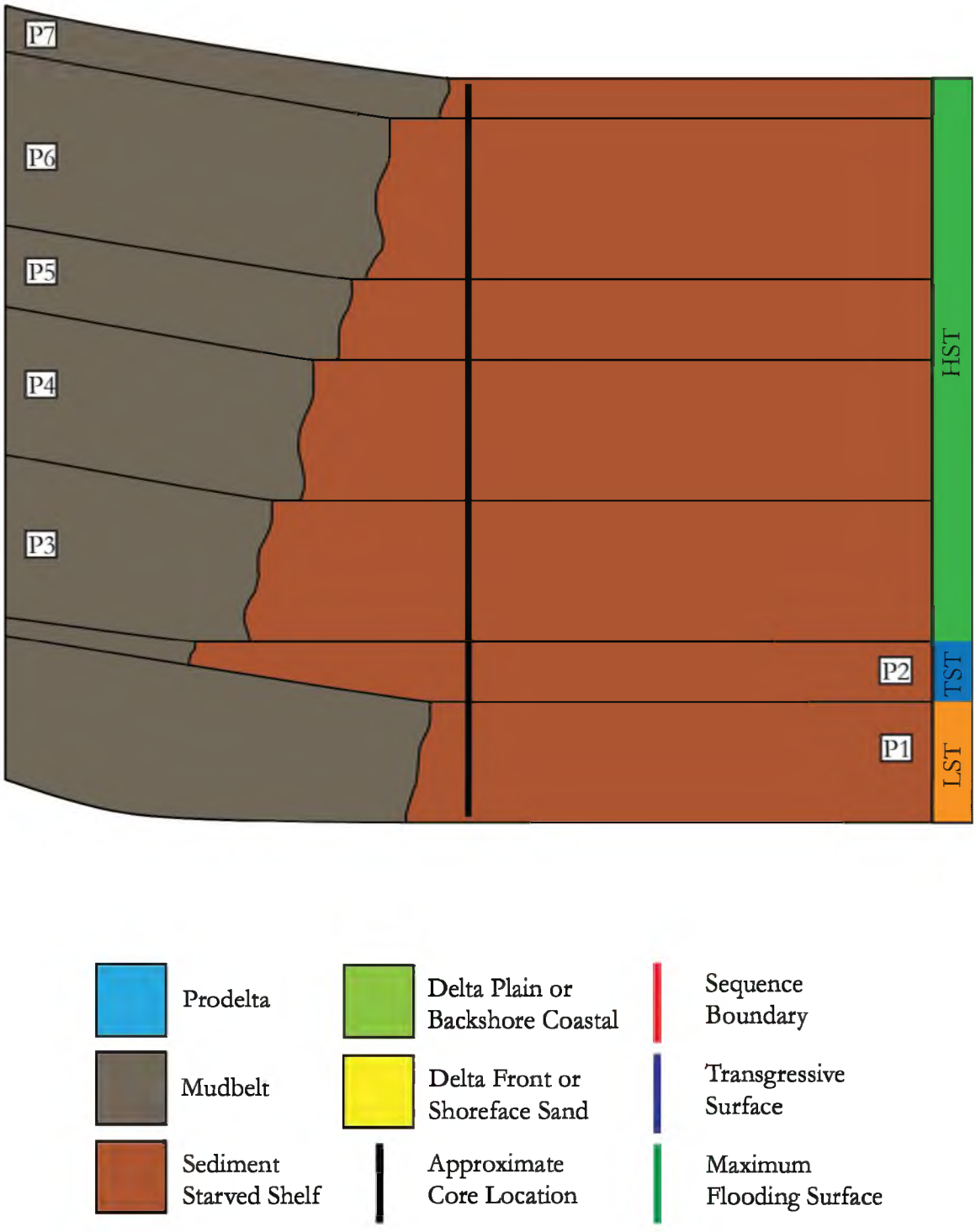

Figure 80: Schematic two dimensional cross section of the Pioneer 2 cored interval. Black line represents approximate location of the core.

Chemostratigraphy

Chemostratigraphy, in a broad sense, is used for the same purposes as lithostratigraphy – that is, it serves as a method to differentiate between different types of rocks. More accurately, chemostratigraphy utilizes a set of chemical data and analyzes the changes in those data over a given depth to separate a set of chemostratigraphic units. Recently, these data have been used to chemically define separate chemostratigraphic units (Jansen et al., 1998; Richter et al., 2006; Rowe et al., 2008). To some degree, these advances have focused on interpreting paleoredox conditions (Rimmer, 2004; Rowe et al., 2012; Rowe et al., 2008; Tribovillard et al., 2006). From a practical standpoint, the purpose of a chemostratigraphic interpretation is to confirm lithological analysis as well as refine lithofacies into sub-units that exhibit chemical variation invisible to the naked eye.

Thus identifying chemostratigraphic intervals of interest becomes akin to examining a log – what the geologist is looking for is variations in ratios of elements that would correlate to a geological change in the mineralogical makeup of the rock (Jansen et al., 1998). In other words, by examining how the ratio of silicon to aluminum changes over a cored interval, one can infer the changes in detrital quartz input in a system relative to the clay content of that system.

In this study, the following ratios are analyzed stratigraphically. Calcium to aluminum ratios (Ca/Al) are examined to trace the change of calcite and micrite relative to clays. Similarly, silicon to aluminum (Si/Al) ratios are used to identify the change of quartz relative to clays (Rowe et al., 2012). Since zirconium is found only in zircon crystals, which are themselves the product of igneous processes, zirconium to aluminum ratios (Zr/Al) are used to indicate detrital input in the system. It follows then that a strong correlation between the Si/Al and Zr/Al ratios is highly indicative that the quartz is indeed detrital rather than

biogenic (Figure 59). This strong positive correlation exists between Zr/Al ratios and Si/Al ratios (Figure 59). This suggests that the majority of quartz in the cored interval is detrital rather than biogenic or diagenetic (Figure 59).

Titanium to aluminum (Ti/Al) ratios along with the niobium to aluminum (Nb/Al) ratios, indicate the amount of heavy mineral variability as both niobium and titanium are found in rutile, the most abundant heavy mineral throughout all cored intervals. Thorium to aluminum (Th/Al) and potassium to aluminum (K/Al) ratios show radioactive element variation throughout the cored interval. Ultimately, these radioactive elements can be followed in a gamma ray log (or spectral gamma ray log). A strong inverse correlation between radioactive elemental abundance and detrital input will support the use of the gamma ray log as a tool to reliably interpret detrital input in a system, and consequently develop strongly supported sequence stratigraphic interpretations of the Mancos interval as a whole.

This inverse relationship is somewhat developed between Si/Al and K/Al, with an R^2 value of .47 for Questar 1, .26 for Questar 8, and .60 for Questar 16 (Figure 60). This inverse relationship does not extend to Th/Al ratios (Figure 60), nor does it correlate well to U/Al ratios. In this core, then, a spectral gamma ray would be an ideal tool to infer detrital input, but a standard gamma ray tool may also be of use, assuming the majority of radioactivity is sourced from the decay of potassium.

Following this, stratigraphic patterns begin to emerge in each individual ratio. Qualitative observations can be performed on the curves for each of these ratios. Similar to log analysis in wells, patterns can be interpreted on multiple scales. Since measurements are taken every three feet, it is difficult to interpret at a higher resolution with confidence. Qualitative measurements can include trends of an increasing or decreasing ratio, rapid

changes in the values of ratios, as well as overall character of the curve (e.g. sawtooth patterns or more numerically consistent ratios).

Questar 1

Chemostratigraphic intervals A – N in Questar 1 are defined below and in Figure 81. From the base of the Questar 1 cored interval to 13,478', four distinct chemostratigraphic intervals emerge: intervals A through D (Figure 81). From the base of the core to 13,489' all ratios fluctuate rapidly between high and low values (chemostratigraphic interval A; Figure 81). This is an interval that oscillates rapidly between intervals of aluminum abundance and aluminum depletion. Following this rapid oscillation, there are three distinct chemostratigraphic intervals that show an oscillation of relative calcium depletion (interval B; Figure 81), followed by relative calcium abundance (interval C; Figure 81), and a third interval of low amounts of calcium relative to aluminum (interval D; Figure 81). In these three intervals, Zr/Al ratios are held relatively constant indicating detrital input into the system was constant.

Overlying the first four chemostratigraphic intervals A through D is chemostratigraphic interval E which is defined by a gradual increase in Si/Al and mirrored by an increase in Zr/Al abundance (Figure 81). This indicates a gradual increase in the detrital quartz followed at the top of chemostratigraphic interval E by a rapid decline in detrital quartz content (base of interval F; Figure 81). Throughout interval E, Ti/Al ratios initially increase in abundance, but are then held notably constant. Nb/Al ratios are more variable, but values vary about a consistent mean value.

Chemostratigraphic interval F is defined at the base by the rapid drop in Ca/Al and Si/Al ratios. Following this initial decrease in Ca/Al and Si/Al, both ratios begin to increase

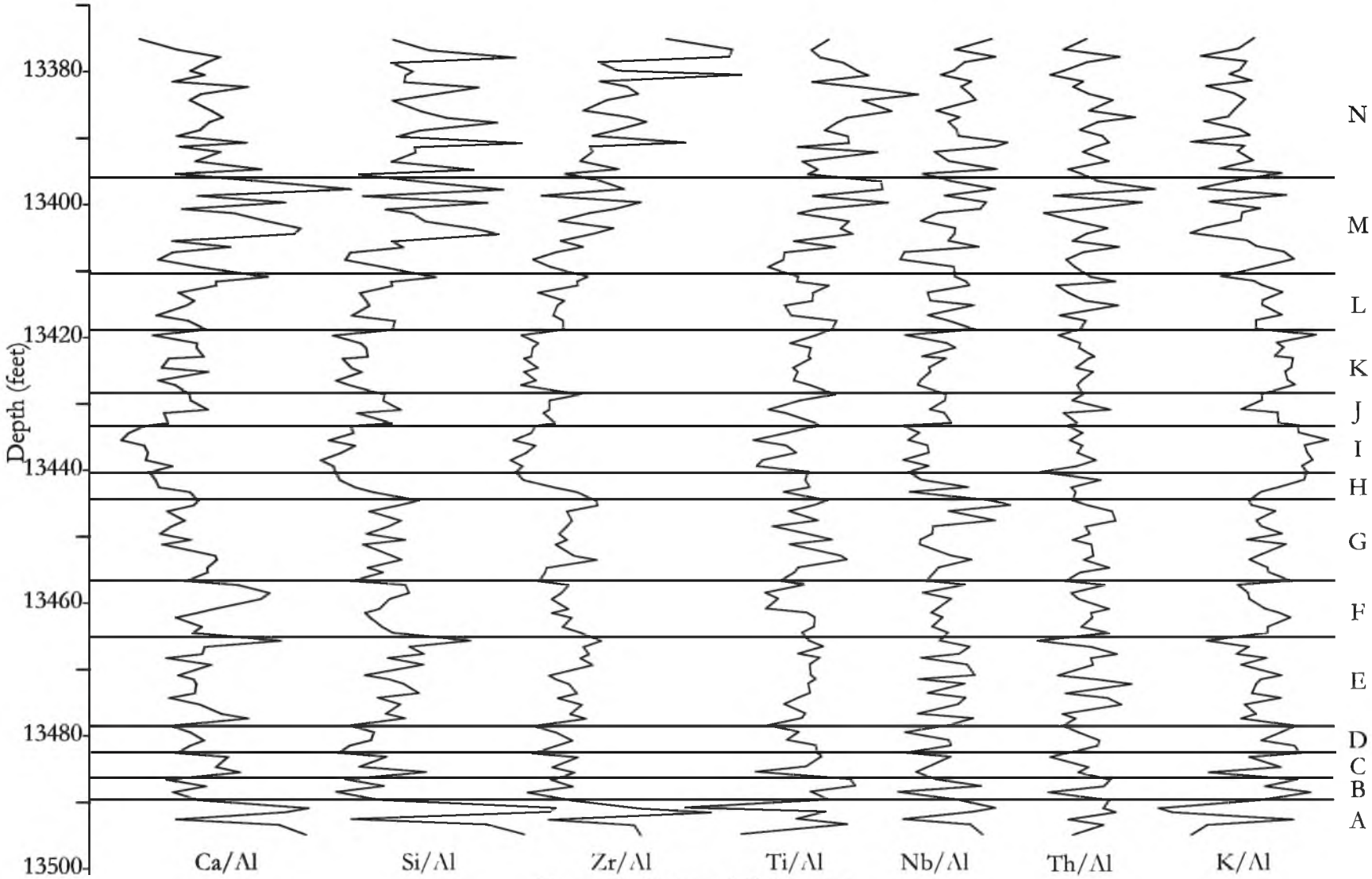

Figure 81: Questar 1 XRF ratios

again. However, the Zr/Al signal consistently declines in this interval. This would suggest that the increase in Ca/Al and Si/Al are not related to an increased detrital input. This could indicate either an increase in biogenic activity at the top of this interval, or a change in diagenetic history compared to the surrounding intervals. A strong decrease in Ti/Al values is recorded in the same depth range as the increase in Ca/Al at the top of interval F. This may indicate a subtle change in the clay content – a lower amount of rutile in the illite also indicates a reduced detrital influence. Chemostratigraphic interval F is topped by a sudden drop in Ca/Al. Chemostratigraphic interval G then shows a subtle increase in Si/Al values coupled with an increase in Zr/Al. This is a strong indicator for an increase in detrital quartz input in the system. Additionally, at the top of this interval Nb/Al ratios increase dramatically. This increase is not mirrored in Ti/Al ratios, which would suggest that Ti and Nb are not exclusively found in the same minerals.

Chemostratigraphic interval H is defined by the rapid decrease in Si/Al and a corresponding decrease in Zr/Al. This decrease takes place over several feet. The Ca/Al ratio also decreases, although, it is far less dramatic than the change in Si/Al or Zr/Al. The base of chemostratigraphic interval I is then marked where this decrease in Si/Al and Zr/Al levels off. Throughout interval I Si/Al and Zr/Al ratios stay relatively constant. Ca/Al ratios, however, decrease throughout interval I. Additionally, interval I marks the lowest values throughout the entire core of Ca/Al, Si/Al, Zr/Al, and Ti/Al. This interval is topped by a sudden increase in Ca/Al which is mirrored by an increase in Si/Al and Zr/Al. Importantly, when looking at the entire cored interval, the lowest detrital quartz signal occurs in chemostratigraphic interval I, which is accompanied by the highest ratio of K/Al in the entire cored interval. Additionally, the most dramatic signal signifying a sudden change to a lower detrital quartz input is demonstrated in chemostratigraphic interval H.

Chemostratigraphic interval J is bounded above and below by comparatively low values of Si/Al and Zr/Al. This is a strong indicator for a brief period of deposition where there is an increased detrital quartz signal.

Chemostratigraphic interval K bears a striking similarity to interval I in that very low values of Si/Al and Zr/Al remain consistent over this 10 foot interval. However, unlike interval I, interval K has higher ratios of Ca/Al that are consistent rather than decreasing. Ti/Al and Nb/Al ratios are also consistent throughout this interval suggesting little change in heavy element abundance.

Chemostratigraphic interval L's base is defined by an increase in both Si/Al and Zr/Al ratios. Throughout this interval, values of Ca/Al, Si/Al, and Zr/Al are generally increasing, but Ti/Al and Nb/Al values, while variable, vary about a constant mean value. Chemostratigraphic interval M directly overlies interval L and is defined at the base by an in initial drop in all ratios, followed by a strong increase in all ratios. This interval is highly variable for all ratios, but the variation about a mean shows that the mean values are generally showing a strong trend to increase. Chemostratigraphic interval N, on the other hand is defined by the subsequent drop in Ca/Al compared to a still increasing Zr/Al ratio. In interval N, we see that the variation for Si/Al is quite high, but all peaks correspond to peaks in Zr/Al as well. This suggests that high quartz values are tied to increases in detrital input. However, Zr/Al ratios increase throughout interval N, and that increase is not replicated in the Si/Al curve. This would indicate that the detrital input is not limited to quartz, but also includes other aluminosilicate minerals.

Throughout Questar 1, there are several larger scale patterns that emerge through XRF analysis. These patterns occur on multiple chemostratigraphic interval scales. First, there are no fewer than four major trends that have developed (Figure 82).

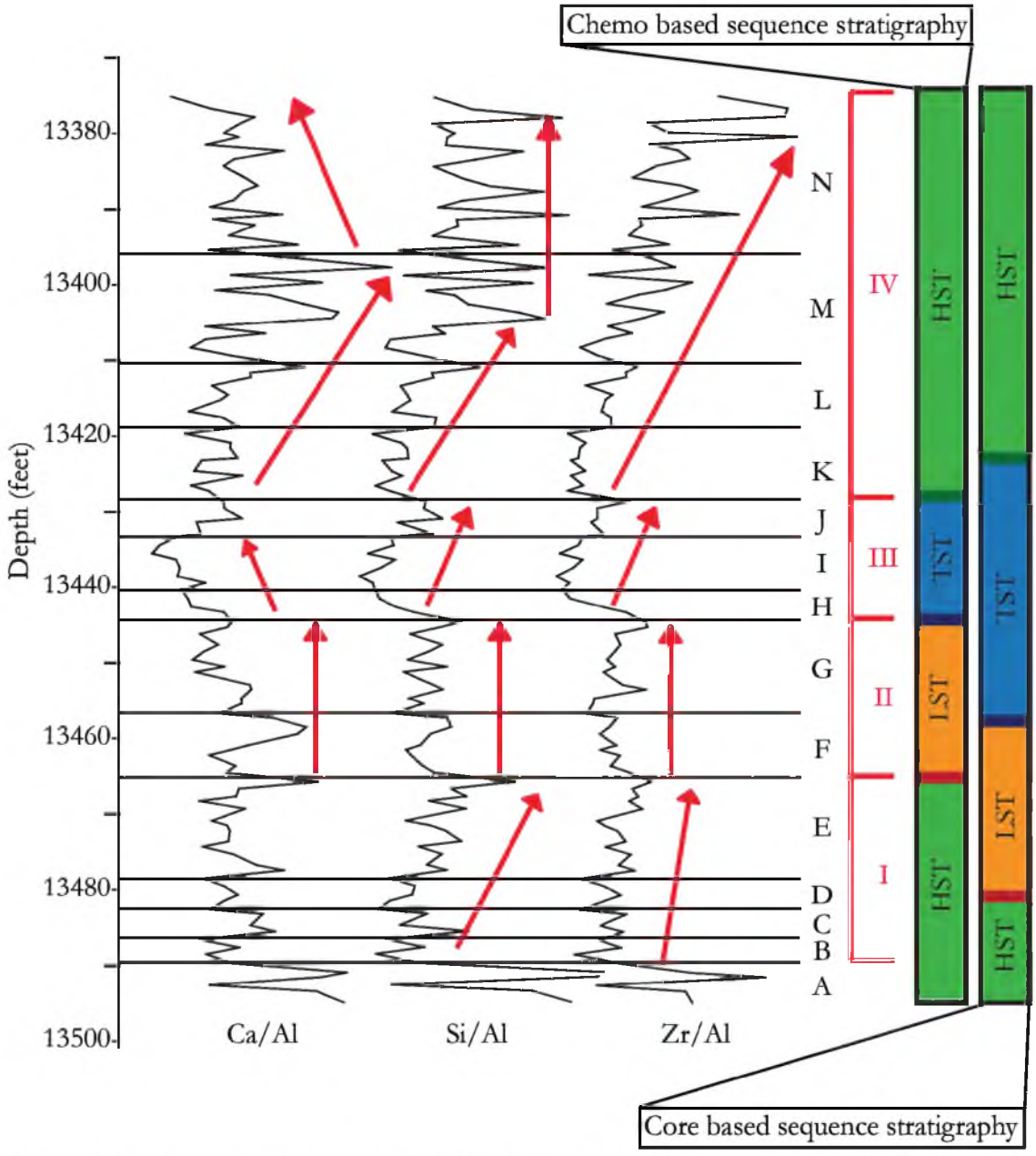

Figure 82: Questar 1 XRF ratios for Ca/Al, Si/Al, and Z/Al. 4 larger (multiple chemostratigraphic intevals) patterns emerge. Interval I represents an increase in detrital quartz into the system. Following a decrease in detrital interval II is a generally constant with respect to detrital input. Interval III represents a dramatic decrease in detrital input, followed by a slight increase. Interval IV is a marked by a dramatic increase in detrital content - not all of which can be attributed to quartz. Two sequence stratigraphic interpretations are far right. Leftmost is a chemostratigraphically based interpretation. Rightmost is the core based sequence stratigraphic interpretation

Chemostratigraphic intervals B through E show a strong signal of increased detrital quartz input into the system through time. Chemostratigraphic intervals F and G indicate a relative decline in detrital quartz input, followed by a period of constant detrital quartz input. Chemostratigraphic intervals H through J represent a dramatic shift to very little detrital quartz input in the system followed by an increase in detrital quartz input. Similarly, intervals K through N show a strong trend from a low detrital quartz signal to an abundance of detrital quartz input (Figure 82).

These large scale trends can be directly compared to sequence stratigraphic interpretations of the core. In this cored interval, there are 4 individual systems tracts that are identified. At the base of the core, a highstand systems tract correlates well to chemostratigraphic intervals A through D (Figure 82; Figure 6). An increased detrital signal correlates well to the interpreted lowstand systems tract based at ~13,480' (Figure 82; Figure 6). Chemostratigraphic interval I includes the top of the highstand as well as the base of the lowstand systems tracts. Chemostratigraphic interval II marks the beginning of the decreased detrital signal previously discussed. However, this decreased detrital signal is consistent throughout chemostratigraphic interval II. This is interpreted as a lowstand systems tract. An alternative interpretation would place the base of the transgressive systems tract at the base of this chemostratigraphic interval (Figure 82; Figure 6). The transgressive systems tract continues through chemostratigraphic interval III, where it is capped by chemostratigraphic interval IV (Figure 82). This final chemostratigraphic interval marks the gradual and significant shift to more proximal environments, and is characteristic of well-developed highstand systems tracts.

Questar 8

A similar approach to that used in describing the Questar 1 cored interval was applied in examining the Questar 8 cored interval. Nine individual chemostratigraphic intervals are identified (Figure 83). Chemostratigraphic analysis of Questar 8 yields subtle trends that may be invisible to the naked eye when directly examining the core. Questar 8 is largely aggradational, with relatively unchanging lithofacies and interpreted proximity to shoreline throughout lower two-thirds of the core. However, the chemostratigraphic evidence suggests fluctuations in detrital input. Chemostratigraphic interval A (Figure 83) shows that the basal ~40 feet of this core show pulses of Si/Al and Zr/Al curves. This is interpreted to represent periodic pulses of sediment into the system. Generally, in this chemostratigraphic interval, however, there is an increased detrital signal through time (i.e. Si/Al increases throughout chemostratigraphic interval A).

Chemostratigraphic interval B (Figure 83) shows an extended interval when all detrital signals dramatically shift suggesting lower influence. Simultaneously, the clay indicators increase. This is overlain by chemostratigraphic interval C which shows the reverse signal from chemostratigraphic interval A – successive pulses of sedimentation are progressively becoming less dominated by detrital input. This trend continues, but slows down in chemostratigraphic interval D.

Following this, a brief pulse of detrital calcium is seen in chemostratigraphic interval E (Figure 83), when the Ca/Al signal continues to decrease, while detrital quartz stays constant (interval F; Figure 83).

Intervals G and I (Figure 83) are similar in that they show an increased detrital signal throughout their thicknesses. Interval H, on the other hand shows relative consistency in the

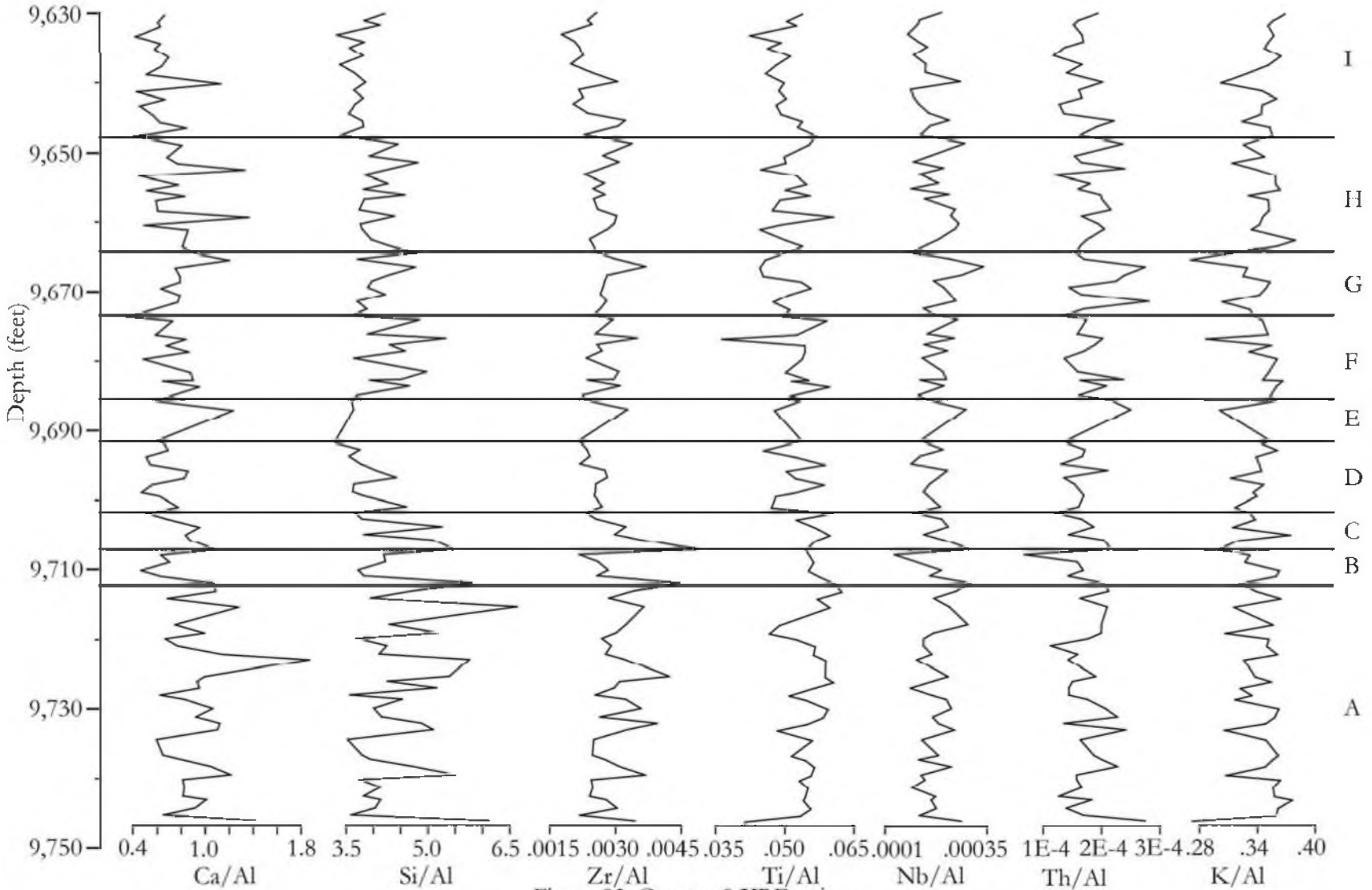

Figure 83: Questar 8 XRF ratios

detrital signal. Interval G, additionally, is defined at its base by a very sudden decrease in detrital quartz content.

These groups of chemostratigraphic intervals define three large scale changes in the chemostratigraphic character of the Questar 8 cored interval (Figure 84). Interval I is similar to interval IV found in Questar 1 (Figure 82). Interval II, however suggests an overall shift to lower detrital input through time. Interval three shows an overall lower detrital influence, but each chemostratigraphic interval still shifts towards an increased detrital signal. These three intervals can be directly compared to the sequence stratigraphic interpretation based on the lithologies. Three sequence stratigraphic systems tracts are identified in this cored interval (Figure 7). The chemostratigraphic data suggest that a revision of the exact placement of these systems tracts may be in order.

Interval I (Figure 84) represents a highstand systems tract, in line with both previously identified chemostratigraphic trends of highstand systems tracts (Figure 82) as well as direct observations of the core. The saw tooth pattern exhibited at the top of interval A and through interval B (Figure 84) is very similar to the pattern shown at the top of the Questar 1 chemostratigraphic interval IV (Figure 82). However, between chemostratigraphic intervals C and D, within Interval II (Figure 84), a transgression is recorded. This transgressive "surface" appears to span nearly 20 feet of the core, although the majority of the decrease in detrital input occurs in chemostratigraphic interval C (Figure 84). Interval III (Figure 84) yields further differences in interpretation. In the core, the top of this interval this is identified as an early (and distal) highstand systems tract (Figure 7). Chemostratigraphic stacking patterns suggest, however, that the overall stacking of individual parasequences may still be retrogradational. Note the shift at the base of interval

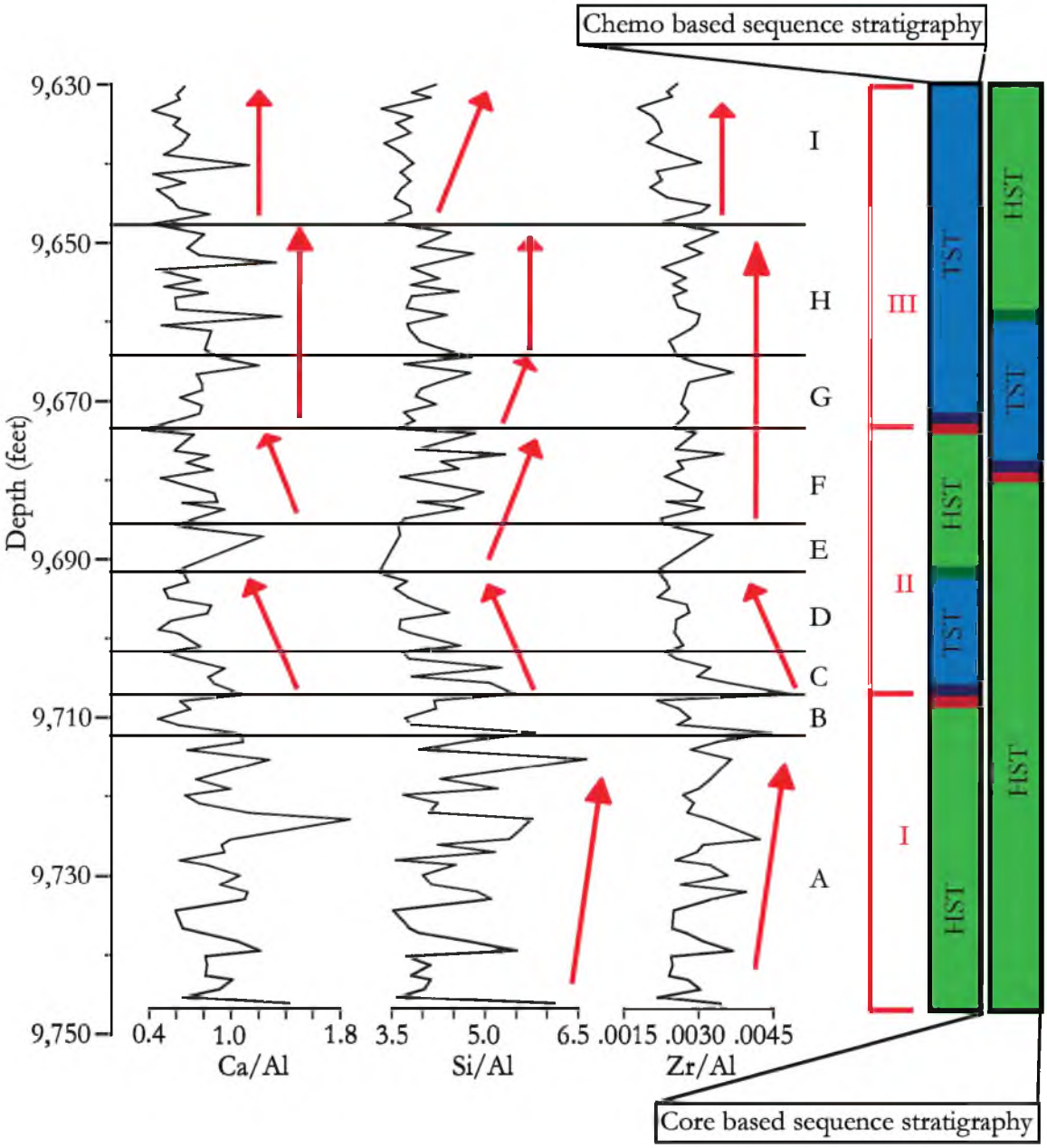

Figure 84: Questar 8 XRF ratios for Ca/Al, Si/Al, and Z/Al. Three large scale patterns emerge. Interval I represents an increase in detrital quartz into the system, with a brief punctualtion of little detrital input. Interval II marks a gradual decrease in detrital input. Interval III represents intervals that generally increase in detrital input, but their own bases are subsequently lower in detrital signals. Two sequence stratigraphic interpretations are far right. Leftmost is a chemostratigraphically based interpretation. Rightmost is the core based sequence stratigraphic interpretation

F, G, and I in the Si/Al curve in Figure 84.

Ultimately, these chemostratigraphic data suggest that what was identified in the core as the transgressive systems tract, and overlying highstand systems tract, may represent a single transgression. Additionally, the basal highstand systems tract in the core could be subdivided using chemostratigraphic data to include a transgressive systems tract.

Questar 16

Following the same procedures as outlined in the Questar 1 chemostratigraphy discussion above, nine distinct chemostratigraphic intervals are identified in the Questar 16 cored interval. Unlike Questar 8, however, the patterns identified in the Questar 16 align very well with identified stacking patterns and previously interpreted sequence stratigraphy.

Chemostratigraphic interval A, D, and F (Figure 85) all show similar trends of an abruptly increasing detrital signal. While the Si/Al signal deflects more in interval D, relative to intervals A and F, a better defined trend is recorded in interval F (Figure 85). Chemostratigraphic intervals B, C, and E do not record precise matches to individual parasequences (Figure 85; Figure 8; Figure 86); however they record a generally unchanging trend of constant detrital input into the system.

Chemostratigraphic interval G marks a sudden deflection towards lower detrital input (Figure 85). This is evidenced best in the Ca/Al, Si/Al, and Zr/Al curves. This sudden departure marks the lowest values for Zr/Al in the entire curve, and very low values in the Si/Al curve. Chemostratigraphic interval H shows a well-developed gradual shift toward lower detrital input, returning the very low values recorded in chemostratigraphic interval I (Figure 85).

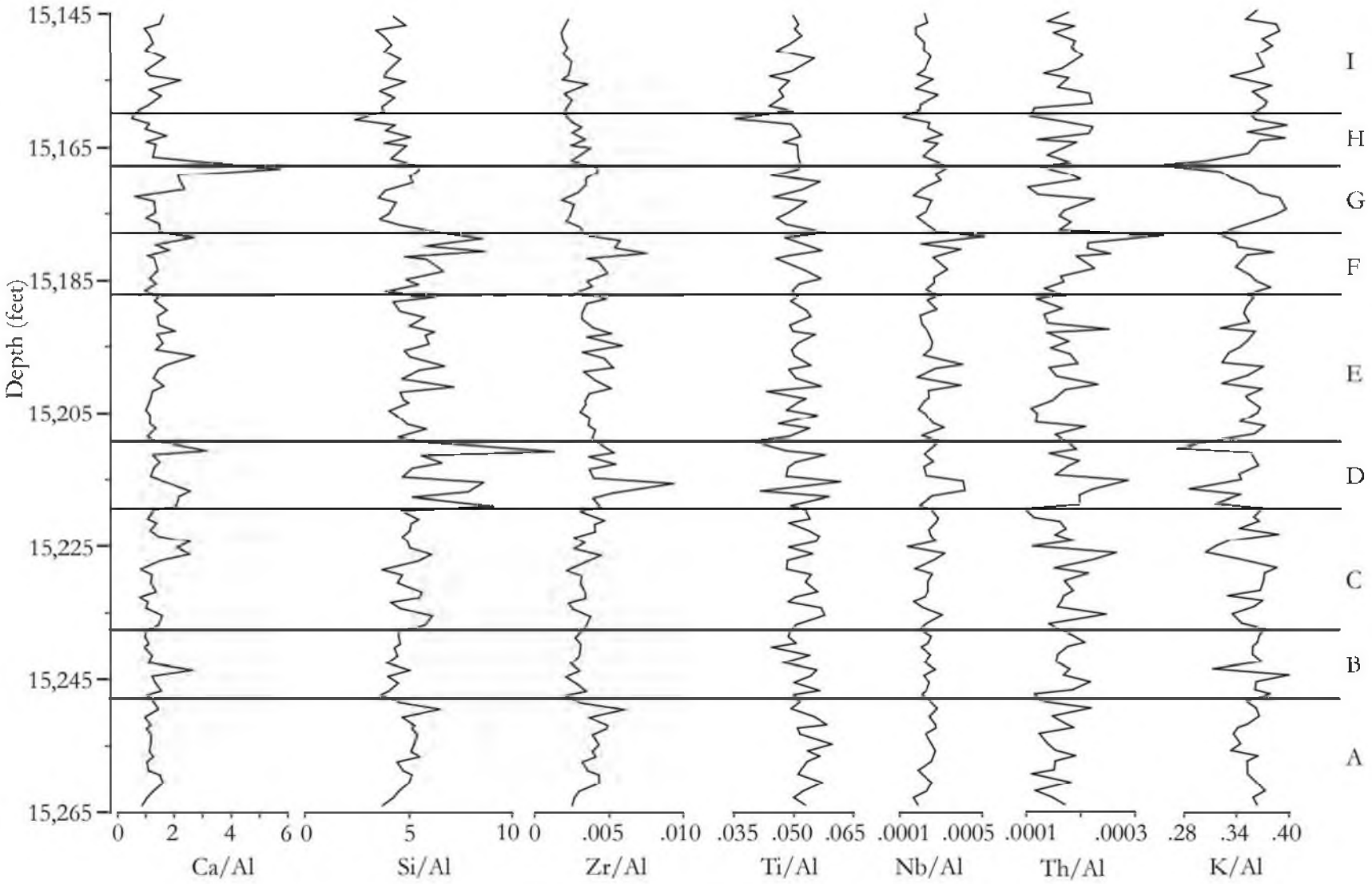

Figure 85: Questar 16 XRF ratios

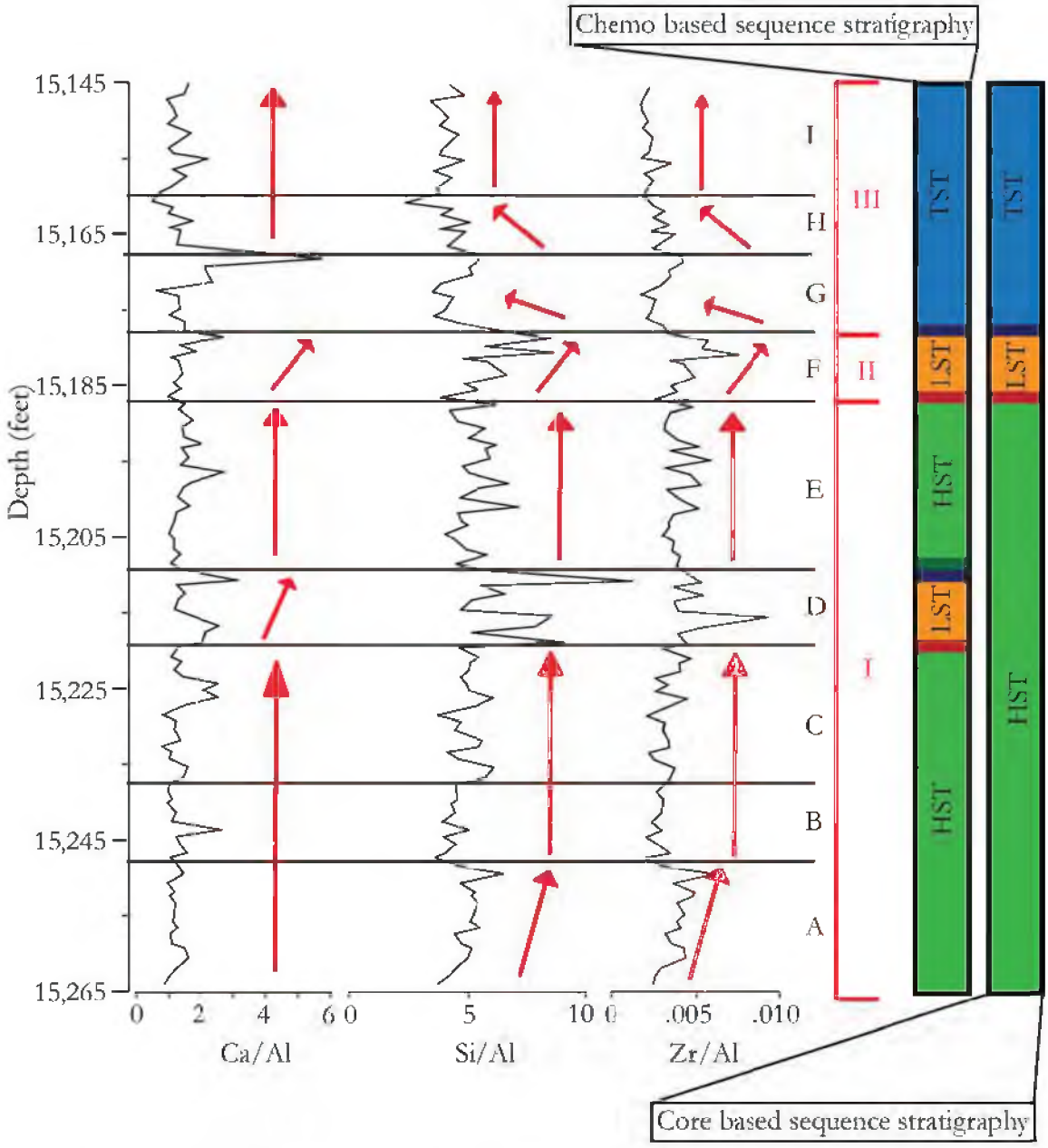

Figure 86: Questar 16 XRF ratios for Ca/Al, Si/Al, and Z/Al. Three large scale patterns emerge. Interval I represents a gradual increase of detrital input into the system. Interval D shows a brief punctuation of high detrital input. Interval II marks a very high amount of detrital input in the system. Interval III show a significant shift away from detrital input into the system. This shift is sudden at first (interval G) and gradual from thereafter (intervals H and I). Two sequence stratigraphic interpretations are far right. Leftmost is a chemostratigraphically based interpretation. Rightmost is the core based sequence stratigraphic interpretation

Three distinct large scale chemostratigraphic intervals emerge from this analysis that match very well against the sequence stratigraphic interpretation that has been applied to the Questar 16 cored interval (Figure 86; Figure 8). Chemostratigraphic interval I correlates very well to the highstand systems tract present at the base of the core. Similar to previously identified highstand systems tracts, the chemostratigraphy indicates multiple pulses of sediment into the system, with a trend to generally increased detrital input throughout the intervals (Figure 82; Figure 84; Figure 86).

The sudden and consistent deflection of detrital indicators throughout chemostratigraphic interval II indicates a sudden landward shift in lithofacies (Figure 86). This landward shift is the lowstand systems tract in the sequence stratigraphic interpretation. The base and top of chemostratigraphic interval II match perfectly with the identified lowstand systems tract (Figure 86; Figure 8). Chemostratigraphic interval D presents an element of complexity. The sudden deflection towards an increased detrital signal in interval D is of similar magnitude and thickness to that in interval F (Figure 86; Figure 85). This landward shift is also observed in the core (Figure 8) but this landward shift was not deemed significant enough to merit identification of a larger lowstand systems tract. It is possible that neither of these intervals represents a lowstand systems tract, and rather they are merely a very proximal representation of a highstand systems tract.

The base of the overlying chemostratigraphic interval III represents a sudden shift to a much lower detrital input into the system (Figure 86). This matches observations (Figure 70) and interpretations (Figure 8) of the lowermost transgressive systems tract. Throughout chemostratigraphic interval III there is a gradual shift towards a lower detrital influence. Of note, interval H (Figure 86) exhibits a gradual shift towards a lower detrital signal. These

trends are consistent with previous observations of lithology and interpretations of a transgressive or retrogradational stacking pattern (Figure 8).

Discussion

In all five studied cored intervals, the sequence stratigraphic model that has historically been applied to far more proximal environments appears to hold in these more distal offshore deposits of the Mancos Shale. There are, however, several complexities that arise in detailed analysis which may be typical of the overall genetic architecture of this system. Generally speaking, the transgressive systems tracts are the simplest to identify in core. Highstand systems tracts dominate the architecture, with lowstand systems tracts represented poorly. Additional complexities arise when correlating across the Uinta Basin.

Transgressive systems tracts in marginal strata are notoriously difficult to identify, and characteristic lithologies can be cryptic (Arnott, 1995; Cattaneo et al., 2002; Sixsmith et al., 2008). Commonly, the lack of accommodation space, as well as a landward transport direction of sediment coupled with erosive surfaces, results in very poor preservation potential. In the nearshore realm, transgressive deposits can be identified based on documentation of distinct surfaces (e.g., ravinement surfaces, transgressive surfaces, etc.) (Cattaneo et al., 2002). There are of course numerous examples of transgressive deposits in a myriad of environments(Cattaneo et al., 2002; Labune et al., 2008; Nelson et al., 2009), but their identification can be challenging. In the cored intervals studied in the Mancos shale, however, transgressive systems tracts are the easiest systems to identify, and their identification may very well be the most accurately identified throughout all cored intervals. Transgressive systems tracts are unique, in that they are the only systems tract that can have retrogradational stacking patterns (i.e., underlying parasequences are more distal than

overlying parasequences). That makes even a single retrogradational parasequence diagnostic of a transgression of some magnitude. Larger (and potentially longer lasting) transgressions compound the effect, and contain within several parasequences that are retrogradationally stacked. By having the ability to confidently place a transgressive systems tract, it allows context to be generated for underlying and overlying systems tracts.

By thickness, the most dominant systems tract present in this study is not the easily identified transgressive systems tract. Rather, it is the highstand systems tract, characterized by comparatively distal parasequences with aggradational (rarely progradational) stacking patterns. This is somewhat in line with the sequence stratigraphic model, but differs in a key aspect. In the sequence stratigraphic model, early highstand systems tracts are aggradational as sediment supply roughly equals accommodation space. As the highstand systems tract progresses, sediment supply begins to outpace accommodation space, and this results in a shift to progradational stacking patterns. In these cored intervals, progradation is rare in all highstand systems tracts. Consequently, the sediment supply/accommodation space paradigm must be slightly altered to apply to distal environments. The lack of progradational late highstand systems tracts suggests that at no point during the highstand does sedimentation rate outpace accommodation space.

In this study, the lowstand systems tract is commonly thin and sometimes absent altogether. Lowstand systems tracts are characterized in traditional sequence stratigraphic models as containing distinct proximal shifts in parasequences that are stacked in progradational to aggradational stacking patterns. Where lowstand systems tracts have been identified in this study, they are always associated with a sudden proximal shift in facies or depositional environment, marking a sequence boundary. This proximal shift is not easily tracked through grain size variation – instead it is most clearly demonstrated by examining

the environments of deposition associated with individual parasequences. Progradation is more common in the few lowstand systems tracts, compared to highstand systems tracts. This is consistent with the previously discussed notion of accommodation space being far more available in distal realms. A lowstand that would shift environments of deposition significantly landward could certainly be of a great enough magnitude to impact the balance of sediment supply and accommodation space.

Of related significance is the cryptic nature of sequence boundaries in these successions. Where lowstand systems tracts are present, the sequence boundary is marked by a sudden landward shift in facies and the environment of deposition, as one might expect. However, where lowstand systems tracts are absent, sequence boundaries and transgressive surfaces are combined surfaces. It is important to note that subtle drops in sea level may not be recorded due to a model of deposition that is not sensitive enough.

There is a trend throughout all five cored intervals concerning the interaction between highstand systems tracts and lowstand systems tracts. Lowstand systems tracts are thin or non-existent, and highstand systems tracts are thick, and commonly bounded both above and below by transgressive systems tracts. The combination of these two factors suggests that all cored intervals are representative of an overall aggrading or prograding coastal mudbelt system, where mud-dominated sediment supply kept pace with (resulting in aggradation) or outpaced (resulting in progradation) the creation of accommodation via basin subsidence and eustatic variations. There is no reason that relative sea level must decrease following an increase – if sea-level was to continue to increase, the lowstand systems tract would be omitted, and the highstands would be bounded above and below by transgressive systems tracts. Given that this is the precise pattern evidenced throughout the

5 cored intervals, the overarching depositional motif is one of a prograding coastal mudbelt, with a generally rising relative sea level.

Chemostratigraphic methods have shown that chemostratigraphy is not refined enough to separate individual lithofacies (see Chapter 1 for statistical analysis) but larger scale trends do emerge. In the cases of Questar 1 and Questar 16 chemostratigraphic data aligns very well with parasequences. In Questar 8, this alignment is less well developed. In all cored intervals, trends emerged that either lend credence or raise questions regarding the sequence stratigraphic interpretation. Certainly, the 20-100 foot scale trends of chemostratigraphic intervals show the most promise for further analysis. Radioactive chemostratigraphy can be tied to gamma ray measurements throughout the cored intervals, which suggests that a robust sequence stratigraphic interpretation can be developed through use of logging tools alone.

The model identified herein is a preliminary one that is left to be tested regionally. Sequence stratigraphic models are composed of systems tracts and associated sequence stratigraphic surfaces that are correlative throughout entire basins. The five cores that are discussed in detail do not correlate between each other, because they are cored at different depths and stratigraphic intervals. However, the RGU-1 core cored through the entirety of the Lower Blue Gate member of the Mancos Shale. Kennedy (2011) provides a sequence stratigraphic interpretation of the Blue Gate Member of the Mancos Shale, which should, according to the sequence stratigraphic model, be correlative across the basin to the Pioneer 1, Pioneer 2, and Questar 16 cored intervals.

The basal 300 feet of the Blue Gate Member (Figure 87) are interpreted to belong to the transgressive systems tract (Kennedy, 2011). Above a maximum flooding surface at

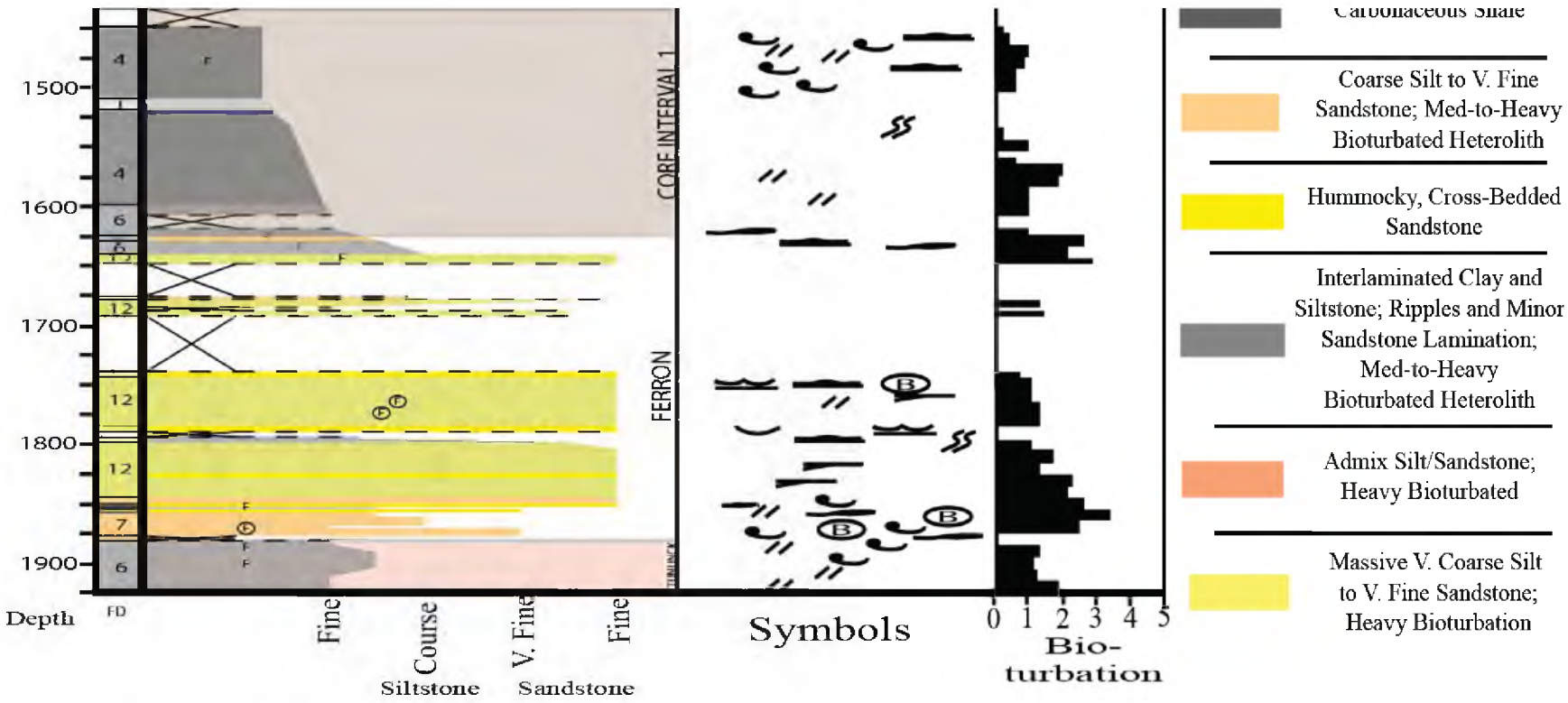

FIgure 87: Core log of the River Gas Unit #1 (RGU-1) core from Kennedy, 2011. Note the difference in scale between the RGU-1 core and the Questar and Pioneer cores in this study. The RGU-1 core is ~1800 feet thick, compared to Questar and Pioneer cres, which are ~120 feet thick. Core Interval 1 and 2 are interpreted to be a transgressive systems tract, with core intervals 3 through 6 representing a highstand systes tract.

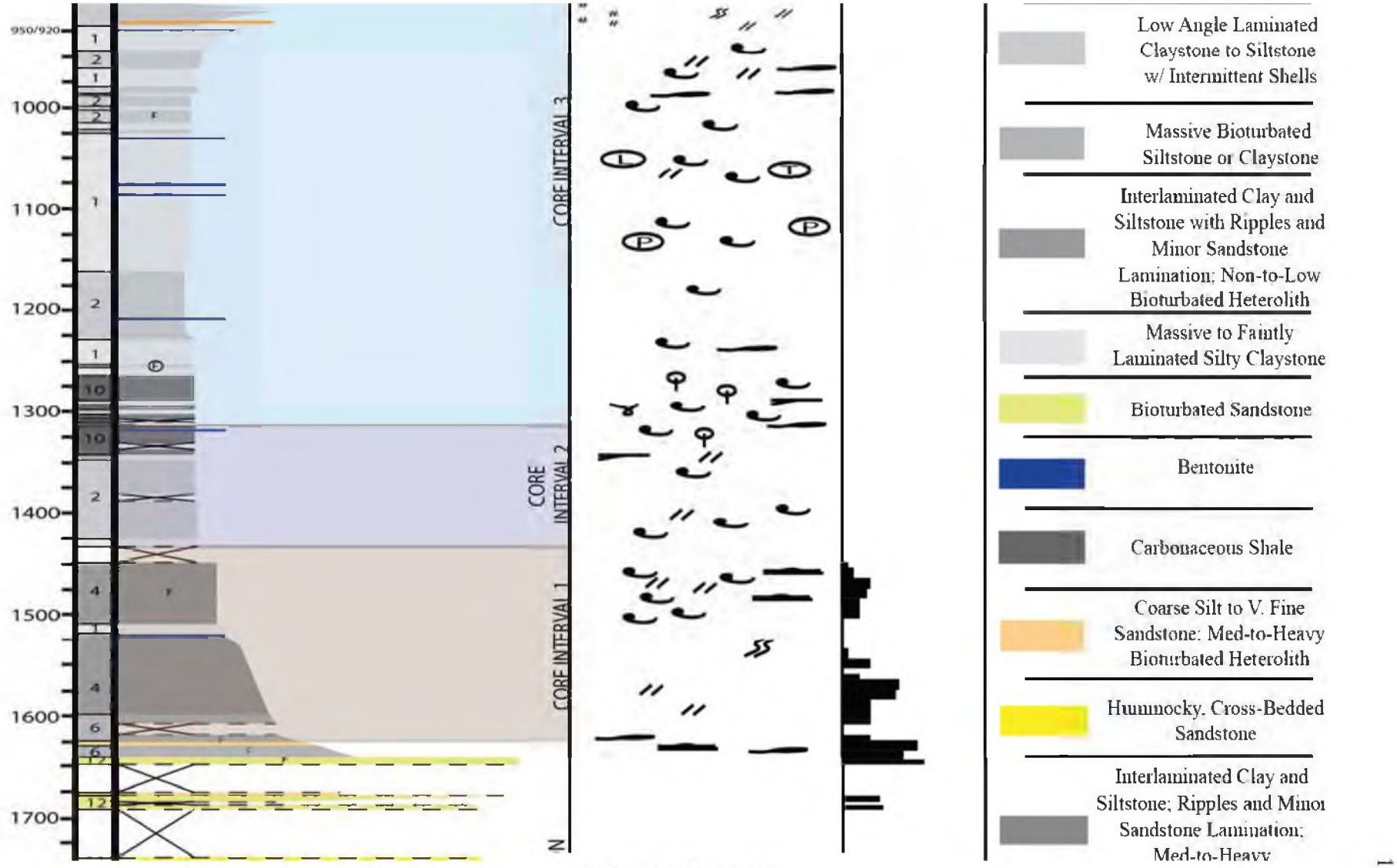

Figure 87. Continued

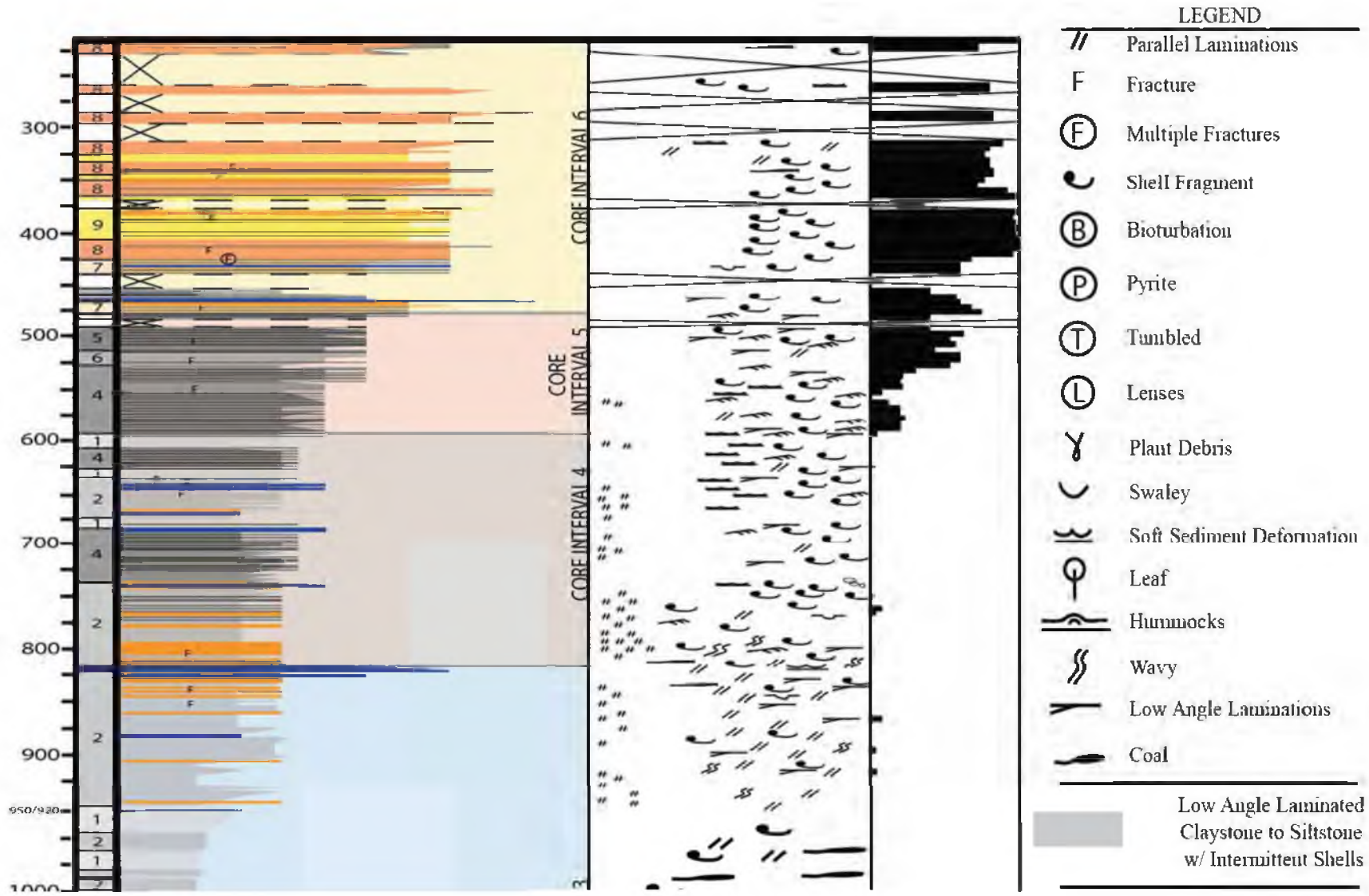

Figure 87: Continued

1310', all sediments belong to a highstand systems tract (~1100 feet) (Figure 87). By comparison, systems tracts in the other five cored intervals are on the order of 10 to 100 feet, with average sizes on the order of 30 feet. There is an order of magnitude difference in scales between the thickness of sequences identified in the RGU-1 core and the other five cored intervals.

It is most likely that the sequences and their component systems tracts in the Pioneer and Questar cored intervals are higher order packages that weren't observed in the RGU-1 core (Kennedy, 2011). Due to the thickness of the RGU-1 core, detailed analysis was necessarily less detailed than the analysis associated with the much thinner Questar and Pioneer cores. As a result, the systems tracts that are present in the Questar 16 core may, in fact, be correlative to the RGU-1 core, but the systems tracts would be higher order oscillations in the 300 to 1000 foot thick systems tracts described in the RGU-1 core (Kennedy, 2011). In essence, the RGU-1 core most likely represents one sequence set with component stacked sequences that are the same order of thickness as the sequences observed in the Questar and Pioneer cored intervals.

Evidence supporting this theory exists in the upper 800 feet of the RGU-1 core (Figure 87). Core intervals are used as parasequence proxies in analyzing the RGU-1 core (Kennedy, 2011), yet it is clear that there are more detailed changes in grain size that occur within these core intervals. In fact, these changes in grain size occur on the order of 10 feet, as described by Kennedy (2011). This is the same order of magnitude thickness that parasequences in the Pioneer and Questar cores are observed. It is not difficult to imagine a higher order sequence stratigraphic analysis of the RGU-1 core, completed with the specific goal of identifying parasequences that are approximately 10 feet thick. Lamination

abundance in the RGU-1 core follows this trend of being highly variable on the 10 foot scale as well (Figure 87; Kennedy, 2011).

Furthermore, if the systems tracts of the Pioneer and Questar cores were to compose sequence sets found in the RGU-1 core, then the trends observed on the largest scale within the Pioneer and Questar cores should fit within the sequence stratigraphic framework of the RGU-1 core. Similar to the Pioneer and Questar cores, the RGU-1 core is composed of a transgressive systems tract that is minor by thickness, overlain by a highstand systems tract that comprises the majority of the core by thickness. The Blue Gate Member is recording an overall sea-level rise, and progradational patterns are occur on a very large (~1000 foot) scale coarsening upwards sequence. Similar to the Pioneer and Questar core, the Blue Gate Member records a large scale motif of a prograding mudbelt associated with sea level rise. Thus, the sequence stratigraphic style and framework of the Pioneer and Questar wells fits with the sequence stratigraphic style and framework of the RGU-1 core, albeit at a higher order. Systems tracts have been identified in separate studies that display thicknesses on the same order of magnitude in mudstone systems in completely different environments (Abouelresh et al., 2012).

Finally, with the purpose of identifying key zones for completion in a very thick Mancos Shale, these techniques have yielded a critical finding: depending on the variables that one wishes to track, sequence stratigraphic models make it possible to trace key features into the basin. Two potential targets are found in lithologic analysis: lithofacies 8 for its high organic carbon values and calcite content, and lithofacies 9 for its high quartz content, and increased grain size.

In Chapter 1, it was noted that the highest TOC values and also highest calcite content are found in lithofacies 8. High TOC implies a higher gas storage capacity and

additional calcite content may impart a brittle quality to the rock, suggesting this lithofacies is a potential target reservoir unit. Lithofacies 8 is found exclusively in transgressive systems tracts and very early (and very distal) highstand systems tracts. These systems tracts and their associated surfaces should be correlative throughout the basin. Similar findings exist in the Barnett formations in the east-central Fort Worth Basin (Abouelresh et al., 2012) where the tops of transgressive systems tracts were found to have increased TOC values compared to surrounding packages. Similar trends are identified in the Mancos Shale in the San Juan basin, where transgressive systems tracts were identified to have increased TOC values compared to other systems tracts (Pasley et al., 1991). Studies in multiple basins suggest that the best source rock potential (e.g., highest TOC values) exist commonly in transgressive systems tracts, although their precise location within the transgressive systems tract is still debated (Lash et al., 2011).

Lithofacies 9, on the other hand, was demonstrated to have low values of TOC. However, the average grain size was largest in lithofacies 9 and the quartz content was markedly higher. This suggests that lithofacies 9 could make for an excellent reservoir. Lithofacies 9 occurs exclusively in proximal lowstand systems tracts. This exhibits a second systems tract that could be traced and mapped throughout the basin.

Thus, intelligent development of the Mancos Shale could hinge on tracing these distal transgressive systems tracts as well as their subsequent early highstand systems tracts, as well as proximal expressions of lowstand systems tracts across the basin. Because transgressive systems tracts are the most easily identified systems tract in this succession, this exercise may prove relatively straightforward and fruitful.

Conclusions

Parasequences, the building block for sequence stratigraphic analysis, are identified in all 5 cored intervals on the order of 3 feet to 80 feet thick. Rather than being defined by coarsening upward lithologies, these parasequences are more specifically defined by an increase in siltstone interlamination frequency and thickness upwards, coupled with noting where lithofacies shift sharply from proximal to distal environments of deposition, based on a depositional scheme established in Chapter 1. Parasequences are compared against each other and progradational, aggradational, and retrogradational vertical stacking patterns are identified. These stacking pattern interpretations are based on comparing the proximity to the shoreline of the base and the top of individual parasequences to the tops and bases of underlying parasequences.

Stacking patterns are used to assign systems tracts to sets of individual parasequences. This exercise revealed several key observations. First, transgressive systems tracts are the most easy to reliably identify with characteristic retrogradational stacking patterns. Highstand systems tracts, which accounted for the majority of the sediment volume in the five cored intervals, are identified by aggradational stacking patterns and rare progradational stacking. The dominance of aggradational stacking patterns relative to progradational stacking reflects seemingly limitless accommodation space in the offshore relative to their updip shallow marine shoreface deposit counterparts. This is a key difference in offshore sequence stratigraphic stacking patterns to be noted for future studies. To be classified as a lowstand systems tract, stacking patterns are generally aggradational or progradational and environments of deposition are considerably more proximal to the paleo-shoreline relative to the underlying package. Where lowstand systems tracts are present, sequence boundaries are relatively straightforward to recognize due to the landward shift in

environment of deposition. However, in general, sequence boundaries are difficult to identify in these offshore deposits without complete analysis of surrounding systems tracts. Where lowstand systems tract are absent, sequence boundaries are interpreted to exist as a surface combined with the transgressive surface, between highstand systems tracts and transgressive systems tracts. In this case, sequence boundary identification is much more cryptic.

Chemostratigraphic data suggest that in Questar 1 and Questar 16 excellent correlation exists between parasequences and small scale chemostratigraphic trends, namely reflected in chemical proxies for detrital input. Better correlations exist between sequence stratigraphic systems tract interpretations and large scale (~20-100 foot) trends exhibited in the chemostratigraphy. Future work should focus on developing these correlations to logs that are present within wells to create a robust sequence stratigraphic interpretation of wells that are not cored.

Finally, these sequences are compared to identified sequences in the RGU-1 core. The sequences are scaled differently, but the higher order sequences of the Questar and Pioneer cores fit with the rising sea level and progradational interpretations of the RGU-1 core. Broadly, the Questar and Pioneer cored intervals are interpreted to represent a prograding mudbelt system with a rising sea-level. The relative abundance by thickness of aggradational highstand systems tracts relative to transgressive systems tracts and lowstand systems tracts reflects an overall sequence architecture that records a dominantly aggrading to prograding coastal mud belt, in which mud sediment supply and deposition rates kept pace with or outpaced accommodation via basin subsidence and eustasy. The combination of facies, paleoenvironmental and sequence stratigraphic analysis performed here suggests

more ideal reservoir targets are found in distal transgressive systems tract packages and early highstand systems tract. This model should be tested regionally throughout the basin.

Thus, with limited alteration of an established model of sequence stratigraphy can be applied to siliciclastically dominated mudstone systems, like the Mancos Shale. This can lead to improved prediction and identification of high grade zones for shale gas extraction in the Mancos Shale, but moreover, this study provides evidence that multiple scales of sequence stratigraphy are applicable to mudstone sedimentology.

APPENDIX A

WHOLE BOX CORE PHOTOS

Appendix A is a compilation of whole-box photographs from all cores that are examined in this study. Each core is read from bottom right to top left, with the deepest core on the bottom right, and shallowing upwards. Detailed core logs can be directly compared to these photos for verification of primary structures and facies contacts.

Pioneer core 1 box 1 of 12

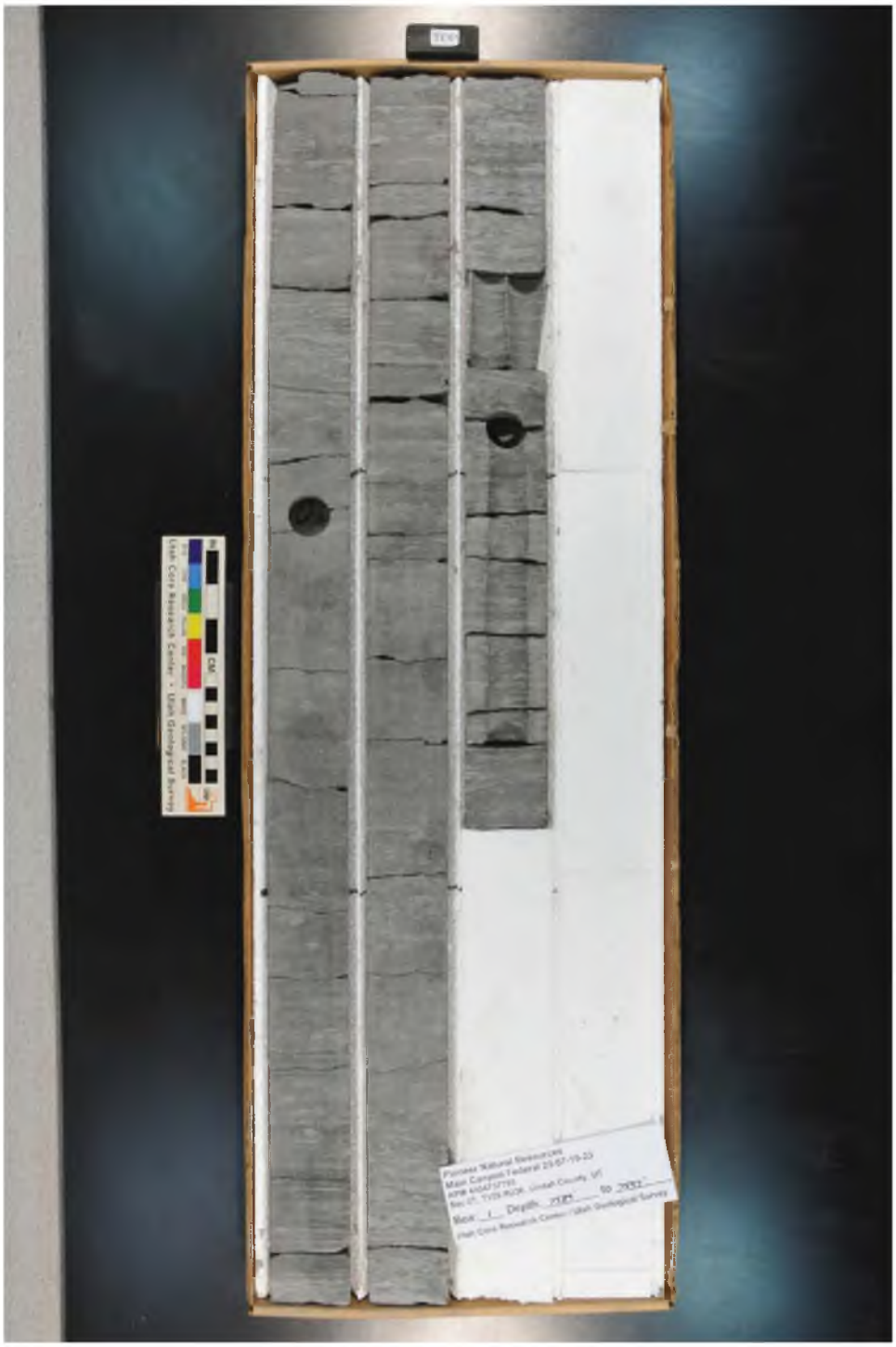

Pioneer core 1 box 2 of 12

Pioneer core 1 box 3 of 12

Pioneer core 1 box 4 of 12

Pioneer core 1 box 5 of 12

Pioneer core 1 box 6 of 12

Pioneer core 1 box 7 of 12

Pioneer core 1 box 8 of 12

Pioneer core 1 box 9 of 12

Pioneer core 1 box 10 of 12

Pioneer core 1 box 11 of 12

Pioneer core 1 box 12 of 12

Pioneer core 2 box 1 of 15

Pioneer core 2 box 2 of 15

Pioneer core 2 box 3 of 15

Pioneer core 2 box 4 of 15

Pioneer core 2 box 5 of 15

Pioneer core 2 box 6 of 15

Pioneer core 2 box 7 of 15

Pioneer core 2 box 8 of 15

Pioneer core 2 box 9 of 15

Pioneer core 2 box 10 of 15

Pioneer core 2 box 11 of 15

Pioneer core 2 box 12 of 15

Pioneer core 2 box 13 of 15

Pioneer core 2 box 14 of 15

Pioneer core 2 box 15 of 15

Questar core 1 box 1 of 11

Questar core 1 box 2 of 11

Questar core 1 box 3 of 11

Questar core 1 box 4 of 11

Questar core 1 box 5 of 11

Questar core 1 box 6 of 11

Questar core 1 box 7 of 11

Questar core 1 box 8 of 11

Questar core 1 box 9 of 11

Questar core 1 box 10 of 11

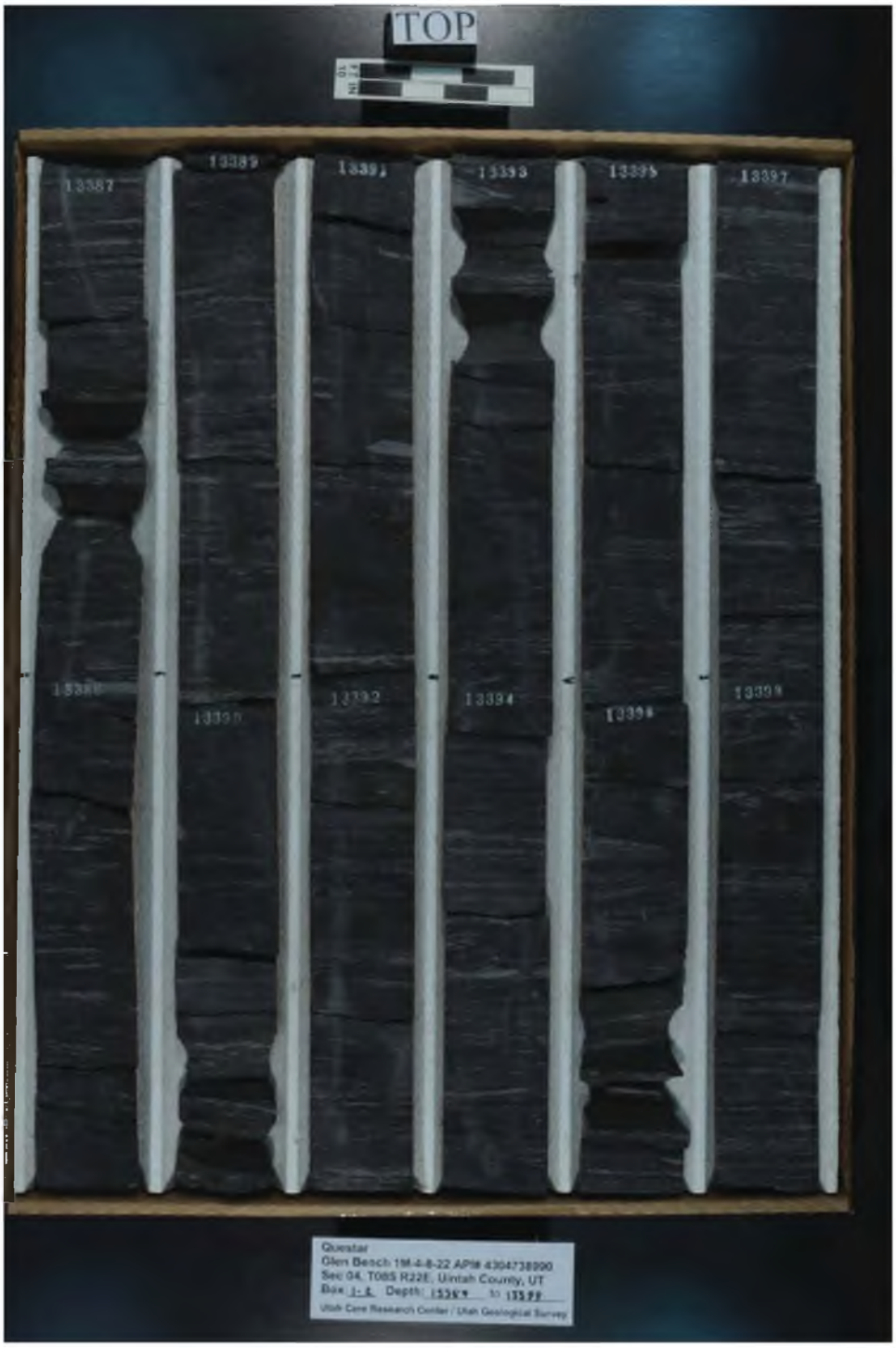

Questar core 1 box 11 of 11

Questar core 8 box 1 of 17

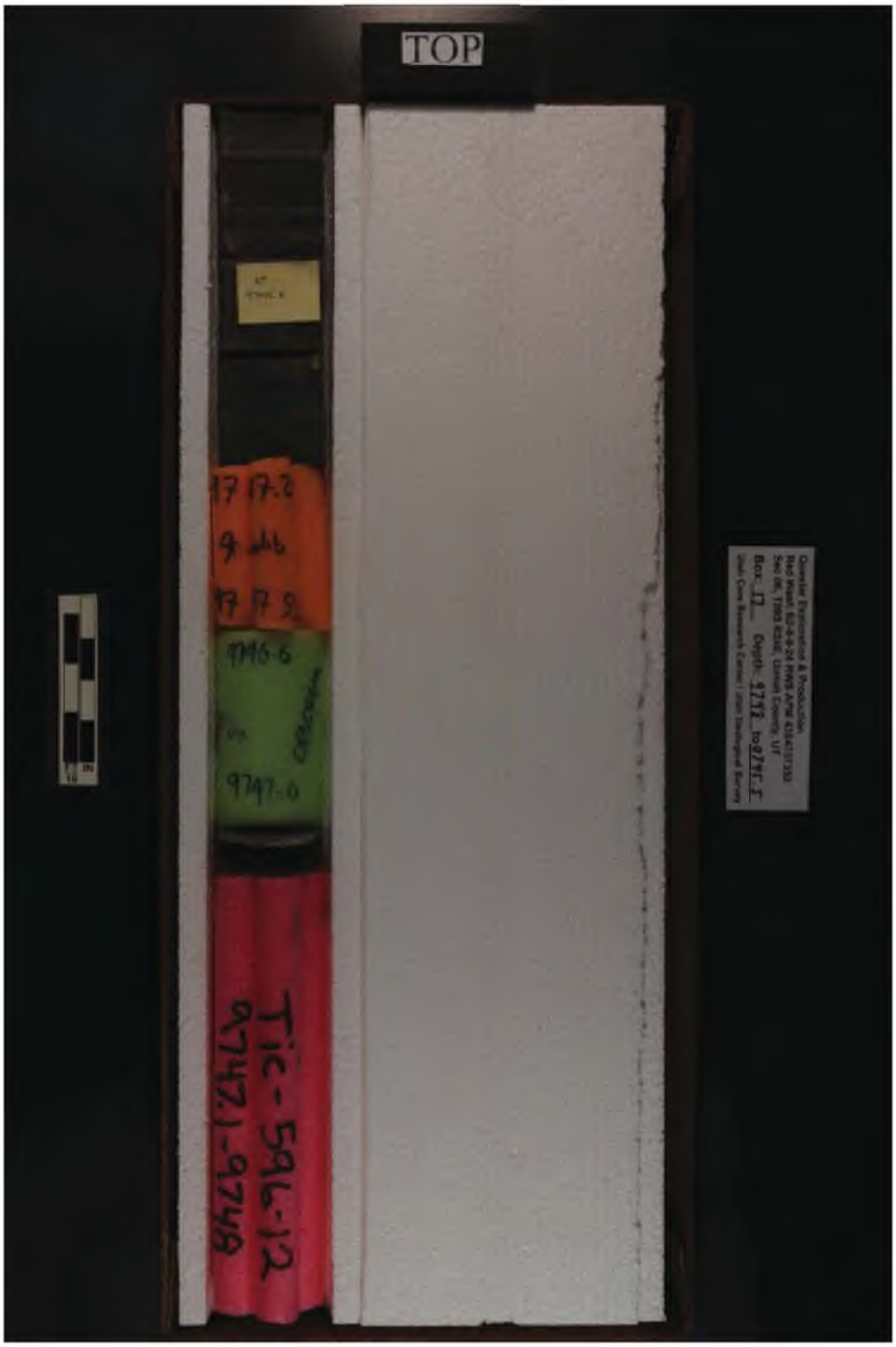

Questar core 8 box 2 of 17

Questar core 8 box 3 of 17

Questar core 8 box 4 of 17

Questar core 8 box 5 of 17

Questar core 8 box 6 of 17

Questar core 8 box 7 of 17

Questar core 8 box 8 of 17


Questar Exploration & Production
Red Wash 80-6-9-24 RWS API# 4304737332
Sec 06, T09S R24E, Uintah County, UT
Box: 10 Depth: 9701.7 to 9694.5
Utah Core Research Center | Utah Geological Survey
TICORA 596-8
9700-9701

Questar core 8 box 9 of 17

Questar core 8 box 10 of 17

Questar core 8 box 11 of 17

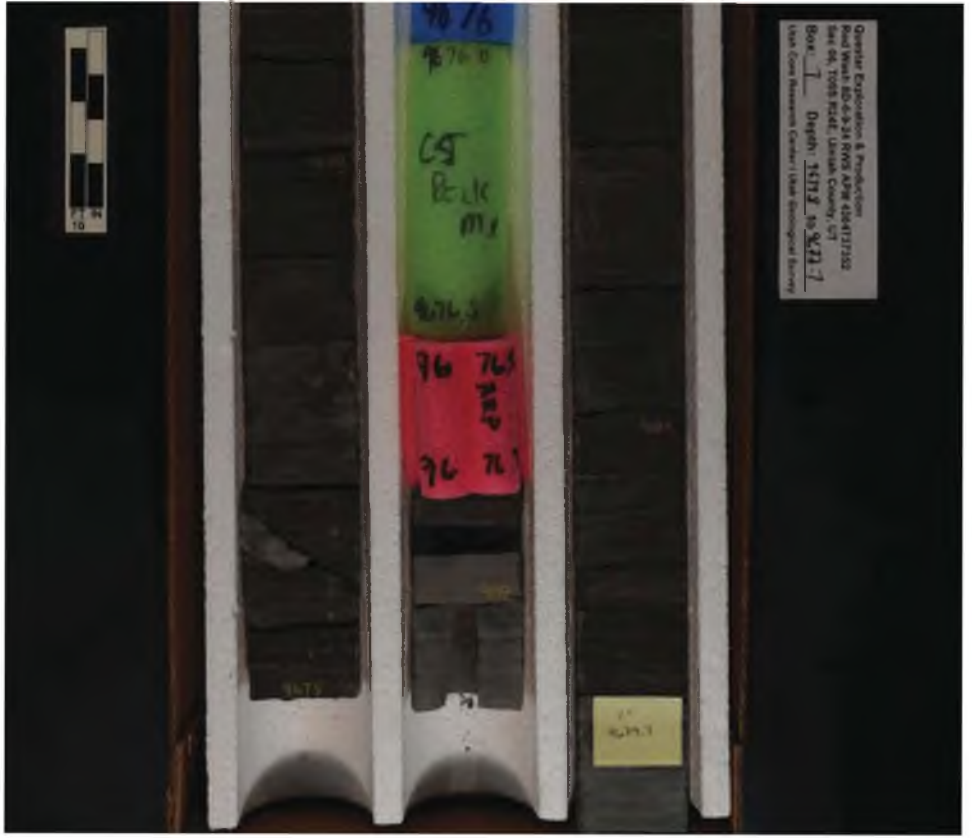
Operator Exploration & Production
Box: 1 Depth: 9572 to 9577
CS
BULK
MI
9576
96 76
REP
96 76

Questar core 8 box 12 of 17

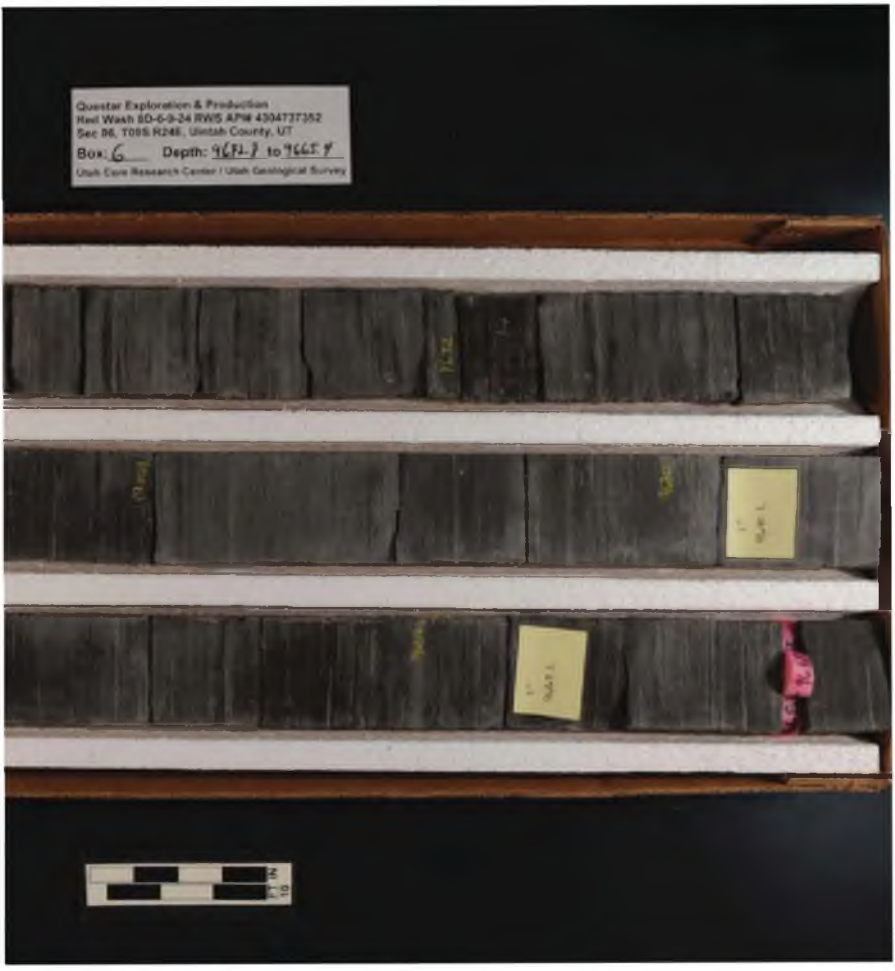
Questar Exploration & Production
Red Wash SD-6-9-24 RWS API# 4304737352
Sec 06, T09S R24E, Uintah County, UT
Box: 6 Depth: 9671.7 to 9685.4
Utah Core Research Center / Utah Geological Survey

Questar core 8 box 13 of 17

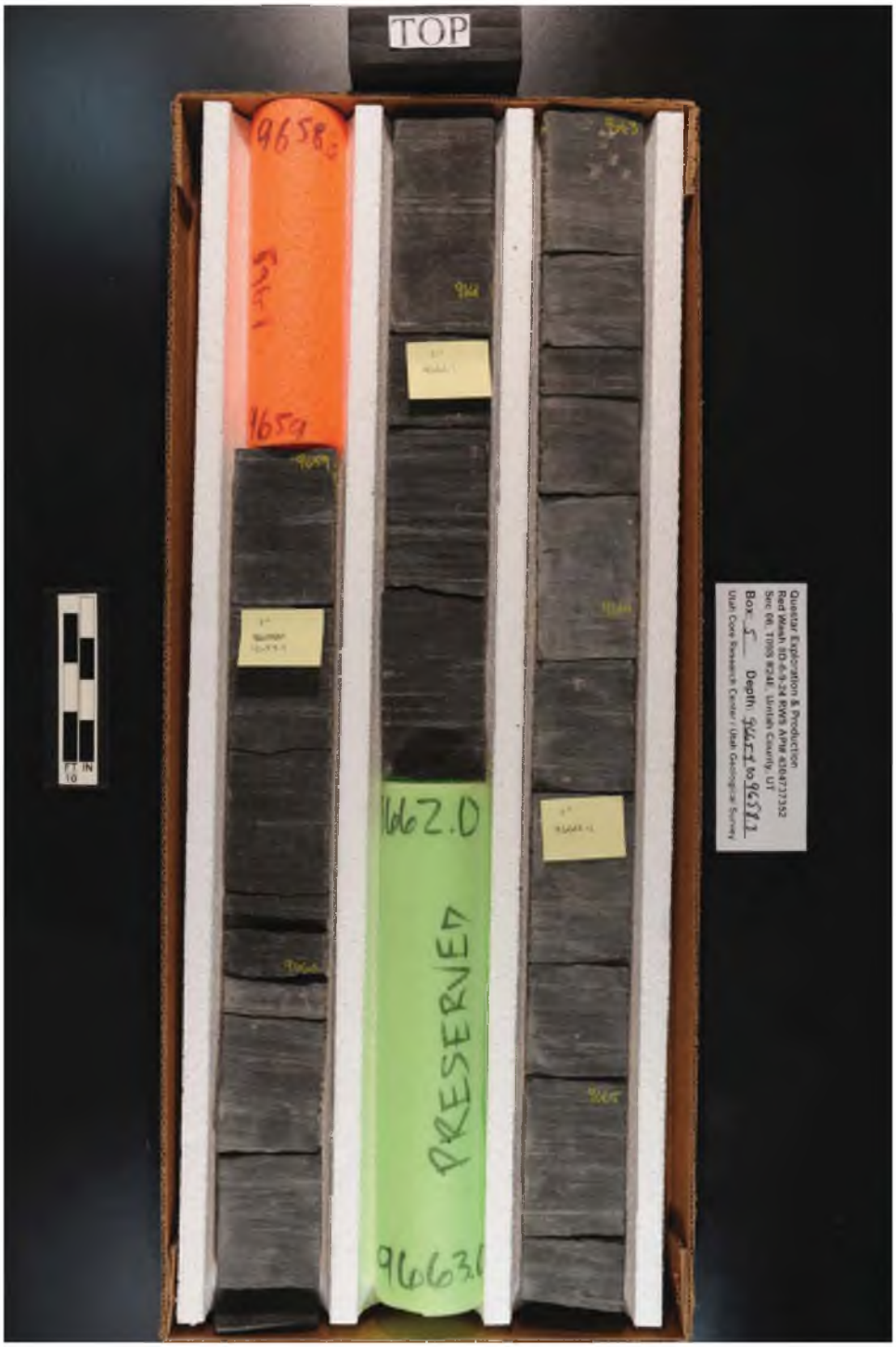

Questar core 8 box 14 of 17

Questar core 8 box 15 of 17

Questar core 8 box 16 of 17

Questar 8 box 17 of 17

Questar Exploration & Production
Red Wash 6D-6-9-24 RWS API# 4304737352
Sec 06, T09S R24E, Uintah County, UT
Box: 1 Depth: 9637 to 9650
Utah Core Research Center / Utah Geological Survey
9633.0
PRESERVED
9634.1
9631
9631.2
9631.5
9632
9632.1

Questar 16 box 1 of 17

Questar 16 box 2 of 17

Questar 16 box 3 of 17

Questar 16 box 4 of 17

Questar 16 box 5 of 17

Questar 16 box 6 of 17

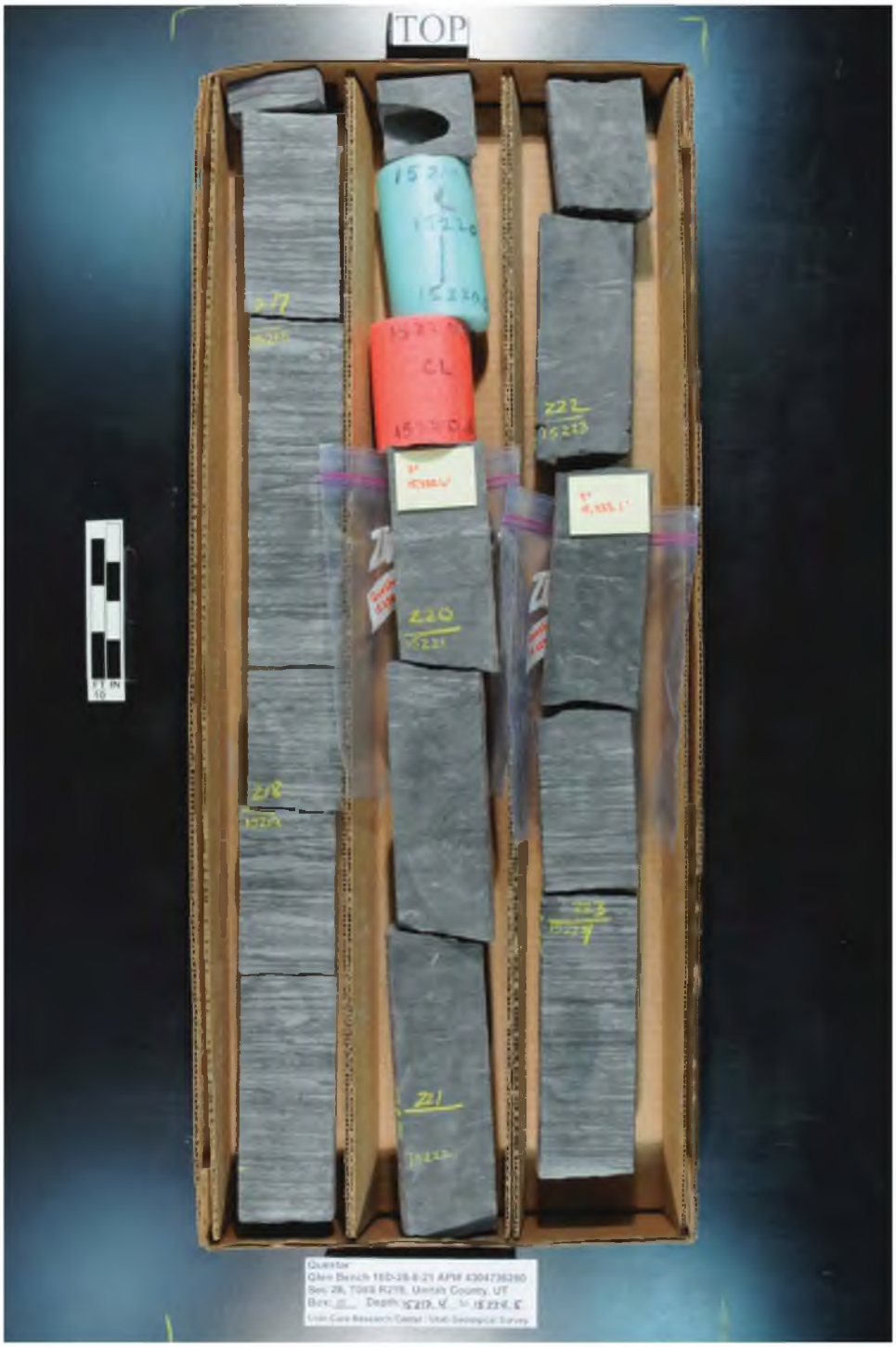

Questar 16 box 7 of 17

Questar 16 box 8 of 17

Questar 16 box 9 of 17

Questar 16 box 10 of 17

Questar 16 box 11 of 17

Questar 16 box 12 of 17

Questar 16 box 13 of 17

Questar 16 box 14 of 17

Questar 16 box 15 of 17

Questar 16 box 16 of 17

Questar 16 box 17 of 17

APPENDIX B

CLOSE-UP CORE PHOTOS

Appendix B comprises all detailed close-up photos that were taken from the Questar and Pioneer cored intervals. Each photograph includes a card that shows the depth from which the sample was taken, as well as what that photograph is showing.

Pioneer core close-ups

Pioneer core close-ups

Pioneer core close-ups

Pioneer core close-ups

Pioneer core close-ups

Pioneer core close-ups

Pioneer core close-ups

Pioneer core close-ups

Pioneer core close-ups

Questar 1 close-ups

Questar 1 close-ups

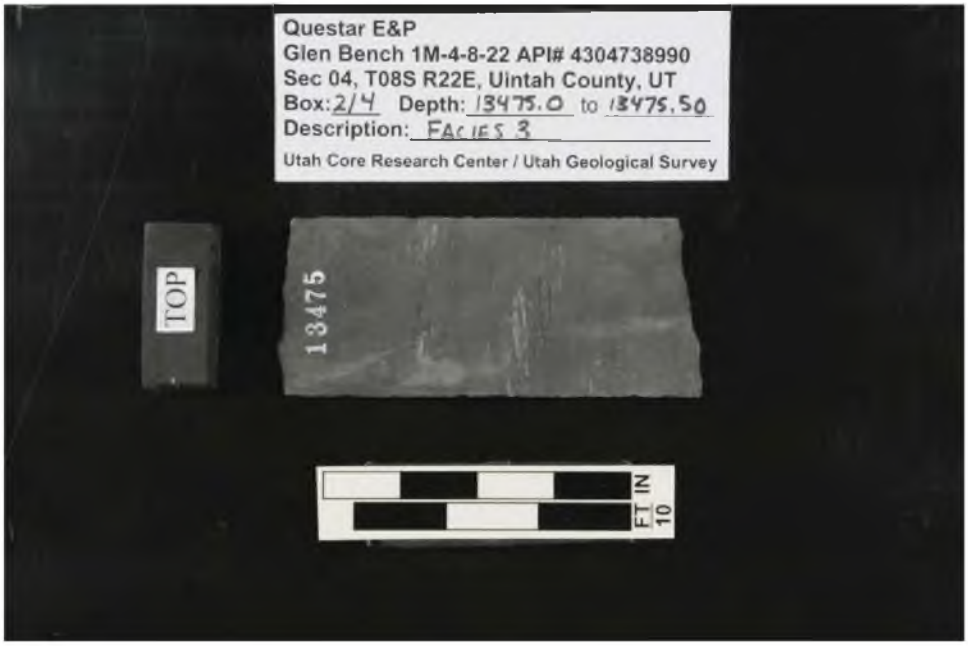

Questar 1 close-ups

Questar 1 close-ups

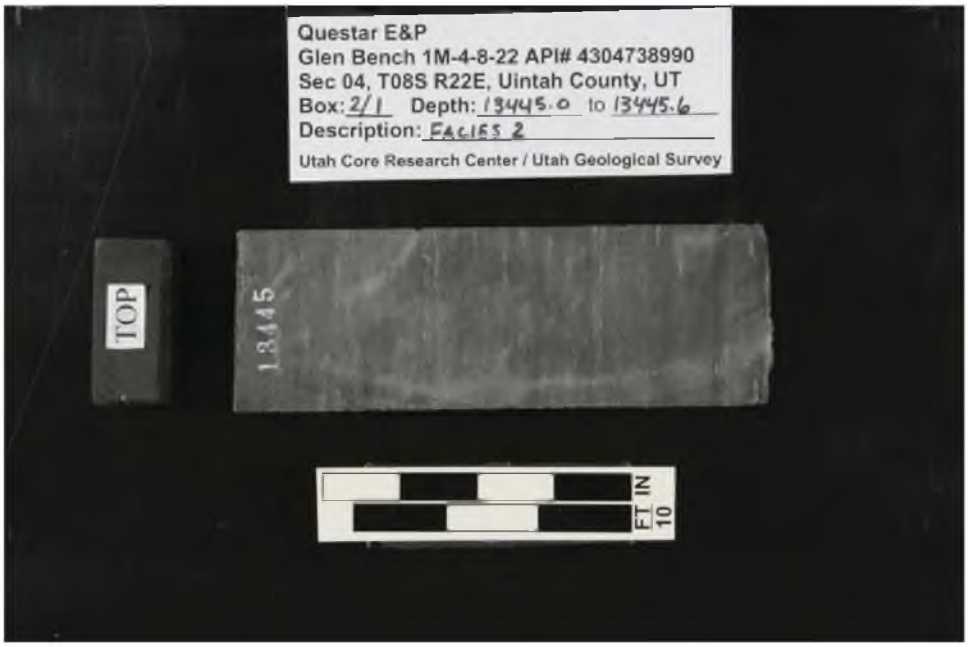

Questar 1 close-ups

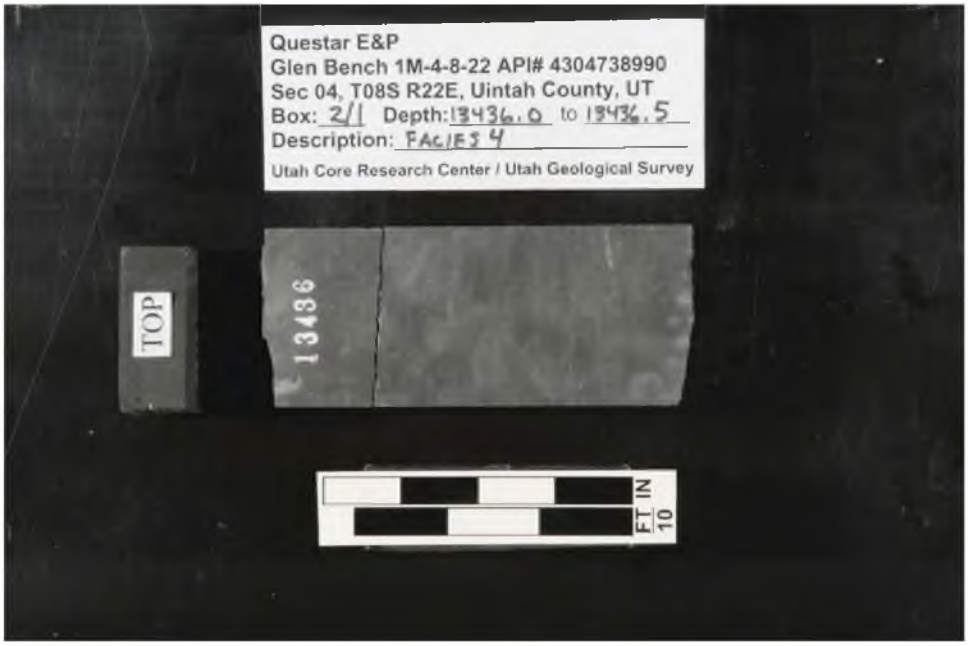

Questar 1 close-ups

Questar 1 close-ups

Questar 1 close-ups

Questar 1 close-ups

Questar 1 close-ups

Questar 1 close-ups

Questar 1 close-ups

Questar 1 close-ups

Questar 8 close-ups

Questar 8 close-ups

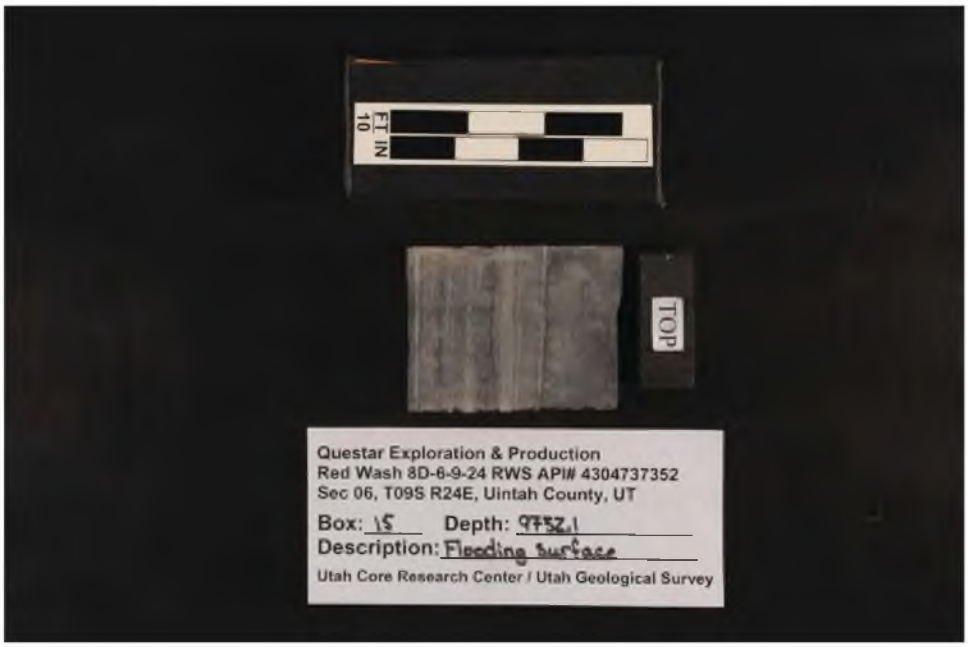

Questar 8 close-ups

Questar 8 close-ups

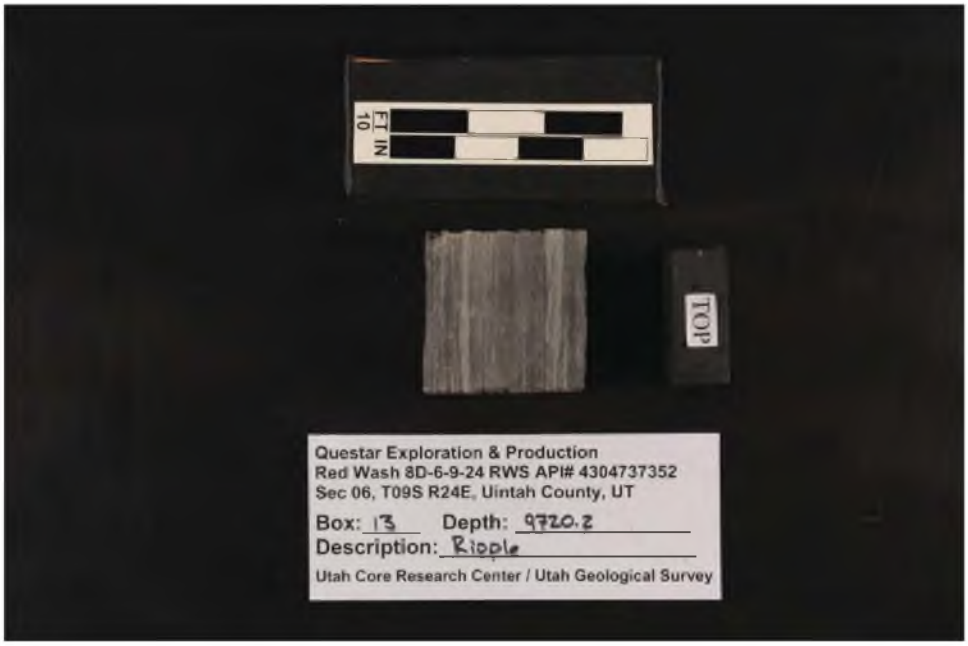

Questar 8 close-ups

Questar 8 close-ups

Questar 8 close-ups

Questar 8 close-ups

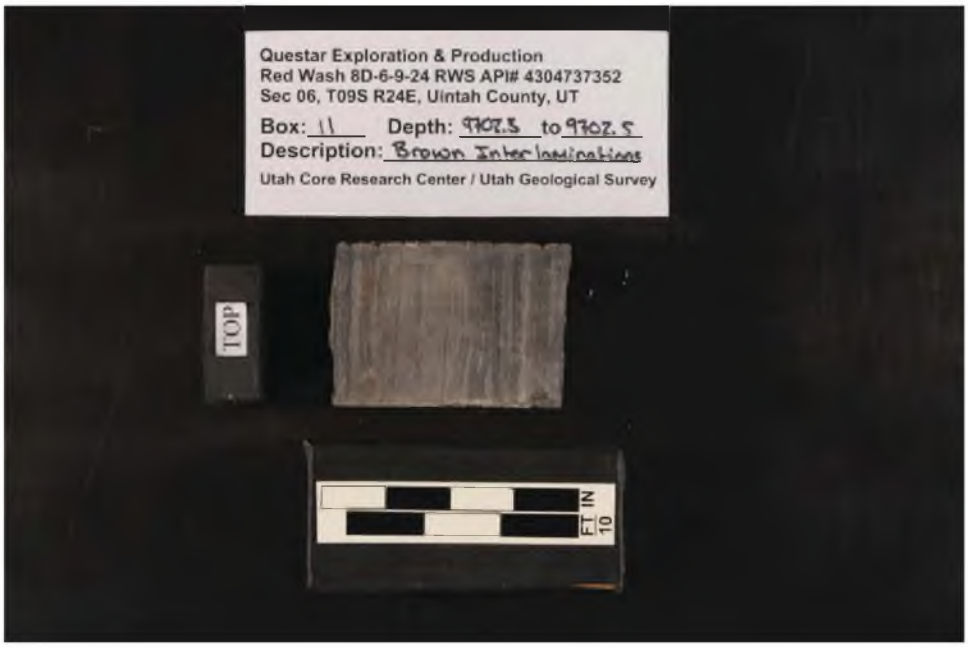

Questar 8 close-ups

Questar 8 close-ups

Questar 8 close-ups

Questar 8 close-ups

Questar 8 close-ups

Questar 16 close-ups

Questar 16 close-ups

Questar 16 close-ups

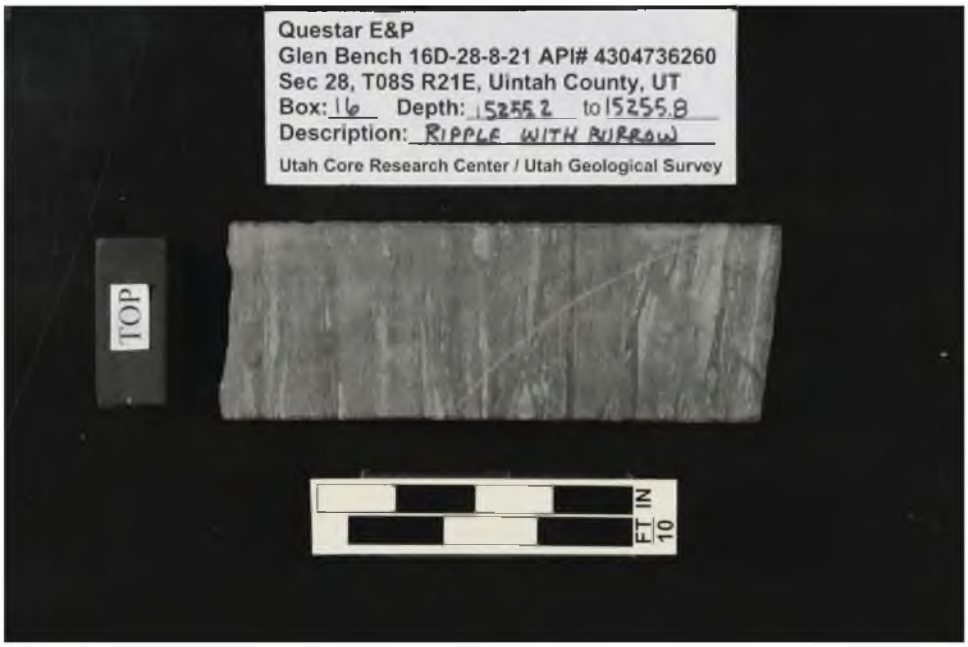

Questar 16 close-ups

Questar 16 close-ups

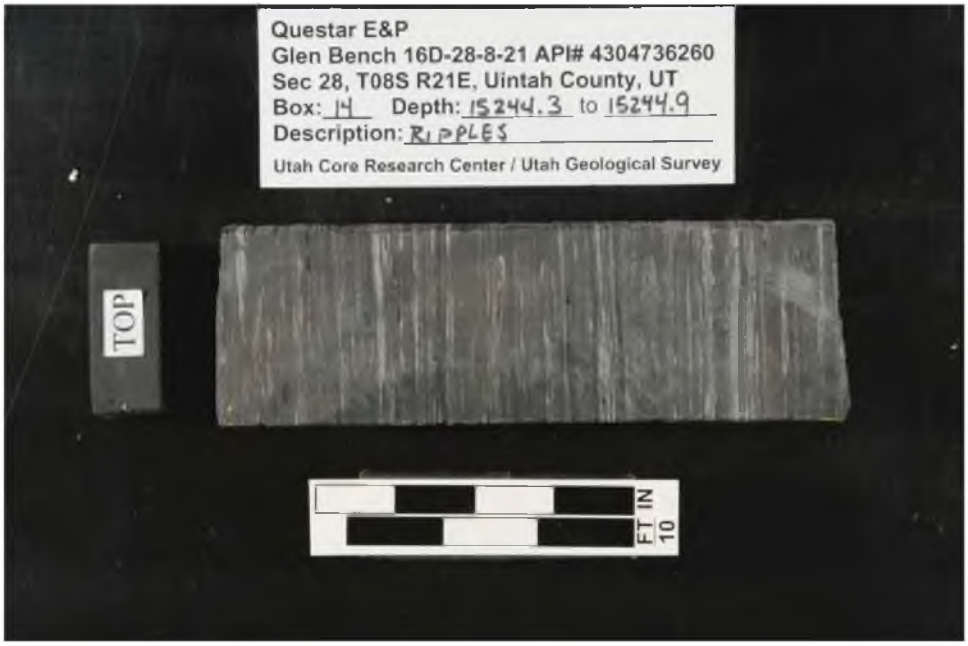

Questar 16 close-ups

Questar 16 close-ups

Questar 16 close-ups

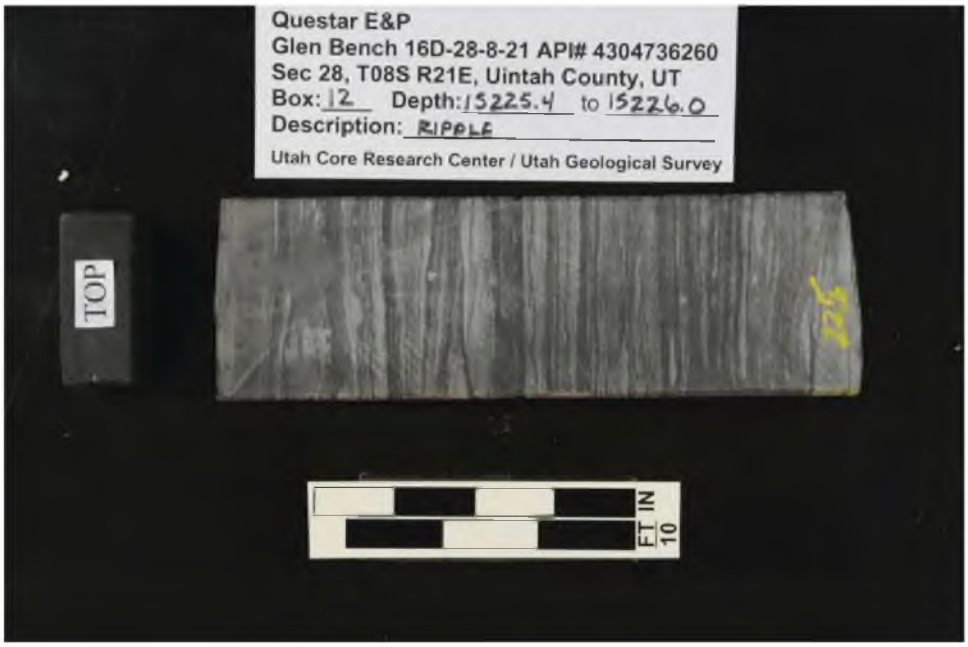

Questar 16 close-ups

Questar 16 close-ups

Questar 16 close-ups

Questar 16 close-ups

Questar 16 close-ups

Questar 16 close-ups

Questar 16 close-ups

Questar 16 close-ups

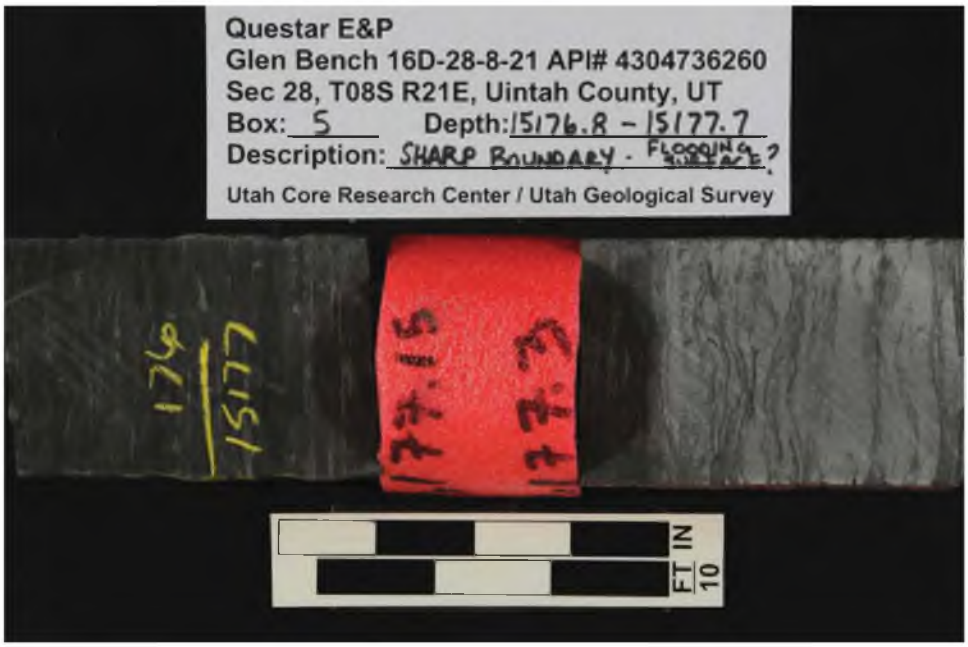

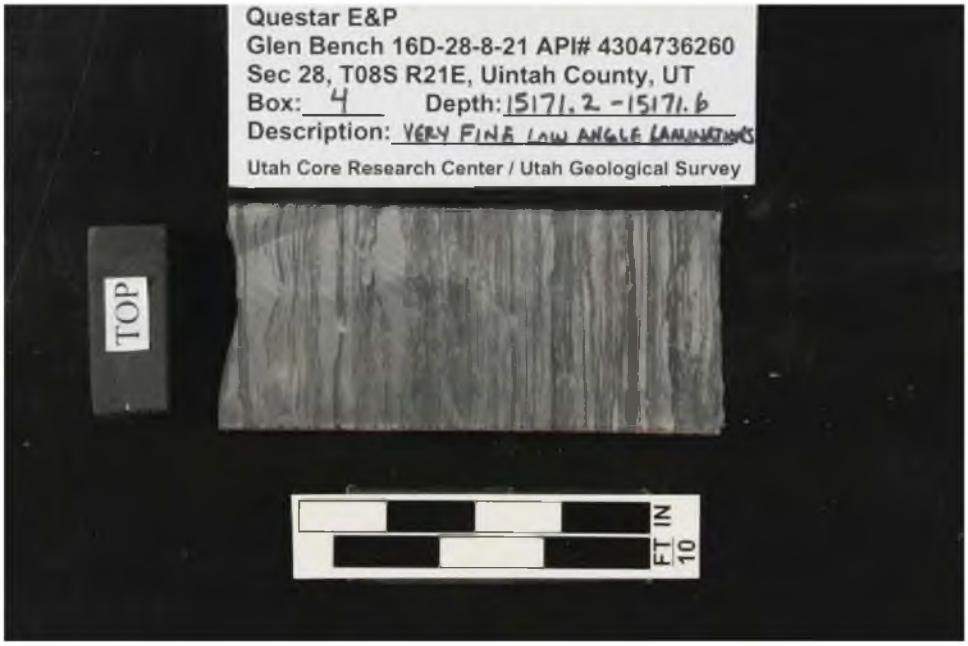

Questar 16 close-ups

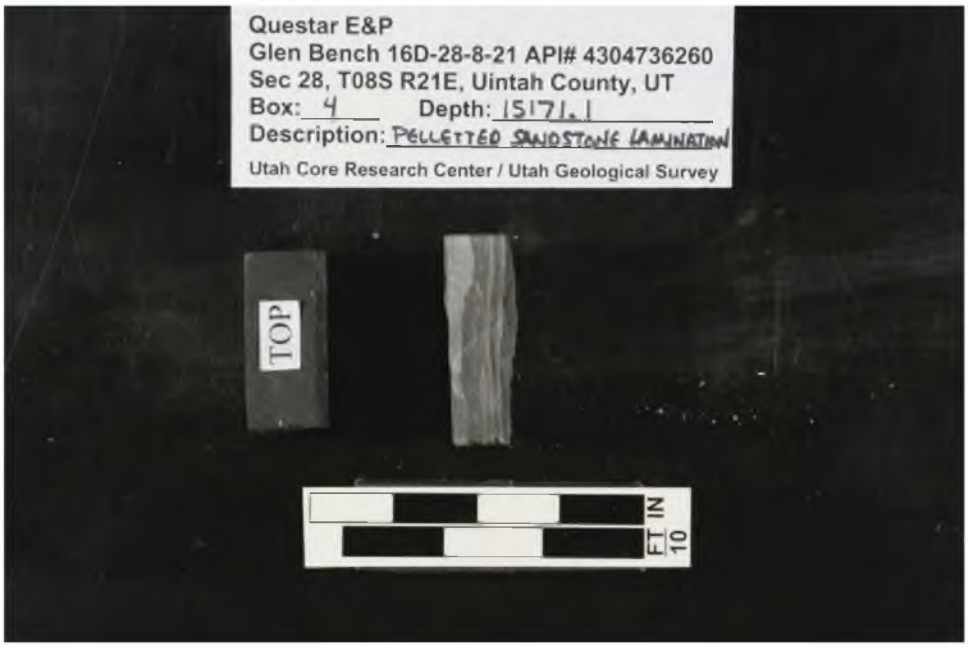

Questar 16 close-ups

Questar 16 close-ups

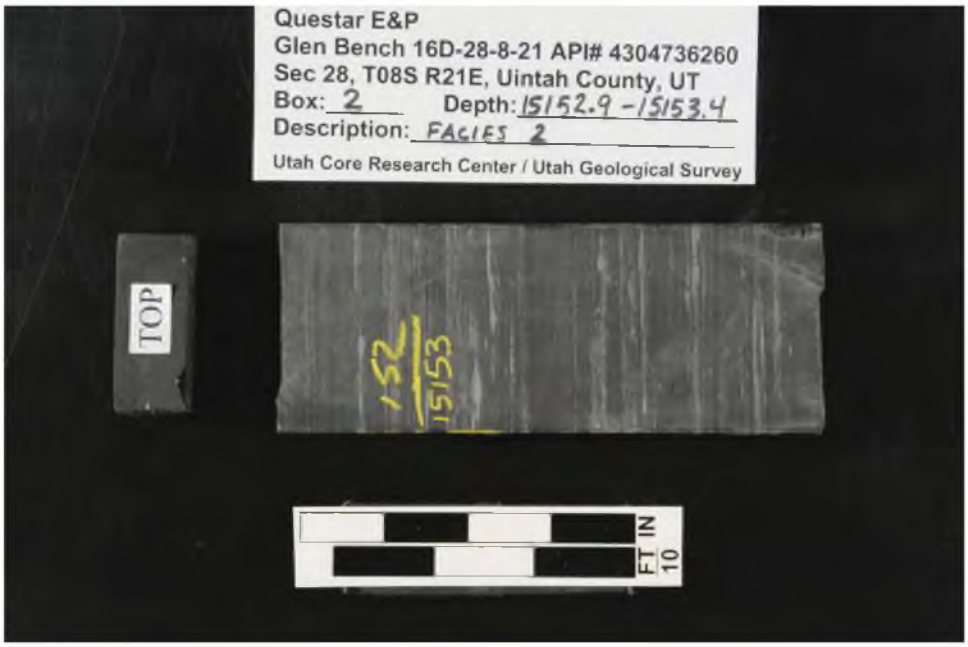

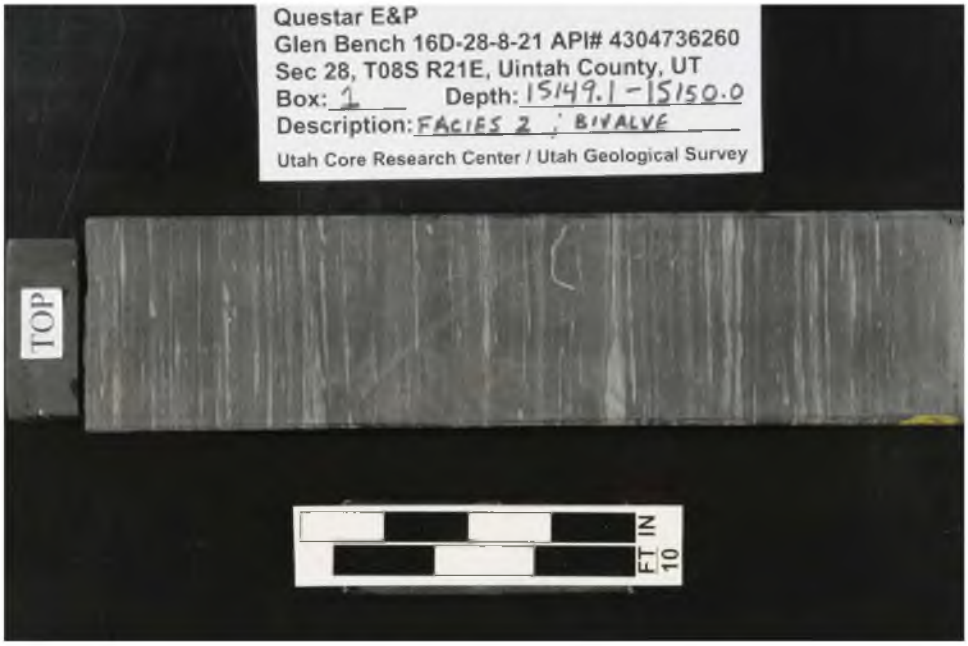

APPENDIX C

CALIBRATED XRF DATA DABLES

Appendix C comprises all of the calibrated XRF data from samples in the Questar 1, Questar 8 and Questar 16 wells, as well as data from the RGU-1 core. These data have been collected by the handheld instrument and run through the matrix specific calibration program written by Dr. Rowe at the University of Texas at Arlington. Values for each element are given in weight percent, and depths are in feet. Samples were run twice, once for major element analysis, and once for trace element analysis.

Questar 1 XRF – major elements

Sample ID	Depth (ft.)	MgKa1	AlKa1	SiKa1	P Ka1	S Ka1	K Ka1	CaKa1	BaLa1
QST(1)-MAJ-001	13375.1	1.5043758	4.3763583	28.8539913	0.0981965	0.4045790	1.3786772	4.7635827	0.0864417
QST(1)-MAJ-002	13376.7	1.5434968	4.7698799	28.6550579	0.1535600	0.4895298	1.5383685	4.6570183	0.0879641
QST(1)-MAJ-003	13377.8	1.6908219	6.8456837	26.6664672	0.1404760	0.5675948	2.3976166	3.7483339	0.0613879
QST(1)-MAJ-004	13378.6	1.3236148	4.2790749	29.9041598	0.1849410	0.6989142	1.1879245	4.2929766	0.0773169
QST(1)-MAJ-005	13379.9	1.0320838	4.1411823	29.3078375	0.0720344	0.4729961	1.0542928	4.5525722	0.0558222
QST(1)-MAJ-006	13380.5	1.4380584	6.1932895	26.7126943	0.1297331	0.6520605	2.0513560	3.9804987	0.0373932
QST(1)-MAJ-007	13381.5	1.4155675	7.2181000	26.4102254	0.1429577	0.7431560	2.5699885	3.8578079	0.0330006
QST(1)-MAJ-008	13382.3	1.6547980	6.0562094	26.6281172	0.1661197	0.8387442	2.1150205	4.0581029	0.0390160
QST(1)-MAJ-009	13383.4	1.2950984	6.9590722	26.5296952	0.1465349	0.9897221	2.4313892	3.5401694	0.0186461
QST(1)-MAJ-010	13384.3	1.2532684	5.3718092	27.1507891	0.1307910	0.6172230	1.5531414	4.3678792	0.0772292
QST(1)-MAJ-011	13385.9	1.6011405	6.4551670	25.9493680	0.1304305	0.7025776	2.2708057	4.6081873	0.0458089
QST(1)-MAJ-012	13386.9	1.6323899	5.9418921	26.3618650	0.1298426	0.7906823	1.9594819	4.5321995	0.0212608
QST(1)-MAJ-013	13387.6	1.6308500	7.0063099	25.9016570	0.1173050	0.7630703	2.4631498	3.8549808	0.0368386
QST(1)-MAJ-014	13388.8	1.6622938	6.7761695	26.2302141	0.1441561	0.7413183	2.4106665	4.0983628	0.0462085
QST(1)-MAJ-015	13389.7	1.4033965	6.3361571	26.6147705	0.1091027	0.6737147	2.0788628	4.2008528	0.0512460
QST(1)-MAJ-016	13390.7	1.5702318	6.3282991	26.8575957	0.1249507	0.7328993	2.2689874	3.8421323	0.0449030
QST(1)-MAJ-017	13391.3	1.6479128	6.8517224	26.4305307	0.1231678	0.7361607	2.4241894	3.5819162	0.0520801
QST(1)-MAJ-018	13392.1	1.5332950	5.6655534	26.7756172	0.0960618	0.7413342	1.8753626	4.7987139	0.0450816
QST(1)-MAJ-019	13393.5	1.7962583	5.9865936	26.5223930	0.1356247	0.7187280	2.0252744	4.4107509	0.0661379
QST(1)-MAJ-020	13394.7	1.5495405	5.8885511	27.3996834	0.0889253	0.7215823	1.9124488	3.8048111	0.0218805
QST(1)-MAJ-021	13395.4	1.7314809	6.4134644	27.6032956	0.1420456	0.8716213	2.2727521	3.3280011	0.0424271
QST(1)-MAJ-022	13396.5	1.7814374	5.7055024	28.2031949	0.1584330	0.4902169	1.9856222	3.5662940	0.0566209
QST(1)-MAJ-023	13397.7	1.7667596	5.7949293	27.2576661	0.1568045	0.6740939	2.0272582	3.6592566	0.0460901
QST(1)-MAJ-024	13398.7	1.3877459	6.1356918	27.4363150	0.1433543	0.5938897	2.0738355	3.8006670	0.0238080
QST(1)-MAJ-025	13399.7	1.6272837	6.6620300	27.3418000	0.1034678	0.5952798	2.2776070	3.7058188	-0.0077857
QST(1)-MAJ-026	13400.7	1.5381238	5.5735746	27.9389577	0.1700062	0.8584732	1.8760859	3.8648986	0.0274223
QST(1)-MAJ-027	13401.3	1.7150562	6.2177072	27.7277990	0.1256388	0.7601555	2.1297636	3.1477735	0.0734814
QST(1)-MAJ-028	13402.5	1.6693495	5.5458402	27.8387750	0.1677945	0.6201676	1.8299967	3.6387958	0.0749076
QST(1)-MAJ-029	13403.6	1.3081069	5.7345747	27.4878456	0.1347026	0.6603232	1.9523225	3.8224648	0.0788592
QST(1)-MAJ-030	13404.4	1.5479359	4.8811263	28.0458945	0.0705017	0.6215829	1.5334822	4.7941802	0.0487555
QST(1)-MAJ-031	13405.5	1.6156496	6.1093469	27.7096855	0.1705476	0.6423491	2.1423975	3.7656063	0.0453869

Questar 1 XRF – major elements

Sample ID	Depth (ft.)	TiKa1	V Ka1	CrKa1	MnKa1	FeKa1	ZrKa1	Ca/Al	Si/Al	Zr/Al
QST(1)-MAJ-001	13375.1	0.2041026	0.0060568	0.0107089	0.0323094	1.8777632	0.0159326	1.0884809	6.5931510	0.0036406
QST(1)-MAJ-002	13376.7	0.2819753	0.0122897	0.0084096	0.0286552	2.1011862	0.0168692	0.9763387	6.0075010	0.0035366
QST(1)-MAJ-003	13377.8	0.3638677	0.0220332	0.0070113	0.0263643	2.4818866	0.0159831	0.5475470	3.8953695	0.0023348
QST(1)-MAJ-004	13378.6	0.2419707	0.0154093	0.0086591	0.0305035	2.1116737	0.0198233	1.0032488	6.9884637	0.0046326
QST(1)-MAJ-005	13379.9	0.1657458	0.0090536	0.0085391	0.0257030	1.8968923	0.0149741	1.0993412	7.0771667	0.0036159
QST(1)-MAJ-006	13380.5	0.3523943	0.0198718	0.0079245	0.0284445	2.3485561	0.0165194	0.6427115	4.3131674	0.0026673
QST(1)-MAJ-007	13381.5	0.3955704	0.0259869	0.0061519	0.0282969	2.6110833	0.0147332	0.5344631	3.6588888	0.0020411
QST(1)-MAJ-008	13382.3	0.3636804	0.0216703	0.0074768	0.0261268	2.5508744	0.0161840	0.6700731	4.3968290	0.0026723
QST(1)-MAJ-009	13383.4	0.4136794	0.0263753	0.0070394	0.0239545	2.8253372	0.0164580	0.5087128	3.8122460	0.0023650
QST(1)-MAJ-010	13384.3	0.2596934	0.0138846	0.0090051	0.0310476	2.3026456	0.0144669	0.8131114	5.0543100	0.0026931
QST(1)-MAJ-011	13385.9	0.3502423	0.0181029	0.0068565	0.0334257	2.7479215	0.0154107	0.7138758	4.0199375	0.0023873
QST(1)-MAJ-012	13386.9	0.3331213	0.0224047	0.0068231	0.0303396	2.5561300	0.0162723	0.7627536	4.4366112	0.0027386
QST(1)-MAJ-013	13387.6	0.3892946	0.0289133	0.0059037	0.0253858	2.7398974	0.0147717	0.5502156	3.6969043	0.0021083
QST(1)-MAJ-014	13388.8	0.3751743	0.0208249	0.0086649	0.0275569	2.7066534	0.0164889	0.6048200	3.8709501	0.0024334
QST(1)-MAJ-015	13389.7	0.3294886	0.0206888	0.0078655	0.0274714	2.5601090	0.0168661	0.6629969	4.2004594	0.0026619
QST(1)-MAJ-016	13390.7	0.3378330	0.0217660	0.0082504	0.0298211	2.7297447	0.0155149	0.6071351	4.2440465	0.0024517
QST(1)-MAJ-017	13391.3	0.3408748	0.0253439	0.0072249	0.0271718	2.6926074	0.0144669	0.5227760	3.8575017	0.0021114
QST(1)-MAJ-018	13392.1	0.3044665	0.0145928	0.0100852	0.0301499	2.6110039	0.0161809	0.8469983	4.7260374	0.0028560
QST(1)-MAJ-019	13393.5	0.3243024	0.0175918	0.0077628	0.0301930	2.5162486	0.0158283	0.7367714	4.4302979	0.0026440
QST(1)-MAJ-020	13394.7	0.3043241	0.0146347	0.0084637	0.0307018	2.3837318	0.0164609	0.6461371	4.6530434	0.0027954
QST(1)-MAJ-021	13395.4	0.3424458	0.0193638	0.0076638	0.0308875	2.6423385	0.0158080	0.5189085	4.3039602	0.0024648
QST(1)-MAJ-022	13396.5	0.3121611	0.0178713	0.0078526	0.0274781	2.3144558	0.0156071	0.6250622	4.9431572	0.0027354
QST(1)-MAJ-023	13397.7	0.3158818	0.0198490	0.0066268	0.0275967	2.4509299	0.0152383	0.6314584	4.7037098	0.0026296
QST(1)-MAJ-024	13398.7	0.3396921	0.0190219	0.0089587	0.0313294	2.5326452	0.0149728	0.6194358	4.4715927	0.0024403
QST(1)-MAJ-025	13399.7	0.3651331	0.0204639	0.0096241	0.0262126	2.5284359	0.0156053	0.5562597	4.1041244	0.0023424
QST(1)-MAJ-026	13400.7	0.3047918	0.0159871	0.0098764	0.0332090	2.5951570	0.0165067	0.6934326	5.0127538	0.0029616
QST(1)-MAJ-027	13401.3	0.3471855	0.0158022	0.0075471	0.0257655	2.4896159	0.0173345	0.5062595	4.4594893	0.0027879
QST(1)-MAJ-028	13402.5	0.2957059	0.0168868	0.0069237	0.0274098	2.2469197	0.0161472	0.6561307	5.0197579	0.0029116
QST(1)-MAJ-029	13403.6	0.3226179	0.0138426	0.0078926	0.0300770	2.4051702	0.0162050	0.6665647	4.7933538	0.0028258
QST(1)-MAJ-030	13404.4	0.2663222	0.0093165	0.0096706	0.0313472	2.0865720	0.0150329	0.9821873	5.7457834	0.0030798
QST(1)-MAJ-031	13405.5	0.3286860	0.0185127	0.0094853	0.0295028	2.4656119	0.0170672	0.6163681	4.5356216	0.0027936

Questar 1 XRF – major elements

Sample ID	Depth (ft.)	MgKa1	AlKa1	SiKa1	P Ka1	S Ka1	K Ka1	CaKa1	BaLa1
QST(1)-MAJ-032	13406.4	1.4500390	6.1576986	26.8866164	0.1365165	0.8892034	2.1441935	4.0282574	0.0282187
QST(1)-MAJ-033	13407.2	1.5606752	6.5491110	27.3926727	0.1141527	0.6973972	2.3689895	3.5721800	0.0262768
QST(1)-MAJ-034	13408.3	1.6747456	6.3856498	26.2488271	0.1399085	0.7615622	2.2556571	4.0638372	0.0143890
QST(1)-MAJ-035	13409.4	1.7053651	6.1293653	26.5498617	0.1117143	0.6330763	2.1169051	4.3252989	0.0481652
QST(1)-MAJ-036	13410.9	1.9364896	5.8040173	26.0388241	0.1555564	0.7107008	1.9574777	5.2294588	0.0609921
QST(1)-MAJ-037	13411.6	1.7872613	5.6541690	27.0947882	0.1481871	0.6264015	1.9454124	5.2929004	0.0717618
QST(1)-MAJ-038	13412.2	1.5491835	5.6166091	26.5937441	0.1227418	0.6681710	1.8449236	4.5260535	0.0291262
QST(1)-MAJ-039	13413.3	1.6943270	6.8261001	26.6160047	0.1810031	0.8438138	2.3777621	4.0067803	0.0325072
QST(1)-MAJ-040	13414.5	1.5799297	6.1274990	26.8488465	0.1738112	0.7352290	2.1517979	4.1537199	0.0446882
QST(1)-MAJ-041	13415.2	1.8830213	6.4237528	26.6524338	0.1661968	0.9829580	2.1386971	4.3516689	0.0394871
QST(1)-MAJ-042	13416.7	1.4628420	5.7430115	26.8290186	0.1353381	0.5177025	1.9591900	4.1172802	0.0297236
QST(1)-MAJ-043	13417.5	1.7848320	5.9765328	27.0404201	0.1302361	0.5175752	2.0492005	4.2487218	0.0095906
QST(1)-MAJ-044	13418.8	1.6170348	6.7834748	27.6433663	0.1574535	0.7205285	2.3225102	3.3225791	0.0405341
QST(1)-MAJ-045	13419.7	1.8749911	5.7886669	27.3921113	0.1417074	0.4388139	1.9325911	3.5181583	0.0269595
QST(1)-MAJ-046	13420.9	1.5087095	6.7257328	27.7922822	0.1530132	0.4565649	2.2848612	3.2246482	0.0287929
QST(1)-MAJ-047	13421.6	1.6291619	6.1817926	27.5857489	0.0780944	0.4239508	2.0782429	3.2531002	0.0860252
QST(1)-MAJ-048	13422.9	1.5563283	5.9713075	27.8368660	0.1199255	0.5299295	2.0291615	3.4769055	0.0229031
QST(1)-MAJ-049	13423.2	1.5412084	6.4415706	26.8834271	0.1464417	0.8437346	2.2187810	3.2835934	0.0732531
QST(1)-MAJ-050	13424.6	1.7379601	5.9783509	27.6606628	0.1402987	0.8592479	1.9781231	3.7103992	0.0374328
QST(1)-MAJ-051	13425.2	1.5127631	5.7277184	28.3070629	0.0609704	0.4290960	1.9543329	3.6663197	0.0375993
QST(1)-MAJ-052	13426.5	1.3997317	6.3922522	27.0389926	0.1563490	0.5168347	2.0772870	3.8642410	0.0385919
QST(1)-MAJ-053	13427.2	1.4724387	6.7511127	26.6952569	0.1218298	0.6199190	2.2578832	3.2079472	0.0319458
QST(1)-MAJ-054	13428.6	1.4269928	7.1777014	26.6528094	0.1423537	0.9036134	2.5074590	3.3063837	0.0285569
QST(1)-MAJ-055	13429.5	1.2683705	7.4379840	27.1179325	0.1230992	0.8197074	2.5316247	3.2387533	0.0214357
QST(1)-MAJ-056	13430.9	1.4496065	7.2755593	26.2783630	0.0928897	0.7860695	2.4856736	3.8598966	0.0492277
QST(1)-MAJ-057	13431.4	1.5188540	7.7414084	26.4611796	0.1586786	1.0210413	2.5897657	3.2537183	0.0534695
QST(1)-MAJ-058	13432.9	1.5434742	7.3379669	27.3742812	0.1649082	0.7347145	2.5362236	3.1484626	0.0657901
QST(1)-MAJ-059	13433.3	1.4831464	6.9453145	27.4365939	0.1474561	0.6166698	2.5113863	2.8712874	0.0281260
QST(1)-MAJ-060	13434.4	1.4916850	7.7803696	27.5504924	0.1505278	0.5633316	2.7436124	2.4751764	0.0451787
QST(1)-MAJ-061	13435.5	1.2920130	7.0426815	27.6383003	0.1427836	0.6101791	2.4502090	2.4588208	0.0390432
QST(1)-MAJ-062	13436.3	1.4741438	7.0091603	27.1995076	0.1455201	0.6164864	2.4446572	2.9470580	0.0237448
QST(1)-MAJ-063	13437.4	1.6068344	6.2718220	28.3480701	0.1446022	0.5692757	2.2508715	3.2146768	0.0610281

Sample ID	Depth (ft.)	TiKa1	V Ka1	CrKa1
QST(1)-MAJ-032	13406.4	0.3400167	0.0207782	0.0085497
QST(1)-MAJ-033	13407.2	0.3619266	0.0213673	0.0088273
QST(1)-MAJ-034	13408.3	0.3469368	0.0254425	0.0076370
QST(1)-MAJ-035	13409.4	0.3036100	0.0146665	0.0087830
QST(1)-MAJ-036	13410.9	0.2957123	0.0192887	0.0078492
QST(1)-MAJ-037	13411.6	0.2794605	0.0162397	0.0075019
QST(1)-MAJ-038	13412.2	0.3033042	0.0195016	0.0088632
QST(1)-MAJ-039	13413.3	0.3494598	0.0269053	0.0075346
QST(1)-MAJ-040	13414.5	0.3242862	0.0228206	0.0083336
QST(1)-MAJ-041	13415.2	0.3425595	0.0230808	0.0085463
QST(1)-MAJ-042	13416.7	0.3390616	0.0188631	0.0101172
QST(1)-MAJ-043	13417.5	0.3482893	0.0227799	0.0075676
QST(1)-MAJ-044	13418.8	0.3546547	0.0188278	0.0109940
QST(1)-MAJ-045	13419.7	0.3317754	0.0176536	0.0073384
QST(1)-MAJ-046	13420.9	0.3651609	0.0220745	0.0082009
QST(1)-MAJ-047	13421.6	0.3110738	0.0147708	0.0062892
QST(1)-MAJ-048	13422.9	0.3323366	0.0196726	0.0102125
QST(1)-MAJ-049	13423.2	0.3365333	0.0211348	0.0071657
QST(1)-MAJ-050	13424.6	0.3297063	0.0198750	0.0082734
QST(1)-MAJ-051	13425.2	0.3251061	0.0137819	0.0075856
QST(1)-MAJ-052	13426.5	0.3298903	0.0177894	0.0072366
QST(1)-MAJ-053	13427.2	0.3691462	0.0257963	0.0086397
QST(1)-MAJ-054	13428.6	0.3886906	0.0258216	0.0088710
QST(1)-MAJ-055	13429.5	0.4056499	0.0300509	0.0075957
QST(1)-MAJ-056	13430.9	0.3522850	0.0219177	0.0093316
QST(1)-MAJ-057	13431.4	0.3805084	0.0258527	0.0080042
QST(1)-MAJ-058	13432.9	0.3895251	0.0243941	0.0086766
QST(1)-MAJ-059	13433.3	0.3604479	0.0278677	0.0077880
QST(1)-MAJ-060	13434.4	0.3738206	0.0239415	0.0081632
QST(1)-MAJ-061	13435.5	0.3664444	0.0296794	0.0064469
QST(1)-MAJ-062	13436.3	0.3906527	0.0314797	0.0080963
QST(1)-MAJ-063	13437.4	0.3469011	0.0226682	0.0085165

- major elements

MnKa1	FeKa1	ZrKa1	Ca/Al	Si/Al	Zr/Al
0.0303160	2.7050743	0.0156370	0.6541823	4.3663418	0.0025394
0.0260606	2.6569082	0.0174419	0.5454450	4.1826551	0.0026632
0.0297348	2.7230695	0.0151827	0.6364015	4.1105961	0.0023776
0.0320219	2.6080572	0.0159906	0.7056683	4.3315842	0.0026089
0.0296269	2.8978189	0.0138045	0.9010067	4.4863450	0.0023784
0.0331307	2.4881943	0.0141723	0.9361058	4.7920019	0.0025065
0.0260560	2.5874677	0.0147216	0.8058338	4.7348397	0.0026211
0.0286038	2.8091732	0.0150327	0.5869794	3.8991524	0.0022022
0.0286411	2.7193970	0.0140445	0.6778818	4.3816974	0.0022920
0.0313148	2.8842408	0.0147972	0.6774340	4.1490441	0.0023035
0.0280293	2.5706454	0.0173100	0.7169201	4.6715941	0.0030141
0.0289951	2.4621326	0.0160751	0.7109008	4.5244326	0.0026897
0.0268004	2.6599056	0.0165103	0.4898049	4.0751041	0.0024339
0.0269145	2.3103883	0.0150454	0.6077666	4.7320241	0.0025991
0.0276642	2.5598342	0.0167131	0.4794493	4.1322311	0.0024849
0.0231164	2.5116356	0.0159984	0.5262390	4.4624191	0.0025880
0.0300129	2.7256244	0.0158866	0.5822687	4.6617707	0.0026605
0.0242576	2.6064106	0.0166570	0.5097504	4.1734274	0.0025859
0.0282819	2.7332881	0.0180658	0.6206392	4.6268048	0.0030219
0.0273235	2.4644673	0.0172277	0.6401013	4.9421184	0.0030078
0.0271625	2.5904141	0.0174935	0.6045195	4.2299634	0.0027367
0.0245299	2.7714868	0.0162926	0.4751731	3.9542010	0.0024133
0.0265466	3.1471383	0.0141584	0.4606466	3.7132792	0.0019726
0.0269787	3.0974946	0.0138621	0.4354343	3.6458713	0.0018637
0.0227304	3.4069851	0.0143494	0.5305292	3.6118684	0.0019723
0.0228598	3.3232420	0.0138568	0.4203006	3.4181351	0.0017900
0.0276069	2.9410862	0.0147779	0.4290647	3.7304994	0.0020139
0.0268586	2.8115918	0.0149483	0.4134136	3.9503746	0.0021523
0.0259861	2.7425761	0.0142807	0.3181309	3.5410262	0.0018355
0.0248743	2.4977291	0.0147440	0.3491313	3.9244001	0.0020935
0.0256071	2.6534331	0.0150903	0.4204581	3.8805658	0.0021529
0.0273623	2.5679692	0.0151587	0.5125587	4.5199099	0.0024169

Questar 1 XRF – major elements

Sample ID	Depth (ft.)	MgKa1	AlKa1	SiKa1	P Ka1
QST(1)-MAJ-064	13438.5	1.3556914	6.8089443	27.1086898	0.1167269
QST(1)-MAJ-065	13439.4	1.5631773	5.9739725	27.8420095	0.0986985
QST(1)-MAJ-066	13440.3	1.5923343	6.2287575	27.3259000	0.1534426
QST(1)-MAJ-067	13441.5	1.4196238	6.1382473	27.0722045	0.1200393
QST(1)-MAJ-068	13442.6	1.6015976	6.8993217	26.7117374	0.1335838
QST(1)-MAJ-069	13443.3	1.5077382	7.1985477	26.3052032	0.1277158
QST(1)-MAJ-070	13444.6	1.5572393	6.5841751	26.6920173	0.1469071
QST(1)-MAJ-071	13445.3	1.6444163	6.9717527	27.1673266	0.1498371
QST(1)-MAJ-072	13446.2	1.6293823	7.0472386	26.4826872	0.1024733
QST(1)-MAJ-073	13447.6	1.5310424	6.4151996	26.6015608	0.1502987
QST(1)-MAJ-074	13448.5	1.7309174	6.5456241	27.0125051	0.1333606
QST(1)-MAJ-075	13449.6	1.5791635	6.5849369	26.6237813	0.1350957
QST(1)-MAJ-076	13450.5	1.5280581	7.4931272	27.0202801	0.1594815
QST(1)-MAJ-077	13451.2	1.6580104	6.0604519	27.4587687	0.0977706
QST(1)-MAJ-078	13452.9	1.5483182	6.0716081	27.7615949	0.1400009
QST(1)-MAJ-079	13453.5	1.5183295	7.0012030	27.3182540	0.1144697
QST(1)-MAJ-080	13454.7	1.4188162	6.4234418	26.8114569	0.1488632
QST(1)-MAJ-081	13455.4	1.3442508	6.4612628	26.6801302	0.0899616
QST(1)-MAJ-082	13456.7	1.4351297	6.7193076	27.0657497	0.1025701
QST(1)-MAJ-083	13457.3	1.8065496	6.0876316	27.5763990	0.1596003
QST(1)-MAJ-084	13458.5	1.7693008	5.9587937	26.8480816	0.0804204
QST(1)-MAJ-085	13459.4	1.6284239	5.3747829	27.9984183	0.1188475
QST(1)-MAJ-086	13460.9	1.6006346	6.2000440	27.2831123	0.1104627
QST(1)-MAJ-087	13461.5	1.4703487	7.1469103	27.1604855	0.0989136
QST(1)-MAJ-088	13462.2	1.5235372	6.9255532	26.8381840	0.1236031
QST(1)-MAJ-089	13463.6	1.7400640	5.8174233	27.3422485	0.1486637
QST(1)-MAJ-090	13464.5	1.3021367	6.1564867	27.8381383	0.0822047
QST(1)-MAJ-091	13465.7	1.4374334	4.6080529	28.5355035	0.1257499
QST(1)-MAJ-092	13466.6	1.8199502	4.8037415	27.9417904	0.1178896
QST(1)-MAJ-093	13467.7	1.8372052	5.4045169	27.2709933	0.1547203
QST(1)-MAJ-094	13468.3	1.5823247	5.6631359	27.4507397	0.0953322
QST(1)-MAJ-095	13469.3	1.5374309	6.2384947	27.5698118	0.1268151

S Ka1	K Ka1	CaKa1	BaLa1
0.5149117	2.2407304	3.3779382	0.0415298
0.6257490	1.8807892	4.0579635	0.0210941
0.6934627	2.0875538	3.7855214	0.0490148
0.7255339	2.0824582	3.6995103	0.0426854
0.8621966	2.4137599	3.7498058	0.0419577
1.0563126	2.3406503	3.4054302	0.0389230
0.6583566	2.3168176	4.4815570	0.0214976
0.7507825	2.3790731	3.3922115	0.0731075
0.7379800	2.3946331	3.6381578	0.0057231
0.6821956	2.2127837	4.2447004	0.0070840
0.6385420	2.3001629	4.1403815	-0.0076012
0.6776395	2.2326078	4.1763998	0.0542051
0.7923234	2.6250029	3.3736195	0.0400263
0.7652633	2.0273970	4.0680404	0.0221391
0.6593602	2.0265118	3.6235730	0.0280886
0.7850031	2.2829135	3.2570030	0.0483448
1.2487535	2.0866823	3.7963906	0.0859779
0.8260861	2.0919217	4.0219952	0.0106355
0.8284473	2.2896017	3.7429221	0.0284670
0.6036196	2.0786622	4.3481776	0.0174205
0.5818133	2.0031886	4.2544464	0.0557253
0.6421727	1.6759472	4.9950844	0.0346396
0.9039404	2.1059874	3.9773081	0.0890475
1.0780621	2.4035291	3.3788113	0.0562448
1.0287802	2.3029665	3.6926137	0.0670630
0.7649964	2.0326392	4.4912876	0.0627051
0.7140104	1.9326289	3.2690058	0.0369296
0.8450765	1.3706434	4.8003516	0.0051655
0.5799739	1.5281910	5.1215995	0.0106120
0.8164516	1.8720268	4.9946028	0.0621229
0.6044675	1.8888801	4.4558406	0.0279862
0.6429731	2.0642075	3.5621052	0.0214135

Questar 1 XRF – major elements

Sample ID	Depth (ft.)	TiKa1	V Ka1	CrKa1	MnKa1	FeKa1	ZrKa1	Ca/Al	Si/Al	Zr/Al
QST(1)-MAJ-064	13438.5	0.3525084	0.0265318	0.0079445	0.0267485	2.5409781	0.0154424	0.4961031	3.9813352	0.0022680
QST(1)-MAJ-065	13439.4	0.2977302	0.0189839	0.0098334	0.0263292	2.4821064	0.0140107	0.6792739	4.6605520	0.0023453
QST(1)-MAJ-066	13440.3	0.3335960	0.0198594	0.0089235	0.0267502	2.6208519	0.0146432	0.6077490	4.3870547	0.0023509
QST(1)-MAJ-067	13441.5	0.3542753	0.0194999	0.0085291	0.0255241	2.7179619	0.0170583	0.6026982	4.4104128	0.0027790
QST(1)-MAJ-068	13442.6	0.3774894	0.0290031	0.0086396	0.0265268	3.0871991	0.0134125	0.5435035	3.8716469	0.0019440
QST(1)-MAJ-069	13443.3	0.3799842	0.0285828	0.0085245	0.0200370	3.1999536	0.0155103	0.4730718	3.6542375	0.0021546
QST(1)-MAJ-070	13444.6	0.3507682	0.0286426	0.0096669	0.0274234	3.1136587	0.0131184	0.6806558	4.0539653	0.0019924
QST(1)-MAJ-071	13445.3	0.3675904	0.0229889	0.0074237	0.0249826	2.9721482	0.0151977	0.4865651	3.8967714	0.0021799
QST(1)-MAJ-072	13446.2	0.3862354	0.0314652	0.0087029	0.0276784	2.9319484	0.0140230	0.5162530	3.7578815	0.0019899
QST(1)-MAJ-073	13447.6	0.3498703	0.0269309	0.0079728	0.0268530	2.7568705	0.0134053	0.6616630	4.1466459	0.0020896
QST(1)-MAJ-074	13448.5	0.3588839	0.0245197	0.0104934	0.0262409	2.7530406	0.0137952	0.6325419	4.1268036	0.0021075
QST(1)-MAJ-075	13449.6	0.3449616	0.0198867	0.0095236	0.0275777	2.7481001	0.0143916	0.6342354	4.0431338	0.0021855
QST(1)-MAJ-076	13450.5	0.4151122	0.0287938	0.0072884	0.0260784	2.9449074	0.0145797	0.4502285	3.6060085	0.0019457
QST(1)-MAJ-077	13451.2	0.3471598	0.0173429	0.0098643	0.0293553	2.7303325	0.0154478	0.6712437	4.5308121	0.0025490
QST(1)-MAJ-078	13452.9	0.3512662	0.0248728	0.0076206	0.0247841	2.7087523	0.0154100	0.5968061	4.5723628	0.0025381
QST(1)-MAJ-079	13453.5	0.3676016	0.0229692	0.0089909	0.0268190	2.6777326	0.0167611	0.4652062	3.9019371	0.0023940
QST(1)-MAJ-080	13454.7	0.3324085	0.0153652	0.0081453	0.0232710	3.1895177	0.0158499	0.5910213	4.1740017	0.0024675
QST(1)-MAJ-081	13455.4	0.3556065	0.0214618	0.0087776	0.0257353	2.6919724	0.0164702	0.6224782	4.1292439	0.0025491
QST(1)-MAJ-082	13456.7	0.3700075	0.0210316	0.0093108	0.0274054	2.8187224	0.0147128	0.5570398	4.0280563	0.0021896
QST(1)-MAJ-083	13457.3	0.3465759	0.0238797	0.0082890	0.0283304	2.6355048	0.0166596	0.7142642	4.5299060	0.0027366
QST(1)-MAJ-084	13458.5	0.3168826	0.0170581	0.0080292	0.0251909	2.7037908	0.0163317	0.7139778	4.5056236	0.0027408
QST(1)-MAJ-085	13459.4	0.2866691	0.0170731	0.0074954	0.0329062	2.5226430	0.0155297	0.9293556	5.2092185	0.0028894
QST(1)-MAJ-086	13460.9	0.3087272	0.0123268	0.0077368	0.0268725	2.7865257	0.0146202	0.6414968	4.4004708	0.0023581
QST(1)-MAJ-087	13461.5	0.3686159	0.0236026	0.0079816	0.0242292	3.0915571	0.0151421	0.4727653	3.8003115	0.0021187
QST(1)-MAJ-088	13462.2	0.3581627	0.0216825	0.0085259	0.0232573	2.8944507	0.0169229	0.5331868	3.8752404	0.0024435
QST(1)-MAJ-089	13463.6	0.3359022	0.0213169	0.0065440	0.0278976	2.6841178	0.0163877	0.7720407	4.7000617	0.0028170
QST(1)-MAJ-090	13464.5	0.3250503	0.0201711	0.0073145	0.0256934	2.6558447	0.0153686	0.5309856	4.5217572	0.0024963
QST(1)-MAJ-091	13465.7	0.2752574	0.0130435	0.0085345	0.0284610	2.5222451	0.0136914	1.0417310	6.1925295	0.0029712
QST(1)-MAJ-092	13466.6	0.2802716	0.0191362	0.0087889	0.0292043	2.4106135	0.0155547	1.0661688	5.8166724	0.0032380
QST(1)-MAJ-093	13467.7	0.3206115	0.0154514	0.0086916	0.0273934	2.7284029	0.0134082	0.9241534	5.0459632	0.0024809
QST(1)-MAJ-094	13468.3	0.3019376	0.0199922	0.0079617	0.0287415	2.4151462	0.0164768	0.7868150	4.8472684	0.0029095
QST(1)-MAJ-095	13469.3	0.3458725	0.0237086	0.0089873	0.0258954	2.5010546	0.0203628	0.5709879	4.4193052	0.0032641

Questar 1 XRF – major elements

Sample ID	Depth (ft.)	MgKa1	AlKa1	SiKa1	P Ka1
QST(1)-MAJ-096	13470.9	1.6586200	4.7068437	28.3176826	0.0896145
QST(1)-MAJ-097	13471.5	1.6055234	6.5865885	26.8452129	0.1133775
QST(1)-MAJ-098	13472.2	1.5714041	4.5017201	28.1987622	0.0979185
QST(1)-MAJ-099	13473.6	1.9322120	5.4699872	27.2384919	0.1295264
QST(1)-MAJ-100	13474.3	1.6062017	6.8487394	27.4766070	0.1515747
QST(1)-MAJ-101	13475.3	1.7471986	4.8810584	28.3305752	0.1314967
QST(1)-MAJ-102	13476.7	1.3118548	6.0436118	27.3014257	0.1289468
QST(1)-MAJ-103	13477.4	1.8240179	5.6522935	27.6626428	0.1501282
QST(1)-MAJ-104	13478.5	1.4350083	5.7966242	28.2589556	0.1118874
QST(1)-MAJ-105	13479.5	1.5151031	4.5440381	29.7753338	0.0948929
QST(1)-MAJ-106	13480.7	1.3718945	5.9270569	27.2601930	0.1166613
QST(1)-MAJ-107	13481.5	1.4431248	5.6928777	28.2392513	0.1334152
QST(1)-MAJ-108	13482.6	1.4207933	4.9026251	30.2411988	0.1309163
QST(1)-MAJ-109	13483.2	1.4596043	5.1800399	27.8560722	0.1102711
QST(1)-MAJ-110	13484.7	1.5477301	5.5894082	27.8177426	0.1086233
QST(1)-MAJ-111	13485.5	1.6578528	6.1047007	27.6929934	0.1187221
QST(1)-MAJ-112	13486.6	1.7300472	5.4501523	28.0913052	0.1372604
QST(1)-MAJ-113	13487.6	1.3465951	4.8805131	28.6639739	0.1218043
QST(1)-MAJ-114	13488.5	1.5499033	5.9177471	27.9134506	0.1176069
QST(1)-MAJ-115	13489.7	1.5675906	5.7120637	27.0318742	0.1030206
QST(1)-MAJ-116	13490.9	1.5544493	5.7703315	27.9759686	0.1322537
QST(1)-MAJ-117	13491.5	1.8049971	5.9670947	26.9247166	0.1138544
QST(1)-MAJ-118	13492.6	1.5839369	4.6247877	29.8539349	0.0736137
QST(1)-MAJ-119	13493.4	1.4943625	5.6410954	28.7857605	0.1698867
QST(1)-MAJ-120	13494.9	1.3416414	6.1809214	28.0810837	0.1122264
Max Values		1.9364896	7.7803696	30.2411988	0.1849410
Stdev		0.1582886	0.3913590	0.9695528	0.0704240
(dx/x)^2		0.0066814	0.0025302	0.0010279	0.1450022
d(Ca/Al)/(Ca/Al)		0.0652314			
d(Si/Al)/(Si/Al)		0.0596495			
d(Zr/Al)/(Zr/Al)		0.0523580			
Max Ca/Al		1.2780316			
Max Si/Al		7.0771667			
MaxZr/Al		0.0050638			
d(Ca/Al)		0.0833678			
d(Si/Al)		0.4221492			
d(Zr/Al)		0.0002651			

S Ka1	K Ka1	CaKa1	BaLa1
0.6089516	1.5628614	4.7143111	0.0033099
0.8011510	2.3275237	4.1969206	0.0369981
0.5631439	1.4491204	5.7533405	0.0131502
0.6036963	1.8313037	4.9298724	-0.0003647
1.0910268	2.2768471	3.7412041	0.0524755
0.5771422	1.6627973	4.4042199	0.0485965
0.7984488	1.9955382	3.7973785	0.0660402
1.0325031	1.8419959	4.1312813	0.0325977
0.8676350	1.9093644	3.2593653	0.0459773
0.4839453	1.3787738	3.8164591	0.0108164
0.6756923	1.9625890	3.2615070	0.0297623
0.6966769	1.8551422	3.6800160	0.0181399
0.6509188	1.5058983	3.3623838	0.0368047
0.6534612	1.7485157	3.8450922	0.0509810
0.5079873	1.8074551	3.8801038	-0.0146798
0.8142420	1.9179317	3.6884481	-0.0320255
0.6156489	1.8036116	3.5399134	0.0180132
0.5660464	1.5272560	4.1290274	0.0121017
0.5575788	1.9825211	3.1555580	0.0556490
0.7188437	1.7608293	3.8081883	0.0387037
0.5756009	1.8642771	3.4986471	0.0547709
0.4957377	1.9299974	4.0323269	0.0250377
0.3765015	1.4757185	3.3736766	0.0587911
0.5689354	1.8479066	3.1144615	0.0734245
0.6188571	2.0068174	2.4407970	0.0480602
1.2487535	2.7436124	5.7533405	0.0890475
0.1470273	0.1495092	0.2389519	
0.0138625	0.0029695	0.0017250	

Questar 1 XRF – major elements

Sample ID	Depth (ft.)	TiKa1	V Ka1	CrKa1	MnKa1	FeKa1	ZrKa1	Ca/Al	Si/Al	Zr/Al
QST(1)-MAJ-096	13470.9	0.3010256	0.0152372	0.0098873	0.0292884	2.4256269	0.0171337	1.0015865	6.0162785	0.0036402
QST(1)-MAJ-097	13471.5	0.3628170	0.0223516	0.0096050	0.0272858	2.8493423	0.0147162	0.6371919	4.0757386	0.0022343
QST(1)-MAJ-098	13472.2	0.2849253	0.0140435	0.0086649	0.0331731	2.2840591	0.0152539	1.2780316	6.2639972	0.0033885
QST(1)-MAJ-099	13473.6	0.3451161	0.0193471	0.0092063	0.0295263	2.4904664	0.0167631	0.9012585	4.9796263	0.0030646
QST(1)-MAJ-100	13474.3	0.3732114	0.0271795	0.0077369	0.0274005	2.8964049	0.0175637	0.5462617	4.0119218	0.0025645
QST(1)-MAJ-101	13475.3	0.2715466	0.0147271	0.0082028	0.0296185	2.3173197	0.0161914	0.9023084	5.8041869	0.0033172
QST(1)-MAJ-102	13476.7	0.3254205	0.0132973	0.0079331	0.0245100	2.5194587	0.0168409	0.6283293	4.5174023	0.0027866
QST(1)-MAJ-103	13477.4	0.3542966	0.0239092	0.0066567	0.0267907	2.6807923	0.0167315	0.7309035	4.8940564	0.0029601
QST(1)-MAJ-104	13478.5	0.3086949	0.0171075	0.0067372	0.0256975	2.5440637	0.0168851	0.5622868	4.8750712	0.0029129
QST(1)-MAJ-105	13479.5	0.2694977	0.0158136	0.0086545	0.0261117	2.1502272	0.0193809	0.8398827	6.5526153	0.0042651
QST(1)-MAJ-106	13480.7	0.3508618	0.0268712	0.0072807	0.0221933	2.4681148	0.0175477	0.5502743	4.5992798	0.0029606
QST(1)-MAJ-107	13481.5	0.3215190	0.0170504	0.0078566	0.0266304	2.4547110	0.0187648	0.6464246	4.9604528	0.0032962
QST(1)-MAJ-108	13482.6	0.2840831	0.0145916	0.0092210	0.0263510	2.3828184	0.0181990	0.6858334	6.1683686	0.0037121
QST(1)-MAJ-109	13483.2	0.3059769	0.0165237	0.0093521	0.0293516	2.5958357	0.0179809	0.7422901	5.3775787	0.0034712
QST(1)-MAJ-110	13484.7	0.3596474	0.0231420	0.0077606	0.0220831	2.4094127	0.0158088	0.6941887	4.9768672	0.0028283
QST(1)-MAJ-111	13485.5	0.3717483	0.0234732	0.0093854	0.0253267	2.6669694	0.0193352	0.6041980	4.5363393	0.0031673
QST(1)-MAJ-112	13486.6	0.3677653	0.0175706	0.0085934	0.0257957	2.4922053	0.0196221	0.6495073	5.1542239	0.0036003
QST(1)-MAJ-113	13487.6	0.2967551	0.0160845	0.0080130	0.0301964	2.3273226	0.0167845	0.8460232	5.8731476	0.0034391
QST(1)-MAJ-114	13488.5	0.3253874	0.0184547	0.0080784	0.0254855	2.5197556	0.0180584	0.5332364	4.7169050	0.0030516
QST(1)-MAJ-115	13489.7	0.3519812	0.0143931	0.0094675	0.0253823	2.6433166	0.0289250	0.6666922	4.7324182	0.0050638
QST(1)-MAJ-116	13490.9	0.3486821	0.0204789	0.0070883	0.0244920	2.3093740	0.0190589	0.6063165	4.8482429	0.0033029
QST(1)-MAJ-117	13491.5	0.3500144	0.0189404	0.0086836	0.0266898	2.3121822	0.0180593	0.6757605	4.5121986	0.0030265
QST(1)-MAJ-118	13492.6	0.2587124	0.0107468	0.0060694	0.0248687	1.8822525	0.0225682	0.7294771	6.4552011	0.0048798
QST(1)-MAJ-119	13493.4	0.3097171	0.0174164	0.0062771	0.0257421	2.1596393	0.0277574	0.5521023	5.1028672	0.0049206
QST(1)-MAJ-120	13494.9	0.3517781	0.0197371	0.0082693	0.0201066	2.3091769	0.0247467	0.3948921	4.5431873	0.0040037
Max Values		0.4151122	0.0314797	0.0109940	0.0334257	3.4069851	0.0289250			
Stdev		0.0154875	0.0041700	0.0029422	0.0041256	0.0176753	0.0004203			
(dx/x)^2		0.0013920	0.0175474	0.0716193	0.0152337	0.0000269	0.0002112			

Sample ID	Depth (ft.)	NiKa1	CuKa1	ZnKa1	ThLa1
QST(1)-TRC-001	13375.1	0.0021251	0.0048941	0.0082436	0.0006364
QST(1)-TRC-002	13376.7	0.0057028	0.0017054	0.0099447	0.0008602
QST(1)-TRC-003	13377.8	0.0039565	0.0002468	0.0099031	0.0009610
QST(1)-TRC-004	13378.6	0.0087449	0.0018985	0.0105375	0.0008317
QST(1)-TRC-005	13379.9	0.0057806	0.0013329	0.0093315	0.0007463
QST(1)-TRC-006	13380.5	0.0049562	-0.0009686	0.0117614	0.0011564
QST(1)-TRC-007	13381.5	0.0032194	0.0024820	0.0135841	0.0008490
QST(1)-TRC-008	13382.3	0.0033539	0.0031966	0.0097377	0.0010943
QST(1)-TRC-009	13383.4	0.0081796	0.0048184	0.0119338	0.0013085
QST(1)-TRC-010	13384.3	0.0052258	0.0058656	0.0132094	0.0008153
QST(1)-TRC-011	13385.9	0.0089724	0.0079696	0.0128804	0.0010511
QST(1)-TRC-012	13386.9	0.0051791	-0.0023294	0.0116436	0.0007127
QST(1)-TRC-013	13387.6	0.0058159	0.0028933	0.0102836	0.0009715
QST(1)-TRC-014	13388.8	0.0039149	0.0055864	0.0104721	0.0011760
QST(1)-TRC-015	13389.7	0.0087905	0.0035350	0.0114411	0.0011124
QST(1)-TRC-016	13390.7	0.0059474	0.0024547	0.0114325	0.0009650
QST(1)-TRC-017	13391.3	0.0032939	0.0033367	0.0140869	0.0009152
QST(1)-TRC-018	13392.1	0.0087793	0.0033844	0.0130777	0.0008419
QST(1)-TRC-019	13393.5	0.0040577	0.0032298	0.0099983	0.0008003
QST(1)-TRC-020	13394.7	0.0025523	0.0041930	0.0136805	0.0011808
QST(1)-TRC-021	13395.4	0.0038820	0.0057274	0.0105117	0.0011863
QST(1)-TRC-022	13396.5	0.0052789	-0.0002046	0.0116287	0.0007818
QST(1)-TRC-023	13397.7	0.0032087	0.0019723	0.0116295	0.0012310
QST(1)-TRC-024	13398.7	0.0057619	0.0021069	0.0124504	0.0010577
QST(1)-TRC-025	13399.7	0.0064851	0.0050925	0.0090207	0.0008540
QST(1)-TRC-026	13400.7	0.0060761	0.0032457	0.0089283	0.0009381
QST(1)-TRC-027	13401.3	0.0061809	0.0006086	0.0123688	0.0010319
QST(1)-TRC-028	13402.5	0.0053920	0.0043676	0.0110643	0.0010845
QST(1)-TRC-029	13403.6	-0.0000846	-0.0004445	0.0103209	0.0009544
QST(1)-TRC-030	13404.4	0.0054651	0.0010372	0.0129033	0.0005125
QST(1)-TRC-031	13405.5	0.0114635	0.0041694	0.0122624	0.0011392

– trace elements

RbKa1	U La1	SrKa1	Y Ka1	ZrKa1	NbKa1	MoKa1
0.0081592	0.0001412	0.0140554	0.0020624	0.0159326	0.0011343	0.0007940
0.0066729	0.0003667	0.0135293	0.0026885	0.0168692	0.0011712	0.0007931
0.0095691	0.0002702	0.0151403	0.0024961	0.0159831	0.0011676	0.0005211
0.0050519	0.0007353	0.0136193	0.0028982	0.0198233	0.0010588	0.0009348
0.0062390	0.0008750	0.0132955	0.0021041	0.0149741	0.0011315	0.0004494
0.0091810	0.0010421	0.0154772	0.0019550	0.0165194	0.0014379	0.0004463
0.0121062	0.0002721	0.0166589	0.0026438	0.0147332	0.0011919	0.0004974
0.0123261	-0.0000955	0.0166548	0.0022586	0.0161840	0.0015585	0.0002558
0.0129491	0.0007251	0.0201233	0.0031716	0.0164580	0.0014458	0.0005049
0.0082580	-0.0001102	0.0148665	0.0021534	0.0144669	0.0009940	0.0005960
0.0125648	0.0003980	0.0179044	0.0027950	0.0154107	0.0012815	0.0004760
0.0102860	0.0002554	0.0140205	0.0023787	0.0162723	0.0013267	0.0004172
0.0105465	0.0006954	0.0162025	0.0024145	0.0147717	0.0012140	0.0007012
0.0126009	0.0007155	0.0171604	0.0025964	0.0164889	0.0015176	0.0001524
0.0121465	0.0001501	0.0174674	0.0028630	0.0168661	0.0014049	0.0004469
0.0119267	0.0005566	0.0171891	0.0025490	0.0155149	0.0010934	0.0006065
0.0134312	0.0005078	0.0174062	0.0023038	0.0144669	0.0015007	-0.0000619
0.0122178	0.0003636	0.0162547	0.0024293	0.0161809	0.0014093	0.0007258
0.0108625	0.0011223	0.0152410	0.0027513	0.0158283	0.0011184	0.0008138
0.0098059	0.0007259	0.0147989	0.0022972	0.0164609	0.0013648	0.0003384
0.0118326	0.0007631	0.0144164	0.0023078	0.0158080	0.0015402	0.0005269
0.0103193	0.0010047	0.0127655	0.0029587	0.0156071	0.0011282	0.0005426
0.0104389	0.0003838	0.0153801	0.0022242	0.0152383	0.0013852	0.0005152
0.0110707	0.0007052	0.0160214	0.0028354	0.0149728	0.0011518	0.0003127
0.0133779	0.0013177	0.0153419	0.0025015	0.0156053	0.0016681	0.0004896
0.0109432	0.0006037	0.0143075	0.0023108	0.0165067	0.0013481	0.0004452
0.0117376	0.0007582	0.0147075	0.0025671	0.0173345	0.0011852	0.0006194
0.0100137	0.0007570	0.0144891	0.0025072	0.0161472	0.0012925	0.0005423
0.0102965	0.0003779	0.0149340	0.0027564	0.0162050	0.0014040	0.0003259
0.0077618	0.0006836	0.0152061	0.0022583	0.0150329	0.0010309	0.0008815
0.0112182	0.0013763	0.0156489	0.0029482	0.0170672	0.0013466	0.0004976

Sample ID	Depth (ft.)	NiKa1	CuKa1	ZnKa1	ThLa1
QST(1)-TRC-032	13406.4	0.0030137	0.0016482	0.0113955	0.0009551
QST(1)-TRC-033	13407.2	0.0036123	-0.0006011	0.0122925	0.0010972
QST(1)-TRC-034	13408.3	0.0044197	0.0065543	0.0137109	0.0010614
QST(1)-TRC-035	13409.4	0.0048256	0.0045275	0.0135056	0.0011420
QST(1)-TRC-036	13410.9	0.0053924	0.0023351	0.0112348	0.0008817
QST(1)-TRC-037	13411.6	0.0082420	-0.0000397	0.0153867	0.0008122
QST(1)-TRC-038	13412.2	0.0091168	0.0049617	0.0151323	0.0010187
QST(1)-TRC-039	13413.3	0.0046365	0.0028895	0.0126856	0.0009341
QST(1)-TRC-040	13414.5	0.0058290	0.0021710	0.0123380	0.0009413
QST(1)-TRC-041	13415.2	0.0070578	0.0059192	0.0112317	0.0011993
QST(1)-TRC-042	13416.7	0.0063650	0.0035888	0.0112858	0.0009073
QST(1)-TRC-043	13417.5	0.0076008	0.0055957	0.0126638	0.0010082
QST(1)-TRC-044	13418.8	0.0058588	0.0056025	0.0152055	0.0011301
QST(1)-TRC-045	13419.7	0.0035323	0.0015261	0.0105667	0.0008414
QST(1)-TRC-046	13420.9	0.0084006	0.0012398	0.0106258	0.0011074
QST(1)-TRC-047	13421.6	0.0020534	0.0041049	0.0114835	0.0009878
QST(1)-TRC-048	13422.9	0.0061185	0.0045868	0.0127281	0.0011584
QST(1)-TRC-049	13423.2	0.0045412	0.0041675	0.0117303	0.0012241
QST(1)-TRC-050	13424.6	0.0038376	0.0003849	0.0099151	0.0009710
QST(1)-TRC-051	13425.2	0.0055439	0.0043501	0.0151115	0.0008323
QST(1)-TRC-052	13426.5	0.0083301	0.0036823	0.0135321	0.0009495
QST(1)-TRC-053	13427.2	0.0048120	-0.0008883	0.0156930	0.0009691
QST(1)-TRC-054	13428.6	0.0036791	0.0042989	0.0106462	0.0012685
QST(1)-TRC-055	13429.5	0.0038814	0.0013727	0.0159811	0.0008042
QST(1)-TRC-056	13430.9	0.0045660	0.0031934	0.0180787	0.0010897
QST(1)-TRC-057	13431.4	0.0053111	0.0029165	0.0157885	0.0013271
QST(1)-TRC-058	13432.9	0.0065371	0.0021412	0.0120145	0.0011048
QST(1)-TRC-059	13433.3	0.0093710	0.0040627	0.0156272	0.0010849
QST(1)-TRC-060	13434.4	0.0060257	0.0036534	0.0118286	0.0011039
QST(1)-TRC-061	13435.5	0.0059455	0.0025686	0.0155815	0.0011008
QST(1)-TRC-062	13436.3	0.0055012	0.0032953	0.0138222	0.0009675
QST(1)-TRC-063	13437.4	0.0042708	0.0011095	0.0110366	0.0009429

– trace elements

RbKa1	U La1	SrKa1	Y Ka1	ZrKa1	NbKa1	MoKa1
0.0114524	0.0004303	0.0148403	0.0024651	0.0156370	0.0012494	0.0004909
0.0125214	0.0011552	0.0169380	0.0022246	0.0174419	0.0014048	0.0002843
0.0108730	0.0003662	0.0152863	0.0027222	0.0151827	0.0012898	0.0003131
0.0124185	0.0004407	0.0157461	0.0023577	0.0159906	0.0012780	0.0004235
0.0113719	-0.0001565	0.0166451	0.0021259	0.0138045	0.0013000	0.0003199
0.0109121	0.0003533	0.0157821	0.0023357	0.0141723	0.0010888	0.0006272
0.0131388	0.0008553	0.0164993	0.0031204	0.0147216	0.0013440	0.0003346
0.0129472	0.0005956	0.0170782	0.0027849	0.0150327	0.0013409	0.0004851
0.0120707	0.0002567	0.0207082	0.0029884	0.0140445	0.0012592	0.0002988
0.0130955	0.0006151	0.0205711	0.0028424	0.0147972	0.0013494	0.0004687
0.0107293	0.0000044	0.0140638	0.0029800	0.0173100	0.0014181	0.0001199
0.0123548	0.0007540	0.0157817	0.0028362	0.0160751	0.0013372	0.0006153
0.0132091	0.0003345	0.0161846	0.0032910	0.0165103	0.0012813	0.0003171
0.0119669	0.0004568	0.0129806	0.0025767	0.0150454	0.0010984	0.0005852
0.0135114	-0.0001826	0.0147666	0.0028534	0.0167131	0.0013667	0.0003828
0.0110023	0.0001348	0.0139045	0.0025053	0.0159984	0.0012616	0.0004002
0.0119434	0.0000394	0.0152805	0.0024431	0.0158866	0.0016305	0.0002986
0.0140847	0.0003175	0.0174763	0.0026955	0.0166570	0.0014258	0.0004754
0.0123066	-0.0006523	0.0154025	0.0027201	0.0180658	0.0017350	-0.0000190
0.0114117	0.0003912	0.0148940	0.0027673	0.0172277	0.0015277	0.0002009
0.0125435	0.0017121	0.0153427	0.0022754	0.0174935	0.0011362	0.0006383
0.0106400	0.0001518	0.0201906	0.0026647	0.0162926	0.0016390	-0.0001332
0.0133444	0.0001008	0.0150788	0.0024061	0.0141584	0.0013690	0.0002806
0.0101012	0.0006043	0.0145377	0.0025144	0.0138621	0.0013116	0.0007134
0.0131985	0.0002574	0.0169403	0.0024452	0.0143494	0.0014478	0.0004004
0.0114571	-0.0001551	0.0164156	0.0020325	0.0138568	0.0013212	0.0004635
0.0134607	0.0005247	0.0159279	0.0024855	0.0147779	0.0014618	0.0000454
0.0148591	0.0006429	0.0154281	0.0027741	0.0149483	0.0013728	0.0002166
0.0148218	0.0009851	0.0152671	0.0026636	0.0142807	0.0013727	0.0003562
0.0134642	0.0011391	0.0153318	0.0024889	0.0147440	0.0013276	0.0002610
0.0141972	0.0003826	0.0162757	0.0030626	0.0150903	0.0011818	0.0004553
0.0137909	-0.0000232	0.0176336	0.0026661	0.0151587	0.0014071	0.0002824

Sample ID	Depth (ft.)	NiKa1	CuKa1	ZnKa1	ThLa1
QST(1)-TRC-064	13438.5	0.0034605	0.0014313	0.0115843	0.0009186
QST(1)-TRC-065	13439.4	0.0054036	0.0043422	0.0153500	0.0011244
QST(1)-TRC-066	13440.3	0.0042119	0.0022555	0.0129143	0.0009011
QST(1)-TRC-067	13441.5	0.0052204	0.0024681	0.0142998	0.0009636
QST(1)-TRC-068	13442.6	0.0086502	0.0048564	0.0135009	0.0010384
QST(1)-TRC-069	13443.3	0.0043601	0.0039996	0.0137398	0.0011174
QST(1)-TRC-070	13444.6	0.0043649	0.0025805	0.0138476	0.0011071
QST(1)-TRC-071	13445.3	0.0062668	0.0051800	0.0133160	0.0010366
QST(1)-TRC-072	13446.2	0.0090535	0.0039277	0.0131796	0.0011502
QST(1)-TRC-073	13447.6	0.0047346	0.0027884	0.0116186	0.0010898
QST(1)-TRC-074	13448.5	0.0031255	0.0011947	0.0111188	0.0009979
QST(1)-TRC-075	13449.6	0.0062573	0.0018707	0.0147697	0.0010137
QST(1)-TRC-076	13450.5	0.0025353	0.0011397	0.0115878	0.0009689
QST(1)-TRC-077	13451.2	0.0024322	0.0029205	0.0119081	0.0009311
QST(1)-TRC-078	13452.9	0.0060529	0.0013330	0.0097041	0.0009724
QST(1)-TRC-079	13453.5	0.0045765	-0.0016034	0.0085541	0.0009113
QST(1)-TRC-080	13454.7	0.0042577	0.0025945	0.0094840	0.0012641
QST(1)-TRC-081	13455.4	0.0105664	0.0029659	0.0140208	0.0010310
QST(1)-TRC-082	13456.7	0.0046486	0.0030228	0.0118005	0.0009411
QST(1)-TRC-083	13457.3	0.0076457	0.0047132	0.0107987	0.0007731
QST(1)-TRC-084	13458.5	0.0076124	0.0010572	0.0119833	0.0011539
QST(1)-TRC-085	13459.4	0.0076644	0.0046672	0.0159782	0.0008868
QST(1)-TRC-086	13460.9	0.0050423	0.0009319	0.0131158	0.0009145
QST(1)-TRC-087	13461.5	0.0058210	0.0049819	0.0099517	0.0009853
QST(1)-TRC-088	13462.2	0.0039166	0.0041086	0.0102848	0.0010879
QST(1)-TRC-089	13463.6	0.0046273	-0.0005565	0.0097182	0.0011500
QST(1)-TRC-090	13464.5	0.0055538	0.0013074	0.0099272	0.0008934
QST(1)-TRC-091	13465.7	0.0048023	0.0040248	0.0099309	0.0007430
QST(1)-TRC-092	13466.6	0.0041947	0.0022749	0.0099423	0.0008887
QST(1)-TRC-093	13467.7	0.0074422	0.0027181	0.0128140	0.0007932
QST(1)-TRC-094	13468.3	0.0021473	0.0037115	0.0116005	0.0006364
QST(1)-TRC-095	13469.3	0.0062390	0.0042531	0.0123432	0.0010082

– trace elements

RbKa1	U La1	SrKa1	Y Ka1	ZrKa1	NbKa1	MoKa1
0.0125407	0.0011653	0.0162591	0.0026955	0.0154424	0.0014730	-0.0000308
0.0112388	0.0004328	0.0155917	0.0026584	0.0140107	0.0011970	0.0003845
0.0128738	0.0010923	0.0168899	0.0025026	0.0146432	0.0013544	0.0003215
0.0119793	0.0008805	0.0171712	0.0024377	0.0170583	0.0013396	0.0005556
0.0130609	0.0008040	0.0166703	0.0024876	0.0134125	0.0012886	0.0005416
0.0147145	0.0015536	0.0178141	0.0023722	0.0155103	0.0013680	0.0004898
0.0120979	0.0007666	0.0171092	0.0022179	0.0131184	0.0013237	0.0004285
0.0144056	0.0002772	0.0176674	0.0024670	0.0151977	0.0013891	0.0000895
0.0144096	0.0006272	0.0178937	0.0024240	0.0140230	0.0015372	0.0003033
0.0119013	0.0008897	0.0166605	0.0023523	0.0134053	0.0012308	0.0003737
0.0127891	-0.0004690	0.0170108	0.0026619	0.0137952	0.0014970	0.0001952
0.0113290	-0.0004585	0.0158437	0.0025924	0.0143916	0.0014427	0.0003245
0.0135411	-0.0003646	0.0165023	0.0027940	0.0145797	0.0012960	0.0004242
0.0109812	0.0002612	0.0157956	0.0023918	0.0154478	0.0015145	-0.0000136
0.0103629	0.0010404	0.0143591	0.0023269	0.0154100	0.0013392	0.0005129
0.0108012	0.0005053	0.0146322	0.0024884	0.0167611	0.0013864	0.0000990
0.0097394	0.0004513	0.0155682	0.0021753	0.0158499	0.0016036	0.0005408
0.0121917	0.0007507	0.0161814	0.0025635	0.0164702	0.0012975	0.0005738
0.0109747	-0.0001353	0.0160044	0.0025901	0.0147128	0.0013290	0.0004424
0.0134644	0.0009407	0.0161753	0.0030197	0.0166596	0.0014878	0.0004142
0.0114769	0.0011458	0.0160580	0.0024728	0.0163317	0.0014334	0.0003788
0.0108512	0.0002709	0.0180683	0.0031624	0.0155297	0.0012274	0.0005742
0.0111608	0.0004377	0.0164169	0.0022847	0.0146202	0.0014085	0.0005290
0.0116807	0.0000344	0.0166355	0.0025054	0.0151421	0.0011965	0.0008594
0.0090380	0.0007857	0.0147306	0.0021037	0.0169229	0.0011910	0.0011296
0.0128065	0.0005527	0.0168405	0.0026100	0.0163877	0.0014823	0.0002359
0.0117880	-0.0000208	0.0150266	0.0026073	0.0153686	0.0013607	0.0005272
0.0081814	0.0003638	0.0158829	0.0022937	0.0136914	0.0010510	0.0008865
0.0091265	0.0016650	0.0153347	0.0022148	0.0155547	0.0010990	0.0007381
0.0065829	0.0005539	0.0182865	0.0020279	0.0134082	0.0010289	0.0006043
0.0119588	0.0006114	0.0153422	0.0028814	0.0164768	0.0011856	0.0009166
0.0118406	0.0007249	0.0150108	0.0024789	0.0203628	0.0016016	0.0008411

Questar 1 XRF – trace elements

Sample ID	Depth (ft.)	NiKa1	CuKa1	ZnKa1	ThLa1	RbKa1	U La1	SrKa1	Y Ka1	ZrKa1	NbKa1	MoKa1
QST(1)-TRC-096	13470.9	0.0059149	0.0006188	0.0111757	0.0010535	0.0093199	-0.0001163	0.0154424	0.0023615	0.0171337	0.0012389	0.0005523
QST(1)-TRC-097	13471.5	0.0046106	0.0010965	0.0082367	0.0008147	0.0110355	0.0013953	0.0169430	0.0024383	0.0147162	0.0014295	0.0001815
QST(1)-TRC-098	13472.2	0.0090167	0.0025514	0.0102717	0.0010750	0.0105220	0.0011500	0.0177633	0.0026459	0.0152539	0.0012294	0.0004902
QST(1)-TRC-099	13473.6	0.0077512	0.0011479	0.0113396	0.0009498	0.0120568	0.0011069	0.0168736	0.0030395	0.0167631	0.0012224	0.0008933
QST(1)-TRC-100	13474.3	0.0035936	0.0018716	0.0114203	0.0010629	0.0124805	0.0004135	0.0158933	0.0025280	0.0175637	0.0013208	0.0004260
QST(1)-TRC-101	13475.3	0.0028742	0.0036448	0.0092710	0.0006843	0.0098100	0.0016028	0.0144798	0.0024883	0.0161914	0.0013419	0.0005530
QST(1)-TRC-102	13476.7	0.0027565	0.0035927	0.0094845	0.0011238	0.0110427	0.0015508	0.0163802	0.0024899	0.0168409	0.0013370	0.0003091
QST(1)-TRC-103	13477.4	0.0067374	0.0044960	0.0099442	0.0008864	0.0088435	0.0005152	0.0148148	0.0024898	0.0167315	0.0011623	0.0005447
QST(1)-TRC-104	13478.5	0.0090091	-0.0002782	0.0095736	0.0009932	0.0137750	0.0007257	0.0165401	0.0025092	0.0168851	0.0015872	0.0003288
QST(1)-TRC-105	13479.5	0.0082245	0.0021545	0.0106905	0.0008473	0.0111133	0.0004757	0.0169003	0.0025715	0.0193809	0.0013031	0.0009090
QST(1)-TRC-106	13480.7	0.0068226	0.0002584	0.0113060	0.0010603	0.0122188	0.0011867	0.0160956	0.0028696	0.0175477	0.0013758	0.0006996
QST(1)-TRC-107	13481.5	0.0044784	0.0058129	0.0132089	0.0008723	0.0105050	0.0017033	0.0147189	0.0025056	0.0187648	0.0013120	0.0006518
QST(1)-TRC-108	13482.6	0.0041148	0.0005129	0.0111818	0.0008530	0.0094085	-0.0003401	0.0141409	0.0024633	0.0181990	0.0010843	0.0009830
QST(1)-TRC-109	13483.2	0.0050050	0.0033295	0.0105659	0.0011200	0.0092130	0.0008944	0.0137431	0.0022024	0.0179809	0.0012097	0.0007807
QST(1)-TRC-110	13484.7	0.0016120	0.0005254	0.0087113	0.0009153	0.0096842	0.0000870	0.0149092	0.0024702	0.0158088	0.0011592	0.0004950
QST(1)-TRC-111	13485.5	0.0057633	0.0027425	0.0097020	0.0011650	0.0103552	0.0003826	0.0149826	0.0021132	0.0193352	0.0015362	0.0005310
QST(1)-TRC-112	13486.6	0.0022978	0.0002510	0.0089532	0.0008926	0.0105818	0.0009169	0.0137548	0.0029216	0.0196221	0.0013353	0.0005746
QST(1)-TRC-113	13487.6	0.0051512	0.0011130	0.0073752	0.0007113	0.0095839	0.0012393	0.0138520	0.0024493	0.0167845	0.0011480	0.0007079
QST(1)-TRC-114	13488.5	0.0078812	0.0028462	0.0104198	0.0009309	0.0120089	0.0001815	0.0156861	0.0024347	0.0180584	0.0014609	0.0004143
QST(1)-TRC-115	13489.7	0.0042036	-0.0002484	0.0120201	0.0006837	0.0073339	0.0003016	0.0165686	0.0031346	0.0289250	0.0012149	0.0014552
QST(1)-TRC-116	13490.9	0.0044673	0.0032511	0.0124177	0.0007796	0.0105624	0.0006951	0.0149747	0.0030167	0.0190589	0.0013099	0.0005269
QST(1)-TRC-117	13491.5	0.0026268	0.0021024	0.0092664	0.0009638	0.0111637	0.0002987	0.0145064	0.0021801	0.0180593	0.0014268	0.0003022
QST(1)-TRC-118	13492.6	0.0070337	-0.0002355	0.0069432	0.0009204	0.0090185	0.0008091	0.0131132	0.0023878	0.0225682	0.0012652	0.0011544
QST(1)-TRC-119	13493.4	0.0062726	0.0014659	0.0094002	0.0007599	0.0090286	-0.0001358	0.0127780	0.0024971	0.0277574	0.0012884	0.0010974
QST(1)-TRC-120	13494.9	0.0046378	0.0004214	0.0109354	0.0009947	0.0111666	0.0000362	0.0140905	0.0026687	0.0247467	0.0016667	0.0008003
Max Values		0.0114635	0.0079696	0.0180787	0.0013271	0.0148591	0.0017121	0.0207082	0.0032910	0.0289250	0.0017350	0.0014552
Std Dev		0.0019571	0.0028852	0.0021975	0.0001276	0.0005511	0.0003919	0.0011559	0.0001768	0.0004203	0.0001039	0.0001303
(dx/x)^2		0.0291452	0.1310619	0.0147754	0.0092459	0.0013757	0.0524012	0.0031158	0.0028849	0.0002112	0.0035841	0.0080189

Questar 8 XRF – major elements

Sample ID	Depth (ft.)	MgKa1	AlKa1	SiKa1	P Ka1	S Ka1	K Ka1	CaKa1
QST(8)-MA]-001	9631.3	1.6406419	4.3893060	26.9122042	0.1184051	1.5749676	1.1925674	6.2537120
QST(8)-MA]-002	9632.3	1.6455126	7.1267657	25.7068188	0.2056735	1.1276033	2.5626909	4.6491980
QST(8)-MA]-003	9632.9	1.6920106	5.9256714	24.0006469	0.1811488	1.2218485	2.1433141	5.4457943
QST(8)-MA]-004	9634.3	1.6850619	5.7174999	23.7202305	0.1300659	2.5928328	2.1539164	5.7833947
QST(8)-MA]-005	9635.3	1.7063098	6.4706002	24.8178400	0.1547344	0.9380141	2.3157221	5.2858539
QST(8)-MA]-006	9636.1	1.6633683	6.2293106	25.8101622	0.1947692	0.9895065	2.2201366	5.1514029
QST(8)-MA]-007	9637.3	1.3093540	6.5400927	24.5213106	0.1074628	0.8899355	2.3803519	5.3283674
QST(8)-MA]-008	9638.6	1.8505261	4.8253756	26.6694646	0.1234043	0.8766861	1.4824186	5.8628175
QST(8)-MA]-009	9639.8	1.6178914	5.3993313	25.5282436	0.1624774	0.7958760	1.8789031	5.6407751
QST(8)-MA]-010	9641.1	1.5213463	6.3288857	25.0502164	0.1229546	0.8353820	2.2530203	5.0390761
QST(8)-MA]-011	9642.2	1.7550490	6.8605771	26.1150626	0.1656480	0.9522851	2.4827307	4.4458479
QST(8)-MA]-012	9643.3	1.4243139	6.8584283	24.2792992	0.3158433	1.6705853	2.3931148	4.0772102
QST(8)-MA]-013	9644.2	1.4301937	5.1374246	26.2691433	0.1552862	0.7140608	1.5686556	5.6689114
QST(8)-MA]-014	9645.5	1.6195809	5.1721437	25.3026222	0.1649837	1.0841750	1.8028746	5.8063925
QST(8)-MA]-015	9646.5	1.6705090	5.8165701	24.2210898	0.1469365	0.8363693	2.0829158	5.3715750
QST(8)-MA]-016	9647.3	1.5732417	5.5900563	22.4895764	0.1418537	1.0477884	2.0260607	5.9471742
QST(8)-MA]-017	9648.5	1.4792483	5.7455869	26.1219353	0.1689276	0.6707833	1.8162950	4.7511701
QST(8)-MA]-018	9649.8	1.5007637	7.1429008	25.5858311	0.1613874	0.9088647	2.3864634	4.4660470
QST(8)-MA]-019	9651.5	1.8383279	4.9929094	25.8159312	0.1103231	1.7133983	1.6065628	4.7654406
QST(8)-MA]-020	9652.4	1.5640904	5.8468367	24.9686562	0.2155974	1.7409003	2.0739209	5.4590540
QST(8)-MA]-021	9653.3	1.4517625	5.0610317	27.3766126	0.0898234	0.7932972	1.7087746	5.0436541
QST(8)-MA]-022	9654.2	1.6543014	4.1858693	24.1817850	0.2142750	1.1168925	1.3626926	7.8421664
QST(8)-MA]-023	9655.5	1.3682459	5.5945586	23.0589402	0.1739222	1.0991812	2.0198277	6.3773342
QST(8)-MA]-024	9656.3	1.7750392	5.9916766	25.5304340	0.1978008	1.0770863	2.0950335	4.6115299
QST(8)-MA]-025	9657.1	1.5773221	6.6256427	24.5510774	0.1506839	1.1904682	2.3324372	4.4249093
QST(8)-MA]-026	9657.7	1.3606914	5.0988100	26.5887922	0.1285963	0.7035628	1.5617567	5.0736791
QST(8)-MA]-027	9659.2	3.6802763	5.3323139	22.9557553	0.2093053	1.1474896	1.9008615	3.9917670
QST(8)-MA]-028	9660.1	1.6936040	4.2448204	28.2117168	0.1276944	0.5970417	1.3377279	5.4335558
QST(8)-MA]-029	9661.2	1.6174138	6.2674445	24.8611842	0.1814090	1.0289590	2.2850116	4.2934881
QST(8)-MA]-030	9661.9	1.9318012	5.1368922	24.2329004	0.2198263	0.8330708	1.7427864	5.5890791
QST(8)-MA]-031	9663.4	1.6102142	4.6743974	27.2285136	0.1587721	0.6823912	1.5003247	5.0068887
QST(8)-MA]-032	9664.2	1.6670963	6.7203926	25.8140640	0.1797336	0.9783907	2.4170051	4.1984034
QST(8)-MA]-033	9665.3	1.5888155	6.6847183	24.9700766	0.1173325	1.1741546	2.4266387	3.1057404
QST(8)-MA]-034	9666.2	1.3709429	6.0450153	25.5951169	0.1284036	0.8953616	1.9750361	4.2550866
QST(8)-MA]-035	9667.3	1.7643331	6.1021920	25.6692718	0.1197587	0.8149759	2.0248187	3.8504732
QST(8)-MA]-036	9668.5	1.3629472	4.8496428	26.6876306	0.0927269	0.4930339	1.4472196	5.3097236

Questar 8 XRF – major elements

Sample ID	Depth (ft.)	BaLa1	TiKa1	V Ka1	CrKa1	MnKa1	FeKa1	ZrKa1
QST(8)-MA1-001	9631.3	0.1963302	0.1819663	0.0074113	0.0111320	0.0271468	1.9150286	0.0143342
QST(8)-MA1-002	9632.3	0.1216107	0.3812817	0.0320813	0.0074534	0.0293136	2.9847427	0.0142445
QST(8)-MA1-003	9632.9	0.1842092	0.3303625	0.0257251	0.0083838	0.0286170	2.8498830	0.0169244
QST(8)-MA1-004	9634.3	0.1637898	0.3097361	0.0219050	0.0080693	0.0304192	2.5826733	0.0149072
QST(8)-MA1-005	9635.3	0.1257597	0.3529736	0.0192546	0.0085892	0.0285180	2.6692808	0.0144356
QST(8)-MA1-006	9636.1	0.1081261	0.3435777	0.0274160	0.0082572	0.0299732	2.7008104	0.0142966
QST(8)-MA1-007	9637.3	0.1407272	0.3484425	0.0199437	0.0114053	0.0297795	2.7872707	0.0148409
QST(8)-MA1-008	9638.6	0.1732818	0.2693257	0.0133904	0.0100010	0.0301695	2.1152403	0.0169064
QST(8)-MA1-009	9639.8	0.1049406	0.3054630	0.0204534	0.0089896	0.0311026	2.3739685	0.0157227
QST(8)-MA1-010	9641.1	0.1314575	0.3456097	0.0187223	0.0095086	0.0300449	2.5891035	0.0162789
QST(8)-MA1-011	9642.2	0.0690885	0.3540324	0.0233545	0.0082111	0.0280063	2.6507590	0.0156673
QST(8)-MA1-012	9643.3	0.2526371	0.3847582	0.0263396	0.0082316	0.0242185	2.6633680	0.0159415
QST(8)-MA1-013	9644.2	0.1165505	0.2490692	0.0150138	0.0087558	0.0323236	2.0870189	0.0157924
QST(8)-MA1-014	9645.5	0.1873269	0.2845387	0.0160356	0.0078440	0.0343903	2.4342032	0.0194526
QST(8)-MA1-015	9646.5	0.1300881	0.3400203	0.0225675	0.0075219	0.0314300	2.6175715	0.0143138
QST(8)-MA1-016	9647.3	0.1569838	0.3326682	0.0238916	0.0078550	0.0403811	2.7539186	0.0189931
QST(8)-MA1-017	9648.5	0.0962322	0.3144619	0.0141817	0.0094280	0.0284990	2.4417795	0.0175032
QST(8)-MA1-018	9649.8	0.0838937	0.3645043	0.0269672	0.0064625	0.0315533	2.6867793	0.0167516
QST(8)-MA1-019	9651.5	0.3386269	0.2797454	0.0038855	0.0083688	0.0220195	2.2370533	0.0138974
QST(8)-MA1-020	9652.4	0.1185651	0.3550086	0.0242981	0.0084203	0.0297890	2.7518792	0.0170177
QST(8)-MA1-021	9653.3	0.0229583	0.2982426	0.0193118	0.0085608	0.0332757	2.3767444	0.0204546
QST(8)-MA1-022	9654.2	0.0846463	0.2470087	0.0148678	0.0096709	0.0346349	2.5189448	0.0126750
QST(8)-MA1-023	9655.5	0.2093050	0.3153752	0.0176004	0.0102179	0.0320306	2.5649717	0.0144542
QST(8)-MA1-024	9656.3	0.2677219	0.3400305	0.0288521	0.0077091	0.0268740	2.5366045	0.0163360
QST(8)-MA1-025	9657.1	0.1767708	0.3484869	0.0206502	0.0073969	0.0298712	2.6894101	0.0165884
QST(8)-MA1-026	9657.7	0.1609267	0.2384434	0.0048458	0.0092659	0.0277588	2.1317763	0.0144068
QST(8)-MA1-027	9659.2	0.2864469	0.2609214	0.0107492	0.0091421	0.0260831	2.4556687	0.0162785
QST(8)-MA1-028	9660.1	0.0085195	0.2543149	0.0123251	0.0080377	0.0358696	2.2074563	0.0146994
QST(8)-MA1-029	9661.2	0.1725224	0.3585212	0.0197810	0.0072319	0.0247340	2.7934294	0.0166739
QST(8)-MA1-030	9661.9	0.1687972	0.3210523	0.0184373	0.0079680	0.0300344	2.3034838	0.0164988
QST(8)-MA1-031	9663.4	0.1257199	0.2852768	0.0156327	0.0078397	0.0341418	2.4618210	0.0200416
QST(8)-MA1-032	9664.2	0.1817730	0.3871759	0.0219881	0.0075356	0.0247505	2.6003671	0.0161069
QST(8)-MA1-033	9665.3	0.2660576	0.3694979	0.0212671	0.0063314	0.0195254	2.5597396	0.0176616
QST(8)-MA1-034	9666.2	0.1783497	0.3408585	0.0217820	0.0082020	0.0279023	2.5168158	0.0145515
QST(8)-MA1-035	9667.3	0.1572479	0.3387393	0.0208991	0.0075664	0.0222055	2.5091322	0.0120890
QST(8)-MA1-036	9668.5	0.0523469	0.2650092	0.0165333	0.0079012	0.0299190	2.5143126	0.0226719

Questar 8 XRF – major elements

Sample ID	Depth (ft.)	MgKa1	AlKa1	SiKa1	P Ka1	S Ka1	K Ka1	CaKa1
QST(8)-MAJ-037	9669.3	1.6071984	5.1674446	26.3084064	0.1448456	0.7914757	1.6543444	4.5357720
QST(8)-MAJ-038	9670.2	1.6833638	6.0873903	23.3740485	0.1888388	1.0605861	2.2804996	5.0970071
QST(8)-MAJ-039	9671.2	1.2291659	5.0502509	26.6382138	0.1819471	0.7907827	1.5844950	4.8257470
QST(8)-MAJ-040	9672.2	1.5604608	6.2898877	23.9350302	0.1196688	2.2619227	2.1234359	4.3730995
QST(8)-MAJ-041	9673.3	1.2843439	7.0892322	26.0619879	0.1025302	1.0650092	2.3523446	3.6391396
QST(8)-MAJ-042	9674.3	1.4308404	5.7786981	26.7071122	0.0606621	0.6755518	1.8275023	4.4898802
QST(8)-MAJ-043	9674.9	1.5800965	6.2569022	23.8762304	0.1331803	2.2278179	2.1228744	3.8702176
QST(8)-MAJ-044	9676.9	1.3316869	6.9166579	25.1636341	0.1284575	1.0729138	2.3200484	3.2373222
QST(8)-MAJ-045	9677.5	1.3902944	7.0618055	25.8251352	0.1229727	0.9049450	2.4464783	3.9477821
QST(8)-MAJ-046	9678.4	1.5736720	5.9331237	26.3316934	0.0826379	0.7086734	1.8486786	4.9123608
QST(8)-MAJ-047	9679.3	1.4695273	6.0534960	24.5648569	0.1379287	1.5028339	2.0827089	5.1887167
QST(8)-MAJ-048	9680.3	1.3945451	6.7459052	25.5216191	0.1437396	1.0660384	2.3065461	3.6535634
QST(8)-MAJ-049	9682.2	1.4232618	7.1806356	25.6283655	0.1062537	1.2530827	2.4309326	3.6515727
QST(8)-MAJ-050	9683.3	1.2135892	6.4716221	24.3843577	0.0933601	0.8681017	2.3356341	4.4691768
QST(8)-MAJ-051	9683.4	1.6946905	7.2766894	24.2967729	0.1314631	1.5026344	2.5092515	4.8132447
QST(8)-MAJ-052	9684.2	1.6662521	7.3798496	24.6438870	0.1446697	1.2823351	2.5999919	4.4635905
QST(8)-MAJ-053	9685.5	5.8379068	4.4335368	16.1888454	0.3547361	5.0448789	1.3333271	5.4764466
QST(8)-MAJ-054	9686.3	2.3652320	6.8442140	24.7681479	0.2614338	1.1680648	2.4547559	4.0558488
QST(8)-MAJ-055	9687.6	1.5852757	6.7227035	25.0147118	0.2008729	1.1371740	2.3774625	4.7904240
QST(8)-MAJ-056	9691.9	1.5800994	5.5173716	25.7942075	0.1471567	0.7077154	1.9847286	5.2637917
QST(8)-MAJ-057	9692.5	1.8135358	5.6560010	25.5790272	0.1481837	0.7065132	1.9539166	5.1027624
QST(8)-MAJ-058	9693.4	1.6112319	6.5467607	25.8571997	0.1561335	0.7021797	2.3992748	4.2308198
QST(8)-MAJ-059	9694.3	1.9304257	5.5432005	27.6591105	0.1689318	0.6463830	1.9499712	4.8769981
QST(8)-MAJ-060	9695.4	1.4731304	7.3117203	26.7501474	0.1579136	1.0828637	2.6365482	3.5418108
QST(8)-MAJ-061	9696.3	1.3019799	5.6648180	26.0382391	0.1233830	1.2903971	1.8752757	4.9074219
QST(8)-MAJ-062	9697.3	1.5058551	6.0903419	26.2943476	0.1111140	0.7030668	2.1596543	4.1158357
QST(8)-MAJ-063	9698.2	5.2529745	4.3202912	23.0704104	0.2978261	1.2767371	1.2355761	3.6260733
QST(8)-MAJ-064	9699.3	1.1726262	6.4986746	25.4047381	0.1001200	0.8683300	2.2812695	3.8081277
QST(8)-MAJ-065	9699.8	1.5480756	5.5854730	27.1258309	0.1271629	0.7450860	1.9281726	4.0729769
QST(8)-MAJ-066	9701.4	1.3224648	7.5369001	27.1007003	0.1241627	0.8280470	2.5336579	2.6477465
QST(8)-MAJ-067	9702.2	1.5462595	6.8337394	26.6232440	0.1070902	0.7091281	2.2687823	3.7910092
QST(8)-MAJ-068	9703.1	4.7100083	5.3200873	19.7672681	0.3218138	4.6947136	1.6131076	4.1077724
QST(8)-MAJ-069	9704.2	1.6019339	6.0282541	25.5163649	0.1510757	1.5586410	2.0609614	4.7661897
QST(8)-MAJ-070	9705.3	1.8562925	6.5531822	25.6450428	0.1305863	0.9575392	2.2861329	4.1388529
QST(8)-MAJ-071	9706.1	1.3138323	6.0609134	24.1728758	0.1897965	2.8874854	2.1404444	4.7943487
QST(8)-MAJ-072	9707.5	2.7977658	5.6634255	24.1888518	0.2067181	1.8198855	1.8387979	4.4797126

Questar 8 XRF – major elements

Sample ID	Depth (ft.)	BaLa1	TiKa1	V Ka1	CrKa1	MnKa1	FeKa1	ZrKa1
QST(8)-MA1-037	9669.3	0.0579088	0.2938125	0.0175736	0.0071480	0.0280277	2.5028482	0.0175816
QST(8)-MA1-038	9670.2	0.1946818	0.3647750	0.0200702	0.0080472	0.0293671	2.7531114	0.0169612
QST(8)-MA1-039	9671.2	0.1459149	0.2865261	0.0185240	0.0081022	0.0285205	2.3648852	0.0153655
QST(8)-MA1-040	9672.2	0.2773006	0.3307274	0.0145034	0.0100698	0.0205457	2.7494983	0.0149375
QST(8)-MA1-041	9673.3	0.0640002	0.4283640	0.0204050	0.0068187	0.0242363	2.8961623	0.0150835
QST(8)-MA1-042	9674.3	0.0575280	0.2727486	0.0209185	0.0088592	0.0287759	2.6242105	0.0144950
QST(8)-MA1-043	9674.9	-0.0139295	0.3012908	-0.0303202	0.0103820	0.0094909	2.5639470	0.0146410
QST(8)-MA1-044	9676.9	0.0802480	0.3622040	0.0202824	0.0073009	0.0238691	2.7144331	0.0163476
QST(8)-MA1-045	9677.5	0.0917215	0.4142109	0.0262069	0.0069976	0.0258630	2.7433906	0.0166945
QST(8)-MA1-046	9678.4	0.0177804	0.3113042	0.0202162	0.0087494	0.0360742	2.5204102	0.0155588
QST(8)-MA1-047	9679.3	0.2934308	0.3054698	0.0040696	0.0080673	0.0292511	2.8887261	0.0155865
QST(8)-MA1-048	9680.3	0.1929857	0.3974779	0.0252818	0.0071417	0.0215876	2.7137069	0.0135007
QST(8)-MA1-049	9682.2	0.1636507	0.3765085	0.0260746	0.0083673	0.0217127	2.7472414	0.0160224
QST(8)-MA1-050	9683.3	0.2137300	0.2943239	0.0222496	0.0095729	0.0298332	3.0471332	0.0140127
QST(8)-MA1-051	9683.4	0.0849257	0.3701498	0.0253238	0.0066717	0.0309636	3.1561955	0.0148162
QST(8)-MA1-052	9684.2	0.0762558	0.3968166	0.0289589	0.0075809	0.0331523	3.3226797	0.0148842
QST(8)-MA1-053	9685.5	0.2529033	0.2121269	0.0277984	0.0102419	0.0300414	2.7010551	0.0137064
QST(8)-MA1-054	9686.3	0.0566298	0.3649912	0.0301304	0.0076816	0.0313643	3.2980501	0.0145602
QST(8)-MA1-055	9687.6	0.1142369	0.3446688	0.0268196	0.0089428	0.0312893	3.0445208	0.0139429
QST(8)-MA1-056	9691.9	0.0680821	0.3303497	0.0201601	0.0079862	0.0276262	2.4857349	0.0160582
QST(8)-MA1-057	9692.5	0.0715447	0.3129919	0.0223728	0.0081967	0.0287411	2.4368753	0.0156521
QST(8)-MA1-058	9693.4	0.0716929	0.3377424	0.0215837	0.0079434	0.0314697	2.8041019	0.0141626
QST(8)-MA1-059	9694.3	0.0508818	0.2787073	0.0130131	0.0092131	0.0347993	2.8500867	0.0160008
QST(8)-MA1-060	9695.4	0.0699769	0.3940837	0.0243813	0.0092602	0.0252328	2.8570971	0.0157479
QST(8)-MA1-061	9696.3	0.1013368	0.3087673	0.0251580	0.0076815	0.0342281	2.4711967	0.0142384
QST(8)-MA1-062	9697.3	0.0254553	0.3317170	0.0219331	0.0076661	0.0309006	2.5527242	0.0146069
QST(8)-MA1-063	9698.2	0.2193997	0.1573927	0.0034146	0.0102902	0.0345491	2.4383210	0.0142938
QST(8)-MA1-064	9699.3	0.2000790	0.3424995	0.0229436	0.0087446	0.0250785	2.5349691	0.0153366
QST(8)-MA1-065	9699.8	0.0558102	0.3309364	0.0234645	0.0074071	0.0272436	2.3817209	0.0153817
QST(8)-MA1-066	9701.4	0.1310004	0.3745512	0.0284136	0.0079467	0.0206375	2.5279229	0.0173357
QST(8)-MA1-067	9702.2	0.0914099	0.3496111	0.0199152	0.0087238	0.0261564	2.5277839	0.0168533
QST(8)-MA1-068	9703.1	0.1794745	0.2531576	0.0222131	0.0074500	0.0292139	2.4270139	0.0138901
QST(8)-MA1-069	9704.2	0.1135351	0.3071240	0.0182657	0.0087869	0.0337039	2.7408371	0.0149378
QST(8)-MA1-070	9705.3	0.1639828	0.3657333	0.0219143	0.0081995	0.0272563	2.7084350	0.0165675
QST(8)-MA1-071	9706.1	0.1760193	0.3252654	0.0292594	0.0078185	0.0324393	2.8091343	0.0156445
QST(8)-MA1-072	9707.5	0.1817357	0.2570885	0.0112189	0.0066954	0.0317091	2.5493564	0.0148926

Questar 8 XRF – major elements

Sample ID	Depth (ft.)	MgKa1	AlKa1	SiKa1	P Ka1	S Ka1	K Ka1	CaKa1
QST(8)-MAI-073	9708.3	8.4291498	4.0797635	19.5207835	0.3660827	0.9687723	1.3427755	3.0661403
QST(8)-MAI-074	9709.3	5.3306102	4.4550046	16.5853000	0.3246039	5.7655589	1.2029497	5.3538886
QST(8)-MAI-075	9710.5	1.5066300	5.4433789	26.1378634	0.1255059	0.6583477	1.6847117	5.0508641
QST(8)-MAI-076	9711.3	1.6333448	5.9482915	25.4754107	0.1475876	0.7118810	2.1468958	4.8281209
QST(8)-MAI-077	9712.3	1.6698129	6.3808504	25.3828440	0.1159225	0.7979040	2.4213606	5.2845083
QST(8)-MAI-078	9713.4	6.2268401	4.6610591	17.7539683	0.3188754	3.3108421	1.5552893	3.9973223
QST(8)-MAI-079	9714.4	7.9646115	5.0594381	19.1076586	0.3624773	1.0831968	1.7309152	2.4850099
QST(8)-MAI-080	9715.6	1.3537894	5.1071614	22.5056440	0.2387214	4.9761940	1.7651007	6.9778589
QST(8)-MAI-081	9718.1	5.0629423	5.6819838	21.3529319	0.3125175	1.0797868	2.0011676	3.4337197
QST(8)-MAI-082	9719.3	1.9756141	6.7355955	25.9152900	0.1375655	0.9921282	2.3668390	3.9802421
QST(8)-MAI-083	9720.1	1.7822027	5.7089288	26.2243581	0.1293741	0.9023406	1.8854128	4.7489868
QST(8)-MAI-084	9721.1	1.7628362	6.9377169	26.6029291	0.1232973	0.6346731	2.5236459	3.5516846
QST(8)-MAI-085	9722.3	1.8409272	5.9657544	25.5458706	0.1668610	1.2381969	2.1427194	4.6378675
QST(8)-MAI-086	9723.1	1.5453947	6.8803375	26.4398221	0.1520037	0.9050632	2.4682026	3.1120246
QST(8)-MAI-087	9725.6	3.4189555	4.5077494	19.5345741	0.3546240	3.2504241	1.5226744	5.9983887
QST(8)-MAI-088	9726.3	2.1109830	5.4291127	26.2286852	0.1059234	1.4077771	1.7003282	4.1911307
QST(8)-MAI-089	9727.2	1.5813325	6.2882752	24.7931963	0.1868106	1.2825577	2.1846230	4.2912574
QST(8)-MAI-090	9728.2	4.0932282	4.9167494	21.9625930	0.2573086	1.7170745	1.5983940	3.9648162
QST(8)-MAI-091	9728.8	1.3859081	7.5990215	25.9691256	0.1332661	1.2386104	2.7029593	3.1737921
QST(8)-MAI-092	9730.1	3.2877442	5.5435907	21.2668371	0.2916328	1.7054273	1.9565441	4.6852123
QST(8)-MAI-093	9731.3	4.6654471	5.3674187	20.4746471	0.3094548	1.5968964	1.7370064	3.3405238
QST(8)-MAI-094	9732.2	1.2668921	7.0902689	25.2832962	0.1772634	1.8619602	2.4358609	4.0081595
QST(8)-MAI-095	9733.1	1.7771269	6.9278413	25.4882453	0.1600590	1.3243507	2.3903910	3.1578798
QST(8)-MAI-096	9734.5	1.8659669	6.5014374	24.8858112	0.2015821	1.0660792	2.3412030	4.3203910
QST(8)-MAI-097	9736.7	2.3713093	6.7800018	24.8100679	0.2263356	2.1685771	2.3359991	2.9244846
QST(8)-MAI-098	9737.3	4.1794910	4.9335332	19.0995215	0.3217534	4.5594077	1.4893838	5.5762951
QST(8)-MAI-099	9738.3	1.9107298	6.6790193	24.5275226	0.2312259	1.4594242	2.1942215	3.3978445
QST(8)-MAI-100	9739.5	1.1763689	7.2572709	24.6985454	0.1574565	1.7949727	2.5488110	4.6274984
QST(8)-MAI-101	9740.2	1.6452726	6.4959548	24.8749831	0.1247021	0.8859965	2.3682798	4.5162349
QST(8)-MAI-102	9741.3	1.9404449	6.6983767	24.0437949	0.1702611	2.9253836	2.3275140	3.8834511
QST(8)-MAI-103	9742.6	1.5756044	6.7862422	26.1708849	0.0906679	1.4178108	2.3814869	4.2600506
QST(8)-MAI-104	9743.1	1.2328463	7.8559243	26.3690394	0.1784350	0.9175826	2.8063023	3.3342926
QST(8)-MAI-105	9744.3	1.4727929	6.3877204	26.4856384	0.1294746	1.2145676	2.2429222	4.0068039
QST(8)-MAI-106	9745.3	1.6432816	6.6247848	25.5409430	0.1548388	1.2463357	2.3551957	4.0194363
QST(8)-MAI-107	9746.1	1.2006397	5.9400911	25.1503384	0.0990794	0.8422288	2.1912447	3.9303672

Questar 8 XRF – major elements

Sample ID	Depth (ft.)	BaLa1	TiKa1	V Ka1	CrKa1	MnKa1	FeKa1	ZrKa1
QST(8)-MA1-073	9708.3	0.1985093	0.1822876	0.0139049	0.0107983	0.0322860	2.7764424	0.0143303
QST(8)-MA1-074	9709.3	0.1978838	0.2043565	0.0256379	0.0095532	0.0289218	2.2354041	0.0125383
QST(8)-MA1-075	9710.5	0.0937691	0.2712522	0.0156268	0.0074675	0.0298054	2.1884656	0.0130478
QST(8)-MA1-076	9711.3	0.0852499	0.3208912	0.0192038	0.0086667	0.0315760	2.6830583	0.0137099
QST(8)-MA1-077	9712.3	0.1026555	0.3214335	0.0235369	0.0077878	0.0319665	2.7079977	0.0142259
QST(8)-MA1-078	9713.4	0.3009667	0.2083343	0.0206736	0.0097214	0.0302465	2.7534929	0.0123693
QST(8)-MA1-079	9714.4	0.1685170	0.2497036	0.0172157	0.0114549	0.0278709	2.9450255	0.0140718
QST(8)-MA1-080	9715.6	0.1407636	0.3101723	0.0285645	0.0075196	0.0327908	2.8001230	0.0144700
QST(8)-MA1-081	9718.1	0.1761058	0.2693284	0.0201143	0.0098620	0.0306995	2.8518108	0.0136908
QST(8)-MA1-082	9719.3	0.1726292	0.3306281	0.0276845	0.0079368	0.0257895	2.6763147	0.0155831
QST(8)-MA1-083	9720.1	0.0583322	0.3173688	0.0294717	0.0075363	0.0300507	2.4746441	0.0146668
QST(8)-MA1-084	9721.1	0.0911053	0.3482449	0.0248109	0.0084249	0.0232212	2.8603819	0.0159639
QST(8)-MA1-085	9722.3	0.1197976	0.3271640	0.0283145	0.0076217	0.0300256	2.7884365	0.0153290
QST(8)-MA1-086	9723.1	0.1309191	0.3609728	0.0253901	0.0079960	0.0219097	2.7729365	0.0144134
QST(8)-MA1-087	9725.6	0.3351944	0.2023517	0.0090350	0.0070890	0.0332668	3.1711320	0.0113255
QST(8)-MA1-088	9726.3	0.1496587	0.2732834	0.0171551	0.0078479	0.0270019	2.2891980	0.0156778
QST(8)-MA1-089	9727.2	0.2010303	0.3142340	0.0125105	0.0088651	0.0251693	2.5965491	0.0159334
QST(8)-MA1-090	9728.2	0.2389254	0.2724424	0.0171174	0.0079775	0.0209940	2.3789055	0.0157408
QST(8)-MA1-091	9728.8	0.0757636	0.4330494	0.0270503	0.0100059	0.0222798	3.0725629	0.0160446
QST(8)-MA1-092	9730.1	0.2667382	0.2933595	0.0242919	0.0076511	0.0284342	2.6220242	0.0158929
QST(8)-MA1-093	9731.3	0.3168621	0.2894403	0.0104105	0.0079696	0.0168289	2.7022283	0.0163106
QST(8)-MA1-094	9732.2	0.0979380	0.3495841	0.0202006	0.0089073	0.0238879	2.9041758	0.0155244
QST(8)-MA1-095	9733.1	0.1297616	0.3342194	0.0246689	0.0079892	0.0225536	2.6393208	0.0127586
QST(8)-MA1-096	9734.5	0.0972343	0.3277303	0.0283647	0.0088948	0.0285945	3.1439950	0.0135053
QST(8)-MA1-097	9736.7	0.1462615	0.3309420	0.0189305	0.0089974	0.0237276	3.2081321	0.0134303
QST(8)-MA1-098	9737.3	0.2572002	0.2464139	0.0230348	0.0083824	0.0411217	2.8534265	0.0140997
QST(8)-MA1-099	9738.3	0.0755942	0.3066960	0.0225755	0.0088638	0.0268227	2.7786221	0.0151058
QST(8)-MA1-100	9739.5	0.1236844	0.3495530	0.0289667	0.0094963	0.0244151	3.3364278	0.0130133
QST(8)-MA1-101	9740.2	0.0681210	0.3332934	0.0293364	0.0080648	0.0294308	3.1185715	0.0135372
QST(8)-MA1-102	9741.3	0.1901243	0.3108402	0.0248432	0.0068683	0.0208749	2.8396376	0.0134009
QST(8)-MA1-103	9742.6	0.0386998	0.3346474	0.0252383	0.0092836	0.0282517	3.1112634	0.0127810
QST(8)-MA1-104	9743.1	0.1779223	0.3339962	0.0293142	0.0106443	0.0206757	2.7741380	0.0124995
QST(8)-MA1-105	9744.3	0.0896562	0.3365290	0.0246342	0.0084657	0.0274061	2.4671389	0.0145555
QST(8)-MA1-106	9745.3	0.1433822	0.3349059	0.0243256	0.0086565	0.0263362	2.6343336	0.0145067
QST(8)-MA1-107	9746.1	0.1484823	0.3205543	0.0240099	0.0096792	0.0243497	2.5381529	0.0142082

Questar 8 XRF – trace elements

Sample ID	Depth (ft.)	NiKa1	CuKa1	ZnKa1	ThLa1	RbKa1	U La1	SrKa1	Y Ka1	ZrKa1	NbKa1	MoKa1
QST(8)-TRC-001	9631.3	0.0063323	0.0058660	0.0114019	0.0012035	0.0110459	0.0002476	0.0186123	0.0021289	0.0143342	0.0012525	0.0004420
QST(8)-TRC-002	9632.3	0.0049790	0.0061029	0.0130725	0.0012005	0.0122421	0.0005153	0.0263392	0.0020205	0.0142445	0.0013080	0.0005616
QST(8)-TRC-003	9632.9	0.0061710	0.0072026	0.0110943	0.0008226	0.0111995	0.0005845	0.0180058	0.0029384	0.0169244	0.0013300	0.0003800
QST(8)-TRC-004	9634.3	0.0041390	0.0036633	0.0113849	0.0010440	0.0095421	-0.0003863	0.0213172	0.0020859	0.0149072	0.0012139	0.0004119
QST(8)-TRC-005	9635.3	0.0035974	0.0072430	0.0125985	0.0008148	0.0112260	0.0009461	0.0206259	0.0029620	0.0144356	0.0014398	0.0002968
QST(8)-TRC-006	9636.1	0.0048018	0.0035580	0.0085483	0.0010304	0.0096163	-0.0002957	0.0172526	0.0023148	0.0142966	0.0010320	0.0003755
QST(8)-TRC-007	9637.3	0.0043771	0.0062926	0.0123928	0.0010263	0.0114922	-0.0001041	0.0198745	0.0021336	0.0148409	0.0012868	0.0002981
QST(8)-TRC-008	9638.6	0.0066223	0.0075859	0.0124338	0.0007551	0.0087621	-0.0001139	0.0191441	0.0024640	0.0169064	0.0009048	0.0005861
QST(8)-TRC-009	9639.8	0.0087791	0.0063329	0.0142322	0.0012242	0.0101423	0.0000003	0.0205149	0.0025078	0.0157227	0.0014094	0.0004693
QST(8)-TRC-010	9641.1	0.0055204	0.0056892	0.0112594	0.0012621	0.0117380	-0.0002126	0.0206445	0.0027199	0.0162789	0.0011481	0.0004674
QST(8)-TRC-011	9642.2	0.0064391	0.0074869	0.0134485	0.0012768	0.0118198	0.0002416	0.0215820	0.0024132	0.0156673	0.0015775	0.0000323
QST(8)-TRC-012	9643.3	-0.0000257	0.0072027	0.0120826	0.0011161	0.0090702	0.0007647	0.0269228	0.0023291	0.0159415	0.0012983	0.0003357
QST(8)-TRC-013	9644.2	0.0080586	0.0061394	0.0136213	0.0012385	0.0129884	0.0013254	0.0195819	0.0025084	0.0157924	0.0013802	0.0003142
QST(8)-TRC-014	9645.5	0.0058252	0.0046179	0.0120310	0.0006967	0.0061751	0.0002780	0.0201167	0.0021548	0.0194526	0.0011917	0.0006076
QST(8)-TRC-015	9646.5	0.0069499	0.0054412	0.0174037	0.0013176	0.0098855	-0.0000534	0.0194759	0.0023768	0.0143138	0.0012542	0.0006224
QST(8)-TRC-016	9647.3	0.0069826	0.0084981	0.0118482	0.0011513	0.0100498	-0.0013395	0.0190232	0.0021954	0.0189931	0.0014611	0.0005053
QST(8)-TRC-017	9648.5	0.0074256	0.0042992	0.0114679	0.0010032	0.0111201	0.0003789	0.0167748	0.0027426	0.0175032	0.0014304	0.0002828
QST(8)-TRC-018	9649.8	0.0090786	0.0107287	0.0136082	0.0010234	0.0132102	0.0009260	0.0178641	0.0024269	0.0167516	0.0015228	0.0002839
QST(8)-TRC-019	9651.5	0.0052621	0.0051674	0.0113985	0.0007148	0.0062317	0.0002858	0.0174791	0.0020639	0.0138974	0.0008055	0.0007696
QST(8)-TRC-020	9652.4	0.0064561	0.0076028	0.0131262	0.0008735	0.0078568	0.0001914	0.0242465	0.0027080	0.0170177	0.0012444	0.0004920
QST(8)-TRC-021	9653.3	0.0072916	0.0096197	0.0095081	0.0009566	0.0095952	0.0010027	0.0145367	0.0025460	0.0204546	0.0012819	0.0008455
QST(8)-TRC-022	9654.2	0.0035061	0.0038425	0.0141806	0.0005944	0.0048678	0.0009124	0.0284349	0.0023997	0.0126750	0.0007396	0.0005746
QST(8)-TRC-023	9655.5	0.0045160	0.0039161	0.0150631	0.0008861	0.0109465	0.0010715	0.0245634	0.0023215	0.0144542	0.0011940	0.0003003
QST(8)-TRC-024	9656.3	0.0056625	0.0047768	0.0141103	0.0006690	0.0117438	-0.0002149	0.0162664	0.0027279	0.0163360	0.0011587	0.0004361
QST(8)-TRC-025	9657.1	0.0030394	0.0069885	0.0111589	0.0011701	0.0122647	0.0006763	0.0238940	0.0025119	0.0165884	0.0012844	0.0005250
QST(8)-TRC-026	9657.7	0.0089151	0.0082469	0.0152681	0.0010127	0.0096151	-0.0002992	0.0221971	0.0024687	0.0144068	0.0011113	0.0006810
QST(8)-TRC-027	9659.2	0.0086316	0.0081957	0.0116122	0.0010611	0.0143218	0.0009979	0.0223891	0.0029645	0.0162785	0.0016062	-0.0001139
QST(8)-TRC-028	9660.1	0.0039202	0.0069538	0.0109371	0.0008861	0.0073205	0.0005997	0.0148062	0.0024432	0.0146994	0.0010887	0.0004442
QST(8)-TRC-029	9661.2	0.0047639	0.0052856	0.0149750	0.0010184	0.0109584	-0.0004895	0.0220296	0.0023679	0.0166739	0.0013713	0.0004925
QST(8)-TRC-030	9661.9	0.0069564	0.0052455	0.0161146	0.0010864	0.0108594	0.0001171	0.0243332	0.0028480	0.0164988	0.0013973	0.0004332
QST(8)-TRC-031	9663.4	0.0044203	0.0066734	0.0148741	0.0009495	0.0085704	0.0004199	0.0219266	0.0026622	0.0200416	0.0014399	0.0007471
QST(8)-TRC-032	9664.2	0.0062702	0.0055643	0.0130715	0.0009528	0.0106563	0.0003636	0.0209720	0.0026959	0.0161069	0.0014047	0.0004231
QST(8)-TRC-033	9665.3	0.0067802	0.0039090	0.0150568	0.0011224	0.0123228	-0.0001540	0.0201269	0.0027063	0.0176616	0.0015806	0.0001189
QST(8)-TRC-034	9666.2	0.0053692	0.0018723	0.0107263	0.0009529	0.0078099	-0.0000209	0.0157525	0.0022779	0.0145515	0.0010596	0.0005921
QST(8)-TRC-035	9667.3	0.0055034	0.0038687	0.0092038	0.0004074	0.0028431	-0.0002376	0.0225364	0.0022979	0.0120890	0.0007458	0.0006463
QST(8)-TRC-036	9668.5	0.0069248	0.0057369	0.0175003	0.0010456	0.0116712	0.0009244	0.0177125	0.0028523	0.0226719	0.0014946	0.0006358

Questar 8 XRF – trace elements

Sample ID	Depth (ft.)	NiKa1	CuKa1	ZnKa1	ThLa1	RbKa1	U La1	SrKa1	Y Ka1	ZrKa1	NbKa1	MoKa1
QST(8)-TRC-037	9669.3	0.0040084	0.0043415	0.0138416	0.0010502	0.0101800	0.0009291	0.0200169	0.0022915	0.0175816	0.0012537	0.0004012
QST(8)-TRC-038	9670.2	0.0066347	0.0036802	0.0139792	0.0008698	0.0100064	-0.0002265	0.0189944	0.0026528	0.0169612	0.0011826	0.0005339
QST(8)-TRC-039	9671.2	0.0050041	0.0080525	0.0136154	0.0009383	0.0104386	0.0003749	0.0209567	0.0023763	0.0153655	0.0012794	0.0003464
QST(8)-TRC-040	9672.2	0.0014578	0.0033570	0.0135849	0.0010377	0.0112755	0.0008390	0.0238663	0.0024740	0.0149375	0.0014950	0.0004053
QST(8)-TRC-041	9673.3	0.0040224	0.0036371	0.0126809	0.0008356	0.0083277	-0.0000427	0.0166459	0.0022249	0.0150835	0.0011807	0.0005987
QST(8)-TRC-042	9674.3	0.0033294	0.0032087	0.0091146	0.0009237	0.0110601	0.0005122	0.0135176	0.0018820	0.0144950	0.0013573	0.0004412
QST(8)-TRC-043	9674.9	0.0026717	0.0075671	0.0150391	0.0010566	0.0106628	0.0004726	0.0152959	0.0024300	0.0146410	0.0012713	0.0002557
QST(8)-TRC-044	9676.9	0.0080280	0.0027155	0.0121267	0.0011359	0.0137975	0.0004101	0.0177946	0.0027708	0.0163476	0.0013380	0.0003091
QST(8)-TRC-045	9677.5	0.0049841	0.0040550	0.0095921	0.0010796	0.0120794	0.0003320	0.0176014	0.0022533	0.0166945	0.0014695	-0.0000182
QST(8)-TRC-046	9678.4	0.0016294	0.0043715	0.0103549	0.0007989	0.0118231	0.0011774	0.0176864	0.0027377	0.0155588	0.0013646	0.0002966
QST(8)-TRC-047	9679.3	0.0079836	0.0045285	0.0110652	0.0012691	0.0124637	0.0004946	0.0196007	0.0024815	0.0155865	0.0015223	0.0003054
QST(8)-TRC-048	9680.3	0.0083461	0.0014419	0.0122851	0.0008746	0.0085765	0.0011970	0.0156621	0.0020708	0.0135007	0.0010997	0.0003554
QST(8)-TRC-049	9682.2	0.0085739	0.0016859	0.0139102	0.0011955	0.0135217	0.0017782	0.0189630	0.0024485	0.0160224	0.0013291	0.0004285
QST(8)-TRC-050	9683.3	0.0077528	0.0091688	0.0499997	0.0011048	0.0115825	0.0001613	0.0238935	0.0025240	0.0140127	0.0015564	0.0001416
QST(8)-TRC-051	9683.4	0.0058956	0.0028867	0.0123768	0.0010273	0.0114462	0.0001521	0.0204657	0.0023230	0.0148162	0.0014696	0.0004234
QST(8)-TRC-052	9684.2	0.0031806	0.0055641	0.0104915	0.0010494	0.0120369	0.0003480	0.0223284	0.0024477	0.0148842	0.0014000	0.0002454
QST(8)-TRC-053	9685.5	0.0088805	0.0036452	0.0089227	0.0011049	0.0137700	-0.0002683	0.0222026	0.0024874	0.0137064	0.0013139	0.0003292
QST(8)-TRC-054	9686.3	0.0069800	0.0021304	0.0104264	0.0014786	0.0114629	-0.0002220	0.0191073	0.0021331	0.0145602	0.0014093	0.0003937
QST(8)-TRC-055	9687.6	0.0038887	0.0003355	0.0110713	0.0010794	0.0109503	-0.0000101	0.0182142	0.0022204	0.0139429	0.0012181	0.0002109
QST(8)-TRC-056	9691.9	0.0088622	0.0065054	0.0134317	0.0011452	0.0117144	-0.0004654	0.0175284	0.0024325	0.0160582	0.0013419	0.0002485
QST(8)-TRC-057	9692.5	0.0028119	0.0042060	0.0097073	0.0013384	0.0106311	0.0011729	0.0201574	0.0021690	0.0156521	0.0014093	0.0003529
QST(8)-TRC-058	9693.4	0.0061836	0.0020351	0.0172835	0.0010640	0.0119663	0.0004409	0.0130221	0.0023852	0.0141626	0.0012131	0.0004316
QST(8)-TRC-059	9694.3	0.0069011	0.0024247	0.0100522	0.0008784	0.0141619	0.0010587	0.0202431	0.0030769	0.0160008	0.0013311	0.0003991
QST(8)-TRC-060	9695.4	0.0075486	0.0039006	0.0128130	0.0009906	0.0143775	0.0002065	0.0302023	0.0032627	0.0157479	0.0013931	0.0004098
QST(8)-TRC-061	9696.3	0.0056637	0.0027496	0.0111020	0.0009597	0.0100860	0.0008273	0.0162383	0.0022887	0.0142384	0.0014245	0.0004213
QST(8)-TRC-062	9697.3	0.0058473	0.0031423	0.0132997	0.0011442	0.0127121	0.0005118	0.0200253	0.0024507	0.0146069	0.0011868	0.0005123
QST(8)-TRC-063	9698.2	0.0052772	0.0023626	0.0103918	0.0008691	0.0109440	0.0002137	0.0155321	0.0024576	0.0142938	0.0011592	0.0004290
QST(8)-TRC-064	9699.3	0.0014782	0.0026589	0.0127458	0.0010263	0.0118327	0.0002044	0.0184228	0.0026384	0.0153366	0.0013159	0.0001367
QST(8)-TRC-065	9699.8	0.0056964	0.0056893	0.0144346	0.0009683	0.0123697	0.0004646	0.0191205	0.0029277	0.0153817	0.0015392	0.0004353
QST(8)-TRC-066	9701.4	0.0068759	0.0051809	0.0122883	0.0009906	0.0147812	0.0000723	0.0166482	0.0028391	0.0173357	0.0017131	0.0002792
QST(8)-TRC-067	9702.2	0.0073509	0.0053582	0.0157673	0.0011544	0.0132012	0.0013874	0.0213512	0.0029415	0.0168533	0.0013197	0.0002872
QST(8)-TRC-068	9703.1	0.0092796	0.0034207	0.0108032	0.0014921	0.0113919	-0.0002920	0.0184678	0.0021259	0.0138901	0.0014428	0.0001757
QST(8)-TRC-069	9704.2	0.0041968	0.0055356	0.0118623	0.0009898	0.0113961	0.0004985	0.0177287	0.0023268	0.0149378	0.0015564	0.0000198
QST(8)-TRC-070	9705.3	0.0031076	0.0027411	0.0115023	0.0009404	0.0125870	0.0004273	0.0170767	0.0026913	0.0165675	0.0015839	-0.0000865
QST(8)-TRC-071	9706.1	0.0052657	0.0038933	0.0164739	0.0013587	0.0118661	0.0021095	0.0235931	0.0025526	0.0156445	0.0013214	0.0002979
QST(8)-TRC-072	9707.5	0.0062617	0.0072160	0.0121307	0.0013459	0.0145291	-0.0005880	0.0240004	0.0022607	0.0148926	0.0016200	0.0003151

Questar 8 XRF – trace elements

Sample ID	Depth (ft.)	NiKa1	CuKa1	ZnKa1	ThLa1	RbKa1	U La1	SrKa1	Y Ka1	ZrKa1	NbKa1	MoKa1
QST(8)-TRC-073	9708.3	0.0072193	0.0016975	0.0117259	0.0011186	0.0128156	0.0004204	0.0177837	0.0025100	0.0143303	0.0013832	0.0002045
QST(8)-TRC-074	9709.3	0.0036874	0.0013119	0.0117203	0.0007549	0.0116828	0.0002956	0.0146765	0.0026594	0.0125383	0.0011437	0.0005890
QST(8)-TRC-075	9710.5	0.0045449	0.0046764	0.0168904	0.0008405	0.0085269	0.0006258	0.0167720	0.0024679	0.0130478	0.0008742	0.0005078
QST(8)-TRC-076	9711.3	0.0058092	0.0057979	0.0126502	0.0009736	0.0128648	0.0007137	0.0189137	0.0030567	0.0137099	0.0011987	0.0005482
QST(8)-TRC-077	9712.3	0.0069245	0.0059520	0.0167103	0.0011121	0.0139036	-0.0002527	0.0193456	0.0028536	0.0142259	0.0014711	-0.0000607
QST(8)-TRC-078	9713.4	0.0057200	0.0008454	0.0139770	0.0009513	0.0103702	0.0014017	0.0185577	0.0020502	0.0123693	0.0012644	0.0005223
QST(8)-TRC-079	9714.4	0.0050079	0.0046566	0.0120462	0.0009803	0.0115400	0.0002536	0.0125032	0.0026350	0.0140718	0.0014115	0.0003578
QST(8)-TRC-080	9715.6	0.0041550	0.0013062	0.0133665	0.0008434	0.0105550	-0.0004893	0.0196610	0.0024095	0.0144700	0.0013286	0.0006523
QST(8)-TRC-081	9718.1	0.0047850	0.0037650	0.0109458	0.0012226	0.0115045	0.0000340	0.0154717	0.0023767	0.0136908	0.0015361	0.0001543
QST(8)-TRC-082	9719.3	0.0048724	0.0021703	0.0109998	0.0013470	0.0099334	0.0002531	0.0159046	0.0017823	0.0155831	0.0013224	0.0004256
QST(8)-TRC-083	9720.1	0.0046055	0.0028755	0.0102196	0.0011279	0.0112327	-0.0000487	0.0168991	0.0024824	0.0146668	0.0014585	0.0003903
QST(8)-TRC-084	9721.1	0.0081610	0.0085802	0.0147506	0.0011047	0.0147240	0.0010049	0.0159767	0.0022925	0.0159639	0.0011333	0.0005598
QST(8)-TRC-085	9722.3	0.0059667	0.0015901	0.0120960	0.0010726	0.0132660	0.0003421	0.0180016	0.0027643	0.0153290	0.0013738	0.0002000
QST(8)-TRC-086	9723.1	0.0059498	0.0036478	0.0126823	0.0008084	0.0113449	-0.0002221	0.0183422	0.0027278	0.0144134	0.0012581	0.0005938
QST(8)-TRC-087	9725.6	0.0043601	0.0064115	0.0115135	0.0010772	0.0116444	0.0010822	0.0391320	0.0024968	0.0113255	0.0010933	0.0003180
QST(8)-TRC-088	9726.3	0.0046796	0.0022218	0.0110053	0.0008935	0.0095640	0.0002473	0.0118939	0.0020475	0.0156778	0.0009166	0.0009670
QST(8)-TRC-089	9727.2	0.0050471	0.0040094	0.0112162	0.0009624	0.0107994	0.0004045	0.0320827	0.0029321	0.0159334	0.0013376	0.0003597
QST(8)-TRC-090	9728.2	0.0053512	0.0000295	0.0119310	0.0011579	0.0130916	-0.0000354	0.0519594	0.0027028	0.0157408	0.0014423	0.0000070
QST(8)-TRC-091	9728.8	0.0031689	0.0027686	0.0142986	0.0012326	0.0109460	-0.0001900	0.0258323	0.0021368	0.0160446	0.0014208	0.0003056
QST(8)-TRC-092	9730.1	0.0064120	0.0045213	0.0125192	0.0010626	0.0142137	0.0004136	0.0254428	0.0025940	0.0158929	0.0011590	0.0006160
QST(8)-TRC-093	9731.3	0.0040336	0.0042023	0.0124726	0.0011846	0.0107888	0.0004648	0.0260353	0.0023540	0.0163106	0.0013726	0.0004933
QST(8)-TRC-094	9732.2	0.0074242	0.0040248	0.0102551	0.0009548	0.0122246	0.0016021	0.0166592	0.0021894	0.0155244	0.0014643	0.0003826
QST(8)-TRC-095	9733.1	0.0046142	-0.0016162	0.0115212	0.0008780	0.0115215	0.0005830	0.0230630	0.0023197	0.0127586	0.0012561	0.0003611
QST(8)-TRC-096	9734.5	0.0081587	0.0011531	0.0114033	0.0010771	0.0124273	-0.0006429	0.0220747	0.0021410	0.0135053	0.0011049	0.0009359
QST(8)-TRC-097	9736.7	0.0073704	0.0038688	0.0111604	0.0010895	0.0126912	-0.0001583	0.0263517	0.0024969	0.0134303	0.0010998	0.0005812
QST(8)-TRC-098	9737.3	0.0070832	-0.0002674	0.0140240	0.0009910	0.0115050	0.0006598	0.0324216	0.0025624	0.0140997	0.0013940	0.0004053
QST(8)-TRC-099	9738.3	0.0089908	0.0001300	0.0134370	0.0009321	0.0128382	0.0008496	0.0275017	0.0023614	0.0151058	0.0013233	0.0006510
QST(8)-TRC-100	9739.5	0.0057742	0.0057386	0.0088769	0.0012033	0.0138487	0.0005143	0.0253424	0.0029615	0.0130133	0.0014440	0.0002744
QST(8)-TRC-101	9740.2	0.0057770	0.0044089	0.0152331	0.0007590	0.0124734	0.0005967	0.0201114	0.0027330	0.0135372	0.0011003	0.0005653
QST(8)-TRC-102	9741.3	0.0026947	0.0017353	0.0099442	0.0009093	0.0126363	0.0001014	0.0150179	0.0023997	0.0134009	0.0013650	0.0001647
QST(8)-TRC-103	9742.6	0.0075390	0.0048063	0.0134189	0.0011423	0.0135031	0.0008506	0.0166738	0.0023225	0.0127810	0.0012200	0.0008235
QST(8)-TRC-104	9743.1	0.0044937	0.0029680	0.0122204	0.0013024	0.0121204	0.0008976	0.0270203	0.0024710	0.0124995	0.0012284	0.0005301
QST(8)-TRC-105	9744.3	0.0079814	0.0049804	0.0097486	0.0009675	0.0125672	0.0010504	0.0240916	0.0028961	0.0145555	0.0011562	0.0005888
QST(8)-TRC-106	9745.3	0.0051546	0.0049218	0.0109177	0.0010535	0.0124044	0.0000567	0.0189564	0.0025707	0.0145067	0.0012283	0.0003444
QST(8)-TRC-107	9746.1	0.0058633	0.0061046	0.0111585	0.0011519	0.0116893	0.0002938	0.0181738	0.0022416	0.0142082	0.0014128	0.0001380

Sample ID	Depth (ft.)	MgKa1	AlKa1	SiKa1
QST(16)-MAJ-001	15145.3	1.6123784	6.6532672	24.9968832
QST(16)-MAJ-002	15146.6	1.6257994	5.8424438	24.8377439
QST(16)-MAJ-003	15147.3	1.4848580	5.4478065	24.6525667
QST(16)-MAJ-004	15148.3	1.6248119	4.8202316	24.1718766
QST(16)-MAJ-005	15149.5	1.8058190	4.8700322	25.1514126
QST(16)-MAJ-006	15150.5	1.5271808	5.4228979	25.7241211
QST(16)-MAJ-007	15151.7	1.5647563	5.7051485	25.3851074
QST(16)-MAJ-008	15153.7	1.3512794	4.8311514	26.7196596
QST(16)-MAJ-009	15154.4	1.5608137	5.1397075	26.2993252
QST(16)-MAJ-010	15155.1	1.4166031	5.0394518	26.4934501
QST(16)-MAJ-011	15156.5	1.4887335	4.9220108	26.7065587
QST(16)-MAJ-012	15157.4	1.3469197	5.2109300	26.9295079
QST(16)-MAJ-013	15158.8	1.3960612	4.9312081	26.0701395
QST(16)-MAJ-014	15159.5	1.5190200	5.4943556	25.8302957
QST(16)-MAJ-015	15160.7	1.4009594	4.1520986	27.0402748
QST(16)-MAJ-016	15161.5	1.8480327	5.3580108	24.4335325
QST(16)-MAJ-017	15162.3	1.6902861	6.5771413	23.8509613
QST(16)-MAJ-018	15163.3	1.7512076	5.5729227	22.5704176
QST(16)-MAJ-019	15164.2	1.8400455	5.4009695	24.3213833
QST(16)-MAJ-020	15164.6	1.8258204	5.8313099	23.3586437
QST(16)-MAJ-021	15166.5	2.0880593	4.1951723	21.2246618
QST(16)-MAJ-022	15167.6	1.7766110	6.1052365	24.0984573
QST(16)-MAJ-023	15168.3	1.6493869	5.4446661	24.3314066
QST(16)-MAJ-024	15169.3	1.9800776	5.7026091	24.6295443
QST(16)-MAJ-025	15170.2	1.6206905	5.3681448	24.7202584
QST(16)-MAJ-026	15171.4	1.4894439	5.6960738	25.8090086
QST(16)-MAJ-027	15172.5	1.7815284	5.6576791	25.6390366
QST(16)-MAJ-028	15173.2	1.5189588	4.5853494	26.5411776
QST(16)-MAJ-029	15174.9	1.8447633	4.3132531	26.5074166
QST(16)-MAJ-030	15175.7	1.4273934	5.5399981	25.5179747
QST(16)-MAJ-031	15176.6	1.8133380	5.9855299	24.8074036
QST(16)-MAJ-032	15177.8	1.5065930	5.1441469	28.3769633
QST(16)-MAJ-033	15178.6	1.7342062	4.5502705	25.6837576

– major elements

P Ka1	S Ka1	K Ka1	CaKa1	BaLa1	TiKa1
0.1478687	0.9445255	2.4192158	5.8187133	0.0664106	0.3509711
0.2061960	1.2221339	2.0978954	6.0566800	0.1955988	0.2915718
0.1287115	1.0104620	2.0307079	6.8284189	0.1249843	0.2851498
0.1729083	0.8649536	1.7500001	7.7319855	0.0730616	0.2754861
0.1813182	1.0540046	1.7191469	7.2525320	0.2721153	0.2483578
0.1745903	0.8606863	1.9130135	5.9867069	0.1427003	0.2801219
0.2315780	1.1484187	2.0091950	5.9585069	0.1047440	0.3040453
0.1632343	0.7021846	1.7612353	6.0991825	0.0235442	0.2722529
0.1519055	0.8865137	1.7154275	5.8055939	0.1255208	0.2744941
0.1830878	0.7259446	1.7375008	5.9196493	0.0442965	0.3001985
0.1422747	0.5386869	1.6566983	5.8699571	0.0182160	0.2532950
0.1206485	0.7166570	1.7817542	5.3838210	0.0398033	0.2648608
0.1360157	0.8334310	1.7386629	5.7987263	0.0393816	0.2873213
0.1549527	0.8162541	2.0113750	5.3308203	0.1245731	0.3027414
0.1255590	0.5363488	1.5055618	6.0331302	0.1102539	0.2044954
0.1503672	0.9090760	1.8821078	6.8803935	0.0943825	0.2755921
0.1552125	0.9528975	2.4884174	6.9124259	0.0729030	0.3285665
0.1820217	1.2119954	2.0127284	8.6657677	0.0825160	0.3143294
0.1575754	1.0339239	1.9595826	7.2304662	0.1444373	0.2699925
0.1239650	1.0097893	2.3321416	7.1461207	0.0648578	0.3160034
0.1181182	0.9036711	1.3126332	11.1356718	0.2459101	0.2335165
0.1356458	0.9116870	2.2561040	6.6693022	0.1468508	0.2873089
0.1497649	1.0037633	1.9514993	6.6728644	0.0789849	0.2935360
0.2131758	1.0729384	2.0466648	5.4820662	0.2404842	0.2528931
0.1748949	1.2893867	1.9547063	5.9098320	0.2624616	0.2709604
0.1171888	0.6342376	2.0859312	5.5438979	0.0231261	0.2765445
0.1715062	0.9716987	2.1084643	5.7926002	0.0563420	0.2782713
0.1435655	0.6668885	1.5878532	6.6489890	-0.0091124	0.2317021
0.1435855	0.6844781	1.4469153	6.8208465	0.0885821	0.2491466
0.1514658	0.8202199	1.9966843	5.5951590	0.0269531	0.3150324
0.1196653	0.8446030	2.2144836	6.4315204	0.0729573	0.2904744
0.0710684	0.6264201	1.6967531	4.0768800	0.0953149	0.2588217
0.1410688	0.6805656	1.6713883	6.1939490	0.1294242	0.2543173

Sample ID	Depth (ft.)	V Ka1	CrKa1	MnKa1
QST(16)-MAJ-001	15145.3	0.0222486	0.0108849	0.0283603
QST(16)-MAJ-002	15146.6	0.0166108	0.0087547	0.0274623
QST(16)-MAJ-003	15147.3	0.0159953	0.0101364	0.0293181
QST(16)-MAJ-004	15148.3	0.0155357	0.0100403	0.0341897
QST(16)-MAJ-005	15149.5	0.0076739	0.0103944	0.0318522
QST(16)-MAJ-006	15150.5	0.0141484	0.0083360	0.0283423
QST(16)-MAJ-007	15151.7	0.0151773	0.0087382	0.0266771
QST(16)-MAJ-008	15153.7	0.0159177	0.0080452	0.0284194
QST(16)-MAJ-009	15154.4	0.0187885	0.0075212	0.0277740
QST(16)-MAJ-010	15155.1	0.0163276	0.0095355	0.0269206
QST(16)-MAJ-011	15156.5	0.0132488	0.0100455	0.0262878
QST(16)-MAJ-012	15157.4	0.0128847	0.0103342	0.0276345
QST(16)-MAJ-013	15158.8	0.0140266	0.0081265	0.0277964
QST(16)-MAJ-014	15159.5	0.0147000	0.0088741	0.0247613
QST(16)-MAJ-015	15160.7	0.0050240	0.0067427	0.0324019
QST(16)-MAJ-016	15161.5	0.0165522	0.0074605	0.0289294
QST(16)-MAJ-017	15162.3	0.0230941	0.0092437	0.0279377
QST(16)-MAJ-018	15163.3	0.0220594	0.0088684	0.0283112
QST(16)-MAJ-019	15164.2	0.0188967	0.0090098	0.0269022
QST(16)-MAJ-020	15164.6	0.0283778	0.0090126	0.0286408
QST(16)-MAJ-021	15166.5	0.0213034	0.0106233	0.0398066
QST(16)-MAJ-022	15167.6	0.0220921	0.0095600	0.0289806
QST(16)-MAJ-023	15168.3	0.0205021	0.0088094	0.0278645
QST(16)-MAJ-024	15169.3	0.0185738	0.0075472	0.0235966
QST(16)-MAJ-025	15170.2	0.0197748	0.0084770	0.0211351
QST(16)-MAJ-026	15171.4	0.0216394	0.0082406	0.0275984
QST(16)-MAJ-027	15172.5	0.0200631	0.0079552	0.0249026
QST(16)-MAJ-028	15173.2	0.0222421	0.0077276	0.0263879
QST(16)-MAJ-029	15174.9	0.0148965	0.0081238	0.0294705
QST(16)-MAJ-030	15175.7	0.0230734	0.0078186	0.0360485
QST(16)-MAJ-031	15176.6	0.0209311	0.0092831	0.0233935
QST(16)-MAJ-032	15177.8	0.0086524	0.0087032	0.0251585
QST(16)-MAJ-033	15178.6	0.0185575	0.0066807	0.0276760

major elements

FeKa1	ZrKa1	Ca/Al	Si/Al	Zr/Al
2.0814183	0.0175647	0.8745648	3.7570839	0.0026400
2.2334575	0.0163342	1.0366689	4.2512594	0.0027958
2.0823508	0.0170058	1.2534254	4.5252280	0.0031216
1.7902778	0.0218854	1.6040693	5.0146712	0.0045403
1.9265752	0.0219047	1.4892164	5.1645270	0.0044979
1.9544211	0.0202797	1.1039682	4.7436116	0.0037396
2.1170830	0.0190681	1.0444087	4.4495086	0.0033423
1.8698370	0.0207067	1.2624697	5.5307022	0.0042861
1.9915606	0.0207860	1.1295573	5.1168915	0.0040442
1.7313868	0.0226769	1.1746614	5.2572087	0.0044999
1.8782224	0.0199606	1.1925933	5.4259448	0.0040554
1.8128914	0.0260537	1.0331785	5.1678890	0.0049998
1.9312990	0.0252237	1.1759241	5.2867652	0.0051151
2.0024970	0.0210595	0.9702358	4.7012421	0.0038329
1.6763406	0.0259714	1.4530316	6.5124357	0.0062550
2.2061076	0.0169936	1.2841321	4.5601873	0.0031716
2.3807437	0.0140550	1.0509773	3.6263416	0.0021369
2.3163019	0.0201596	1.5549772	4.0500144	0.0036174
2.3624166	0.0159192	1.3387349	4.5031514	0.0029475
2.3787903	0.0127920	1.2254743	4.0057284	0.0021937
2.2081733	0.0133420	2.6544016	5.0593064	0.0031803
2.1438573	0.0155990	1.0923905	3.9471784	0.0025550
2.2579573	0.0171009	1.2255783	4.4688519	0.0031409
2.1118085	0.0182914	0.9613260	4.3189958	0.0032075
2.1402002	0.0174456	1.1009077	4.6049910	0.0032498
1.9909516	0.0163019	0.9732841	4.5310173	0.0028619
2.0709261	0.0187894	1.0238474	4.5317233	0.0033210
1.8467811	0.0166421	1.4500507	5.7882563	0.0036294
2.0788894	0.0168819	1.5813694	6.1455742	0.0039140
1.9282649	0.0149781	1.0099568	4.6061342	0.0027036
2.0757218	0.0143225	1.0745114	4.1445626	0.0023929
1.7245263	0.0184333	0.7925279	5.5163594	0.0035834
1.6895765	0.0161595	1.3612266	5.6444464	0.0035513

Sample ID	Depth (ft.)	MgKa1	AlKa1	SiKa1
QST(16)-MAJ-034	15179.7	1.7538846	5.5410029	24.8349837
QST(16)-MAJ-035	15180.5	1.6024349	5.3126745	24.9794033
QST(16)-MAJ-036	15181.3	2.0086094	6.6360187	24.7196524
QST(16)-MAJ-037	15181.7	1.3707715	4.7915947	26.1447133
QST(16)-MAJ-038	15183.5	1.8117147	3.8861555	23.7081861
QST(16)-MAJ-039	15184.7	1.9396916	4.4738556	22.6673628
QST(16)-MAJ-040	15185.5	1.7557096	4.2305164	20.9667077
QST(16)-MAJ-041	15186.5	1.6447643	5.0374594	23.7601907
QST(16)-MAJ-042	15187.5	1.2282876	4.9642036	25.0879834
QST(16)-MAJ-043	15188.2	1.5072308	4.9247804	25.2482697
QST(16)-MAJ-044	15189.6	1.5166157	4.9089380	26.9043108
QST(16)-MAJ-045	15190.5	1.8315114	5.3086043	24.7426262
QST(16)-MAJ-046	15191.8	1.4183008	3.1240397	28.3696277
QST(16)-MAJ-047	15192.7	2.0794978	4.3831216	22.7611420
QST(16)-MAJ-048	15193.2	1.3559883	3.3117860	26.1867631
QST(16)-MAJ-049	15194.5	1.1338729	3.2798962	28.2498173
QST(16)-MAJ-050	15195.5	1.3263886	5.1646748	24.3448097
QST(16)-MAJ-051	15196.4	1.8169256	4.9739292	25.7554952
QST(16)-MAJ-052	15197.8	1.4579221	4.0755892	26.9584717
QST(16)-MAJ-053	15198.4	1.5646289	4.7405888	26.6398165
QST(16)-MAJ-054	15199.7	1.0276373	2.4777708	29.8351578
QST(16)-MAJ-055	15200.9	1.3907347	4.5777095	26.7881266
QST(16)-MAJ-056	15201.7	1.5485603	5.7472279	25.9645241
QST(16)-MAJ-057	15202.8	1.2286219	4.6129901	26.9910850
QST(16)-MAJ-058	15203.3	1.4532234	5.2671169	26.0848437
QST(16)-MAJ-059	15204.5	1.4764249	5.6132126	25.1373979
QST(16)-MAJ-060	15205.3	1.6988849	6.2014005	25.2022973
QST(16)-MAJ-061	15206.6	1.5724551	5.2234003	26.1509339
QST(16)-MAJ-062	15207.3	1.5707285	5.4475350	25.8829691
QST(16)-MAJ-063	15208.5	1.5230579	5.3705588	24.7024930
QST(16)-MAJ-064	15209.3	1.0163013	3.7668005	27.0708955
QST(16)-MAJ-065	15210.7	1.4857495	5.0720334	23.7518815
QST(16)-MAJ-066	15211.3	1.2568909	4.6405668	25.5497558

– major elements

P Ka1	S Ka1	K Ka1	CaKa1	BaLa1	TiKa1
0.1448355	0.7074941	2.0562239	6.5144986	0.0203389	0.2930396
0.1704595	0.7328189	1.9774851	6.4953863	0.0747030	0.2882503
0.1713653	1.0688414	2.5623713	5.4353602	0.1185439	0.3193458
0.1177273	0.7102971	1.6419455	7.2037880	0.0726826	0.2315191
0.1986860	0.6424774	1.1834716	9.8679561	0.1024407	0.2122968
0.2321965	0.9406492	1.4202018	9.3802540	0.1595745	0.2175957
0.3032947	1.1975867	1.4128211	10.7730974	0.0525817	0.2351428
0.1682186	0.8416945	1.9549664	7.1940234	0.1104791	0.2834480
0.0936954	1.0255239	1.7060906	5.7928726	0.2065503	0.2654347
0.2339790	1.0315423	1.8026853	6.7991139	0.2382897	0.2396009
0.2354697	0.9550408	1.7671780	5.2599146	0.1663916	0.2649496
0.2312787	1.0753110	1.9642712	6.8260147	0.1002944	0.2804216
0.1605605	0.6872134	0.9858607	6.4713950	0.1394939	0.1538074
0.1698908	1.1916126	1.5122339	9.5101483	0.1190782	0.2579217
0.0451064	0.6933986	0.9473391	8.4878434	0.1858148	0.1378810
0.1688446	0.9963168	1.1334341	5.4399278	0.1916748	0.2024189
0.1247164	1.0973499	1.7727055	6.0729283	0.2957580	0.2480061
0.1244159	0.7235637	1.8171772	6.4054967	0.1307906	0.2409405
0.1567926	0.6825956	1.4729572	6.0808887	0.0446654	0.2051166
0.1690571	1.1688952	1.6905425	5.8950656	0.1620702	0.2742634
0.0795627	0.4948222	0.6734759	7.7912699	0.0814219	0.1189091
0.1389871	0.7480254	1.4772129	6.4657638	0.1827217	0.1806378
0.1048364	0.8246819	2.0726356	6.0938010	0.0522694	0.2810202
0.1610053	0.5567330	1.7193174	6.2291603	0.0661569	0.2484452
0.2185431	1.1048708	1.8134601	6.0575774	0.1142874	0.2428815
0.2072123	0.8752212	2.0437537	6.4630108	0.0496326	0.3127412
0.1579254	0.8659603	2.2775694	6.2401441	0.0618998	0.2981252
0.2004520	1.2511690	1.8484453	5.8889188	0.1990138	0.2669504
0.2281685	0.8394360	1.9116950	6.3697597	0.0580340	0.2886060
0.1406706	0.8447560	1.9847200	6.6289433	0.1199425	0.2318327
0.3021777	1.4089276	1.2174637	6.1501829	0.3831097	0.2141311
0.1501268	1.8672162	1.7912130	6.4513139	0.2893496	0.2558813
0.1689280	1.1413280	1.7201071	6.7361246	0.0920893	0.2257604

Sample ID	Depth (ft.)	V Ka1	CrKa1	MnKa1
QST(16)-MAJ-034	15179.7	0.0204741	0.0089330	0.0267083
QST(16)-MAJ-035	15180.5	0.0186727	0.0081271	0.0246749
QST(16)-MAJ-036	15181.3	0.0226859	0.0075969	0.0234448
QST(16)-MAJ-037	15181.7	0.0138887	0.0080708	0.0297410
QST(16)-MAJ-038	15183.5	0.0120242	0.0121227	0.0329106
QST(16)-MAJ-039	15184.7	0.0149858	0.0088582	0.0350833
QST(16)-MAJ-040	15185.5	0.0184927	0.0097794	0.0392142
QST(16)-MAJ-041	15186.5	0.0169435	0.0071853	0.0245053
QST(16)-MAJ-042	15187.5	0.0228561	0.0088736	0.0218463
QST(16)-MAJ-043	15188.2	0.0172509	0.0096035	0.0255223
QST(16)-MAJ-044	15189.6	0.0137459	0.0088763	0.0241615
QST(16)-MAJ-045	15190.5	0.0222237	0.0076670	0.0225068
QST(16)-MAJ-046	15191.8	0.0044562	0.0100927	0.0201444
QST(16)-MAJ-047	15192.7	0.0156988	0.0111902	0.0349180
QST(16)-MAJ-048	15193.2	0.0096370	0.0109304	0.0291922
QST(16)-MAJ-049	15194.5	0.0128137	0.0104041	0.0218108
QST(16)-MAJ-050	15195.5	0.0183497	0.0088304	0.0224581
QST(16)-MAJ-051	15196.4	0.0102289	0.0090580	0.0213868
QST(16)-MAJ-052	15197.8	0.0063068	0.0096447	0.0260272
QST(16)-MAJ-053	15198.4	0.0187011	0.0089268	0.0254425
QST(16)-MAJ-054	15199.7	0.0072138	0.0103078	0.0307657
QST(16)-MAJ-055	15200.9	0.0120131	0.0097075	0.0267415
QST(16)-MAJ-056	15201.7	0.0142729	0.0097945	0.0274570
QST(16)-MAJ-057	15202.8	0.0081374	0.0096448	0.0237008
QST(16)-MAJ-058	15203.3	0.0146983	0.0089922	0.0255702
QST(16)-MAJ-059	15204.5	0.0196607	0.0092673	0.0245351
QST(16)-MAJ-060	15205.3	0.0211527	0.0073413	0.0199346
QST(16)-MAJ-061	15206.6	0.0170229	0.0084324	0.0257886
QST(16)-MAJ-062	15207.3	0.0191230	0.0079444	0.0237881
QST(16)-MAJ-063	15208.5	0.0114460	0.0081585	0.0223743
QST(16)-MAJ-064	15209.3	0.0156016	0.0091335	0.0182391
QST(16)-MAJ-065	15210.7	-0.0094161	0.0097003	0.0109689
QST(16)-MAJ-066	15211.3	0.0153284	0.0086853	0.0201020

major elements

FeKa1	ZrKa1	Ca/Al	Si/Al	Zr/Al
1.9268575	0.0178820	1.1756894	4.4820377	0.0032272
1.7732256	0.0175584	1.2226208	4.7018509	0.0033050
2.1945817	0.0150043	0.8190694	3.7250727	0.0022610
1.9387253	0.0171718	1.5034218	5.4563699	0.0035837
2.0995116	0.0180925	2.5392592	6.1006786	0.0046556
2.4272020	0.0123581	2.0966824	5.0666282	0.0027623
2.4410400	0.0148438	2.5465207	4.9560635	0.0035087
1.8004033	0.0140809	1.4281055	4.7167012	0.0027952
1.6746271	0.0210508	1.1669289	5.0537781	0.0042405
1.6688677	0.0207329	1.3805923	5.1267808	0.0042099
1.5633346	0.0240291	1.0714975	5.4806784	0.0048950
1.8115174	0.0171595	1.2858398	4.6608533	0.0032324
1.5434793	0.0144900	2.0714829	9.0810714	0.0046382
2.1413776	0.0180147	2.1697204	5.1929068	0.0041100
1.5453050	0.0182878	2.5629202	7.9071422	0.0055220
1.4266389	0.0317932	1.6585671	8.6130219	0.0096934
1.5944643	0.0214293	1.1758588	4.7137159	0.0041492
1.4930325	0.0190602	1.2878142	5.1780985	0.0038320
1.5498109	0.0229715	1.4920269	6.6146194	0.0056364
1.6381671	0.0180527	1.2435302	5.6195164	0.0038081
1.2013269	0.0136672	3.1444675	12.0411289	0.0055159
1.6010397	0.0206002	1.4124452	5.8518625	0.0045001
1.7392340	0.0233065	1.0603027	4.5177475	0.0040553
1.4629168	0.0196450	1.3503520	5.8511040	0.0042586
1.7461245	0.0199418	1.1500746	4.9523950	0.0037861
1.7231094	0.0216740	1.1513925	4.4782551	0.0038612
1.7461130	0.0198781	1.0062476	4.0639687	0.0032054
1.8027636	0.0187825	1.1274110	5.0064962	0.0035958
1.7894678	0.0193069	1.1692921	4.7513176	0.0035442
1.6983186	0.0205614	1.2343117	4.5996132	0.0038285
1.4283408	0.0202416	1.6327339	7.1867081	0.0053737
1.7195674	0.0215749	1.2719384	4.6829111	0.0042537
1.8526075	0.0159511	1.4515737	5.5057403	0.0034373

Sample ID	Depth (ft.)	MgKa1	AlKa1	SiKa1
QST(16)-MAJ-067	15212.4	1.4806900	3.8794855	26.2088526
QST(16)-MAJ-068	15213.2	1.3289362	4.0241896	20.3884239
QST(16)-MAJ-069	15214.5	1.8242952	5.1996012	24.9685742
QST(16)-MAJ-070	15215.3	1.2538748	4.4028566	26.3224283
QST(16)-MAJ-071	15216.7	1.3374831	4.3038880	24.9970816
QST(16)-MAJ-072	15217.5	1.7194808	3.9729382	24.8128876
QST(16)-MAJ-073	15218.8	1.6980321	4.8448855	24.4283550
QST(16)-MAJ-074	15219.5	1.6380825	4.5162192	26.0640949
QST(16)-MAJ-075	15220.8	1.3577941	4.9991895	22.9256017
QST(16)-MAJ-076	15221.4	1.6439902	5.6606767	24.1367576
QST(16)-MAJ-077	15222.5	1.5715145	4.2366299	26.3322897
QST(16)-MAJ-078	15223.4	1.9667865	6.2012387	24.1187772
QST(16)-MAJ-079	15224.3	1.3805091	4.8768264	26.6416225
QST(16)-MAJ-080	15225.2	1.5169438	5.2872133	25.8325793
QST(16)-MAJ-081	15226.2	1.4247383	4.2032002	28.1319628
QST(16)-MAJ-082	15227.2	1.2251364	4.5622861	26.7935506
QST(16)-MAJ-083	15228.5	1.1876455	5.4375208	26.2280537
QST(16)-MAJ-084	15229.3	1.1270935	3.4215746	29.6475822
QST(16)-MAJ-085	15230.4	1.6222664	4.5717863	26.5938397
QST(16)-MAJ-086	15231.8	1.1817884	3.1138738	26.6144111
QST(16)-MAJ-087	15232.6	1.2683097	4.1046780	27.6586237
QST(16)-MAJ-088	15233.3	1.7656138	5.0964802	23.5307869
QST(16)-MAJ-089	15234.2	1.8772318	6.6103753	23.7276049
QST(16)-MAJ-090	15235.3	1.4636077	5.8064247	23.5114287
QST(16)-MAJ-091	15236.7	1.6947669	5.5084891	24.2096004
QST(16)-MAJ-092	15237.5	1.6412527	7.3691752	26.0045034
QST(16)-MAJ-093	15238.5	2.2920810	4.8492138	18.8430122
QST(16)-MAJ-094	15239.5	1.9564200	4.3366693	22.5669939
QST(16)-MAJ-095	15240.1	2.0924757	4.4993683	22.7961071
QST(16)-MAJ-096	15241.3	2.2712958	2.9566738	16.2332276
QST(16)-MAJ-097	15242.5	2.2028046	3.4934433	19.0597059
QST(16)-MAJ-098	15243.6	1.8068196	5.9372731	24.6939384
QST(16)-MAJ-099	15244.5	1.5414569	4.9881187	24.4323159

– major elements

P Ka1	S Ka1	K Ka1	CaKa1	BaLa1	TiKa1
0.1411846	0.8909470	1.2545833	6.5751981	0.0222196	0.2102339
0.1889571	1.3617594	1.3306765	10.9442440	0.3016058	0.2014476
0.2026700	1.1303917	1.7900473	7.0650452	0.0671311	0.2568024
0.2088359	0.9698411	1.5551131	7.0526186	0.1486287	0.2239913
0.1049695	0.8214922	1.5553226	6.0031224	0.0276911	0.2376600
0.1214683	0.7495705	1.2760925	8.0751545	0.1154965	0.1974270
0.1649353	1.1230182	1.7195659	7.1041515	0.1241786	0.2369457
0.1521805	0.7451652	1.5749882	6.3711758	0.0813872	0.2448467
0.1203810	1.1016918	1.7551901	8.7264309	0.0203919	0.2652039
0.2215082	1.1954926	2.0339494	7.4161881	0.1229052	0.2781721
0.1313944	0.5831555	1.4935882	6.2904695	0.0778037	0.2161162
0.1308690	1.0870023	2.3501403	6.0541575	0.0475708	0.3074693
0.1276609	0.7368067	1.7647880	6.6731864	0.0281851	0.2498911
0.1499996	0.7930621	1.8823144	6.0652123	0.1115619	0.3002765
0.1399857	0.6441463	1.4261837	5.9795388	0.0441985	0.2221977
0.0755924	0.7023569	1.6062091	5.9130992	0.1728221	0.2073764
0.1652721	0.9161471	2.0781174	5.8156962	0.0469587	0.2633022
0.1439955	0.5259276	1.1686869	6.2472543	0.0481890	0.1949786
0.2159582	1.1723136	1.5526804	6.1596859	0.1982275	0.2426921
0.2312454	1.0107296	0.9917194	8.3840875	0.0828927	0.1486272
0.1362797	1.0617652	1.3794810	6.1250111	0.0223353	0.2371238
0.1219516	0.7349472	1.8580801	7.5225185	0.0771455	0.2445070
0.1311344	1.0210777	2.5450794	6.7743396	0.1226950	0.3019359
0.1525694	1.0209817	2.3037772	7.7729568	0.0925623	0.2813636
0.2709385	1.0212911	2.1443432	7.1194787	0.0372380	0.2924213
0.1368374	1.1372970	2.6993658	4.5107982	0.0515862	0.3306030
0.3188752	1.4227141	1.7326348	11.5017997	0.1450620	0.2525658
0.1313436	0.9430294	1.4403362	9.5914401	0.0431322	0.2451380
0.1881648	0.9582373	1.4495943	9.5653434	0.1425751	0.1994120
0.1974849	0.8792891	0.7417105	16.8850018	0.3020492	0.1511386
0.1808339	0.8043913	1.0695120	13.7301964	0.0475857	0.1806540
0.1400355	0.7229185	2.0998640	7.4068108	0.0243881	0.3031604
0.1948262	1.1658122	1.8304861	6.7673785	0.0249907	0.2533985

Sample ID	Depth (ft.)	V Ka1	CrKa1	MnKa1
QST(16)-MAJ-067	15212.4	0.0138304	0.0089586	0.0228460
QST(16)-MAJ-068	15213.2	0.0195084	0.0080970	0.0253728
QST(16)-MAJ-069	15214.5	0.0132243	0.0091202	0.0277930
QST(16)-MAJ-070	15215.3	0.0131619	0.0098153	0.0195388
QST(16)-MAJ-071	15216.7	0.0194799	0.0089144	0.0242614
QST(16)-MAJ-072	15217.5	0.0131663	0.0109695	0.0286638
QST(16)-MAJ-073	15218.8	0.0155587	0.0081276	0.0240598
QST(16)-MAJ-074	15219.5	0.0139268	0.0077995	0.0236617
QST(16)-MAJ-075	15220.8	0.0165942	0.0106286	0.0297694
QST(16)-MAJ-076	15221.4	0.0158071	0.0087823	0.0236018
QST(16)-MAJ-077	15222.5	0.0091532	0.0082117	0.0236800
QST(16)-MAJ-078	15223.4	0.0180299	0.0078753	0.0253646
QST(16)-MAJ-079	15224.3	0.0177531	0.0107276	0.0238998
QST(16)-MAJ-080	15225.2	0.0192431	0.0074743	0.0287915
QST(16)-MAJ-081	15226.2	0.0098158	0.0096153	0.0280343
QST(16)-MAJ-082	15227.2	0.0118806	0.0095551	0.0247091
QST(16)-MAJ-083	15228.5	0.0139861	0.0076352	0.0354783
QST(16)-MAJ-084	15229.3	0.0093536	0.0096467	0.0291369
QST(16)-MAJ-085	15230.4	0.0113131	0.0095715	0.0242920
QST(16)-MAJ-086	15231.8	0.0042029	0.0101233	0.0251764
QST(16)-MAJ-087	15232.6	0.0160199	0.0086107	0.0286288
QST(16)-MAJ-088	15233.3	0.0137287	0.0100975	0.0253395
QST(16)-MAJ-089	15234.2	0.0188124	0.0099363	0.0235672
QST(16)-MAJ-090	15235.3	0.0207442	0.0106880	0.0249281
QST(16)-MAJ-091	15236.7	0.0174440	0.0089832	0.0269348
QST(16)-MAJ-092	15237.5	0.0288610	0.0084929	0.0234659
QST(16)-MAJ-093	15238.5	0.0294416	0.0075493	0.0349307
QST(16)-MAJ-094	15239.5	0.0153187	0.0091462	0.0262982
QST(16)-MAJ-095	15240.1	0.0120012	0.0098964	0.0282523
QST(16)-MAJ-096	15241.3	0.0144276	0.0076752	0.0421950
QST(16)-MAJ-097	15242.5	0.0164355	0.0089065	0.0360842
QST(16)-MAJ-098	15243.6	0.0220747	0.0083704	0.0236178
QST(16)-MAJ-099	15244.5	0.0218570	0.0075948	0.0240385

major elements

FeKa1	ZrKa1	Ca/Al	Si/Al	Zr/Al
1.6921493	0.0213067	1.6948634	6.7557548	0.0054921
1.8384139	0.0195557	2.7196144	5.0664670	0.0048595
1.8559833	0.0174560	1.3587667	4.8020172	0.0033572
1.4894157	0.0267518	1.6018279	5.9784887	0.0060760
1.8721468	0.0157946	1.3948138	5.8080233	0.0036698
1.8159829	0.0214177	2.0325397	6.2454753	0.0053909
1.9822439	0.0198255	1.4663198	5.0420913	0.0040920
1.5583568	0.0150324	1.4107322	5.7712201	0.0033285
1.8769794	0.0166934	1.7455692	4.5858638	0.0033392
1.6284061	0.0207368	1.3101239	4.2639350	0.0036633
1.4167538	0.0211939	1.4847814	6.2153859	0.0050025
2.0912984	0.0172701	0.9762820	3.8893483	0.0027849
1.8563196	0.0196881	1.3683461	5.4629016	0.0040371
1.7902727	0.0195103	1.1471473	4.8858591	0.0036901
1.8654674	0.0214712	1.4226158	6.6929867	0.0051083
1.6086375	0.0201892	1.2960825	5.8728344	0.0044252
1.9595992	0.0200237	1.0695492	4.8235317	0.0036825
1.5853675	0.0265744	1.8258419	8.6648943	0.0077667
1.6679849	0.0254977	1.3473258	5.8169472	0.0055772
1.4692325	0.0185000	2.6924943	8.5470423	0.0059412
1.6590134	0.0145521	1.4922026	6.7383176	0.0035452
2.0040401	0.0163038	1.4760223	4.6170662	0.0031990
1.9830423	0.0148358	1.0248041	3.5894490	0.0022443
1.9635887	0.0144695	1.3386821	4.0492092	0.0024920
1.8513784	0.0152698	1.2924558	4.3949620	0.0027720
2.0727200	0.0141007	0.6121171	3.5288214	0.0019135
2.5402298	0.0148161	2.3718896	3.8857871	0.0030554
1.9628933	0.0156552	2.2117066	5.2037618	0.0036100
2.1029921	0.0161748	2.1259303	5.0665128	0.0035949
2.5220768	0.0129856	5.7108098	5.4903681	0.0043920
2.1138706	0.0152636	3.9302760	5.4558509	0.0043692
1.7358060	0.0155887	1.2475105	4.1591381	0.0026256
2.1347382	0.0195058	1.3566996	4.8981024	0.0039104

Questar 16 XRF – major elements

Sample ID	Depth (ft.)	MgKa1	AlKa1	SiKa1	P Ka1	S Ka1	K Ka1	CaKa1	BaLa1	TiKa1
QST(16)-MAJ-100	15245.5	1.7777568	6.3423260	24.3106580	0.2082598	1.1810016	2.5081542	6.4447971	0.0598205	0.3002514
QST(16)-MAJ-101	15246.7	1.9565723	4.5766735	23.2889067	0.2115104	1.1406519	1.6140356	7.9240916	0.1103062	0.2363760
QST(16)-MAJ-102	15247.3	1.5170990	6.1589791	23.9926011	0.2236011	1.3363702	2.4490683	6.0673844	0.0768832	0.3111940
QST(16)-MAJ-103	15248.4	1.5069537	5.7333496	25.0085084	0.2147443	1.0502756	2.0772332	6.4404967	0.0854331	0.2826805
QST(16)-MAJ-104	15249.4	1.5137165	9.5072793	22.6869390	0.1752405	1.2691771	3.3849137	4.7264671	0.0366086	0.3359732
QST(16)-MAJ-105	15250.6	1.6531849	6.7696478	25.8372937	0.2387277	1.4827983	2.5173222	4.9022021	0.2055915	0.3366162
QST(16)-MAJ-106	15251.8	1.6338514	6.3031003	23.3970342	0.1604537	1.1689128	2.3634784	6.7338601	0.1256649	0.2758838
QST(16)-MAJ-107	15252.3	1.6207755	5.3996311	23.3569305	0.1333773	0.9445712	1.9350155	8.2851493	0.0685441	0.2553853
QST(16)-MAJ-108	15253.2	1.6910867	6.5612401	23.5457168	0.1844303	1.0402376	2.4951068	7.3670616	0.0503157	0.3032194
QST(16)-MAJ-109	15254.7	1.4408229	4.5413829	22.0154047	0.1917102	1.1927134	1.5124769	10.1029479	0.1746396	0.2215088
QST(16)-MAJ-110	15255.7	1.7671998	6.2649950	24.0029499	0.1766303	1.1988699	2.2344315	7.2011869	0.1359482	0.2751806
QST(16)-MAJ-111	15256.5	1.5442827	6.2513377	24.4712783	0.1407578	0.9626825	2.3222800	6.1693297	0.0785580	0.3080840
QST(16)-MAJ-112	15257.3	1.7600659	4.9492751	22.8301768	0.1636503	1.1161149	1.7971043	8.2834228	0.0244704	0.2724942
QST(16)-MAJ-113	15258.6	2.0188476	6.4318028	24.5800238	0.1223455	1.0393625	2.4471871	6.2432005	0.2102957	0.2929610
QST(16)-MAJ-114	15259.2	1.6908210	5.7638046	24.1425330	0.1534905	0.9809333	2.1274776	7.1116923	0.0247149	0.2820517
QST(16)-MAJ-115	15260.5	1.5974109	6.1975958	23.8223468	0.1592416	1.2343683	2.4094540	6.9455643	0.0283748	0.3214141
QST(16)-MAJ-116	15261.8	1.7044783	6.8427156	23.4995302	0.1221540	1.3201771	2.6335280	6.3806462	0.0272556	0.3431689
QST(16)-MAJ-117	15262.8	2.0002715	5.0574643	24.6230948	0.1357912	0.8869129	1.7716179	7.4571997	0.0148969	0.2582997
QST(16)-MAJ-118	15263.9	1.7665156	5.3350193	22.8557791	0.1930526	1.1721289	1.9350452	8.5178361	0.0532675	0.2656063
Max Values		2.2920810	9.5072793	29.8351578	0.3188752	1.8672162	3.3849137	16.8850018	0.3831097	0.3509711
Stdev		0.1582886	0.3913590	0.9695528	0.0704240	0.1470273	0.1495092	0.2389519		0.0154875
(dx/x)^2		0.0047691	0.0016945	0.0010561	0.0487752	0.0062002	0.0019509	0.0002003		0.0019472
d(Ca/Al)/(Ca/Al)		0.0435288								
d(Si/Al)/(Si/Al)		0.0524456								
d(Zr/Al)/(Zr/Al)		0.0432353								
Max Ca/Al		5.7108098								
Max Si/Al		12.0411289								
MaxZr/Al		0.0096934								
d(Ca/Al)		0.2485848								
d(Si/Al)		0.6315042								
d(Zr/Al)		0.0004191								

Sample ID	Depth (ft.)	V Ka1	CrKa1	MnKa1
QST(16)-MAJ-100	15245.5	0.0228696	0.0088830	0.0258466
QST(16)-MAJ-101	15246.7	0.0208326	0.0085708	0.0282547
QST(16)-MAJ-102	15247.3	0.0267448	0.0068414	0.0254472
QST(16)-MAJ-103	15248.4	0.0182556	0.0097833	0.0268048
QST(16)-MAJ-104	15249.4	0.0368320	0.0072027	0.0215300
QST(16)-MAJ-105	15250.6	0.0320796	0.0079875	0.0208424
QST(16)-MAJ-106	15251.8	0.0220141	0.0087833	0.0218710
QST(16)-MAJ-107	15252.3	0.0235853	0.0090323	0.0243356
QST(16)-MAJ-108	15253.2	0.0286253	0.0085685	0.0255286
QST(16)-MAJ-109	15254.7	0.0232010	0.0099852	0.0209824
QST(16)-MAJ-110	15255.7	0.0258288	0.0096440	0.0210925
QST(16)-MAJ-111	15256.5	0.0236881	0.0085282	0.0243294
QST(16)-MAJ-112	15257.3	0.0258410	0.0088205	0.0199703
QST(16)-MAJ-113	15258.6	0.0278665	0.0107967	0.0233965
QST(16)-MAJ-114	15259.2	0.0239321	0.0103820	0.0227694
QST(16)-MAJ-115	15260.5	0.0370181	0.0089684	0.0247540
QST(16)-MAJ-116	15261.8	0.0339226	0.0082523	0.0244494
QST(16)-MAJ-117	15262.8	0.0214457	0.0094459	0.0243345
QST(16)-MAJ-118	15263.9	0.0199485	0.0115087	0.0230474
Max Values		0.0370181	0.0121227	0.0421950
Stdev		0.0041700	0.0029422	0.0041256
(dx/x)^2		0.0126896	0.0589041	0.0095597

major elements

	FeKa1	ZrKa1	Ca/Al	Si/Al	Zr/Al
	2.1756424	0.0162572	1.0161567	3.8330824	0.0025633
	2.1955238	0.0162388	1.7314085	5.0886100	0.0035482
	2.1639761	0.0164369	0.9851283	3.8955484	0.0026688
	2.0991674	0.0188599	1.1233393	4.3619368	0.0032895
	2.5236928	0.0251187	0.4971419	2.3862704	0.0026420
	2.1681996	0.0140655	0.7241443	3.8166378	0.0020777
	2.3985119	0.0138342	1.0683409	3.7119882	0.0021948
	2.0603432	0.0142183	1.5343917	4.3256530	0.0026332
	2.2615217	0.0139044	1.1228154	3.5886077	0.0021192
	2.0041863	0.0169058	2.2246413	4.8477315	0.0037226
	2.2935668	0.0122032	1.1494322	3.8312800	0.0019478
	2.1255701	0.0149274	0.9868815	3.9145667	0.0023879
	2.2998049	0.0128844	1.6736638	4.6128324	0.0026033
	2.1465731	0.0130284	0.9706766	3.8216383	0.0020256
	2.2538671	0.0132622	1.2338538	4.1886453	0.0023009
	2.4624181	0.0123904	1.1206869	3.8438045	0.0019992
	2.5812259	0.0130061	0.9324728	3.4342404	0.0019007
	2.2425227	0.0103553	1.4744938	4.8686640	0.0020475
	2.2849268	0.0126644	1.5965896	4.2841043	0.0023738
	2.5812259	0.0317932	5.7108098	12.0411289	0.0096934
	0.0176753	0.0004203			
	0.0000469	0.0001748			

Questar 16 XRF – trace elements

Sample ID	Depth (ft.)	NiKa1	CuKa1	ZnKa1	ThLa1	RbKa1	U La1	SrKa1	Y Ka1	ZrKa1	NbKa1	MoKa1
QST(16)-TRC-001	15145.3	0.0047981	0.0056539	0.0110415	0.0011348	0.0113030	0.0017892	0.0236852	0.0019813	0.0175647	0.0012395	0.0004467
QST(16)-TRC-002	15146.6	0.0036858	0.0043400	0.0131494	0.0008620	0.0081173	0.0014034	0.0225979	0.0020055	0.0163342	0.0009670	0.0009060
QST(16)-TRC-003	15147.3	0.0056676	0.0075704	0.0127644	0.0006350	0.0077660	0.0006303	0.0264746	0.0025761	0.0170058	0.0012589	0.0003887
QST(16)-TRC-004	15148.3	0.0044040	0.0049695	0.0104149	0.0008744	0.0080153	0.0014209	0.0275514	0.0022254	0.0218854	0.0012338	0.0007517
QST(16)-TRC-005	15149.5	0.0023985	0.0053502	0.0066944	0.0005355	0.0039240	0.0007606	0.0291883	0.0025249	0.0219047	0.0010119	0.0009900
QST(16)-TRC-006	15150.5	0.0018849	0.0076578	0.0096648	0.0008204	0.0089875	0.0001684	0.0231904	0.0023103	0.0202797	0.0010261	0.0007848
QST(16)-TRC-007	15151.7	0.0058990	0.0031307	0.0101282	0.0008733	0.0110866	0.0004779	0.0230261	0.0023962	0.0190681	0.0014487	0.0005162
QST(16)-TRC-008	15153.7	0.0017144	0.0056707	0.0105758	0.0009185	0.0099477	0.0006964	0.0256772	0.0025616	0.0207067	0.0012755	0.0009035
QST(16)-TRC-009	15154.4	0.0032568	0.0022453	0.0090975	0.0007909	0.0080902	0.0008859	0.0201892	0.0020640	0.0207860	0.0014042	0.0007809
QST(16)-TRC-010	15155.1	0.0011016	0.0106841	0.0106775	0.0007020	0.0094269	-0.0001892	0.0256382	0.0029100	0.0226769	0.0012868	0.0008873
QST(16)-TRC-011	15156.5	0.0045583	0.0032598	0.0072515	0.0006110	0.0072026	0.0008953	0.0192894	0.0025757	0.0199606	0.0011111	0.0009731
QST(16)-TRC-012	15157.4	0.0040036	0.0057757	0.0109257	0.0009741	0.0091984	0.0004780	0.0225855	0.0021276	0.0260537	0.0014369	0.0010979
QST(16)-TRC-013	15158.8	0.0100409	0.0047881	0.0091560	0.0008575	0.0074703	0.0011671	0.0214549	0.0022908	0.0252237	0.0013502	0.0014219
QST(16)-TRC-014	15159.5	0.0015898	0.0068745	0.0076184	0.0008127	0.0086883	0.0010741	0.0220383	0.0022221	0.0210595	0.0013456	0.0010325
QST(16)-TRC-015	15160.7	0.0068151	0.0065063	0.0099059	0.0009074	0.0059694	0.0002633	0.0247715	0.0024790	0.0259714	0.0011733	0.0013298
QST(16)-TRC-016	15161.5	0.0070409	0.0035803	0.0139984	0.0006801	0.0101350	0.0005283	0.0289303	0.0028116	0.0169936	0.0013374	0.0006048
QST(16)-TRC-017	15162.3	0.0040523	0.0067214	0.0122681	0.0007608	0.0116742	0.0008213	0.0279283	0.0025203	0.0140550	0.0013673	0.0005791
QST(16)-TRC-018	15163.3	0.0053217	0.0068242	0.0093493	0.0010293	0.0100853	0.0005843	0.0334087	0.0025369	0.0201596	0.0012762	0.0008846
QST(16)-TRC-019	15164.2	0.0031716	0.0076598	0.0158412	0.0011722	0.0104186	0.0002953	0.0256775	0.0024141	0.0159192	0.0013145	0.0005644
QST(16)-TRC-020	15164.6	0.0046178	0.0059769	0.0345829	0.0009821	0.0117654	0.0004937	0.0252717	0.0023890	0.0127920	0.0012618	0.0001771
QST(16)-TRC-021	15166.5	0.0096427	0.0092399	0.0118149	0.0007535	0.0107327	0.0004534	0.0272569	0.0025573	0.0133420	0.0011464	0.0005728
QST(16)-TRC-022	15167.6	0.0017544	0.0050829	0.0091707	0.0009425	0.0095990	-0.0011567	0.0239163	0.0022603	0.0155990	0.0013409	0.0003261
QST(16)-TRC-023	15168.3	0.0041805	0.0045331	0.0107743	0.0008598	0.0114176	0.0002978	0.0230431	0.0024667	0.0171009	0.0013594	0.0004724
QST(16)-TRC-024	15169.3	0.0048217	0.0104132	0.0115392	0.0010033	0.0113626	0.0014881	0.0258118	0.0023923	0.0182914	0.0011616	0.0004432
QST(16)-TRC-025	15170.2	0.0041156	0.0063360	0.0111464	0.0011120	0.0095901	0.0001337	0.0248547	0.0020528	0.0174456	0.0012802	0.0005704
QST(16)-TRC-026	15171.4	0.0060542	0.0036336	0.0099961	0.0010573	0.0096711	0.0007409	0.0204029	0.0020084	0.0163019	0.0014417	0.0005651
QST(16)-TRC-027	15172.5	0.0061077	0.0027111	0.0099432	0.0009029	0.0099827	0.0012806	0.0238313	0.0025496	0.0187894	0.0010947	0.0006476
QST(16)-TRC-028	15173.2	0.0021673	0.0068145	0.0071958	0.0006501	0.0059985	0.0004796	0.0238202	0.0018909	0.0166421	0.0010241	0.0006643

Questar 16 XRF – trace elements

Sample ID	Depth (ft.)	NiKa1	CuKa1	ZnKa1	ThLa1	RbKa1	U La1	SrKa1	Y Ka1	ZrKa1	NbKa1	MoKa1
QST(16)-TRC-029	15174.9	0.0080057	0.0068202	0.0126333	0.0010649	0.0123855	0.0012623	0.0188689	0.0027820	0.0168819	0.0013231	0.0004701
QST(16)-TRC-030	15175.7	0.0049044	0.0070561	0.0093524	0.0008711	0.0076827	0.0013550	0.0257232	0.0026494	0.0149781	0.0011677	0.0007298
QST(16)-TRC-031	15176.6	0.0067480	0.0075955	0.0108011	0.0009868	0.0049664	0.0006468	0.0326898	0.0023568	0.0143225	0.0010024	0.0006955
QST(16)-TRC-032	15177.8	0.0040420	0.0055625	0.0087665	0.0008670	0.0083737	0.0006453	0.0230704	0.0023794	0.0184333	0.0011467	0.0008145
QST(16)-TRC-033	15178.6	0.0035100	0.0040755	0.0074035	0.0008467	0.0094273	0.0012431	0.0250693	0.0025904	0.0161595	0.0010793	0.0006833
QST(16)-TRC-034	15179.7	0.0063840	0.0077080	0.0105818	0.0009434	0.0112237	0.0002198	0.0239360	0.0024954	0.0178820	0.0013146	0.0005410
QST(16)-TRC-035	15180.5	0.0075976	0.0032845	0.0075686	0.0011337	0.0095398	0.0009194	0.0208202	0.0022643	0.0175584	0.0013744	0.0004683
QST(16)-TRC-036	15181.3	0.0052773	0.0051541	0.0095353	0.0010084	0.0075992	0.0010860	0.0237129	0.0018285	0.0150043	0.0011460	0.0005252
QST(16)-TRC-037	15181.7	0.0047040	0.0064183	0.0107347	0.0010782	0.0101667	0.0000599	0.0226083	0.0022145	0.0171718	0.0012803	0.0006556
QST(16)-TRC-038	15183.5	0.0013776	0.0026790	0.0098711	0.0010299	0.0083666	-0.0001564	0.0306951	0.0018096	0.0180925	0.0012370	0.0007866
QST(16)-TRC-039	15184.7	0.0016851	0.0048944	0.0088402	0.0005009	0.0035735	0.0003958	0.0414343	0.0020293	0.0123581	0.0006119	0.0010337
QST(16)-TRC-040	15185.5	0.0082712	0.0041671	0.0083861	0.0007984	0.0095437	0.0010716	0.0331754	0.0019859	0.0148438	0.0011694	0.0007510
QST(16)-TRC-041	15186.5	0.0020870	0.0052985	0.0080537	0.0007699	0.0086125	0.0005831	0.0321724	0.0021894	0.0140809	0.0012686	0.0005709
QST(16)-TRC-042	15187.5	0.0068262	0.0070509	0.0114391	0.0008570	0.0094150	0.0005105	0.0317616	0.0023309	0.0210508	0.0012041	0.0009479
QST(16)-TRC-043	15188.2	0.0046973	0.0042845	0.0111153	0.0007966	0.0085501	0.0005729	0.0262419	0.0022725	0.0207329	0.0013637	0.0008980
QST(16)-TRC-044	15189.6	-0.0015388	0.0062261	0.0070117	0.0005620	0.0088447	0.0009177	0.0237310	0.0026310	0.0240291	0.0014141	0.0006985
QST(16)-TRC-045	15190.5	0.0024203	0.0028601	0.0088924	0.0005128	0.0080056	0.0006907	0.0257304	0.0021694	0.0171595	0.0013379	0.0004646
QST(16)-TRC-046	15191.8	0.0046717	0.0086302	0.0090093	0.0006186	0.0037912	0.0008655	0.0274469	0.0021017	0.0144900	0.0006175	0.0009573
QST(16)-TRC-047	15192.7	0.0016841	0.0031249	0.0100078	0.0008656	0.0074063	0.0008104	0.0277414	0.0020455	0.0180147	0.0011370	0.0007120
QST(16)-TRC-048	15193.2	0.0055002	0.0050092	0.0104014	0.0007284	0.0091608	-0.0002020	0.0255660	0.0023118	0.0182878	0.0013771	0.0009670
QST(16)-TRC-049	15194.5	0.0078817	0.0043863	0.0114246	0.0009415	0.0084612	0.0002282	0.0305258	0.0026345	0.0317932	0.0013351	0.0016846
QST(16)-TRC-050	15195.5	0.0045540	0.0070722	0.0112072	0.0007924	0.0078858	0.0002734	0.0255499	0.0025879	0.0214293	0.0011781	0.0008010
QST(16)-TRC-051	15196.4	0.0021514	0.0059384	0.0100299	0.0008778	0.0093311	0.0004450	0.0287931	0.0021348	0.0190602	0.0010766	0.0007118
QST(16)-TRC-052	15197.8	0.0029893	0.0079301	0.0084991	0.0008029	0.0083085	0.0002720	0.0217975	0.0018597	0.0229715	0.0010758	0.0007933
QST(16)-TRC-053	15198.4	0.0044952	0.0025455	0.0099099	0.0006762	0.0090786	-0.0003272	0.0214515	0.0022063	0.0180527	0.0010405	0.0006043
QST(16)-TRC-054	15199.7	0.0010684	0.0030100	0.0054295	0.0004754	0.0031738	0.0003243	0.0314002	0.0026777	0.0136672	0.0006050	0.0008083
QST(16)-TRC-055	15200.9	0.0046821	0.0062709	0.0084553	0.0007777	0.0087807	0.0004115	0.0256970	0.0024327	0.0206002	0.0013617	0.0007733
QST(16)-TRC-056	15201.7	0.0033689	0.0051871	0.0108541	0.0008824	0.0070310	0.0000464	0.0271952	0.0027460	0.0233065	0.0011876	0.0009210
QST(16)-TRC-057	15202.8	0.0030313	0.0035403	0.0097184	0.0009603	0.0093677	0.0002005	0.0279254	0.0021761	0.0196450	0.0014528	0.0005291
QST(16)-TRC-058	15203.3	0.0044391	0.0019833	0.0084817	0.0006193	0.0093531	0.0012832	0.0287453	0.0026203	0.0199418	0.0013752	0.0007831

Questar 16 XRF – trace elements

Sample ID	Depth (ft.)	NiKa1	CuKa1	ZnKa1	ThLa1	RbKa1	U La1	SrKa1	Y Ka1	ZrKa1	NbKa1	MoKa1
QST(16)-TRC-059	15204.5	0.0045602	0.0040724	0.0104498	0.0006766	0.0081054	0.0010102	0.0253424	0.0026370	0.0216740	0.0012758	0.0012793
QST(16)-TRC-060	15205.3	0.0009960	0.0050134	0.0089355	0.0006765	0.0096232	-0.0001845	0.0252115	0.0026864	0.0198781	0.0011781	0.0009283
QST(16)-TRC-061	15206.6	0.0040816	0.0022943	0.0083265	0.0007753	0.0088730	-0.0007614	0.0290086	0.0021587	0.0187825	0.0011359	0.0005160
QST(16)-TRC-062	15207.3	0.0027133	0.0031664	0.0108683	0.0008462	0.0106291	0.0010085	0.0249986	0.0023590	0.0193069	0.0013222	0.0006870
QST(16)-TRC-063	15208.5	0.0079939	0.0078375	0.0102778	0.0009218	0.0109974	0.0008185	0.0298108	0.0022977	0.0205614	0.0012911	0.0009080
QST(16)-TRC-064	15209.3	0.0041183	0.0085010	0.0110212	0.0008726	0.0102590	0.0016998	0.0455578	0.0024534	0.0202416	0.0014926	0.0007251
QST(16)-TRC-065	15210.7	0.0018203	0.0049357	0.0085841	0.0007906	0.0070036	0.0007362	0.0314899	0.0022234	0.0215749	0.0009265	0.0009754
QST(16)-TRC-066	15211.3	0.0025001	0.0040513	0.0077382	0.0006608	0.0086277	0.0011941	0.0336207	0.0023022	0.0159511	0.0012737	0.0005357
QST(16)-TRC-067	15212.4	0.0059347	0.0065690	0.0100240	0.0007538	0.0091448	0.0001716	0.0328470	0.0028625	0.0213067	0.0015660	0.0007469
QST(16)-TRC-068	15213.2	0.0073233	0.0054075	0.0114230	0.0007261	0.0059357	0.0003542	0.0386809	0.0024235	0.0195557	0.0008631	0.0013073
QST(16)-TRC-069	15214.5	0.0066239	0.0086661	0.0127367	0.0007538	0.0093083	-0.0002266	0.0298067	0.0021725	0.0174560	0.0013086	0.0008549
QST(16)-TRC-070	15215.3	0.0044454	0.0050529	0.0089195	0.0007835	0.0064013	0.0001439	0.0363659	0.0026720	0.0267518	0.0011417	0.0018236
QST(16)-TRC-071	15216.7	0.0011421	0.0007458	0.0072114	0.0005947	0.0057983	0.0001641	0.0349330	0.0021856	0.0157946	0.0010392	0.0006502
QST(16)-TRC-072	15217.5	0.0081003	0.0075246	0.0106868	0.0010022	0.0066260	0.0002074	0.0369037	0.0018173	0.0214177	0.0009233	0.0013091
QST(16)-TRC-073	15218.8	0.0041044	0.0088140	0.0096151	0.0006770	0.0063721	0.0003239	0.0362370	0.0020173	0.0198255	0.0010028	0.0011339
QST(16)-TRC-074	15219.5	0.0046100	0.0076824	0.0075064	0.0006003	0.0046814	0.0005161	0.0347490	0.0018146	0.0150324	0.0008946	0.0011701
QST(16)-TRC-075	15220.8	0.0023254	0.0064482	0.0099441	0.0008322	0.0085620	0.0003714	0.0313303	0.0024870	0.0166934	0.0014032	0.0004174
QST(16)-TRC-076	15221.4	0.0029725	0.0020541	0.0089046	0.0006746	0.0088571	0.0001075	0.0370328	0.0020091	0.0207368	0.0013248	0.0005549
QST(16)-TRC-077	15222.5	0.0054435	0.0057387	0.0085309	0.0007266	0.0084440	0.0011363	0.0271298	0.0022050	0.0211939	0.0012627	0.0006897
QST(16)-TRC-078	15223.4	0.0046087	0.0057357	0.0095238	0.0008278	0.0105099	0.0008059	0.0210983	0.0022373	0.0172701	0.0014166	0.0008280
QST(16)-TRC-079	15224.3	0.0059451	0.0047769	0.0113244	0.0008238	0.0111387	0.0011573	0.0220075	0.0026074	0.0196881	0.0013095	0.0005601
QST(16)-TRC-080	15225.2	0.0035520	0.0065136	0.0082787	0.0008622	0.0120175	-0.0003667	0.0212869	0.0028636	0.0195103	0.0014114	0.0007642
QST(16)-TRC-081	15226.2	0.0028486	0.0063234	0.0082035	0.0009469	0.0083977	0.0002934	0.0238443	0.0023815	0.0214712	0.0013948	0.0009622
QST(16)-TRC-082	15227.2	0.0043904	0.0065214	0.0117146	0.0008747	0.0105019	0.0004153	0.0236961	0.0021281	0.0201892	0.0012005	0.0009397
QST(16)-TRC-083	15228.5	0.0054476	0.0053043	0.0098796	0.0013833	0.0129178	0.0006457	0.0284440	0.0020356	0.0200237	0.0016700	0.0005455
QST(16)-TRC-084	15229.3	0.0060143	0.0055761	0.0296176	0.0007255	0.0091348	0.0006771	0.0297893	0.0024773	0.0265744	0.0013521	0.0012604
QST(16)-TRC-085	15230.4	0.0022313	0.0061669	0.0157881	0.0009764	0.0056628	0.0017972	0.0321139	0.0025153	0.0254977	0.0009246	0.0013979
QST(16)-TRC-086	15231.8	0.0002873	0.0071235	0.0090061	0.0010889	0.0112103	0.0019534	0.0321729	0.0022692	0.0185000	0.0015850	0.0007592
QST(16)-TRC-087	15232.6	0.0041192	0.0055231	0.0063747	0.0006620	0.0061849	0.0001703	0.0312224	0.0016812	0.0145521	0.0011455	0.0006350

Questar 16 XRF – trace elements

Sample ID	Depth (ft.)	NiKa1	CuKa1	ZnKa1	ThLa1	RbKa1	U La1	SrKa1	Y Ka1	ZrKa1	NbKa1	MoKa1
QST(16)-TRC-088	15233.3	0.0063462	0.0027151	0.0179580	0.0009264	0.0103671	0.0001838	0.0266899	0.0020998	0.0163038	0.0011264	0.0007248
QST(16)-TRC-089	15234.2	0.0070497	0.0082786	0.0137357	0.0010618	0.0134396	0.0002247	0.0243444	0.0020238	0.0148358	0.0012063	0.0008285
QST(16)-TRC-090	15235.3	0.0064336	0.0050179	0.0153142	0.0009835	0.0115986	0.0004127	0.0288204	0.0028483	0.0144695	0.0013218	0.0004809
QST(16)-TRC-091	15236.7	0.0051433	0.0061329	0.0112976	0.0012403	0.0115035	0.0003791	0.0304105	0.0022676	0.0152698	0.0014087	0.0007925
QST(16)-TRC-092	15237.5	0.0067600	0.0058647	0.0134392	0.0008993	0.0099451	0.0006395	0.0247356	0.0023551	0.0141007	0.0012166	0.0008202
QST(16)-TRC-093	15238.5	0.0025755	0.0043978	0.0063588	0.0004994	0.0052595	0.0006187	0.0337212	0.0020970	0.0148161	0.0010381	0.0007331
QST(16)-TRC-094	15239.5	0.0045827	0.0036160	0.0098818	0.0008626	0.0068039	0.0008048	0.0300685	0.0022532	0.0156552	0.0013016	0.0011339
QST(16)-TRC-095	15240.1	0.0065517	0.0075992	0.0104795	0.0007809	0.0079519	0.0001668	0.0296774	0.0020421	0.0161748	0.0012229	0.0007206
QST(16)-TRC-096	15241.3	0.0037548	0.0027277	0.0059577	0.0003665	0.0040779	0.0012099	0.0332715	0.0016171	0.0129856	0.0009776	0.0005223
QST(16)-TRC-097	15242.5	0.0019877	0.0037771	0.0083498	0.0006311	0.0053132	0.0008652	0.0360612	0.0022071	0.0152636	0.0010647	0.0009880
QST(16)-TRC-098	15243.6	0.0069566	0.0072492	0.0117742	0.0008246	0.0100411	0.0002035	0.0238867	0.0020786	0.0155887	0.0012620	0.0006135
QST(16)-TRC-099	15244.5	0.0063413	0.0059087	0.0121314	0.0009578	0.0095330	0.0005549	0.0321483	0.0024777	0.0195058	0.0014215	0.0006849
QST(16)-TRC-100	15245.5	0.0053057	0.0056995	0.0117612	0.0007625	0.0097591	0.0002830	0.0259889	0.0023484	0.0162572	0.0013679	0.0004504
QST(16)-TRC-101	15246.7	0.0082937	0.0090230	0.0122204	0.0009808	0.0091913	0.0012788	0.0335924	0.0025084	0.0162388	0.0014026	0.0008771
QST(16)-TRC-102	15247.3	0.0088705	0.0083327	0.0125993	0.0013686	0.0120094	-0.0000531	0.0288892	0.0025005	0.0164369	0.0014597	0.0005588
QST(16)-TRC-103	15248.4	0.0065369	0.0097615	0.0103474	0.0009595	0.0113211	0.0010302	0.0256582	0.0024162	0.0188599	0.0014093	0.0007596
QST(16)-TRC-104	15249.4	0.0018526	0.0067255	0.0081432	0.0010153	0.0099500	0.0007482	0.0316957	0.0025303	0.0251187	0.0011012	0.0014015
QST(16)-TRC-105	15250.6	0.0030760	0.0053581	0.0147090	0.0007812	0.0122430	0.0009042	0.0269275	0.0024923	0.0140655	0.0013355	0.0005820
QST(16)-TRC-106	15251.8	0.0035794	0.0055933	0.0174921	0.0013897	0.0122322	0.0003353	0.0241485	0.0025256	0.0138342	0.0012586	0.0005570
QST(16)-TRC-107	15252.3	0.0056979	0.0069290	0.0135680	0.0011648	0.0116572	0.0012117	0.0372696	0.0022866	0.0142183	0.0015359	0.0002300
QST(16)-TRC-108	15253.2	0.0038783	0.0110321	0.0135086	0.0010342	0.0112722	0.0011209	0.0279986	0.0024084	0.0139044	0.0011531	0.0005342
QST(16)-TRC-109	15254.7	0.0057619	0.0016172	0.0120226	0.0008069	0.0073829	0.0006115	0.0310634	0.0025128	0.0169058	0.0011897	0.0013131
QST(16)-TRC-110	15255.7	0.0049730	0.0022133	0.0149578	0.0008294	0.0097630	0.0000043	0.0228647	0.0021969	0.0122032	0.0011500	0.0004637
QST(16)-TRC-111	15256.5	0.0093020	0.0093163	0.0113953	0.0010340	0.0138634	0.0009595	0.0323768	0.0025922	0.0149274	0.0013734	0.0010071
QST(16)-TRC-112	15257.3	0.0068603	0.0057971	0.0120348	0.0010051	0.0116934	0.0003182	0.0233880	0.0021748	0.0128844	0.0012418	0.0007293
QST(16)-TRC-113	15258.6	0.0041911	0.0060058	0.0120205	0.0011796	0.0105617	0.0008551	0.0310231	0.0021698	0.0130284	0.0014026	0.0007800
QST(16)-TRC-114	15259.2	0.0092566	0.0066219	0.0105342	0.0010919	0.0098786	0.0008605	0.0233957	0.0021109	0.0132622	0.0012707	0.0009799
QST(16)-TRC-115	15260.5	0.0057813	0.0093925	0.0159722	0.0009326	0.0123552	0.0003827	0.0251189	0.0025405	0.0123904	0.0011126	0.0007270
QST(16)-TRC-116	15261.8	0.0057011	0.0069801	0.0122963	0.0012894	0.0116989	0.0010922	0.0206400	0.0020012	0.0130061	0.0012265	0.0008086
QST(16)-TRC-117	15262.8	0.0054354	0.0079889	0.0151130	0.0007033	0.0091392	0.0011548	0.0243326	0.0024529	0.0103553	0.0011906	0.0008997
QST(16)-TRC-118	15263.9	0.0056720	0.0064433	0.0113379	0.0009469	0.0108016	0.0007152	0.0270112	0.0019184	0.0126644	0.0011897	0.0006288

RGU-1 top half major elements

Sample ID	Depth (ft.)	MgKa1	AlKa1	SiKa1	P Ka1	S Ka1	K Ka1	CaKa1
RGU(T)-MAJ-001	926.0	1.3671014	5.6240665	23.4135594	0.0407264	0.4210239	1.7990630	4.0913374
RGU(T)-MAJ-002	923.7	0.9146379	4.6472371	20.3080453	0.0683032	0.4730264	1.5988876	6.9961515
RGU(T)-MAJ-003	947.3	1.7276048	5.4520925	22.5872574	0.0612535	0.6659504	1.8353389	6.2150354
RGU(T)-MAJ-004	944.2	1.4643919	5.6015185	22.4461200	0.0947362	1.1765899	1.8174074	5.0167430
RGU(T)-MAJ-005	941.5	1.5152413	5.7397748	22.7361845	0.0623136	0.8108168	1.8896055	5.5982127
RGU(T)-MAJ-006	938.2	1.7586387	5.2199659	22.1609328	0.0921983	0.4347979	1.8003836	6.5577897
RGU(T)-MAJ-007	935.2	1.6200118	5.3953383	22.9987290	0.0614400	0.4963079	1.7662677	5.3532934
RGU(T)-MAJ-008	932.4	1.4692798	5.6475202	22.5743720	0.0503843	0.4543823	1.8797232	5.1827577
RGU(T)-MAJ-009	929.5	1.4462606	5.4475988	22.7858561	0.1038988	0.6496825	1.7926180	6.1254183
RGU(T)-MAJ-010	926.7	1.3572500	5.1441836	21.1069112	0.0602135	0.6260714	1.6396755	8.3772020
RGU(T)-MAJ-011	923.2	1.3031438	5.1681356	21.1147818	0.0986267	0.6582382	1.6458367	8.1505298
RGU(T)-MAJ-012	920.8	1.4017028	5.1694678	22.4315488	0.0501556	0.5981432	1.7684606	6.9184050
RGU(T)-MAJ-013	917.3	1.4733769	5.3817084	23.1999748	0.0699634	0.5834304	1.7769289	5.5240787
RGU(T)-MAJ-014	914.2	1.5236936	4.7475112	20.2938758	0.0476926	0.8222224	1.5504620	9.2733503
RGU(T)-MAJ-015	911.6	1.4746957	5.0423309	20.8878184	0.0779537	0.8530418	1.6906234	7.6897363
RGU(T)-MAJ-016	911.5	0.9191433	2.8828944	27.0223156	0.0309700	0.3873001	1.1840990	4.2385117
RGU(T)-MAJ-017	908.5	1.3519838	4.7600987	19.4663666	0.0584188	0.9454917	1.4991667	10.3131389
RGU(T)-MAJ-018	905.5	1.3576725	4.9728648	19.8785659	0.0829175	0.8787771	1.5469699	9.4951257
RGU(T)-MAJ-019	902.2	1.3830108	5.2110017	21.6438697	0.0457423	0.9113843	1.9219515	5.0290073
RGU(T)-MAJ-020	899.3	1.5986216	5.5742543	22.4509531	0.0573110	0.7250026	1.8413886	6.1994390
RGU(T)-MAJ-021	896.8	1.3529211	5.4630130	21.8810562	0.0672512	0.9908938	1.7699135	7.4756276
RGU(T)-MAJ-022	893.7	1.4866129	4.0991244	18.7695580	0.0916267	0.8790612	1.4126364	10.8240942
RGU(T)-MAJ-023	890.2	1.5525315	5.7571982	23.2975701	0.0963536	1.0872402	1.9285585	5.1750379
RGU(T)-MAJ-024	887.4	1.4203713	5.3226039	21.2972910	0.0797372	0.8205537	1.7100721	8.2164874
RGU(T)-MAJ-025	884.6	1.5311337	5.6342088	22.6061180	0.0590208	0.6193228	1.8334438	5.9596848
RGU(T)-MAJ-026	881.2	1.4623983	5.5858669	22.3372910	0.0491751	0.7638294	1.8043990	6.0532411
RGU(T)-MAJ-027	880.2	0.0879243	8.9586047	20.2892072	-0.0273289	0.2038922	0.8382991	0.2158925
RGU(T)-MAJ-028	878.6	1.3661945	5.2718803	22.8872777	0.0406755	0.7757861	1.7273632	5.6949183
RGU(T)-MAJ-029	875.4	1.4191009	4.4936258	19.0341501	0.0764349	0.9630894	1.4595032	10.6626236

RGU-1 top half major elements

Sample ID	Depth (ft.)	BaLa1	TiKa1	V Ka1
RGU(T)-MAJ-001	926.0	-0.0473366	0.3083519	0.0190974
RGU(T)-MAJ-002	923.7	-0.0992864	0.2748062	0.0149974
RGU(T)-MAJ-003	947.3	-0.0536707	0.3140306	0.0153552
RGU(T)-MAJ-004	944.2	-0.0601048	0.3011024	0.0161057
RGU(T)-MAJ-005	941.5	-0.0260673	0.2905354	0.0130861
RGU(T)-MAJ-006	938.2	-0.0326771	0.2768256	0.0111494
RGU(T)-MAJ-007	935.2	-0.0789441	0.3066177	0.0163709
RGU(T)-MAJ-008	932.4	-0.0553382	0.3048271	0.0199192
RGU(T)-MAJ-009	929.5	-0.0325773	0.2822102	0.0108428
RGU(T)-MAJ-010	926.7	-0.0400324	0.2637895	0.0124526
RGU(T)-MAJ-011	923.2	-0.0552215	0.2780279	0.0145737
RGU(T)-MAJ-012	920.8	-0.0295229	0.2624887	0.0067972
RGU(T)-MAJ-013	917.3	-0.0420878	0.2839481	0.0117364
RGU(T)-MAJ-014	914.2	-0.0165925	0.2439077	0.0168022
RGU(T)-MAJ-015	911.6	-0.0389058	0.2697211	0.0199754
RGU(T)-MAJ-016	911.5	-0.0520182	0.2090121	0.0010038
RGU(T)-MAJ-017	908.5	-0.0616802	0.2520652	0.0119899
RGU(T)-MAJ-018	905.5	-0.0918810	0.2810536	0.0209082
RGU(T)-MAJ-019	902.2	-0.0412987	0.3124220	0.0155796
RGU(T)-MAJ-020	899.3	-0.0533595	0.3060063	0.0175668
RGU(T)-MAJ-021	896.8	-0.0572919	0.2881242	0.0143173
RGU(T)-MAJ-022	893.7	-0.0565318	0.2553399	0.0161904
RGU(T)-MAJ-023	890.2	-0.0347014	0.2867380	0.0123606
RGU(T)-MAJ-024	887.4	-0.0350168	0.2662358	0.0131214
RGU(T)-MAJ-025	884.6	-0.0825292	0.3011919	0.0174467
RGU(T)-MAJ-026	881.2	-0.0384309	0.2765518	0.0107512
RGU(T)-MAJ-027	880.2	-0.1388330	0.1962004	0.0114122
RGU(T)-MAJ-028	878.6	-0.0180534	0.2621123	0.0091358
RGU(T)-MAJ-029	875.4	-0.0948878	0.2681529	0.0165512

CrKa1	MnKa1	FeKa1
0.0017933	0.0189576	2.5850843
0.0051024	0.0236611	2.5903860
0.0030398	0.0225001	2.9493570
0.0023465	0.0226199	3.4125241
0.0031651	0.0227617	2.8075594
0.0035129	0.0262684	2.7366818
0.0024082	0.0216038	2.8220901
0.0024120	0.0219021	2.8404208
0.0043154	0.0217185	2.7433599
0.0043879	0.0203457	2.5610110
0.0021982	0.0226323	2.5839948
0.0056350	0.0247508	2.6113417
0.0038622	0.0223791	2.6446963
0.0034767	0.0209939	2.5042444
0.0027211	0.0240354	2.6410183
0.0016360	0.0159866	1.4296180
0.0049577	0.0236196	2.6546910
0.0040699	0.0194811	2.6855741
0.0036970	0.0202931	2.9398365
0.0026100	0.0207118	2.6070449
0.0044858	0.0165321	2.6549292
0.0023934	0.0176339	2.5045243
0.0032568	0.0239195	2.8866050
0.0047346	0.0207223	2.5265583
0.0019458	0.0173380	2.5554004
0.0028446	0.0220540	2.5266350
-0.0024753	0.0106971	1.2631979
0.0031710	0.0197910	2.5026792
0.0039988	0.0212693	2.7186542

RGU-1 top half major elements

Sample ID	Depth (ft.)	MgKa1	AlKa1	SiKa1	P Ka1	S Ka1	K Ka1	CaKa1
RGU(T)-MAJ-030	872.1	1.7296056	5.9514032	23.2830475	0.0556149	0.9033603	1.9730016	4.7225818
RGU(T)-MAJ-031	*	1.5560183	6.1882363	24.1868475	0.1153073	0.8986586	2.2732800	5.5087308
RGU(T)-MAJ-032	*	1.4875207	6.3079344	23.3889815	0.1563333	0.9925487	2.1564335	7.2454394
RGU(T)-MAJ-033	*	1.6943352	5.4599919	20.7080247	0.1591749	1.0041031	1.8542356	10.0963902
RGU(T)-MAJ-034	*	1.5024961	5.2173731	21.0832937	0.2069315	1.1541094	1.8341005	10.2106638
RGU(T)-MAJ-035	859.1	1.6217722	3.8769985	17.3313544	0.0999549	0.7615501	1.3110670	12.4252038
RGU(T)-MAJ-036	856.5	1.2880162	5.3843160	22.3961168	0.0472416	0.7323952	1.7752534	6.5045891
RGU(T)-MAJ-037	853.1	1.8047099	4.1042781	18.2791274	0.0904710	0.9398512	1.3521382	11.1258040
RGU(T)-MAJ-038	850.1	1.2955799	5.8077388	23.2049746	0.0491018	0.7917972	1.8524669	4.8462766
RGU(T)-MAJ-039	847.0	1.6060656	5.9322578	22.7819701	0.0855575	0.8937119	1.8622044	5.2641677
RGU(T)-MAJ-040	844.5	1.6895537	5.1038222	21.3157557	0.0115943	0.9943133	1.6335253	7.4323098
RGU(T)-MAJ-041	841.2	1.4249246	4.6767646	20.2318034	0.0467419	1.0172474	1.5231038	9.6796833
RGU(T)-MAJ-042	838.4	1.3235214	5.1151435	21.2876153	0.0881264	1.2059802	1.5989455	7.5088416
RGU(T)-MAJ-043	835.7	1.3011063	4.8243339	20.3179668	0.0157008	1.0221935	1.5367301	8.7978642
RGU(T)-MAJ-044	831.9	1.4938644	5.5914344	22.2377036	0.0372808	1.3431192	1.7417809	6.8115519
RGU(T)-MAJ-045	829.9	1.6960589	4.7233655	18.6504786	0.0171744	1.0331028	1.4460942	11.3497665
RGU(T)-MAJ-046	826.5	1.3770328	4.2877647	18.0604662	0.0323204	0.8342495	1.3699795	11.7324873
RGU(T)-MAJ-047	823.6	1.4520366	5.9007263	23.4830975	0.0610437	0.6642334	1.9105833	5.2727350
RGU(T)-MAJ-048	821.9	1.0854381	4.7096883	23.5530262	0.0039094	0.5527691	1.6364224	6.8747812
RGU(T)-MAJ-049	821.4	0.9992887	6.2066095	23.3459937	0.0218889	0.3362602	0.9413253	1.4165977
RGU(T)-MAJ-050	820.7	0.8671077	6.8867152	22.4863005	-0.0196094	0.0797849	0.6532697	0.6832957
RGU(T)-MAJ-051	816.7	0.6618218	5.0329961	25.8345500	-0.0232368	0.0457127	0.2543822	0.3943421
RGU(T)-MAJ-052	813.2	1.4250210	5.3490689	22.1061359	0.0234398	0.7707150	1.5943672	7.0556438
RGU(T)-MAJ-053	810.5	1.7014281	3.8168678	16.9511042	0.1608669	0.5442915	1.2035464	13.2865427
RGU(T)-MAJ-054	807.5	1.3615236	3.6394065	16.2449850	0.0665643	0.7865878	1.1983315	13.9403736
RGU(T)-MAJ-055	804.5	1.4428652	4.9532152	19.7814055	0.0273859	0.8322358	1.4856563	9.7382608
RGU(T)-MAJ-056	800.5	1.3017422	5.3290879	22.0094167	0.0509907	0.8558735	1.6167561	7.1074425
RGU(T)-MAJ-057	797.3	1.4583190	5.2870913	21.5429269	0.0520397	1.2365298	1.5529275	7.2604988
RGU(T)-MAJ-058	794.2	1.3191721	4.6313455	20.9447815	0.0176989	1.0268185	1.4406843	8.5157810

RGU-1 top half major elements

Sample ID	Depth (ft.)	BaLa1	TiKa1	V Ka1
RGU(T)-MAJ-030	872.1	-0.0616251	0.3269047	0.0178382
RGU(T)-MAJ-031	*	0.0413083	0.3153431	0.0232692
RGU(T)-MAJ-032	*	0.0238414	0.3182288	0.0219072
RGU(T)-MAJ-033	*	0.0037843	0.2781701	0.0204269
RGU(T)-MAJ-034	*	0.0305719	0.2629877	0.0161800
RGU(T)-MAJ-035	859.1	-0.0418816	0.2115220	0.0132543
RGU(T)-MAJ-036	856.5	-0.0246734	0.2652040	0.0074748
RGU(T)-MAJ-037	853.1	-0.0442386	0.2445719	0.0135915
RGU(T)-MAJ-038	850.1	-0.0603997	0.3026858	0.0174913
RGU(T)-MAJ-039	847.0	-0.0420542	0.3145193	0.0137326
RGU(T)-MAJ-040	844.5	-0.0387952	0.2610785	0.0162682
RGU(T)-MAJ-041	841.2	-0.0766471	0.2654204	0.0184901
RGU(T)-MAJ-042	838.4	-0.0717059	0.2897861	0.0196117
RGU(T)-MAJ-043	835.7	0.0091543	0.2300043	0.0105891
RGU(T)-MAJ-044	831.9	-0.0084446	0.2781378	0.0185996
RGU(T)-MAJ-045	829.9	-0.0528953	0.2270896	0.0162761
RGU(T)-MAJ-046	826.5	-0.0371403	0.2109163	0.0128718
RGU(T)-MAJ-047	823.6	0.0041691	0.2501612	0.0144724
RGU(T)-MAJ-048	821.9	-0.0591515	0.2348143	0.0107330
RGU(T)-MAJ-049	821.4	0.0280287	0.5039153	0.0045751
RGU(T)-MAJ-050	820.7	-0.0759011	0.2156003	0.0100281
RGU(T)-MAJ-051	816.7	-0.0673533	0.1472303	0.0014353
RGU(T)-MAJ-052	813.2	-0.0448514	0.2492006	0.0133298
RGU(T)-MAJ-053	810.5	-0.1031166	0.2112443	0.0136404
RGU(T)-MAJ-054	807.5	-0.0582712	0.2086594	0.0174642
RGU(T)-MAJ-055	804.5	-0.0776083	0.2629738	0.0162269
RGU(T)-MAJ-056	800.5	-0.0563147	0.2768857	0.0166078
RGU(T)-MAJ-057	797.3	-0.0481882	0.2560613	0.0163222
RGU(T)-MAJ-058	794.2	-0.0579159	0.2331419	0.0102877

	CrKa1	MnKa1	FeKa1
	0.0030944	0.0193159	2.9644760
	0.0065469	0.0261985	2.5784830
	0.0077978	0.0282481	2.5776504
	0.0092270	0.0255491	2.5622641
	0.0101099	0.0276703	2.4489992
	0.0037508	0.0251671	2.7800047
	0.0047242	0.0236363	2.3022956
	0.0026950	0.0217269	2.6218467
	0.0032319	0.0194675	2.4595752
	0.0027307	0.0184717	2.5605952
	0.0029182	0.0200147	2.4232414
	0.0038414	0.0177365	2.3975063
	0.0041094	0.0165135	2.4706247
	0.0037488	0.0157367	2.2617395
	0.0043522	0.0172635	2.7442652
	0.0047585	0.0192847	2.3088624
	0.0043890	0.0206643	2.1989734
	0.0031576	0.0154364	2.2840179
	0.0048007	0.0142227	1.8886816
	-0.0012562	0.0108671	2.1327272
	-0.0007909	0.0235835	1.7887372
	-0.0014459	0.0133595	1.6708318
	0.0035076	0.0138886	2.3411584
	0.0033611	0.0317861	2.4785799
	0.0015282	0.0168536	2.2001706
	0.0060003	0.0130334	2.3906729
	0.0034179	0.0134505	2.3944193
	0.0033853	0.0125497	2.6319090
	0.0049232	0.0188860	2.3585426

RGU-1 top half major elements

Sample ID	Depth (ft.)	MgKa1	AlKa1	SiKa1	P Ka1	S Ka1	K Ka1	CaKa1
RGU(T)-MAJ-059	791.7	1.2408467	4.1205532	19.2215581	0.0255203	1.1390614	1.2410339	10.2381598
RGU(T)-MAJ-060	788.2	1.2862906	5.3255822	22.7403774	0.0190904	0.7584765	1.7013584	6.2770953
RGU(T)-MAJ-061	785.2	1.2608047	5.1633285	21.9433606	0.0360329	0.7726932	1.6322491	7.2374055
RGU(T)-MAJ-062	782.3	1.4213487	6.1255988	24.0849606	0.0518594	0.7128760	1.9196415	5.1617062
RGU(T)-MAJ-063	779.4	1.6716111	5.3412602	23.4543853	0.0671042	0.9706765	1.7215406	5.7359129
RGU(T)-MAJ-064	776.8	1.4040537	4.9130472	23.5435404	0.0740738	0.8289705	1.5631047	6.1833931
RGU(T)-MAJ-065	773.1	1.3819901	5.0779079	23.1274984	0.0352085	0.8083816	1.6606310	6.3590147
RGU(T)-MAJ-066	770.4	1.3841331	5.3524535	22.6933821	0.0453279	0.6172025	1.7245477	5.4991952
RGU(T)-MAJ-067	767.3	1.5754520	5.1512740	21.7396550	0.0565977	0.8318051	1.6806200	7.2479753
RGU(T)-MAJ-068	764.6	1.4090686	5.3400275	21.2315528	0.0489598	1.0716273	1.5864223	7.4590783
RGU(T)-MAJ-069	761.6	1.2638438	5.3621231	22.5297478	0.0209566	0.7974618	1.6951693	6.2882130
RGU(T)-MAJ-070	758.2	1.4133954	4.7611760	19.7321341	0.0703659	0.7728186	1.4557247	9.4642330
RGU(T)-MAJ-071	755.4	1.2939641	5.3305279	21.7048620	0.0772085	0.8029668	1.6966880	7.1953262
RGU(T)-MAJ-072	752.3	1.1667737	4.8640117	20.5194478	0.0593154	0.7929027	1.5462875	8.8968106
RGU(T)-MAJ-073	749.2	1.3376088	4.2811626	20.2060937	0.0821399	0.8249523	1.3768515	9.5724849
RGU(T)-MAJ-074	746.9	1.3051361	5.4559338	22.5112088	0.0418555	0.7669641	1.7041510	6.2888113
RGU(T)-MAJ-075	743.1	1.3681654	4.7989719	22.0231896	0.0319228	1.1094420	1.5645825	6.9597424
RGU(T)-MAJ-076	740.3	1.4787385	4.7330869	22.0955137	0.0610065	1.2738023	1.4816062	6.9891284
RGU(T)-MAJ-077	737.5	1.4700038	4.6517888	21.6696695	0.0590387	1.1112932	1.4534448	7.9543894
RGU(T)-MAJ-078	734.5	1.4613858	4.7130106	21.4761571	0.0533608	0.8744614	1.5028530	8.0261818
RGU(T)-MAJ-079	731.4	1.3060146	4.6433556	22.7112934	0.0388190	0.8024989	1.5078520	6.4864971
RGU(T)-MAJ-080	729.4	1.2675943	4.7795789	21.6996088	0.0691430	0.8858720	1.4889497	7.4018182
RGU(T)-MAJ-081	726.6	1.0573623	5.1598225	23.1942560	0.0118496	0.8177467	1.6182923	6.2247292
RGU(T)-MAJ-082	723.7	1.3355072	5.1714896	22.0934517	0.0668738	0.9604075	1.6058167	7.3310679
RGU(T)-MAJ-083	720.5	1.1480622	6.4696288	23.6645521	0.0448599	0.3514844	1.6469949	4.1146334
RGU(T)-MAJ-084	717.2	1.2467004	4.7548217	21.7013183	0.0083130	0.7739923	1.4623550	7.6712285
RGU(T)-MAJ-085	714.5	1.1265543	4.7871199	21.7563429	0.0369788	0.8610496	1.5036694	8.0813738
RGU(T)-MAJ-086	711.7	1.1603909	5.3451518	22.4660698	0.0077206	0.8699946	1.6230813	6.7694177
RGU(T)-MAJ-087	708.3	1.2209496	5.2843203	22.6559325	0.0246896	1.0038182	1.6511161	6.0909216

RGU-1 top half major elements

Sample ID	Depth (ft.)	BaLa1	TiKa1	V Ka1
RGU(T)-MAJ-059	791.7	-0.0735010	0.2134600	0.0126825
RGU(T)-MAJ-060	788.2	-0.0531231	0.2722166	0.0127436
RGU(T)-MAJ-061	785.2	-0.0523351	0.2727013	0.0147956
RGU(T)-MAJ-062	782.3	-0.0490710	0.3035074	0.0190633
RGU(T)-MAJ-063	779.4	-0.0157912	0.2632677	0.0136384
RGU(T)-MAJ-064	776.8	-0.0493410	0.2567091	0.0098355
RGU(T)-MAJ-065	773.1	-0.0625330	0.2792581	0.0155346
RGU(T)-MAJ-066	770.4	-0.0597630	0.2882314	0.0151082
RGU(T)-MAJ-067	767.3	-0.0409818	0.2674735	0.0172174
RGU(T)-MAJ-068	764.6	-0.0600942	0.2729427	0.0147412
RGU(T)-MAJ-069	761.6	-0.0135513	0.2629672	0.0101922
RGU(T)-MAJ-070	758.2	-0.0599737	0.2391179	0.0138891
RGU(T)-MAJ-071	755.4	-0.0148031	0.2690562	0.0174940
RGU(T)-MAJ-072	752.3	-0.0515601	0.2490330	0.0130978
RGU(T)-MAJ-073	749.2	-0.0873076	0.2527417	0.0162056
RGU(T)-MAJ-074	746.9	-0.0305361	0.2774030	0.0139823
RGU(T)-MAJ-075	743.1	-0.0305884	0.2457814	0.0141768
RGU(T)-MAJ-076	740.3	-0.1070705	0.2709492	0.0155751
RGU(T)-MAJ-077	737.5	-0.0302460	0.2293308	0.0105028
RGU(T)-MAJ-078	734.5	-0.0059175	0.2407608	0.0112645
RGU(T)-MAJ-079	731.4	-0.0825536	0.2695219	0.0114670
RGU(T)-MAJ-080	729.4	-0.0135206	0.2481968	0.0148521
RGU(T)-MAJ-081	726.6	-0.0225092	0.2782892	0.0099241
RGU(T)-MAJ-082	723.7	-0.0342861	0.2728941	0.0137310
RGU(T)-MAJ-083	720.5	-0.0870042	0.3280660	0.0103977
RGU(T)-MAJ-084	717.2	-0.0591569	0.2564267	0.0154317
RGU(T)-MAJ-085	714.5	-0.0591051	0.2692046	0.0155920
RGU(T)-MAJ-086	711.7	-0.0658513	0.2882390	0.0144468
RGU(T)-MAJ-087	708.3	-0.0211725	0.2565387	0.0103886

	CrKa1	MnKa1	FeKa1
	0.0043431	0.0130339	2.3976629
	0.0046091	0.0171238	2.4458436
	0.0052594	0.0161323	2.5124615
	0.0039736	0.0190078	2.5389163
	0.0028479	0.0201529	2.6667222
	0.0038268	0.0185059	2.3366771
	0.0033987	0.0195286	2.4667609
	0.0042795	0.0180794	2.3911939
	0.0020552	0.0184414	2.5541884
	0.0033234	0.0193465	2.7351199
	0.0054181	0.0194334	2.5242053
	0.0029262	0.0141717	2.2580563
	0.0031480	0.0174364	2.5758319
	0.0052077	0.0192546	2.4292748
	0.0048905	0.0171721	2.3101906
	0.0038962	0.0158208	2.4727742
	0.0030242	0.0199039	2.5933561
	0.0032149	0.0215298	2.7517412
	0.0046086	0.0171189	2.5344566
	0.0036569	0.0155920	2.3497052
	0.0046287	0.0174314	2.3522657
	0.0023840	0.0186161	2.4340521
	0.0045232	0.0144576	2.4429563
	0.0040903	0.0150749	2.5115539
	0.0032854	0.0158561	2.6305762
	0.0051831	0.0139594	2.3203036
	0.0052114	0.0153253	2.3140934
	0.0043334	0.0188828	2.5801849
	0.0036855	0.0175466	2.6753869

RGU-1 top half major elements

Sample ID	Depth (ft.)	MgKa1	AlKa1	SiKa1	P Ka1	S Ka1	K Ka1	CaKa1
RGU(T)-MAJ-088	705.1	1.4364488	5.2595509	22.5622181	0.0526445	0.7310041	1.6832872	6.2246975
RGU(T)-MAJ-089	702.5	1.3716891	4.7329075	22.1883684	0.0239802	0.7090007	1.4499406	7.6095604
RGU(T)-MAJ-090	699.5	1.2315599	5.0821475	22.2389166	0.0138298	0.7643519	1.6032149	6.7018733
RGU(T)-MAJ-091	696.3	1.5243037	5.8361908	23.4636069	0.0408824	0.7745902	1.8252511	5.3814111
RGU(T)-MAJ-092	693.2	1.2631888	4.9630549	23.5728940	0.0453272	0.6312144	1.5663532	5.3296055
RGU(T)-MAJ-093	690.3	1.4404928	5.8740436	23.4537499	0.0410258	0.8374061	1.7988623	5.0046562
RGU(T)-MAJ-094	687.2	1.3425007	5.4180423	21.5492431	0.0351508	0.8157066	1.5575805	7.9886807
RGU(T)-MAJ-095	684.2	1.1615978	5.2458831	22.3895562	0.0323654	0.6008650	1.7827082	5.1906140
RGU(T)-MAJ-096	681.5	1.2379144	5.1428201	22.2593701	0.0588404	0.7916414	1.6113629	6.5130794
RGU(T)-MAJ-097	678.4	1.5077785	5.7353600	23.8444758	0.0601336	0.6526650	1.8032437	5.4382014
RGU(T)-MAJ-098	675.4	1.5512899	5.5344598	24.1102116	0.0484630	0.5436298	1.8118914	4.8362673
RGU(T)-MAJ-099	672.5	1.6198965	4.6857580	21.9857708	0.0441869	0.6640039	1.5918679	7.6752848
RGU(T)-MAJ-100	669.3	1.2983546	4.8275565	24.7242326	0.0391684	0.5691177	1.6330125	5.3870359
RGU(T)-MAJ-101	668.7	0.8310327	8.2446396	19.9395588	0.0753657	1.2593205	0.3501869	1.6386455
RGU(T)-MAJ-102	666.6	1.5449570	5.6991944	23.1626502	0.0362441	0.5586227	1.7019877	5.3134106
RGU(T)-MAJ-103	663.5	1.4338457	4.9153369	21.7354313	0.0451986	0.7119536	1.4768762	7.4334099
RGU(T)-MAJ-104	660.3	1.1858040	5.1015224	23.2475773	0.0482634	0.6848230	1.5463573	5.9020251
RGU(T)-MAJ-105	657.2	1.0675293	5.4495767	23.1904102	0.0397351	0.5220072	1.7313918	4.3819992
RGU(T)-MAJ-106	654.4	1.6541464	4.8993344	22.0583791	0.0265169	0.8062090	1.5481149	6.7175733
RGU(T)-MAJ-107	651.4	1.4500015	4.7224028	22.1796725	0.0370802	0.5890017	1.5953005	5.7890111
RGU(T)-MAJ-108	648.7	1.3252460	5.5351599	23.7302572	0.0219376	0.7450450	1.6919491	5.1077724
RGU(T)-MAJ-109	645.1	1.4395311	5.5085459	23.7952800	0.0426603	0.6094446	1.6921340	4.5592385
RGU(T)-MAJ-110	642.1	1.3458384	5.6120020	23.1238366	0.0601458	0.7981689	1.7092983	5.4771410
RGU(T)-MAJ-111	639.7	1.3628794	5.1686019	22.7948142	0.0300675	1.0223069	1.5904513	6.3127109
RGU(T)-MAJ-112	636.2	1.6691636	5.6608027	23.8139498	0.0311145	0.8396783	1.7679318	5.1428034
RGU(T)-MAJ-113	633.8	1.4080695	5.5578787	23.2473658	0.0328126	0.6679396	1.7068598	5.3167403
RGU(T)-MAJ-114	630.1	1.3439215	5.0859092	22.0531933	0.0218363	0.6413030	1.6682715	5.3240838
RGU(T)-MAJ-115	627.5	1.4279504	5.1744719	23.2968524	0.0530633	0.7148550	1.6935510	5.7368353
RGU(T)-MAJ-116	624.3	1.3015095	5.8953654	23.3159713	0.0163001	0.7382755	1.7723050	5.4380393

RGU-1 top half major elements

Sample ID	Depth (ft.)	BaLa1	TiKa1	V Ka1	CrKa1	MnKa1	FeKa1
RGU(T)-MAJ-088	705.1	-0.0611802	0.2688207	0.0128049	0.0032564	0.0158839	2.2810993
RGU(T)-MAJ-089	702.5	-0.0598731	0.2443699	0.0103857	0.0048629	0.0175379	2.2135867
RGU(T)-MAJ-090	699.5	-0.1096374	0.2927713	0.0170631	0.0042462	0.0154646	2.5124930
RGU(T)-MAJ-091	696.3	-0.0514232	0.2892322	0.0135989	0.0049546	0.0183962	2.5878723
RGU(T)-MAJ-092	693.2	-0.0660859	0.2702714	0.0098978	0.0022787	0.0194216	2.1541497
RGU(T)-MAJ-093	690.3	-0.0180807	0.2806770	0.0118280	0.0039422	0.0167059	2.6390186
RGU(T)-MAJ-094	687.2	-0.0294853	0.2518153	0.0108045	0.0044374	0.0170361	2.4274255
RGU(T)-MAJ-095	684.2	-0.0667561	0.3055840	0.0169996	0.0030995	0.0188751	2.4912288
RGU(T)-MAJ-096	681.5	-0.0350165	0.2669469	0.0136264	0.0032680	0.0181319	2.4769068
RGU(T)-MAJ-097	678.4	-0.0061488	0.2583663	0.0091641	0.0039555	0.0216227	2.4248053
RGU(T)-MAJ-098	675.4	-0.0702900	0.3034858	0.0147903	0.0030555	0.0195757	2.3632213
RGU(T)-MAJ-099	672.5	-0.0308569	0.2414906	0.0110096	0.0046803	0.0211861	2.3859203
RGU(T)-MAJ-100	669.3	-0.0511900	0.2615925	0.0123484	0.0044995	0.0201158	2.3469859
RGU(T)-MAJ-101	668.7	0.0357315	0.4301687	0.0053403	-0.0025802	0.0165055	2.9215960
RGU(T)-MAJ-102	666.6	-0.0291978	0.2480585	0.0094568	0.0024887	0.0198932	2.4724690
RGU(T)-MAJ-103	663.5	-0.0513366	0.2480963	0.0122788	0.0028102	0.0197529	2.4775368
RGU(T)-MAJ-104	660.3	-0.0569815	0.2628282	0.0129035	0.0031966	0.0200180	2.3101535
RGU(T)-MAJ-105	657.2	-0.0561603	0.2954772	0.0124415	0.0031681	0.0162083	2.3985934
RGU(T)-MAJ-106	654.4	-0.0642897	0.2652078	0.0125734	0.0040353	0.0189546	2.5478246
RGU(T)-MAJ-107	651.4	-0.0451200	0.2558838	0.0140421	0.0042334	0.0187103	2.3253088
RGU(T)-MAJ-108	648.7	-0.0383584	0.2856537	0.0144543	0.0021201	0.0183913	2.4656285
RGU(T)-MAJ-109	645.1	-0.0489457	0.2818756	0.0131777	0.0029105	0.0178976	2.2724695
RGU(T)-MAJ-110	642.1	-0.0435121	0.2987189	0.0151687	0.0031958	0.0178080	2.5786326
RGU(T)-MAJ-111	639.7	-0.0598322	0.2878002	0.0190435	0.0024999	0.0223134	2.6882650
RGU(T)-MAJ-112	636.2	-0.0244641	0.2822617	0.0126006	0.0042671	0.0224205	2.5855681
RGU(T)-MAJ-113	633.8	-0.0523410	0.2886370	0.0112806	0.0045483	0.0191011	2.3558502
RGU(T)-MAJ-114	630.1	-0.0835965	0.2938550	0.0180330	0.0024260	0.0143843	2.4505912
RGU(T)-MAJ-115	627.5	-0.0566681	0.2775305	0.0129801	0.0041942	0.0208934	2.4954876
RGU(T)-MAJ-116	624.3	-0.0422565	0.2866971	0.0130774	0.0038045	0.0179299	2.6220282

RGU-1 top half major elements

Sample ID	Depth (ft.)	MgKa1	AlKa1	SiKa1	P Ka1	S Ka1	K Ka1	CaKa1
RGU(T)-MAJ-117	621.1	1.4386193	4.7707885	23.9142562	0.0873423	0.6933448	1.4769966	5.5386637
RGU(T)-MAJ-118	618.5	1.4204448	5.2186202	23.6446981	0.0309151	0.7671638	1.6589383	5.5113390
RGU(T)-MAJ-119	615.2	1.2720752	5.1989637	23.6725817	0.0433030	0.6270608	1.6790436	5.3849421
RGU(T)-MAJ-120	612.4	1.3446818	5.8226570	23.4641867	0.0390566	0.5703759	1.7994966	5.1909809
RGU(T)-MAJ-121	609.4	1.4276991	5.1508752	22.3720485	0.0561787	0.6685082	1.5822628	6.4767825
RGU(T)-MAJ-122	606.6	1.2678892	5.4111980	24.2176290	0.0229754	0.5401131	1.7002945	5.2010310
RGU(T)-MAJ-123	603.7	1.3876798	5.4456919	24.0111777	0.0481754	0.6681371	1.7220173	4.8758186
RGU(T)-MAJ-124	600.5	1.1633318	5.1808752	23.5894909	0.0796587	0.6060326	1.6715520	5.7023150
RGU(T)-MAJ-125	597.4	1.5184067	5.1826168	23.5933952	0.0671532	0.6189579	1.6548318	5.3595521
RGU(T)-MAJ-126	594.2	1.5074293	4.8107169	23.7263094	0.0385995	0.4904051	1.5817709	5.8590203
RGU(T)-MAJ-127	591.5	1.3985951	5.1847579	23.4806010	0.0269367	0.6421346	1.6577894	5.1454240
RGU(T)-MAJ-128	588.3	1.3027914	5.6062790	23.8167198	0.0364142	0.5278733	1.7530215	4.9360309
RGU(T)-MAJ-129	585.6	1.2921439	4.3205635	24.3616872	0.0316922	0.5811009	1.4903198	5.3863346
RGU(T)-MAJ-130	582.6	1.3325176	3.7784959	23.8171283	0.0277549	0.6098069	1.2630468	6.9323445
RGU(T)-MAJ-131	*	1.4340402	5.1263706	23.0690674	0.1204256	0.6700274	1.8192405	6.1539841
RGU(T)-MAJ-132	*	1.7134248	5.5272099	24.0251320	0.0854251	0.8729491	1.8585308	6.7586976
RGU(T)-MAJ-133	*	1.3697957	5.3883384	24.7668249	0.1183088	0.7661439	1.8649021	6.4999601
RGU(T)-MAJ-134	*	1.4203417	5.6085929	26.0497101	0.1161553	0.6157008	1.9081822	5.1056193
RGU(T)-MAJ-135	571.4	1.4346045	4.0973817	23.1599393	0.0758761	0.5922254	1.2994341	6.9198200
RGU(T)-MAJ-136	568.3	1.2344497	5.3332398	24.3848932	0.0192545	0.5190488	1.6889976	4.2261726
RGU(T)-MAJ-137	565.5	1.4812094	5.6791338	23.6454080	0.0535277	0.6373016	1.8044673	4.5247288
RGU(T)-MAJ-138	562.4	1.3554178	5.1556168	23.5458981	0.0267381	0.5293273	1.7193939	4.7227829
RGU(T)-MAJ-139	559.1	1.3618261	5.4362249	23.3356854	0.0150300	0.6537345	1.7312324	5.0199587
RGU(T)-MAJ-140	556.5	1.6537788	4.9879732	22.9539877	0.0393496	0.6632697	1.6187538	5.9953713
RGU(T)-MAJ-141	553.6	1.3957199	4.0053785	24.8877705	0.0306853	0.5593696	1.3060782	5.9024971
RGU(T)-MAJ-142	550.4	1.3512572	4.7664419	23.3305983	0.0532785	0.5833891	1.5894526	5.5224074
RGU(T)-MAJ-143	547.5	1.5217450	4.8737918	24.2559700	0.0627844	0.5377519	1.6033469	5.3612540
RGU(T)-MAJ-144	544.5	1.1536499	4.2389749	24.7365604	0.0488337	0.4444069	1.4624522	4.9546566
RGU(T)-MAJ-145	541.5	1.3480402	4.2867058	23.7886131	0.0629128	0.6035584	1.4866447	6.4349289

RGU-1 top half major elements

Sample ID	Depth (ft.)	BaLa1	TiKa1	V Ka1
RGU(T)-MAJ-117	621.1	-0.0538483	0.2621630	0.0110481
RGU(T)-MAJ-118	618.5	-0.0370759	0.2811465	0.0086885
RGU(T)-MAJ-119	615.2	-0.0759874	0.3060674	0.0154653
RGU(T)-MAJ-120	612.4	-0.0652726	0.3185939	0.0142033
RGU(T)-MAJ-121	609.4	-0.0210944	0.2604855	0.0104506
RGU(T)-MAJ-122	606.6	-0.0754340	0.2816649	0.0112080
RGU(T)-MAJ-123	603.7	-0.0394040	0.2846229	0.0085067
RGU(T)-MAJ-124	600.5	-0.0144741	0.2533267	0.0087573
RGU(T)-MAJ-125	597.4	-0.0577896	0.2723447	0.0107661
RGU(T)-MAJ-126	594.2	-0.0250457	0.2523013	0.0058459
RGU(T)-MAJ-127	591.5	-0.0326088	0.2680021	0.0095050
RGU(T)-MAJ-128	588.3	-0.0495351	0.2921756	0.0124233
RGU(T)-MAJ-129	585.6	-0.0585221	0.2468141	0.0097937
RGU(T)-MAJ-130	582.6	-0.0298627	0.2094122	0.0051725
RGU(T)-MAJ-131	*	0.0292624	0.2758831	0.0137558
RGU(T)-MAJ-132	*	0.0180825	0.2871422	0.0163530
RGU(T)-MAJ-133	*	0.0037210	0.2773994	0.0170653
RGU(T)-MAJ-134	*	0.0581092	0.2623663	0.0155368
RGU(T)-MAJ-135	571.4	-0.0245116	0.2288648	0.0040410
RGU(T)-MAJ-136	568.3	-0.0380651	0.2720621	0.0078367
RGU(T)-MAJ-137	565.5	-0.0725377	0.3060760	0.0151628
RGU(T)-MAJ-138	562.4	-0.0616727	0.2937693	0.0091898
RGU(T)-MAJ-139	559.1	-0.0623056	0.2847064	0.0130679
RGU(T)-MAJ-140	556.5	-0.0740842	0.2794703	0.0110027
RGU(T)-MAJ-141	553.6	-0.0395562	0.2174769	0.0034863
RGU(T)-MAJ-142	550.4	-0.0281179	0.2672178	0.0108348
RGU(T)-MAJ-143	547.5	-0.0399057	0.2683235	0.0097165
RGU(T)-MAJ-144	544.5	-0.0739110	0.2618006	0.0091308
RGU(T)-MAJ-145	541.5	-0.0270298	0.2318160	0.0061579

CrKa1	MnKa1	FeKa1
0.0027332	0.0169469	2.2042160
0.0040234	0.0190187	2.5259168
0.0028651	0.0189647	2.4212156
0.0031043	0.0180108	2.4782849
0.0033608	0.0205633	2.4902387
0.0042217	0.0208049	2.2142345
0.0055496	0.0164234	2.3191178
0.0028573	0.0219427	2.3746434
0.0027457	0.0212771	2.2293932
0.0048770	0.0207646	2.0930671
0.0034798	0.0204187	2.3242851
0.0040474	0.0170077	2.2720255
0.0028463	0.0202237	2.0856396
0.0044665	0.0211895	1.9194863
0.0079834	0.0271096	2.2160722
0.0077840	0.0243754	2.3519228
0.0088071	0.0252450	2.2940696
0.0082411	0.0266454	1.9533699
0.0038050	0.0211467	1.9811384
0.0042459	0.0152880	2.1454388
0.0033725	0.0189069	2.4859192
0.0033835	0.0191383	2.3074844
0.0031956	0.0201583	2.5154261
0.0036425	0.0237327	2.4148541
0.0043529	0.0184355	1.8596600
0.0011789	0.0167370	2.1232407
0.0028818	0.0183808	2.1431332
0.0031288	0.0204542	1.8208672
0.0042044	0.0212070	2.0467186

RGU-1 top half major elements

Sample ID	Depth (ft.)	MgKa1	AlKa1	SiKa1	P Ka1	S Ka1	K Ka1	CaKa1
RGU(T)-MAJ-146	538.6	1.3446728	4.7045910	23.3850003	0.0379670	0.4510483	1.5550498	5.5479531
RGU(T)-MAJ-147	535.5	1.1831093	3.6627974	25.5453007	0.0733437	0.4976250	1.2627471	5.3633429
RGU(T)-MAJ-148	532.5	1.5539129	4.9805978	23.8318775	0.0264560	0.4500265	1.6281616	5.1793348
RGU(T)-MAJ-149	529.5	1.3683731	4.0122315	24.4460458	0.0018531	0.5740028	1.3082317	5.9350939
RGU(T)-MAJ-150	526.2	1.3913811	4.2833163	23.8525172	0.0285206	0.4332059	1.4853495	5.8612672
RGU(T)-MAJ-151	523.3	1.2487324	3.0099330	23.7455150	0.0452054	0.4133793	1.1354570	7.8097627
RGU(T)-MAJ-152	*	1.6216741	4.6026790	25.0817926	0.2050983	0.5199760	1.7105280	6.3227104
RGU(T)-MAJ-153	*	1.8164045	5.0923764	23.5206283	0.1343065	0.6251550	1.8149873	6.9773033
RGU(T)-MAJ-154	*	1.6844744	6.1196281	24.5498507	0.1164457	0.6676802	2.0844417	6.6372747
RGU(T)-MAJ-155	511.3	1.1702125	4.6509816	24.6489789	0.0543960	0.7035752	1.5321513	4.7740760
RGU(T)-MAJ-156	508.6	1.1220952	3.9061369	25.1495581	0.0666037	0.5108643	1.4045043	4.9487509
RGU(T)-MAJ-157	505.6	1.2516153	3.6783501	19.6342631	0.0204528	1.0313880	1.2934118	7.1931228
RGU(T)-MAJ-158	502.5	1.5818102	4.8429266	23.4087119	0.0543825	0.6379775	1.6822808	5.1819193
RGU(T)-MAJ-159	499.3	1.2779354	4.0467803	24.9662794	0.0331693	0.5239176	1.4075364	5.2308924
RGU(T)-MAJ-160	496.4	0.9464888	3.0667921	26.2041870	0.0367176	0.4595850	1.1561676	5.7540297
RGU(T)-MAJ-161	493.1	1.2372865	4.4308703	24.4712227	0.0375814	0.5724977	1.4425916	5.2307759
RGU(T)-MAJ-162	483.7	1.1218026	3.0755311	26.8054722	0.0646820	0.3764257	1.2278024	4.6889824
RGU(T)-MAJ-163	482.1	1.3514806	5.6646374	23.8203744	0.0356601	0.3356417	1.7129329	4.8727015
RGU(T)-MAJ-164	479.7	1.3966050	4.2493222	24.9799284	0.0348749	0.5697121	1.5388352	4.3392088
RGU(T)-MAJ-165	476.5	1.1708288	3.0788952	27.3748627	0.0211770	0.4448447	1.2461251	4.1121029
RGU(T)-MAJ-166	473.4	1.0191924	3.0872136	26.2018891	0.0488238	0.3840961	1.3009294	4.5457106
RGU(T)-MAJ-167	470.3	0.7597188	3.1295680	27.3703545	0.0410826	0.3300249	1.2748316	4.1297730
RGU(T)-MAJ-168	467.7	1.2323287	3.6370639	26.0501167	0.0721479	0.4979127	1.4325753	4.4077596
RGU(T)-MAJ-169	467.1	0.9679491	7.4656195	18.5721300	0.0390753	0.5093374	0.6090922	1.4261104
RGU(T)-MAJ-170	465.6	1.4601412	5.1430254	24.3854494	0.0577126	0.3522156	1.2125211	3.1491153
RGU(T)-MAJ-171	462.4	1.6305659	5.2031288	23.9434040	0.0501662	0.4675474	1.4555833	4.0799905
RGU(T)-MAJ-172	459.3	1.2182584	4.7463843	24.2718016	0.0579353	0.4530139	1.4945013	3.7907776
RGU(T)-MAJ-173	456.5	1.2559701	5.5497893	23.9137281	0.0478821	0.4815322	1.5893153	3.4975002
RGU(T)-MAJ-174	454.2	1.0737364	3.3338430	25.6982392	0.0005743	0.3274812	1.2431147	3.8179863

RGU-1 top half major elements

Sample ID	Depth (ft.)	BaLa1	TiKa1	V Ka1
RGU(T)-MAJ-146	538.6	-0.0304354	0.2378800	0.0065255
RGU(T)-MAJ-147	535.5	-0.0593442	0.2129676	0.0067172
RGU(T)-MAJ-148	532.5	-0.0546376	0.2633031	0.0115670
RGU(T)-MAJ-149	529.5	-0.0596768	0.2205574	0.0041461
RGU(T)-MAJ-150	526.2	-0.0547227	0.2601734	0.0067479
RGU(T)-MAJ-151	523.3	-0.1119119	0.1903678	0.0053951
RGU(T)-MAJ-152	*	-0.0028153	0.2476067	0.0093510
RGU(T)-MAJ-153	*	0.0251852	0.2427439	0.0134267
RGU(T)-MAJ-154	*	-0.0218934	0.3000592	0.0155006
RGU(T)-MAJ-155	511.3	-0.0605090	0.2754648	0.0067263
RGU(T)-MAJ-156	508.6	-0.0260076	0.2168696	0.0034776
RGU(T)-MAJ-157	505.6	0.1377924	0.2230533	-0.0139861
RGU(T)-MAJ-158	502.5	-0.0344148	0.2682636	0.0099402
RGU(T)-MAJ-159	499.3	-0.0501948	0.2545859	0.0064934
RGU(T)-MAJ-160	496.4	-0.0413168	0.1996820	-0.0009702
RGU(T)-MAJ-161	493.1	-0.0490695	0.2435466	0.0071635
RGU(T)-MAJ-162	483.7	-0.0562703	0.1919764	0.0040740
RGU(T)-MAJ-163	482.1	-0.0406140	0.3010223	0.0105280
RGU(T)-MAJ-164	479.7	-0.0475956	0.2624960	0.0069255
RGU(T)-MAJ-165	476.5	-0.0557024	0.1869507	0.0009594
RGU(T)-MAJ-166	473.4	-0.0791464	0.2241156	0.0060000
RGU(T)-MAJ-167	470.3	-0.1055534	0.2000667	0.0030667
RGU(T)-MAJ-168	467.7	-0.0629317	0.2294081	0.0086479
RGU(T)-MAJ-169	467.1	-0.0588854	0.4483705	0.0111378
RGU(T)-MAJ-170	465.6	-0.0680324	0.2674159	0.0080342
RGU(T)-MAJ-171	462.4	-0.0911269	0.2746539	0.0144848
RGU(T)-MAJ-172	459.3	-0.0694249	0.2772862	0.0082633
RGU(T)-MAJ-173	456.5	-0.0284345	0.2540440	0.0044621
RGU(T)-MAJ-174	454.2	-0.0703676	0.1815858	0.0020684

	CrKa1	MnKa1	FeKa1
	0.0034163	0.0165693	1.9649341
	0.0016780	0.0283371	1.7217175
	0.0027265	0.0198986	1.9504243
	0.0036047	0.0235221	1.9776822
	0.0049250	0.0196619	1.9112054
	0.0045705	0.0253766	1.5113934
	0.0085843	0.0280543	1.8913664
	0.0073807	0.0257967	2.0930797
	0.0096208	0.0284589	2.1542443
	0.0032636	0.0188026	2.1262560
	0.0024949	0.0173574	1.7585091
	0.0043428	0.0036085	1.7297545
	0.0013268	0.0185953	2.2505245
	0.0034141	0.0181963	1.9251261
	0.0052761	0.0201734	1.5739629
	0.0026147	0.0186441	1.9201374
	0.0038929	0.0207210	1.5599340
	0.0031930	0.0238908	2.7121501
	0.0031200	0.0213303	1.9665414
	0.0039931	0.0185295	1.3628000
	0.0035492	0.0148692	1.4075081
	0.0023825	0.0198514	1.5329403
	0.0019988	0.0206016	1.7590759
	-0.0011847	0.0249733	2.8646729
	0.0006103	0.0196243	1.9961356
	0.0015038	0.0196663	2.1930667
	0.0002586	0.0204131	2.0348210
	0.0012104	0.0186414	2.0007616
	0.0017107	0.0214177	1.4157647

RGU-1 top half major elements

Sample ID	Depth (ft.)	MgKa1	AlKa1	SiKa1	P Ka1	S Ka1	K Ka1	CaKa1
RGU(T)-MAJ-175	438.8	0.7048548	2.2332925	27.2188256	0.0693856	0.3282697	0.9471537	3.7062864
RGU(T)-MAJ-176	435.3	1.1265605	2.6998246	26.4641246	0.0486798	0.4013092	0.9874127	4.2709820
RGU(T)-MAJ-177	433.6	1.0104485	1.2422220	24.5117943	0.0062733	0.3171682	0.6728093	11.1116225
RGU(T)-MAJ-178	433.3	1.2618685	0.3660764	6.5418936	0.0952239	0.1209107	0.2146683	29.6793485
RGU(T)-MAJ-179	430.2	1.0319706	2.5216493	27.6734254	0.0240523	0.3473604	1.0944388	3.3801873
RGU(T)-MAJ-180	427.2	0.8917184	2.0658704	29.0314127	0.0407267	0.3407521	0.8951508	2.9160971
RGU(T)-MAJ-181	424.6	0.7897376	2.3312931	28.1783440	0.0190850	0.3886223	0.9666206	4.4290783
RGU(T)-MAJ-182	421.4	0.8105508	1.8218475	28.4804560	-0.0081008	0.3061576	0.8112879	4.8132174
RGU(T)-MAJ-183	418.5	0.6308418	2.6058083	27.3686194	0.0018603	0.4421467	1.0196017	3.0183971
RGU(T)-MAJ-184	415.7	1.1070992	4.6149216	23.6835508	0.0414887	0.4445129	1.5750579	3.4988735
RGU(T)-MAJ-185	412.5	1.0813839	4.3035191	23.6356124	0.0024013	0.5793592	1.4399350	5.0015005
RGU(T)-MAJ-186	409.4	1.2733484	3.6868805	24.5712908	0.0869705	0.6543856	1.2279077	4.9016656
RGU(T)-MAJ-187	406.3	1.1922492	4.8705654	22.8667983	0.0484089	0.6613597	1.5577599	6.2274453
RGU(T)-MAJ-188	403.3	1.2966621	4.0601331	23.6395483	0.0281867	0.4289194	1.4049651	5.0365372
RGU(T)-MAJ-189	400.2	1.5527256	4.1941586	24.0492917	0.0540251	0.5148115	1.5140243	4.6903048
RGU(T)-MAJ-190	397.3	1.1789935	3.7936338	23.8883190	0.0228907	0.3295197	1.3933499	4.8017260
RGU(T)-MAJ-191	394.5	1.0505818	4.7530715	23.5089849	0.0342130	0.4440378	1.5713488	4.9114899
RGU(T)-MAJ-192	391.2	1.0158626	3.8228577	24.6235645	0.0443652	0.3990210	1.4318988	4.4083883
RGU(T)-MAJ-193	388.3	1.3244431	4.2931904	23.6245596	0.0350992	0.5510369	1.5472928	5.3087589
RGU(T)-MAJ-194	385.6	0.9984021	3.6850359	24.8408568	0.0094669	0.4361208	1.3759199	4.5508799
RGU(T)-MAJ-195	382.1	0.6324228	2.0196244	26.9603608	0.0153520	0.3267605	0.9661695	5.2254124
RGU(T)-MAJ-196	379.9	1.0967235	4.0544548	24.2472759	0.0140028	0.3387810	1.4536971	4.8678712
RGU(T)-MAJ-197	*	1.6912840	4.8609480	24.1035711	0.1733642	0.5712545	1.7883715	6.6572592
RGU(T)-MAJ-198	*	1.4346108	5.6742704	23.7506587	0.1232236	0.6612024	2.0413794	6.5870316
RGU(T)-MAJ-199	*	1.2343821	5.4886342	24.0842036	0.1463039	0.8822454	1.9470600	6.5257931
RGU(T)-MAJ-200	*	1.4051312	4.5312986	25.7688678	0.1223996	0.5238848	1.6873361	5.5577736
RGU(T)-MAJ-201	360.5	1.0756657	3.2333427	24.3852941	0.0309554	0.4682305	1.2466342	5.3633311
RGU(T)-MAJ-202	355.8	0.6005370	2.4272597	26.5810969	0.0443599	0.2829040	1.0041748	5.0086734
RGU(T)-MAJ-203	351.8	0.7180053	2.6655409	25.2848801	0.0265234	0.4327496	1.0512061	5.9943220

RGU-1 top half major elements

Sample ID	Depth (ft.)	BaLa1	TiKa1	V Ka1
RGU(T)-MAJ-175	438.8	-0.0597680	0.1944006	-0.0018152
RGU(T)-MAJ-176	435.3	-0.0805689	0.1786993	0.0020128
RGU(T)-MAJ-177	433.6	-0.0816512	0.1547240	-0.0019928
RGU(T)-MAJ-178	433.3	-0.2049855	0.0790184	0.0078482
RGU(T)-MAJ-179	430.2	-0.0739008	0.1668305	-0.0001575
RGU(T)-MAJ-180	427.2	-0.0792076	0.1253764	-0.0005809
RGU(T)-MAJ-181	424.6	-0.0515436	0.1832750	-0.0019798
RGU(T)-MAJ-182	421.4	-0.1026602	0.1455764	-0.0013596
RGU(T)-MAJ-183	418.5	-0.0802699	0.1878325	0.0002071
RGU(T)-MAJ-184	415.7	-0.0446013	0.2480036	0.0047971
RGU(T)-MAJ-185	412.5	-0.0851261	0.2539672	0.0061877
RGU(T)-MAJ-186	409.4	-0.0678722	0.2004423	0.0054293
RGU(T)-MAJ-187	406.3	-0.0884242	0.2587882	0.0094785
RGU(T)-MAJ-188	403.3	-0.0860280	0.2371153	0.0046782
RGU(T)-MAJ-189	400.2	-0.0640556	0.2312764	0.0070803
RGU(T)-MAJ-190	397.3	-0.0646829	0.2281692	0.0046076
RGU(T)-MAJ-191	394.5	-0.0599381	0.2569093	0.0093684
RGU(T)-MAJ-192	391.2	-0.1399148	0.2590368	0.0094153
RGU(T)-MAJ-193	388.3	-0.0786813	0.2620139	0.0107826
RGU(T)-MAJ-194	385.6	-0.0823205	0.2348770	0.0079139
RGU(T)-MAJ-195	382.1	-0.0511895	0.1736037	-0.0015862
RGU(T)-MAJ-196	379.9	-0.0640821	0.2588704	0.0065456
RGU(T)-MAJ-197	*	0.0209052	0.2599778	0.0124554
RGU(T)-MAJ-198	*	0.0425558	0.2676424	0.0116971
RGU(T)-MAJ-199	*	0.0036415	0.2645784	0.0180461
RGU(T)-MAJ-200	*	-0.0219307	0.2523312	0.0148358
RGU(T)-MAJ-201	360.5	-0.0414018	0.1974197	0.0043816
RGU(T)-MAJ-202	355.8	-0.0256771	0.1316454	-0.0027165
RGU(T)-MAJ-203	351.8	-0.0523080	0.1887908	-0.0006155

CrKa1	MnKa1	FeKa1
0.0004818	0.0114761	1.1394262
0.0015135	0.0145038	1.2406889
0.0074213	0.0259497	0.8767082
-0.0031304	0.0208541	0.6607323
0.0000580	0.0139684	1.1817649
0.0019929	0.0122989	1.0674489
0.0058939	0.0176689	1.1928894
0.0020142	0.0162461	1.0005405
-0.0004166	0.0110668	1.3823380
0.0011825	0.0135705	1.7976773
0.0028632	0.0158870	1.9208860
0.0019842	0.0122068	1.7174672
0.0050723	0.0204734	2.1086734
0.0044764	0.0148410	1.7591578
0.0030220	0.0170881	1.8492838
0.0015863	0.0195690	1.7394621
0.0013178	0.0196146	2.0453201
0.0022432	0.0179247	1.7137041
0.0018762	0.0179297	1.9209230
0.0003555	0.0146503	1.5652906
0.0022200	0.0145976	1.1477404
0.0020288	0.0156236	1.6496012
0.0068179	0.0281738	1.7784848
0.0084116	0.0270995	2.0659406
0.0076030	0.0277995	2.0602361
0.0072837	0.0253594	1.5634398
0.0021091	0.0168335	1.5312544
0.0018383	0.0167358	1.0325359
0.0039057	0.0196385	1.3451842

RGU-1 top half major elements

Sample ID	Depth (ft.)	MgKa1	AlKa1	SiKa1	P Ka1	S Ka1	K Ka1	CaKa1
RGU(T)-MAJ-204	350.9	1.0542097	3.7301944	24.7268667	0.0268443	0.4239816	1.3902087	4.9342049
RGU(T)-MAJ-205	348.4	0.8959936	3.2584949	24.7740728	0.0241913	0.5150667	1.2615397	5.2690154
RGU(T)-MAJ-206	345.4	1.0931209	2.9741724	24.9162283	0.0586343	0.4808402	1.1959529	5.1551146
RGU(T)-MAJ-207	342.5	1.1299789	2.6617779	25.2890255	0.0833527	0.4485474	1.1917333	5.2324027
RGU(T)-MAJ-208	339.5	1.0801596	2.9554289	24.7524728	0.0223915	0.3440856	1.2732677	5.4388058
RGU(T)-MAJ-209	336.7	0.8391652	3.1297447	25.8911976	0.0388537	0.2729239	1.2681124	4.2470469
RGU(T)-MAJ-210	334.4	1.2967293	3.6631021	24.0276603	0.0351013	0.5707431	1.4021410	5.2011278
RGU(T)-MAJ-211	331.3	0.9999481	3.5288701	25.3090088	0.0104144	0.3434012	1.3337214	4.7517522
RGU(T)-MAJ-212	328.5	1.1925626	3.4132523	25.8276112	0.0504190	0.3429423	1.3442010	4.4994498
RGU(T)-MAJ-213	325.4	0.9887136	3.1644027	25.1051191	0.0731365	0.5095602	1.2568347	5.2105134
RGU(T)-MAJ-214	322.5	0.8367823	2.2232121	25.4848286	0.0411429	0.3746620	0.9247865	6.0792348
RGU(T)-MAJ-215	319.6	1.0941717	3.0615834	24.9401584	0.0664409	0.5496202	1.2069878	5.1505560
RGU(T)-MAJ-216	316.2	0.7634718	3.1668753	25.2608230	0.0273958	0.3645293	1.3578962	5.0426571
RGU(T)-MAJ-217	295.2	0.7704835	2.3937579	27.1145267	-0.0028843	0.2820137	1.0903195	3.7842376
RGU(T)-MAJ-218	292.2	0.7391037	1.4512769	26.1857908	-0.0489651	0.3003181	0.7879647	8.4384545
RGU(T)-MAJ-219	289.6	0.7578716	2.0665619	27.7248851	0.0090015	0.2588153	0.9242700	3.9420485
RGU(T)-MAJ-220	267.5	0.8904918	2.6049127	27.4237609	-0.0042018	0.5109767	1.1029623	4.1004467
RGU(T)-MAJ-221	264.5	0.6960124	2.3614729	27.3985561	0.0736224	0.3145018	0.9688865	3.5163406
RGU(T)-MAJ-222	261.6	1.1231660	4.4111254	24.9868667	0.0432985	0.6861228	1.4661007	4.5454906
RGU(T)-MAJ-223	229.8	1.1628419	3.4547343	26.3743437	0.0126423	0.4923215	1.3037581	4.3896291
RGU(T)-MAJ-224	226.2	0.7999677	2.8759961	27.5317504	0.0288113	0.4264591	1.1950163	3.3508461
RGU(T)-MAJ-225	223.2	0.8268363	2.9052971	27.7827265	0.0226443	0.4223721	1.1280929	3.8569625
RGU(T)-MAJ-226	220.3	0.5708528	1.5813663	29.0784336	0.0523913	0.3183843	0.7941230	5.1711450

RGU-1 top half major elements

Sample ID	Depth (ft.)	BaLa1	TiKa1	V Ka1	CrKa1	MnKa1	FeKa1
RGU(T)-MAJ-204	350.9	-0.0909417	0.2339159	0.0034327	0.0028477	0.0197950	1.6637206
RGU(T)-MAJ-205	348.4	-0.0734155	0.2149505	0.0021508	0.0030690	0.0162497	1.6353711
RGU(T)-MAJ-206	345.4	-0.1122516	0.2130102	0.0084467	0.0027905	0.0177980	1.5200670
RGU(T)-MAJ-207	342.5	-0.0503021	0.2111918	0.0006846	0.0026706	0.0173909	1.5606499
RGU(T)-MAJ-208	339.5	-0.0796751	0.2166543	0.0047221	0.0026421	0.0179067	1.5090202
RGU(T)-MAJ-209	336.7	-0.0844530	0.2058032	0.0042934	0.0013552	0.0145095	1.2797703
RGU(T)-MAJ-210	334.4	-0.0464608	0.2595714	0.0033306	0.0033499	0.0213166	1.9026842
RGU(T)-MAJ-211	331.3	-0.0645731	0.2056916	0.0043566	0.0013480	0.0208886	1.5225643
RGU(T)-MAJ-212	328.5	-0.0302739	0.2552602	0.0029687	0.0014671	0.0181106	1.5413154
RGU(T)-MAJ-213	325.4	-0.0432690	0.2162263	0.0040631	0.0017479	0.0178998	1.6230067
RGU(T)-MAJ-214	322.5	-0.0874620	0.1523965	-0.0006058	0.0036455	0.0192925	1.2796504
RGU(T)-MAJ-215	319.6	-0.0597753	0.1957981	0.0055628	0.0012296	0.0179435	1.6161699
RGU(T)-MAJ-216	316.2	-0.0634237	0.2118982	0.0015800	0.0041280	0.0185361	1.4979267
RGU(T)-MAJ-217	295.2	-0.0689496	0.1833799	0.0009994	0.0022511	0.0154916	1.1704304
RGU(T)-MAJ-218	292.2	-0.0690271	0.1399034	-0.0022594	0.0055653	0.0188144	0.9802084
RGU(T)-MAJ-219	289.6	-0.0396555	0.1698043	-0.0003623	0.0015663	0.0214195	1.0651687
RGU(T)-MAJ-220	267.5	-0.1098864	0.1698083	-0.0015744	0.0036596	0.0249135	1.3196597
RGU(T)-MAJ-221	264.5	-0.0466245	0.1429059	-0.0016390	0.0019682	0.0177140	1.1143114
RGU(T)-MAJ-222	261.6	-0.0458901	0.2441527	0.0055913	0.0025749	0.0148020	1.8132749
RGU(T)-MAJ-223	229.8	-0.0163073	0.2302878	-0.0002807	0.0032878	0.0186022	1.4615783
RGU(T)-MAJ-224	226.2	-0.0844065	0.2355086	-0.0002398	0.0007506	0.0126952	1.2624214
RGU(T)-MAJ-225	223.2	-0.0653928	0.2178609	0.0015625	0.0018997	0.0183899	1.2763714
RGU(T)-MAJ-226	220.3	-0.0297991	0.1406706	-0.0035074	0.0035339	0.0186635	0.8298641
* = Uncertain Depth Measurement (i.e., core crushed, core loose and not filling core box, dubious core box measurements)							

RGU-1 top half trace elements

Sample ID	Depth (ft.)	NiKa1	CuKa1	ZnKa1	ThLa1	RbKa1	U La1	SrKa1	Y Ka1	ZrKa1	NbKa1	MoKa1
RGU(T)-TRC-001	926	0.0030542	-0.0052227	0.0058592	0.0006741	0.0101454	0.0003911	0.0172690	0.0019838	0.0131753	0.0011809	0.0006277
RGU(T)-TRC-002	923.7	0.0038903	-0.0008182	0.0100710	0.0009633	0.0099363	0.0005259	0.0310269	0.0025982	0.0135576	0.0014450	0.0000877
RGU(T)-TRC-003	947.3	0.0042184	0.0020771	0.0089677	0.0010361	0.0128838	0.0005199	0.0203414	0.0020772	0.0120964	0.0010697	0.0000991
RGU(T)-TRC-004	944.2	0.0081615	-0.0033406	0.0170328	0.0010213	0.0124813	0.0010470	0.0178881	0.0024026	0.0132440	0.0012342	0.0002888
RGU(T)-TRC-005	941.5	0.0052298	-0.0016489	0.0096169	0.0009356	0.0109908	0.0002717	0.0182476	0.0023442	0.0120862	0.0013105	0.0001061
RGU(T)-TRC-006	938.2	0.0084370	0.0001345	0.0137258	0.0010492	0.0127043	0.0004705	0.0223579	0.0026992	0.0124238	0.0012884	0.0002181
RGU(T)-TRC-007	935.2	0.0075531	0.0020046	0.0180939	0.0009747	0.0116291	0.0002598	0.0193743	0.0026262	0.0133819	0.0011008	0.0003622
RGU(T)-TRC-008	932.4	0.0045428	-0.0003889	0.0099999	0.0009427	0.0118805	0.0001148	0.0180499	0.0020470	0.0124504	0.0012796	0.0002713
RGU(T)-TRC-009	929.5	0.0079227	-0.0013812	0.0103798	0.0009801	0.0111053	0.0000682	0.0213746	0.0024627	0.0123416	0.0013191	0.0003436
RGU(T)-TRC-010	926.7	0.0070976	0.0012313	0.0109526	0.0012043	0.0123003	0.0004132	0.0220596	0.0022020	0.0124404	0.0009904	0.0006303
RGU(T)-TRC-011	923.2	0.0018501	-0.0001257	0.0058178	0.0005773	0.0104212	-0.0001161	0.0229778	0.0021840	0.0108849	0.0010963	0.0003914
RGU(T)-TRC-012	920.8	0.0020677	-0.0001879	0.0109795	0.0008182	0.0095510	0.0013531	0.0220013	0.0024185	0.0110696	0.0011260	0.0000941
RGU(T)-TRC-013	917.3	0.0074446	0.0036876	0.0111537	0.0007204	0.0139553	0.0000608	0.0214828	0.0027674	0.0139526	0.0010368	0.0003398
RGU(T)-TRC-014	914.2	0.0090368	-0.0026997	0.0094756	0.0009191	0.0089782	0.0011971	0.0272478	0.0019336	0.0122222	0.0011754	0.0007259
RGU(T)-TRC-015	911.6	0.0069160	-0.0007900	0.0111400	0.0006634	0.0115866	0.0008859	0.0227435	0.0025474	0.0115491	0.0009332	0.0007942
RGU(T)-TRC-016	911.5	0.0048484	-0.0012451	0.0073966	0.0006187	0.0095233	0.0009545	0.0125128	0.0025825	0.0261945	0.0011901	0.0010736
RGU(T)-TRC-017	908.5	0.0056154	0.0003855	0.0097736	0.0008132	0.0111921	0.0003272	0.0342242	0.0020221	0.0111563	0.0010573	0.0007180
RGU(T)-TRC-018	905.5	0.0044477	-0.0018356	0.0104446	0.0006488	0.0093800	0.0009082	0.0444844	0.0022614	0.0101358	0.0011552	0.0004840
RGU(T)-TRC-019	902.2	0.0045170	0.0006030	0.0128054	0.0007681	0.0136567	-0.0000613	0.0196293	0.0025196	0.0120238	0.0011714	0.0005031
RGU(T)-TRC-020	899.3	0.0049486	0.0007915	0.0083230	0.0010207	0.0126234	0.0009125	0.0214357	0.0021949	0.0128814	0.0012521	0.0002407
RGU(T)-TRC-021	896.8	0.0042659	-0.0035452	0.0096143	0.0008808	0.0103286	0.0007851	0.0242072	0.0020504	0.0108642	0.0013009	0.0004978
RGU(T)-TRC-022	893.7	0.0068081	0.0004108	0.0111171	0.0006592	0.0107458	0.0011032	0.0310001	0.0019116	0.0106801	0.0009810	0.0006848
RGU(T)-TRC-023	890.2	0.0050934	0.0014801	0.0107282	0.0010688	0.0130870	0.0012472	0.0177217	0.0025669	0.0134671	0.0015882	0.0003898
RGU(T)-TRC-024	887.4	0.0043707	-0.0020573	0.0094024	0.0010486	0.0105764	0.0004592	0.0238681	0.0016221	0.0106794	0.0011071	0.0002927
RGU(T)-TRC-025	884.6	0.0040603	-0.0014717	0.0077197	0.0008906	0.0130123	-0.0000673	0.0226162	0.0021685	0.0129132	0.0011242	0.0003185
RGU(T)-TRC-026	881.2	0.0053368	0.0015787	0.0091300	0.0011030	0.0112868	0.0008527	0.0232627	0.0020790	0.0117387	0.0010761	0.0004023
RGU(T)-TRC-027	880.2	0.0023671	-0.0024836	0.0064187	0.0020836	0.0026277	0.0005384	0.0385760	0.0014935	0.0203283	0.0008660	0.0013635
RGU(T)-TRC-028	878.6	0.0098399	-0.0011161	0.0160591	0.0011118	0.0117626	0.0000614	0.0199254	0.0027811	0.0139126	0.0015197	0.0002126
RGU(T)-TRC-029	875.4	0.0070602	-0.0017820	0.0110403	0.0008976	0.0099816	0.0001958	0.0265389	0.0017874	0.0103976	0.0009261	0.0021067

RGU-1 top half trace elements

Sample ID	Depth (ft.)	NiKa1	CuKa1	ZnKa1	ThLa1	RbKa1	U La1	SrKa1	Y Ka1	ZrKa1	NbKa1	MoKa1
RGU(T)-TRC-030	872.1	0.0063964	0.0007217	0.0114447	0.0008850	0.0131713	0.0003849	0.0189574	0.0025218	0.0129914	0.0012823	0.0003546
RGU(T)-TRC-031	*	0.0058887	0.0059971	0.0157309	0.0011926	0.0123103	0.0002218	0.0180462	0.0023854	0.0123617	0.0014031	0.0004057
RGU(T)-TRC-032	*	0.0056709	0.0012303	0.0097493	0.0008987	0.0133075	0.0000551	0.0218557	0.0021510	0.0120909	0.0012931	0.0004395
RGU(T)-TRC-033	*	0.0063640	0.0056219	0.0099830	0.0008346	0.0111178	0.0000513	0.0249648	0.0021291	0.0119993	0.0010940	0.0010133
RGU(T)-TRC-034	*	0.0039163	0.0025391	0.0077304	0.0009001	0.0100139	0.0003299	0.0213851	0.0023979	0.0108231	0.0010477	0.0012207
RGU(T)-TRC-035	859.1	0.0042702	-0.0025826	0.0064435	0.0006295	0.0075758	0.0009851	0.0259837	0.0016775	0.0090113	0.0007870	0.0011222
RGU(T)-TRC-036	856.5	0.0062380	-0.0026572	0.0078203	0.0008491	0.0108652	0.0007425	0.0192324	0.0019937	0.0126551	0.0012616	0.0002146
RGU(T)-TRC-037	853.1	0.0057394	0.0015541	0.0078055	0.0007810	0.0091676	0.0005702	0.0306497	0.0022100	0.0098076	0.0008264	0.0017015
RGU(T)-TRC-038	850.1	0.0076063	-0.0053904	0.0111295	0.0009878	0.0112320	0.0011661	0.0156909	0.0022081	0.0150843	0.0013426	0.0007259
RGU(T)-TRC-039	847	0.0070285	-0.0015467	0.0119476	0.0008534	0.0132746	0.0008882	0.0198416	0.0027566	0.0144954	0.0012626	0.0001746
RGU(T)-TRC-040	844.5	0.0091296	0.0009726	0.0084786	0.0008162	0.0107184	0.0007936	0.0232238	0.0021376	0.0116809	0.0011328	0.0015233
RGU(T)-TRC-041	841.2	0.0115872	0.0013631	0.0121057	0.0008290	0.0103352	0.0003196	0.0333224	0.0022174	0.0114175	0.0010562	0.0017987
RGU(T)-TRC-042	838.4	0.0133270	0.0005547	0.0112711	0.0008221	0.0124954	0.0016429	0.0191535	0.0025314	0.0130336	0.0015420	0.0017522
RGU(T)-TRC-043	835.7	0.0090134	-0.0010885	0.0101224	0.0006744	0.0111683	0.0007894	0.0249501	0.0025565	0.0107916	0.0010158	0.0012250
RGU(T)-TRC-044	831.9	0.0084021	-0.0015624	0.0120709	0.0008767	0.0116004	0.0008133	0.0215904	0.0020674	0.0106008	0.0010053	0.0027874
RGU(T)-TRC-045	829.9	0.0043440	-0.0002070	0.0097836	0.0007710	0.0107152	0.0010278	0.0317258	0.0018695	0.0086803	0.0010899	0.0028177
RGU(T)-TRC-046	826.5	0.0078029	-0.0022289	0.0107469	0.0005614	0.0113862	0.0014281	0.0330396	0.0017104	0.0094718	0.0010761	0.0012075
RGU(T)-TRC-047	823.6	0.0053579	-0.0021462	0.0120910	0.0009034	0.0128464	0.0007394	0.0255563	0.0019163	0.0108137	0.0011683	0.0011218
RGU(T)-TRC-048	821.9	0.0024728	-0.0040695	0.0066742	0.0009137	0.0109592	-0.0000032	0.0281657	0.0019907	0.0099995	0.0010583	0.0008204
RGU(T)-TRC-049	821.4	0.0046534	-0.0015352	0.0126377	0.0012358	0.0033377	0.0008566	0.0788637	0.0014179	0.0354283	0.0030460	0.0005444
RGU(T)-TRC-050	820.7	0.0024851	-0.0019707	0.0090570	0.0016193	0.0024880	0.0007516	0.0501705	0.0010916	0.0184073	0.0019232	0.0006267
RGU(T)-TRC-051	816.7	0.0021844	-0.0007784	0.0071523	0.0012130	0.0008001	0.0011231	0.0411616	0.0009920	0.0147745	0.0022646	-0.0002082
RGU(T)-TRC-052	813.2	0.0034727	-0.0008121	0.0080205	0.0008774	0.0100783	0.0004399	0.0260904	0.0017699	0.0110863	0.0014126	0.0010908
RGU(T)-TRC-053	810.5	0.0046401	-0.0023984	0.0114672	0.0007448	0.0074993	0.0004888	0.0526470	0.0014406	0.0074111	0.0008578	0.0006568
RGU(T)-TRC-054	807.5	0.0071786	-0.0033984	0.0063649	0.0006123	0.0094799	-0.0003779	0.1009138	0.0022236	0.0057794	0.0009273	0.0013306
RGU(T)-TRC-055	804.5	0.0043580	-0.0002511	0.0101715	0.0008969	0.0109638	0.0007623	0.0361250	0.0015612	0.0101238	0.0011960	0.0009429
RGU(T)-TRC-056	800.5	0.0099643	-0.0010595	0.0090190	0.0011137	0.0122707	-0.0003099	0.0262254	0.0018020	0.0117781	0.0010303	0.0012975
RGU(T)-TRC-057	797.3	0.0043106	-0.0016597	0.0103395	0.0009009	0.0100322	-0.0001272	0.0244089	0.0018956	0.0096410	0.0013862	0.0012807
RGU(T)-TRC-058	794.2	0.0056763	-0.0019041	0.0066759	0.0007287	0.0102426	0.0000157	0.0284694	0.0024599	0.0097685	0.0010365	0.0016258

RGU-1 top half trace elements

Sample ID	Depth (ft.)	NiKa1	CuKa1	ZnKa1	ThLa1	RbKa1	U La1	SrKa1	Y Ka1	ZrKa1	NbKa1	MoKa1
RGU(T)-TRC-059	791.7	0.0051758	0.0004661	0.0098526	0.0009699	0.0123546	0.0011663	0.0248559	0.0023237	0.0114152	0.0009689	0.0026732
RGU(T)-TRC-060	788.2	0.0056041	-0.0017216	0.0103388	0.0009243	0.0117218	0.0002641	0.0227697	0.0020965	0.0104467	0.0011838	0.0006369
RGU(T)-TRC-061	785.2	0.0069899	-0.0002407	0.0128647	0.0009887	0.0130133	0.0003695	0.0239571	0.0020556	0.0120832	0.0012521	0.0007701
RGU(T)-TRC-062	782.3	0.0045600	0.0004256	0.0128049	0.0008257	0.0121189	0.0002218	0.0228582	0.0023883	0.0111335	0.0012342	0.0004932
RGU(T)-TRC-063	779.4	0.0065079	-0.0030349	0.0099179	0.0008212	0.0113500	-0.0002571	0.0203983	0.0025295	0.0110467	0.0011689	0.0006589
RGU(T)-TRC-064	776.8	0.0047018	-0.0033362	0.0117599	0.0008855	0.0101701	0.0003313	0.0224437	0.0019759	0.0112782	0.0013209	0.0009144
RGU(T)-TRC-065	773.1	0.0068050	-0.0003657	0.0090640	0.0010088	0.0110105	0.0002952	0.0215421	0.0019049	0.0104849	0.0010520	0.0008082
RGU(T)-TRC-066	770.4	0.0050050	0.0000290	0.0094809	0.0010172	0.0130827	0.0008051	0.0227950	0.0024226	0.0125278	0.0008737	0.0009184
RGU(T)-TRC-067	767.3	0.0066918	-0.0003146	0.0114099	0.0008422	0.0127704	0.0003864	0.0226737	0.0019842	0.0109336	0.0010948	0.0010718
RGU(T)-TRC-068	764.6	0.0048282	-0.0003639	0.0082635	0.0007653	0.0115231	0.0007203	0.0284191	0.0020330	0.0116743	0.0011283	0.0011315
RGU(T)-TRC-069	761.6	0.0083798	-0.0010995	0.0116594	0.0009804	0.0120295	0.0002158	0.0239210	0.0022142	0.0115284	0.0012370	0.0007411
RGU(T)-TRC-070	758.2	0.0068658	0.0027381	0.0151943	0.0009055	0.0123499	0.0016094	0.0317375	0.0027322	0.0117376	0.0010330	0.0020601
RGU(T)-TRC-071	755.4	0.0049734	-0.0005174	0.0107093	0.0007694	0.0134970	0.0005703	0.0218798	0.0020426	0.0112018	0.0011346	0.0013009
RGU(T)-TRC-072	752.3	0.0048586	-0.0010347	0.0094919	0.0009205	0.0114799	0.0003373	0.0259194	0.0023431	0.0109663	0.0009815	0.0009424
RGU(T)-TRC-073	749.2	0.0005007	-0.0022721	0.0128059	0.0006349	0.0072063	-0.0002849	0.0279207	0.0020123	0.0115716	0.0010678	0.0008596
RGU(T)-TRC-074	746.9	0.0048054	-0.0025648	0.0090444	0.0007060	0.0112319	0.0012889	0.0293852	0.0019264	0.0116184	0.0014064	0.0009086
RGU(T)-TRC-075	743.1	0.0077457	0.0010773	0.0101475	0.0007908	0.0110598	0.0008819	0.0262347	0.0024308	0.0113519	0.0012275	0.0007097
RGU(T)-TRC-076	740.3	0.0058278	-0.0004023	0.0110025	0.0006646	0.0123765	-0.0009297	0.0270489	0.0019461	0.0117308	0.0012058	0.0012307
RGU(T)-TRC-077	737.5	0.0013936	0.0018388	0.0085871	0.0006037	0.0119062	0.0009351	0.0281697	0.0024842	0.0119219	0.0009702	0.0016509
RGU(T)-TRC-078	734.5	0.0063900	-0.0012687	0.0096766	0.0008104	0.0115156	0.0019399	0.0278596	0.0020967	0.0130934	0.0012344	0.0014914
RGU(T)-TRC-079	731.4	0.0066468	0.0011738	0.0094607	0.0009550	0.0123136	0.0001375	0.0231109	0.0023360	0.0125294	0.0011863	0.0015384
RGU(T)-TRC-080	729.4	0.0064539	-0.0002177	0.0093422	0.0009422	0.0109927	0.0006445	0.0219754	0.0020224	0.0120378	0.0011072	0.0015929
RGU(T)-TRC-081	726.6	0.0062282	0.0033320	0.0107888	0.0009510	0.0112661	0.0009255	0.0239493	0.0018996	0.0136267	0.0009813	0.0013633
RGU(T)-TRC-082	723.7	0.0071889	-0.0006301	0.0095935	0.0011823	0.0107955	0.0003856	0.0232632	0.0017915	0.0131550	0.0013627	0.0009370
RGU(T)-TRC-083	720.5	0.0057914	-0.0004981	0.0076011	0.0010423	0.0104799	0.0005756	0.0188943	0.0024993	0.0188926	0.0015740	0.0003450
RGU(T)-TRC-084	717.2	0.0045902	-0.0005367	0.0086866	0.0008380	0.0125739	0.0008107	0.0262026	0.0022445	0.0122568	0.0011175	0.0015064
RGU(T)-TRC-085	714.5	0.0095053	0.0016990	0.0092522	0.0008142	0.0107851	0.0020264	0.0345311	0.0029163	0.0127775	0.0010594	0.0014297
RGU(T)-TRC-086	711.7	0.0058139	-0.0030412	0.0073454	0.0009099	0.0101276	0.0003466	0.0209354	0.0022268	0.0117597	0.0011309	0.0009549
RGU(T)-TRC-087	708.3	0.0072137	0.0036618	0.0121445	0.0010206	0.0117499	0.0001533	0.0215629	0.0027156	0.0119324	0.0011543	0.0009633

RGU-1 top half trace elements

Sample ID	Depth (ft.)	NiKa1	CuKa1	ZnKa1	ThLa1	RbKa1	U La1	SrKa1	Y Ka1	ZrKa1	NbKa1	MoKa1
RGU(T)-TRC-088	705.1	0.0051224	-0.0007682	0.0095266	0.0009568	0.0107769	0.0000515	0.0190661	0.0020811	0.0115266	0.0011229	0.0004645
RGU(T)-TRC-089	702.5	0.0056536	0.0019878	0.0107984	0.0008386	0.0113390	0.0000555	0.0249419	0.0023343	0.0142183	0.0012446	0.0005772
RGU(T)-TRC-090	699.5	0.0065728	0.0007025	0.0104794	0.0010194	0.0126900	-0.0004932	0.0260285	0.0024500	0.0137017	0.0014515	0.0008281
RGU(T)-TRC-091	696.3	0.0072438	0.0021550	0.0107027	0.0010201	0.0134647	0.0006922	0.0190475	0.0023803	0.0128443	0.0012536	0.0005579
RGU(T)-TRC-092	693.2	0.0019271	-0.0012130	0.0072640	0.0008487	0.0103643	0.0012374	0.0169593	0.0021945	0.0180325	0.0013224	0.0008189
RGU(T)-TRC-093	690.3	0.0032512	-0.0008910	0.0076827	0.0009841	0.0108263	0.0003070	0.0233391	0.0021265	0.0122269	0.0010883	0.0007113
RGU(T)-TRC-094	687.2	0.0077964	0.0007702	0.0159256	0.0008121	0.0108768	0.0000590	0.0282666	0.0028963	0.0121696	0.0009126	0.0010959
RGU(T)-TRC-095	684.2	0.0078312	0.0010874	0.0106052	0.0011784	0.0125223	0.0000531	0.0215212	0.0023523	0.0136074	0.0010831	0.0007522
RGU(T)-TRC-096	681.5	0.0056785	0.0015835	0.0104065	0.0007926	0.0129277	0.0000146	0.0191906	0.0021794	0.0121962	0.0011938	0.0006527
RGU(T)-TRC-097	678.4	0.0081773	-0.0016935	0.0102759	0.0008806	0.0126493	0.0001753	0.0178442	0.0024627	0.0124095	0.0010980	0.0005006
RGU(T)-TRC-098	675.4	0.0024594	-0.0021208	0.0073509	0.0008843	0.0115504	0.0008732	0.0163741	0.0021382	0.0122631	0.0011263	0.0003779
RGU(T)-TRC-099	672.5	-0.0002392	-0.0023975	0.0081407	0.0006832	0.0121432	-0.0002399	0.0191944	0.0027537	0.0120558	0.0010710	0.0005659
RGU(T)-TRC-100	669.3	0.0018526	0.0012846	0.0092992	0.0009454	0.0107905	0.0007889	0.0190617	0.0022358	0.0127748	0.0012340	0.0004495
RGU(T)-TRC-101	668.7	0.0043071	-0.0022264	0.0404620	0.0011498	0.0012615	0.0007058	0.0905887	0.0013119	0.0245557	0.0021066	0.0017977
RGU(T)-TRC-102	666.6	0.0060568	-0.0047763	0.0107187	0.0007913	0.0116789	0.0007272	0.0209502	0.0022564	0.0118558	0.0012328	0.0005574
RGU(T)-TRC-103	663.5	0.0090301	-0.0004355	0.0108821	0.0010473	0.0104180	0.0013729	0.0285038	0.0018980	0.0121411	0.0010091	0.0009317
RGU(T)-TRC-104	660.3	0.0038067	0.0006989	0.0081079	0.0008186	0.0106759	0.0002861	0.0217977	0.0022813	0.0133277	0.0010410	0.0011227
RGU(T)-TRC-105	657.2	0.0045487	0.0005159	0.0092130	0.0009203	0.0112927	0.0009815	0.0200226	0.0022809	0.0136445	0.0013957	0.0008989
RGU(T)-TRC-106	654.4	0.0091828	-0.0006420	0.0117493	0.0010100	0.0110774	0.0004317	0.0221265	0.0022282	0.0133883	0.0012221	0.0010824
RGU(T)-TRC-107	651.4	0.0074532	-0.0028479	0.0117853	0.0008137	0.0110711	0.0003846	0.0203621	0.0025331	0.0117886	0.0013439	0.0006959
RGU(T)-TRC-108	648.7	0.0087973	0.0001133	0.0083839	0.0007795	0.0134471	-0.0001711	0.0200549	0.0027646	0.0123130	0.0010222	0.0011341
RGU(T)-TRC-109	645.1	0.0055373	-0.0017079	0.0094976	0.0010129	0.0106200	-0.0000732	0.0192793	0.0022783	0.0138341	0.0015643	0.0004207
RGU(T)-TRC-110	642.1	0.0112587	0.0013322	0.0115746	0.0009653	0.0128758	0.0000556	0.0205829	0.0024626	0.0142210	0.0011329	0.0008963
RGU(T)-TRC-111	639.7	0.0029728	0.0003438	0.0106468	0.0009128	0.0105693	0.0000631	0.0192671	0.0020874	0.0138911	0.0014067	0.0011180
RGU(T)-TRC-112	636.2	0.0013762	-0.0018234	0.0072318	0.0008956	0.0110173	-0.0001673	0.0173050	0.0018424	0.0129366	0.0012950	0.0005347
RGU(T)-TRC-113	633.8	0.0061909	-0.0000204	0.0099581	0.0009315	0.0113810	0.0008939	0.0231651	0.0027071	0.0143348	0.0009347	0.0008092
RGU(T)-TRC-114	630.1	0.0040923	-0.0003055	0.0092374	0.0009318	0.0115650	0.0002483	0.0199860	0.0018237	0.0128936	0.0013678	0.0005879
RGU(T)-TRC-115	627.5	0.0068217	0.0021334	0.0085631	0.0006372	0.0114391	0.0005216	0.0268339	0.0031982	0.0133456	0.0011697	0.0003824
RGU(T)-TRC-116	624.3	0.0042275	0.0008023	0.0104195	0.0009905	0.0115725	0.0010337	0.0230104	0.0022872	0.0134954	0.0012197	0.0014022

RGU-1 top half trace elements

Sample ID	Depth (ft.)	NiKa1	CuKa1	ZnKa1	ThLa1	RbKa1	U La1	SrKa1	Y Ka1	ZrKa1	NbKa1	MoKa1
RGU(T)-TRC-117	621.1	0.0071130	-0.0000917	0.0103915	0.0008277	0.0120677	0.0006153	0.0174409	0.0026559	0.0164608	0.0012508	0.0009796
RGU(T)-TRC-118	618.5	0.0050428	0.0023869	0.0097576	0.0008629	0.0129053	0.0005461	0.0218939	0.0024697	0.0128043	0.0012776	0.0002480
RGU(T)-TRC-119	615.2	0.0022400	-0.0023684	0.0082970	0.0007752	0.0083410	0.0005353	0.0192772	0.0022860	0.0160374	0.0011206	0.0006853
RGU(T)-TRC-120	612.4	0.0102129	-0.0026453	0.0092380	0.0008867	0.0126904	-0.0002127	0.0234586	0.0022687	0.0127153	0.0012287	0.0003923
RGU(T)-TRC-121	609.4	0.0054358	0.0028382	0.0065120	0.0009055	0.0130231	0.0005975	0.0177557	0.0020313	0.0136719	0.0012854	0.0008668
RGU(T)-TRC-122	606.6	0.0032464	0.0028148	0.0089706	0.0008866	0.0119012	0.0002565	0.0189018	0.0027094	0.0149099	0.0013057	0.0003122
RGU(T)-TRC-123	603.7	0.0070364	-0.0011465	0.0098120	0.0009228	0.0109211	0.0004116	0.0158783	0.0026416	0.0153945	0.0012101	0.0004670
RGU(T)-TRC-124	600.5	0.0031763	-0.0012066	0.0080150	0.0008347	0.0097523	0.0009699	0.0177668	0.0021151	0.0141063	0.0010833	0.0004224
RGU(T)-TRC-125	597.4	0.0082433	0.0032306	0.0075901	0.0008574	0.0116013	0.0001952	0.0183262	0.0026260	0.0154056	0.0012116	0.0003916
RGU(T)-TRC-126	594.2	0.0035838	0.0026434	0.0090125	0.0009602	0.0115234	0.0005072	0.0202254	0.0027888	0.0153695	0.0010643	0.0007145
RGU(T)-TRC-127	591.5	0.0037466	-0.0016436	0.0087094	0.0007465	0.0108624	0.0004494	0.0178838	0.0024068	0.0144944	0.0011730	0.0004048
RGU(T)-TRC-128	588.3	0.0086970	-0.0027783	0.0091919	0.0010143	0.0122517	0.0006099	0.0200094	0.0025059	0.0155887	0.0009979	0.0005708
RGU(T)-TRC-129	585.6	0.0072775	-0.0019331	0.0094580	0.0009427	0.0119308	0.0003421	0.0195910	0.0026457	0.0152923	0.0012942	0.0005425
RGU(T)-TRC-130	582.6	0.0080319	-0.0007000	0.0062890	0.0009429	0.0116642	0.0000293	0.0215300	0.0028058	0.0152161	0.0013109	0.0005447
RGU(T)-TRC-131	*	0.0036427	0.0001967	0.0095632	0.0010119	0.0086047	0.0005825	0.0174550	0.0021918	0.0162464	0.0010721	0.0006522
RGU(T)-TRC-132	*	-0.0009213	0.0050524	0.0094070	0.0011880	0.0099767	0.0005289	0.0198827	0.0021952	0.0140215	0.0011921	0.0005810
RGU(T)-TRC-133	*	0.0041844	0.0010572	0.0099326	0.0009801	0.0099858	0.0007509	0.0196802	0.0022836	0.0154429	0.0012005	0.0005423
RGU(T)-TRC-134	*	0.0051279	-0.0000304	0.0074191	0.0009819	0.0112279	0.0005579	0.0156825	0.0025040	0.0157520	0.0010958	0.0005392
RGU(T)-TRC-135	571.4	0.0035045	-0.0015753	0.0090522	0.0008161	0.0118888	0.0008939	0.0194442	0.0022515	0.0171853	0.0012706	0.0007922
RGU(T)-TRC-136	568.3	0.0071978	-0.0003293	0.0110959	0.0011219	0.0110889	0.0008677	0.0161214	0.0028091	0.0158685	0.0014308	0.0006738
RGU(T)-TRC-137	565.5	0.0074124	-0.0030582	0.0073027	0.0012234	0.0110924	0.0002870	0.0169503	0.0026384	0.0147566	0.0012111	0.0005106
RGU(T)-TRC-138	562.4	0.0028177	0.0030731	0.0140726	0.0006586	0.0117478	0.0003548	0.0180434	0.0025006	0.0170876	0.0014604	0.0005493
RGU(T)-TRC-139	559.1	0.0047361	0.0014091	0.0092528	0.0008565	0.0114002	0.0003015	0.0184284	0.0024761	0.0135551	0.0011971	0.0007486
RGU(T)-TRC-140	556.5	0.0037721	0.0016333	0.0061796	0.0008306	0.0123337	0.0006864	0.0168373	0.0024046	0.0134803	0.0011432	0.0005823
RGU(T)-TRC-141	553.6	0.0031596	0.0022943	0.0065911	0.0005880	0.0079819	0.0000655	0.0177830	0.0021264	0.0126192	0.0006828	0.0009557
RGU(T)-TRC-142	550.4	0.0018689	-0.0019369	0.0066935	0.0008577	0.0096265	-0.0005581	0.0174664	0.0024569	0.0181421	0.0011437	0.0009703
RGU(T)-TRC-143	547.5	0.0030484	-0.0025460	0.0082515	0.0006852	0.0100728	0.0006746	0.0182870	0.0024251	0.0155973	0.0009824	0.0007988
RGU(T)-TRC-144	544.5	0.0035809	-0.0027822	0.0082432	0.0008511	0.0102706	0.0002900	0.0182178	0.0020945	0.0205677	0.0012479	0.0013335
RGU(T)-TRC-145	541.5	0.0003973	-0.0018704	0.0058406	0.0008098	0.0076736	0.0001142	0.0180982	0.0024647	0.0181915	0.0009673	0.0009514

RGU-1 top half trace elements

Sample ID	Depth (ft.)	NiKa1	CuKa1	ZnKa1	ThLa1	RbKa1	U La1	SrKa1	Y Ka1	ZrKa1	NbKa1	MoKa1
RGU(T)-TRC-146	538.6	0.0043176	0.0029552	0.0060029	0.0006947	0.0105632	0.0005527	0.0176215	0.0025277	0.0178243	0.0010294	0.0008708
RGU(T)-TRC-147	535.5	-0.0005904	-0.0047173	0.0075660	0.0007540	0.0079185	-0.0002929	0.0156013	0.0022630	0.0240232	0.0011627	0.0011898
RGU(T)-TRC-148	532.5	0.0036996	-0.0021431	0.0059783	0.0007851	0.0097271	0.0000558	0.0168595	0.0027242	0.0179321	0.0010329	0.0006917
RGU(T)-TRC-149	529.5	0.0054294	-0.0020760	0.0056230	0.0007848	0.0109176	-0.0010423	0.0172103	0.0020486	0.0193976	0.0011526	0.0011413
RGU(T)-TRC-150	526.2	0.0020027	-0.0009357	0.0057064	0.0007470	0.0101003	0.0008590	0.0184706	0.0023712	0.0158997	0.0011653	0.0005551
RGU(T)-TRC-151	523.3	0.0004727	-0.0010078	0.0051978	0.0006957	0.0081275	0.0000494	0.0160017	0.0022201	0.0230554	0.0014274	0.0005622
RGU(T)-TRC-152	*	0.0069820	0.0032436	0.0071420	0.0007507	0.0110577	0.0015467	0.0187451	0.0024918	0.0186759	0.0010652	0.0008811
RGU(T)-TRC-153	*	0.0058069	0.0009521	0.0088866	0.0010125	0.0105770	0.0005921	0.0172684	0.0023445	0.0162542	0.0010847	0.0007467
RGU(T)-TRC-154	*	0.0046604	0.0018421	0.0074747	0.0008118	0.0098699	0.0002656	0.0168932	0.0028299	0.0163225	0.0012498	0.0003363
RGU(T)-TRC-155	511.3	0.0030052	-0.0020361	0.0081763	0.0007436	0.0093651	0.0001495	0.0147517	0.0023718	0.0174103	0.0010698	0.0009090
RGU(T)-TRC-156	508.6	0.0005217	-0.0043124	0.0071566	0.0005431	0.0114196	0.0001124	0.0146328	0.0024993	0.0202892	0.0010498	0.0010400
RGU(T)-TRC-157	505.6	0.0016077	-0.0023878	0.0069231	0.0006987	0.0089764	0.0005355	0.0150862	0.0020894	0.0203483	0.0011973	0.0010749
RGU(T)-TRC-158	502.5	0.0011968	-0.0047262	0.0066407	0.0006103	0.0101589	0.0001007	0.0162458	0.0021519	0.0207040	0.0011156	0.0010351
RGU(T)-TRC-159	499.3	0.0018569	0.0003597	0.0051082	0.0009378	0.0095548	0.0004722	0.0185559	0.0022774	0.0170559	0.0011755	0.0007641
RGU(T)-TRC-160	496.4	-0.0006911	-0.0014980	0.0045413	0.0006592	0.0069260	0.0004731	0.0151307	0.0023310	0.0230200	0.0009196	0.0013220
RGU(T)-TRC-161	493.1	0.0057048	-0.0028791	0.0064282	0.0008534	0.0101515	0.0003132	0.0163196	0.0025408	0.0184203	0.0012661	0.0009932
RGU(T)-TRC-162	483.7	-0.0000709	-0.0026627	0.0038899	0.0007073	0.0084294	0.0000205	0.0136144	0.0020651	0.0210794	0.0010007	0.0014403
RGU(T)-TRC-163	482.1	0.0004355	-0.0015790	0.0063696	0.0006378	0.0099840	-0.0008659	0.0177335	0.0023452	0.0144037	0.0010348	0.0005020
RGU(T)-TRC-164	479.7	0.0024727	-0.0027015	0.0056224	0.0007597	0.0105741	0.0000968	0.0137223	0.0025920	0.0156948	0.0009749	0.0006839
RGU(T)-TRC-165	476.5	0.0008980	-0.0036810	0.0041971	0.0007759	0.0073803	-0.0002800	0.0119433	0.0018642	0.0197736	0.0011349	0.0008576
RGU(T)-TRC-166	473.4	0.0023178	-0.0020479	0.0045726	0.0006249	0.0086800	-0.0006589	0.0138283	0.0024159	0.0225550	0.0010960	0.0011521
RGU(T)-TRC-167	470.3	-0.0021948	-0.0020153	0.0058079	0.0003656	0.0081265	0.0002366	0.0131606	0.0021578	0.0190821	0.0009204	0.0009374
RGU(T)-TRC-168	467.7	0.0000047	-0.0032079	0.0045996	0.0005440	0.0103070	-0.0005896	0.0147216	0.0027996	0.0162720	0.0012350	0.0005941
RGU(T)-TRC-169	467.1	0.0025858	-0.0020241	0.0127889	0.0008026	0.0034660	0.0012935	0.0609818	0.0014834	0.0275114	0.0021197	0.0008664
RGU(T)-TRC-170	465.6	0.0028249	-0.0027263	0.0085400	0.0007522	0.0077164	-0.0002865	0.0286870	0.0022569	0.0201935	0.0016379	0.0004935
RGU(T)-TRC-171	462.4	0.0036797	-0.0033331	0.0045258	0.0010405	0.0093417	0.0002767	0.0218298	0.0019351	0.0156049	0.0012020	0.0005873
RGU(T)-TRC-172	459.3	0.0014473	0.0000218	0.0067142	0.0009424	0.0097144	0.0005338	0.0192452	0.0024578	0.0217128	0.0011913	0.0009592
RGU(T)-TRC-173	456.5	0.0053672	-0.0025131	0.0050666	0.0005165	0.0099290	0.0002198	0.0154703	0.0028959	0.0218705	0.0011134	0.0008876
RGU(T)-TRC-174	454.2	0.0043192	0.0000471	0.0033346	0.0005827	0.0080630	0.0002294	0.0130668	0.0025296	0.0224442	0.0011382	0.0009573

RGU-1 top half trace elements

Sample ID	Depth (ft.)	NiKa1	CuKa1	ZnKa1	ThLa1	RbKa1	U La1	SrKa1	Y Ka1	ZrKa1	NbKa1	MoKa1
RGU(T)-TRC-175	438.8	0.0018037	-0.0021657	0.0057549	0.0005493	0.0077976	-0.0000109	0.0118942	0.0022689	0.0275882	0.0009913	0.0014648
RGU(T)-TRC-176	435.3	0.0011336	-0.0035929	0.0050337	0.0005113	0.0083500	-0.0004696	0.0114772	0.0025332	0.0281736	0.0010560	0.0017390
RGU(T)-TRC-177	433.6	0.0024153	-0.0017934	0.0044751	0.0005597	0.0064437	0.0004472	0.0134237	0.0024344	0.0275351	0.0008945	0.0018334
RGU(T)-TRC-178	433.3	0.0008677	-0.0052876	0.0007985	0.0001722	0.0014310	0.0003182	0.0302277	0.0006045	0.0070505	0.0002203	0.0009938
RGU(T)-TRC-179	430.2	0.0019720	-0.0006491	0.0026359	0.0008119	0.0068344	0.0001020	0.0103127	0.0024678	0.0307991	0.0011604	0.0018113
RGU(T)-TRC-180	427.2	-0.0006228	-0.0017074	0.0049375	0.0007369	0.0069325	0.0004262	0.0096251	0.0021895	0.0311376	0.0011739	0.0018172
RGU(T)-TRC-181	424.6	0.0012862	-0.0014302	0.0052981	0.0006357	0.0075566	0.0004143	0.0115339	0.0021891	0.0318654	0.0009771	0.0019571
RGU(T)-TRC-182	421.4	0.0014002	0.0002831	0.0049470	0.0005826	0.0066927	0.0003098	0.0104056	0.0024225	0.0400759	0.0011731	0.0024477
RGU(T)-TRC-183	418.5	0.0025661	-0.0010901	0.0047602	0.0005916	0.0070704	0.0000271	0.0102138	0.0022315	0.0353661	0.0012896	0.0021894
RGU(T)-TRC-184	415.7	-0.0019156	-0.0006788	0.0049246	0.0004668	0.0094663	-0.0003869	0.0112670	0.0024461	0.0300334	0.0010797	0.0016562
RGU(T)-TRC-185	412.5	0.0036932	-0.0017294	0.0036825	0.0007066	0.0104352	0.0000462	0.0156896	0.0024665	0.0193734	0.0011882	0.0013608
RGU(T)-TRC-186	409.4	-0.0025213	-0.0019601	0.0037181	0.0004996	0.0059291	0.0001515	0.0158279	0.0025697	0.0335760	0.0012500	0.0022550
RGU(T)-TRC-187	406.3	0.0014489	-0.0007162	0.0075149	0.0007895	0.0098338	0.0004690	0.0199523	0.0021631	0.0168377	0.0008766	0.0010199
RGU(T)-TRC-188	403.3	0.0036310	-0.0025424	0.0047711	0.0005747	0.0096622	-0.0002528	0.0147518	0.0025870	0.0166533	0.0010591	0.0009192
RGU(T)-TRC-189	400.2	0.0011232	-0.0023805	0.0057138	0.0006259	0.0088488	-0.0006893	0.0143629	0.0025906	0.0219051	0.0012127	0.0008711
RGU(T)-TRC-190	397.3	0.0026820	-0.0030042	0.0061298	0.0007292	0.0096133	0.0005451	0.0142979	0.0023242	0.0206995	0.0011323	0.0006806
RGU(T)-TRC-191	394.5	0.0026327	-0.0025379	0.0053980	0.0008354	0.0098406	-0.0002739	0.0151678	0.0025899	0.0219267	0.0012871	0.0010596
RGU(T)-TRC-192	391.2	0.0002396	-0.0015265	0.0042365	0.0006659	0.0107152	-0.0002916	0.0135089	0.0019815	0.0230410	0.0013419	0.0010494
RGU(T)-TRC-193	388.3	0.0038554	-0.0025909	0.0047774	0.0006856	0.0096686	-0.0005530	0.0140009	0.0022321	0.0181840	0.0010433	0.0010144
RGU(T)-TRC-194	385.6	0.0009013	-0.0003864	0.0039010	0.0007739	0.0093856	0.0000788	0.0152271	0.0023825	0.0173951	0.0008420	0.0010809
RGU(T)-TRC-195	382.1	0.0026857	-0.0033671	0.0043793	0.0006154	0.0076932	-0.0001273	0.0131694	0.0020623	0.0217184	0.0011075	0.0011997
RGU(T)-TRC-196	379.9	0.0011586	0.0011070	0.0031458	0.0005511	0.0095027	0.0003860	0.0142661	0.0023720	0.0198950	0.0010269	0.0011632
RGU(T)-TRC-197	*	0.0044813	0.0042191	0.0098814	0.0007116	0.0109080	0.0005132	0.0169219	0.0026106	0.0195638	0.0010411	0.0006819
RGU(T)-TRC-198	*	0.0024237	0.0016923	0.0084475	0.0007750	0.0094063	-0.0000559	0.0162393	0.0021288	0.0183072	0.0009135	0.0009927
RGU(T)-TRC-199	*	0.0014753	0.0006528	0.0048182	0.0006474	0.0071512	0.0002805	0.0149433	0.0022369	0.0224763	0.0010107	0.0014387
RGU(T)-TRC-200	*	0.0019666	-0.0002836	0.0070517	0.0006242	0.0096475	0.0008859	0.0157651	0.0028263	0.0241515	0.0011159	0.0011613
RGU(T)-TRC-201	360.5	-0.0000875	-0.0035795	0.0057361	0.0006636	0.0086575	0.0004152	0.0153298	0.0024528	0.0192227	0.0010700	0.0010573
RGU(T)-TRC-202	355.8	0.0021437	-0.0025761	0.0049901	0.0005685	0.0070717	-0.0000956	0.0138659	0.0023659	0.0221965	0.0009524	0.0011300
RGU(T)-TRC-203	351.8	0.0013306	-0.0030465	0.0041376	0.0003607	0.0077427	0.0002976	0.0163001	0.0025276	0.0279586	0.0009963	0.0018237

RGU-1 top half trace elements

Sample ID	Depth (ft.)	NiKa1	CuKa1	ZnKa1	ThLa1	RbKa1	U La1	SrKa1	Y Ka1	ZrKa1	NbKa1	MoKa1
RGU(T)-TRC-204	350.9	0.0016652	-0.0043678	0.0054643	0.0005605	0.0077228	0.0000832	0.0135766	0.0022445	0.0196617	0.0012237	0.0010338
RGU(T)-TRC-205	348.4	0.0018031	-0.0038722	0.0049881	0.0006041	0.0080724	0.0004196	0.0162937	0.0024278	0.0197092	0.0010555	0.0008746
RGU(T)-TRC-206	345.4	0.0006051	-0.0028923	0.0065004	0.0006235	0.0080476	0.0005628	0.0147345	0.0020875	0.0220093	0.0010437	0.0013033
RGU(T)-TRC-207	342.5	0.0032257	-0.0033426	0.0066007	0.0006340	0.0093595	0.0003821	0.0157859	0.0023647	0.0227323	0.0011170	0.0012650
RGU(T)-TRC-208	339.5	0.0020647	-0.0029623	0.0026708	0.0006137	0.0063049	0.0000777	0.0128194	0.0023311	0.0312984	0.0010802	0.0020196
RGU(T)-TRC-209	336.7	0.0004039	-0.0004747	0.0057236	0.0008236	0.0078811	-0.0002559	0.0131505	0.0021955	0.0274843	0.0011203	0.0015430
RGU(T)-TRC-210	334.4	0.0000179	-0.0016433	0.0049788	0.0006951	0.0096585	0.0000453	0.0149733	0.0025969	0.0264711	0.0013636	0.0012699
RGU(T)-TRC-211	331.3	0.0024447	-0.0039284	0.0088897	0.0005997	0.0092567	-0.0005669	0.0150678	0.0021957	0.0203144	0.0011989	0.0009852
RGU(T)-TRC-212	328.5	0.0037181	-0.0022442	0.0047645	0.0006362	0.0073188	-0.0000429	0.0122127	0.0019391	0.0257551	0.0010039	0.0015003
RGU(T)-TRC-213	325.4	0.0027606	-0.0042282	0.0051224	0.0005668	0.0090915	0.0006250	0.0144102	0.0021678	0.0235152	0.0011703	0.0010397
RGU(T)-TRC-214	322.5	-0.0002536	-0.0012130	0.0044916	0.0004773	0.0079292	-0.0001816	0.0129332	0.0023742	0.0234586	0.0010882	0.0012256
RGU(T)-TRC-215	319.6	0.0054058	-0.0028408	0.0060186	0.0008279	0.0082548	-0.0005265	0.0137562	0.0020947	0.0219262	0.0011875	0.0008047
RGU(T)-TRC-216	316.2	0.0010069	-0.0023979	0.0051748	0.0007139	0.0091403	-0.0000673	0.0146051	0.0024779	0.0262460	0.0012962	0.0011264
RGU(T)-TRC-217	295.2	0.0000465	-0.0032820	0.0034556	0.0005165	0.0079606	-0.0005361	0.0123822	0.0024992	0.0281578	0.0011157	0.0016509
RGU(T)-TRC-218	292.2	-0.0001268	-0.0025044	0.0046704	0.0003621	0.0043929	-0.0000087	0.0164334	0.0035385	0.0612916	0.0016262	0.0037483
RGU(T)-TRC-219	289.6	0.0001674	-0.0050800	0.0043123	0.0003181	0.0080144	0.0001847	0.0129687	0.0025447	0.0285451	0.0010416	0.0011961
RGU(T)-TRC-220	267.5	0.0009538	-0.0037068	0.0037340	0.0007719	0.0054090	0.0000396	0.0104765	0.0020274	0.0281844	0.0009632	0.0015424
RGU(T)-TRC-221	264.5	0.0026149	-0.0033109	0.0046556	0.0005566	0.0065193	0.0000760	0.0108916	0.0026090	0.0406757	0.0010848	0.0024896
RGU(T)-TRC-222	261.6	0.0021399	-0.0022044	0.0055728	0.0008097	0.0097792	0.0002069	0.0157091	0.0021637	0.0282037	0.0013599	0.0014344
RGU(T)-TRC-223	229.8	0.0008287	-0.0023535	0.0045517	0.0006609	0.0064386	-0.0005256	0.0123840	0.0025556	0.0368977	0.0013419	0.0021657
RGU(T)-TRC-224	226.2	0.0022667	-0.0022235	0.0037700	0.0007004	0.0083035	0.0001623	0.0126464	0.0026583	0.0412481	0.0012216	0.0024858
RGU(T)-TRC-225	223.2	0.0041861	0.0002388	0.0047152	0.0004953	0.0081898	0.0004659	0.0124492	0.0027658	0.0373838	0.0012068	0.0021382
RGU(T)-TRC-226	220.3	-0.0007197	-0.0012983	0.0034002	0.0004484	0.0045076	0.0007448	0.0133994	0.0032359	0.0546178	0.0013082	0.0030451

* = Uncertain Depth Measurement (i.e., core crushed, core loose and not filling core box, dubious core box measurements)

REFERENCES

Abouelresh, M. O., & Slatt, R. M. (2012). Lithofacies and sequence stratigraphy of the Barnett Shale in east-central Fort Worth Basin, Texas. *AAPG Bulletin, 96*(1), 1-22. doi: 10.1306/04261110116

Allison, M. A., & Nittrouer, C. A. (1998). Identifying Accretionary Mud Shorefaces in the Geologic Record: Insights from the Modern Amazon Dispersal System. In J. Schieber, W. Zimmerle & P. Sethi (Eds.), *Shales and Mudstones I* (pp. 147-161). Stuttgart: E. Schweizerbar'sche Verlasbuchhandlung.

Anderson, D. S., & Harris, N. B. (2006). Integrated Sequence Stratigraphic and Geochemical Resource Characterization of the Lower Mancos Shale, Uinta Basin, Utah (Vol. Open-File Report, pp. 219). Salt Lake City: Utah Geological Survey.

Anderson, T. (2012). Eagle Ford Ternary Diagram. In tri-plot_Mineral_types.xls (Ed.), *Excel.* EGI Internal Report: EGI.

Arnott, R. W. C. (1995). The parasequence definition; are transgressive deposits inadequately addressed? *Journal of Sedimentary Research, 65*(1), 1-6.

Bann, K. L., Tye, S. C., MacEachern, J. A., Fielding, C. R., & Jones, B. G. (2008). Ichnological and Sedimentologic Signatures of Mixed Wave- and Storm-Dominated Deltaic Deposits: Examples from the Early Permain Sydney Basin, Australia. *SEPM Special Publication: Recent Advances in Models of Siliciclastic Shallow-Marine Stratigraphy, 90*, 293-332.

Bhattacharya, J. P. (2010). Deltas. In N. P. James & R. W. Dalrymple (Eds.), *Facies Models 4* (pp. 233 - 264). St. John's, Newfoundland and Labrador, Canada: Canadian Sedimentology Research Group.

Birgenheier, L. P., Johnson, C., Kennedy, A. D., Horton, B., & McLennan, J. (2011, April 11, 2011). *Integrated Sedimentary, Geochemical, and Geomechanical Evaluation of the Mancos Shale, Uinta Basin, Utah.* Paper presented at the AAPG Annual Convention and Exposition, Houston, TX.

Bohacs, K. (2011). [Grain Size Determination in Mudstones].

Bohacs, K., Lazar, R., & Anonymous. (2008). *The role of sequence stratigraphy in unraveling and applying the complex controls on mudstone reservoir properties.* Paper presented at the AAPG 2008 Annual Convention and Exhibition, San Antonio, TX, United States.

Boyce, M. L., & Carr, T. R. (2009). *Lithostratigraphy and Petrophysics of the Devonian Marcellus Interval in West Virginia and Southwestern Pennsylvania.* Paper presented at the 29th Annual GCSSEPM Foundation Bob F. Perkins Research Conference, Houston, TX. http://search.proquest.com/docview/916837583?accountid=14677

Bruner, K. R., & Smosna, R. (2011). A Comparative Study of the Mississippian Barnett Shale, Fort Worth Basin, and Devonian Marcellus Shale, Appalachian Basin. In D. J. Soeder (Ed.). National Energy Technology Laboratory: U.S. Department of Energy.

Cattaneo, A., & Steel, R. J. (2002). Transgressive deposits: a review of their variability. *Earth-Science Reviews, 62*, 187-228.

Catuneanu, O. (2008). *Principles of sequence stratigraphy*. Linacre House, Jordan Hill, Oxford, OX2 8DP, UK: Elsevier.

Chidsey, T. C., morgan, C. D., Ressetar, R., Birgenheier, L. P., Bereskin, S. R., & Schamel, S. (2011). EMD Gas Shales Committee Annual Report - 2011, Utah Shales, U.S., 54.

Coe, A. L. (2003). *The sedimentary record of sea-level change*. Cambridge, UK: Cambridge university press.

Cole, R. D. Y., Robert G.; Willis, Grant C. (1997). The Prairie Canyon Member, A New Unit of the Upper Cretaceous Mancos Shale, West-Central Colorado and East-Central Utah (Vol. Miscellaneous Publication, pp. 26): Utah Geological Survey.

Council, G. W. P. (2009). Modern Shale Gas Development in the United States: A Primer (pp. 116): U.S. Department of Energy.

Cross, C. W., & Purington, C. W. (Cartographer). (1899). Description of the Telluride Quadrangle, Colorado.

DeCelles, P. G. (1994). Late Cretaceous-Paleocene synorogenic sedimentation and kinematic history of the Sevier thrust belt, northeast Utah and southwest Wyoming. *Geological Society of America Bulletin, 106*, 23-56.

DeCelles, P. G., & Giles, K., A. (1996). Foreland basin systems. *Basin Research, 8*(2), 105-123.

Dickinson, W. R., Klute, M. A., Hayes, M. J., Janecke, S. U., Lundin, E. R., McKittrick, M. A., & Olivares, M. D. (1988). Paleogeographic and paleotectonic setting of Laramide sedimentary basins in the central Rocky Mountain region. *Geological Society of America Bulletin, 100*(7), 1023-1039.

Dumitrescu, M. (2002). *Organic Carbon-Sulfur-Iron Relationships in Condensed Intervals of the Cretaceous Mancos Shale.* Master of Science, University of Nebraska, Lincoln, Nebraska.

Energy Information Administration, U. S. (2011). Annual Energy Outlook 2011 with Projections to 2035 (pp. 246). Washington, DC 20585: U.S. Department of Energy.

Haberlah, D., Owen, M., W.S.K., B. P., & Gottlieb, P. (2011). [SEM-EDS Protocol for Subsurface Drilling Mineral Identification and Petrological Classification].

Hampson, G. J., Howell, J. A., & Flint, S. S. (1999). A Sedimentological and Sequence Stratigraphic Re-Interpretation of the Upper Cretaceous Prairie Canyon Member ("Mancos B") and Associated Strata, Book Cliffs Area, Utah, U.S.A. *Journal of Sedimentary Research, 69*(2), 20.

Houseknecht, D. W., Bird, K. J., Schenk, C. J., & Anonymous. (2001). *Sequence stratigraphy of oil- and gas-prospective shelf and shoreface sandstones in the Kingak Shale, National Petroleum Reserve-Alaska (NPRA).* Paper presented at the AAPG 2001 Annual Meeting, Denver, Co, United States.

Hyne, N. J., Laidig, L. W., & Cooper, W. A. (1979). Prodelta sedimentation on a lacustrine delta by clay mineral flocculation. *Journal of Sedimentary Petrology, 49*(4), 1209-1215.

IHS, I. (2012a). Pioneer Main Canyon Federal #23-7-15S-23E. *PI/Dwights PLUS on CD Well Summary Report* Retrieved January 24, 2012

IHS, I. (2012b). Questar Glenn Bench #1M-4-8-22R. *PI/Dwights PLUS on CD Well Summary Report* Retrieved January 24, 2012

IHS, I. (2012c). Questar Glenn Bench #16M-28-8-21. *PI/Dwights PLUS on CD Well Summary Report* Retrieved January 24, 2012

IHS, I. (2012d). Questar Red Wash #8ML-6-9-24. *PI/Dwights PLUS on CD Well Summary Report* Retrieved January 24, 2012

Jansen, J. H. F., Van der Gaast, S. J., Koster, B., & Vaars, A. J. (1998). CORTEX, a shipboard XRF-scanner for element analyses in split sediment cores. *Marine Geology, 151*(1-4), 143-153.

Johnson, R. C. (2003). Depositional Framework of the Upper Cretaceous Mancos Shale and the Lower Part of the Upper Cretaceous Mesaverde Group, Western Colorado and Eastern Utah *Petroleum Systems and Geolgoic Assessment of Oil and Gas in the Uinta-Piceance Province, Utah and Colorado* (1.0 ed., pp. 29). Denver, CO 80225: U.S. Geological Survey, Information Services.

Kauffman, E. G. (1977). Geological and biological overview; Western Interior Cretaceous basin. *The Mountain Geologist, 14*(3-4), 75-99.

Kauffman, E. G. (1984). Paleobiogeography and evolutionary response dynamic in the Cretaceous Western Interior seaway of North America. *Geological Association of Canada - Special Paper, 27*(273-306).

Kennedy, A. D. (2011). *Geologic Predictors of the Hydrocarbon Extraction Potential of the Mancos Shale.* Master of Science, University of Utah, Salt Lake City, Utah.

Kirschbaum, M. A. (2003). Geologic Assessment of Undiscovered Oil and Gas Resources of the Mancos/Mowry Total Petroleum System, Uinta Piceance Province, Utah and Colorado *Petroleum Systems and Geologic Assessment of Oil and Gas in the Uinta-Piceance Province, Utah and Colorado: U.S. Geological Survey Digital Data Series DDS-69-B* (1.0 ed., pp. 51). Denver, CO 80225: U.S. Geological Survey, Information Services.

Labune, C., Tesson, M., & Gensous, B. (2008). Variability of the transgressive stacking pattern under environmental changes control: Example from the Post-Glacial deposits of the Gulf of Lions inner-shelf, Mediterranean, France. *Continental Shelf Research, 28*(9), 1138-1152.

Lash, G. G., & Engelder, T. (2011). Thickness trends and sequence stratigraphy of the Middle Devonian Marcellus Formation, Appalachian Basin: Implications for Acadian foreland basin evolution. *AAPG Bulletin, 95*(1), 61-103. doi: 10.1306/06301009150

Leckie, R. M., Kirkland, J. I., & Elder, W. P. (1997, October 1-4, 1997). *Stratigraphic framework and correlation of a principal reference section of the Mancos Shale (Upper Cretaceous), Mesa Verde, Colorado.* Paper presented at the New Mexico Geological Society, 48th annual field conference, Cortez, NM, United States.

Livaccari, R. F. (1991). Role of crustal thickening and extensional collapse in the tectonic evolution of the Sevier-Laramide Orogeny, Western United States. *Geology, 19*(11), 1104-1107. doi: 0091-7613

Loucks, R. G., & Ruppel, S. C. (2007). Mississippian Barnett Shale: Lithofacies and depositional setting of a deep-water shale-gas succession in the Fort Worth Basin, Texas. *AAPG Bulletin, 91*(4), 579-601. doi: 10.1306/11020606059

MacEachern, J. A., Pemberton, G. S., Gingras, M. K., & Bann, K. L. (2010). Ichnology and Facies Models. In N. P. James & R. W. Dalrymple (Eds.), *Facies Models 4* (pp. 19 - 58). St. John's, Newfoundland & Labrador, Canada: Canadian Sedimentology Research Group.

Macquaker, J. H. S., & Adams, A. E. (2003). Maximizing Information From Fine-Grained Sedimentary Rocks: An Inclusive Nomenclature for Mudstones. *Journal of Sedimentary Research, 73*(5), 10.

Macquaker, J. H. S., Taylor, K. G., & Gawthorpe, R. L. (2007). High-Resolution Facies Analyses of Mudstones: Implications for Paleoenvironmental and Sequence Stratigraphic Interpretations of Offshore Ancient Mud-Dominated Successions. *Journal of Sedimentary Research, 77*(4), 324-339. doi: 10.2110/jsr.2007.029

Milligan, T. G., Hill, P. S., & Law, B. A. (2007). Flocculation and the loss of sediment from the Po River plume. *Continental Shelf Research, 27*(3-4), 309-321.

Molenaar, C. M., & Cobban, W. A. (1991). Middle Cretaceous stratigraphy on the south and east sides of the Uinta Basin. *U.S. Geolgoical Survey Bulletin*, 1-34.

Mulder, T., & Syvitsky, J. P. M. (1995). Turbidity currents generated at river mouths during exceptional discharge to the world's oceans. *Journal of Geology, 103*, 285-298.

Mulder, T., Syvitsky, J. P. M., Migeon, S., Faugeres, J.-C., & Savoye, B. (2003). Marine hyperpycnal flows: initiation, behavior and related deposits. A review. *Marine and Petroluem Geology, 20*(6-8), 861-882.

Nadeau, P. H., & Reynolds, R. C., Jr. (1981). Burial and contact metamorphism in the Mancos Shale. *Clays and Clay Minerals, 29*(6), 249-259.

Nelson, D. T., & Jewell, P. (2009). *Insights from mapping surficial deposits associated with the transgressive rise of Lake Bonneville in northwestern Utah.* Paper presented at the Geological Society of America, Rocky Mountain Section, 61st annual meeting, Orem, UT, United States.

Nuccio, V. F., & Roberts, L. N. R. (2003). Thermal Maturity and Oil and Gas Generation History of Petroleum Systems in the Uinta-Piceance Province, Utah and Colorado *Petroleum Systems and Geologic Assessment of Oil and Gas in the Uinta-Piceance Province, Utah and Colorado: U.S. Geological Survey Digital Data Series DDS-69-B.* Denver, CO 80225: U.S. Geological Survey, Information Services.

Parry, W. T. (2011). *Clay Mineral Geochemistry.* CD. Geology and Geophysics. University of Utah.

Pasley, M. A., Gregory, W. A., & Hart, G. F. (1991). Organic matter variations in transgressive and regressive shales. *Organic Geochemistry, 17*(4), 483-509.

Pattison, S. A. J. (2005). Storm-Influenced Prodelta Turbidite Complex in the Lower Kenilworth Member at Hatch Mesa, Book Cliffs, Utah, U.S.A.: Implications for Shallow Marine Facies Models. *Journal of Sedimentary Research, 75*(3), 420-439. doi: 10.2110/jsr.2005.033

Plint. (1988). Sharp-based shoreface sequences and "offshore bars" in the Cardium formation: Their relationship to relative changes in sea level. *SEPM Special Publication: Sea Level Changes: An Integrated Approach, 42*, 357-370.

Plint. (2010). Wave- and Storm-Dominated Shoreline and Shallow-Marine Systems. In N. P. James & R. W. Dalrymple (Eds.), *Facies Models 4* (pp. 167 - 200). St. John's, Newfoundland and Labrador, Canada: Canadian Sedimentology Research Group.

Ressetar, R., & Birgenheier, L. P. (2011). Cretaceous Mancos Shale, Uinta Basin, Utah: Resource Potential and Best Practices for and Emerging Shale-Gas Play - Technology Status Assessment (pp. 8): Utah Department of Natural Resources.

Ressetar, R., & Birgenheier, L. P. (2012). EMD Gas Shales Committee Mid-Year Report, FY 2012, Utah Shales, U.S. (pp. 84): American Association of Petroleum Geologists, Emergy Minerals Division.

Richter, T. O., Van der Gaast, S. J., Koster, B., Vaars, A. J., & Gieles, R. (2006). The Avaatech XRF core scanner; technical description and applications to NE Atlantic sediments. *Geological Society Special Publications, 267*, 39-50.

Rimmer, S. M. (2004). Geochemical paleoredox indicators in Devonian-Mississippian black shales, central Appalachian Basin; USA. *Chemical Geology, 206*(3-4), 373-391.

Rodriguez-Clemente, R., & Tardy, Y. (1987). *Geochemistry and mineral formation in the Earth surface*. Paper presented at the International meeting on geochemistry of the earth surface and processes of mineral formation, Granada, Spain.

Rowe, H., Hughes, N., & Robinson, K. (2012). The quantification and application of handheld energy-dispersive x-ray fluorescence (ED-XRF) in mudrock chemostratigraphy and geochemistry. *Chemical Geology*. doi: 10.1016/j.chemgeo.2011.12.023

Rowe, H., Loucks, R. G., Ruppel, S. C., & Rimmer, S. M. (2008). Mississippian Barnett Formation, Fort Worth Basin, Texas; bulk geochemical inferences and Mo-TOC constraints on the severity of hydrographic restriction. *Chemical Geology, 257*(1-2), 16-25.

Schamel, S. (2006). Shale Gas Resources of Utah: Assessment of Previosly Undeveloped Gas Discoveries (pp. 84). Salt Lake City, UT: Utah Geological Survey.

Schieber, J. (1998). Deposition of Mudstones and Shales: Overview, Problems, and Challenges. In W. Zimmerle & P. Sethi (Eds.), *Shales and Mudstones O* (pp. 131-146). Stuttgart: E. Schweizerbar'sche Verschlagsbuchhandlung.

Schieber, J., Lazar, R., & Bohacs, K. M. (2010). *Sedimentology and Stratigraphy of Shales: Expression and Correlation of Depositional Sequences in the Devonian of Tennessee, Kentucky, and Indiana*. Paper presented at the AAPG 2010 Annual Convention, New Orleans, LA.

Sixsmith, P. J., Hampson, G. J., Gupta, S., Johnson, H. D., & Fofana, J. F. (2008). Facies architecture of a net transgressive sandstone reservoir analog; the Cretaceous Hosta Tongue, New Mexico. *AAPG Bulletin, 92*(4), 513-547.

Sorby, H. C. (1908). On the Application of Quantitative Methods to the Study of the Structure and History of Rocks. *Quarterly Jornal of the Geological Society of London, 64*(1-4), 171-233. doi: 10.1144/GSL.JGS.1908.064.01-04.12

Tribovillard, N., Algeo, T. J., Lyons, T. W., & Riboulleau, A. (2006). Trace metals as paleoredox and paleoproductivity proxies; an update. *Chemical Geology, 232*(1-2), 12-32.

Vakarelov, B. K. (2006). *Controls on Stratigraphic Architecture in Shallow Marine Environments: Tectonic Forcing and Mud Geometries.* Ph. D, University of Texas at Dallas.

Van Olphen, H. (1965). *Parallel plate interaction in clay-water systems.* Paper presented at the Clays and clay minerals; the Fourteenth national conference, Berkeley, CA, USA, United States.

Van Wagoner, J. C. (1995). Overview of sequence stratigraphy of foreland basin deposits: terminology, summary of papers, and glossary of sequence stratigraphy. *American Associate of Petroleum Geolgoists Memoir 64.*

Varban, B. L., & Plint, A. G. (2005). Allostratigraphy of the Kaskapau Formation (Cenomanian-Turonian) in subsurface and outcrop:NE British Columbia and NW Alberta, western Canada foreland basin. *Bulletin of Canadian Petroleum Geolgoy, 53*, 357-389.

Yoshida, S. (2000). Facies architecture and sequence stratigraphy of the Blackhawk Formation and the Castlegate Sandstone (Upper Cretaceous), Book Cliffs, Utah, USA. *Sedimentary Geology, 136*, 239-276.

SUPPLEMENTARY MATERIALS

SCANNED CORE LOGS

Appearing here are the raw core logs that were written at the time of describing the cores. Depths are recorded in feet, and any sedimentary features that were of importance are noted. Detailed stratigraphic findings are detailed in the preceding chapters.

Questar 1 core log – 13,495' – 13,483'

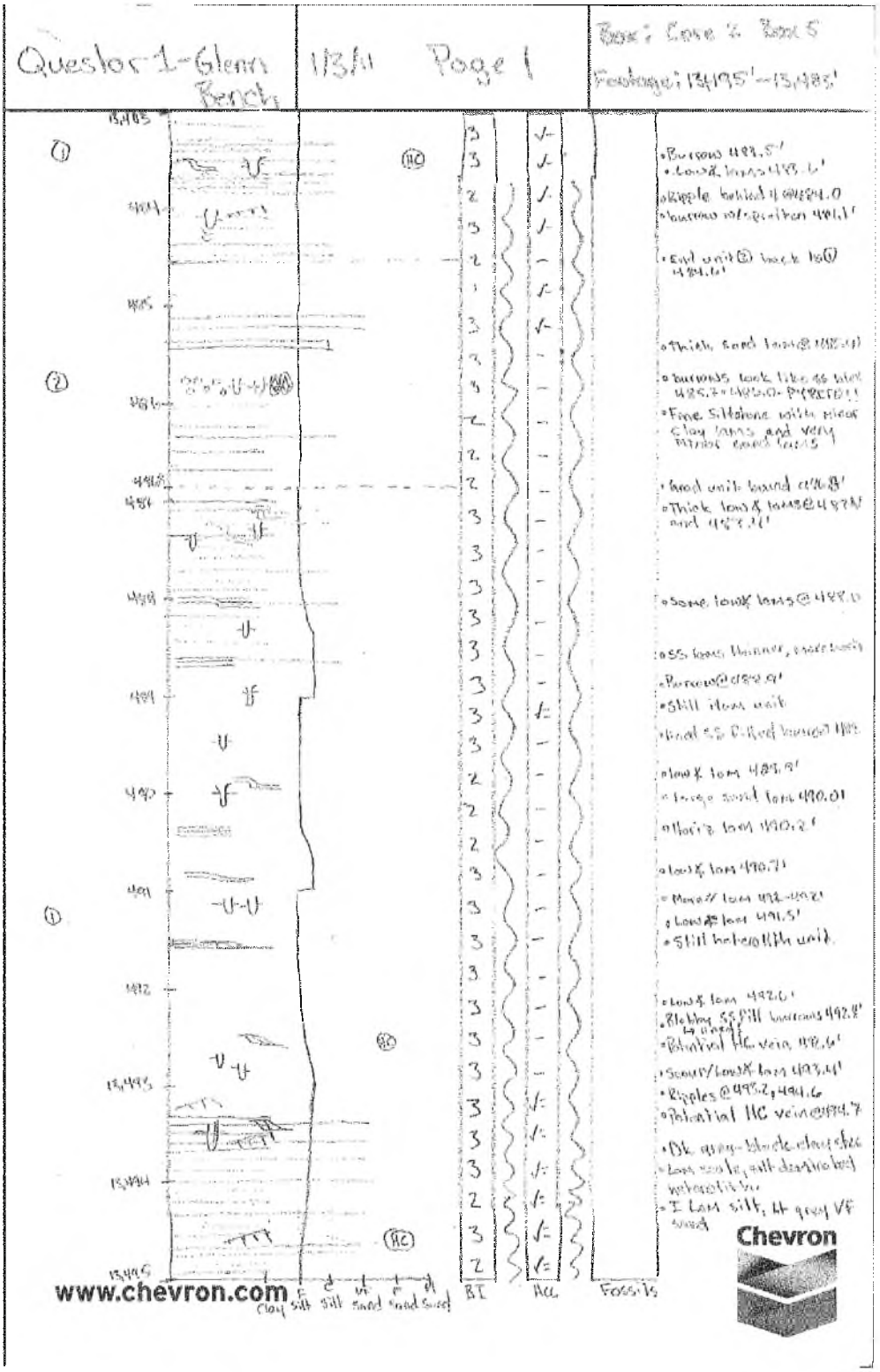

Questar 1 core log - 13,483’ – 13,471’

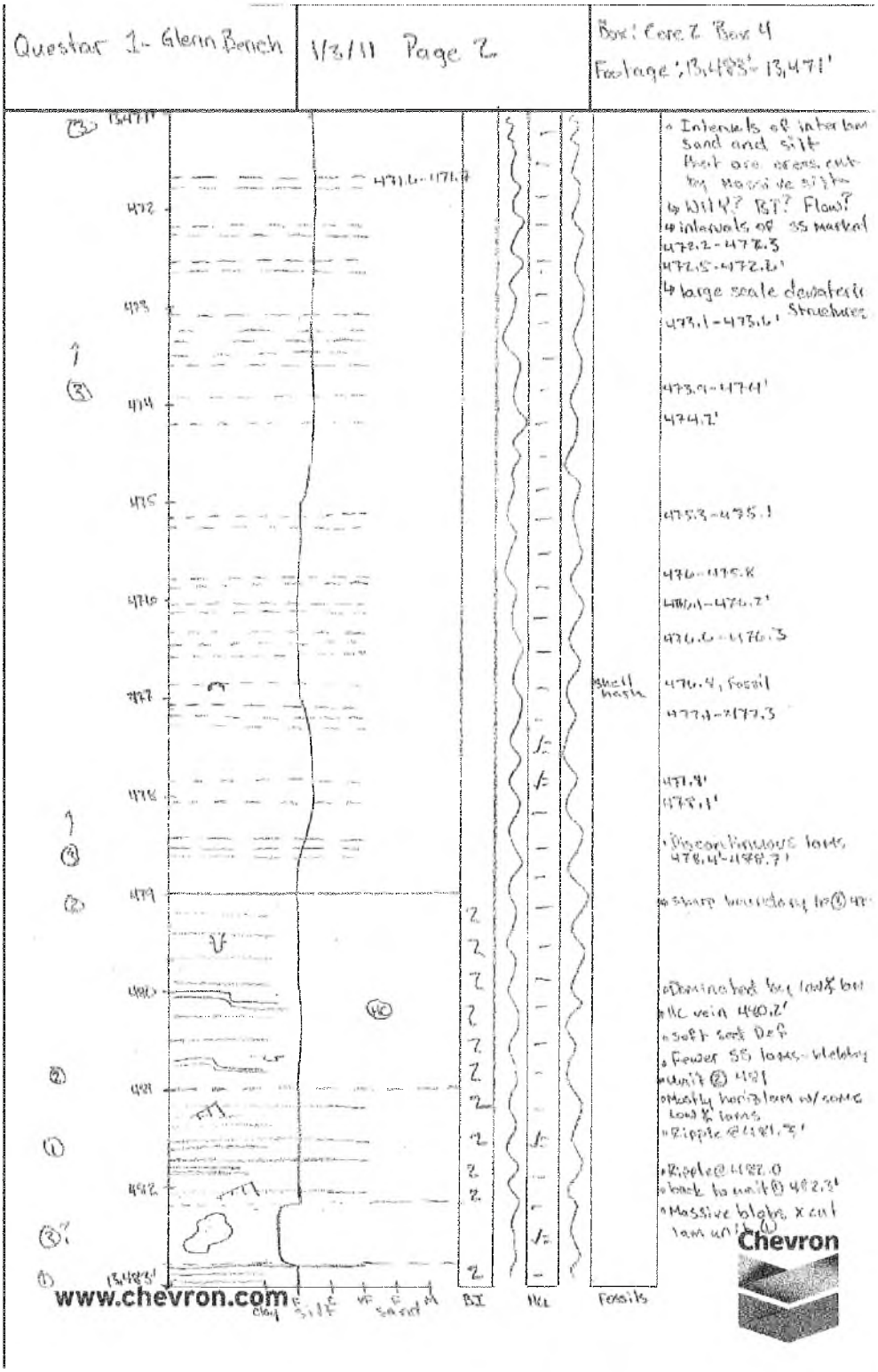

Questar 1 core log - 13,471' – 13,459'

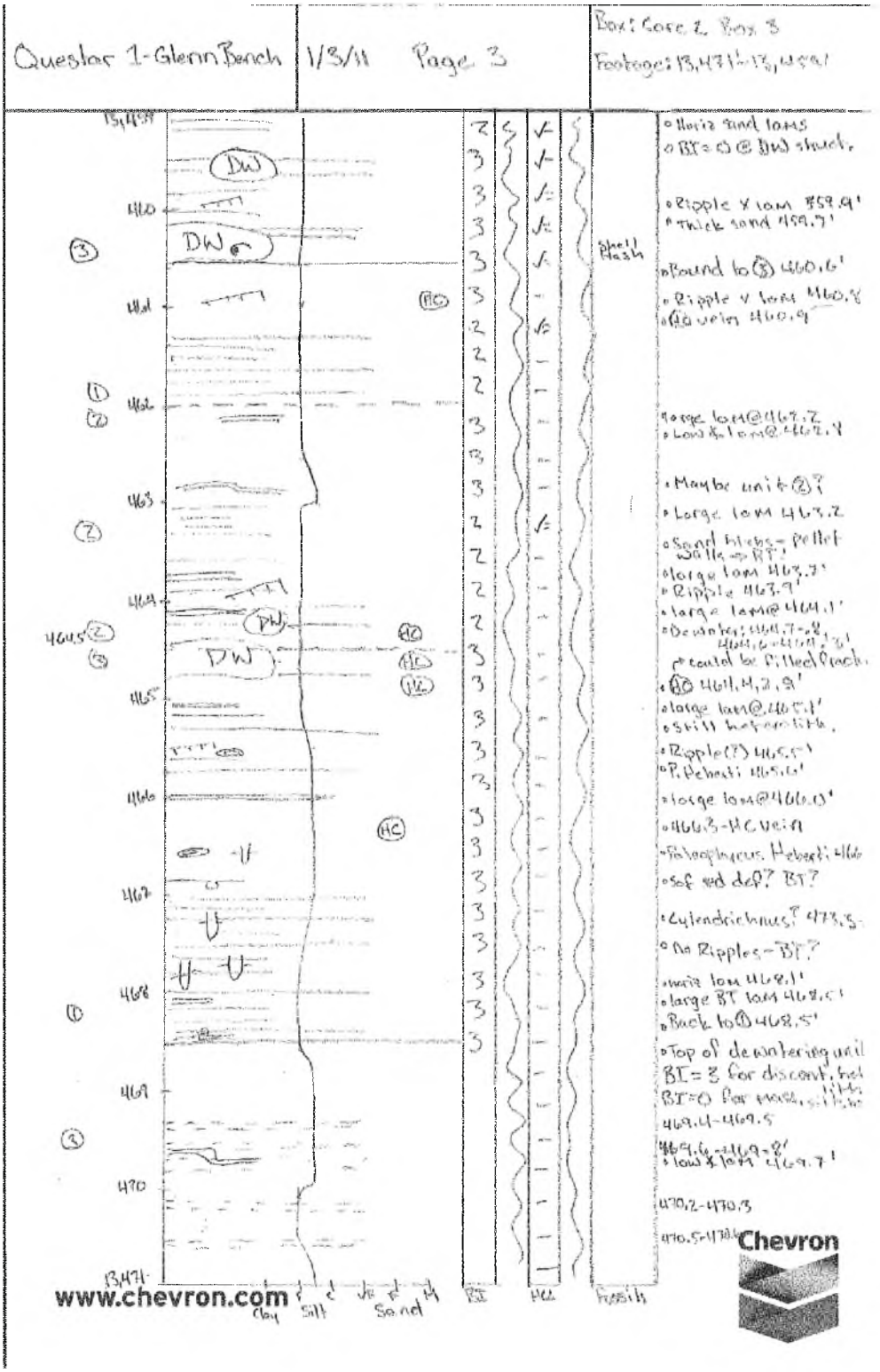

Questar 1 core log - 13,459’ – 13,447’

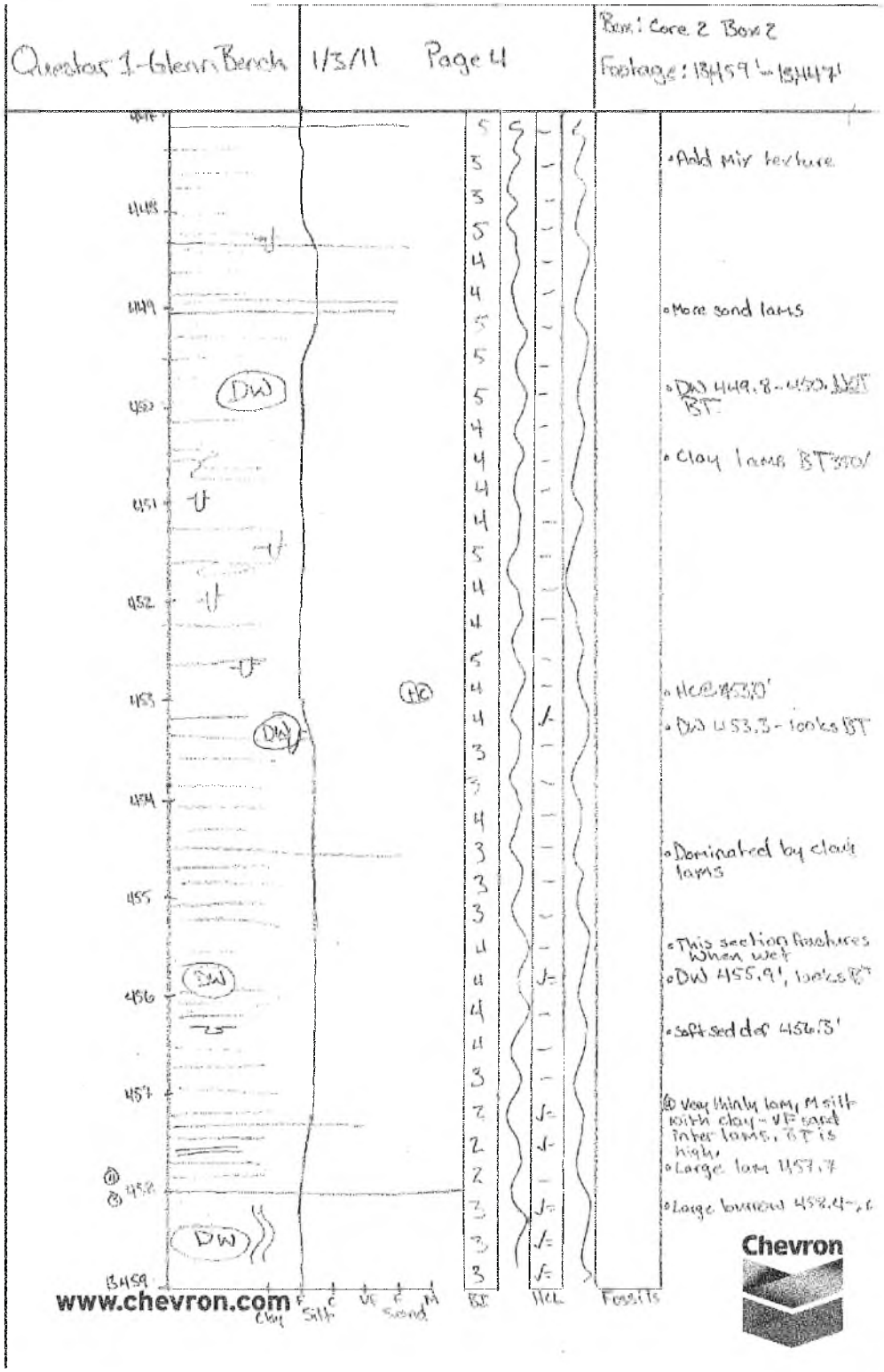

Questar 1 core log - 13,447’ – 13,435’

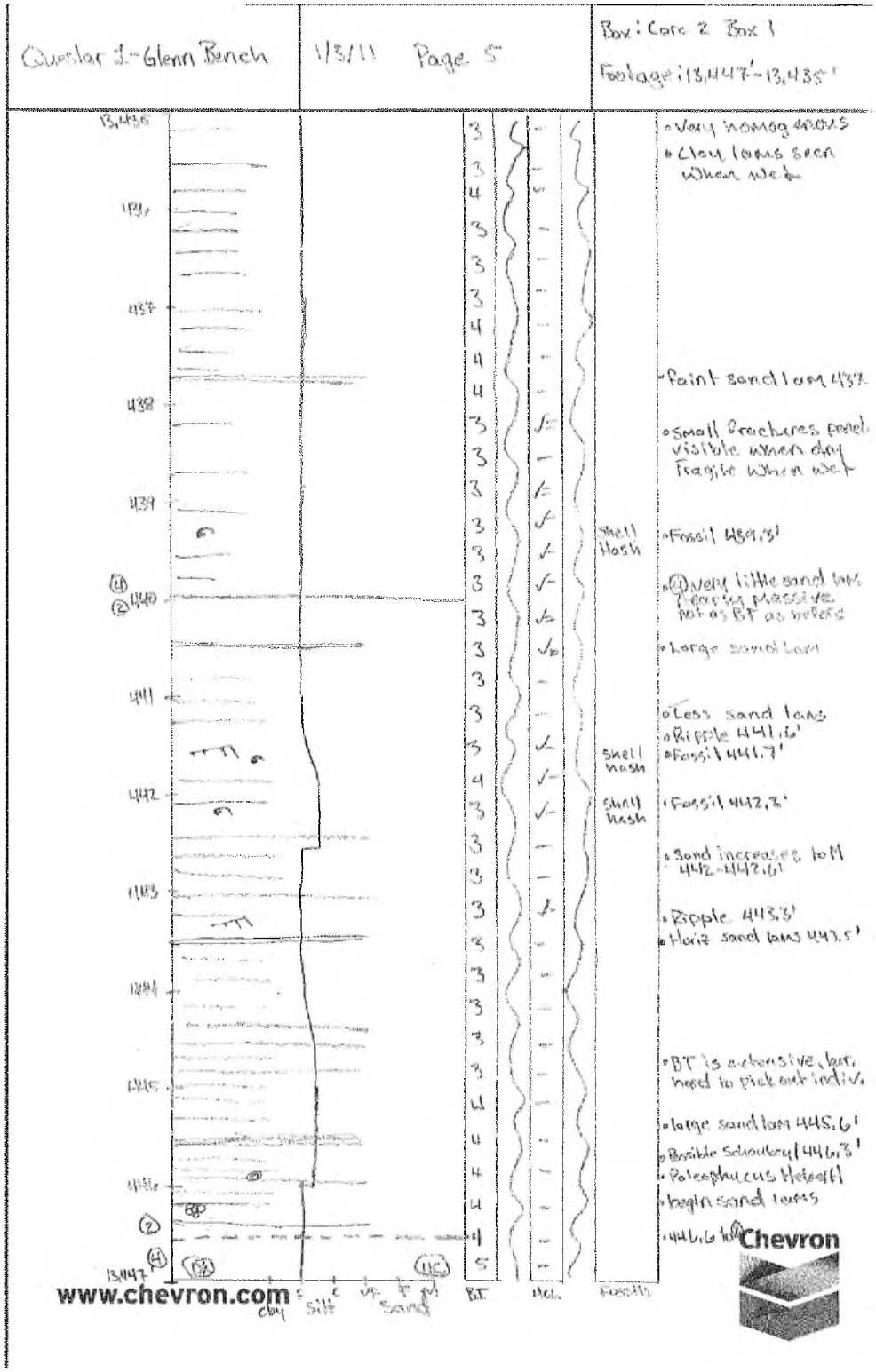

Questar 1 core log - 13,435' – 13,423'

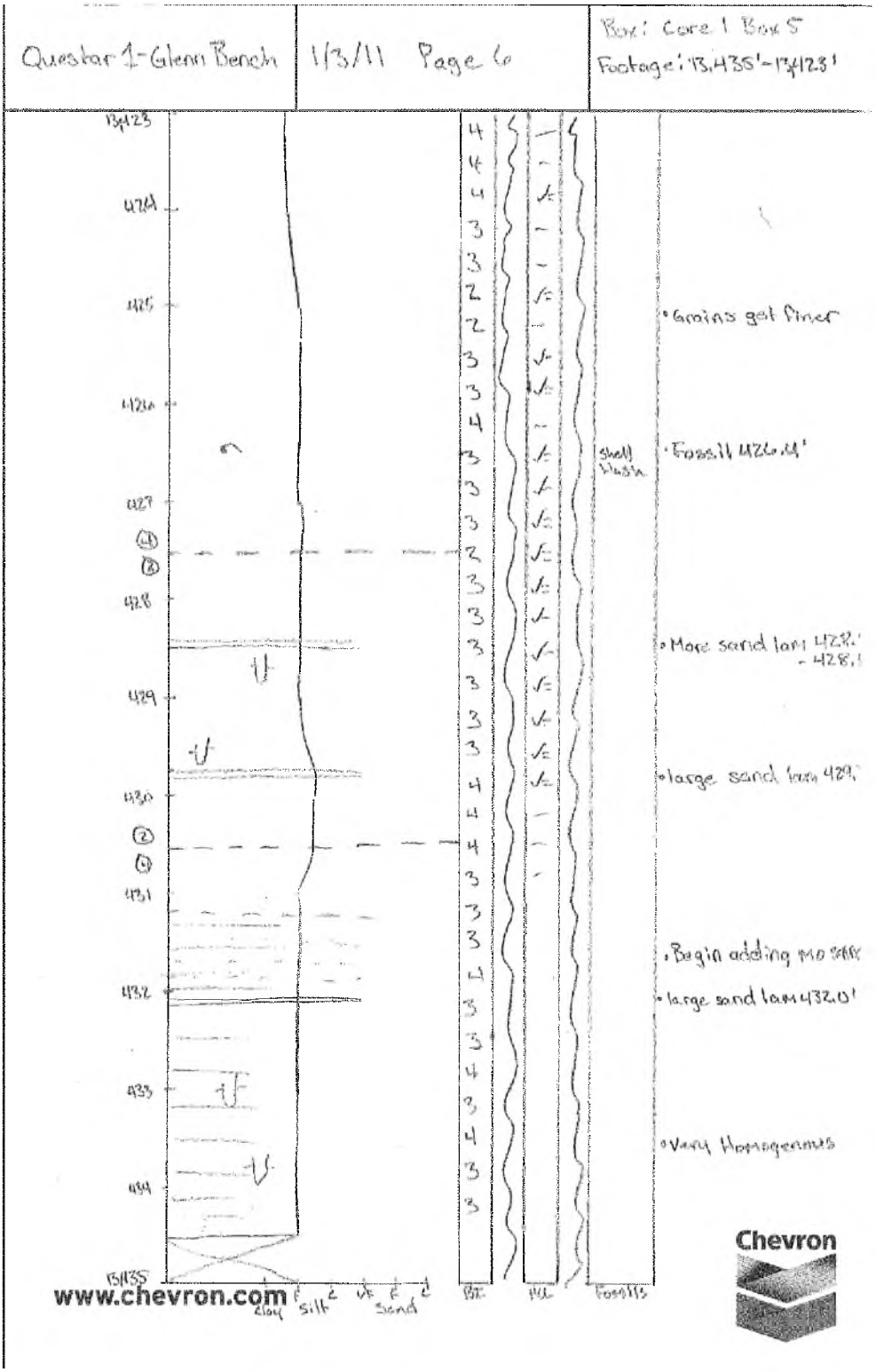

Questar 1 core log - 13,423’ – 13,411’

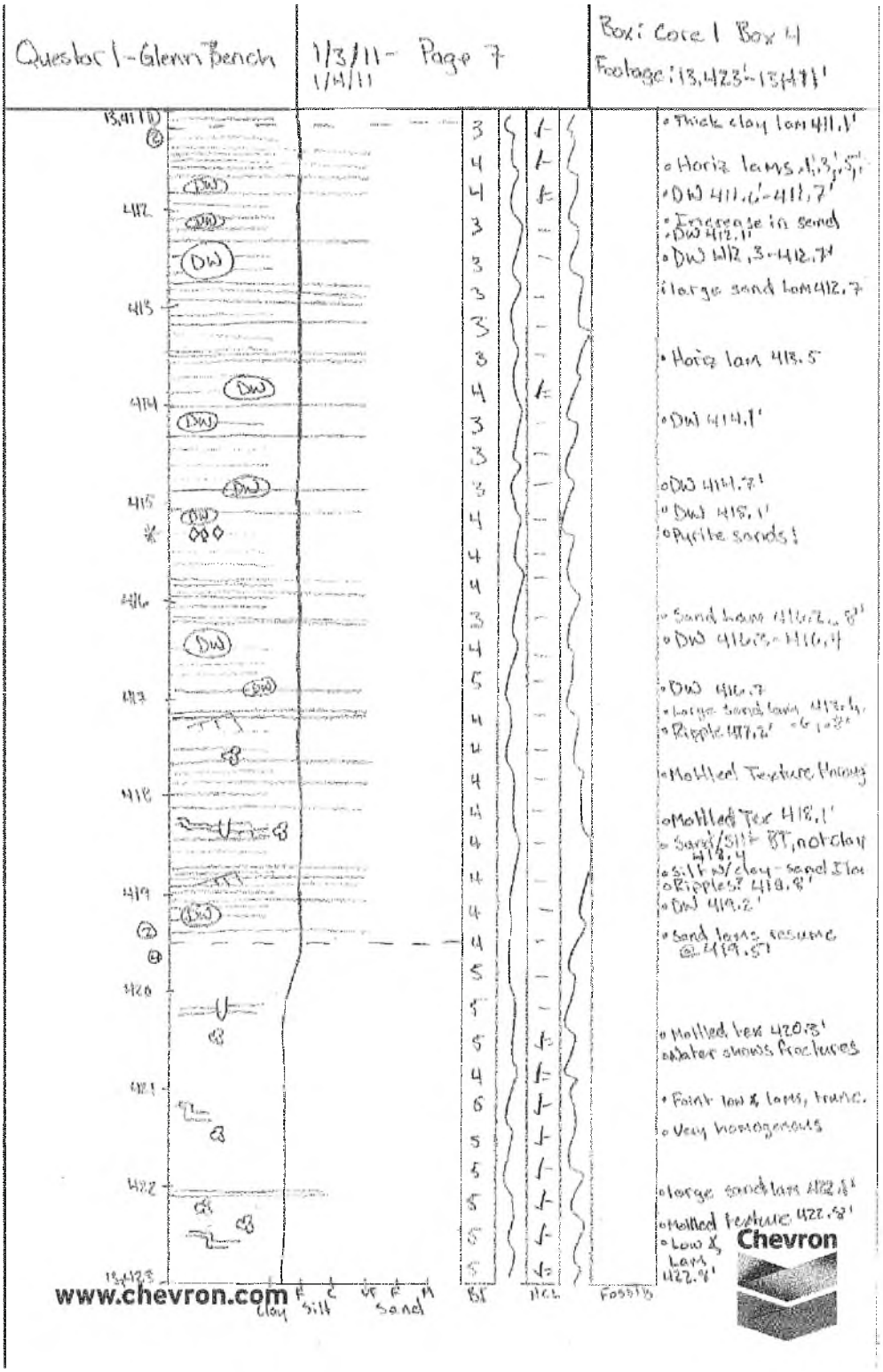

Questar 1 core log - 13,411' – 13,399'

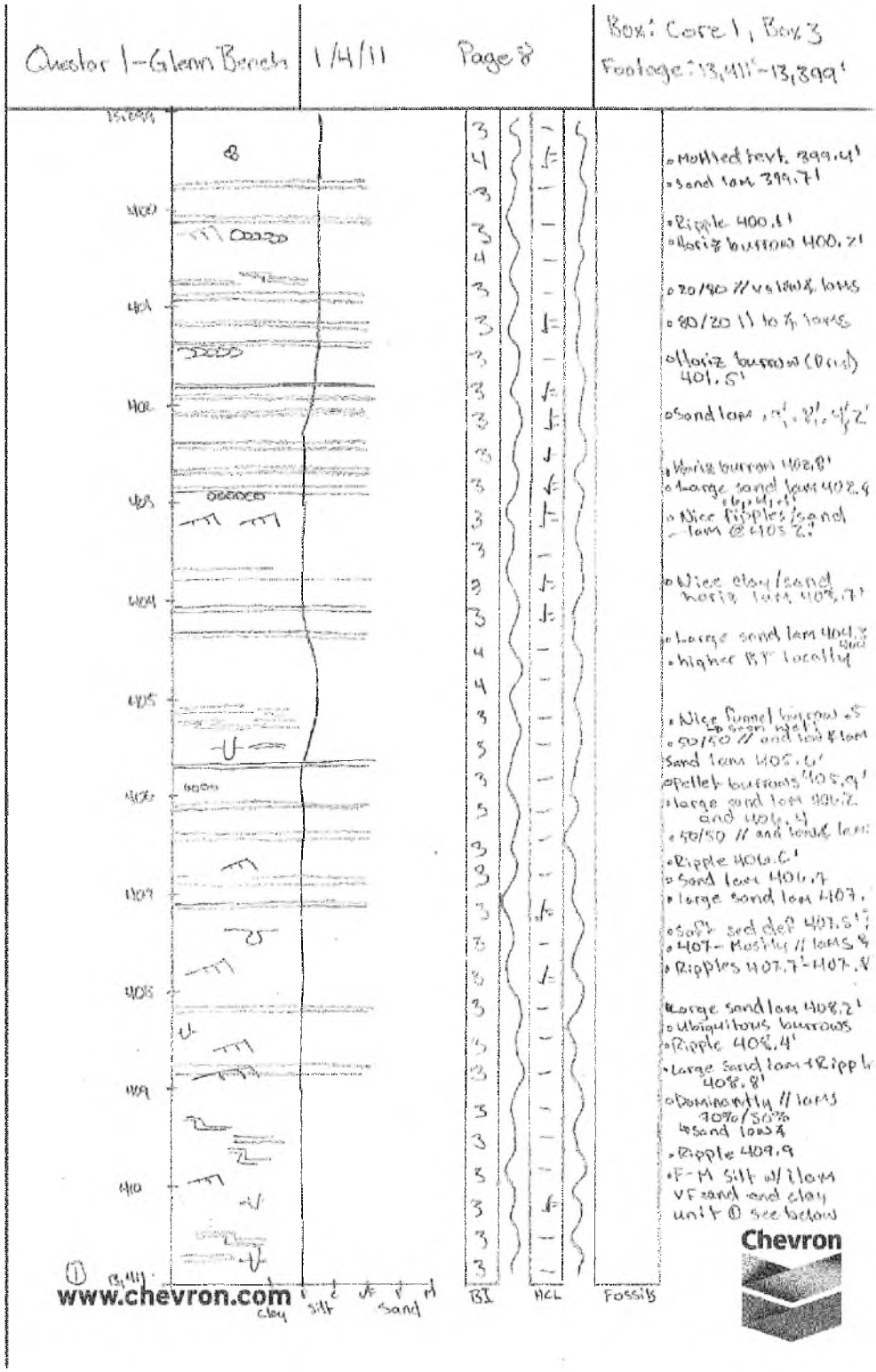

Questar 1 core log - 13,399’ – 13,387’

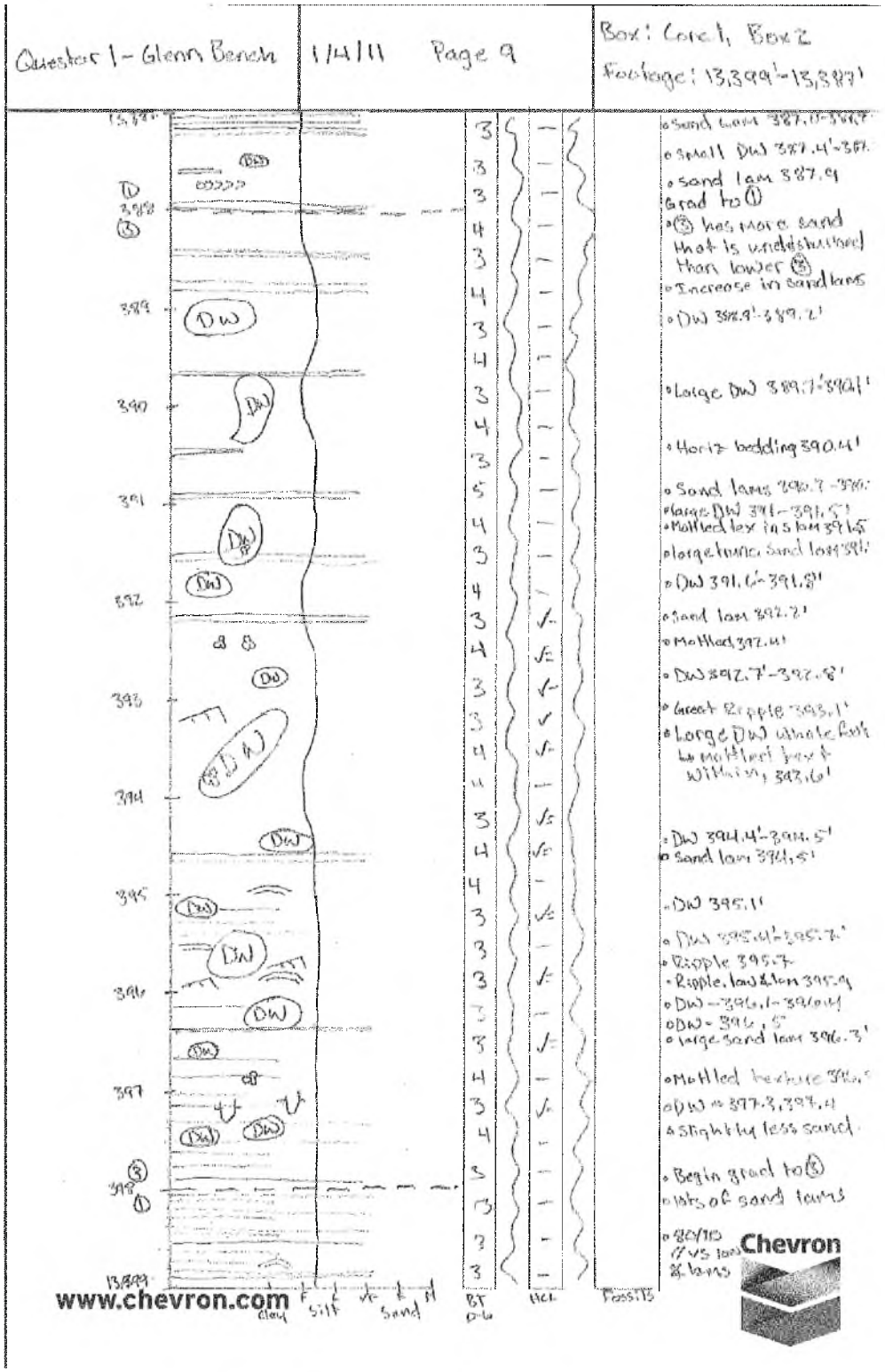

Questar 1 core log - 13,387' – 13,375'

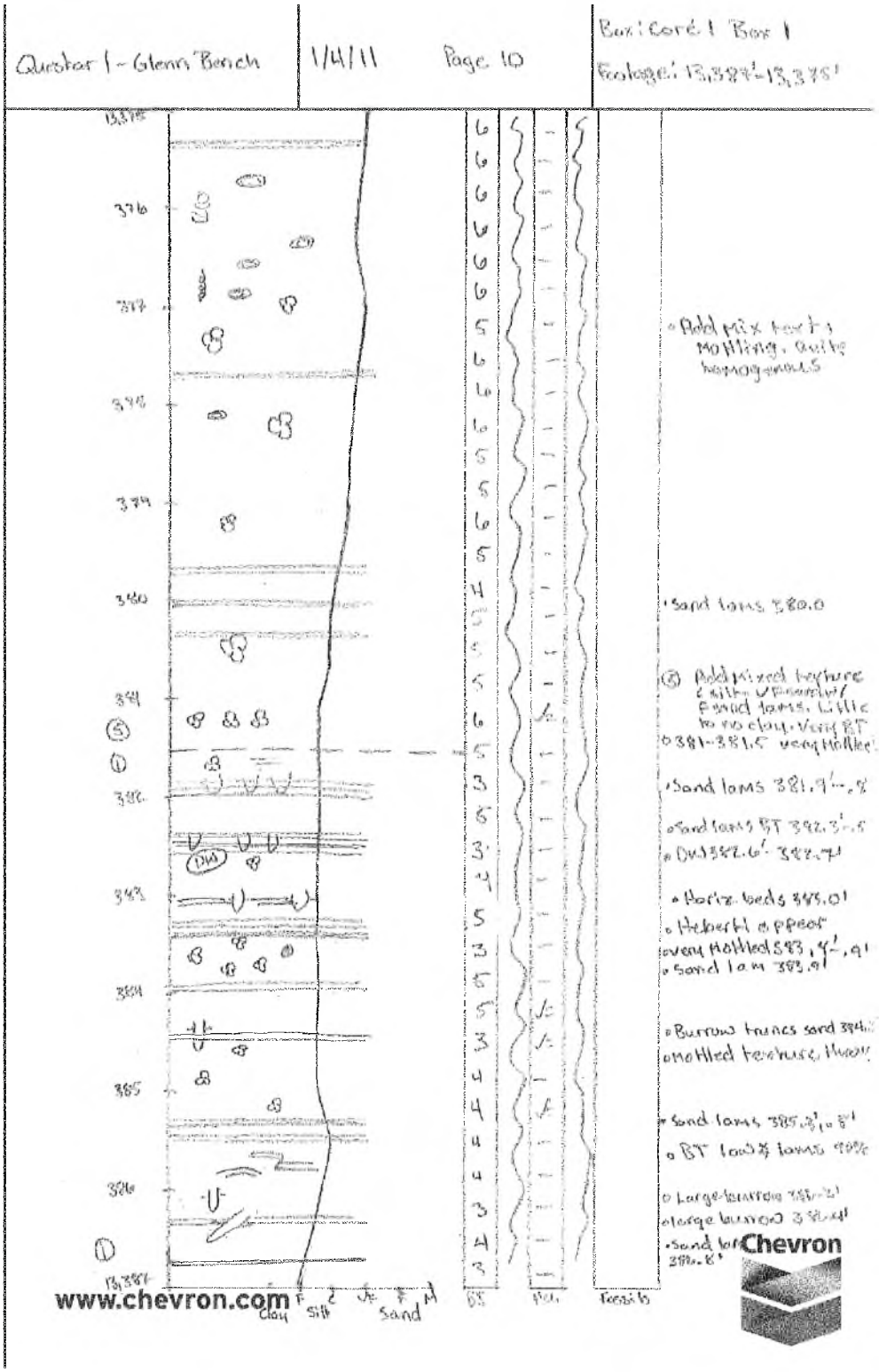

Questar 8 core log – 9,736' – 9,748'

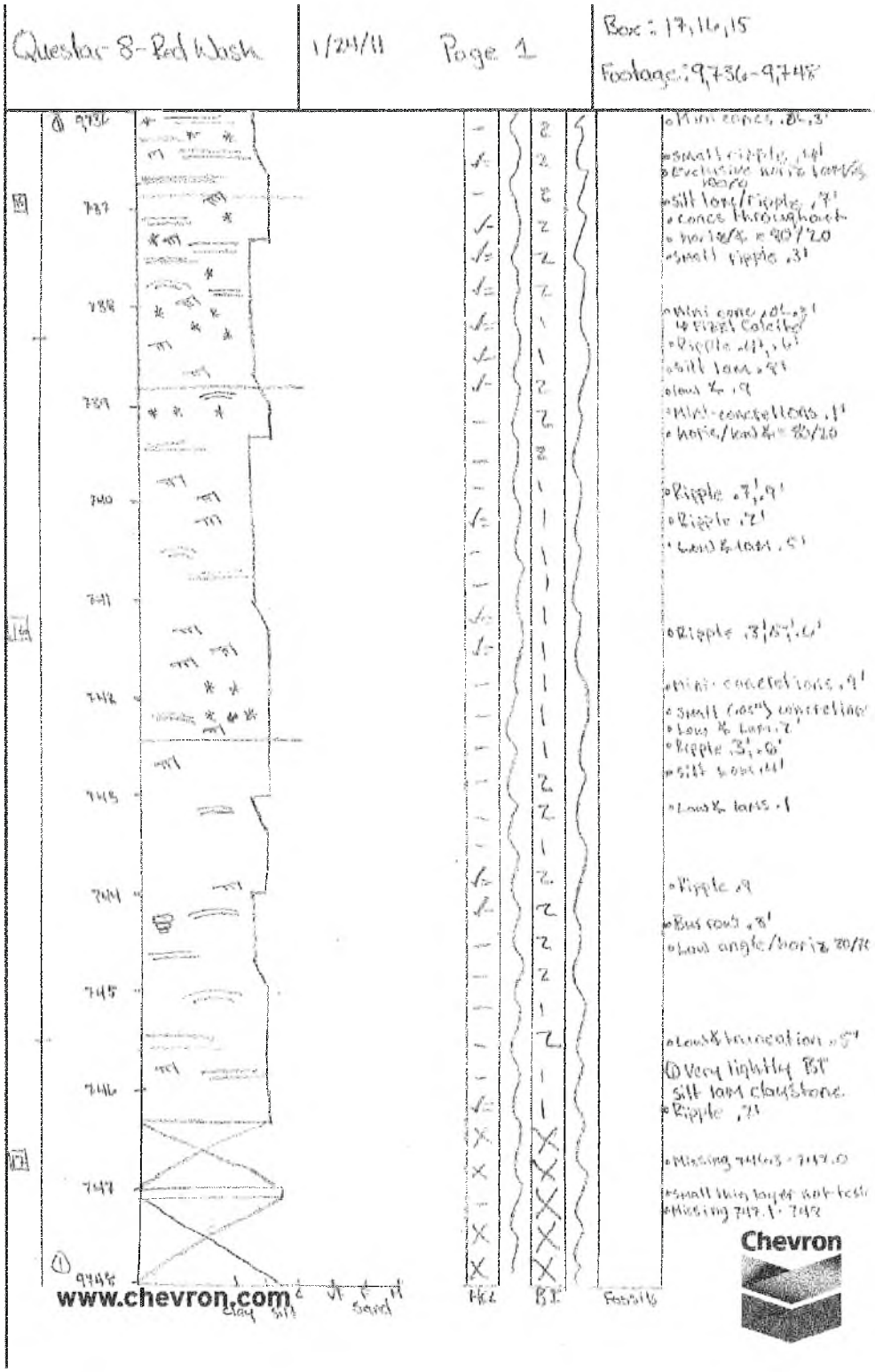

Questar 8 core log – 9,724’ – 9,736’

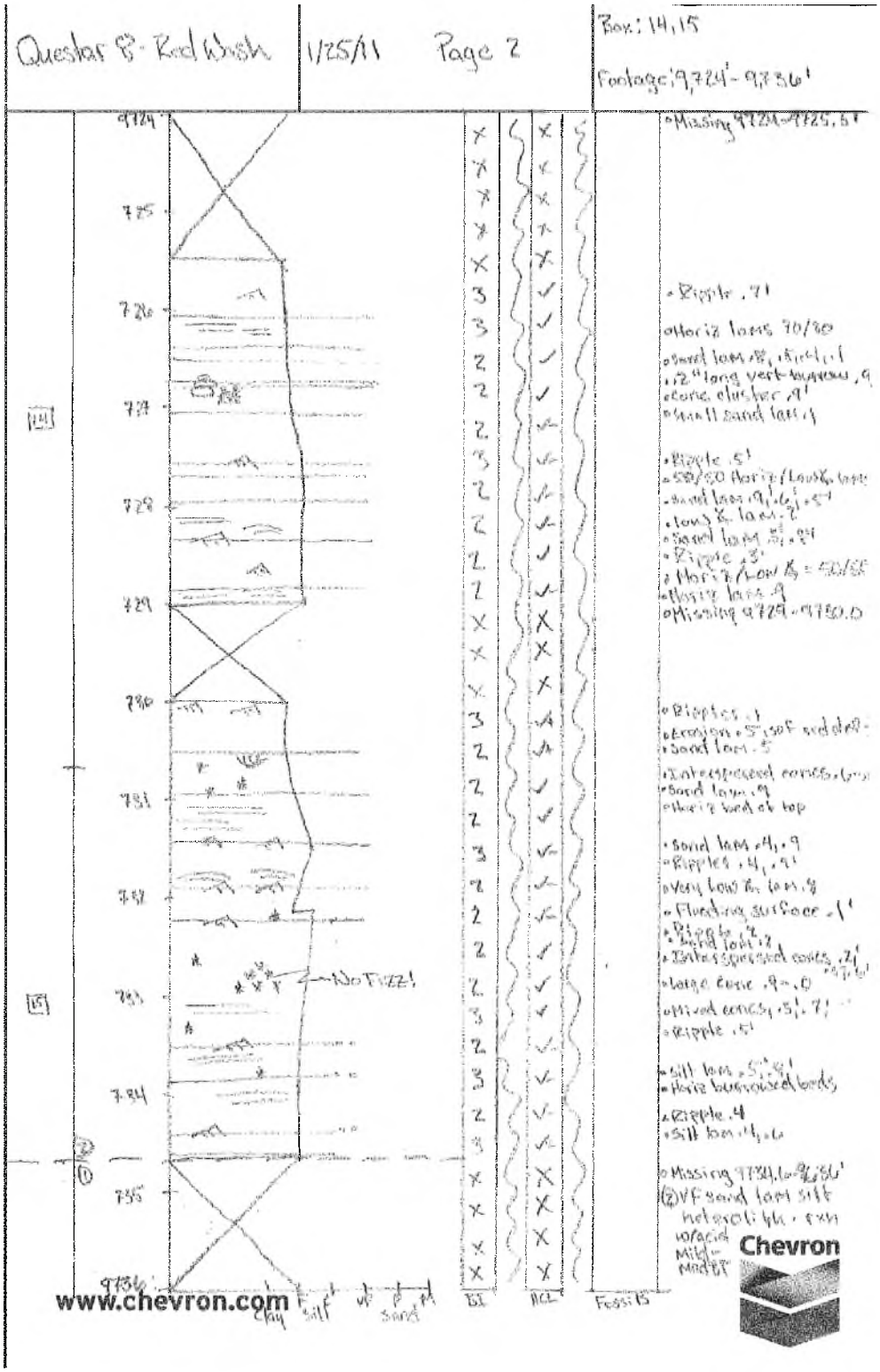

Questar 8 core log – 9,712’ – 9,724’

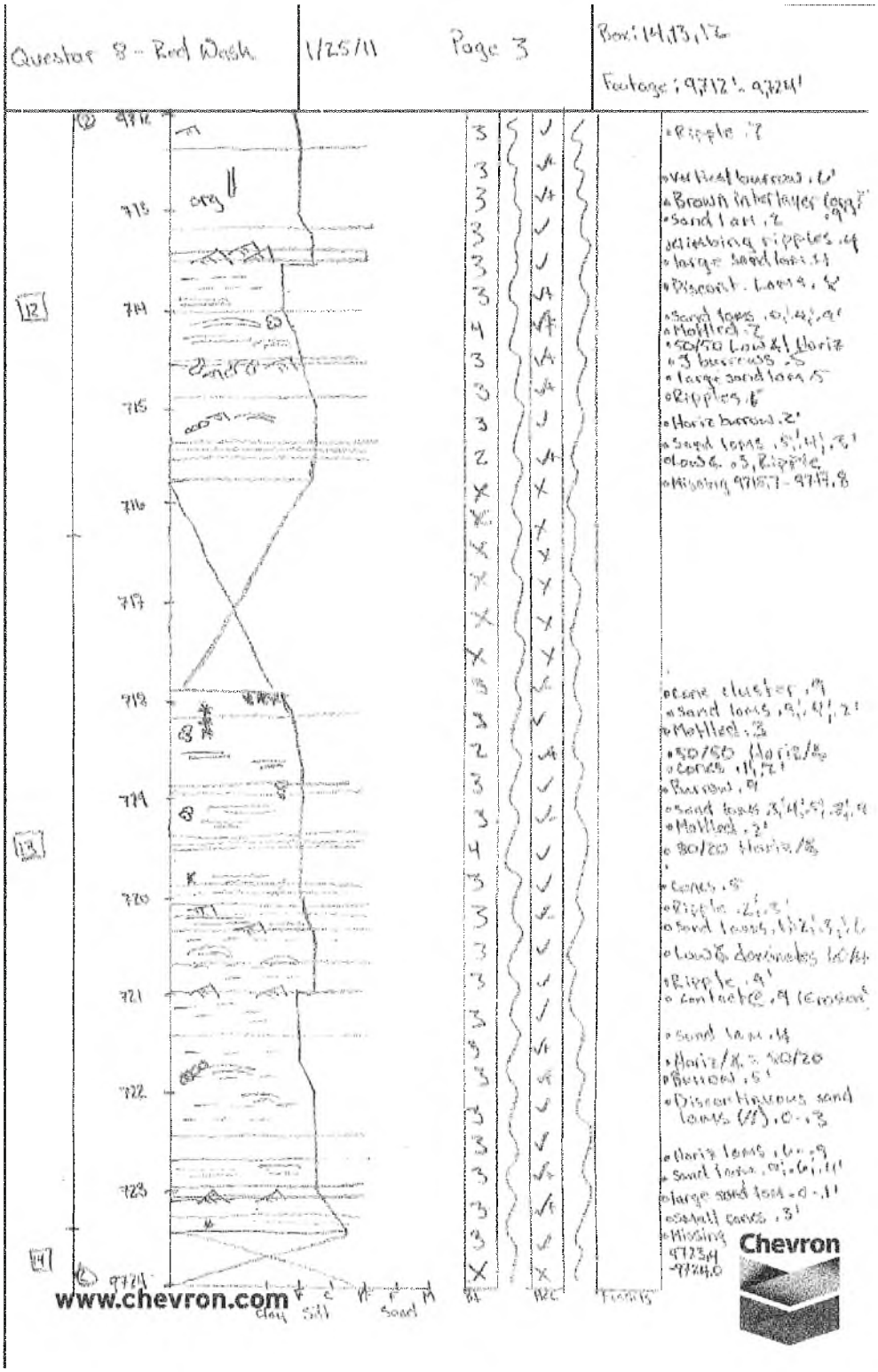

Questar 8 core log – 9,700’ – 9,712’

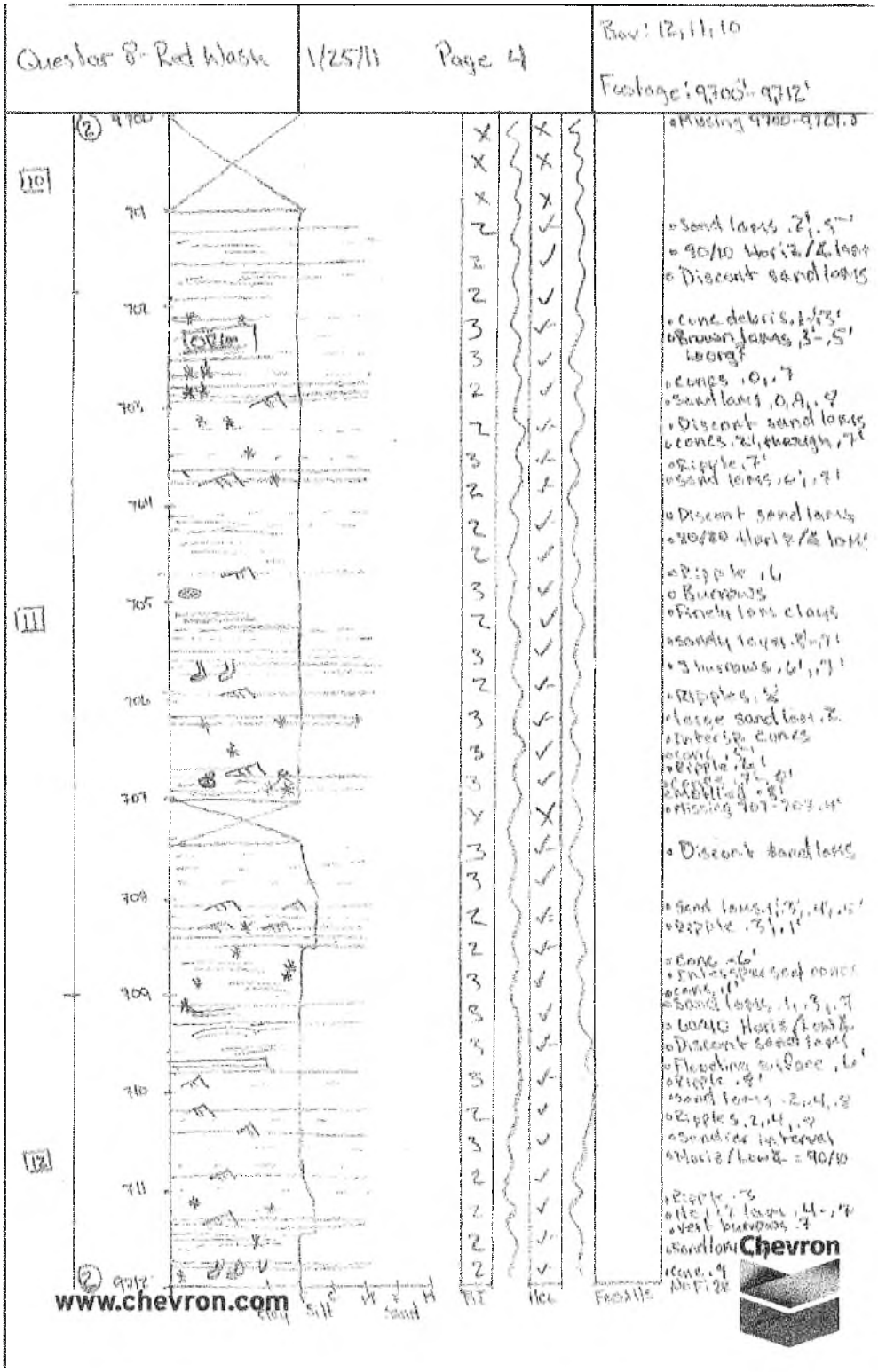

Questar 8 core log – 9,688’ – 9,700’

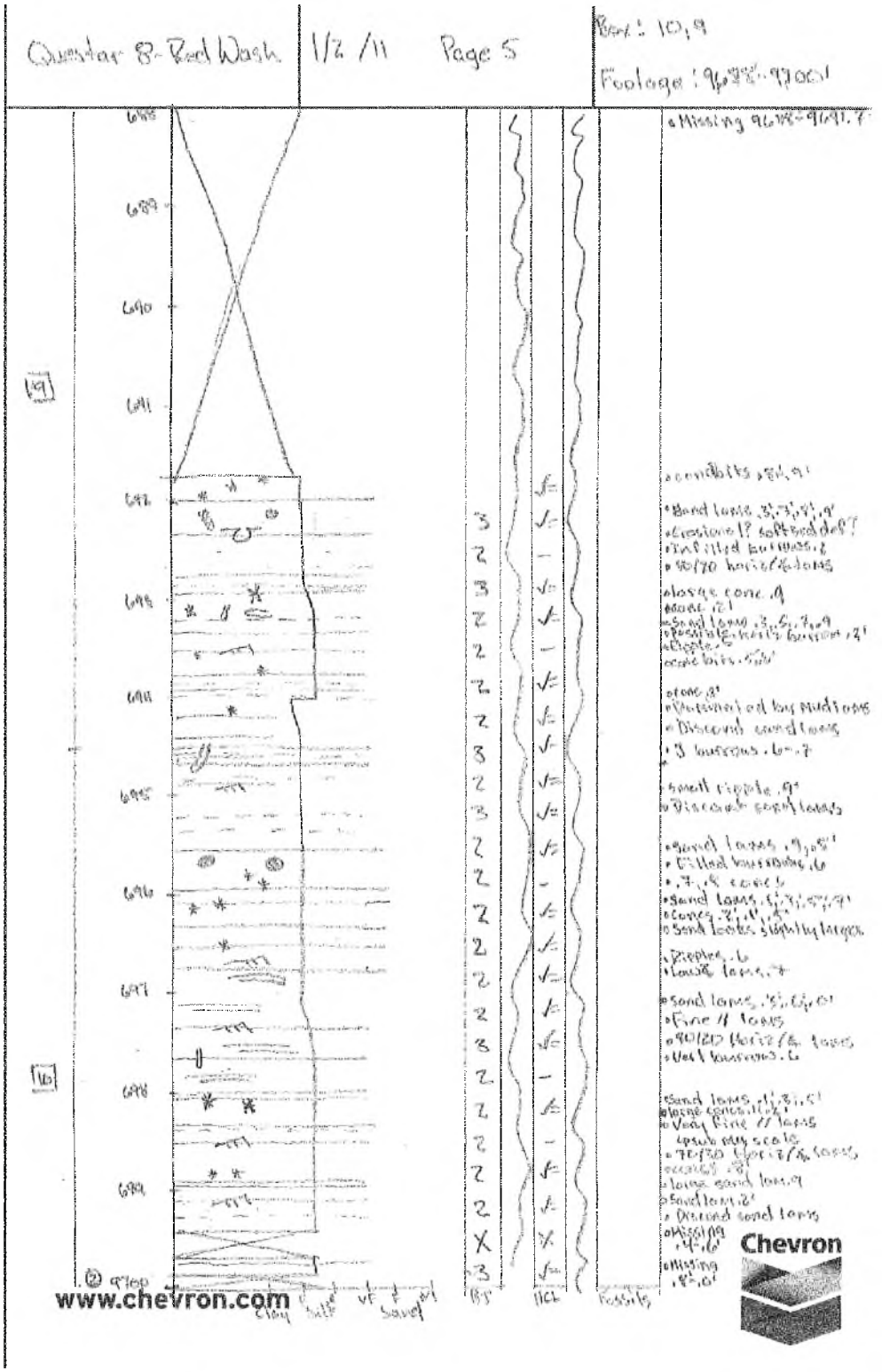

Questar 8 core log – 9,676’ – 9,688’

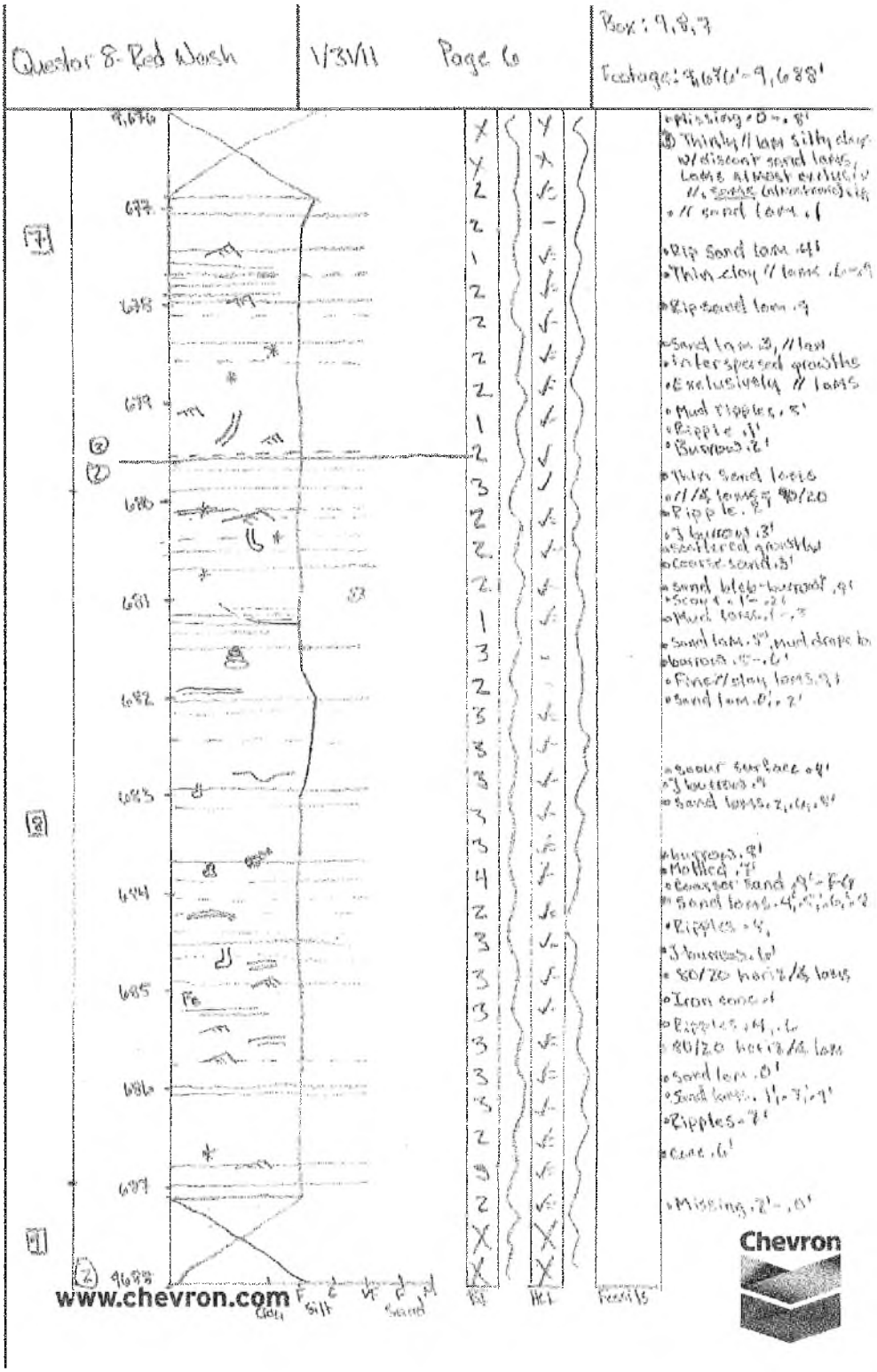

Questar 8 core log – 9,664’ – 9,676’

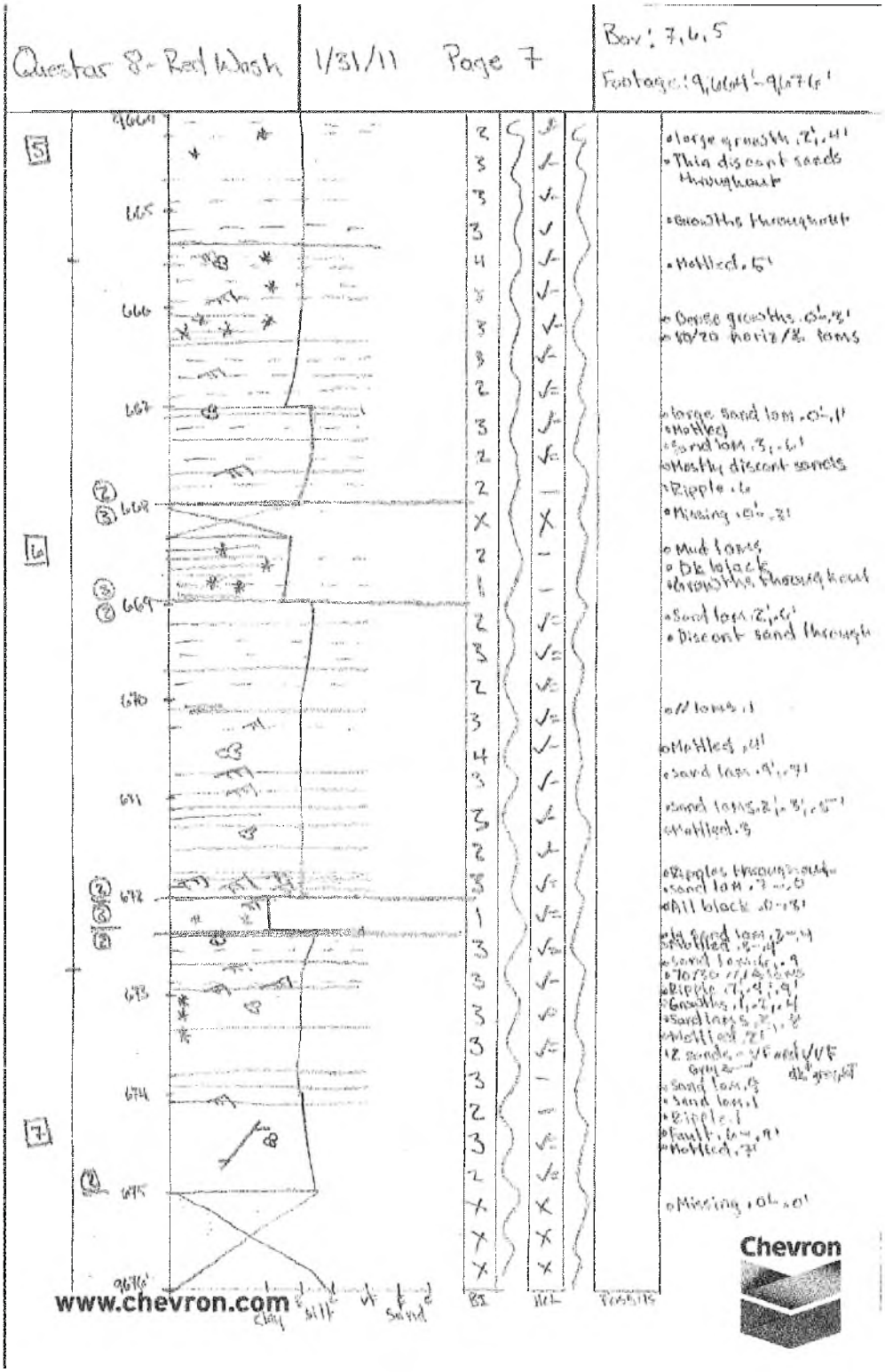

Questar 8 core log – 9,652’ – 9,664’

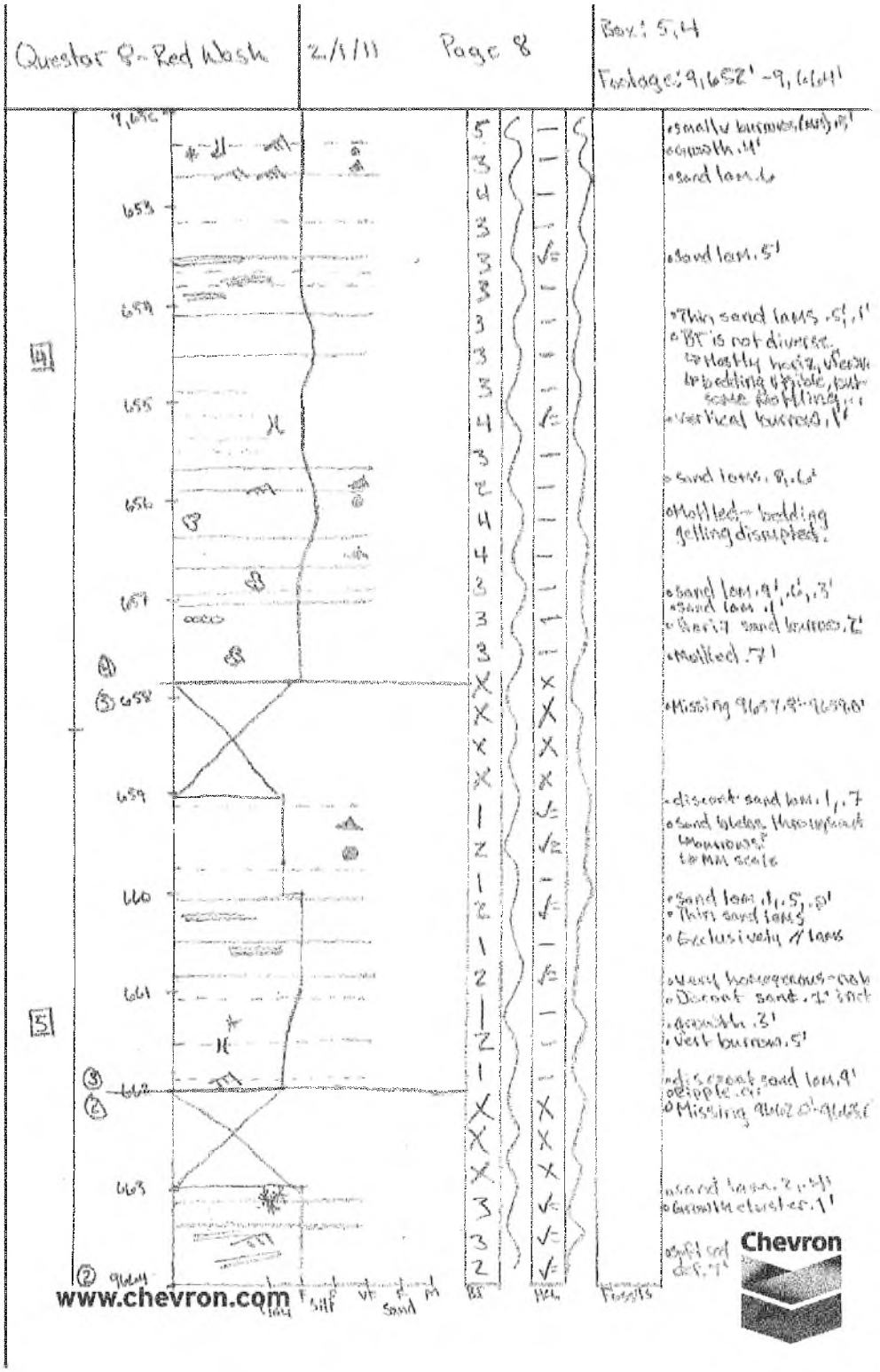

Questar 8 core log – 9,640’ – 9,652’

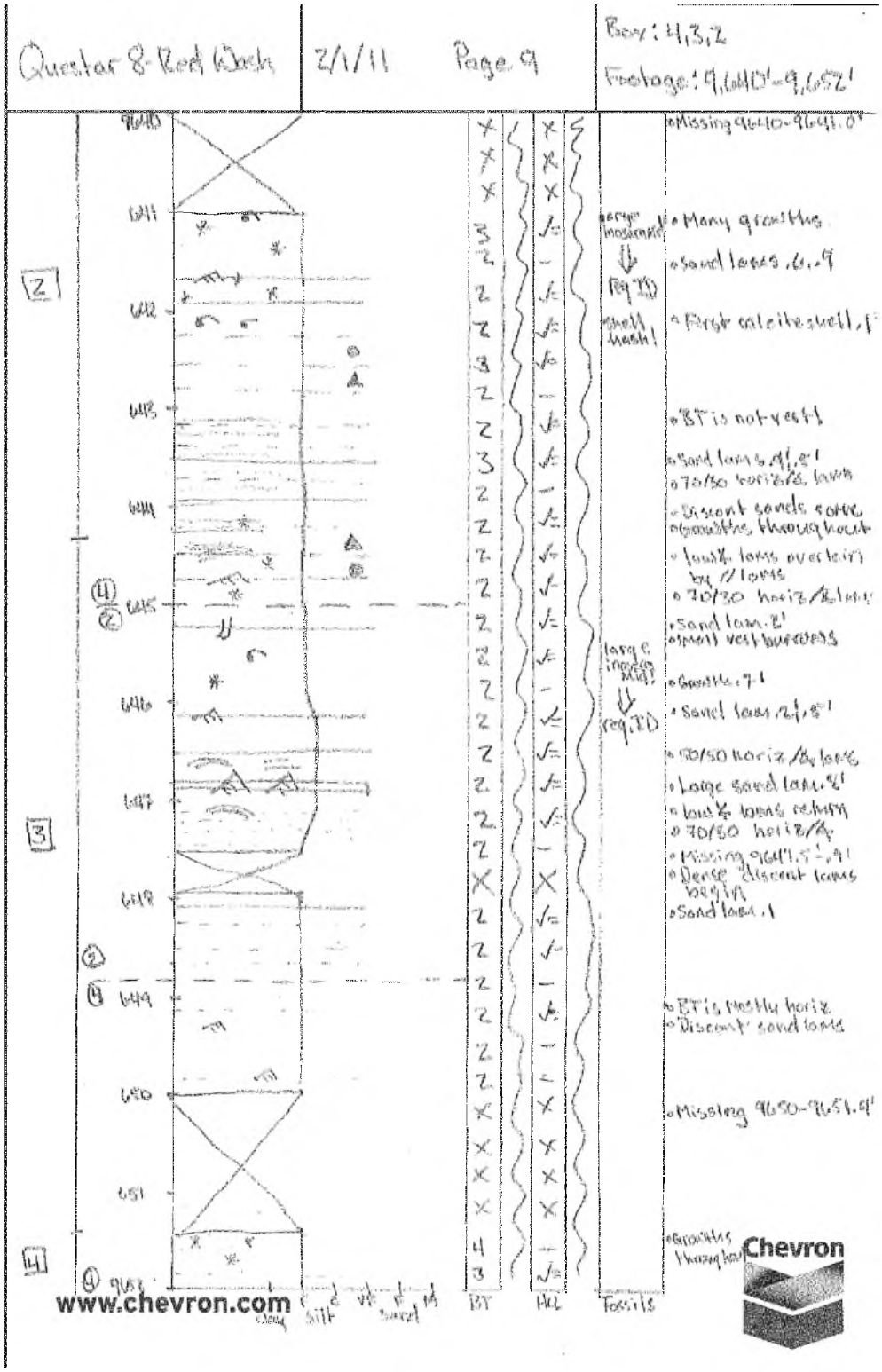

Questar 8 core log – 9,630’ – 9,640’

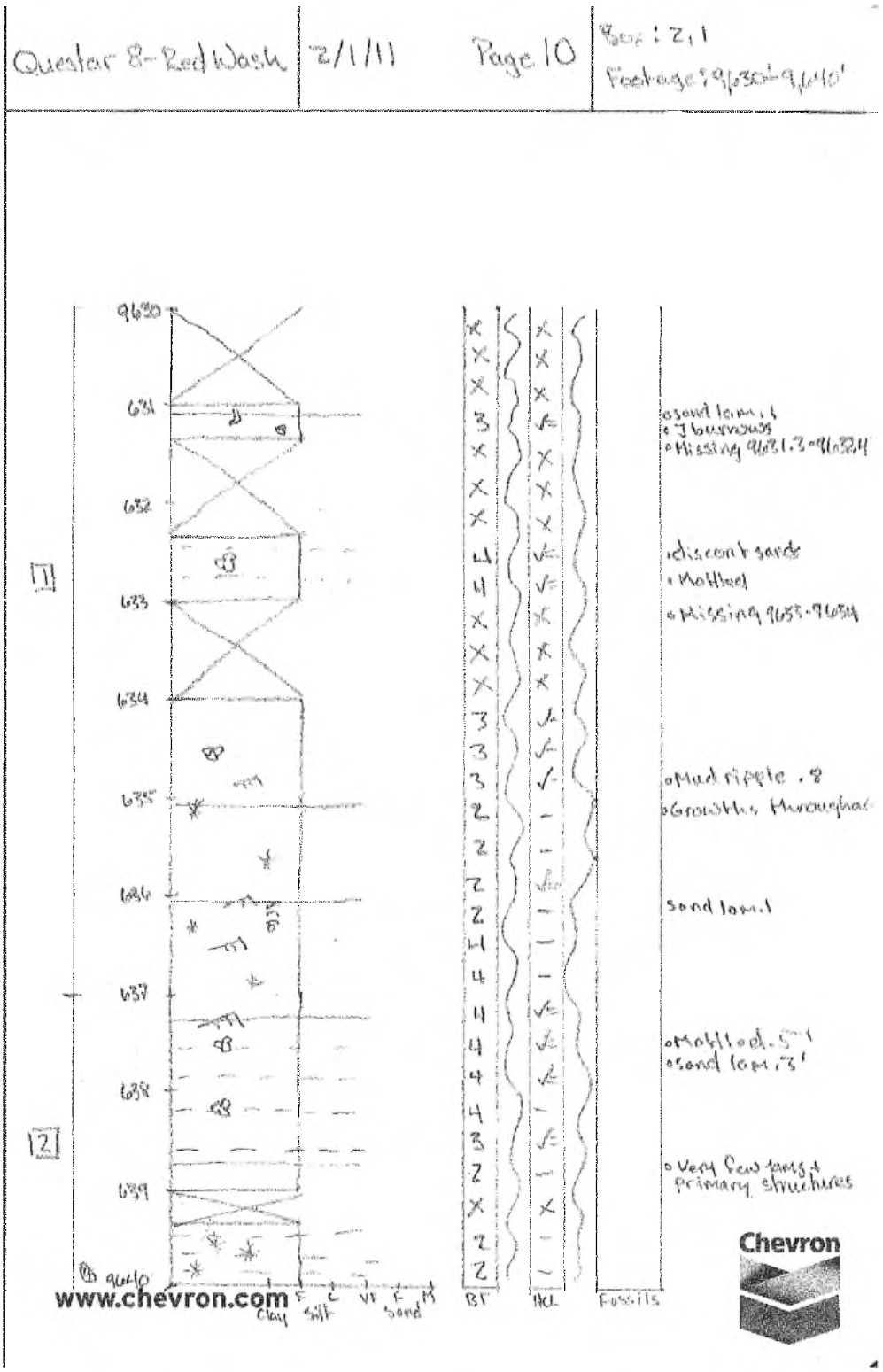

Questar 16 core log – 15,265’ – 15,253’

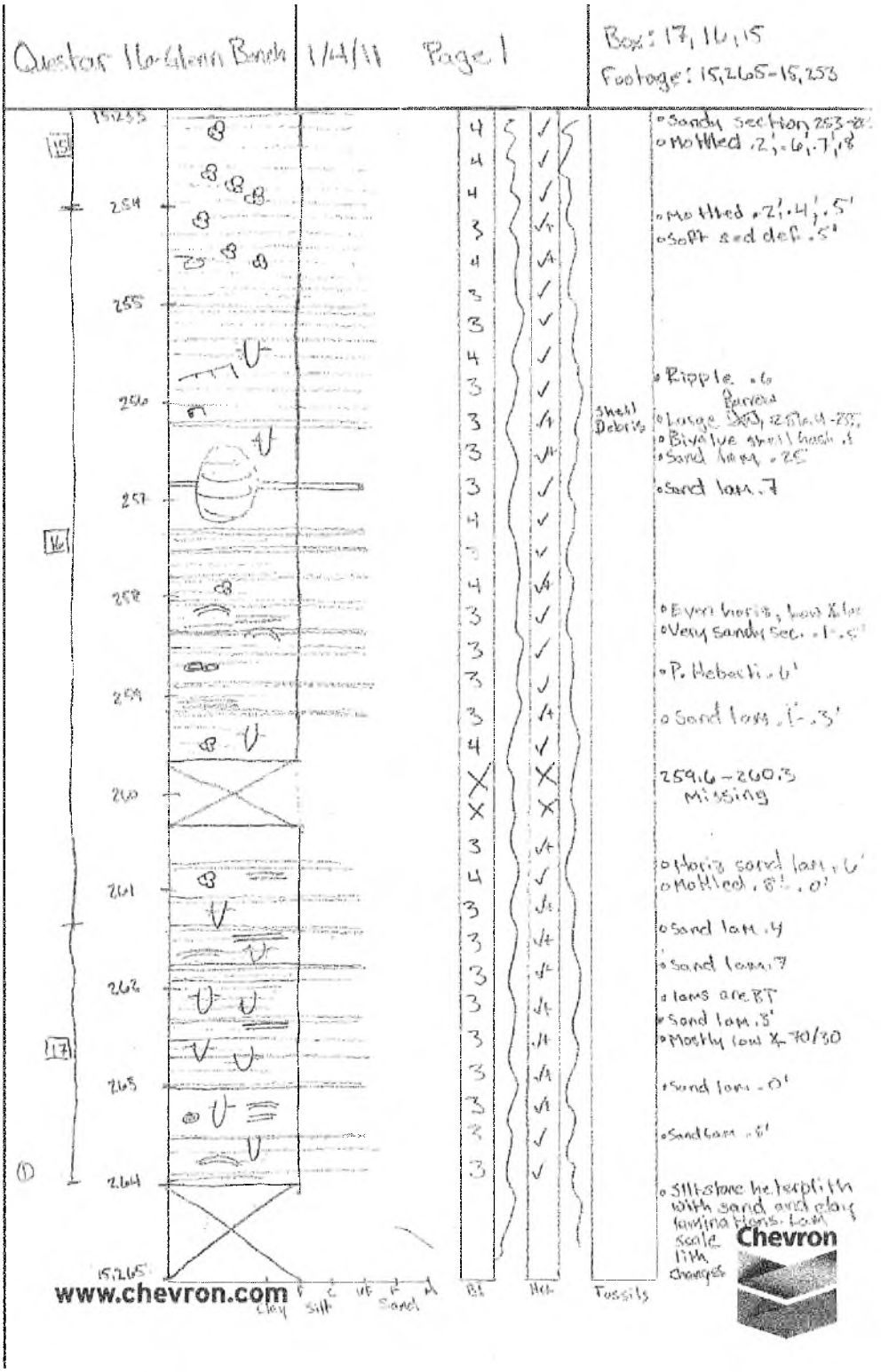

Questar 16 core log – 15,253’ – 15,241’

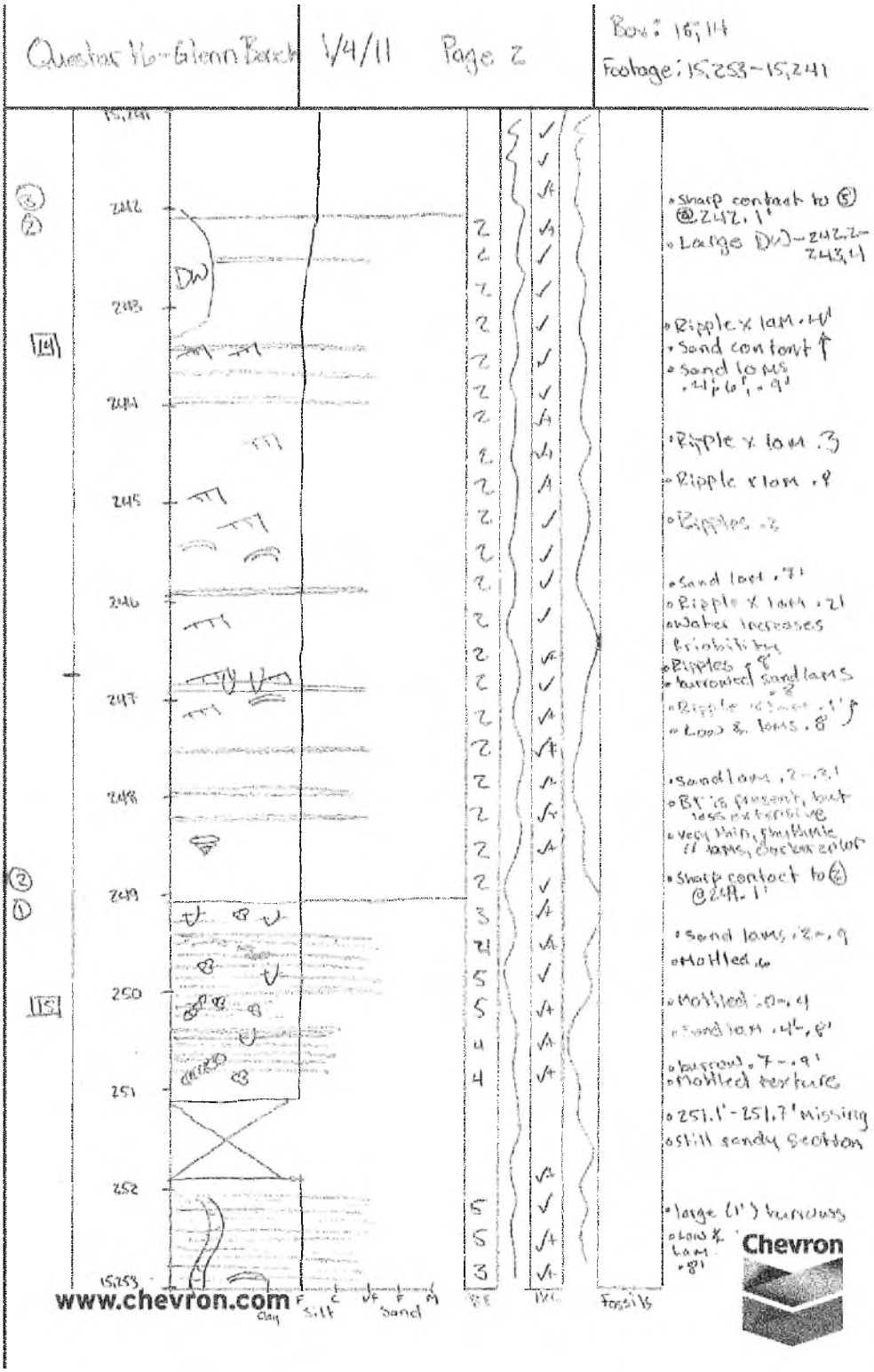

Questar 16 core log – 15,241' – 15,229'

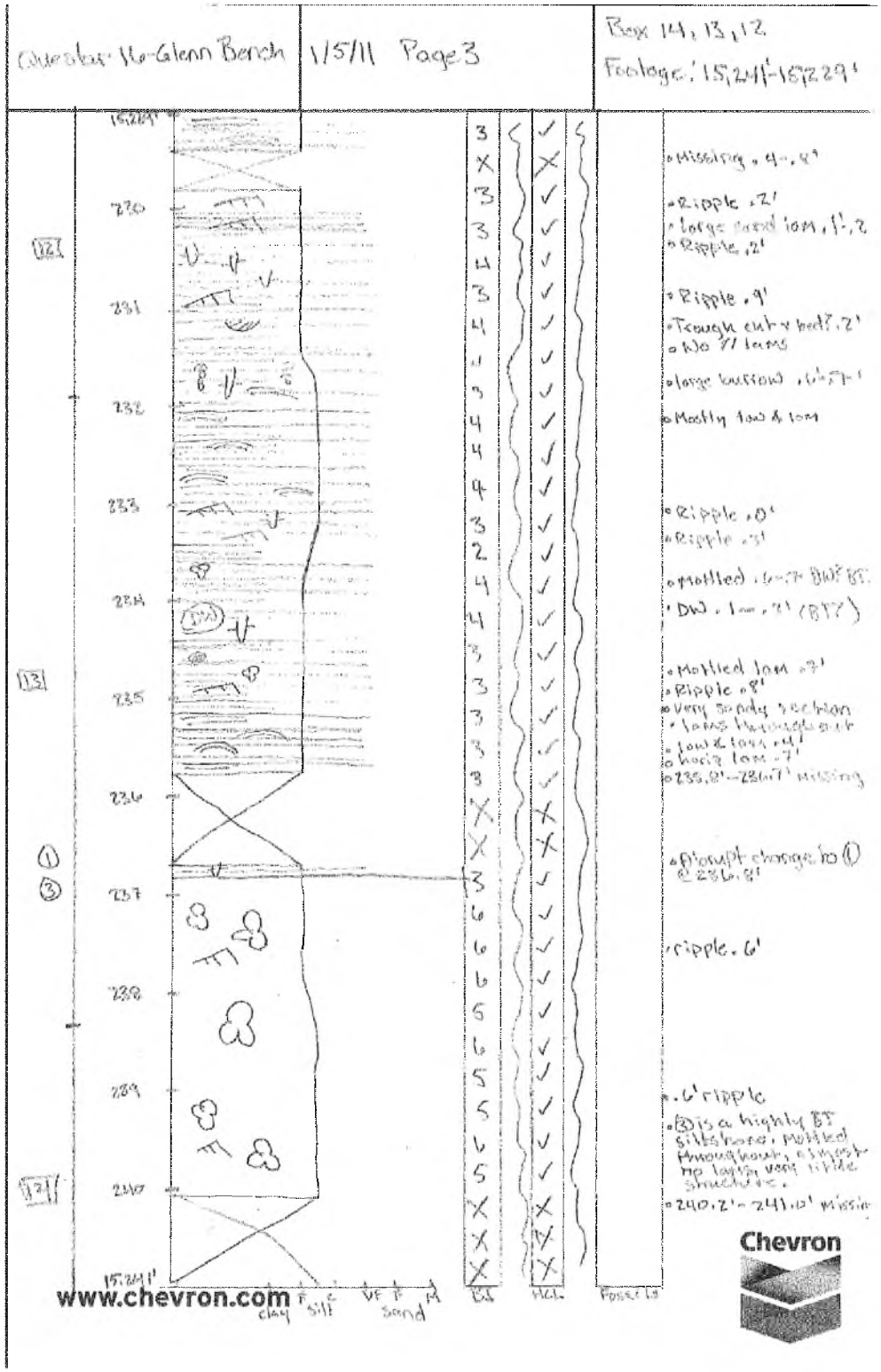

Questar 16 core log – 15,229’ – 15,217’

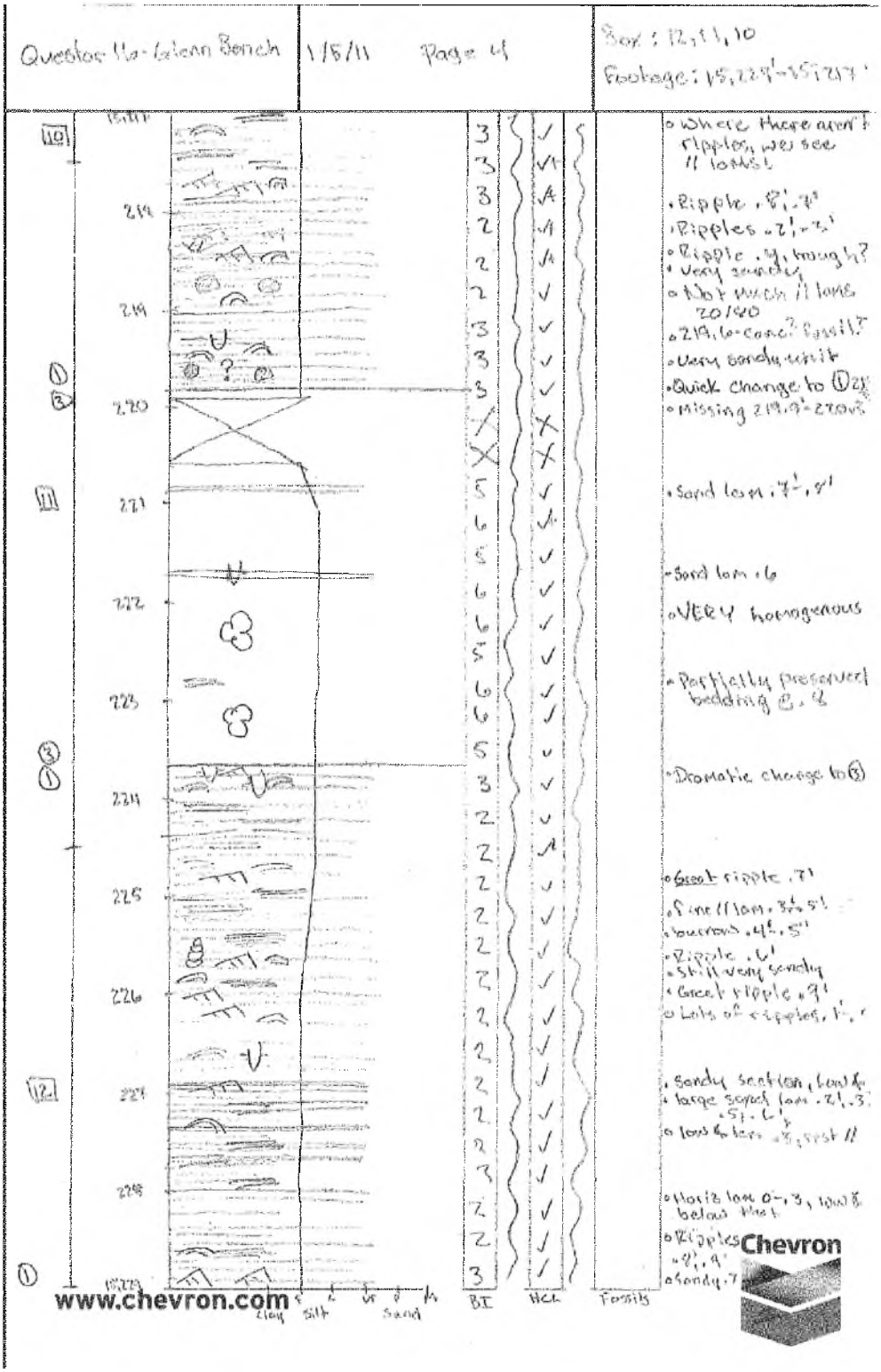

Questar 16 core log – 15,217’ – 15,205’

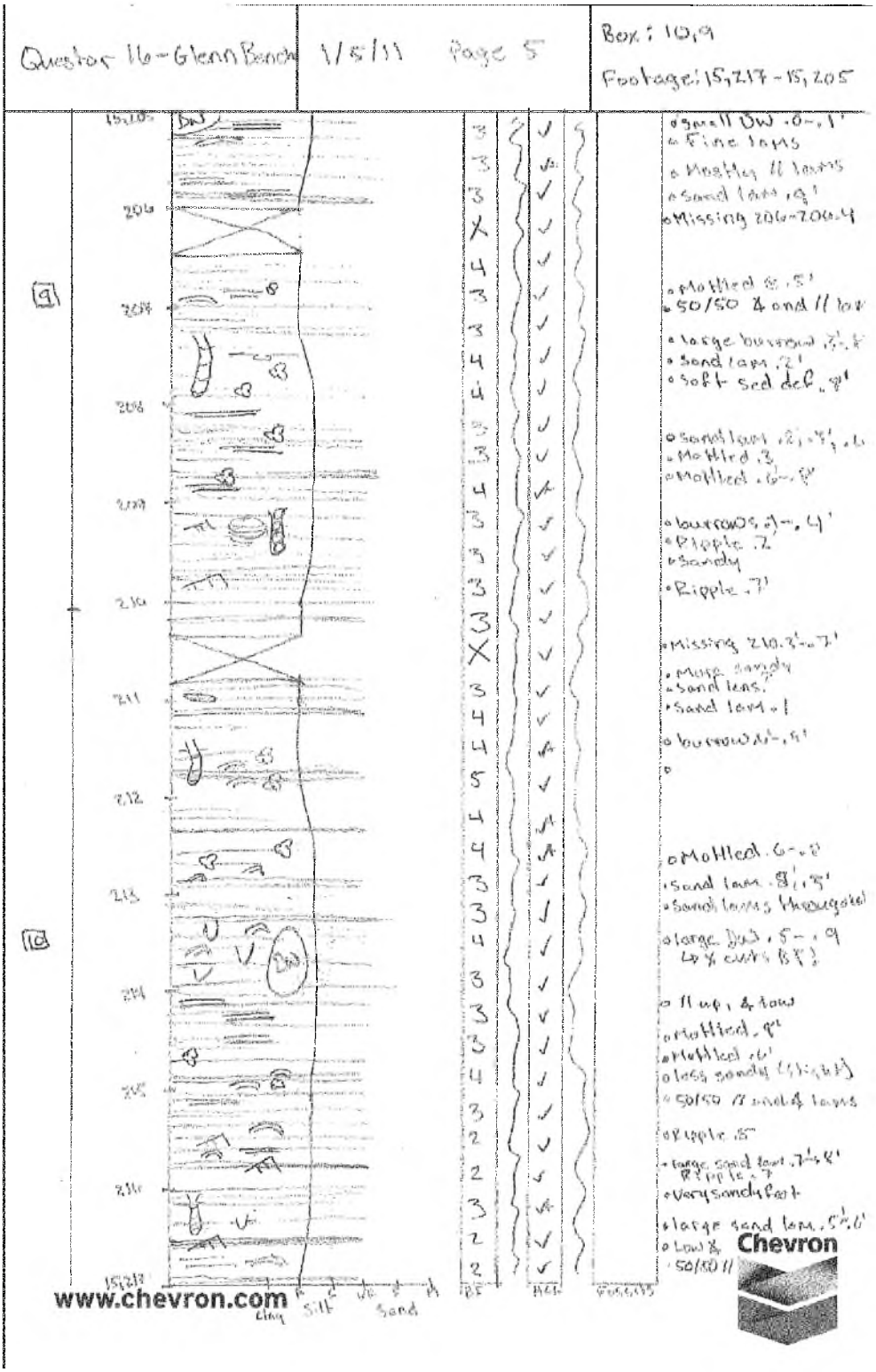

Questar 16 core log – 15,205’ – 15,193’

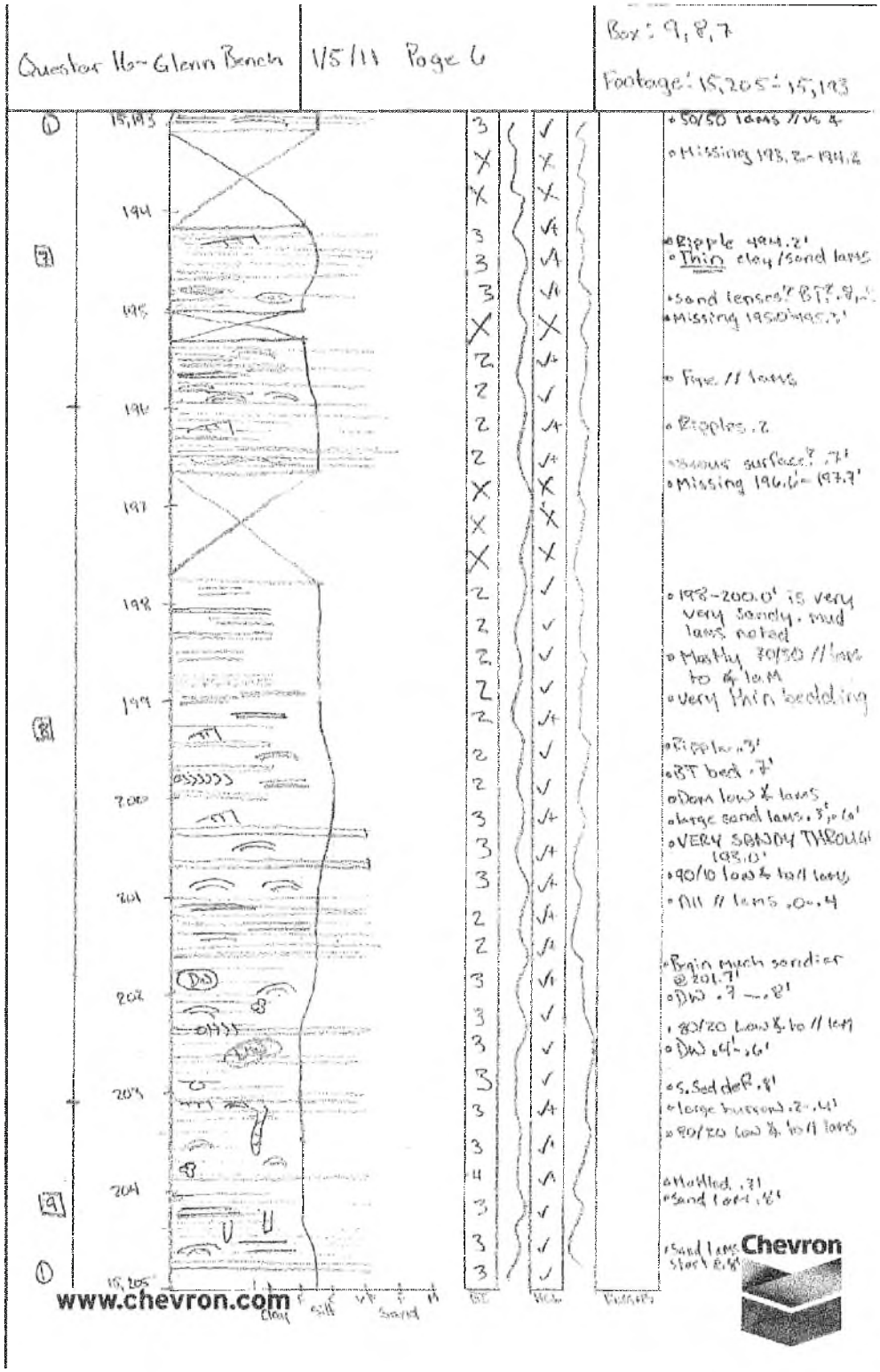

Questar 16 core log – 15,193’ – 15,181’

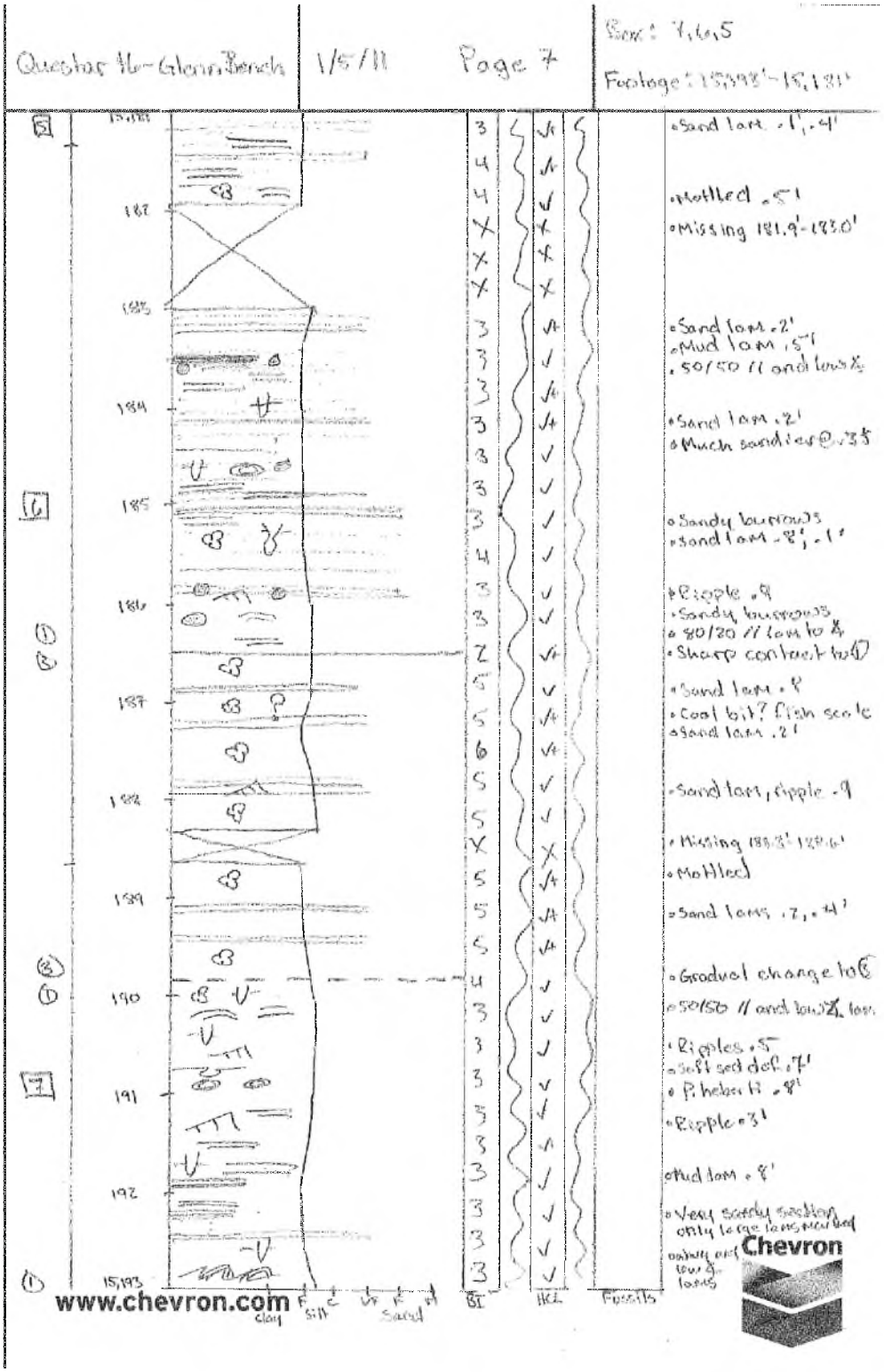

Questar 16 core log – 15,181' – 15,169'

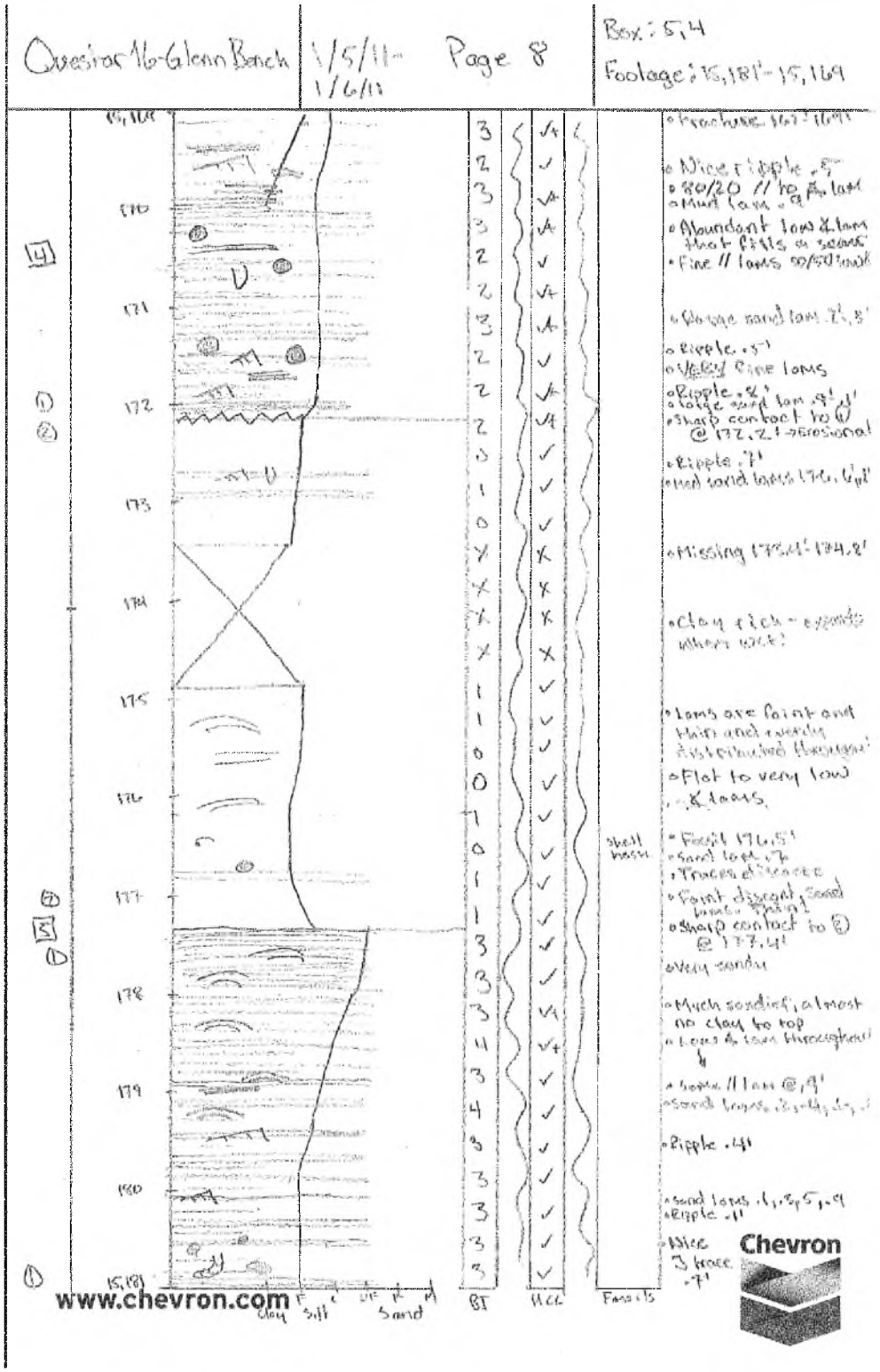

Questar 16 core log – 15,169’ – 15,157’

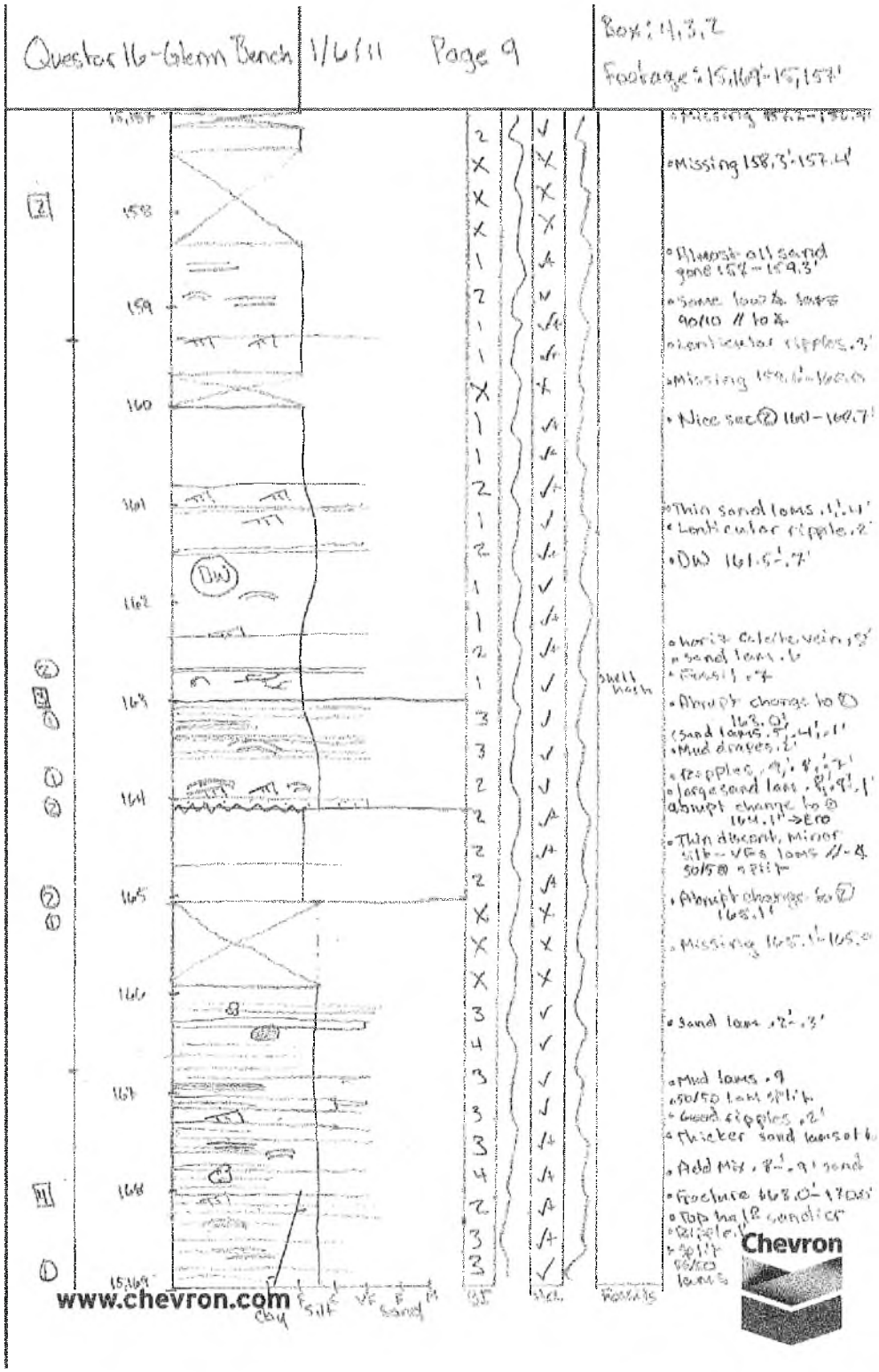

Questar 16 core log – 15,157' – 15,145'

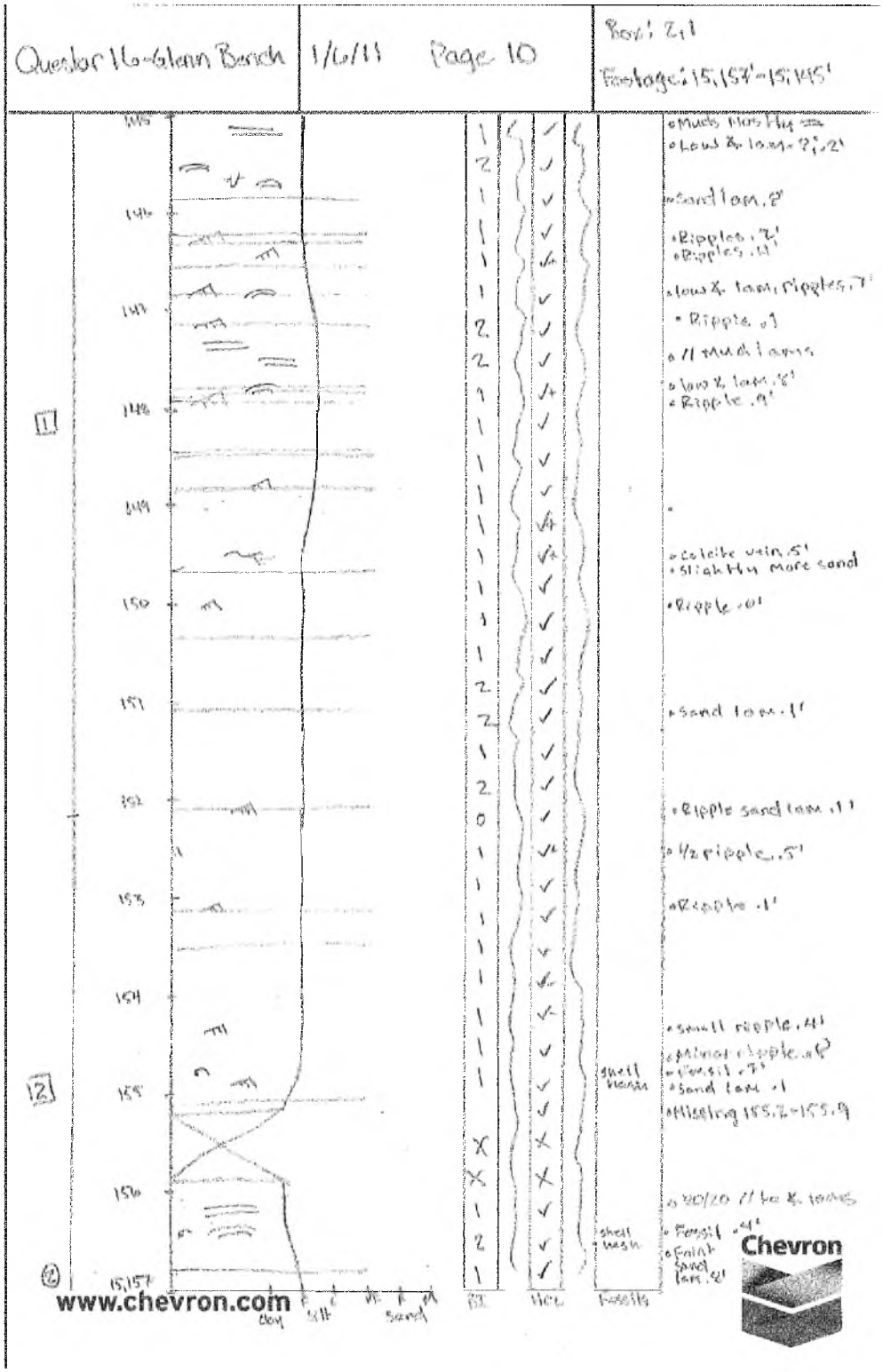

Pioneer 1 core log – 7,597' – 7,577'

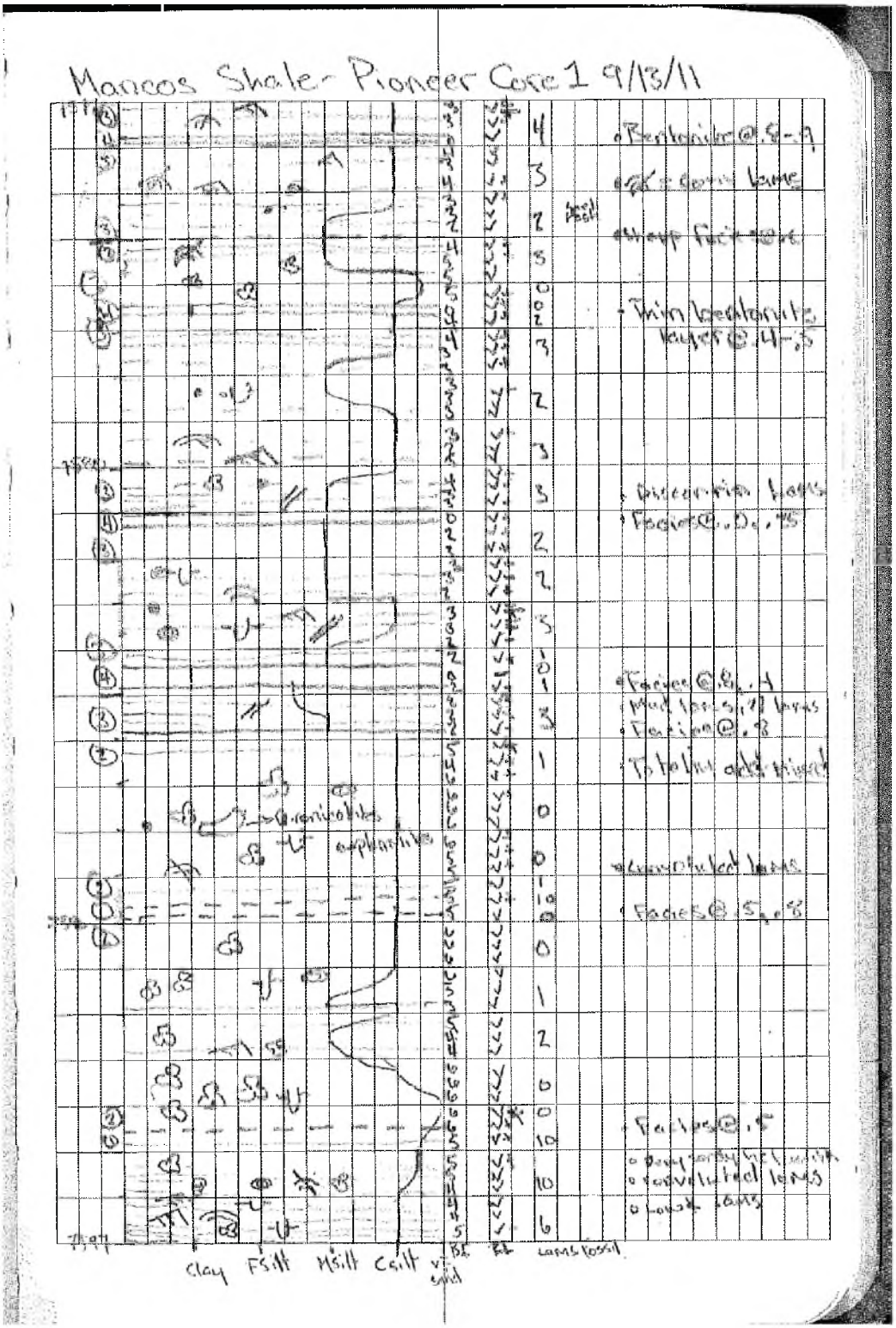

Pioneer 1 core log – 7,572' – 7,547'

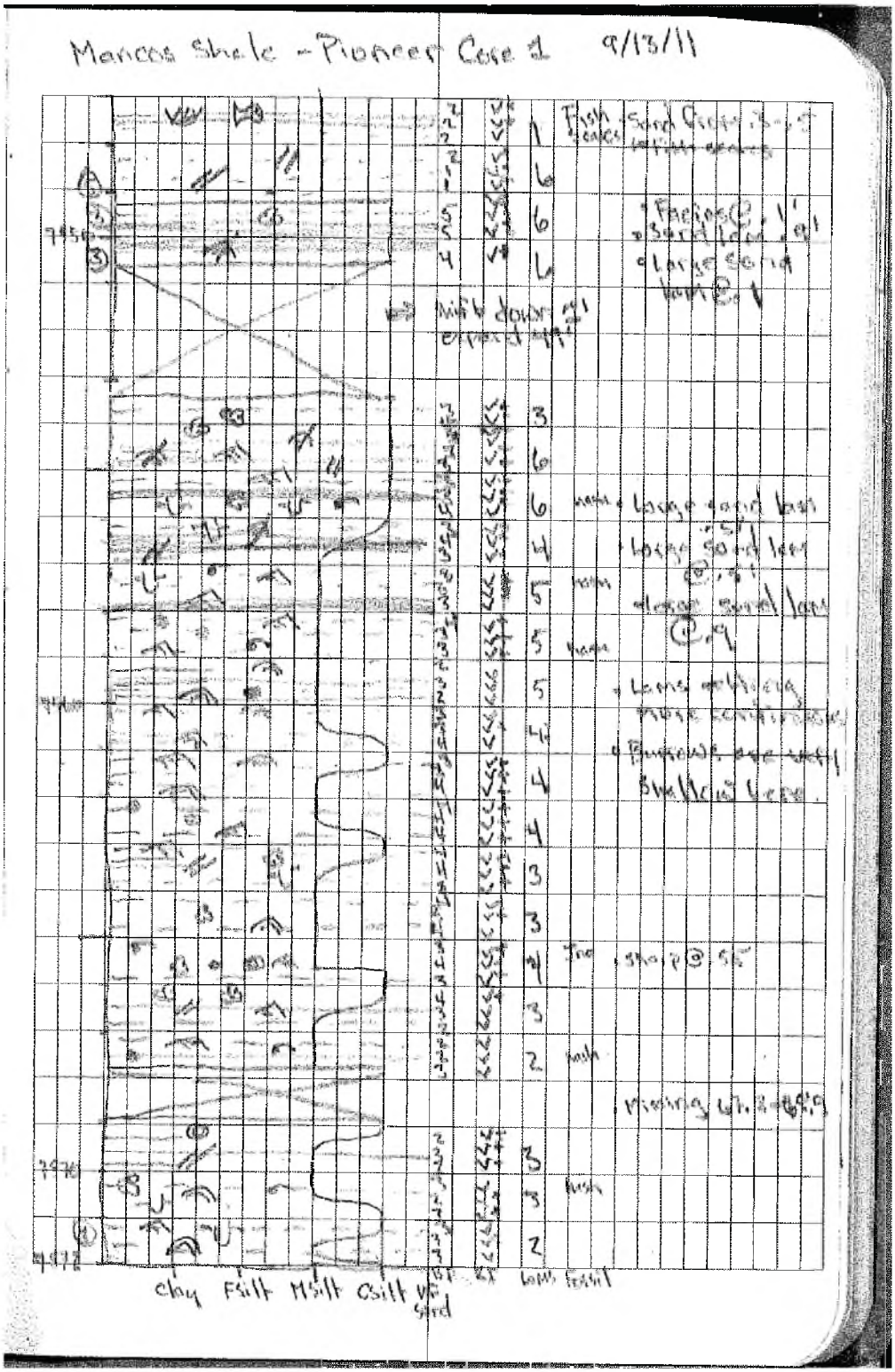

Pioneer 1 core log – 7,547' – 7,522'

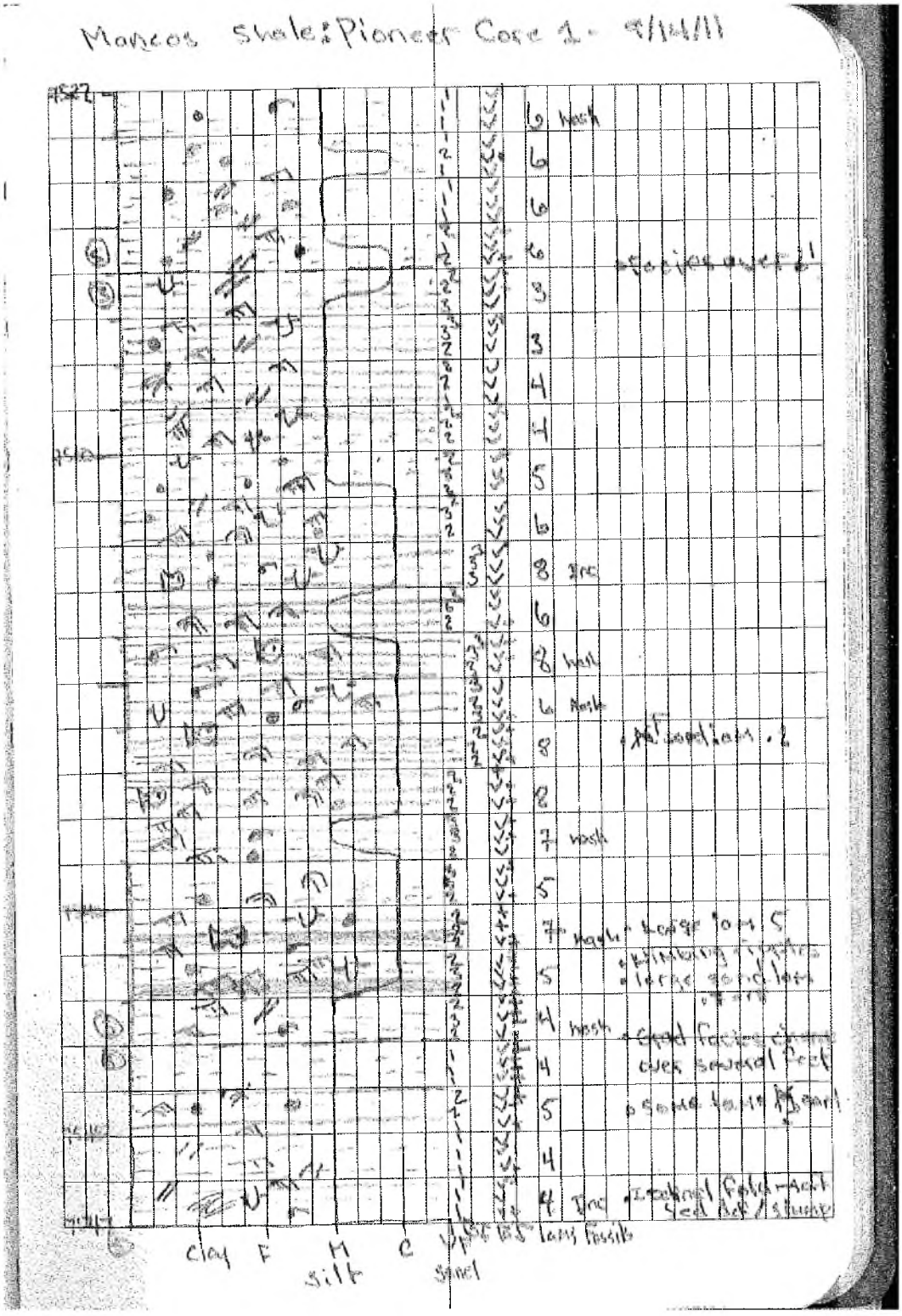

Pioneer 1 core log – 7,522' – 7,497'

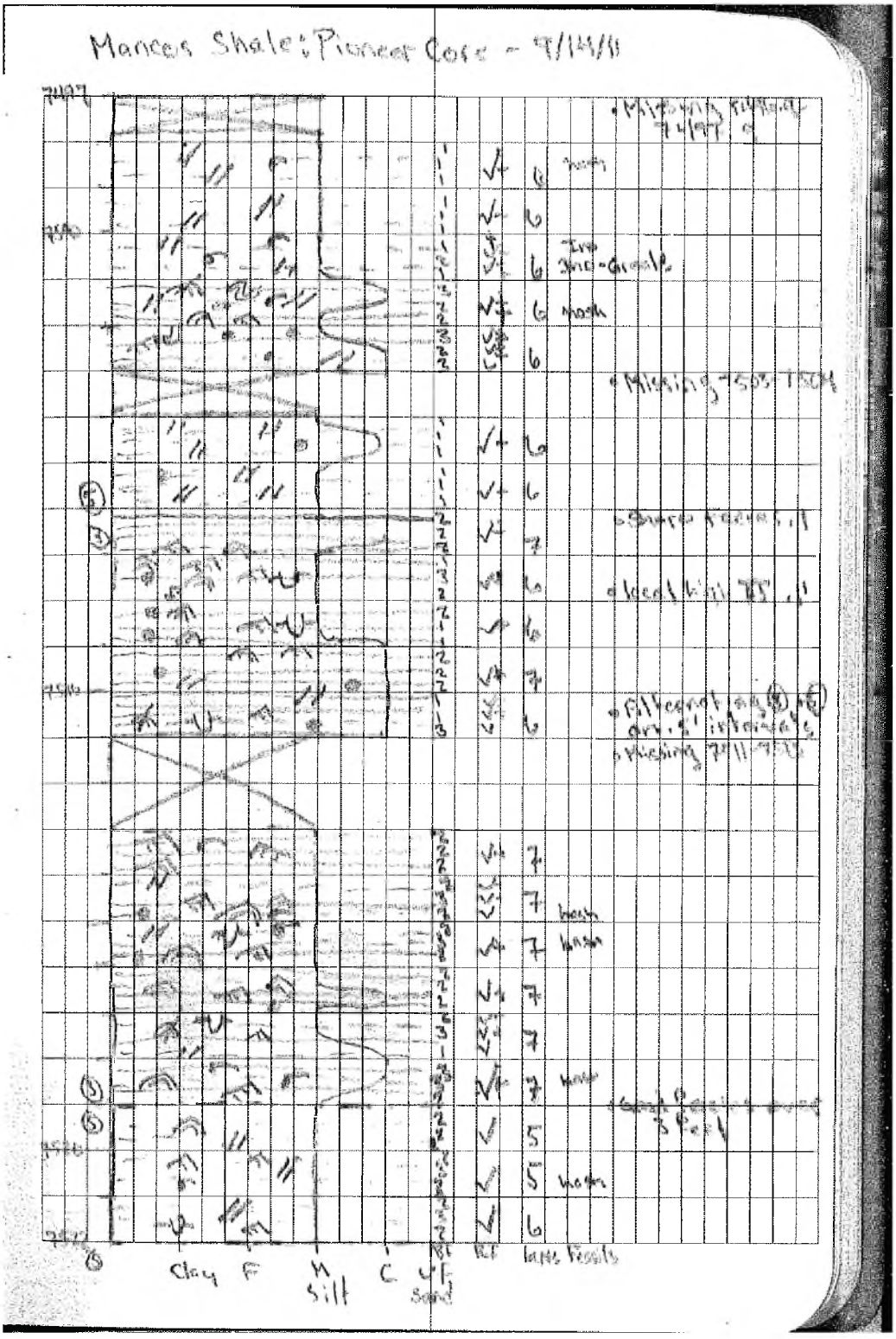

Pioneer 1 core log – 7,497’ – 7,480’

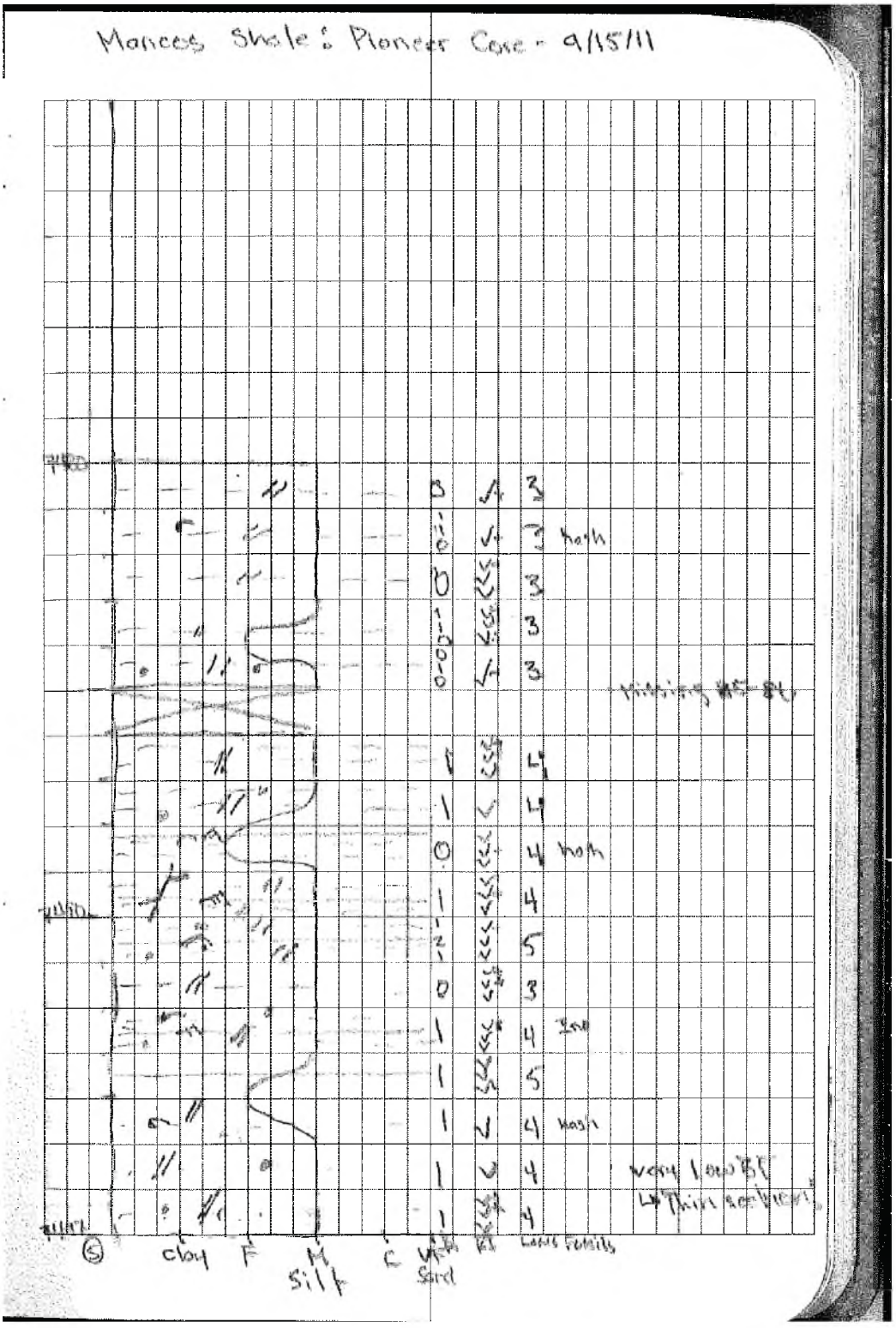

Pioneer 2 core log – 7,135' – 7,110'

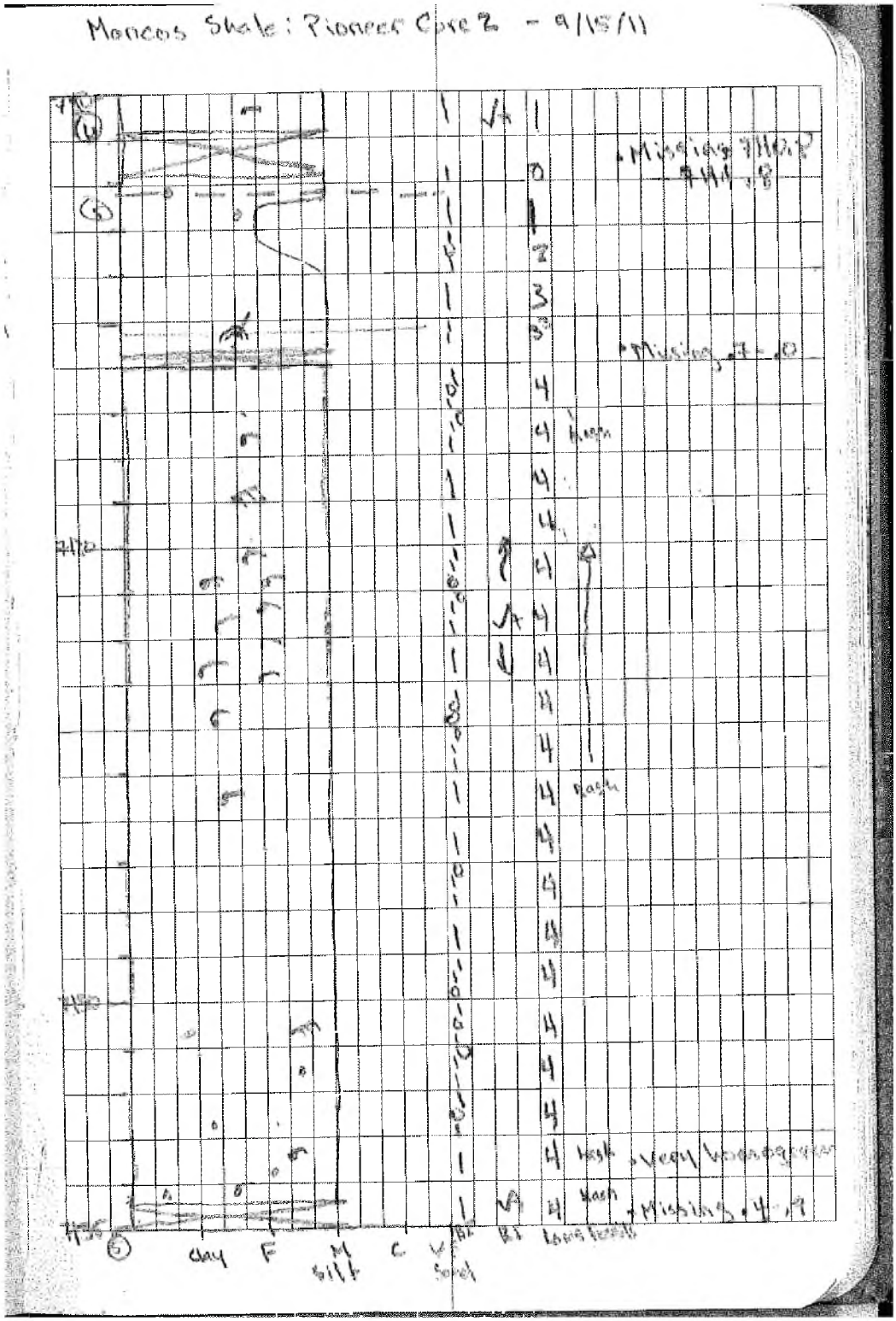

Pioneer 2 core log 7,110' – 7,085'

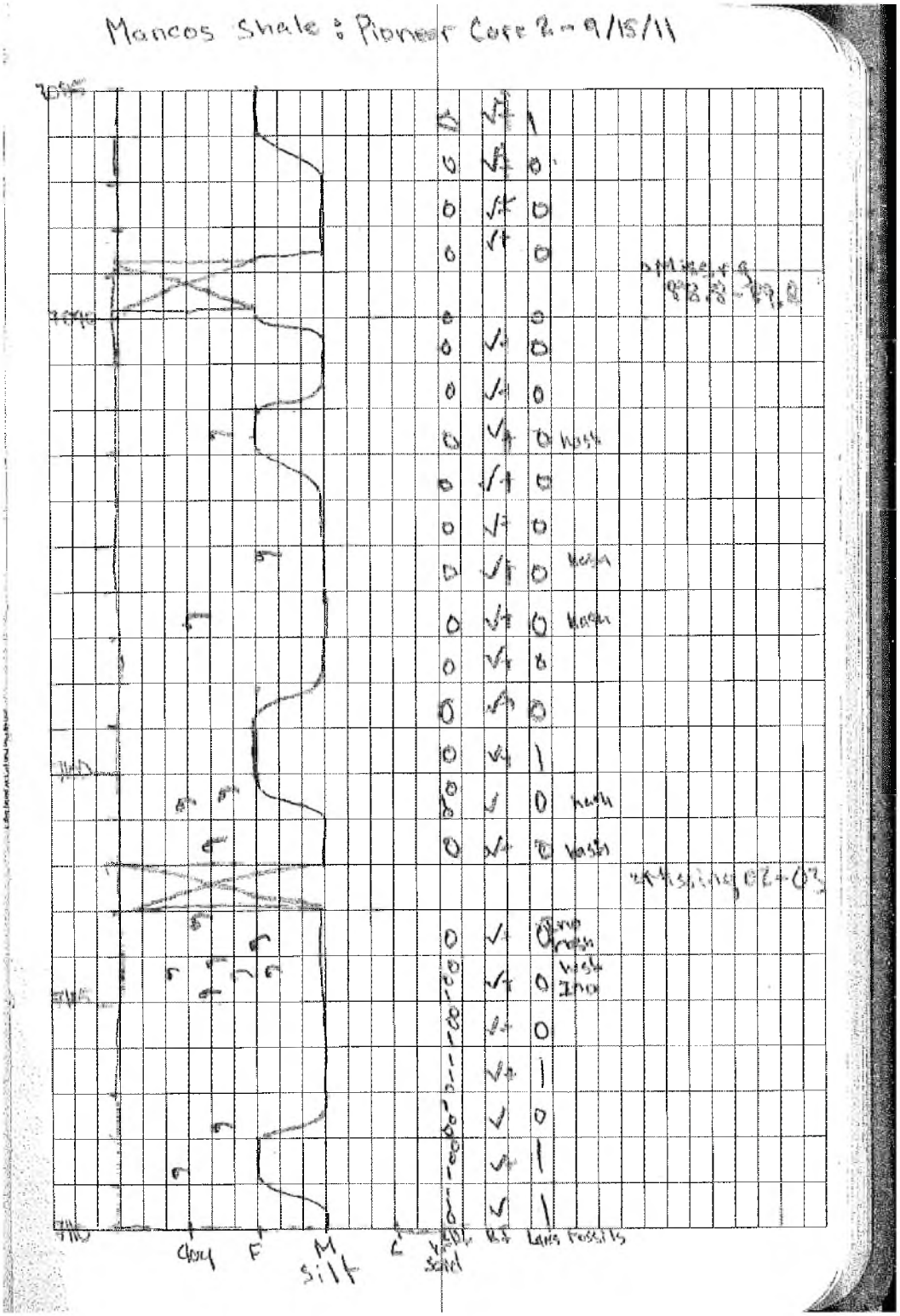

Pioneer 2 core log – 7,085' – 7,060'

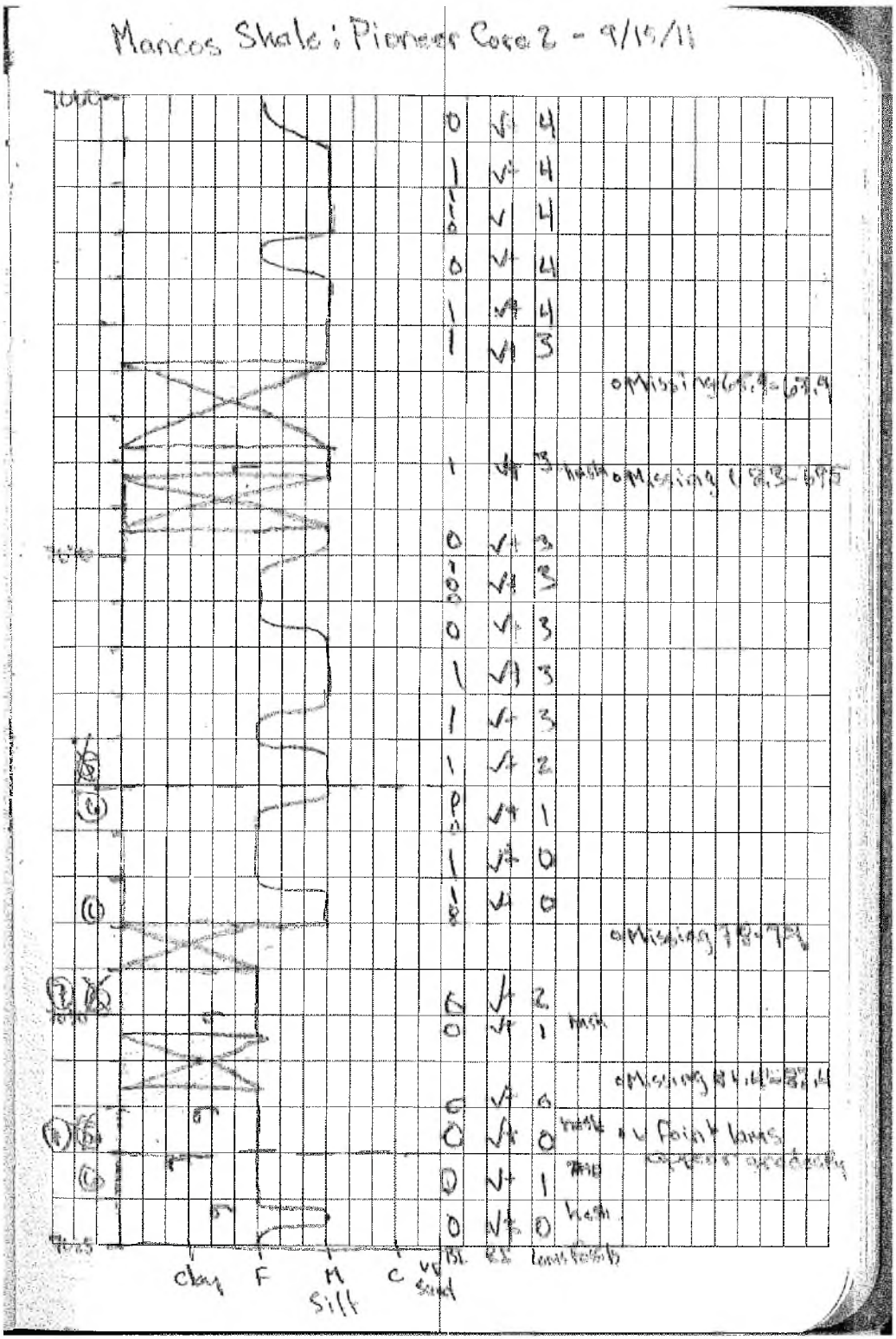

Pioneer 2 core log – 7,060' – 7,035'

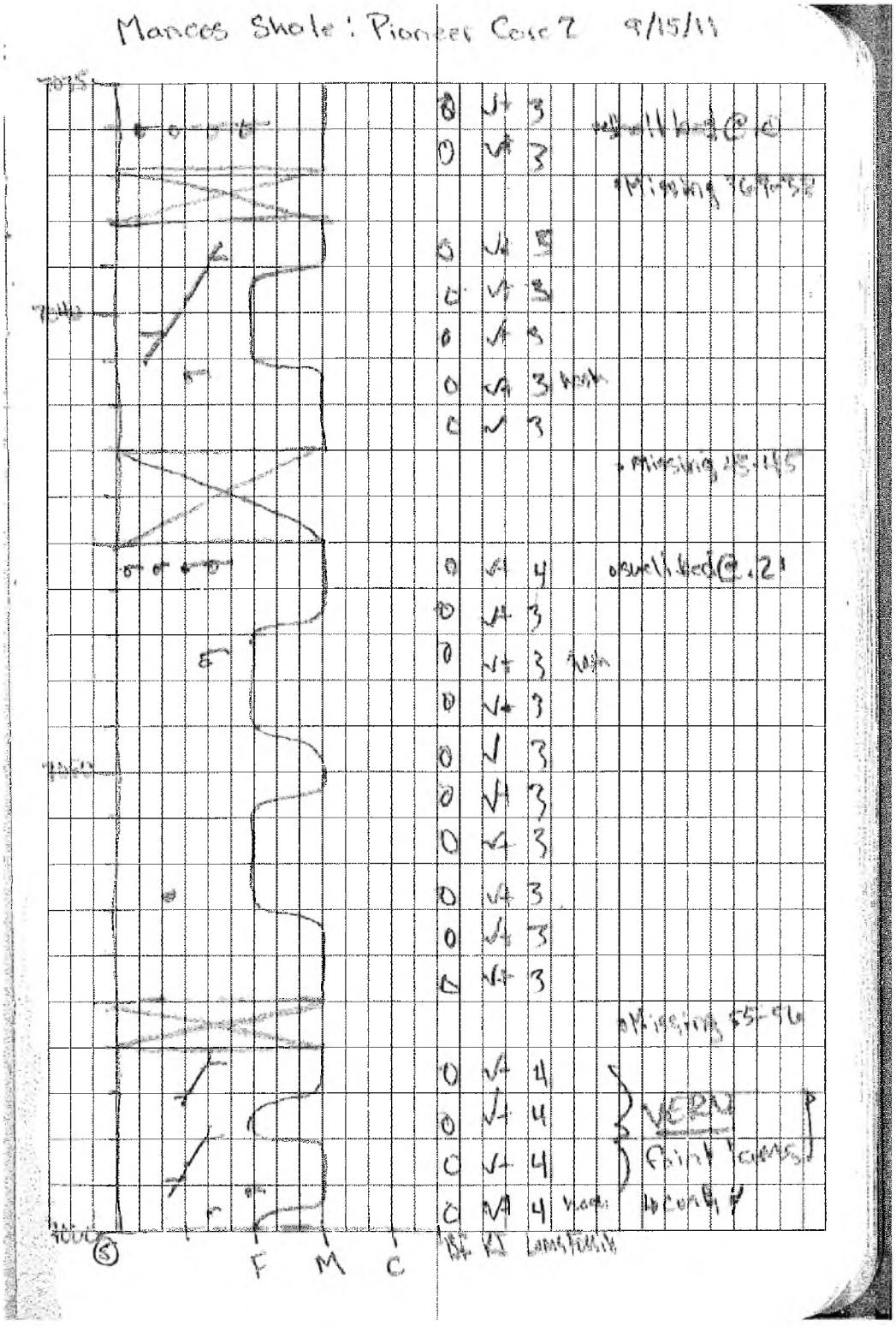

Pioneer 2 core log – 7,035' – 7,010'

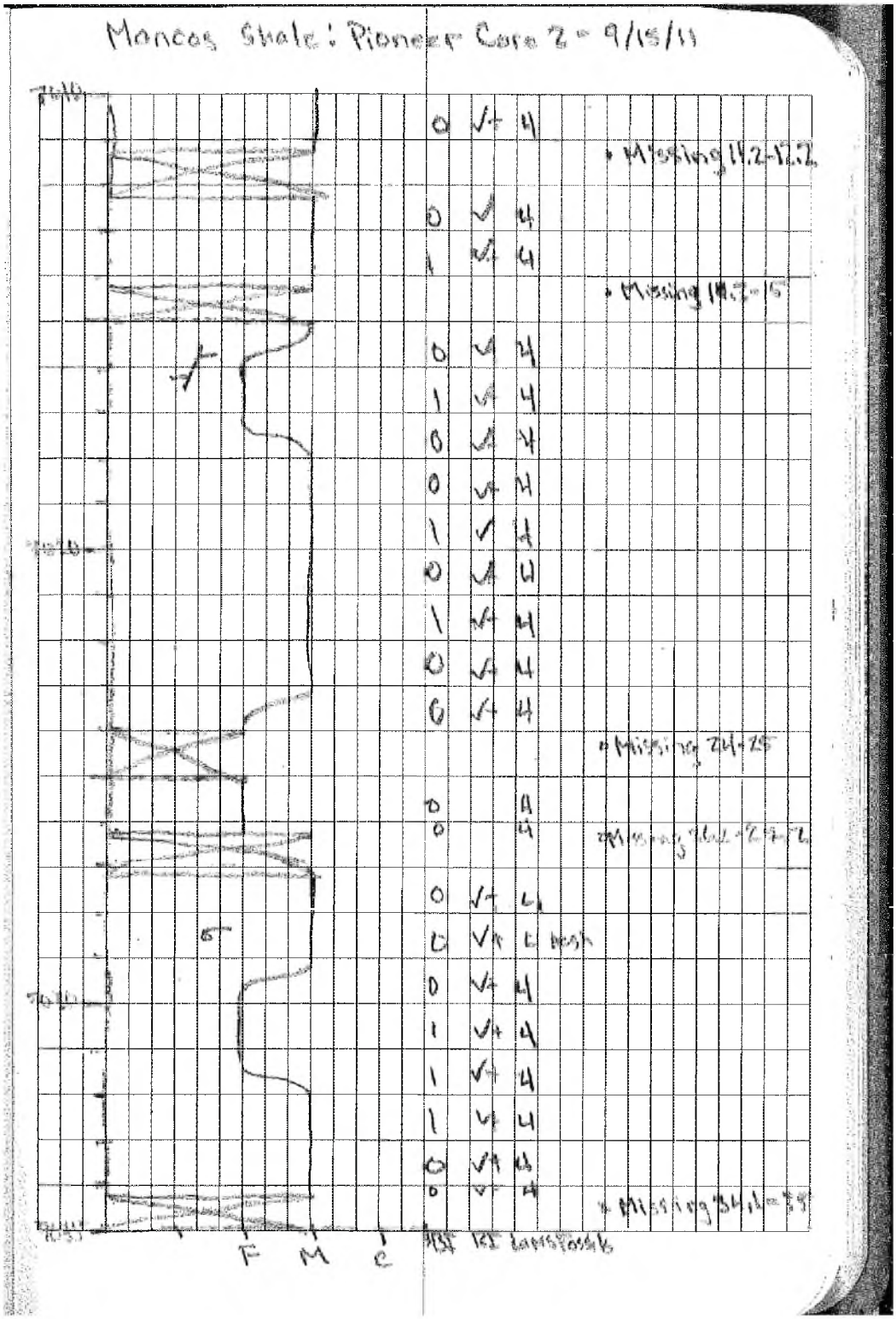

Pioneer 2 core log – 7,010' – 6,995'

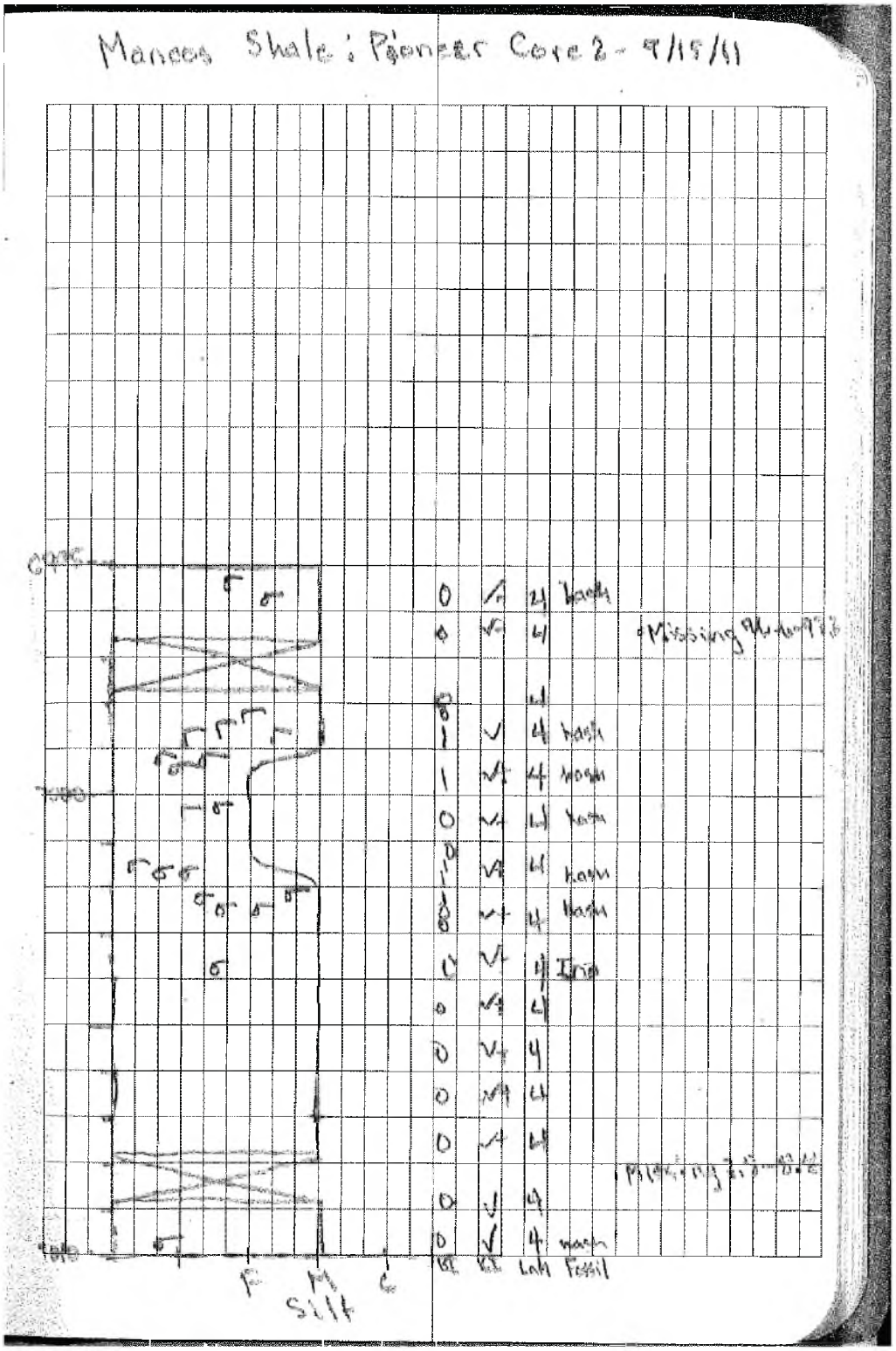

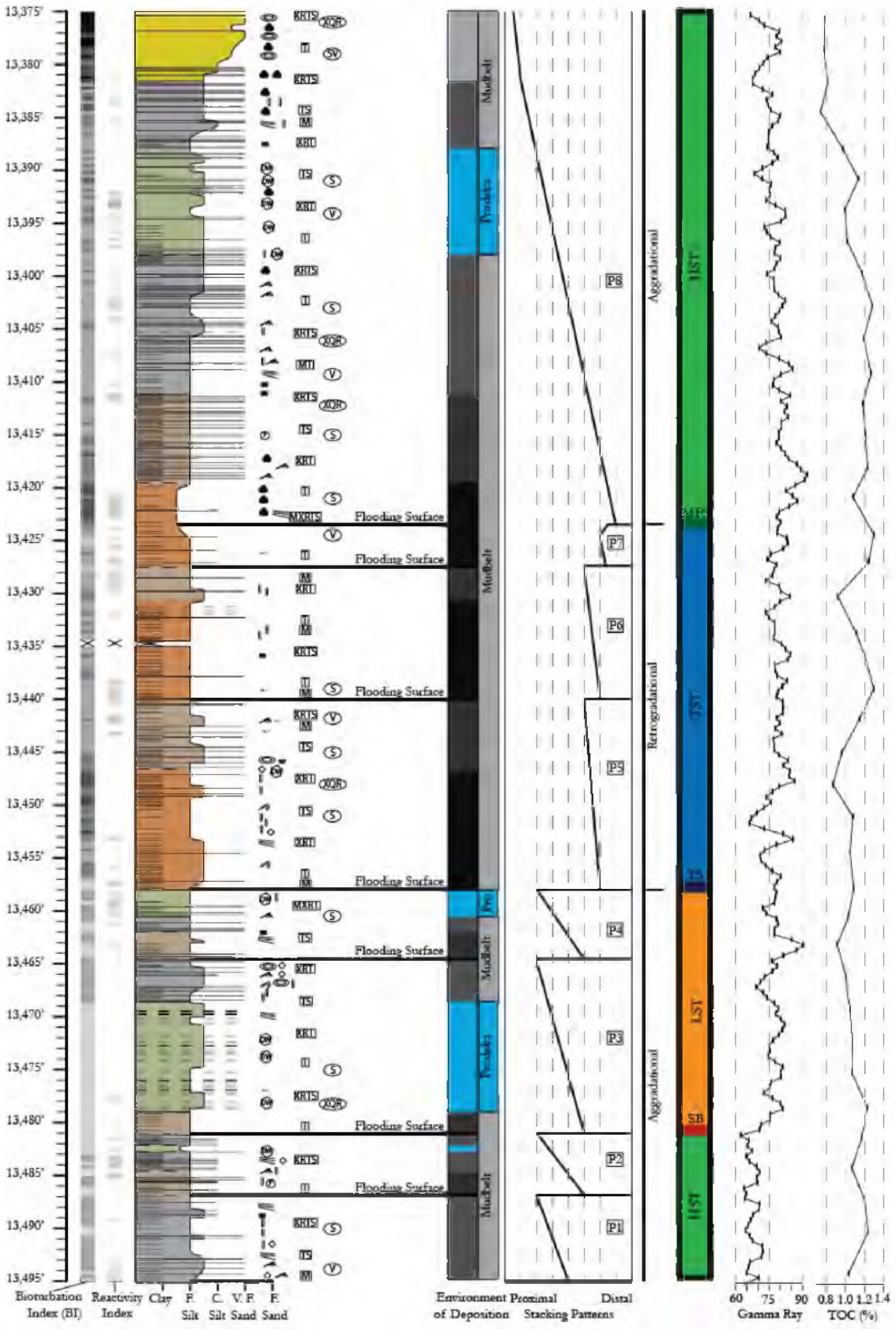

Core Log of Questar 1

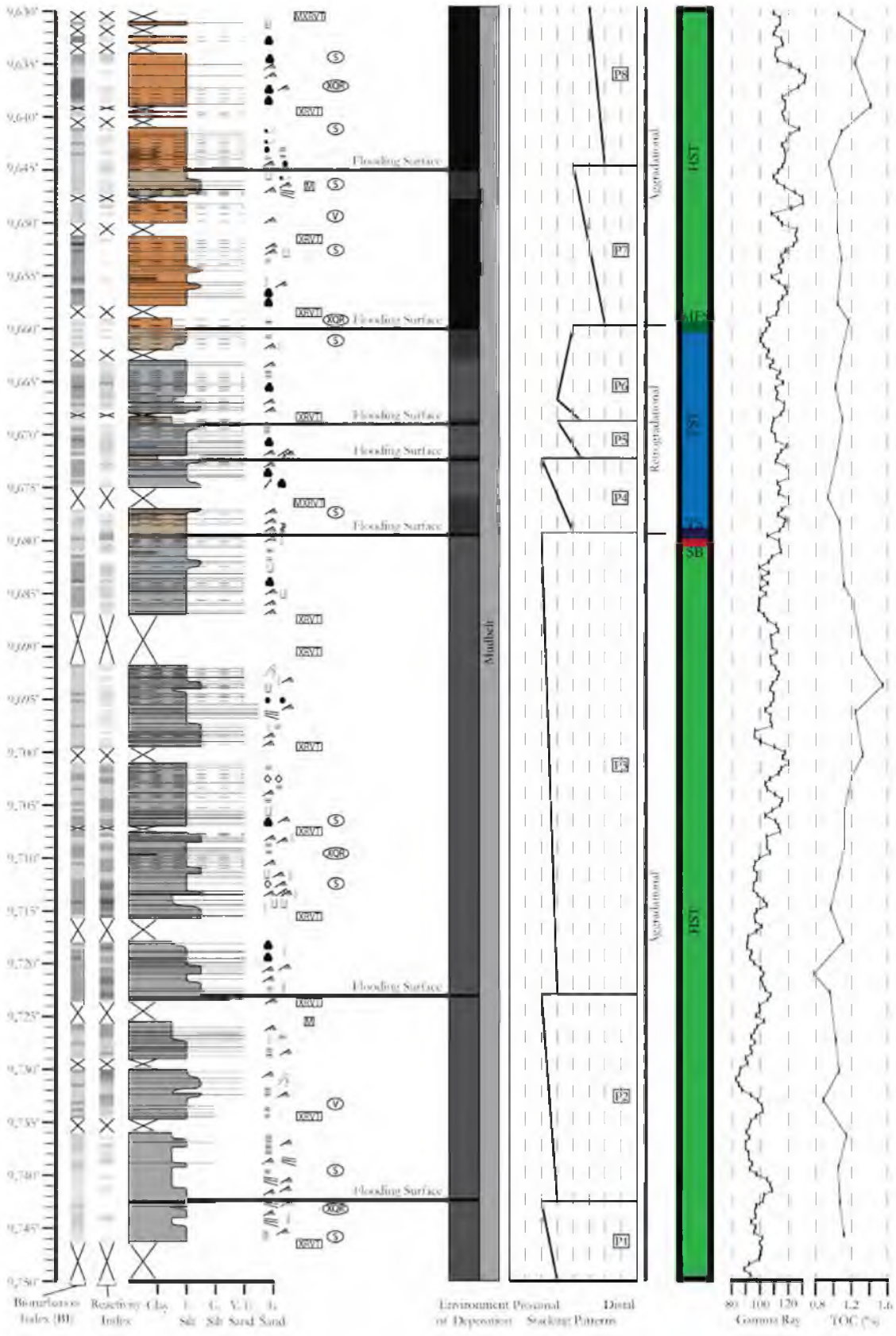

Core Log of Questar 8

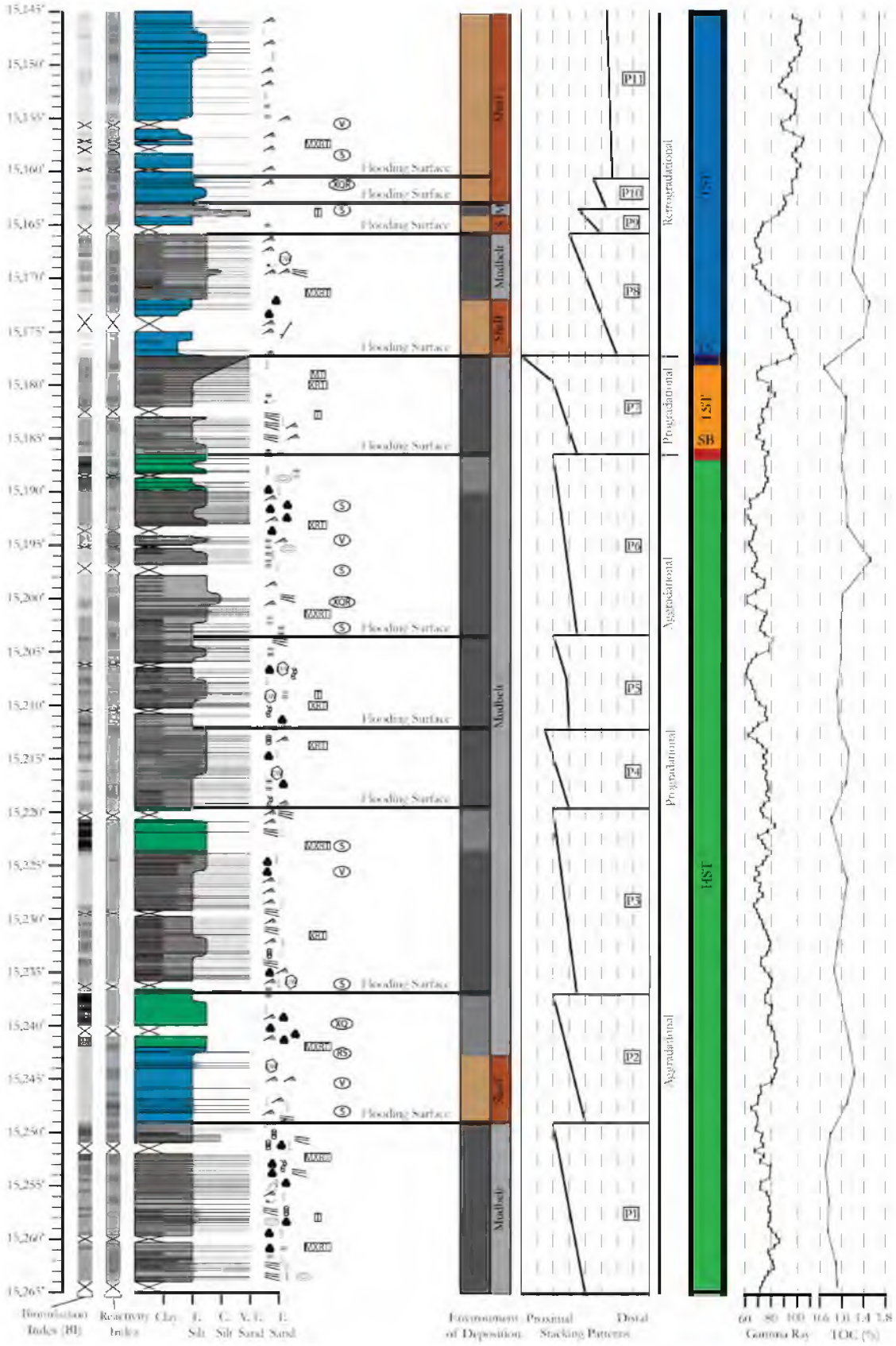

Core Log of Questar 16

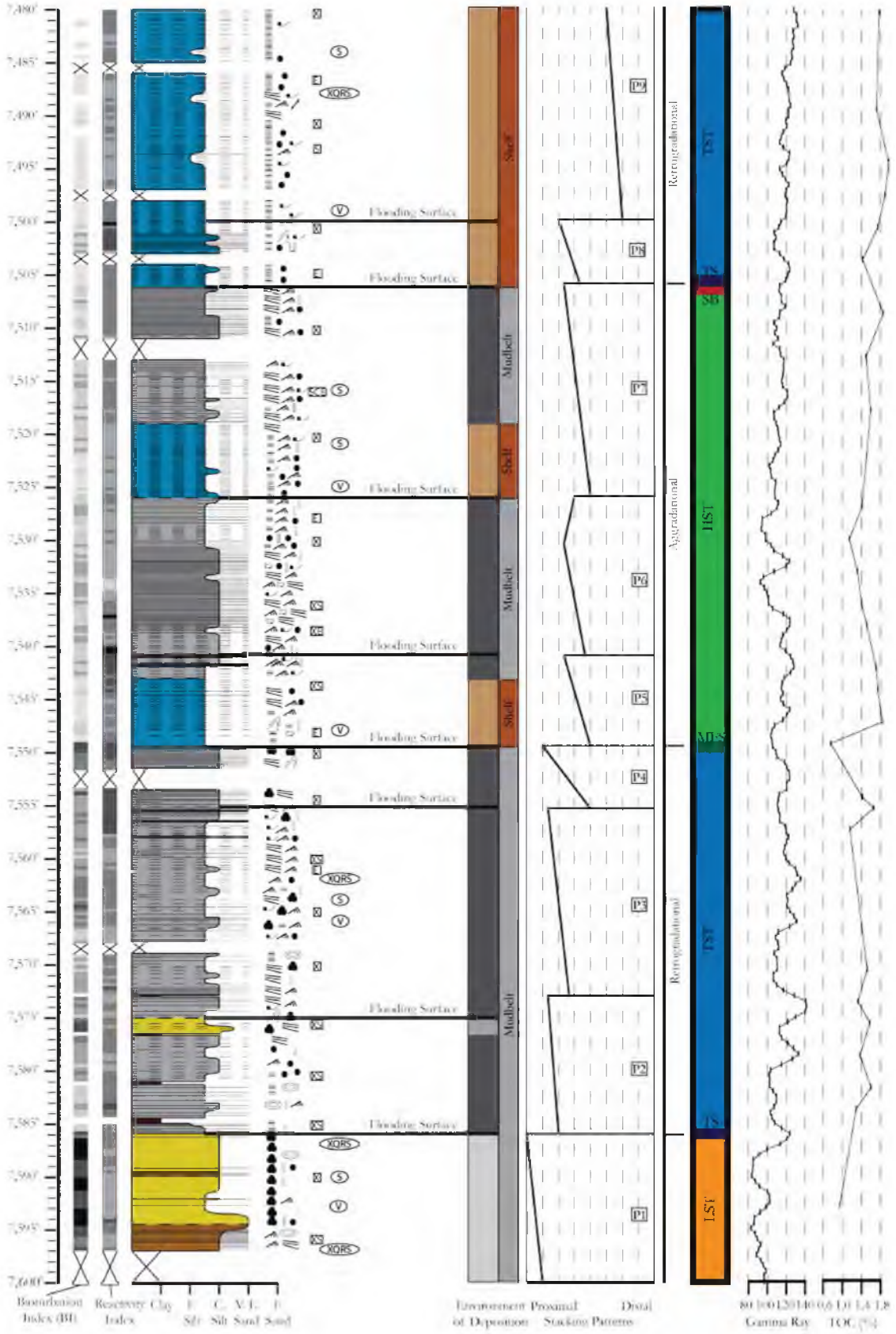

Core Log of Pioneer 1

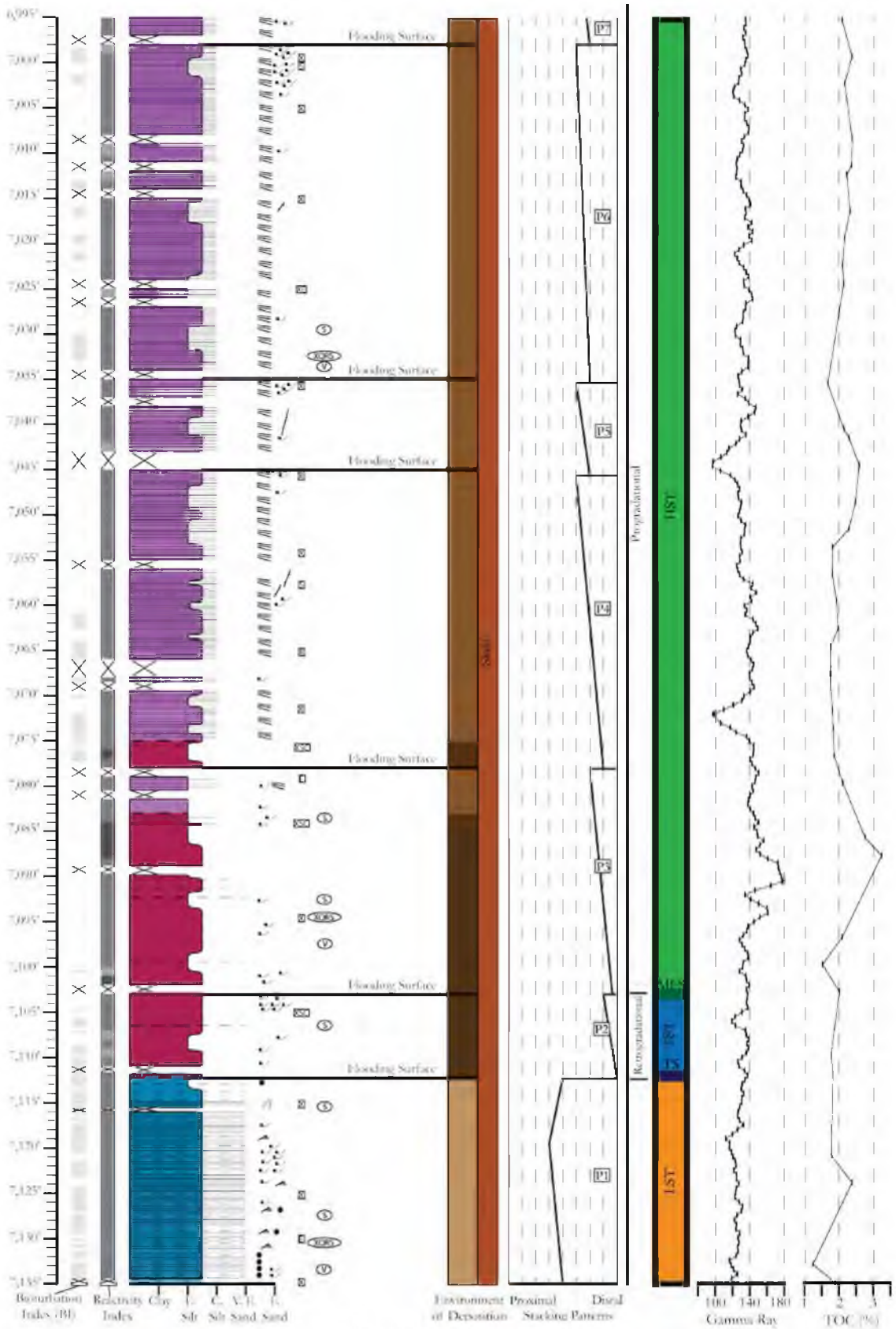

Core Log of Pioneer 2